Ε Θ Ν Ι Κ Ο Μ Ε Τ Σ Ο Β Ι Ο Π Ο Λ Υ Τ Ε Χ Ν Ε Ι Ο

ΣΧΟΛΗ ΠΟΛΙΤΙΚΩΝ ΜΗΧΑΝΙΚΩΝ

ΤΟΜΕΑΣ ΓΕΩΤΕΧΝΙΚΗΣ

Δ Ι Δ Α Κ Τ Ο Ρ Ι Κ Η Δ Ι Α Τ Ρ Ι Β Η

ΣΥΜΒΟΛΗ ΣΤΗΝ ΣΤΑΤΙΚΗ ΚΑΙ ΔΥΝΑΜΙΚΗ ΕΓΚΑΡΣΙΑ ΑΠΟΚΡΙΣΗ ΠΑΣΣΑΛΩΝ ΘΕΜΕΛΙΩΣΕΩΣ

Σπύρος Κ. Γιαννακός

Διπλωματούχος Μηχανικός Μεταλλείων – Μεταλλουργός

Ε.Μ.Π. – 2005

Master of Science in Civil Engineering

U.C. Berkeley – 2006

Επιβλέπων: Γ. ΓΚΑΖΕΤΑΣ, Καθηγητής

Ιούνιος 2013

NATIONAL TECHNICAL UNIVERSITY OF ATHENS
SCHOOL OF CIVIL ENGINEERING
DEPARTMENT OF GEOTECHNICAL ENGINEERING

D O C T O R A L D I S S E R T A T I O N

CONTRIBUTION TO THE STATIC AND DYNAMIC LATERAL RESPONSE OF PILES

Spyros K. Giannakos

Diploma in Mining and Metallurgy Engineering
N.T.U.A. – 2005
Master of Science in Civil Engineering
U.C. Berkeley – 2006

Supervisor: G. GAZETAS, Professor

June 2013

Review Committee

Gazetas George, Professor, NTUA, Athens
Kavvadas Michael, Associate Professor, NTUA, Athens
Gerolymos Nikos, Assistant Professor, NTUA, Athens

Papadopoulos Vassilios, Associate Professor, NTUA, Athens
Sapountzakis Evangelos, Professor, NTUA, Athens
Comodromos Emilios, Professor, UTH, Volos
Pitilakis Dimitrios, Lecturer, AUTH, Thessaloniki

The research for this dissertation was conducted for the project *DARE : Soil-Foundation-Structure Systems Beyond Conventional Seismic "Failure" Thresholds : Application to New or Existing Structures and Monuments*, funded by the European Research Council (ERC) under its IDEAS-Advanced Grant program : ERC-2008-AdG: 228254-DARE.

Συμβολή στην Στατική και Δυναμική Εγκάρσια Απόκριση Πασσάλων Θεμελιώσεως

Εκτενής Περίληψη

Εισαγωγή: Σκοπός της Διατριβής

Η οριζόντια απόκριση πασσάλων θεμελιώσεως υπό στατική και δυναμική φόρτιση αποτελεί ένα πεδίο συνεχούς έρευνας, αφού οι θεμελιώσεις πασσάλων χρησιμοποιούνται συχνά για την θεμελίωση κατασκευών, όπως γέφυρες, ανεμογεννήτριες, πλατφόρμες πετρελαίου. Ειδικότερα, η δυναμική κινηματική και αδρανειακή αλληλεπίδραση του συστήματος εδάφους-πασσάλου-ανωδομής εξαρτάται από ένα σύνολο παραμέτρων, όπως η εδαφική στρωματογραφία και οι εδαφικές ιδιότητες, η μή-γραμμική σχέση τάσεων-παραμορφώσεων του εδάφους και του πασσάλου (μή-γραμμική συμπεριφορά του υλικού) και οι γεωμετρικές μή-γραμμικότητες (αποκόλληση και ολίσθηση).

Οι μέθοδοι ανάλυσης των πασσάλων υπό εγκάρσια φόρτιση μπορούν να κατηγοριοποιηθούν ως εξής: (1) μέθοδοι οριακής ισορροπίας, (2) μέθοδοι δοκού επί ελατηριωτού εδάφους τύπου Winkler, οι οποίες συνήθως βασίζονται σε πειραματικές καμπύλες p-y, (3) μέθοδοι που βασίζονται στην θεωρία συνεχούς μέσου, και (4) μέθοδοι μακρο-στοιχείου. Η μέθοδος οριακής ισορροπίας, η οποία θεωρεί καί τον πάσσαλο καί το έδαφος ως απολύτως πλαστικά υλικά, είναι κατάλληλη μόνον για τον υπολογισμό του οριακού φορτίου του πασσάλου. Στην τρίτη κατηγορία ανήκουν λύσεις με τη θεωρία της ελαστικότητας και λύσεις με μή-γραμμικά προσομοιώματα πεπερασμένων στοιχείων. Τα γραμμικά ελαστικά προσομοιώματα δύναται να χρησιμοποιηθούν εύκολα, εξαιτίας των αναλυτικών εκφράσεων, αλλά αδυνατούν να περιγράψουν την αναπόφευκτη πλαστικοποίηση του εδάφους, ιδίως σε μεγάλες παραμορφώσεις. Τα μή-γραμμικά προσομοιώματα πεπερασμένων στοιχείων συνεχούς μέσου προσπαθούν να αναπαράγουν ρεαλιστικά την πολύπλοκη συμπεριφορά στην διεπιφάνεια εδάφους-

πασσάλου, αλλά η ενσωμάτωσή τους σε αριθμητικούς κώδικες προϋποθέτει την χρήση και βαθμονόμηση προχωρημένων και πολύπλοκων εδαφικών καταστατικών προσομοιωμάτων, μία ιδιαιτέρως χρονοβόρα διαδικασία. Τα προσομοιώματα δοκών επί ελατηριωτού εδάφους τύπου Winkler έχουν αποδειχτεί κατάλληλα για την απόκριση πασσάλων υπό οριζόντια φόρτιση, ενώ επιπλέον μπορούν εύκολα να ενσωματωθούν σε αριθμητικούς κώδικες. Το βασικό μειονέκτημα αυτής της μεθόδου είναι ότι κάθε εδαφικό ελατήριο αποκρίνεται ανεξάρτητα από τα γειτονικά του. Τέλος, η μέθοδος μακρο-στοιχείου επιτρέπει την πλήρη μακροσκοπική προσομοίωση του συστήματος εδάφους-θεμελίωσης σε ελάχιστο χρόνο, όπως και τα προσομοιώματα δοκών επί ελατηριωτού εδάφους τύπου Winkler, ενώ τυτόχρονα όλοι οι βαθμοί ελευθερίας του μακρο-στοιχείου είναι συζευγμένοι.

Σκοπός της διδακτορικής διατριβής είναι η απόκτηση νέων γνώσεων σχετικά με την μή–γραμμική αλληλεπίδραση συστημάτων εδάφους–πασσαλο-θεμελιώσεων υπό στατική και δυναμική φόρτιση και επιπλέον συμβάλλει στην ανάπτυξη ενός καινοτομικού υπολογιστικού πλαισίου (μακρο-στοιχείου) για την αντιμετώπιση της πασσαλο-θεμελίωσης ως ενιαίου συστήματος, στην απόκριση της οποίας συνυπολογίζεται η ταυτόχρονη εξέλιξη όλων των μή–γραμμικών μηχανισμών που την συνθέτουν. Αποτέλεσμα της διατριβής είναι η κατανόηση του ρόλου θεμελιωδών παραγόντων στην αλληλεπίδραση συστημάτων εδάφους–πασσαλο-θεμελίωσης, όπως π.χ. η αλληλεπίδραση πασσάλου–προς–πάσσαλον στην ανελαστική περιοχή της παραμόρφωσης και η δημιουργία πλαστικών αρθρώσεων στον πάσσαλο.

Συνοπτικά, παρουσιάζεται ένα απλοποιημένο εδαφικό καταστατικό προσομοίωμα για την στατική και ανακυκλική συμπεριφορά πασσάλων σε μή-συνεκτικά εδάφη υπό στραγγιζόμενες συνθήκες. Το προσομοίωμα ενσωματώνεται σε ένα τρισδιάστατο κώδικα πεπερασμένων στοιχείων μέσω υπορουτίνας, βαθμονομείται και επαληθεύεται με πειράματα σε φυγοκεντριστή για μεμονωμένους πασσάλους σε άμμο υπό εγκάρσια ανακυκλική φόρτιση, και χρησιμοποιείται για την κατανόηση φαινομένων που παρατηρούνται σε μεμονωμένους και μή πασσάλους υπό ανακυκλική φόρτιση, όπως: (1) το φαινόμενο της σταθεροποίησης της πλαστικής ενέργειας με μειούμενο ρυθμό (plastic shakedown response), (2) η επίδραση των δυο μηχανισμών που προκαλούν το φαινόμενο της σταθεροποίησης της πλαστικής ενέργειας στην απόκριση του πασσάλου, (3) η επιρροή του αριθμού των κύκλων φόρτισης στις

εσωτερικές δομητικές δυνάμεις (μέγιστες και παραμένουσες), και (4) το φαινόμενο της σκιάς και η αποδοτικότητα της πασσαλομάδας.

Επιπλέον, από την θεωρία της οριακής ισορροπίας παρουσιάζονται αναλυτικές εκφράσεις για τις καμπύλες αλληλεπίδρασης μεμονωμένων πασσάλων υπό οριζόντια δύναμη και ροπή ανατροπής για διάφορους εδαφικούς τύπους, καθώς και αναλυτικές εκφράσεις για τον νόμο πλαστικής ροής, τα οποία αποτελούν τη βάση για την ανάπτυξη μακρο-στοιχείου για την απόκριση πασσάλου. Οι εκφράσεις αυτές επαληθεύονται αριθμητικά με μή-γραμμικό ελατηριωτό προσομοίωμα Winkler, αλλά και με τρισδιάστατες αναλύσεις πεπερασμένων στοιχείων (και με το αναπτυχθέν καταστατικό προσομοίωμα), λαμβάνοντας υπόψιν καί το κατακόρυφο φορτίο. Ταυτόχρονα διενεργούνται παραμετρικές αναλύσεις για την επίδραση παραγόντων αντοχής του εδάφους στην ορθότητα των αναλυτικών εκφράσεων. Επιπλέον, η επαλήθευση γίνεται με συγκρίση με αποτελέσματα από πείραμα φυσικής κλίμακας πασσάλου και με πειράματα που διεξήχθησαν στο εργαστήριο Δυναμικής / Εδαφομηχανικής του ΕΜΠ.

Τέλος, διερευνώνται οι επιπτώσεις της διαρροής του πασσάλου στην απόκριση συστήματος εδάφους-πασσάλου-γέφυρας υπό σεισμική φόρτιση με έμφαση στην δομητική ανελαστικότητα. Η αλληλεπίδραση εδάφους-πασσάλου-ανωδομής αναλύεται με δυο μεθόδους: (1) με την μέθοδο του πασσαλου επί ελατηριωτού εδάφους, η οποία πραγματοποιείται σε δύο στάδια: (i) ανάλυση (εν-χρόνω) της ανελαστικής μή-γραμμικής απόκρισης του εδαφικού σχηματισμού, χωρίς την παρουσία πασσάλου, υπό τις εξεταζόμενες σεισμικές διεγέρσεις, και (ii) ανάλυση της απόκρισης του συστήματος εδάφους-πασσάλου-ανωδομής με χρήση μή-γραμμικού ελατηριωτού προσομοιώματος Winkler, το οποίο διεγείρεται με τα αποτελέσματα της ανάλυσης της εδαφικής απόκρισης, και (2) με προσομοίωση της πλήρους σύζευξης της κινηματικής και αδρανειακής αλληλεπίδρασης σε τρισδιάστατο προσομοίωμα πεπερασμένων στοιχείων (και με το καταστατικό προσομοίωμα που αναπτύχθηκε στην παρούσα διατριβή).

Προτείνεται μια μεθοδολογία βαθμονόμησης των ελατηρίων και των αποσβεστήρων της υβριδικής διάταξης που χρησιμοποιείται για το μή-γραμμικό ελατηριωτό προσομοίωμα Winkler. Επιπλέον, εξετάζεται η επίδραση του τύπου του εδαφικού υλικού, του ύψους του βάθρου, και της δυνατότητας ανάπτυξης πλαστικής άρθρωσης στον φορέα πάνω και κάτω από την επιφάνεια του εδάφους στην σεισμική απόκριση του συστήματος σε όρους πλαστιμότητας.

Καταστατικό Προσομοίωμα για την Ανακυκλική Απόκριση Πασσάλων σε Αμμώδες Έδαφος

Στην παρούσα διατριβή αναπτύσσεται ένα απλοποιημένο καταστατικό προσομοίωμα για την ανακυκλική απόκριση πασσάλων σε αμμώδες έδαφος. Το εν λόγω προσομοίωμα είναι επέκταση του προσομοιώματος που βαθμονομήθηκε από τους Gerolymos et al (2005, 2006) για συνεκτικά υλικά. Το προσομοίωμα χαρακτηρίζεται από μή-γραμμικό νόμο κράτυνσης, μή-συσχετισμένο νόμο πλαστικής ροής και τροποποιημένο κριτήριο διαρροής Mohr-Coulomb . Οι παράμετροι του καταστατικού προσομοιώματος βαθμονομούνται να ταιριάζουν με το κριτήτιο αστοχίας Mohr-Coulomb στο επίπεδο των κυρίων τάσεων για κάθε γωνία του εξαγώνου σύμφωνα με την περιβάλλουσα αστοχίας του **Σχήματος 1**. Σύμφωνα με το κριτήριο διαρροής, η τάση διαρροής σ_y ισούται:

$$\sigma_y = \sqrt{3J_2} \tag{1}$$

όπου J_2 η δεύτερη αναλλοίωτος του τανυστή των αποκλινουσών τάσεων που στην αστοχία ικανοποιεί την ακόλουθη εξίσωση:

$$I_1 \sin\varphi + \frac{1}{2}\left[3(1-\sin\varphi)\sin\theta + \sqrt{3}(3+\sin\varphi)\cos\theta\right]\sqrt{J_2} - 3c\cos\varphi = 0 \tag{2}$$

όπου I_1 η πρώτη αναλλοίωτος του τανυστή των κυρίων τάσεων, c η συνοχή, φ η γωνία τριβής και θ η γωνία Lode (Chen and Mizuno, 1990).

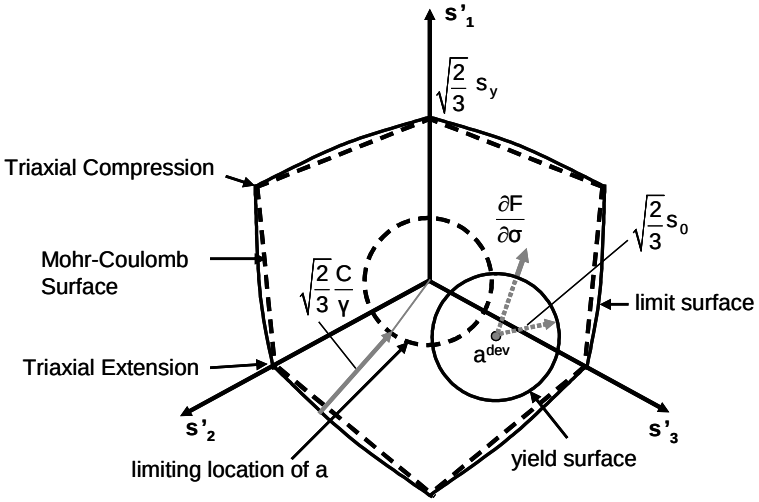

Σχήμα 1: Τρισδιάστατη απεικόνιση του νόμου κράτυνσης του προτεινόμενου καταστατικού προσομοιώματος

Το προσομοίωμα ενσωματώνεται στον κώδικα πεπερασμένων στοιχείων ABAQUS μέσω υπορουτίνας, η οποία συνδέει τις παραμέτρους του προσομοιώματος με την κατακόρυφη τάση, τις κύριες τάσεις και την γωνία Lode σε κάθε βήμα φόρτισης. Η γωνία Lode επιτρέπει την ακριβέστερη προσομοίωση της απόκρισης του εδάφους σε τρισδιάστατο περιβάλλον. Για τον λόγο αυτό εισάγεται μια παράμετρος για την εντατική κατάσταση του εδάφους k (συναρτήσει της γωνίας Lode), η οποία λαμβάνει τιμές από 0 έως 1. Η τιμή k = 0 αντιστοιχεί σε συνθήκες καθαρού τριαξονικού εφελκυσμού, k = 1 σε καθαρή τριαξονική θλίψη, k = 0.5 σε δοκίμη απευθείας διάτμησης.

Το παρόν απλοποιημένο καταστατικό προσομοίωμα δεν λαμβάνει υπόψιν του την διαστολική συμπεριφορά του εδάφους και την εδαφική συμπύκνωση κατά την ανακυκλική φόρτιση. Η επίδραση της διαστολικής συμπεριφοράς είναι συνήθως ασήμαντη, καθώς η εδαφική συμπύκνωση αποτελεί τη δεσπόζουσα συμπεριφορά στην εγκάρσια ανακυκλική απόκριση με μεγάλο αριθμό κύκλων φόρτισης. Η αδυναμία του προτεινόμενου καταστατικού προσομοιώματος για την προσομοίωση της εδαφικής συμπύκνωσης χρησιμοποιήθηκε για την αξιολόγηση του ρόλου των δυο μηχανισμών κράτυνσης (εδαφικής συμπύκνωσης και ενεργοποιημένης εδαφικής αντίστασης σε μεγαλύτερα βάθη) στο παρατηρηθέν φαινόμενο της σταθεροποίησης της πλαστικής ενέργειας με μειούμενο ρυθμό (plastic shakedown response).

Το προτεινόμενο καταστατικό προσομοίωμα βαθμονομείται και επαληθεύεται με τα πειραματικά αποτελέσματα από τρία πειράματα σε φυγοκεντριστή μεμονωμένου πασσάλου σε ξηρή άμμο υπό ανακυκλική εγκάρσια φόρτιση (**Σχήμα 2**) στο Laboratoire Central des Ponts et Chaussées (LCPC) από τους Rosquoët et al (2004). Τα πειράματα P32 και P344 έχουν ασύμμετρη ανακυκλική φόρτιση με διαφορετικό εύρος δυνάμεων, ενώ το πείραμα P330 έχει πλήρη ανακυλική φόρτιση. Το τρισδιάστατο προσομοίωμα πεπερασμένων στοιχείων που χρησιμοποιήθηκε παρουσιάζεται στο **Σχήμα 3**. Το έδαφος προσομοιώνεται με οκτακομβικά στοιχεία συνεχούς μέσου, ενώ ο ελαστικός πάσσαλος με τρισδιάστατα στοιχεία δοκού κατά μήκος του κατακόρυφου άξονά του συνδεδεμένα με κατάλληλους κινηματικούς περιορισμούς με τους κόμβους στην περίμετρό του για την ρεαλιστική προσομοίωση ολόκληρης της γεωμετρίας του πασσάλου. Τα στοιχεία συνεχούς μέσου εντός της περιμέτρου του πασσάλου έχουν μηδενική δυσκαμψία.

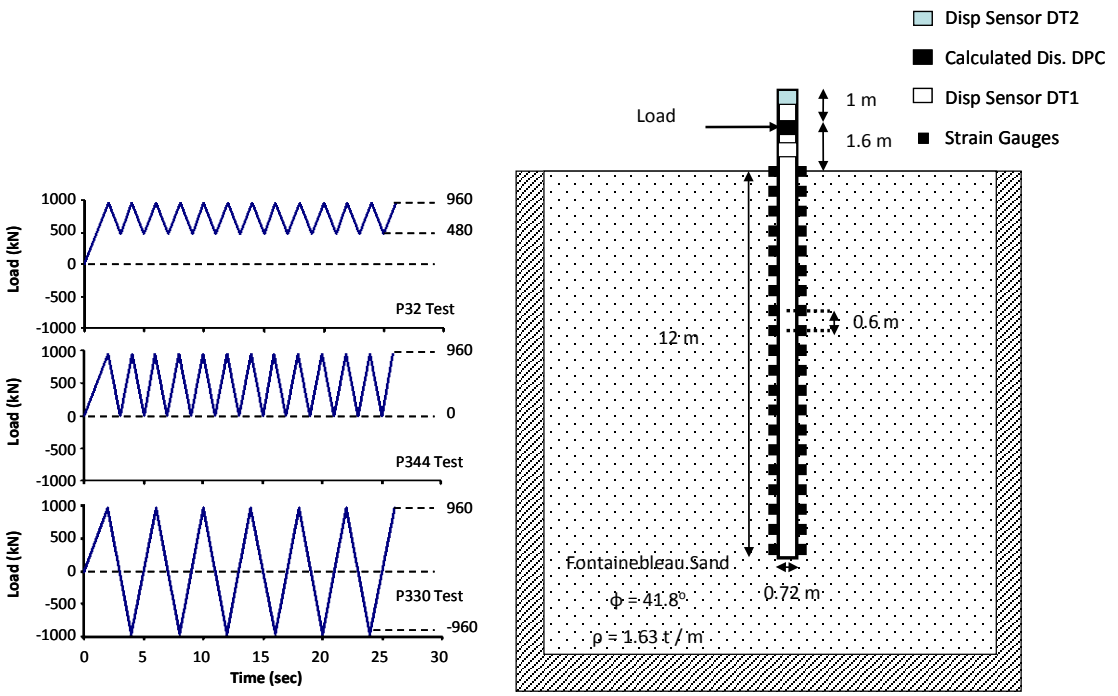

Σχήμα 2: Διάταξη και χρονοϊστορίες φόρτισης των πειραμάτων σε φυγοκεντριστή στο LCPC. Οι διαστάσεις αναφέρονται στο πρωτότυπο

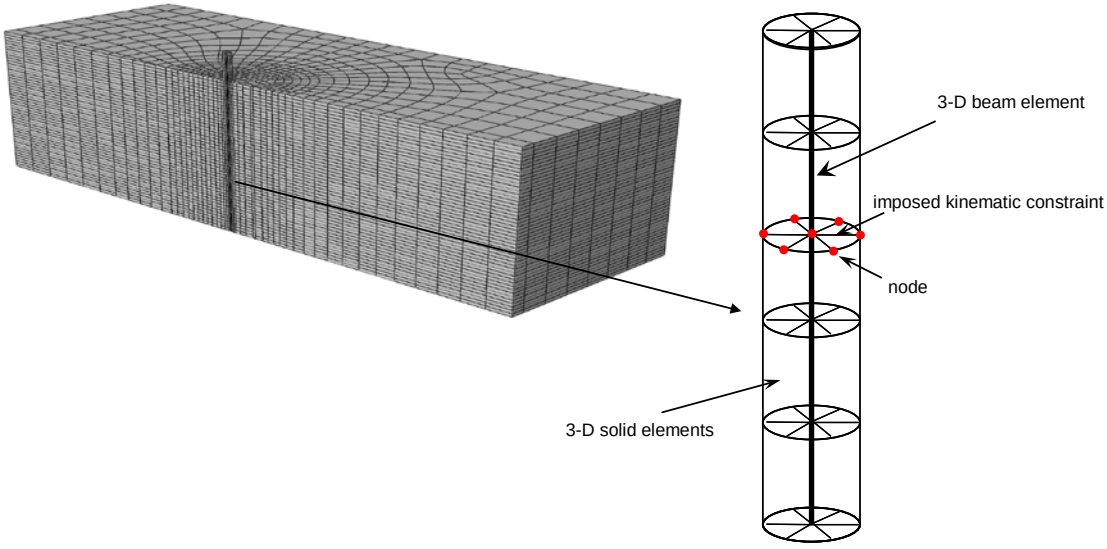

Σχήμα 3: Τρισδιάστατο προσομοίωμα πεπερασμένων στοιχείων των πειραμάτων και του πασσάλου

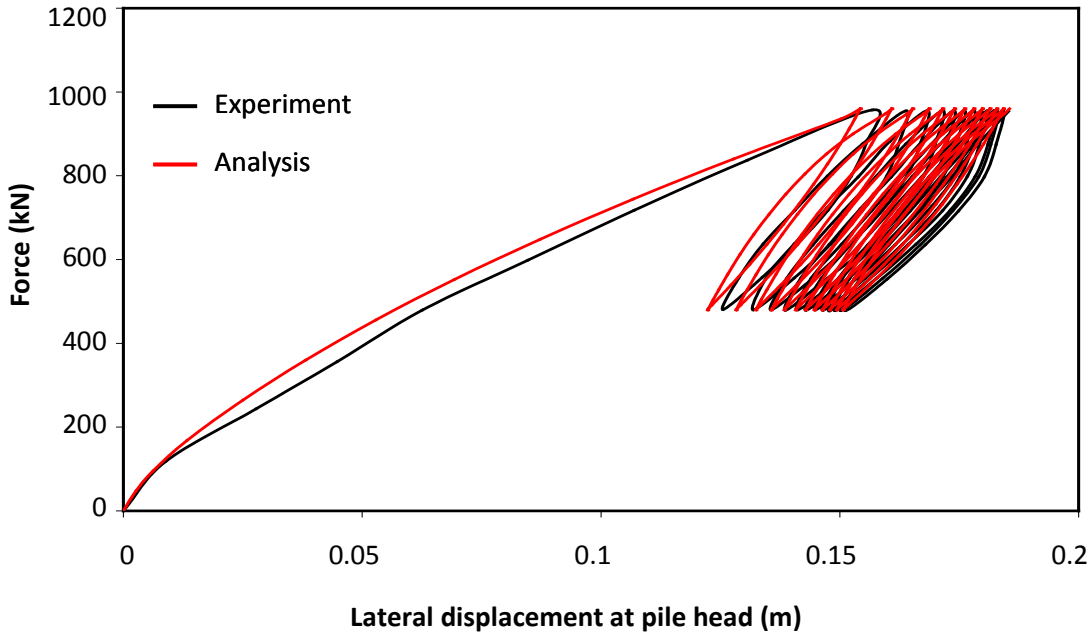

Σχήμα 4: Σύγκριση αποτελεσμάτων δύναμης–μετατόπισης στην κεφαλή του πασσάλου του πειράματος P32 με τα αποτελέσματα της αριθμητικής ανάλυσης

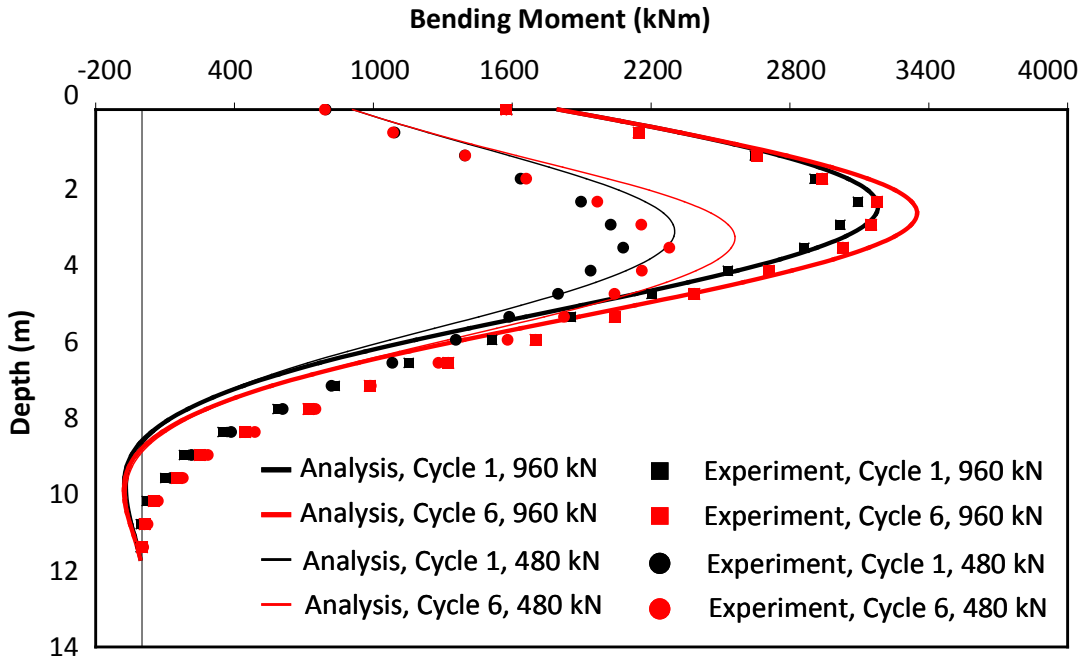

Σχήμα 5: Σύγκριση κατανομών καμπτικών ροπών για το πείραμα P32 κατά την φόρτιση και αποφόρτιση του 1^{ου} και του 6^{ου} κύκλου με τα αποτελέσματα της αριθμητικής ανάλυσης

Η καμπύλη δύναμης–μετατόπισης στην κεφαλή του πασσάλου κατά την αρχική φόρτιση του πειράματος P32 (μέγιστη οριζόντια δύναμη 960 kN και ελάχιστη 480 kN) χρησιμοποιείται για την βαθμονόμηση των παραμέτρων του εδαφικού καταστατικού προσομοιώματος. Στο **Σχήμα 4** παρατηρείται ότι το προσομοίωμα αναπαράγει την κράτυνση (plastic shakedown response) στην απόκριση του πασσάλου. Η εν λόγω απόκριση είναι το αποτέλεσμα δύο μηχανισμών: (1) της εδαφικής συμπύκνωσης, και (2) της "συμπύκνωσης του συστήματος", λόγω της προοδευτικής αύξησης (με τους κύκλους φόρτισης) του όγκου του εδαφικού πρίσματος αστοχίας. Το προταθέν καταστατικό προσομοίωμα αναπαράγει μόνον τον δεύτερο μηχανισμό. Το **Σχήμα 5** απεικονίζει την απορρέουσα κατανομή των καμπτικών ροπών για τον $1^{ο}$ και τον $6^{ο}$ κύκλο φόρτισης. Η γενική σύγκριση των καταγεγραμένων καμπτικών ροπών με τα αποτελέσματα της αριθμητικής ανάλυσης είναι ικανοποιητική. Το προσομοίωμα προβλέπει επιτυχώς το σχήμα της κατανομής των ροπών και την αύξηση των καμπτικών ροπών με τον αυξανόμενο αριθμό των κύκλων φόρτισης. Επιπλέον, προσομοιώνεται επιτυχώς το βάθος της μέγιστης καμπτικής ροπής σε φόρτιση και αποφόρτιση, καθώς και η μετατόπιση της μέγιστης καμπτικής ροπής σε μεγαλύτερα βάθη με την αύξηση του αριθμού των κύκλων φόρτισης.

Το βαθμονομημένο προσομοίωμα από το πείραμα P32 χρησιμοποιείται εν συνεχεία για την πρόβλεψη της απόκρισης των πειραμάτων P344 (πλήρως ασύμμετρη ανακυκλική φόρτιση, χωρίς αλλαγή στο πρόσημο της φόρτισης) και P330 (πλήρως συμμετρική ανακυκλική φόρτιση, με αλλαγή προσήμου φόρτισης). Στο πείραμα P344 η μέγιστη οριζόντια δύναμη είναι 960 kN ενώ η ελάχιστη 0 kN. Στο **Σχήμα 6** συγκρίνονται τα αποτελέσματα του πειράματος και της αριθμητικής προσομοίωσης με την μορφή καμπύλης δύναμης–μετατόπισης στην κεφαλή του πασσάλου. Παρά την διαφορά της παραμένουσας μετατόπισης στο τέλος κάθε σταδίου αποφόρτισης, η σύγκριση είναι αρκετά ικανοποιητική. Στο **Σχήμα 7** γίνεται σύγκριση των αριθμητικών αποτελεσμάτων με τα πειραματικά με την μορφή κατανομών καμπτικών ροπών στο τέλος της φόρτισης και της αποφόρτισης του $1^{ου}$ και του $6^{ου}$ κύκλου. Παρόλο που η κατανομή των καμπτικών ροπών στο τέλος της φόρτισης κάθε κύκλου συμφωνεί με τα πειραματικά δεδομένα, παρατηρείται διαφορά της απόκρισης στο τέλος της αποφόρτισης των κύκλων. Η εν λόγω διαφορά αποδίδεται στην αδυναμία του προσομοιώματος να αναπαράγει την εδαφική συμπύκνωση και χαλάρωση. Έτσι, η ενεργοποιημένη εδαφική

μάζα πίσω από τον πάσσαλο, η οποία ακολουθεί την κίνησή του κατά την φόρτιση στην αριθμητική ανάλυση, προσδίδει μεγαλύτερη αντίσταση στην αποφόρτιση από το χαλαρωμένο έδαφος στο πείραμα.

Τέλος, το **Σχήμα 8** απεικονίζει τις ισοϋψείς των ενεργητικών και παθητικών εντατικών καταστάσεων σε σχέση με την παράμετρο k για τρία διαφορετικά στάδια φόρτισης: (α) στο τέλος της φόρτισης του $1^{ου}$ κύκλου, (β) στο τέλος της αποφόρτισης του $12^{ου}$ κύκλου, και (γ) στο τέλος φόρτισης του $12^{ου}$ κύκλου. k = 0 αντιστοιχεί σε συνθήκες καθαρού τριαξονικού εφελκυσμού, k = 1 σε καθαρή τριαξονική θλίψη, k = 0.5 σε δοκίμη απευθείας διάτμησης. Το φαινόμενο της σταθεροποίησης της πλαστικής ενέργειας με μειούμενο ρυθμό (plastic shakedown response) απεικονίζεται από την αύξηση του τμήματος του εδάφους μπροστά από τον πάσσαλο σε παθητική κατάσταση με τον αριθμό των κύκλων φόρτισης, ενώ το ενεργοποιούμενο εδαφικό τμήμα πίσω από τον πάσσαλο σε ενεργητική κατάσταση μειώνεται. Επιπλέον, στο **Σχήμα 8β** παρατηρείται ότι παρόλο που δεν ασκείται οριζόντια φόρτιση στον πάσσαλο (στάδιο πλήρους αποφόρτισης), ο πάσσαλος δεν επιστρέφει στην αρχική κατακόρυφη θέση, εξαιτίας της αντίστασης του εδαφικού τμήματος το οποίο μετατοπίζεται με τον πάσσαλο κατά τη φόρτιση και καταλαμβάνει πλέον την αρχική θέση του πασσάλου.

Η μετρηθείσα καμπύλη δύναμης−μετατόπισης στην κεφαλή του πασσάλου για το πείραμα P330 (με μέγιστη οριζόντια δύναμη 960 kN και η ελάχιστη -960 kN) συγκρίνεται με τα αποτελέσματα της αριθμητικής ανάλυσης στο **Σχήμα 9**. Στην περίπτωση της πλήρους συμμετρικής ανακυκλικής φόρτισης η μετατόπιση του πασσάλου στα σημεία αλλαγής από φόρτιση σε αποφόρτιση μειώνεται με μειούμενο ρυθμό με τον αριθμό των κύκλων φόρτισης, σε αντίθεση με την περίπτωση της ασύμμετρης φόρτισης. Η κράτυνση αυτή στην απόκριση του πασσάλου οφείλεται στην εκτενή πλαστικοποίηση του εδάφους γύρω από τον πάσσαλο, η οποία οδηγεί στην αύξηση της εδαφικής πίεσης στον πάσσαλο. Επιπλέον, παρατηρείται διαφορά στην μετατόπιση περίπου 1.5 cm στο πέρας της “αρχικής” φόρτισης του πειράματος P330 σε σχέση με τα πειράματα P32 και P344. Αυτό υπονοεί ότι οι αρχικές συνθήκες της άμμου στο πείραμα P330 δεν είναι ίδιες με των πειραμάτων P32 και P344. Τα αποτελέσματα σε αυτή την περίπτωση είναι περισσότερο ποιοτικά παρά ποσοτικά, αφού δεν πραγματοποιήθηκε νέα βαθμονόμηση του προτεινόμενου προσομοιώματος για τις νέες εδαφικές συνθήκες.

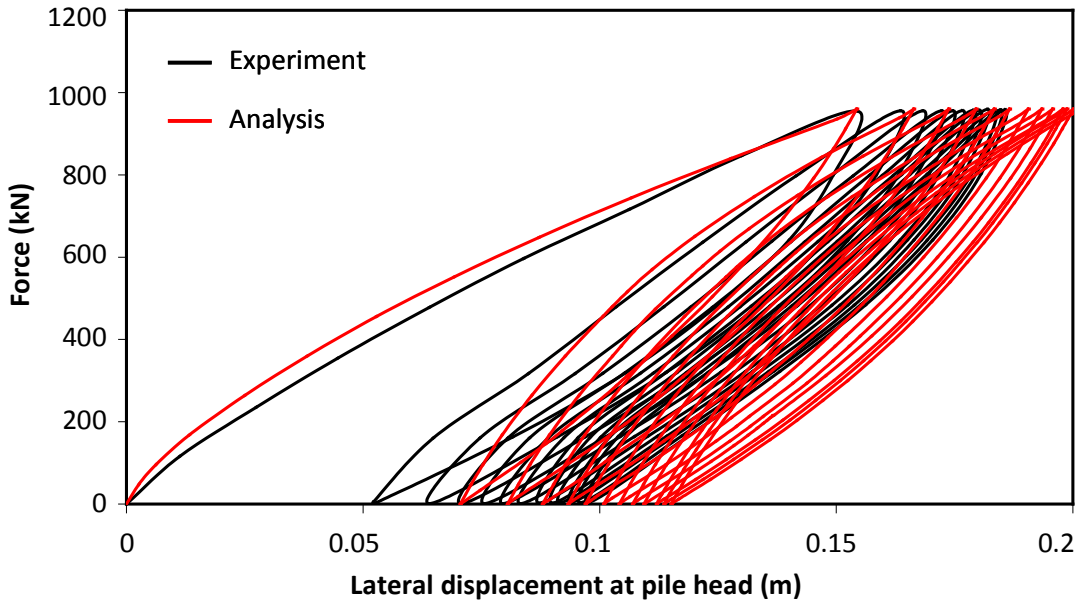

Σχήμα 6: Σύγκριση δύναμης–μετατόπισης στην κεφαλή του πασσάλου του πειράματος P344 με τα αποτελέσματα της αριθμητικής ανάλυσης

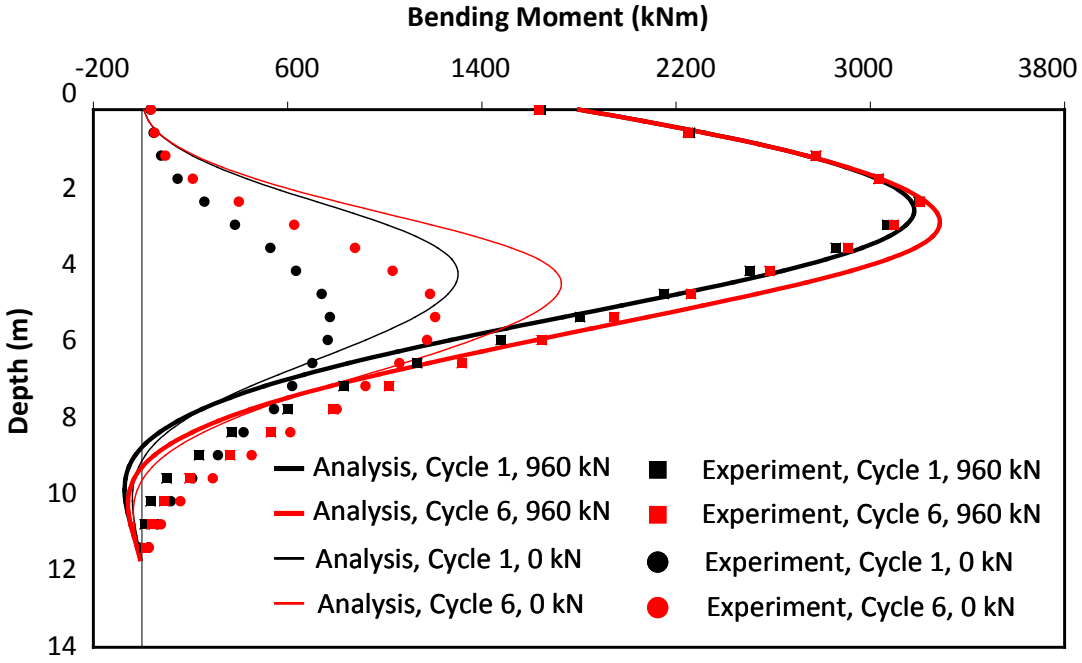

Σχήμα 7: Σύγκριση κατανομών καμπτικών ροπών του πειράματος P344 κατά την φόρτιση και αποφόρτιση του 1^{ου} και του 6^{ου} κύκλου με τα αποτελέσματα της αριθμητικής ανάλυσης

Το **Σχήμα 10** παρουσιάζει την σύγκριση των κατανομών καμπτικών ροπών του πειράματος με τα αποτελέσματα της αριθμητικής ανάλυσης. Για την πλήρη ανακυκλυκή φόρτιση η σύγκριση είναι ικανοποιητική. Ενδιαφέρον παρουσιάζουν οι κατανομές στο τέλος της φόρτισης και στο τέλος της αποφόρτισης, καθώς δεν είναι ακριβώς συμμετρικές, αλλά είναι λίγο μεγαλύτερες προς την κατεύθυνση της "αρχικής φόρτισης". Το εν λόγω φαινόμενο οφείλεται στο γεγονός ότι το τμήμα του εδάφους πίσω από τον πάσσαλο κατά την "αρχική φόρτιση" ρέει με τον πάσσαλο και έτσι αυξάνεται η εδαφική αντίσταση κατά την αποφόρτιση και την φόρτιση προς την αντίθετη κατεύθυνση.

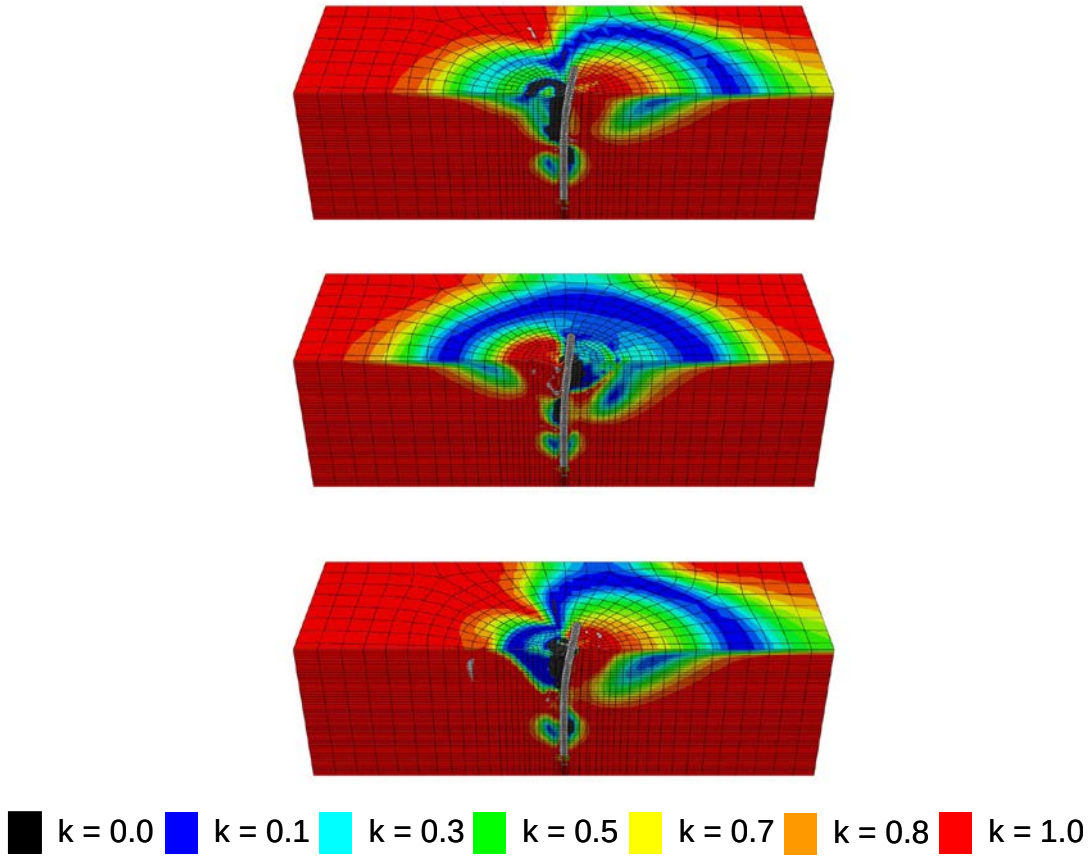

Σχήμα 8: Ισοϋψείς των ενεργητικών και παθητικών εντατικών καταστάσεων σε σχέση με την παράμετρο k για τρία διαφορετικά στάδια φόρτισης: (α) στο τέλος της φόρτισης του 1^{ου} κύκλου, (β) στο τέλος της αποφόρτισης του 12^{ου} κύκλου, και (γ) στο τέλος φόρτισης του 12^{ου} κύκλου. (Συντελεστής μεγέθυνσης: 5)

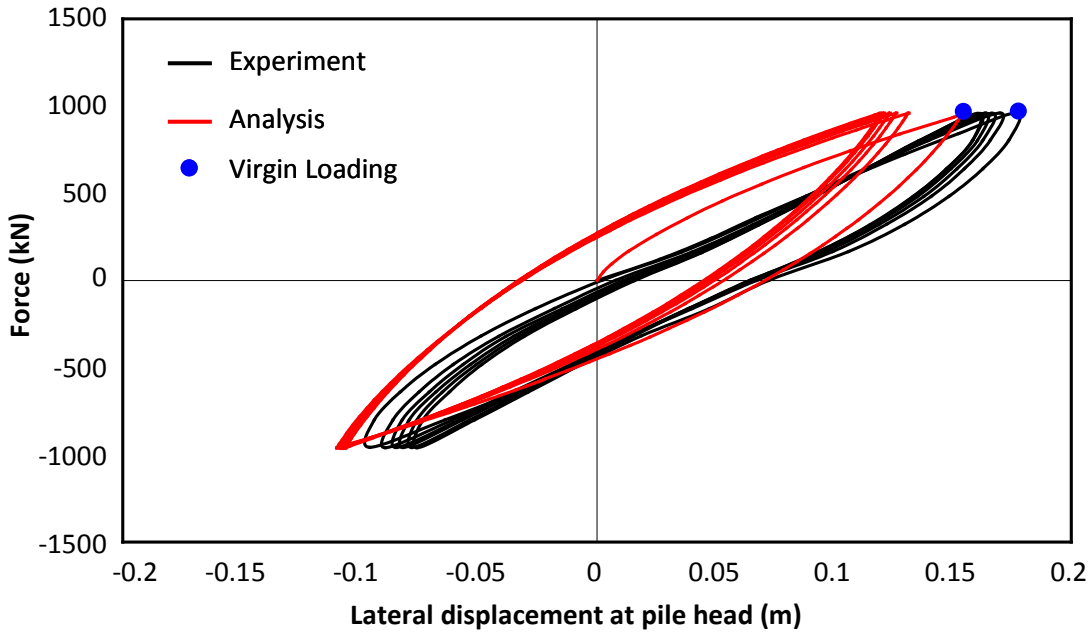

Σχήμα 9: Σύγκριση δύναμης–μετατόπισης στην κεφαλή του πασσάλου του πειράματος P330 με τα αποτελέσματα της αριθμητικής ανάλυσης

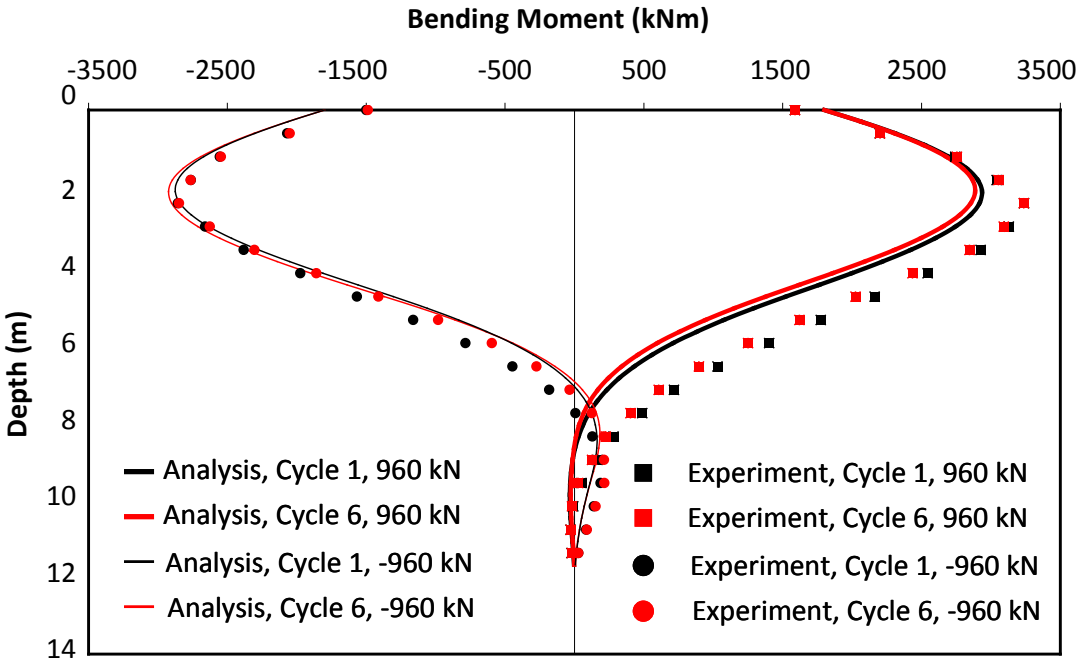

Σχήμα 10: Σύγκριση κατανομών καμπτικών ροπών του πειράματος P330 κατά την φόρτιση και αποφόρτιση του 1^{ου} και του 6^{ου} κύκλου με τα αποτελέσματα της αριθμητικής ανάλυσης

Επειδή το έδαφος μπροστά από τον πάσσαλο θλίβεται και βρίσκεται σε παθητική κατάσταση, ενώ πίσω από τον πάσσαλο βρίσκεται σε ενεργητική κατάσταση, εξετάζεται η επίδραση της μορφής του κριτηρίου διαρροής στο επίπεδο π στην απόκριση του πασσάλου. Εξετάζονται τρία διαφορετικά κριτήρια διαρροής: (α) το προτεινόμενο καταστατικό προσομοίωμα (ορίζεται ως προσομοίωμα CT), όπου το κριτήριο διαρροής εφάπτεται στο εξάγωνο του κριτηρίου αστοχίας Mohr-Coulomb σε κάθε γωνία στο επίπεδο π, (β) ένα αντίστοιχο προσομοίωμα (προσομοίωμα C), όπου το κριτήριο διαρροής είναι ένας κύκλος περιγεγραμμένος στο εξάγωνο του κριτηρίου αστοχίας Mohr-Coulomb στις τρεις γωνίες που αντιστοιχούν σε δοκιμή τριαξονικής θλίψης, και (γ) ένα αντίστοιχο προσομοίωμα (προσομοίωμα T), όπου το κριτήριο διαρροής είναι ένας κύκλος περιγεγραμμένος στο εξάγωνο του κριτηρίου αστοχίας Mohr-Coulomb στις τρεις γωνίες που αντιστοιχούν σε δοκιμή τριαξονικού εφελκυσμού. Οι αναλύσεις πραγματοποιήθηκαν και για τους τρεις τύπους ανακυκλικής φόρτισης των πειράματων. Στο **Σχήμα 11** συγκρίνονται η καμπύλη δύναμης−μετατόπισης στην κεφαλή του πασσάλου του πειράματος P32 με τα αποτελέσματα από τις αριθμητικές αναλύσεις των τριών προσομοιωμάτων. Είναι προφανές ότι το προσομοίωμα CT έχει την καλύτερη απόκριση. Η απόκριση με το προσομοίωμα C είναι κόντα στις πειραματικές τιμές (αφού γενικά η θλίψη είναι αυτή που κυριαρχεί στην απόκριση του συστήματος πασσάλου-εδάφους) αλλά είναι πιο δύσκαμπτη, ενώ η απόκριση με το προσομοίωμα T υπολογίζει μεγαλύτερες μετατοπίσεις. Αντίστοιχη συμπεριφορά παρατηρείται και στις κατανομές των καμπτικών ροπών και των διατμητικών δυνάμεων. Για την περίπτωση της πλήρους ανακυκλικής φόρτισης η σωστή προσομοίωση της τριαξονικής αντοχής σε εφελκυσμό έχει μεγαλύτερη σημασία από ότι στην ασύμμετρη ανακυκλική φόρτιση.

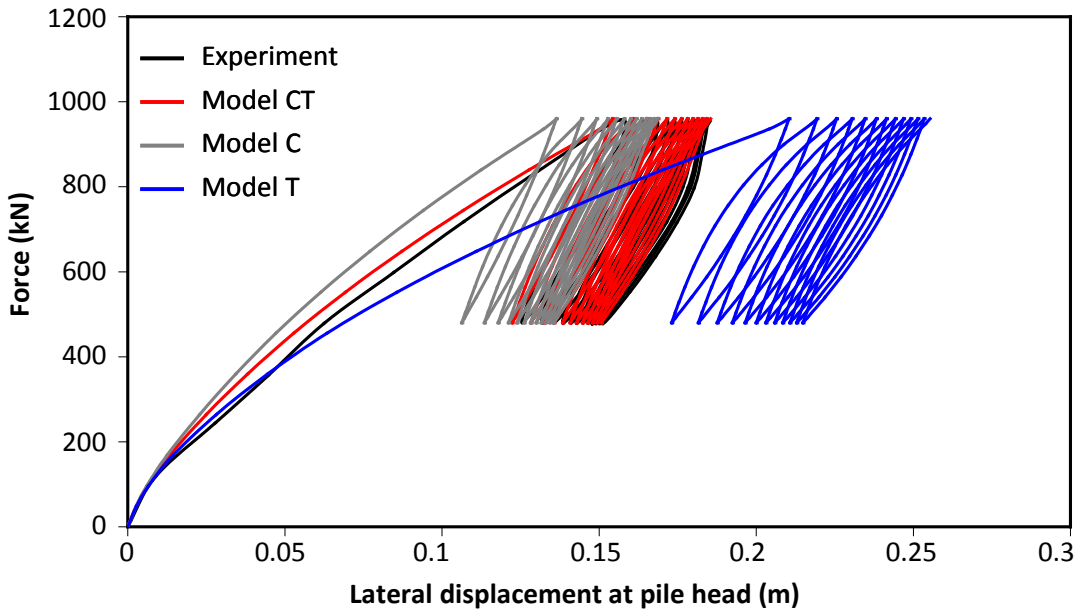

Σχήμα 11: Σύγκριση δύναμης–μετατόπισης στην κεφαλή του πασσάλου του πειράματος P32 με τα αποτελέσματα των αριθμητικών αναλύσεων με τρία διαφορετικά καταστατικά προσομοιώματα

Τρεις δείκτες συμπεριφοράς εισάγονται για την αξιολόγηση των αποτελεσμάτων του συστήματος πασσάλου-εδάφους. Στο **Σχήμα 12α** παρουσιάζεται για το πείραμα P344 ο λόγος του εφαπτομενικού μέτρου σε κάθε σημείο αποφόρτισης–επαναφόρτισης κάθε κύκλου προς το εφαπτομενικό μέτρο στο σημείο αποφόρτισης–επαναφόρτισης του πρώτου κύκλου φόρτισης. Ο δείκτης αυτός είναι ενδεικτικός της ελαστικής συμπεριφοράς του συστήματος πασσάλου-εδάφους. Είναι αξιοσημείωτο ότι το προκύπτον εφαπτομενικό μέτρο από την αριθμητική ανάλυση με το προτεινόμενο καταστατικό προσομοίωμα παραμένει σταθερό, ανεξάρτητο από τους κύκλους φόρτισης, ενώ το εφαπτομενικό μέτρο του πειράματος αυξάνει με τον αριθμό των κύκλων φόρτισης. Η αύξηση αυτή αποδίδεται στην εδαφική συμπύκνωση κατά την ανακυκλική φόρτιση, φαινόμενο που δεν προσομοιώνεται με το προτεινόμενο προσομοίωμα και το οποίο επικρατεί στην ελαστική απόκριση του πασσάλου. Ο λόγος του τέμνοντος μέτρου από το πέρας της αποφόρτισης και το πέρας της επαναφόρτισης στον ίδιο κύκλο φόρτισης προς το τέμνον μέτρο του πρώτου κύκλου φόρτισης, ο οποίος είναι ενδεικτικός της συνολικής συμπεριφοράς του συστήματος πασσάλου-εδάφους κατά την ανακυκλική φόρτιση, απεικονίζεται στο **Σχήμα 12β**. Σε αυτήν την περίπτωση το

τέμνον μέτρο που μετρήθηκε πειραματικώς, αλλά και αυτό που προκύπτει από τις αριθμητικές αναλύσεις αυξάνει με τον αριθμό των κύκλων φόρτισης. Δεδομένου ότι η κράτυνση του συστήματος, λόγω της προοδευτικής αύξησης (με τους κύκλους φόρτισης) του όγκου του εδαφικού πρίσματος αστοχίας, προσομοιώνεται αριθμητικά, η διαφορά στις τιμές του τέμνοντος μέτρου από το πείραμα και την αριθμητική ανάλυση οφείλεται στην εδαφική συμπύκνωση. Ο λόγος της σχετικής μετατόπισης δυο διαδοχικών σημείων επαναφόρτισης–αποφόρτισης στην κεφαλή του πασσάλου ως προς την σχετική μετατόπιση της "αρχικής" φόρτισης και επαναφόρτισης–αποφόρτισης του πρώτου κύκλου δίνεται στο **Σχήμα 12γ**. Σε κάθε κύκλο η μετατόπιση του πασσάλου στα σημεία φόρτισης–αποφόρτισης αυξάνεται με μειούμενο ρυθμό μέχρι να σταθεροποιηθεί ο ρυθμός των πλαστικών παραμορφώσεων. Παρατηρείται ότι τα αποτελέσματα των αριθμητικών αναλύσεων συμφωνούν ικανοποιητικά με τα πειραματικά δεδομένα, υποδεικνύοντας ότι ο μηχανισμός της κράτυνσης του συστήματος υπερισχύει του μηχανισμού της εδαφικής συμπύκνωσης.

Έχοντας συγκρίνει και επαληθεύσει την εγκάρσια απόκριση πασσάλων σε άμμο του προτεινόμενου προσομοιώματος με πειραματικά δεδομένα, το προσομοίωμα χρησιμοποιείται για την ανάλυση 1x2 πασσαλομάδας για τα ίδια τρία πειράματα. Οι πάσσαλοι, οι οποίοι απέχουν απόσταση τριών διαμέτρων από κέντρο σε κέντρο, είναι παράλληλοι προς την διεύθυνση φόρτισης. Οι κεφαλές των πασσάλων έχουν αρθρωτή σύνδεση με τον κεφαλόδεσμο με κατάλληλους κινηματικούς περιορισμούς, ώστε: (α) οι κεφαλές των πασσάλων να έχουν ίδια μετατόπιση όπως σε μια πασσαλομάδα, και (β) τα αποτελέσματα των αναλύσεων να συγκρίνονται απευθείας με αυτά του μεμονωμένου πασσάλου ελεύθερης κεφαλής. Το φορτίο εφαρμόζεται στην μέση του κεφαλοδέσμου με φορά από αριστερά προς τα δεξιά, καθιστώντας τον δεξιά πάσσαλο "πρώτο πάσσαλο" και τον αριστερά "δεύτερο πάσσαλο". Το **Σχήμα 13** απεικονίζει τη τομή του τρισδιάστατου προσομοιώματος πεπερασμένων στοιχείων που χρησιμοποιήθηκε και τις ισοϋψείς των ενεργητικών και παθητικών εντατικών καταστάσεων σε σχέση με την παράμετρο k για το πείραμα P344: (α) στο τέλος της φόρτισης του $1^{ου}$ κύκλου, και (β) στο τέλος φόρτισης του $12^{ου}$ κύκλου. Η εικόνα των ισοϋψών είναι παρόμοια με του **Σχήματος 8** για την απόκριση μεμονωμένου πασσάλου. Σε αυτή την περίπτωση όμως, το φαινόμενο της σκιάς απεικονίζεται με τον σχηματισμό μίας ζώνης χαλάρωσης (k = 0–0.5 αντί για k = 1) ανάμεσα στους δύο πασσάλους.

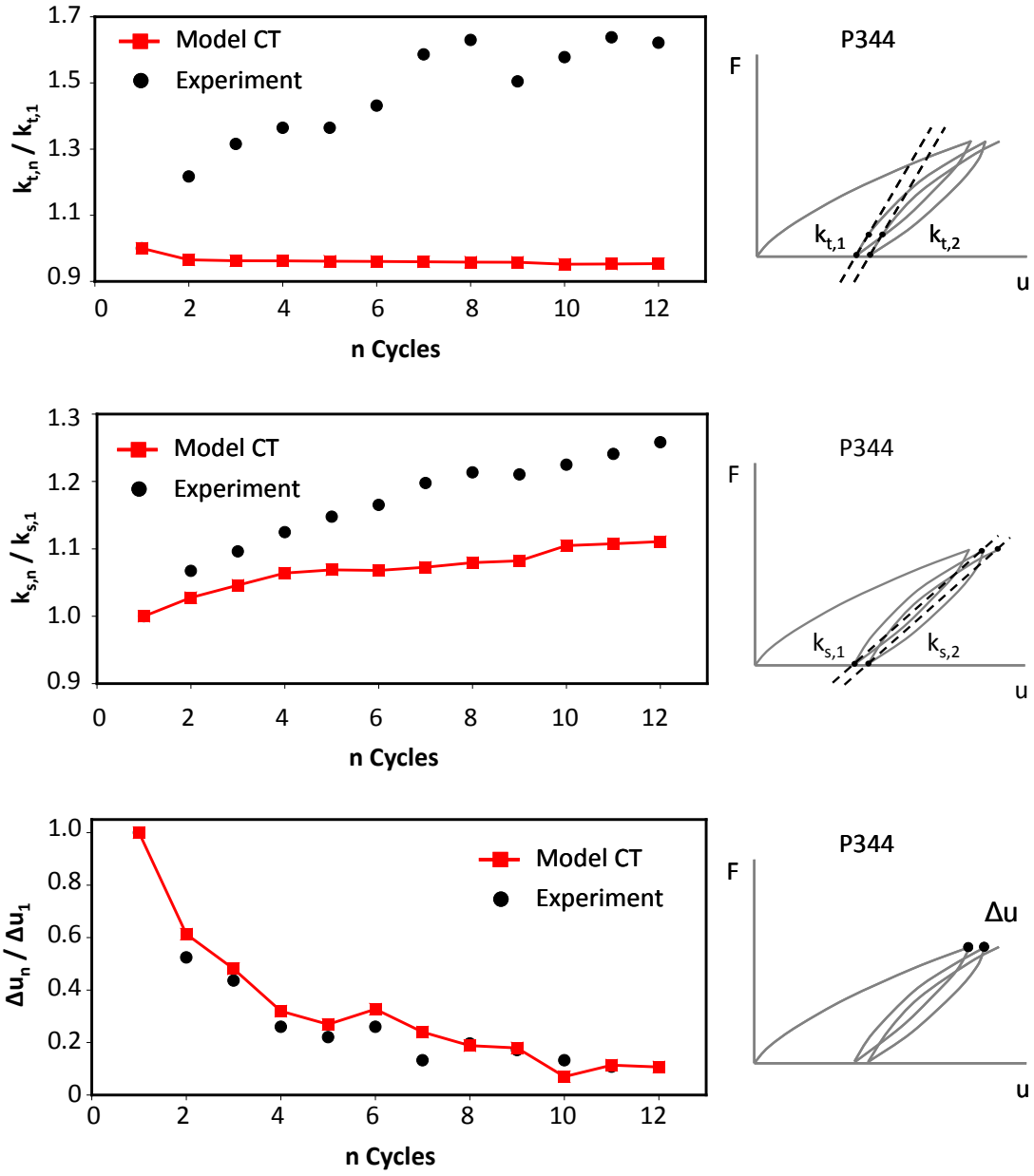

Σχήμα 12: Δείκτες συμπεριφοράς για το πείραμα P344: (α) ο λόγος του εφαπτομενικού μέτρου από κάθε σημείο αποφόρτισης–επαναφόρτισης κάθε κύκλου προς το εφαπτομενικό μέτρο από το σημείο αποφόρτισης-επαναφόρτισης του πρώτου κύκλου φόρτισης, (β) ο λόγος του τέμνοντος μέτρου από το πέρας της αποφόρτισης και το πέρας της επαναφόρτισης στον ίδιο κύκλο φόρτισης προς το τέμνον μέτρο του πρώτου κύκλου φόρτισης, (γ) ο λόγος της σχετικής μετατόπισης δυο διαδοχικών σημείων επαναφόρτισης–αποφόρτισης στην κεφαλή του πασσάλου ως προς την σχετική μετατόπιση της αρχικής φόρτισης και επαναφόρτισης–αποφόρτισης του πρώτου κύκλου

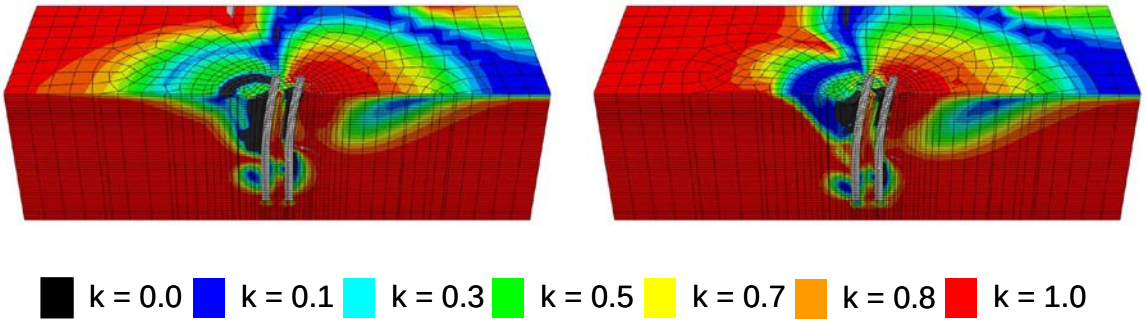

Σχήμα 13: Ισοϋψείς των ενεργητικών και παθητικών εντατικών καταστάσεων σε σχέση με την παράμετρο k του πειράματος P344: (α) στο τέλος της φόρτισης του 1ου κύκλου, και (β) στο τέλος φόρτισης του 12ου κύκλου. (Συντελεστής μεγέθυνσης: 5)

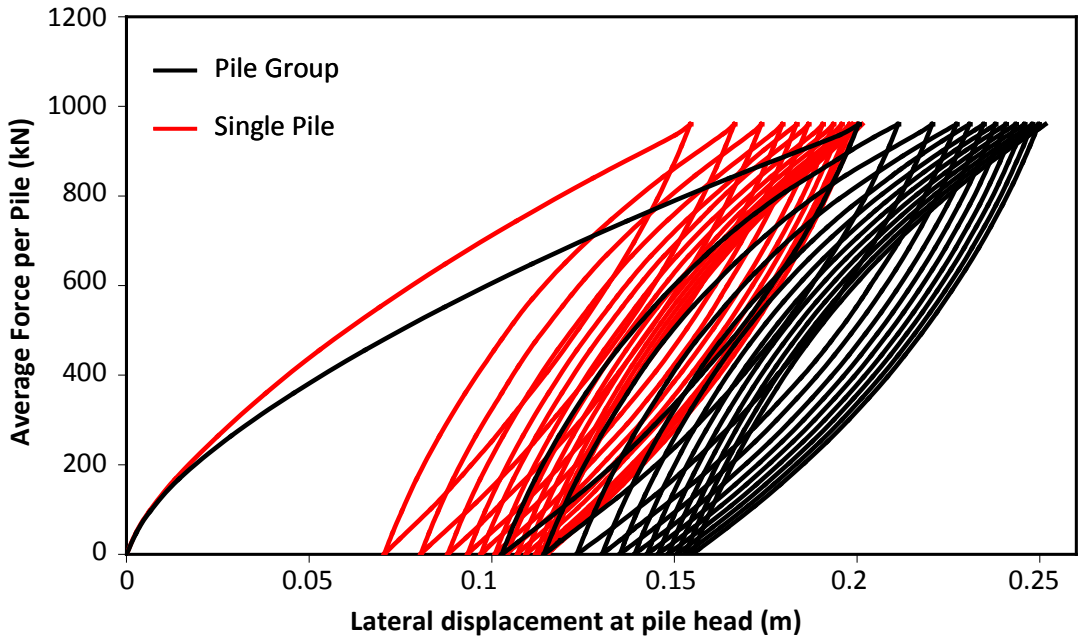

Σχήμα 14: Δύναμη–μετατόπιση του μεμονωμένου πασσάλου και της πασσαλομάδας για την φόρτιση του πειράματος P344

Η επιβαλλόμενη δύναμη στην πασσαλομάδα είναι διπλάσια από ότι στα πειράματα, ώστε η μέση δύναμη ανά πάσσαλο της πασσαλομάδας να είναι ίδια με τον μεμονωμένο πάσσαλο. Το **Σχήμα 14** συγκρίνει την καμπύλη μέσης δύναμης ανά πάσσαλο–μετατόπισης της πασσαλομάδας με την αντίστοιχη του μεμονωμένου

πασσάλου για το πείραμα P344. Για το ίδιο μέσο φορτίο, η μετατόπιση της πασσαλομάδας είναι μεγαλύτερη από του μεμονωμένου πασσάλου. Αυτή η συμπεριφορά οφείλεται στο ότι οι παθητικές ζώνες των πασσάλων της πασσαλομάδας επικαλύπτονται (φαινόμενο της σκιάς) με την αύξηση του οριζόντιου φορτίου, μειώνοντας έτσι την μέση εδαφική αντίσταση στους πασσάλους της πασσαλομάδας. Το φαινόμενο της σκιάς είναι πιο εμφανές όταν μειώνεται η απόσταση των πασσάλων. Όπως και στον μεμονωμένο πάσσαλο, η μετατόπιση της πασσαλομάδας αυξάνεται με μειούμενο ρυθμό με τον αριθμό των κύκλων φόρτισης μέχρι να σταθεροποιηθεί η πλαστική ενέργεια (plastic shakedown response). Επιπλέον, παρατηρείται ότι ο βρόχος δύναμης−μετατόπισης της πασσαλομάδας είναι μεγαλύτερος από τον αντίστοιχο μεμονωμένου πασσάλου, υπονοώντας μεγαλύτερη πλαστικοποίηση του εδάφους.

Η κατανομή των καμπτικών ροπών με το βάθος για κάθε πάσσαλο της πασσαλομάδας δίδεται στο **Σχήμα 15** στην φόρτιση και την αποφόρτιση του $1^{ου}$ και του $6^{ου}$ κύκλου φόρτισης. Στο ίδιο σχήμα γίνεται σύγκριση με τα αποτελέσματα του μεμονωμένου πασσάλου. Παρατηρείται ότι:

- Η μέγιστη καμπτική ροπή αυξάνει με τον αριθμό των κύκλων φόρτισης και μετατοπίζεται σε μεγαλύτερα βάθη εξαιτίας της προοδευτικής πλαστικοποίησης του εδάφους. Παρόμοια συμπεριφορά παρατηρείται στις κατανομές των διατμητικών δυνάμεων και της οριζόντιας εδαφικής αντίδρασης.
- Η μεγαλύτερη καμπτική ροπή αναπτύσσεται στον πρώτο πάσσαλο σε σχέση με τον δεύτερο και τον μεμονωμένο πάσσαλο, ο οποίος έχει μια ενδιάμεση απόκριση από τους πασσάλους της πασσαλομάδας. Η διαφορά στην κατανομή των καμπτικών ροπών μεταξύ του πρώτου και του δεύτερου πασσάλου οφείλεται στον φαινόμενο της σκιάς. Παρόμοια συμπεριφορά παρατηρείται και στις κατανομές των διατμητικών δυνάμεων και της οριζόντιας εδαφικής αντίδρασης.
- Στην αποφόρτιση (μηδενική οριζόντια δύναμη) οι καμπτικές ροπές δεν μηδενίζονται, αλλά διατηρούν μεγάλες τιμές σε σχέση με αυτές από το μέγιστο φόρτιο. Η μείωση των μέγιστων τιμών είναι περίπου 40%. Αντίθετα, για ελαστικό έδαφος οι τιμές αυτές θα μηδενίζονταν.

Τέλος, το **Σχήμα 16** παρουσιάζει τους συντελεστές αποδοτικότητας της 1x2 πασσαλομάδας υπό εγκάρσια φόρτιση σε ύψος 1.6 m από την επιφάνεια του εδάφους

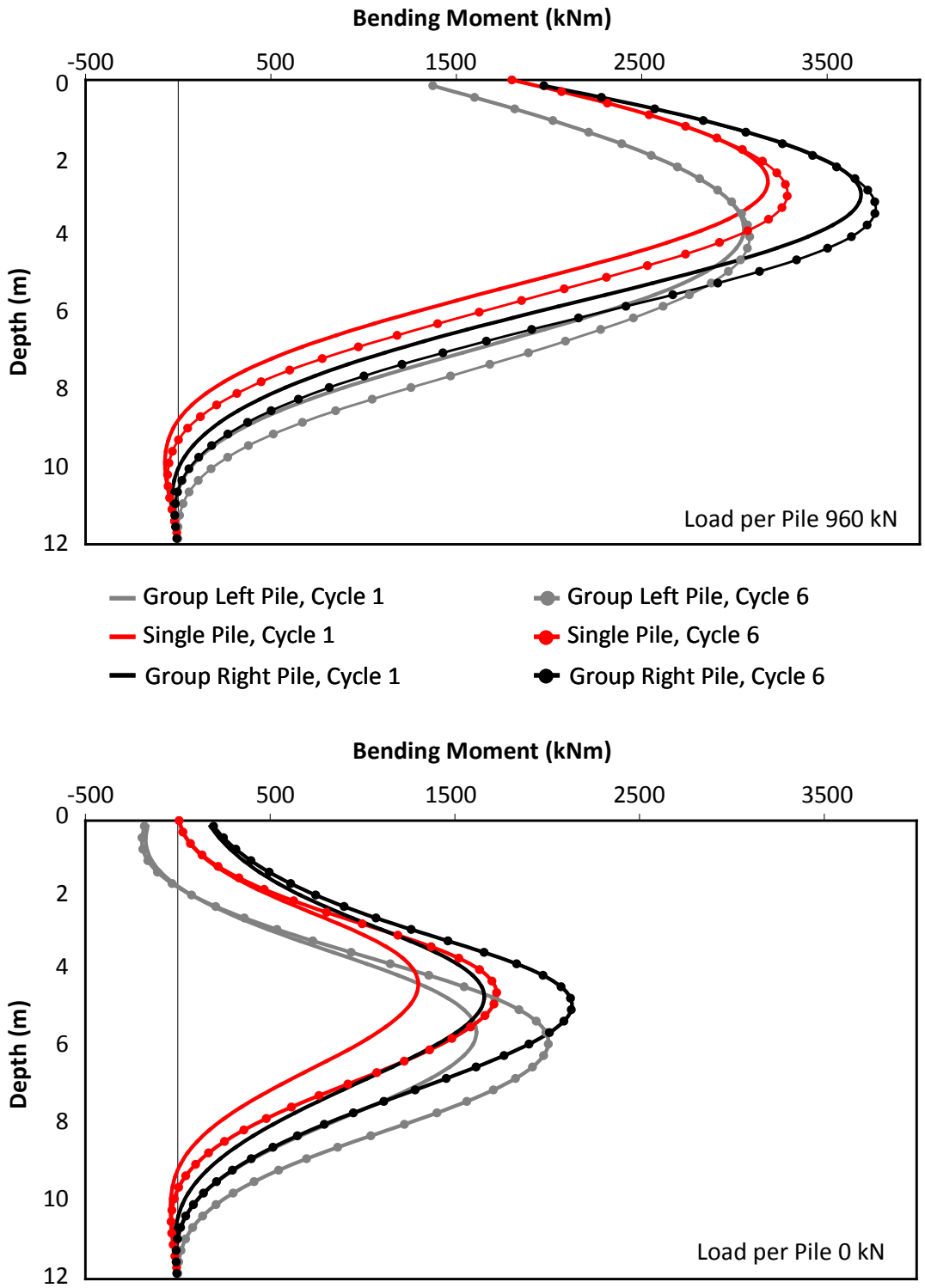

Σχήμα 15: Σύγκριση των κατανομών καμπτικών ροπών της πασσαλομάδας και του μεμονωμένου πασσάλου για το πείραμα P344: (α) στην φόρτιση του 1^{ου} και του 6^{ου} κύκλου για δύναμη 960 kN ανά πάσσαλο, και (β) στην αποφόρτιση του 1^{ου} και του 6^{ου} κύκλου για δύναμη 0 kN ανά πάσσαλο

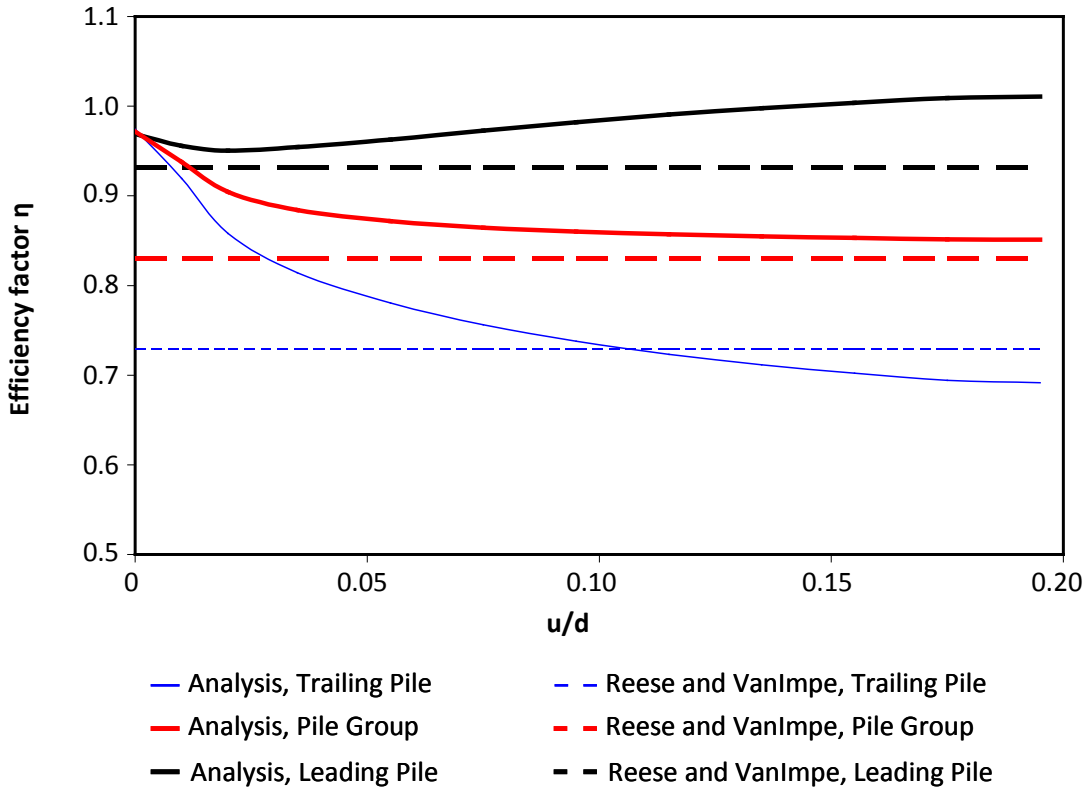

Σχήμα 16: Σύγκριση των συντελεστών αποδοτικότητας για 1x2 πασσαλομάδα υπό οριζόντια φορτίο σε ύψος 1.6 m από την επιφάνεια του εδάφους με τους αντίστοιχους των Reese and Van Impe (2001)

συναρτήσει της οριζόντιας μετατόπισης, όπως προκύπτουν από την ανάλυση με το προτεινόμενο καταστατικό προσομοίωμα και τους αντίστοιχους από τους Reese and Van Impe (2001). Οι ασυμπτωτικές τιμές των συντελεστών αποδοτικότητας από την αριθμητική ανάλυση είναι κοντά στις τιμές των Reese and Van Impe (2001) για μεγάλες μετατοπίσεις. Παρατηρείται μία διαφορά για τον συντελεστή αποδοτικότητας του πρώτου πασσάλου, ο οποίος αρχικά μειώνεται καθώς αυξάνεται η μετατόπιση, αλλά για πολύ μεγάλες μετατοπίσεις επανέρχεται στην αρχική (σχεδόν ελαστική) τιμή ($\eta_L \approx 1$). Η εν λόγω κράτυνση στην συμπεριφορά, αποδίδεται στο φαινόμενο της σταθεροποίησης της πλαστικής ενέργειας με μειούμενο ρυθμό (plastic shakedown response). Αντιθέτως, ο συντελεστής αποδοτικότητας του δεύτερου πασσάλου μειώνεται συνεχώς, εξαιτίας του φαινομένου της σκιάς, αλλά με μειούμενο ρυθμό εξαιτίας της κράτυνσης του συστήματος πασσαλομάδας-έδαφος, φτάνοντας σε μια ασυμπτωτική τιμή ($\eta_T \approx 0.7$). Ξεχωριστό ενδιαφέρον παρουσιάζει ότι όλοι οι συντελεστές αποδοτικότητας από την

αριθμητική ανάλυση για την ελαστική απόκριση είναι πολύ κοντά στο 1 (≈ 0.97), υπονοώντας ότι η αλληλεπίδραση πασσάλου-προς-πάσσαλο έχει αμελητέα επίδραση. Αυτό οφείλεται κυρίως στο γεγονός ότι το σημείο εφαρμογής της φόρτισης είναι ψηλότερα από την επιφάνεια του εδάφους, καθώς και ότι η σύνδεση των πασσάλων με τον κεφαλόδεσμο είναι αρθρωτή.

Προσομοίωση της Εγκάρσιας Απόκρισης Εύκαμπτου Πασσάλου με Μακρο-στοιχείο: Καμπύλες Αλληλεπίδρασης και Νόμος Πλαστικής Ροής – Αναλυτική Έκφραση, Αριθμητική και Πειραματική Επαλήθευση

Η προσομοίωση με μακρο-στοιχείο αποσκοπεί στην αναπαραγωγή της απόκρισης του συστήματος εδάφους-πασσάλου σε μακροσκοπικό επίπεδο με όρους δύναμεων−μετατοπίσεων γύρω από ένα σημείο αναφοράς (την κεφαλή του πασσάλου) και όχι σε επίπεδο εδαφικού στοιχείου. Σύμφωνα με τους Martin and Houlsby (2001) η μαθηματική διατύπωση του μακροστοιχείου (**Σχήμα 17**) απαιτεί αναλυτικές εκφράσεις:

- για την καμπύλη αλληλεπίδρασης του πασσάλου σε όρους αξονικής φόρτισης N, οριζόντιας φόρτισης Q, και ροπής M,
- για το ελαστικό μητρώο δυσκαμψίας,
- για τον νόμο πλαστικής ροής (plastic flow rule), και
- για τον νόμο κράτυνσης (hardening rule).

Εκφράσεις για το ελαστικό μητρώο δυσκαμψίας και τον νόμο κράτυνσης υπάρχουν στην βιβλιογραφία (πχ Gazetas, 1991; Gerolymos and Gazetas, 2005). Για τον λόγο αυτό, στην παρούσα διατριβή αναπτύχθηκαν αναλυτικές εκφράσεις καμπυλών αλληλεπίδρασης και κριτηρίου πλαστικής ροής για μεμονωμένο πάσσαλο. Σε αυτό το πλαίσιο, με αφετηρία την μέθοδο οριακής ισορροπίας του Broms (1964a,b, 1965) παράγονται κλειστού τύπου εκφράσεις για την καμπύλη αλληλεπίδρασης εύκαμπτου μεμονωμένου πασσάλου υπό συνδυασμένη φόρτιση Q–M στην κεφαλή του πασσάλου για διάφορους τύπους εδάφους. Η κεφαλή του πασσάλου συμπίπτει με την επιφάνεια του εδάφους και οι θεωρούμενες θετικές φορές για την φόρτιση και τις επακόλουθες μετακινήσεις ως προς το σημείο αναφοράς παρουσιάζονται στο **Σχήμα 18**. Συγκεκριμένα, παρουσιάζονται καμπύλες αλληλεπίδρασης για εύκαμπτο πάσσαλο σε:

(i) ομοιογενές συνεκτικό έδαφος

(ii) συνεκτικό έδαφος Gibson

(iii) μή-συνεκτικό έδαφος

(iv) δίστρωτο συνεκτικό έδαφος

(v) μή-συνεκτικό έδαφος με την κεφαλή του πασσάλου σε απόσταση e πάνω από την επιφάνεια του εδάφους

Οι καμπύλες αλληλεπίδρασης που προκύπτουν είναι κανονικοποιημένες ως προς τις "καθαρές" αντοχές του συστήματος πασσάλου-εδάφους, δηλαδή σε αποκλειστικώς οριζόντια φόρτιση και σε αποκλειστικώς επιβαλλόμενη ροπή, οι οποίες συμβολίζονται με τον δείκτη "y". Το μεγάλο πλεονέκτημα αυτής της κανονικοποίησης έγκειται στο γεγονός ότι η μορφή των καμπυλών αλληλεπίδρασης δεν επηρεάζεται από άλλες παραμέτρους αντοχής του εδάφους ή του πασσάλου. Οι αναλυτικές εκφράσεις για τις παραπάνω περιπτώσεις καταλήγουν σε μία γενική έκφραση για φόρτιση σε χώρο M-Q:

$$f = \left| \mathrm{sgn}(Q) \left| \frac{Q}{Q_y^*} \right|^B + \mathrm{sgn}(Q) A \left| \frac{Q}{Q_y^*} \right| + \mathrm{sgn}(M) \left| \frac{M}{M_y^*} \right| \right| - 1 = 0 \quad \text{για} \quad \left| \frac{M}{M_y} \right| < 1 \qquad (3)$$

και

$$f = \left| \frac{M}{M_y} \right| - 1 = 0 \quad \text{για} \quad \left| \frac{M}{M_y} \right| = 1 \qquad (4)$$

όπου A, B, Q_y^*, M_y^* σταθερές, ανάλογα με την περίπτωση που μελετάται δίνονται στον **Πίνακα 1**. Η μεθοδολογία αυτή δύναται να εφαρμοστεί και σε αλλές περιπτώσεις, όπως πάσσαλος σε τρίστρωτο σχηματισμό.

Πίνακας 1. Σταθερές καμπυλών αλληλεπίδρασης

Πάσσαλος σε:	A	B	Q_y*	M_y*
Ομοιογενές συνεκτικό έδαφος	0	2	$\left(2P_yM_y\right)^{\frac{1}{2}}$	M_y
Συνεκτικό έδαφος Gibson	0	3/2	$\left(\frac{45}{4}M_y^2a\gamma d\right)^{\frac{1}{3}}$	M_y
Μή-συνεκτικό έδαφος	0	3/2	$\left(\frac{27}{8}M_y^2k_p\gamma d\right)^{\frac{1}{3}}$	M_y
Δίστρωτο συνεκτικό έδαφος με $S_{u1} < S_{u2}$	$\frac{2b\left(P_{y2}-P_{y1}\right)}{\sqrt{2P_{y2}M_y\left(1-\frac{P_{y1}b^2\left(P_{y1}-P_{y2}\right)}{2P_{y2}M_y}\right)}}$	2	$\sqrt{2P_{y2}M_y\left(1-\frac{P_{y1}b^2\left(P_{y1}-P_{y2}\right)}{2P_{y2}M_y}\right)}$	$M_y\left(1-\frac{P_{y1}b^2\left(P_{y1}-P_{y2}\right)}{2P_{y2}M_y}\right)$
Μή-συνεκτικό έδαφος με την κεφαλή του πασσάλου σε απόσταση e πάνω από την επιφάνεια του εδάφους	$\frac{e\left(\frac{27}{8}k_p\gamma dM_y^2\right)^{\frac{1}{3}}}{M_y}$	3/2	$\left(\frac{27}{8}M_y^2k_p\gamma d\right)^{\frac{1}{3}}$	M_y

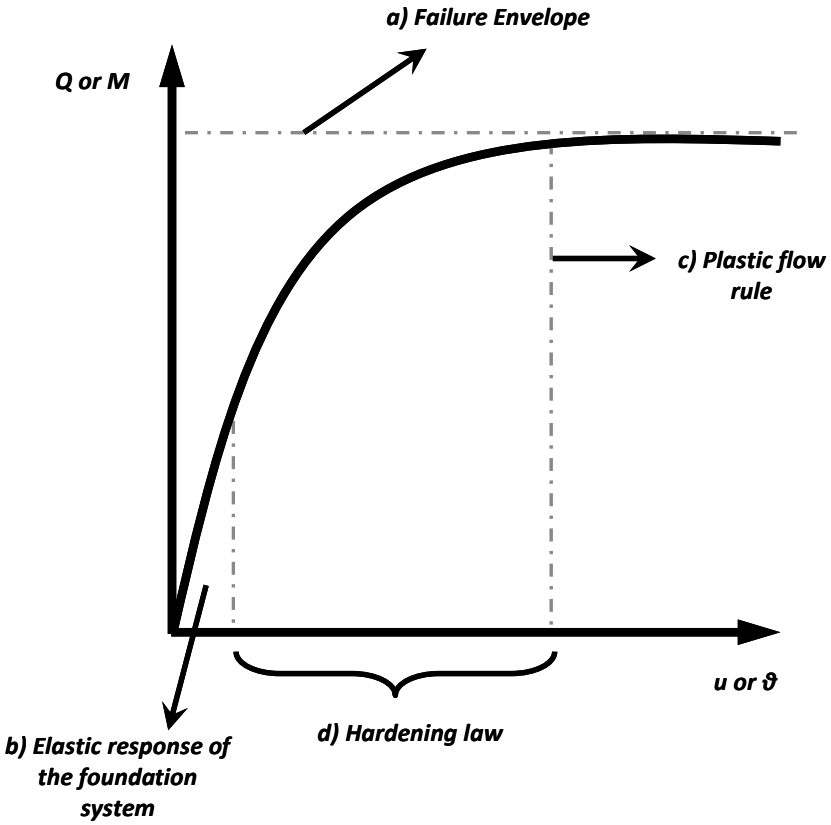

Σχήμα 17: Απαραίτητες εκφράσεις για την δημιουργία ενός μακροστοιχείου και η επιρροή τους στις καμπύλες δύναμης−μετατόπισης και ροπής−στροφής

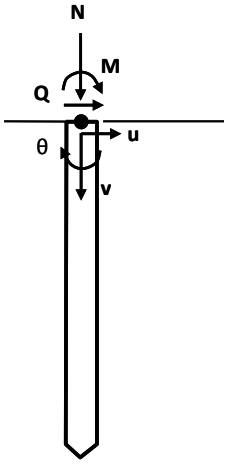

Σχήμα 18: Θετικές φορές φορτίων και μετατοπίσεων

Το **Σχήμα 19** παρουσιάζει την αδιαστατοποιημένη καμπύλη αλληλεπίδρασης για πάσσαλο σε ομοιογενές συνεκτικό έδαφος, η οποία είναι συμμετρική ως προς την αρχή των αξόνων Q/Q_y–M/M_y. Παρατηρείται ότι η μέγιστη ροπή ανατροπής στο σύστημα δεν μπορεί να υπερβεί την ροπή διαρροής του πασσάλου (M_{max} / M_y = 1), καθώς στην

“καθαρή” αντοχή σε επιβαλλόμενη ροπή του συστήματος συμβάλλει μόνον ο πάσσαλος. Όταν η ροπή ανατροπής είναι ομόσημη της οριζόντιας δύναμης, η αντοχή σε οριζόντια δύναμη είναι μικρότερη της “καθαρής” αντοχής σε οριζόντια φόρτιση ($Q / Q_y = 1$, $M / M_y = 0$), εξαιτίας της πρόσθετης δράσης της ροπής. Αντίθετα, όταν η ροπή ανατροπής είναι ετερόσημη με την οριζόντια δύναμη, η αντοχή σε οριζόντια φόρτιση αυξάνει εώς ότου ο πάσσαλος φθάσει στην ροπή διαρροής του, όπου και επιτυγχάνεται η μέγιστη οριζόντια φόρτιση στο σύστημα. Αυτό οφείλεται στο γεγονός ότι η ετερόσημη ροπή συμβάλλει στην αντίσταση του εδάφους στην οριζόντια φόρτιση. Για την περίπτωση ομοιογενούς συνεκτικού υλικού, η μέγιστη οριζόντια φόρτιση επιτυγχάνεται για $Q_{max} / Q_y = 2^{0.5}$.

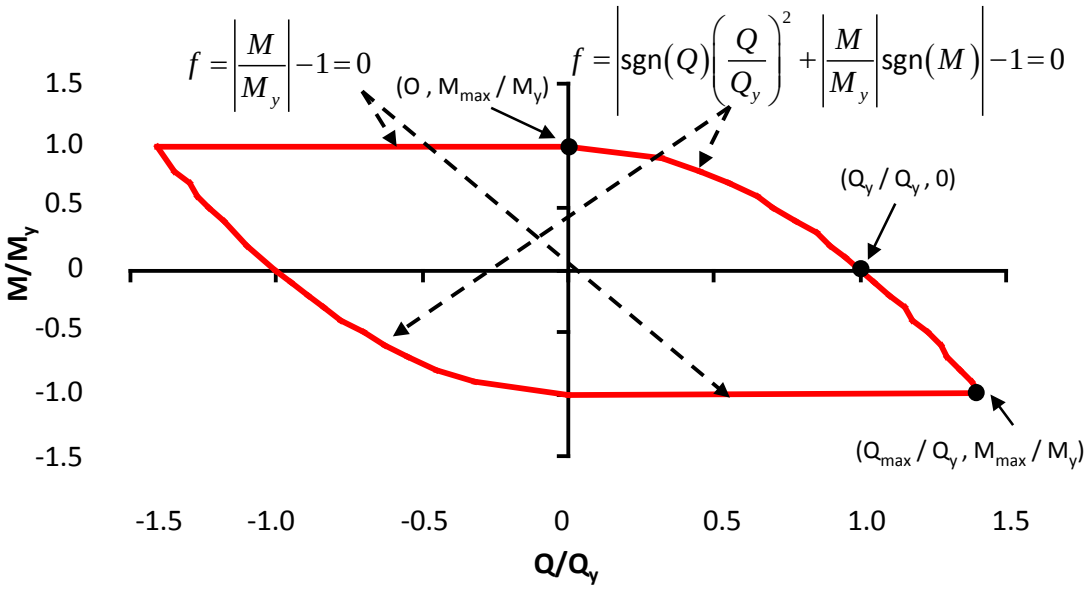

Σχήμα 19: Καμπύλη αλληλεπίδρασης πασσάλου σε ομοιογενές συνεκτικό έδαφος

Το δυναμικό πλαστικοποίησης (platic potential) εκφράζει την σχέση που έχουν οι μεταβολές (increments) των πλαστικών μετακινήσεων (v^{pl}, u^{pl}, θ^{pl}) κατά την στιγμή της αστοχίας σε άμεση συνάρτηση με την μεταβολή της επιφάνειας διαρροής του συστήματος της θεμελίωσης ως προς τα εντατικά μεγέθη M–Q–N. Με την θεώρηση συσχετισμένου νόμου πλαστικής ροής g = f, όπου η συνάρτηση του δυναμικού πλαστικοποίησης g συμπίπτει με την συνάρτηση διαρροής f, δηλαδή για άμεση συσχέτιση των πλαστικών παραμορφώσεων με την καμπύλη αλληλεπίδρασης, η έκφραση του νόμου πλαστικής ροής προκύπτει με παραγώγιση των αναλυτικών

εκφράσεων των καμπυλών αλληλεπίδρασης. Έτσι, ο συσχετισμένος νόμος πλαστικής ροής των μετακινήσεων εκφράζεται στην μορφή:

$$\begin{Bmatrix} \partial u^{pl} \\ \partial \theta^{pl} \end{Bmatrix} = \lambda \begin{Bmatrix} \dfrac{\partial f}{\partial Q} \\ \dfrac{\partial f}{\partial M} \end{Bmatrix} \tag{5}$$

όπου λ ένας μή αρνητικός συντελεστής, ο οποίος δηλώνει το μέγεθος που έχουν οι πλαστική μετακίνηση και στροφή κατά την αστοχία. Οι εκφράσεις που προκύπτουν για τον νόμο πλαστικής ροής στο χώρο Q–M είναι ανεξάρτητες της επιβαλλόμενης ροπής M στον πάσσαλο. Λόγω του συσχετισμένου νόμου πλαστικής ροής, το διάνυσμα των πλαστικών μετατοπίσεων που αρχίζει στην καμπύλη διαρροής και έχει κλίση τον λόγο των πλαστικών μετατοπίσεων προς τις στροφές (δu/δθ) είναι κάθετο στην καμπύλη αλληλεπίδρασης σε αυτό το σημείο.

Επιπλέον, λόγω της συνθήκης της καθετότητας, στα σημεία της μέγιστης ροπής M_{max} ο λόγος της πλαστικής μετατόπισης προς τη στροφή είναι 0, αφού στην κεφαλή του πασσάλου υπάρχει μόνον στροφή, δηλαδή:

$$\frac{\partial f}{\partial Q} = 0 \rightarrow \frac{\partial u^{pl}}{\partial \theta^{pl}} = 0 \qquad \text{για} \qquad \left| \frac{M}{M_y} \right| = 1 \tag{6}$$

Αντίθετα, στο σημείο της μέγιστης οριζόντιας δύναμης Q_{max} εκτός από μετατόπιση υπάρχει και στροφή στην κεφαλή του πασσάλου, αφού εξετάζεται εύκαμπτος πάσσαλος και δεν αστοχεί μόνον το έδαφος.

Η ορθότητα των αναλυτικών εκφράσεων των καμπυλών αλληλεπίδρασης και του κριτηρίου πλαστικής ροής επαληθεύονται με αναλύσεις επιβολής δύναμης σε ελαστοπλαστικό προσομοίωμα δοκού σε ελατηριωτό έδαφος τύπου Winkler και σε πλήρως τρισδιάστατο προσομοίωμα πεπερασμένων στοιχείων. Κάθε ανάλυση ακολουθεί μία συγκεκριμένη διαδρομή φόρτισης στην κεφαλή του πασσάλου έως την αστοχία στον χώρο Q–M. Εκτός από την επαλήθευση της μορφής της καμπύλης αλληλεπίδρασης, από τις αναλύσεις λαμβάνονται και οι επαυξητικές μετατοπίσεις κατά την αστοχία. Έτσι ελέγχεται και η εγκυρότητα του συσχετισμένου νόμου πλαστικής ροής.

Η αναλυτική έκφραση της κάθε χαρακτηριστικής περίπτωσης ελέγχεται ξεχωριστά με ένα προσομοίωμα δοκού σε ελατηριωτό έδαφος τύπου Winkler μέσω ενός χαρακτηριστικού παραδείγματος. Το προσομοίωμα δοκού επί ελατηριωτού εδάφους

Winkler δημιουργείται σε κώδικα πεπερασμένων σημείων. Χρησιμοποιούνται δε δισδιάστατα στοιχεία δοκού για τον πάσσαλο με διγραμμική σχέση ροπής−καμπυλότητας και ελαστοπλαστικά ελατήρια για το έδαφος (**Σχήμα 20**).

Αρχικώς, ελέγχεται η ευαισθησία του προσομοιώματος στην πυκνότητα του καννάβου (κατακόρυφη απόσταση των ελατηρίων). Το **Σχήμα 21** παρουσιάζει την σύγκριση της κανονικοποιημένης καμπύλης αλληλεπίδρασης για πάσσαλο σε ομοιογενές συνεκτικό έδαφος από την αναλυτική έκφραση με τα αποτελέσματα των αριθμητικών αναλύσεων με απόσταση ελατηρίων 1 m, 0.25 m και 0.1 m. Παρατηρείται ότι για αδρό κάνναβο τα αποτελέσματα δίνουν υπεραντοχή του συστήματος για το τμήμα της καμπύλης αλληλεπίδρασης όπου η ροπή υπερισχύει στην απόκριση της οριζόντιας δύναμης, ενώ είναι ετερόσημες. Αντίθετα, για πυκνό κάνναβο οι αριθμητικές αναλύσεις επιβεβαιώνουν πλήρως την αναλυτική καμπύλη αλληλεπίδρασης, αποδεικνύοντας ότι για το εξεταζόμενο πρόβλημα η μεγάλη διακριτοποίηση είναι απαραίτητη. Επιπλέον, παραμετρική διερεύνηση έδειξε ότι η μορφή της καμπύλης αλληλεπίδρασης είναι ανεξάρτητη ορισμένων χαρακτηριστικών παραμέτρων αντοχής του συστήματος πασσάλου-εδάφους, όπως η διάμετρος του πασσάλου, το μέτρο ελαστικότητας του εδάφους, και η αστράγγιστη διατμητική του αντοχή.

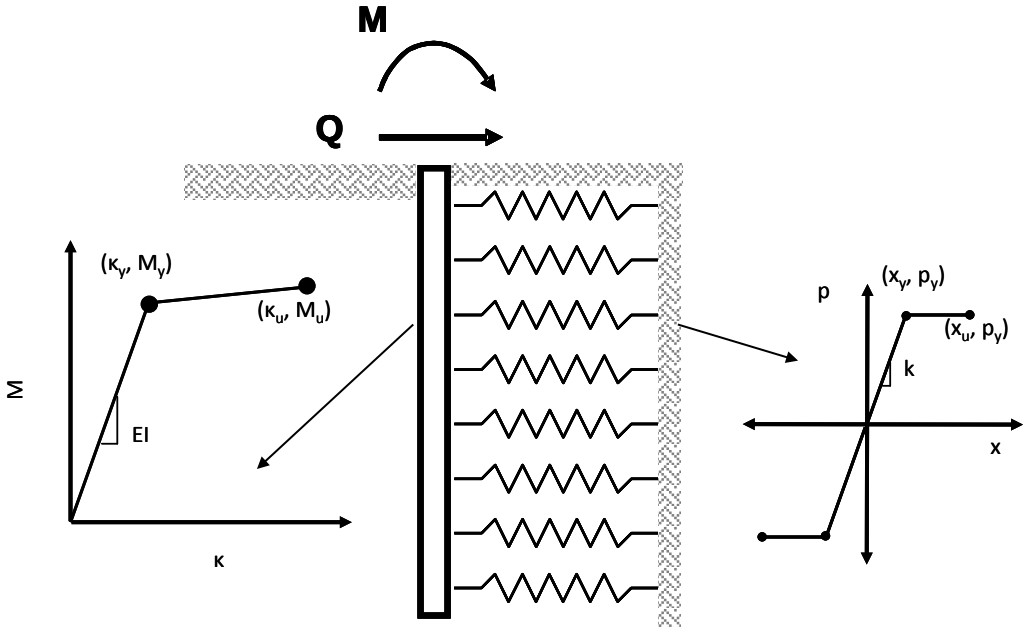

Σχήμα 20: Προσομοίωμα δοκού σε ελατηριωτό έδαφος τύπου Winkler, σχέση ροπής−καμπυλότητας και σχέση εδαφικής αντίδρασης-μετατόπισης

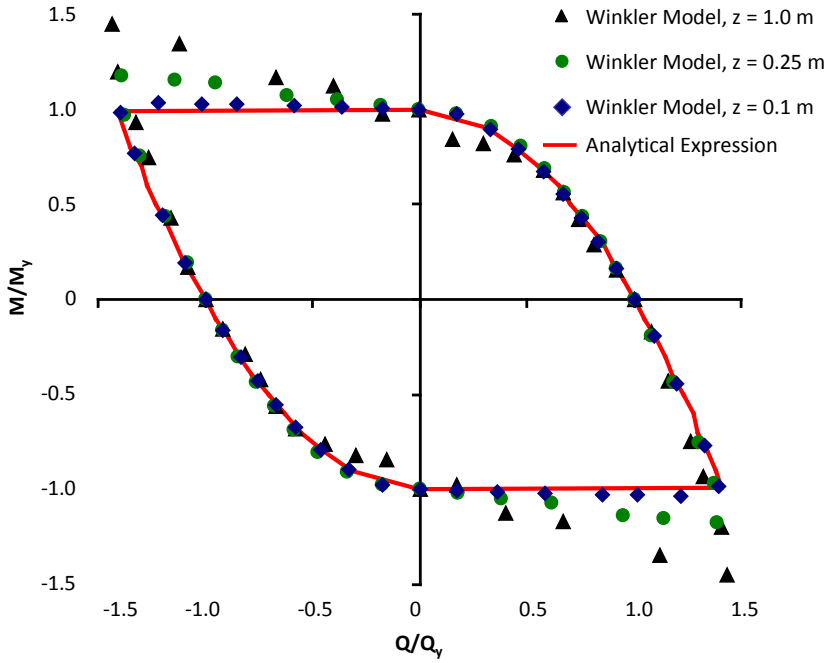

Σχήμα 21: Επίδραση της πυκνότητας του καννάβου των ελατηρίων Winkler στην καμπύλη αλληλεπίδρασης για πάσσαλο σε ομοιογενές συνεκτικό έδαφος

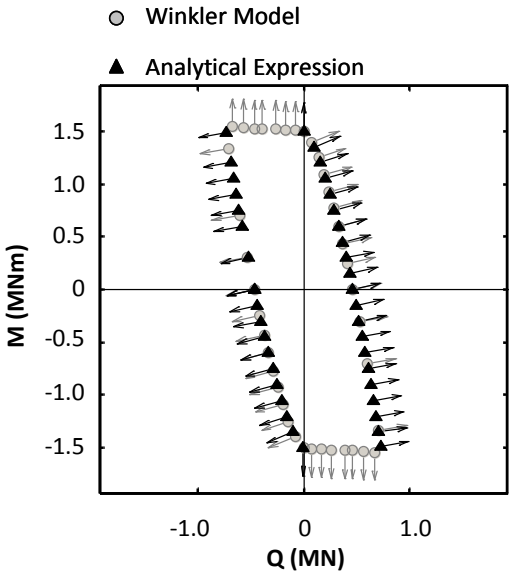

Σχήμα 22: Διανύσματα των μεταβολών των πλαστικών εγκάρσιων μετακινήσεων και στροφών από την αναλυτική έκφραση με την θεώρηση συσχετισμένου νόμου πλαστικής ροής για πάσσαλο σε συνεκτικό έδαφος τύπου Gibson και σύγκριση με τα αποτελέσματα από τις αριθμητικές αναλύσεις κατά την αστοχία

Τα διανύσματα των μεταβολών των πλαστικών εγκαρσίων μετακινήσεων δu^{pl} και στροφών $\delta\theta^{pl}$ από την αναλυτική έκφραση με την θεώρηση συσχετισμένου νόμου πλαστικής ροής για πάσσαλο σε συνεκτικό έδαφος τύπου Gibson και αυτά από τις αριθμητικές αναλύσεις κατά την αστοχία δείχνονται στο **Σχήμα 22**. Τα διανύσματα καί των δύο προσεγγίσεων είναι γραφικώς ίδια και επιπλέον κάθετα στην καμπύλη αλληλεπίδρασης στον μή-κανονικοποιημένο χώρο Q–M. Συνεπώς, η γνώση της αναλυτικής έκφρασης της καμπύλης αλληλεπίδρασης είναι αρκετή για τον προσδιορισμό του νόμου πλαστικής ροής.

Η φυσική σημασία της ισχύος του συσχετισμένου νόμου πλαστικής ροής είναι ότι ο πάσσαλος μετά την αστοχία συμπεριφέρεται ως ένα άκαμπτο στερεό σώμα και άρα το βάθος της πλαστικής άρθρωσης δίδεται από τον λόγο της πλαστικής εγκάρσιας μετακίνησης προς την στροφή. Ορίζοντας ως β την γωνία των ζευγών ροπής οριζόντιας δύναμης QM στην αστοχία, με $\beta = 0^o$ το σημείο $Q = Q_y$ και M = 0 (καθαρή αντοχή σε οριζόντια δύναμη) και πηγαίνοντας αριστερόστροφα στον χώρο $Q/Q_y – M/M_y$, το **Σχήμα 23** απεικονίζει την μεταβολή του λόγου της πλαστικής εγκάρσιας μετακίνησης προς την στροφή στην αστοχία για διάφορα ζεύγη QM και το αντίστοιχο βάθος της πλαστικής άρθρωσης για τα ίδια σημεία. Είναι εμφανές ότι εκτός από τις περιοχές με $\left|M / M_y\right| = 1$ (δηλαδή για $\beta = 90^o - 145^o$ και $\beta = 270^o - 325^o$), όπου η δομητική αστοχία του πασσάλου εκδηλώνεται στην κεφαλή του, ο λόγος της μετακίνησης προς την στροφή συμπίπτει με το βάθος της πλαστικής άρθρωσης.

Το προσομοίωμα δοκού σε ελατηριωτό έδαφος τύπου Winkler χρησιμοποιείται ευρέως για την προσομοίωση μεμονωμένων πασσάλων, αλλά δεν λαμβάνει υπόψιν την πλήρη φυσική του προβλήματος, όπως η γεωμετρική μή-γραμμικότητα. Έτσι, οι αναλυτικές εκφράσεις των καμπυλών αλληλεπίδρασης και του συσχετισμένου νόμου πλαστικής ροής εξετάζονται περαιτέρω με τρισδιάστατες αριθμητικές αναλύσεις πεπερασμένων στοιχείων με την χρήση διαφορετικών καταστατικών προσομοιωμάτων (συμπεριλαμβανομένου και του προτεινομένου) χωρίς συσχετισμένο νόμο πλαστικής ροής, τα οποία προσομοιώνουν καλύτερα την μή γραμμική συμπεριφορά του εδαφικού υλικού. Αποδεικνύεται ότι η μακροσκοπική συμπεριφορά του συστήματος εδάφους-θεμελίωσης δεν επηρεάζεται από τα χαρακτηριστικά του καταστατικού προσομοιώματος των αναλύσεων.

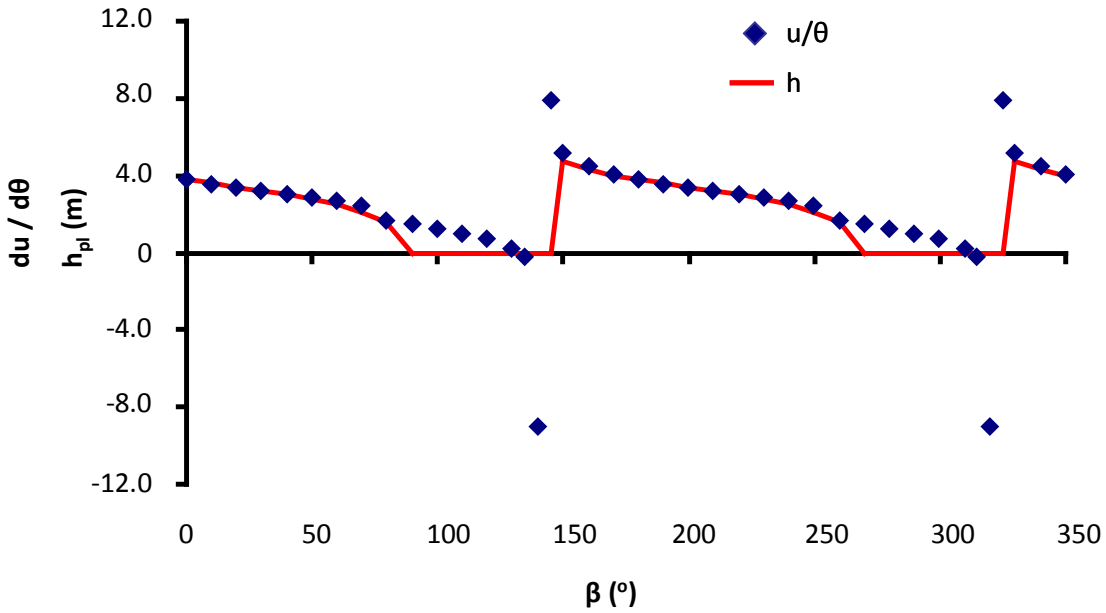

Σχήμα 23: Σύγκριση της μεταβολής του λόγου της πλαστικής εγκάρσιας μετακίνησης προς την στροφή στην αστοχία για διάφορα ζεύγη QM και του αντιστοίχου βάθους της πλαστικής άρθρωσης για τα ίδια σημεία

Επίσης, εξετάζεται η επιρροή της ύπαρξης ή όχι γεωμετρικών μή-γραμμικοτήτων. Τα ζεύγη ροπής M και οριζόντιας δύναμης Q στην αστοχία, κανονικοποιημένα με τις "καθαρές" αντοχές σε ροπή M_y και οριζόντια δύναμη Q_y από τις τρισδιάστατες αριθμητικές αναλύσεις, για πάσσαλο σε ομοιογενές συνεκτικό έδαφος μέ ή χωρίς την ύπαρξη κενού δίδονται στο **Σχήμα 24**. Τα αποτελέσματα των τρισδιάστατων αναλύσεων επαληθεύουν ξανά την αναλυτική έκφραση της καμπύλης αλληλεπίδρασης. Μια μικρή υπεραντοχή παρατηρείται όταν η ροπή στην κεφαλή του πασσάλου είναι ετερόσημη της οριζόντιας δύναμης στο τμήμα όπου η ροπή υπερισχύει της οριζόντιας δύναμης. Αυτή η διαφορά οφείλεται στην πυκνότητα του καννάβου στην κατακόρυφη διεύθυνση (στο συγκεκριμένο προσομοίωμα είναι 0.3 m αντί 0.1 m του ελατηριωτού προσομοιώματος). Η ολίσθηση και η αποκόλληση του εδάφους στον πάσσαλο δεν επηρεάζει την μορφή της *κανονικοποιημένης* καμπύλης αλληλεπίδρασης.

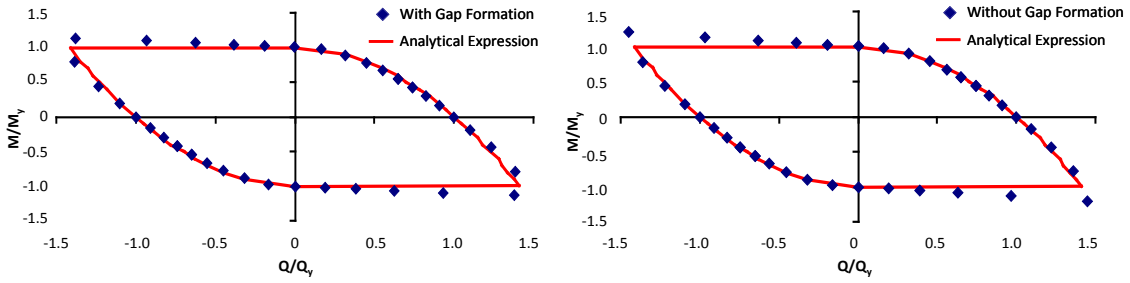

Σχήμα 24: Σύγκριση των αποτελεσμάτων από τις τρισδιάστατες αριθμητικές αναλύσεις (α) με την ύπαρξη κενού, και (β) χωρίς την ύπαρξη κενού με την καμπύλη αλληλεπίδρασης από την αναλυτική έκφραση για πάσσαλο σε ομοιογενές συνεκτικό έδαφος.

Μελετώντας τους μηχανισμούς αστοχίας του πασσάλου διακρίνονται χαρακτηριστικές ζώνες στην καμπύλη αλληλεπίδρασης. Εξαιτίας της συμμετρίας μόνον η μισή καμπύλη αλληλεπίδρασης παρουσιάζεται στο **Σχήμα 25**. Διακρίνονται:

1. Ζώνη ομόσημης M–Q φόρτισης, όπου η ροπή υπερισχύει στην απόκριση του συστήματος. Ο πάσσαλος υπόκειται σε μικρή οριζόντια μετατόπιση και μεγάλη ομόσημη στροφή. Η πλαστική άρθρωση αναπτύσσεται κοντά στην κεφαλή του πασσάλου.
2. Ζώνη ομόσημης M–Q φόρτισης, όπου η οριζόντια δύναμη υπερισχύει στην απόκριση του συστήματος. Ο πάσσαλος υπόκειται σε μεγάλη οριζόντια μετατόπιση και μικρή ομόσημη στροφή. Η πλαστική άρθρωση αναπτύσσεται σε βάθος, κατανεμημένη σε αρκετό μήκος του πασσάλου.
3. Ζώνη ετερόσημης M–Q φόρτισης, όπου η οριζόντια δύναμη υπερισχύει στην απόκριση του συστήματος. Ο πάσσαλος υπόκειται σε μεγάλη οριζόντια μετατόπιση και μικρή ομόσημη στροφή. Η πλαστική άρθρωση αναπτύσσεται ακόμα βαθύτερα κατά μήκος του πασσάλου, αφού η ετερόσημη ροπή αυξάνει την αντίσταση του συστήματος.
4. Ζώνη ετερόσημης M–Q φόρτισης, όπου η ροπή ανατροπής υπερισχύει στην απόκριση του συστήματος. Ο πάσσαλος υπόκειται μόνον σε ετερόσημη στροφή ως προς την κατεύθυνση της δύναμης. Η πλαστική άρθρωση αναπτύσσεται στην κεφαλή του πασσάλου.

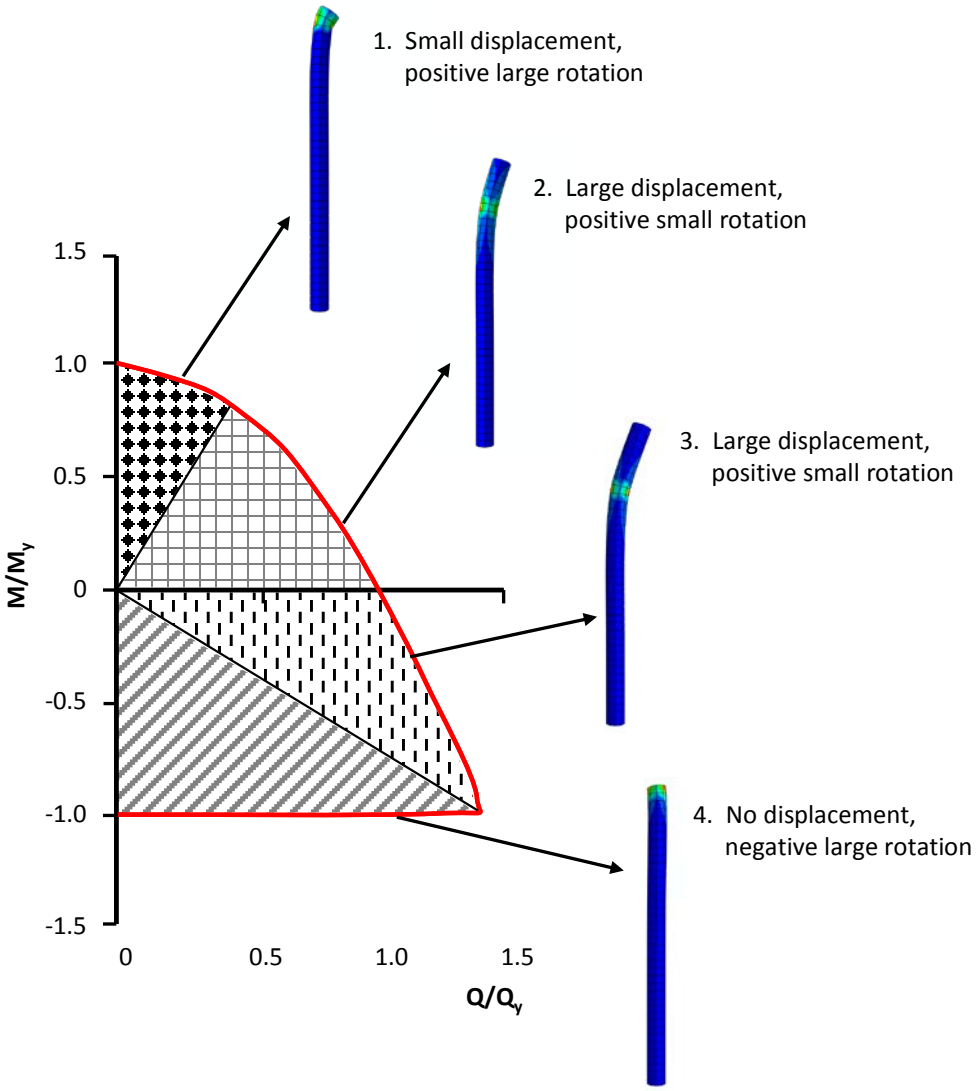

Σχήμα 25: Επίδραση της φόρτισης στην απόκριση του πασσάλου

Το **Σχήμα 26** απεικονίζει τα διανύσματα από την αναλυτική έκφραση με την θεώρηση συσχετισμένου νόμου πλαστικής ροής με τα διανύσματα μετατοπίσεων και στροφών κατά την αστοχία από τις τρισδιάστατες αναλύσεις (α) με την ύπαρξη κενού, και (β) χωρίς την ύπαρξη κενού για πάσσαλο σε ομοιογενές συνεκτικό έδαφος. Είναι εμφανές ότι τα διανύσματα των αριθμητικών αναλύσεων είναι κάθετα στην καμπύλη αλληλεπίδρασης στον χώρο Q–M. Επιπλέον, παρατηρείται ότι η "καθαρή" αντοχή του πασσάλου σε ροπή με τις τρισδιάστατες αναλύσεις είναι ίδια με της αναλυτικής έκφρασης. Στις τρισδιάστατες αναλύσεις χωρίς την ύπαρξη κενού, η "καθαρή" αντοχή του συστήματος σε οριζόντια φόρτιση είναι μεγαλύτερη από της αναλυτικής έκφρασης. Αντίθετα, η "καθαρή" αντοχή του συστήματος σε οριζόντια φόρτιση από τις τρισδιάστατες αναλύσεις με την ύπαρξη κενού είναι περίπου 0.7 φορές επί την

αντίστοιχη από τις τρισδιάστατες αναλύσεις χωρίς κενό. Αυτό είναι αναμενόμενο αποτέλεσμα, αφού η εδαφική αντίσταση p_y μειώνεται με την ύπαρξη του κενού και η "καθαρή" αντοχή του συστήματος σε οριζόντια φόρτιση είναι συνάρτηση της τετραγωνικής ρίζας της εδαφικής αντίστασης. Όμως, παρά την διαφορά στην "καθαρή" αντοχή του συστήματος σε οριζόντια φόρτιση, η μορφή της καμπύλης αλληλεπίδρασης παραμένει αμετάβλητη, κατά συνέπειαν ανεπηρέαστη από την ύπαρξη γεωμετρικών μή-γραμμικοτήτων.

Οι καμπύλες αλληλεπίδρασης που αναπτύχθηκαν έως εδώ δεν λαμβάνουν υπόψιν τους την επίδραση του κατακορύφου φορτίου, όπως συμβαίνει στην πράξη σήμερα. Για τον λόγο αυτό, εξετάζεται με τρισδιάστατες αριθμητικές αναλύσεις η επίδραση του κατακορύφου φορτίου στις καμπύλες αλληλεπίδρασης. Αρχικώς, προσδιορίζονται οι "καθαρές" αντοχές του πασσάλου σε κατακόρυφο φορτίο N_y, οριζόντιο φορτίο Q_y και ροπή ανατροπής M_y. Εν συνεχεία, ένα σταθερό κατακόρυφο φορτίο (ποσοστό της "καθαρής" αντοχής N_y) ασκείται συνεχώς στην κεφαλή του πασσάλου και λαμβάνονται οι καμπύλες αλληλεπίδρασης Q−M για το φορτίο αυτό. Η διαδικασία αυτή πραγματοποιήθηκε για τέσσερες τιμές κατακόρυφου φορτίου: 0, $0.25N_y$, $0.5N_y$ και $0.75N_y$. Οι καμπύλες αλληλεπίδρασης που προέκυψαν είναι ίδιες μεταξύ τους, ανεξάρτητες του κατακόρυφου φορτίου. Με βάση τις τρισδιάστατες αναλύσεις προτείνεται μια πλήρης καμπύλη αλληλεπίδρασης σε αξονική φόρτιση N, οριζόντια φόρτιση Q και καμπτική ροπή M, χωρίς να λαμβάνεται υπόψιν το κριτήριο διαρροής του υλικού του πασσάλου (**Σχήμα 27**).

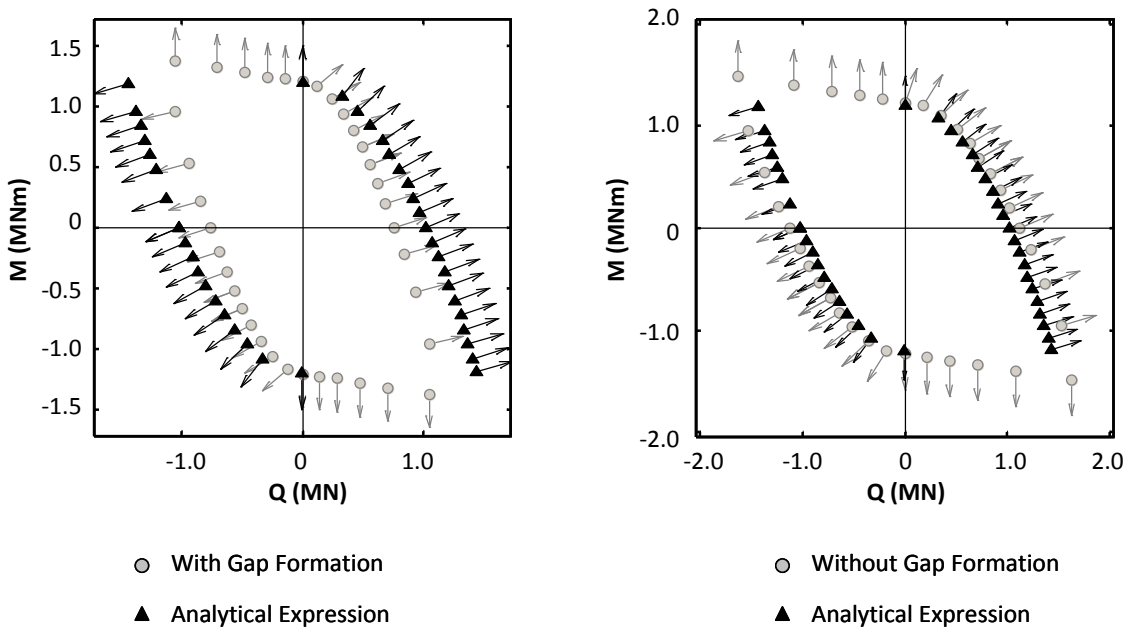

Σχήμα 26: Διανύσματα των μεταβολών των πλαστικών εγκάρσιων μετακινήσεων και στροφών από την αναλυτική έκφραση με την θεώρηση συσχετισμένου νόμου πλαστικής ροής για πάσσαλο σε ομοιγενές συνεκτικό έδαφος και σύγκριση με τα αποτελέσματα από τις αριθμητικές αναλύσεις (α) με την ύπαρξη κενού, και (β) χωρίς την ύπαρξη κενού

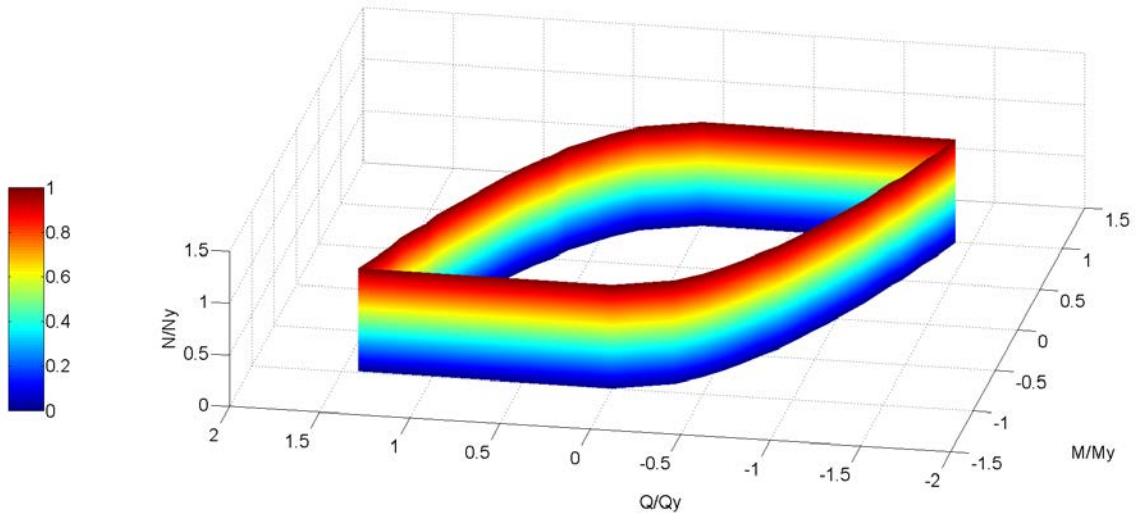

Σχήμα 27: Προτεινόμενη καμπύλη αλληλεπίδρασης για μεμονωμένο πάσσαλο σε ομοιογενές συνεκτικό έδαφος στον τρισδιάστατο χώρο $M/M_y-Q/Q_y-N/N_y$

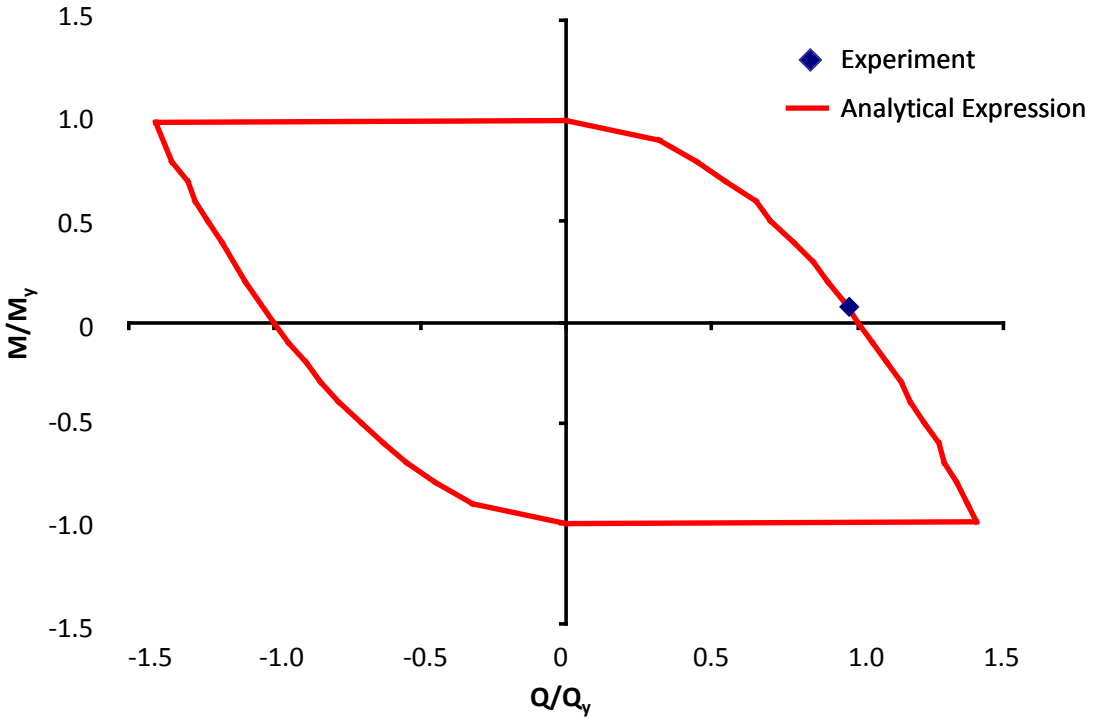

Σχήμα 28: Σύγκριση του αποτελέσματος πειράματος σε φυσική κλίμακα με την καμπύλη αλληλεπίδρασης από την αναλυτική έκφραση

Το αποτέλεσμα μιας δοκιμής φυσικής κλίμακας πασσάλου υπό ορίζόντια φόρτιση, μήκους L = 25 m, διαμέτρου = 0.8 m, και ροπή διαρροής M_{pl} = 800 kNm σε μαλακή άργιλο (Gerolymos, 2013) δίνει ένα σημείο στην καμπύλη αλληλεπίδρασης. Η φόρτιση ασκήθηκε σε ύψος 19 cm από την επιφάνεια του εδάφους και το σημείο αστοχίας σε σχέση με την καμπύλη αλληλεπίδρασης απεικονίζεται στο **Σχήμα 28**.

Για τον ύπαρξη πολλών σημείων αστοχίας στην καμπύλη αλληλεπίδρασης διεξήχθη μία σειρά πειραμάτων μονοτονικώς φορτιζομένων μεμονωμένων πασσάλων σε ξηρή άμμο υπό ροπή και οριζόντια δύναμη έως την αστοχία (Push-over Tests) στο Εργαστήριο Δυναμικής / Εδαφομηχανικής του Εθνικού Μετσοβίου Πολυτεχνείου. Σκοπός της πειραματικής σειράς είναι η πρακτική επαλήθευση της καμπύλης αλληλεπίδρασης Q–M και του συσχετισμένου νόμου πλαστικής ροής μεμονωμένων πασσάλων σε αμμώδες υλικό. Αρχικώς, πραγματοποιήθηκαν πειράματα προκειμένου να εκτιμηθεί η επίδραση παραγόντων όπως η διάμετρος του πασσάλου, η διεπιφάνεια πασσάλου-εδάφους, η πυκνότητα του εδάφους και η θέση του πασσάλου στο κιβώτιο της άμμου:

- Η μέγιστη εδαφική αντίδραση προέκυψε μεγαλύτερη από αυτή που υπολογίζεται με τη μέθοδο Broms με γωνία τριβής της άμμου ίση με αυτήν της κρίσιμης κατάστασης. Δεδόμένου ότι η καμπύλη αλληλεπίδρασης είναι κανονικοποιημένη αυτή η διαφορά εξαλείφεται.
- Τα βάθος της πλαστικής άρθρωσης από την επιφάνεια του εδάφους, καθώς και η εδαφική αντίδραση αυξάνονται με την διάμετρο του πασσάλου.
- Η εδαφική αντίδραση αυξάνεται με την αύξηση της εδαφικής πυκνότητας από D_r = 45% (χαλαρή κατάσταση) σε D_r = 94% (πυκνή κατάσταση). Σημειώνεται ότι, μετά το μέγιστο φορτίο στην πυκνή άμμο, η απόκριση του συστήματος παρουσιάζει χαλάρωση.
- Η θέση του πασσάλου στο κουτί της άμμου, για τις ίδιες πειραματικές συνθήκες, δεν επηρεάζει την απόκριση του πασσάλου σε όρους δυσκαμψίας και "καθαρής" αντοχής σε οριζόντια φόρτιση.
- Εξετάστηκαν τρεις διαφορετικές διεπιφάνειες πασσάλου-εδάφους: (1) χωρίς τεχνητή διεπιφάνεια, (2) με τεχνητή τραχεία διεπιφάνεια από κόλλα και άμμο, και (3) με πολύ τραχεία διεπιφάνεια από γυαλόχαρτο (N 120). Χωρίς την τεχνητή διεπιφάνεια, το έμβολο ολισθαίνει πάνω στην επιφάνεια του πασσάλου με αποτέλεσμα να αλλάζει συνεχώς το σημείο εφαρμογής του φορτίου. Η διαφορά στην απόκριση του πασσάλου με τις δυο άλλες διεπιφάνειες είναι ελάχιστη.

Τελικώς, για τα πειράματα επιλέχθηκε σωληνοειδής πάσσαλος από αλουμίνιο 6063 – F25 με διάμετρο 30x28 mm, με τεχνητή τραχεία διεπιφάνεια από κόλλα και άμμο, σε 60 cm πυκνής άμμου (D_r = 94%), τοποθετημένος στο κέντρο του κιβωτίου της άμμου. Η μονοτονική οριζόντια φόρτιση ασκείται είτε στην κεφαλή του πασσάλου (στην επιφάνεια του εδάφους) είτε σε συγκεκριμένο ύψος πάνω από την επιφάνεια του εδάφους, ώστε να μεταβιβάζεται και ροπή στην κεφαλή του πασσάλου. Σε κάθε πάσσαλο τοποθετούνται μετακινησιόμετρα. Μία χαρακτηριστική τελική διάταξη πειράματος δίδεται στο **Σχήμα 29**.

Σχήμα 29: Τελική διάταξη πειράματος

Συνολικά πραγματοποιήθηκαν δέκα πειράματα: ένα υπό καθαρή οριζόντια δύναμη, ένα υπό καθαρή ροπή, πέντε υπό διαφορετικές ομόσημες φορτίσεις, ένα για έλεγχο της επαναληψιμότητας των πειραμάτων και δυο υπό ετερόσημη φόρτιση. Το **Σχήμα 30** παρουσιάζει την κανονικοποιημένη καμπύλη αλληλεπίδρασης από την αναλυτική έκφραση και τα πειραματικά αποτελέσματα. Παρά την μικρή κλίμακα του πειράματος, η *κανονικοποιημένη* καμπύλη αλληλεπίδρασης επαληθεύεται ικανοποιητικά. Το κόκκινο τρίγωνο στο σχήμα αντιστοιχεί στο πείραμα για τον έλεγχο της επαναληψιμότητας και ενισχύει την σημασία των αποτελεσμάτων.

Το **Σχήμα 31** απεικονίζει τα διανύσματα του λόγου μετακίνησης προς στροφή από την αναλυτική έκφραση με την θεώρηση συσχετισμένου νόμου πλαστικής ροής με τα αποτελέσματα των πειραμάτων. Η κάμψη του πασσάλου δεν επέτρεψε την μέτρηση αυτών των δεδομένων για τις ετερόσημες φορτίσεις. Παρόλα αυτά, για τις ομόσημες φορτίσεις είναι προφανές ότι η θεώρηση της καθετότητας είναι δικαιολογημένη.

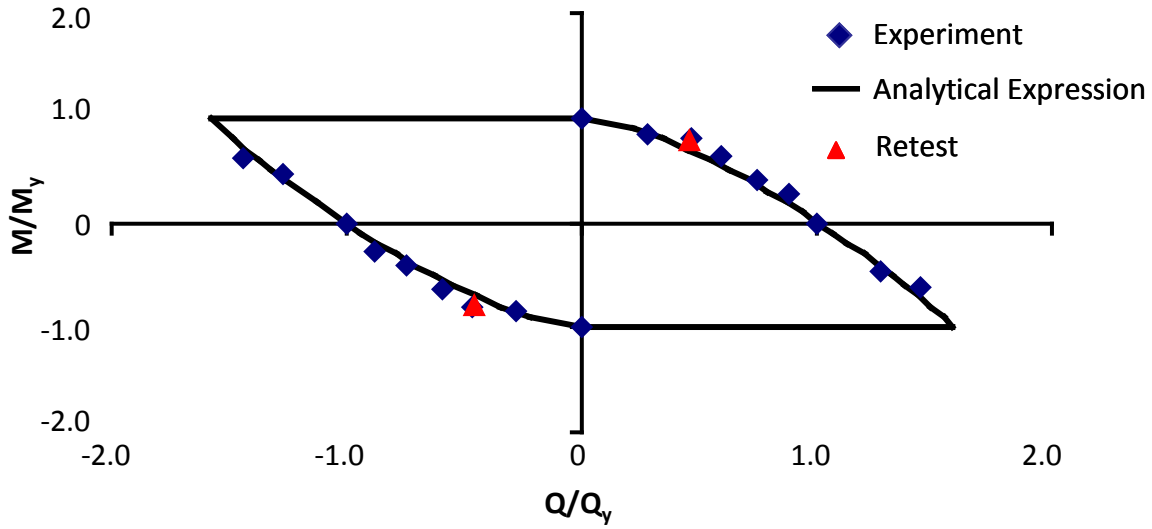

Σχήμα 30: Σύγκριση των πειραματικών αποτελεσμάτων με την καμπύλη αλληλεπίδρασης από την αναλυτική έκφραση για πάσσαλο σε μή-συνεκτικό έδαφος.

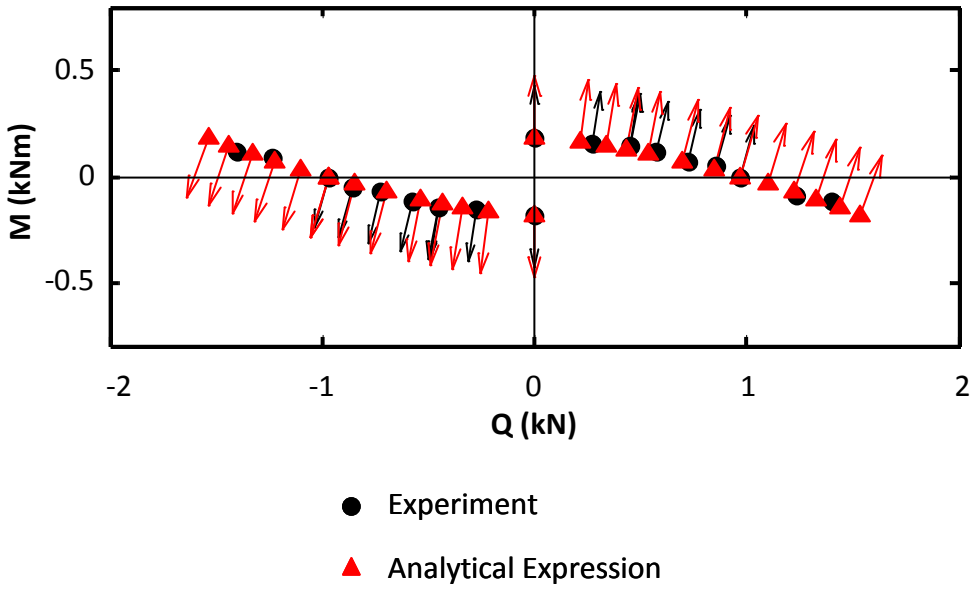

Σχήμα 31: Διανύσματα των μεταβολών των πλαστικών εγκάρσιων μετακινήσεων και στροφών από την αναλυτική έκφραση με την θεώρηση συσχετισμένου νόμου πλαστικής ροής για πάσσαλο σε μή-συνεκτικό έδαφος και σύγκριση με τα πειραματικά αποτελέσματα

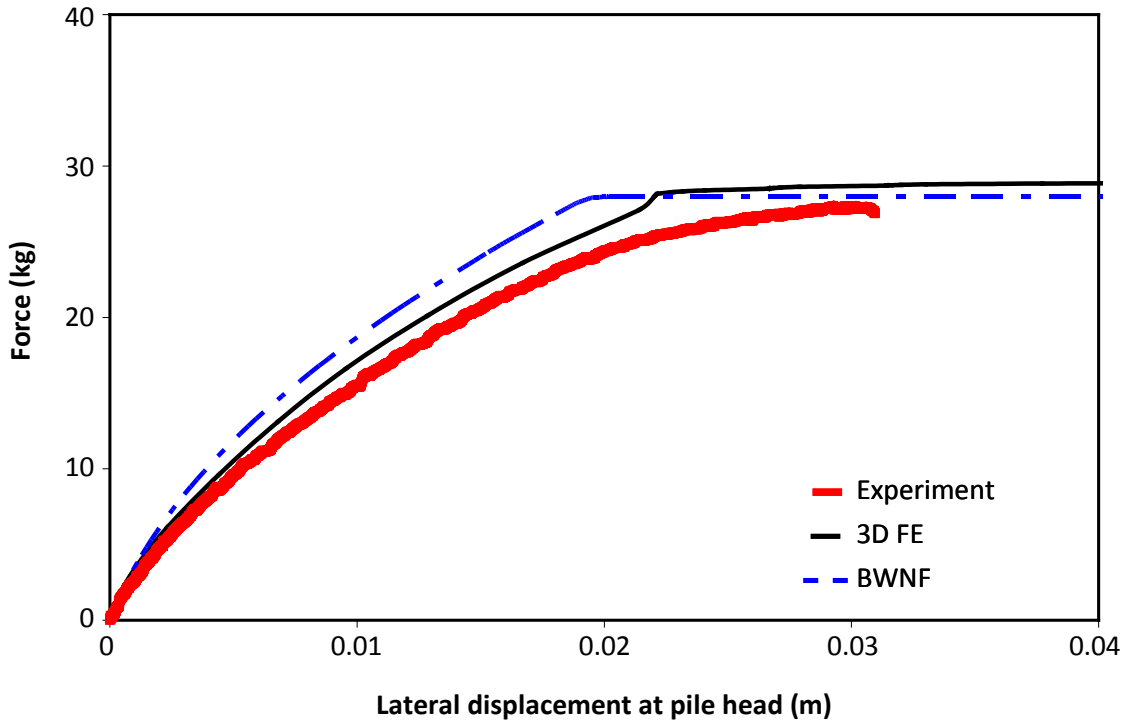

Σχήμα 32: Σύγκριση δύναμης–μετακίνησης στην κεφαλή του πασσάλου για επιβαλλόμενη δύναμη σε ύψος 56 cm με τα αποτελέσματα της τρισδιάστατης ανάλυσης, αλλά και με την πρόβλεψη του απλοποιημένου προσομοιώματος.

Η επαλήθευση των πειραμάτων έγινε με προβλέψεις Class B (Lambe, 1973) μέσω ενός απλοποιημένου προσομοιώματος δοκού επί μή-γραμμικού ελατηριωτού εδάφους τύπου Winkler. Το προσομοίωμα βαθμονομήθηκε με τα πειράματα “καθαρής” αντοχής σε ροπή (για την συμπεριφορά του πασσάλου) και σε οριζόντια δύναμη (για το σύστημα) και εν συνεχεία έγινε πρόβλεψη της απόκρισης του πασσάλου για τα υπόλοιπα οκτώ πειράματα προτού αυτά πραγματοποιηθούν.

Επιπλέον, μετά την ολοκλήρωση των πειραμάτων πραγματοποιήθηκε τρισδιάστατη αριθμητική προσομοίωσή τους με το καταστατικό προσομοίωμα που προτείνεται στην παρούσα διατριβή, τροποποιημένο ώστε να λαμβάνει υπόψιν την μεταβολή της γωνίας τριβής της άμμου με την κατακόρυφη τάση, καθώς και την χαλάρωση του εδαφικού υλικού συναρτήσει της διατμητικής παραμόρφωσης. Το προσομοίωμα βαθμονομείται, όπως και πριν, για “καθαρή” οριζόντια φόρτιση και “καθαρή” ροπή και εν συνεχεία επαληθεύει την απόκριση του συστήματος για τις υπόλοιπες πειραματικές δοκιμές.

Το **Σχήμα 32** συγκρίνει την δύναμη–μετακίνηση στην κεφαλή του πασσάλου για επιβαλλόμενη δύναμη σε ύψος 56 cm με τα αποτελέσματα της τρισδιάστατης ανάλυσης, αλλά και με την πρόβλεψη του απλοποιημένου προσομοιώματος. Είναι εμφανές ότι το απλοποιημένο προσομοίωμα προέβλεψε ικανοποιητικά την απόκριση του πασσάλου. Επιπλέον, η απόκριση σε όρους δυσκαμψίας και μέγιστης δύναμης από την τρισδιάστατη αριθμητική ανάλυση είναι πολύ κοντά στα πειραματικά δεδομένα. Μικρές διαφορές που παρατηρούνται, οφείλονται στην διαστολικότητα του εδάφους, η οποία δεν προσομοιώνεται από το συγκεκριμένο καταστατικό προσομοίωμα.

Εφαρμογή στη Δυναμική Απόκριση Κολωνοπασσάλων Γέφυρας

Έχοντας επαληθεύσει την αξιοπιστία του, το προτεινόμενο καταστατικό προσομοίωμα εφαρμόζεται στην μελέτη της ανελαστικής δυναμικής απόκρισης συστήματος εδάφους-πασσάλου-κατασκευής. Η αλληλεπίδραση εδάφους-πασσάλου-ανωδομής αναλύεται με δυο μεθόδους: (1) Με απλοποιημένη προσομοίωση, η οποία πραγματοποιείται σε δύο στάδια: (i) ανάλυση (εν-χρόνω) της ανελαστικής μη-γραμμικής απόκρισης του εδαφικού σχηματισμού, χωρίς την παρουσία πασσάλου, υπό τις εξεταζόμενες σεισμικές διεγέρσεις και (ii) ανάλυση της απόκρισης εδάφους-πασσάλου-ανωδομής με χρήση μή-γραμμικού υβριδικού ελατηριωτού προσομοιώματος Winkler, το οποίο διεγείρεται σύμφωνα με τα αποτελέσματα της ανάλυσης της εδαφικής απόκρισης, (2) Με προσομοίωση της πλήρους σύζευξης της κινηματικής και αδρανειακής αλληλεπίδρασης σε τρισδιάστατο προσομοίωμα πεπερασμένων στοιχείων.

Αρχικώς, συγκρίνοται τα αποτελέσματα των δυο προσομοιωμάτων για την ελαστική δυναμική απόκριση ενός συστήματος εδάφους-πασσάλου-κατασκευής. Ο κολωνοπάσσαλος θεμελιωμένος σε δίστρωτο αργιλικό έδαφος και μονολιθικά συνδεδεμένος με το κατάστρωμα μιας γέφυρας υποβάλλεται σε σεισμική διέγερση (**Σχήμα 33**). Ελέγχεται η επίδραση των συνόρων του τρισδιάστατου προσομοιώματος στην απόκριση του συστήματος εδάφους–πασσάλου–κατασκευής. Για την ορθότερη προσομοίωση στο τρισδιάστατο προσομοίωμα χρησιμοποιείται ισοδύναμη απόσβεση με το προσομοίωμα δοκού σε ελατηριωτό έδαφος τύπου Winkler. Η επίδραση της διέγερσης στην σεισμική απόκριση διερευνάται μέσω τριών πραγματικών επιταχυνσιογραφημάτων:

• Την καταγραφή του σεισμού του Αιγίου (1995)

• Την καταγραφή του σεισμού της Λευκάδας (2003)

• Την καταγραφή JMA του σεισμού του Kobe (1995)

Σε όλες τις καταγραφές έγινε επικλιμάκια αναγωγή σε PGA = 0.5 g. Τα αποτελέσματα των δυο μεθόδων συγκρίνονται πολύ καλά σε όρους χρονοϊστορίας επιτάχυνσης (**Σχήμα 34**), μετατόπισης, στροφής, φασμάτων απόκρισης και κατανομής μεγίστων ροπών.

Έχοντας συγκρίνει την ελαστική απόκριση του συστήματος με τις δυο διαφορετικές μεθόδους, πραγματοποιείται μία πρώτη διερεύνηση των επιπτώσεων της διαρροής του πασσάλου στην απόκριση συστήματος εδάφους-πασσάλου-γέφυρας υπό σεισμική φόρτιση με έμφαση στην δομητική ανελαστικότητα. Επιπλέον, εξετάζεται η επίδραση του τύπου του εδαφικού υλικού, του ύψους του βάθρου, και της δυνατότητας ανάπτυξης πλαστικής άρθρωσης στον φορέα πάνω και κάτω από την επιφάνεια του εδάφους στην σεισμική απόκριση του συστήματος σε όρους πλαστιμότητας.

Το εξεταζόμενο πρόβλημα παρουσιάζεται στο **Σχήμα 35**. Κολωνοπάσσαλος θεμελιωμένος σε: (α) αργιλικό έδαφος με αυξανόμενη με το βάθος αστράγγιστη διατμητική αντοχή, και (β) αμμώδες έδαφος με γωνία τριβής $\phi = 40^{o}$ και συνοχή c = 5 kPa υποβάλλεται σε σεισμική διέγερση. Η απόσταση της επιφάνειας του εδάφους από το κέντρο μάζας του καταστρώματος ορίζεται ως ύψος του βάθρου H, το οποίο παραμετρικά λαμβάνεται ως H = 5, 10 m. Η διατομή του κολωνοπασσάλου έχει διάμετρο d για το τμήμα κάτω από την επιφάνεια του εδάφους και b (b = 1.5, 3.0 m) για το τμήμα πάνω από την επιφάνεια του εδάφους. Για την διερεύνηση της επιρροής της θέσης της πλαστικής άρθρωσης στην απόκριση του συστήματος η διάμετρος d αυξάνεται κατά 33% σε σχέση με την διάμετρο του βάθρου b, ώστε η πλαστική άρθρωση να δημιουργηθεί πάνω από την επιφάνεια του εδάφους (δηλαδή στο βάθρο και όχι στον πάσσαλο). Έτσι, τα ζεύγη διαμέτρων πασσάλου–βάθρου, d–b, που αναλύονται είναι 1.5–1.5, 2.0–1.5, 3.0–3.0, 4.0–3.0 (σε m). Το μήκος έμπηξης του κολωνοπασσάλου είναι L = 30 m, ενώ το βραχώδες υπόβαθρο θεωρείται στα 50 m βάθος. Συνολικά εξετάζονται 8 διατάξεις κολωνοπασσάλου.

Για κάθε ένα από τα αναλυθέντα δομητικά συστήματα η μάζα του καταστρώματος υπολογίστηκε ώστε η ιδιοπερίοδος του πακτωμένου στη βάση βάθρου να ισούται με T = 0.3 sec. Η μή-γραμμική δομητική συμπεριφορά των κολωνοπασσάλων

απεικονίζεται στο **Σχήμα 36**. Οι καμπύλες αυτές υπολογίστηκαν μέσω του προσομοιώματος BWGG (Gerolymos et al., 2009) με τιμή παραμέτρου n = 1, αρχικό μέτρο δυσκαμψίας EI της μη-ρηγματωμένης διατομής και καμπτική ροπή αντοχής στην στάθμη της επιφάνειας του εδάφους για μέγιστη επιτάχυνση στη μάζα του καταστρώματος a = 0.2 g.

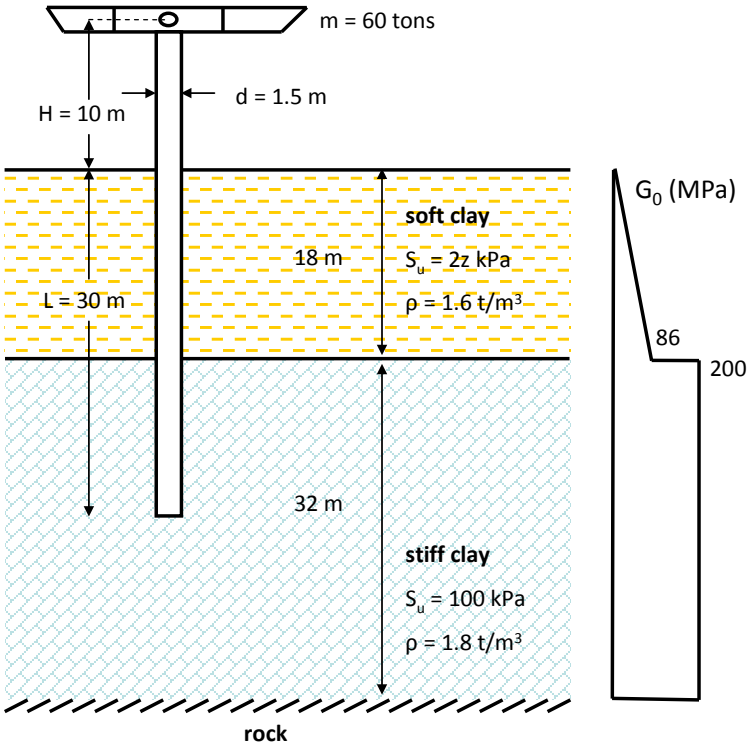

Σχήμα 33: Εξεταζόμενο πρόβλημα για την ελαστική δυναμική απόκριση ενός συστήματος εδάφους-πασσάλου-κατασκευής με ένα πλήρως τρισδιάστατο προσομοίωμα πεπερασμένων στοιχείων και ένα προσομοίωμα δοκού σε ελατηριωτό έδαφος τύπου Winkler

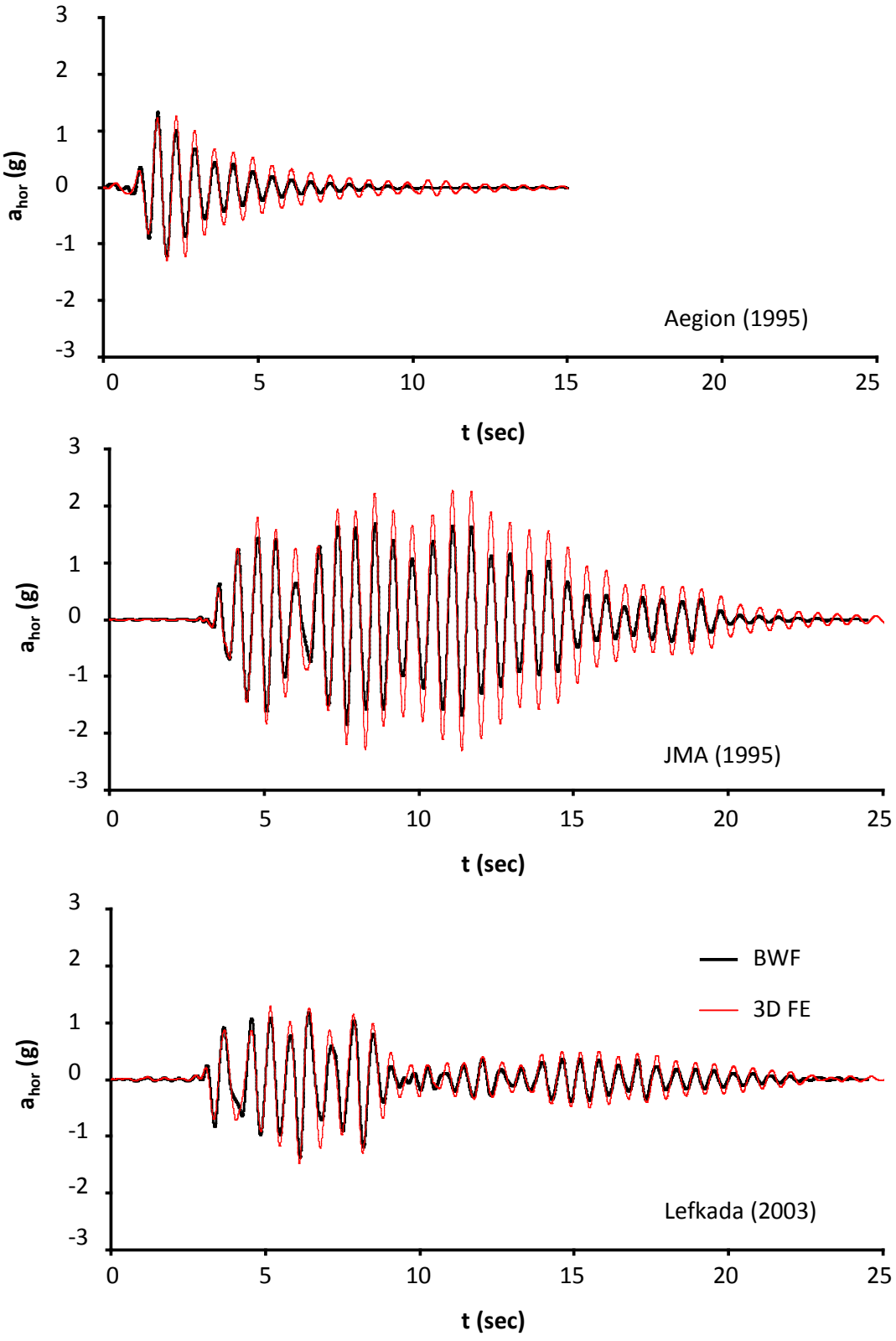

Σχήμα 34: Σύγκριση χρονοϊστοριών επιτάχυνσης στο κατάστρωμα της γέφυρας με το πλήρως τρισδιάστατο προσομοίωμα πεπερασμένων στοιχείων και ένα προσομοίωμα δοκού σε ελατηριωτό έδαφος τύπου Winkler

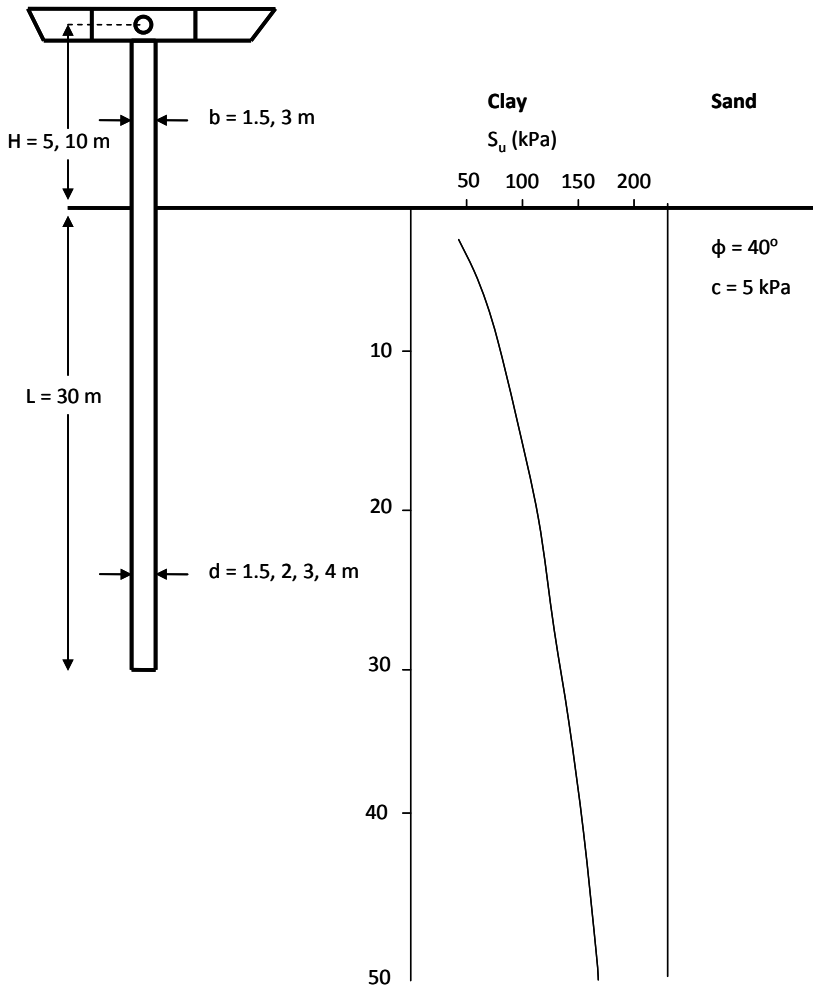

Σχήμα 35: Εξεταζόμενο πρόβλημα για την ανελαστική δυναμική απόκριση ενός συστήματος εδάφους–πασσάλου–κατασκευής

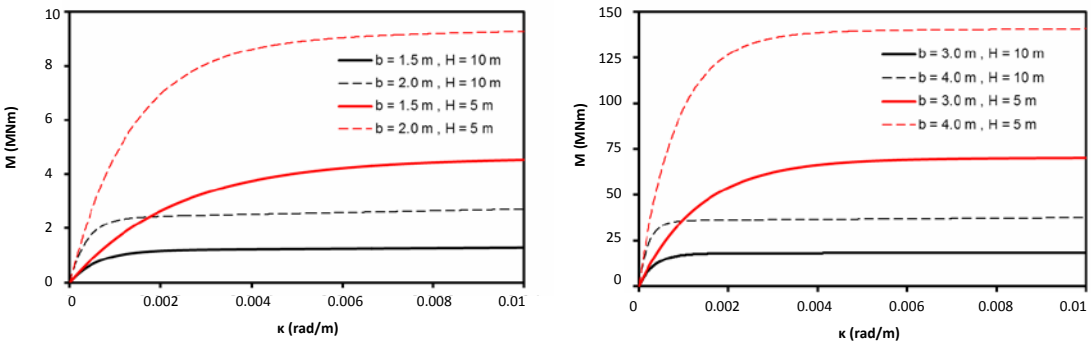

Σχήμα 36: Καμπύλες ροπής–καμπυλότητας για τις παραμετρικές αναλύσεις του εξεταζόμενου προβλήματος

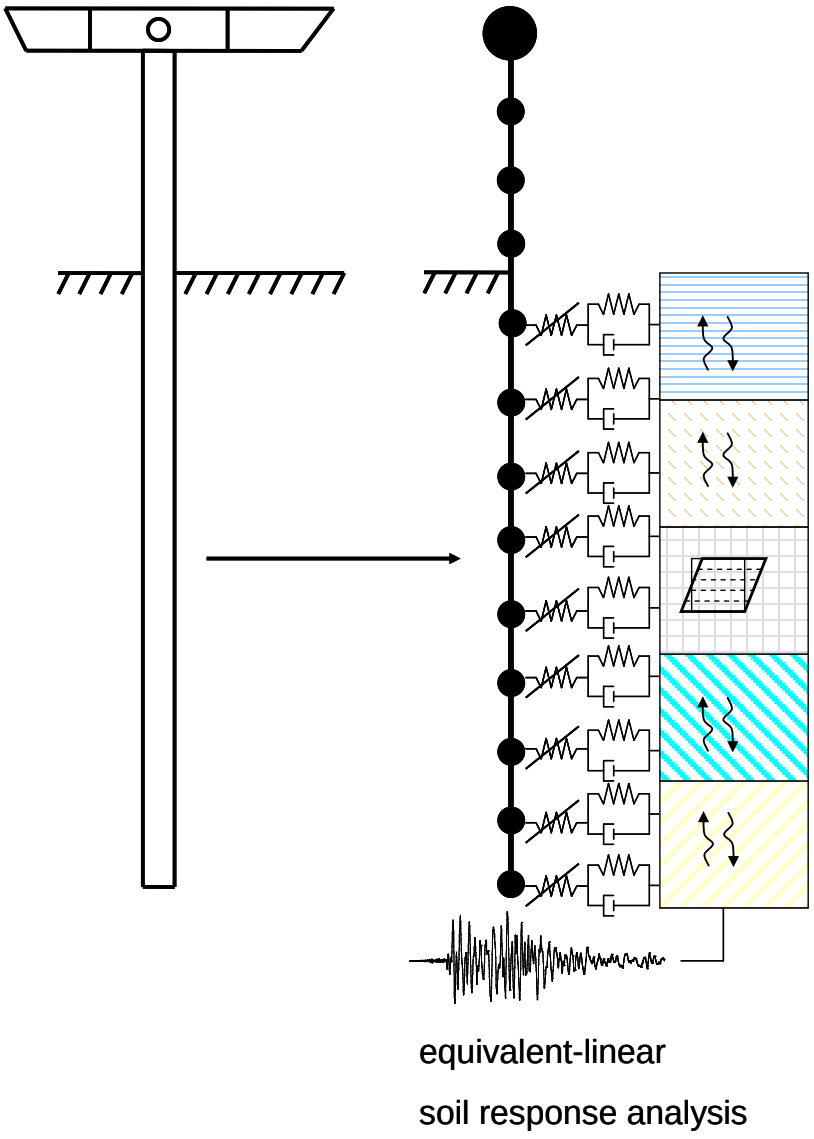

Σχήμα 37: Μή-γραμμικό προσομοίωμα τύπου Winkler

Με στόχο τον περιορισμό των παραμέτρων που υπεισέρχονται στο πρόβλημα, η επίδραση της απόκρισης του εδάφους εκμηδενίστηκε, θεωρώντας ένα μόνον εδαφικό προφίλ για την ανάλυση της μή-γραμμικής απόκρισης του εδαφικού σχηματισμού. Η επίδραση της διέγερσης στην σεισμική απόκριση διερευνάται μέσω των τριών πραγματικών επιταχυνσιογραφημάτων που χρησιμοποιήθηκαν στις ελαστικές αναλύσεις με επικλιμάκια αναγωγή σε 0.5 g και 0.8 g στην επιφάνεια του εδάφους.

Το **Σχήμα 37** παρουσιάζει το μή-γραμμικό προσομοίωμα τύπου Winkler που χρησιμοποιήθηκε. Η αναλύση αποτελείται από δύο στάδια: (1) ανάλυση της ανελαστικής απόκρισης του εδαφικού σχηματισμού, χωρίς την παρουσία της κατασκευής με τον κώδικα SHAKE και (2) ανάλυση της απόκρισης

εδάφους-πασσάλου-ανωδομής σε κατακορύφως διαδιδόμενη διέγερση (από το πρώτο στάδιο) με τον κώδικα OpenSees. Οι εδαφικές χρονοϊστορίες από το SHAKE εισήχθησαν ως διέγερση στο μή-γραμμικό προσομοίωμα τύπου Winkler, ενώ η χρονοϊστορία της επιτάχυνσης στα 30 m χρησιμοποιήθηκε ως διέγερση στο τρισδιάστατο προσομοίωμα πεπερασμένων στοιχείων. Έτσι, ελέγχεται η μονοδιάστατη ανάλυση της ανελαστικής μή-γραμμικής απόκρισης του εδαφικού σχηματισμού με την τρισδιάστατη. Το κατάστρωμα προσομοιώθηκε ως συγκεντρωμένη μάζα στον κορυφαίο κόμβο του κολωνοπασσάλου. Ο κολωνοπάσσαλος διακριτοποιείται σε μή-γραμμικά στοιχεία δοκού μήκους 1.0 m, και η καμπτική συμπεριφορά του ορίζεται μέσω του καταστατικού προσομοιώματος BWGG (Gerolymos & Gazetas 2005). Στο μή-γραμμικό ελατηριωτό προσομοίωμα Winkler χρησιμοποιείται μια υβριδική διάταξη ελατηρίων και αποσβεστήρων. Η συμπεριφορά του εδάφους λαμβάνεται υπόψιν με ένα μή-γραμμικό ελατήριο συνδεδεμένο εν σειρά με μια παράλληλη σύνδεση γραμμικού ελατηρίου και αποσβεστήρα. Για την συγκεκριμένη διάταξη προτείνεται μια μεθοδολογία βαθμονόμησης των σταθερών των ελατηρίων και του αποσβεστήρα (**Σχήμα 38**) σύμφωνα με την οποία οι σταθερές των ελατηρίων και του αποσβεστήρα δίνονται μέσω μιας διαδικασίας βελτιστοποίησης από τις σχέσεις:

$$\mathrm{Re}\left(\frac{k_{el}k_{nl}+i\omega c_{el}k_{nl}}{k_{el}+k_{nl}+i\omega c_{el}}\right)\approx 1.2E_s \tag{5}$$

και

$$\frac{1}{\omega}\mathrm{Im}\left(\frac{k_{el}k_{nl}+i\omega c_{el}k_{nl}}{k_{el}+k_{nl}+i\omega c_{el}}\right)\approx 6\left(\frac{\omega d}{V_s}\right)^{-1/4}\rho_s V_s d \tag{6}$$

όπου k_{el} η σταθερά του γραμμικού ελατηρίου, k_{nl} η σταθερά του μή-γραμμικού ελατηρίου, c_{el} η σταθερά του αποσβεστήρα, E_s το μέτρο ελαστικότητας του εδάφους, V_s η ταχύτητα του διατμητικού κύματος, d η διάμετρος του πασσάλου και ρ_s η πυκνότητα του εδάφους. Τα μή-γραμμικά p-y ελατήρια του εδάφους προσδιορίζονται επίσης από το καταστατικό προσομοίωμα BWGG βαθμονομημένο με τις καμπύλες p-y του Matlock (1970) για άργιλο και των Reese et al (1974) για άμμο (Drosos, 2007).

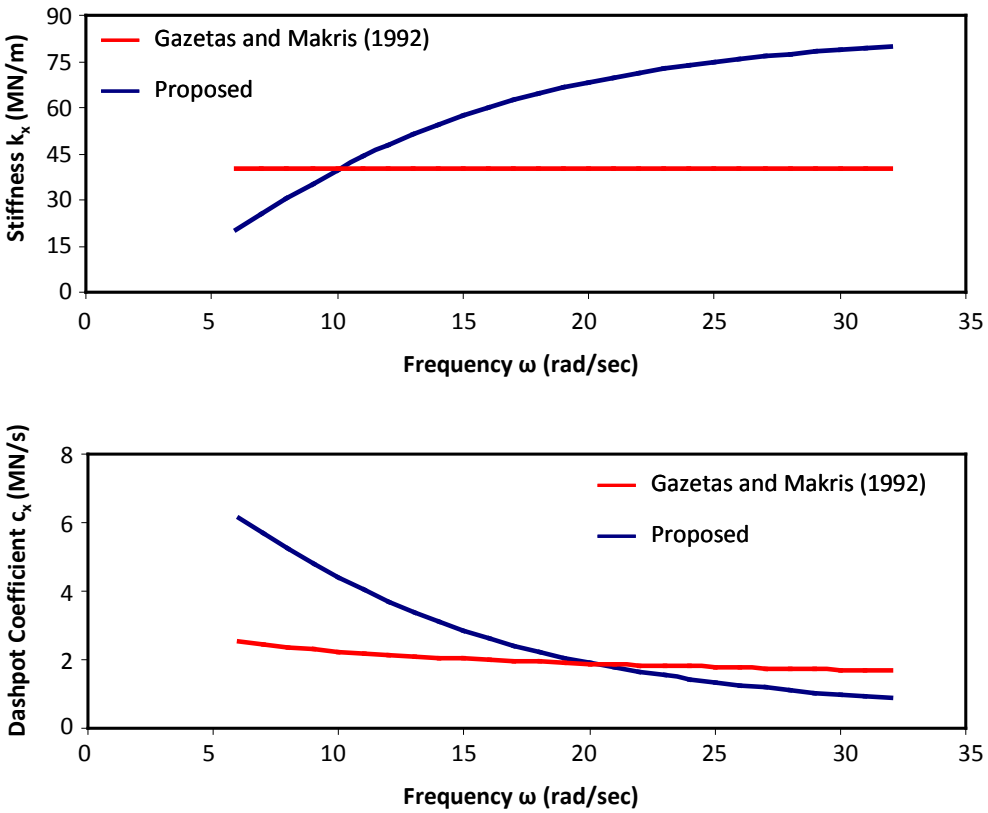

Σχήμα 38: Βαθμονόμηση της δυσκαμψίας k_x και της σταθεράς απόσβεσης c_x της υβριδικής διάταξης του εξεταζομένου προβλήματος

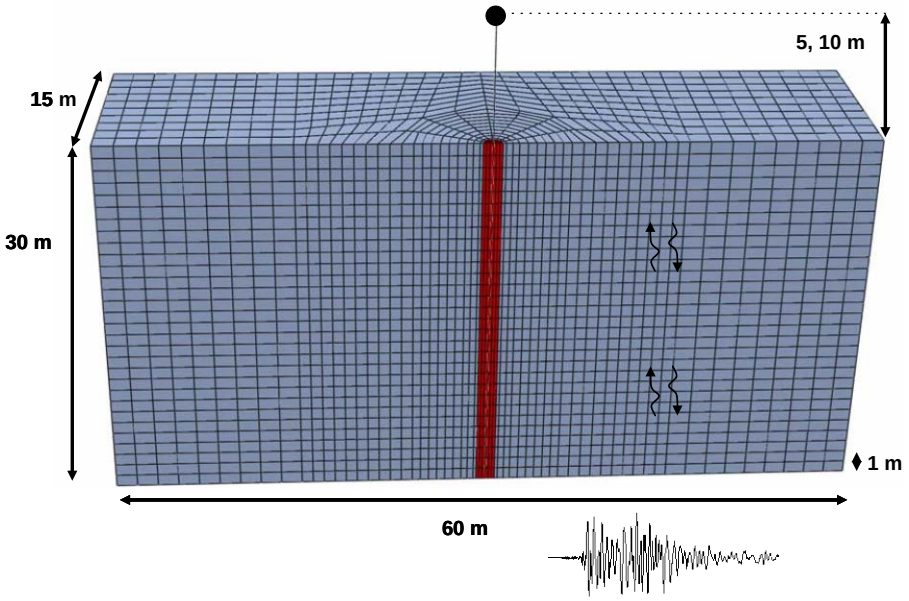

Σχήμα 39: Διακριτοποίηση του καννάβου για το τρισδιάστατο προσομοίωμα πεπερασμένων στοιχείων του εξεταζομένου προβλήματος

Στη δεύτερη μέθοδο η ανάλυση της σεισμικής απόκρισης του εδαφικού σχηματισμού και η ανάλυση της αλληλεπίδρασης εδάφους-πασσάλου-ανωδομής πραγματοποιούνται σε ένα μόνον στάδιο με τον κώδικα πεπερασμένων στοιχείων ABAQUS (**Σχήμα 39**). Το έδαφος προσομοιώνεται με οκτακομβικά στοιχεία συνεχούς μέσου ενώ ο κολωνοπάσσαλος με τρισδιάστατα στοιχεία δοκού κατά μήκος του κατακορύφου άξονά του συνδεδεμένα με κατάλληλους κινηματικούς περιορισμούς με τους κόμβους στην περίμετρό του για την ρεαλιστική προσομοίωση ολόκληρης της γεωμετρίας του κολωνοπασσάλου. Η συμπεριφορά του κολωνοπασσάλου (σε όρους ροπής−καμπυλότητας) ορίζεται από ένα ελαστοπλαστικό προσομοίωμα σύμφωνα με τις καμπύλες του **Σχήματος 36**. Για την ρεαλιστική προσομοίωση της μή-γραμμικής απόκρισης του εδάφους σε ανακυκλική φόρτιση, εισάγονται μέσω υπορουτίνας το καταστατικό προσομοίωμα των Gerolymos et al (2005) για την συμπεριφορά της αργίλου και το προτεινόμενο στην παρούσα διατριβή καταστατικό προσομοίωμα για την συμπεριφορά της άμμου. Οι παράμετροι των δυο καταστατικών προσομοιωμάτων βαθμονομούνται με στόχο την ταύτιση των καμπυλών με τις αντίστοιχες καμπύλες G-γ των Ishibashi and Zhang (1993) από τη βιβλιογραφία. Για το αναπτυχθέν καταστατικό προσομοίωμα ο λόγος του μέτρου διατμήσεως σε ανακυκλική φόρτιση απλής διάτμησης υπολογίζεται από την σχέση:

$$\frac{G}{G_0}=\begin{cases}1, & \gamma<\gamma_y\\ \dfrac{\left(\left(c+p\tan\varphi\right)\cos\varphi\left(1-\dfrac{1}{a}\right)\right)}{\left(\gamma-\dfrac{\left(c+p\tan\varphi\right)\cos\varphi}{aG_0}\right)}\left(1-e^{\dfrac{-\gamma G_0+\dfrac{\left(c+p\tan\varphi\right)\cos\varphi}{a}}{\left(c+p\tan\varphi\right)\cos\varphi\left(1-\dfrac{1}{a}\right)}}\right) & \gamma>\gamma_y\end{cases} \tag{7}$$

και η αύξηση του λόγου υστερητικής απόσβεσης ξ με τη διατμητική παραμόρφωση γ

$$\xi=\begin{cases}0, & \gamma<\gamma_y\\ \dfrac{2}{\pi}\left[\dfrac{1+e^{\dfrac{-\gamma+\dfrac{\left(c+p\tan\varphi\right)\cos\varphi}{aG_0}}{\left(\dfrac{\sqrt{3}\left(c+p\tan\varphi\right)\cos\varphi\left(1-\frac{1}{a}\right)}{\sqrt{3}G_0}\right)}}}{1-e^{\dfrac{-\gamma+\dfrac{\left(c+p\tan\varphi\right)\cos\varphi}{aG_0}}{\left(\dfrac{\left(c+p\tan\varphi\right)\cos\varphi\left(1-\frac{1}{a}\right)}{G_0}\right)}}}-\dfrac{2\dfrac{\left(c+p\tan\varphi\right)\cos\varphi\left(1-\dfrac{1}{a}\right)}{G_0}}{\gamma-\dfrac{\left(c+p\tan\varphi\right)\cos\varphi}{aG_0}}\right] & \gamma>\gamma_y\end{cases} \tag{8}$$

όπου

$$\gamma_y = \frac{(c + p\tan\varphi)\cos\varphi}{aG_0} \quad (9)$$

Κατάλληλοι κινηματικοί περιορισμοί επιβάλλονται στις άκρες του προσομοιώματος, ώστε η κίνηση να είναι όμοια με του ελεύθερου πεδίου. Τέλος, για την μείωση του υπολογιστικού χρόνου, το αρχικό τρισδιάστατο προσομοίωμα τμήθηκε εγκάρσια κατά το ήμισυ χωρίς να επηρεάζονται ποσοτικά τα αποτελέσματα των αναλύσεων.

Αναλύσεις εγκάρσιας μονοτονικής φόρτισης (Pushover Tests) των δυο προσομοιωμάτων προηγήθηκαν των δυναμικών αναλύσεων: (α) με θεώρηση συνθηκών πάκτωσης στην βάση του βάθρου προκειμένου να ελεγθεί η δομητική συμπεριφορά της κατασκευής, και (β) με θεώρηση της αλληλεπίδρασης εδάφους-ανωδομής.

Το **Σχήμα 40** παρουσιάζει τις χρονοϊστορίες της επιτάχυνσης στην επιφάνεια του εδάφους στο ελεύθερο πεδίο για την καταγραφή του JMA και τα αντίστοιχα φάσματα απόκρισης για απόσβεση 5%, όπως προκύπτουν με τις δυο μεθόδους ανάλυσης. Εξάγονται τα ακόλουθα συμπεράσματα:

- Το αυξημένο πλάτος της επιτάχυνσης στις μεγάλες συχνότητες για την τρισδιάστατη ανάλυση σε σχέση με την μή-γραμμική ανάλυση αποδίδεται στην πολύ μικρή απόσβεση Rayleigh του τρισδιάστατου προσομοιώματος. Επιπλέον, η ισοδύναμη γραμμική μέθοδος έχει μεγαλύτερη απόσβεση στην εδαφική απόκριση για υψηλές συχνότητες.
- Σε όλες τις περιπτώσεις, η τρισδιάστατη ανάλυση οδηγεί σε ίσες ή χαμηλότερες τιμές για την μέγιστη εδαφική επιτάχυνση (PGA) σε σχέση με την ισοδύναμη γραμμική μέθοδο, καταδεικνύοντας την επίδραση της “πραγματικής” μή-γραμμικής συμπεριφοράς του εδάφους στην απόκριση.
- Όπως αναμενόταν, η μή-γραμμική απόκριση του εδάφους μειώνει τις φασματικές επιταχύνσεις, ενώ η δεσπόζουσα περίοδος παραμένει η ίδια.
- Στην τρισδιάστατη ανάλυση, η πλαστικοποίηση του εδάφους αυξάνει αυξανομένης της κορυφαίας εδαφικής επιτάχυνσης (PGA). Έτσι, η ενίσχυση της σεισμικής διέγερσης είναι μικρότερη σε σχέση με την ισοδύναμη γραμμική μέθοδο.

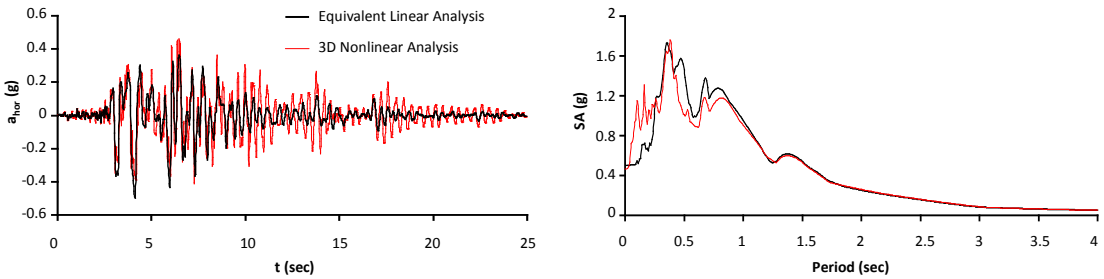

Σχήμα 40: (α) Χρονοϊστορίες της επιτάχυνσης του JMA (Kobe) με επικλιμάκια αναγωγή στο 0.5g στο ελεύθερο πεδίο και (β) φάσμα απόκρισης (ξ = 5%) από την ισοδύναμη γραμμική μέθοδο και την τρισδιάστατη μή-γραμμική ανάλυση για άργιλο

Το **Σχήμα 41** συγκρίνει τις χρονοϊστορίες της επιτάχυνσης στο κατάστρωμα της γέφυρας από τις δύο μεθόδους για κολωνοπάσσαλο διαμέτρου d = 3 m σε αμμώδες έδαφος ως προς το ύψος του βάθρου. Είναι εμφανές ότι η απόκριση του συστήματος από τις τρισδιάστατες αναλύσεις είναι παρόμοια και με την απλοποιημένη μέθοδο. Ενδεικτικά, από τα αποτελέσματα της παραμετρικής διερεύνησης παρατηρούνται ότι:

- Η αύξηση του ύψους του βάθρου αυξάνει την επιτάχυνση στο κατάστρωμα.
- Η μικρότερη διάμετρος του πασσάλου οδηγεί σε μεγαλύτερη επιτάχυνση στο κατάστρωμα.
- Σε σταθερής διαμέτρου κολωνοπασσάλους, η αύξηση της διαμέτρου του πασσάλου μεταβιβάζει τις μέγιστες ροπές σε μεγαλύτερο βάθος.
- Οι σταθερής διαμέτρου κολωνοπάσσαλοι αναπτύσσουν πλαστική άρθρωση εντός του εδάφους και οι πλαστικές στροφές κατανέμονται σε μεγαλύτερο βάθος, μειώνοντας έτσι την μέγιστη καμπυλότητα.
- Με την αύξηση του ύψους του βάθρου η πλαστική άρθρωση μεταβιβάζεται πιο κοντά στην επιφάνια του εδάφους.

Εκτός από τα θεμελιώδη μεγέθη, όπως οι χρονοϊστορίες επιτάχυνσης, που περιγράφουν την σεισμική απόκριση του συστήματος εδάφους–κολωνοπασσάλου–ανωδομής, άλλοι σημαντικοί δείκτες της σεισμικής απόκρισης είναι ο δείκτης καθολικής πλαστιμότητας μ_δ, ο δείκτης τοπικής πλαστιμότητας μ_ϕ, η διαφορική οριζόντια μετακίνηση της ανωδομής ανηγμένη προς το ύψος της γ (drift ratio). Ως δείκτης τοπικής πλαστιμότητας μ_ϕ ορίζεται ο λόγος της μέγιστης καμπυλότητα κ_{max} που επιβάλλεται στην κατασκευή από τον σεισμό προς την καμπυλότητα διαρροής κ_y, που είναι ιδιότητα

της διατομής του κολωνοπασσάλου. Αντίστοιχα, ως δείκτης καθολικής πλαστιμότητας μ_δ ορίζεται ο λόγος της μέγιστης μετακίνησης της ανωδομής u_{max}, την οποία διανύει το τμήμα της κατασκευής πάνω από την επιφάνεια του εδάφους, προς την μετακίνηση διαρροής που είναι ιδιότητα του συστήματος εδάφους-κολωνοπασσάλου-γέφυρας. Τέλος, η διαφορική οριζόντια μετακίνηση της ανωδομής ανηγμένη προς το ύψος της γ ορίζεται ως ο λόγος της μέγιστης οριζόντιας μετακίνησης του καταστρώματος σε σχέση με τη βάση του βάθρου προς το ύψος του βάθρου.

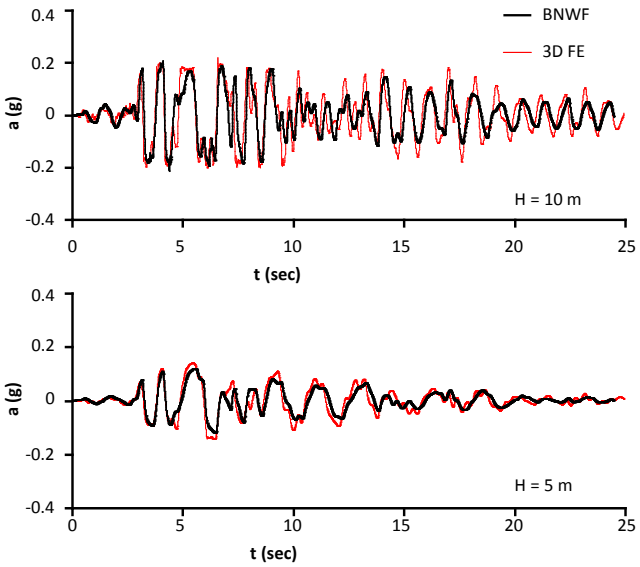

Σχήμα 41: Χρονοϊστορίες της επιτάχυνσης στο κατάστρωμα της γέφυρας για κολωνοπάσσαλο με διάμετρο d = 3 m σε αμμώδες έδαφος (διέγερση JMA 1995 με επικλιμάκια αναγωγή στο 0.8 g)

Το **Σχήμα 42** παρουσιάζει την σύγκριση του δείκτη τοπικής πλαστιμότητας μ_ϕ και της διαφορικής οριζόντιας μετακίνησης της ανωδομής ανηγμένη προς το ύψος της γ% όπως προέκυψαν από το μή-γραμμικό προσομοίωμα τύπου Winkler και το τρισδιάστατο προσομοίωμα πεπερασμένων στοιχείων. Η σύγκριση των δυο παραμέτρων με τις δυο μεθόδους ανάλυσης υποδεικνύει ότι η απόκριση του συστήματος εδάφους-πασσάλου-θεμελίωσης με το τρισδιάστατο προσομοίωμα πεπερασμένων στοιχείων είναι λίγο πιο δύσκαμπτη από την αντίστοιχη με το μή-γραμμικό προσομοίωμα τύπου Winkler. Για τον λόγο αυτό όλα τα αποτελέσματα κατηγοριοποιούνται και ως προς την μέθοδο ανάλυσης που χρησιμοποιήθηκε.

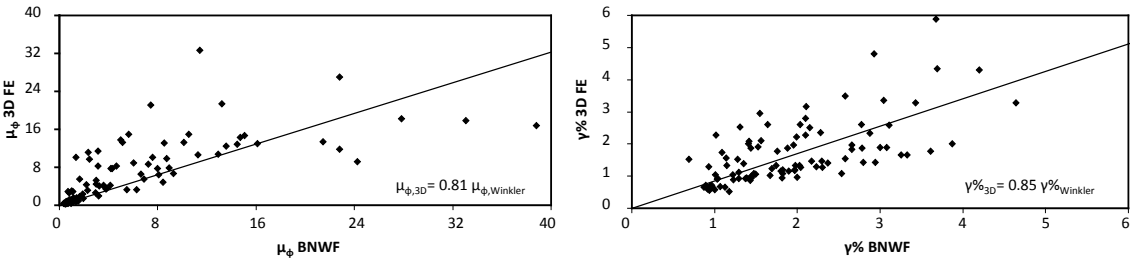

Σχήμα 42: Σύγκριση (α) του δείκτη τοπικής πλαστιμότητας μ_ϕ και (β) του λόγου οριζόντιας μετακίνησης της ανωδομής γ% από το μή-γραμμικό προσομοίωμα τύπου Winkler και το τρισδιάστατο προσομοίωμα πεπερασμένων στοιχείων

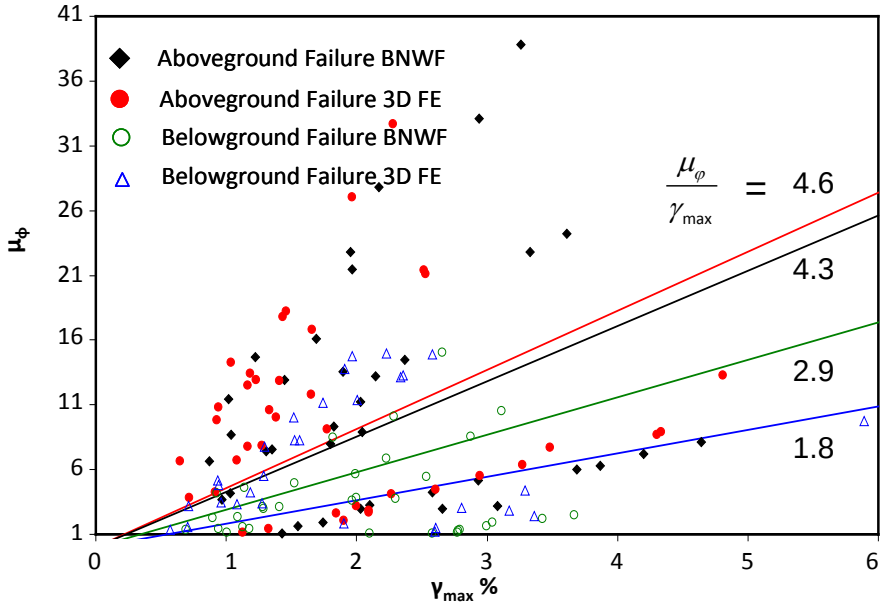

Σχήμα 43: Συσχέτιση του δείκτη τοπικής πλαστιμότητας μ_ϕ και του λόγου οριζόντιας μετακίνησης της ανωδομής γ% για διαφορετικές θέσεις της πλαστικής άρθρωσης με τις δυο εξεταζόμενες μεθόδους ανάλυσης

Το **Σχήμα 43** δείχνει την σχέση του δείκτη τοπικής πλαστιμότητας μ_ϕ και της διαφορικής οριζόντιας μετακίνησης της ανωδομής ανηγμένη προς το ύψος της γ% για θέση της πλαστικής άρθρωσης στον φορέα πάνω και κάτω από την επιφάνεια του εδάφους. Η απαιτούμενη πλαστιμότητα για δεδομένον λόγο οριζόντιας μετακίνησης της ανωδομής και για τις δυο μεθόδους είναι μεγαλύτερη όταν η πλαστική άρθρωση αναπτύσσεται στο βάθρο. Η εν λόγω συμπεριφορά οφείλεται στην κίνηση απαραμόρφωτου σώματος, που αυξάνεται με το βάθος της πλαστικής άρθρωσης και

δεν προκαλεί δομητική αστοχία, επομένως δεν επηρεάζει την απαιτούμενη πλαστιμότητα. Επιπλέον, για την περίπτωση της ανάπτυξης της πλαστικής άρθρωσης στο βάθρο και οι δυο μέθοδοι υπολογισμού καταλήγουν σε παρόμοια συσχέτιση του δείκτη τοπικής πλαστιμότητας μ_ϕ με τον λόγο σχετικής οριζόντιας μετακίνησης της ανωδομής γ.

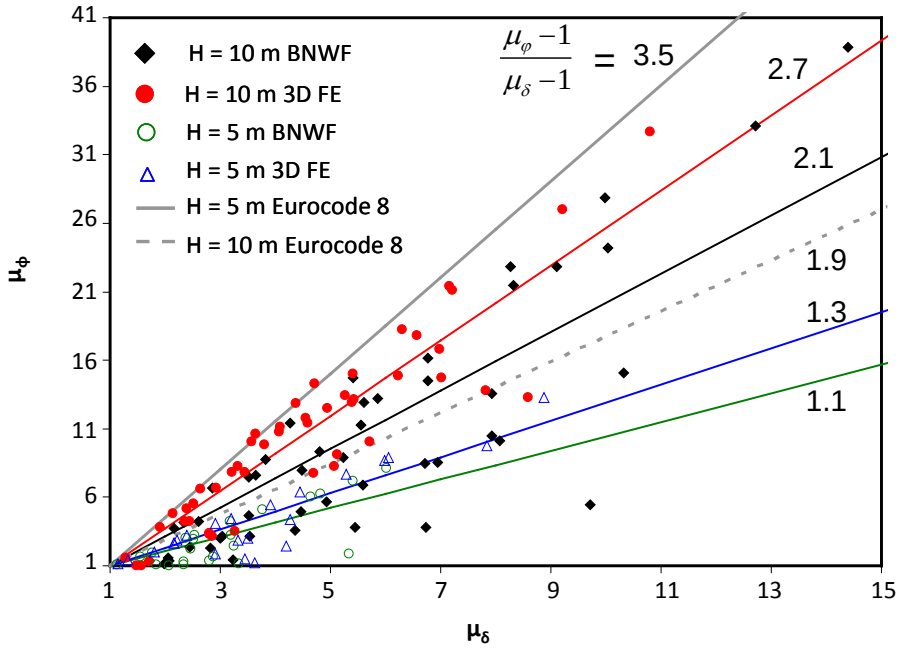

Σχήμα 44: Συσχέτιση του δείκτη τοπικής πλαστιμότητας μ_ϕ και του δείκτη καθολικής πλαστιμότητας μ_δ για διαφορετικά ύψη του βάθρου με τις δυο εξεταζόμενες μεθόδους ανάλυσης και τον Ευρωκώδικα 8

Η επιρροή του ύψους του βάθρου στην συσχέτιση των δεικτών τοπικής και καθολικής πλαστιμότητας μ_ϕ και μ_δ με τις δυο εξεταζόμενες μεθόδους αποτυπώνεται στο **Σχήμα 44** και γίνεται σύγκριση με τον Ευρωκώδικα 8. Το ψηλότερο βάθρο (H = 10 m) παρουσιάζει μεγαλύτερη απαίτηση σε τοπική πλαστιμότητα μ_ϕ για μια δεδομένη καθολική πλαστιμότητα μ_δ, καθώς ο μέσος λόγος $(\mu_\phi - 1) / (\mu_\delta - 1)$ ισούται με 2.7 και 2.1 για το τρισδιάστατο προσομοίωμα πεπερασμένων στοιχείων και το μή-γραμμικό προσομοίωμα τύπου Winkler αντίστοιχα, έναντι 1.3 και 1.1 για το κοντύτερο βάθρο (H = 5 m). Αυτό οφείλεται και στην μεγαλύτερη ενεργό ιδιοπερίοδο του κολωνοπάσσαλου με το κοντύτερου βάθρο (T = 1.15 sec) σε σχέση με το ψηλότερο (T = 0.9 sec), όπως

προέκυψε με ανάλυση Fourier. Επιπλέον, η απαίτηση σε όρους πλαστιμότητας από τον Ευρωκώδικα 8 είναι πιο συντηρητική και από τις δυο μεθόδους ανάλυσης.

Το **Σχήμα 45** παρουσιάζει τις μέσες και ακραίες τιμές του δείκτη καθολικής πλαστιμότητας μ_δ σε σχέση με την θέση της πλαστικής άρθρωσης στον φορέα πάνω και κάτω από την επιφάνεια του εδάφους. Ο ευεργετικός ρόλος της δημιουργίας πλαστικής άρθρωσης κάτω από την επιφάνεια του εδάφους είναι προφανής, καθώς καί οι μέσες καί οι ακραίες τιμές του δείκτη καθολικής πλαστιμότητας μ_δ είναι μικρότερες από τις αντίστοιχες για την πλαστική άρθρωση στο βάθρο. Η συμπεριφορά αυτή παρατηρείται και με τις δυο αριθμητικές μεθόδους.

Για να ελεγχθεί η επίδραση της εδαφικής ενδοσιμότητας στην σεισμική απόκριση του συστήματος πραγματοποιήθηκε παραμετρική διερεύνηση δυο επιπλέον εδαφικών προφιλ: (α) άμμου με γωνία τριβής $\phi = 28^o$ και συνοχή c = 5 kPa σταθερά με το βάθος (ορίζεται ως χαλαρή), και (β) αργίλου με το 20% της αστράγγιστης διατμητικής αντοχής από την αρχική θεώρηση (ορίζεται ως χαλαρή), για τις ίδιες δυναμικές ιδιότητες του εδάφους. Επειδή η μείωση της αντοχής του εδάφους επηρεάζει τις δυναμικές ιδιότητες του εδάφους στο τρισδιάστατο προσομοίωμα (πχ. **Εξισώσεις 7-9**) και κατά συνέπειαν η μέγιστη επιτάχυνση στην επιφάνεια του εδάφους είναι μικρότερη από την επιτάχυνση της επικλιμάκιας αναγωγής, η εδαφική ενδοσιμότητα μελετάται μόνον με το μή-γραμμικό προσομοίωμα τύπου Winkler.

Στο **Σχήμα 46** δείχνεται η συσχέτιση της τοπικής μ_ϕ με την καθολική πλαστιμότητα μ_δ συναρτήσει της ενδοσιμότητας του εδάφους με το μή-γραμμικό προσομοίωμα τύπου Winkler. Δεν παρατηρούνται σημαντικές διαφοροποιήσεις, αφού για δεδομένη πλαστιμότητα σε όρους μετακίνησης, η πλαστιμότητα σε όρους καμπυλότητας ενός κολωνοπασσάλου θεμελιωμένου σε μαλακή άργιλο ή χαλαρή άμμο ελάχιστα διαφέρει από την αντίστοιχη σε στιφρή άργιλο ή πυκνή άμμο.

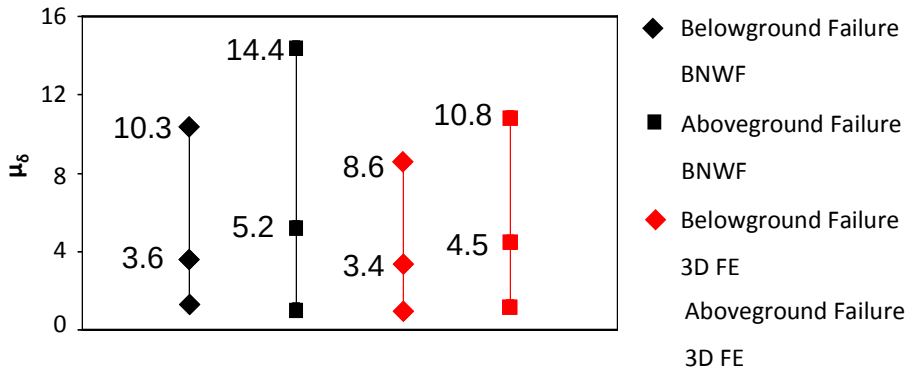

Σχήμα 45: Μέσες και ακραίες τιμές του δείκτη καθολικής πλαστιμότητας μ_δ σε σχέση με την θέση της πλαστικής άρθρωσης στον φορέα πάνω και κάτω από την επιφάνεια του εδάφους

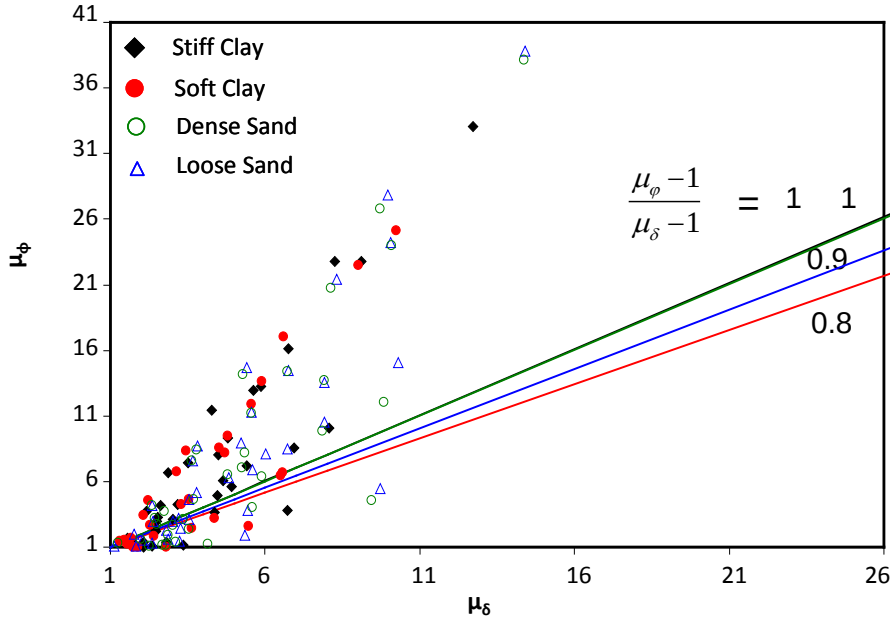

Σχήμα 46: Συσχέτιση των υπολογισμένων δεικτών τοπικής και καθολικής πλαστιμότητας μ_ϕ και μ_δ για διαφορετική εδαφική ενδοσιμότητα με το μή-γραμμικό προσομοίωμα τύπου Winkler

Γενικά, από τις παραμετρικές αναλύσεις των δυο προσομοιωμάτων προκύπτει:

- Για συγκεκριμένη απαίτηση σε δείκτη καθολικής πλαστιμότητας μ_δ, η εμφάνιση της πλαστικής άρθρωσης κάτω από την επιφάνεια του εδάφους μειώνει την απαίτηση σε δείκτη τοπικής πλαστιμότητας μ_ϕ, υποδεικνύοντας την ευεργετική συμπεριφορά της ανελαστικής απόκρισης του πασσάλου.

- Η διάμετρος του βάθρου δεν έχει ιδιαίτερη επιρροή στην συσχέτιση των δεικτών τοπικής και καθολικής πλαστιμότητας.
- Τα ψηλότερα βάθρα, έχουν μεγαλύτερη απαίτηση σε δείκτη τοπικής πλαστιμότητας μ_ϕ, για συγκεκριμένη απαίτηση σε δείκτη καθολικής πλαστιμότητας μ_δ. Η απαίτηση πλαστιμότητας του Ευρωκώδικα 8 είναι συντηρητικότερη σε σύγκριση με τις δυο μεθόδους αναλύσεως.
- Αντιστοίχως, η απαίτηση σε δείκτη τοπικής πλαστιμότητας μ_ϕ, για συγκεκριμένο λόγο οριζόντιας μετακίνησης της ανωδομής γ είναι μεγαλύτερη με την πλαστικοποίηση του βάθρου και με την αύξηση της διαμέτρου και του ύψους του βάθρου.
- Σχετικά με τις μέσες και μέγιστες τιμές που λαμβάνουν οι εξεταζόμενοι όροι πλαστιμότητας κατά τη διάρκεια ενός σεισμού, οι δείκτες τοπικής και καθολικής πλαστιμότητας μ_ϕ και μ_δ, μειώνονται όταν η πλαστική άρθρωση αναπτύσσεται μέσα στο έδαφος. Η αύξηση του ύψους του βάθρου και της διαμέτρου του βάθρου αυξάνουν τις μέσες και μέγιστες τιμές των μ_ϕ και μ_δ, ενώ μειώνουν τις αντίστοιχες του λόγου οριζόντιας μετακίνησης της ανωδομής γ.
- Η συσχέτιση των δεικτών τοπικής και καθολικής πλαστιμότητας επηρεάζεται ελάχιστα από την εδαφική ενδοσιμότητα.
- Για δεδομένο λόγο οριζόντιας μετακίνησης της ανωδομής γ, η απαίτηση σε δείκτη τοπικής πλαστιμότητας μ_ϕ, είναι μεγαλύτερη σε μαλακά εδάφη.

Από τα ανωτέρω τονίζεται ο μικρός ευεργετικός ρόλος της ανελαστικής συμπεριφοράς του εδάφους στην απόκριση της κατασκευής, αλλά κυρίως η μεγάλη ευεργετική επίδραση της ανάπτυξης της πλαστικής άρθρωσης στο φορέα κάτω από την επιφάνεια του εδάφους.

Acknowledgements

This research could not have been possible without the collaboration and support of a number of individuals to whom I would like to extend my sincere thanks. First of all, I wish to express my gratitude to my advisor, **Professor George Gazetas**, whose guidance all these years proved to be invaluable. This work could not have been accomplished without his mentorship and motivation.

I am greatly indebted to **Assistant Professor Nikos Gerolymos** for his continuous help, constructive advice and support throughout this research. His wealth of ideas has enriched this dissertation and is highly appreciated.

I would like to acknowledge **Assistant Professor Ioannis Anastasopoulos** for his beneficial comments and discussions on various engineering topics.

I am also extremely grateful to **Dr. Vassilis Drosos** for his assistance in conducting the experiments and the valuable input to various aspects of this dissertation.

I would like to thank my "officemates" **Thanasis Zafeirakos**, **Panagiota Tasiopoulou** and **Marianna Loli** who were always available to discuss this work and **the SGM Group** for the cooperation and the exchange of ideas.

Acknowledgement also goes to **the members of the Geotechnical Department of the School of Civil Engineering of NTUA** for the stimulating discussions on research (and not only) matters.

Words are not enough to thank **my family**, **my friends** and all **those** who traveled this journey with me. I would like to gratefully thank them for their love and support, especially at difficult times.

This work has been conducted with financial support from **the EU 7th Framework research project** funded through the European Research Council's Programme ''Ideas'', Support for Frontier Research – Advanced Grant, under Contract number ERC-2008-AdG 228254-DARE.

TABLE OF CONTENTS

CHAPTER 1: OVERVIEW OF METHODS OF ANALYSIS OF PILES UNDER LATERAL LOADING

1.1 Introduction 7

1.2 Limit Equilibrium Method 8

1.3 Beam-on-Winkler-Foundation Methods 9

1.4 Methods Based on Continuum Mechanics 15

1.4.1 Elastic Solutions 15

1.4.2 Nonlinear Solutions 21

1.5 Macro-element Method 24

1.6 Scope and Structure 26

References 29

CHAPTER 2: A CONSTITUTIVE MODEL FOR THE CYCLIC RESPONSE OF PILES IN COHESIONLESS SOIL

2.1 Piles under Cyclic Loading 49

2.2 Review of Constitutive Model for Cohesive Soils under Undrained Conditions 56

2.3 Extension to Cohesionless Soils under Drained Conditions 58

2.4 Validation against Centrifuge Experiments 59

2.4.1 Centrifuge Lateral Cyclic Load Pile Experiments 59

2.4.2 Finite Element Modeling 61

2.4.3 Numerical Simulation of the Centrifuge Tests 63

2.4.3.1 Calibration of Model Parameters against Test P32 63

2.4.3.2 Comparison of Numerical Results with Tests P344 (Asymmetric Cyclic Loading) and P330 (Symmetric Cyclic Loading) 64

2.4.4 Influence of the π-plane Shape of the Yield Surface on Pile Response 67

2.4.5 Evaluation of Model Predictions 69

2.5 Application to 1x2 Pile Group 70

2.5.1 Test P344 (Asymmetric Cyclic Loading) 70

2.5.2 Test P32 (Asymmetric Cyclic Loading) 72

2.5.3 Test P330 (Symmetric Cyclic Loading) 73
2.5.4 Efficiency Factors 74
2.6 Summary and Conclusions 75
References 77

CHAPTER 3: MACRO-ELEMENT MODELING OF THE LATERAL RESPONSE OF FLEXIBLE PILES: FAILURE SURFACE AND PLASTIC FLOW RULE – ANALYTICAL FORMULATION

3.1 Macro-element Formulation and Requirements 133
3.2 Failure Envelopes: A Review 135
3.3 Derivation of Failure Envelopes and Plastic Flow Rule for Flexible Piles: A Limit Equilibrium Approach 139
3.3.1 Failure Envelope for Pile in Homogeneous Cohesive Soil 140
3.3.2 Failure Envelope for Pile in Cohesive Gibson Soil 143
3.3.3 Failure Envelope for Pile in Cohesionless Soil 145
3.3.4 Failure Envelope for Pile in Two Cohesive Layers 146
3.3.5 Failure Envelope for Pile-column in Cohesionless Soil with Horizontal Force Q and Moment M at a Distance e from the Ground Surface 149
3.4 Summary and Conclusions 151
References 152

CHAPTER 4: MACRO-ELEMENT MODELING OF THE LATERAL RESPONSE OF FLEXIBLE PILES: FAILURE SURFACE AND PLASTIC FLOW RULE – NUMERICAL VERIFICATION

4.1 Introduction 163
4.2 Winkler Approach 163
4.2.1 Failure Envelope for Pile in Homogeneous Cohesive Soil 164
4.2.2 Failure Envelope for Pile in Cohesive Gibson Soil 167
4.2.3 Failure Envelope for Pile in Nonhomogeneous Cohesionless Soil 168
4.2.4 Failure Envelope for Pile in Two Cohesive Layers with $S_{u1} < S_{u2}$ 169
4.2.5 Failure Envelope for Pile in Cohesionless Soil with Horizontal Force Q

and Moment M at a Distance e from the Ground Surface 169
4.3 3D Finite Element Approach 170
4.3.1 Finite Element Modeling 170
4.3.2 Flexible Pile in Cohesionless Soil – Verification against Different Constitutive Soil Models 171
4.3.3 Flexible Pile in Cohesive Soil – Verification against Geometric Nonlinearities 174
4.3.4 M–Q–N Failure Envelope for Flexible Pile in Cohesive Soil 177
4.4 Summary and Conclusions 180
References 182

CHAPTER 5: MACRO-ELEMENT MODELING OF THE LATERAL RESPONSE OF FLEXIBLE PILES: FAILURE SURFACE AND PLASTIC FLOW RULE – EXPERIMENTAL VALIDATION

5.1 Introduction 215
5.2 Validation against Full-scale Test 215
5.3 Validation against Laboratory Tests 216
5.3.1 Experimental Equipment 217
5.3.2 Model Preparation 219
5.3.3 Experimental Results 220
5.3.3.1 Results of Preliminary Tests 220
5.3.3.2 Results of the Pushover Test Series 222
5.4 Numerical Modeling of the Pushover Tests 224
5.5 Summary and Conclusions 227
References 229

CHAPTER 6: APPLICATION TO THE SEISMIC RESPONSE OF BRIDGE PILE-COLUMNS

6.1 Introduction 251
6.2 Elastic Analysis: Evaluation of the Methods Used 252
6.2.1 Problem Investigated 252
6.2.2 Numerical Models 253

6.2.2.1 Beam-on-Winkler-foundation Model 254
6.2.2.2 3D Finite Element Model 255
6.2.3 Results of Elastic Analyses 256
6.3 Inelastic Analysis 258
6.3.1 Problem Investigated 258
6.3.2 Numerical Modeling 260
6.3.2.1 Beam-on-nonlinear-Winkler-foundation Model 260
6.3.2.2 3D Finite Element Model 263
6.3.3 Results of Parametric Analysis 265
6.3.4 Local and Global Ductility Demands 269
6.3.5 Effect of Soil Compliance 273
6.4 Summary and Conclusions 275
References 277

LIST OF REFERENCES 339

CHAPTER 1:

OVERVIEW OF METHODS OF ANALYSIS OF PILES UNDER LATERAL LOADING

1.1 INTRODUCTION

The lateral response of pile foundation under static or dynamic loading is an area of extensive active research, since pile foundation is widely used to support superstructures such as bridges, wind-turbines and offshore platforms. Especially, the kinematic and inertial interaction constitute a complex and unique phenomenon referred to as the soil–pile–structure interaction which includes a number of parameters, such as the soil stratigraphy and properties, the nonlinear stress–strain behavior of the soil and pile (material nonlinearity) and the geometrical nonlinearities (p–δ effects, separation and slippage).

The methods of analyses of laterally loaded piles can be categorized into four major groups: (i) the limit equilibrium method, (ii) beam-on-Winkler-foundation methods usually based on experimentally derived p-y curves, (iii) methods based on continuum mechanics, and (iv) the macro-element method. The limit equilibrium method considers both the pile and the soil to be perfectly plastic and is suitable only for the ultimate load of a pile. Models of the third group can be either linear elastic continuum models or nonlinear continuum finite element models. Linear elastic models are easily used having closed-form expressions, but they are not capable of describing the inevitable soil inelasticity, especially in large strains. Nonlinear continuum finite element models attempt to reproduce realistically the complicated soil-pile interface behavior, but their implementation in numerical codes presumes the use and calibration of quite advanced and complicated constitutive models, usually an extremely time-consuming task. Beam-on-Winkler-foundation models have been proved sufficient in the prediction of horizontally loaded pile response, while at the same time they can be easily implemented in numerical codes. A drawback of this method is that each soil spring responds independently from the adjacent ones, thus ignoring the shear transfer between the soil

layers. Finally, the macro-element method allows the complete macroscopic simulation of the soil-foundation system with minimum time as the beam-on-Winkler-foundation methods, while all the degrees of freedom of the macro-element are coupled.

The lateral pile response and the soil-pile-structure interaction have been investigated by numerous researchers. In the present chapter, an overview of characteristic methods of analysis available in the literature is presented with emphasis on single piles embedded in non-liquefied soils.

1.2 LIMIT EQUILIBRIUM METHOD

In general, limit analysis provide the equations for the loading that develops the ultimate bending moment on the pile. The main assumption considers the soil and the pile as rigid plastic materials. The failure load of a laterally loaded pile was first treated in detail by Broms (1964a, b, 1965). Different mechanisms of failure were identified depending on the relative length of the pile, the plastic moment of the pile section and the strength of the soil. A key quantity in the solutions was the limiting pressure (or force per unit length of the pile) which the soil was assumed to apply. The ultimate load is found by equations of statics for the distribution of ultimate resistance of soil that puts the pile in equilibrium.

For cohesive soil, Broms assumed a limiting pressure of $9S_u$ where S_u the undrained shear strength of the soil. Close to the ground surface this value is reduced to allow for the different mode of deformation at that region. Randolph and Houlsby (1984) used classical plasticity theory to derive lower and upper bound values of the limiting pressure on a laterally loaded pile from undrained soil. The soil was modeled as a perfectly plastic cohesive material and the calculation of the ultimate lateral resistance at depth to purely horizontal movement reduced to a plain strain problem of plastic theory. Hence, the load is calculated on a long cylinder which moves laterally through an infinite medium. It was found that the load factor varies from $6+\pi$ for a perfectly smooth pile to $5.66+2\pi$ for a perfectly rough pile. Similar results have been obtained by Murff and Hamilton (1993) and Martin and Randolph (2006).

For cohesionless soil, Broms assumed that the ultimate lateral resistance is a factor n (in Broms' case n = 3) times the Rankine passive pressure. Many researchers have proposed different values for the factor n. Fleming et al (1992) proposed a value

equal to the passive earth pressure coefficient n = K_p. Pender (1995) proposed a value of n = 5 times the Rankine passive pressure because it compares well results from finite element analysis. Additionally, Cubrinovski et al (2006) based on full-scale pile tests measured a value of n = 4.5.

Recently, De Simone (2012) extended the Broms' theory for cohesionless soils to account for an arbitrary position of the pile head, considering embedded as well as over-ground restrained and free pile head (**Figures 1.1** and **1.2**). As in Broms' theory, soil and pile are both considered as rigid plastic materials, the collapse mechanisms being: (i) the rigid (short or no hinges) and long (one hinge) pile in case of free head, and (ii) short, intermediate (one hinge) and long (two hinges) in the case of a restrained head, with the soil reaction profiles at an ultimate state condition. Explicit analytic expressions for the collapse load and the geometrical parameters (such as pile length and diameter) of the problem are given for the cases examined.

1.3 BEAM-ON-WINKLER-FOUNDATION METHODS

Originally proposed by Winkler in 1967, Beam-on-Winkler-foundation methods are widely used for the response of single piles. The model represents the soil as an array of uncoupled springs while the pile is modeled as a beam-column element. The springs can be linear elastic or nonlinear and the shapes of the load-deformation relationships are described by empirical p-y curves, where the spring stiffness value is variable, allowing consideration of a non-proportional relationship between the soil resistance per unit pile length p and the lateral displacement y. For dynamic problems, hysteretic energy dissipation in the soil is modeled using nonlinear springs whose parameters are determined experimentally from load-deformation curves while dashpots are also introduced that account for the energy dissipation due to radiation damping under dynamic loading conditions. Regarding seismic excitations, Penzien et al (1964) assumed a lumped mass model and performed the analysis in two stages: (1) the dynamic motion of the free-field is obtained by considering that it is uncoupled from the pile motion (site response analysis), and (2) the free-field motion is applied to the soil-pile system as boundary support movements at the end of each spring element. Although this method ignores the shear transfer between layers of soil and the radial and three-dimensional

components of interaction, it has been adopted by many researchers due to its efficiency and simplicity.

Several researchers have developed recommendations for p-y curves. Based on experiments on single piles in soft clay, Matlock (1970) proposed relationships of the soil resistance p and the lateral soil displacement y for short-term loading, for cyclic loading and after-cyclic loading (**Figure 1.3**). Similarly, Reese et al (1974) developed p-y curves for piles embedded in sand for short term static loading and for cyclic loading, while Reese et al (1975) conducted lateral pile load tests in overconsolidated stiff clay and proposed p-y curves for static and cyclic loading. O'Neill and Murchison (1983) proposed a procedure for developing p-y curves for piles embedded in sands that is recommended by the API (2000). In their study, the failure mechanisms of Reese et al (1974) that correspond to the wedge-shaped and the horizontal plane strain failure mode are retained, but three coefficients that are dimensionless functions of the peak friction angle are introduced in the ultimate soil resistance. Furthermore, the initial modulus is given as a function of either the relative density or the friction angle of the soil. Georgiadis (1983) proposed a procedure for the determination of p-y curves for layered soils. Ashour and Norris (2000) developed the Strain Wedge Model, which allows the assessment of nonlinear p-y curve response of laterally loaded piles based on a 3D soil-pile interaction response through a passive wedge soil developing in front of the pile (**Figure 1.4**). This approach relates the stress-strain-strength behaviour of the layered soil in the 3D wedge model to the 1D BNWF model parameters taking into consideration influences such as pile bending stiffness, pile cross-sectional shape, pile-head fixity, and pile-head. Results have shown very good agreement with actual field tests in sand, clay, and layered soils. Finally, Reese and Van Impe (2001) proposed a procedure for short-term static loading and for cyclic loading for piles embedded in soils that are characterized by both cohesion c and friction ϕ.

Novak (1974) based on beam-on-elastic-foundation model studied the dynamic response of piles to horizontal loading and derived spring and dashpots coefficients assuming plane strain conditions. Matlock et al (1978) proposed a Winkler model for the dynamic response analysis of pile foundations which consists of a frequency-independent nonlinear spring connected in parallel with a linear dashpot which accounts for the radiation damping.

Trochanis et al (1991a) used the experience gained from a three-dimensional parametric study to develop a simplified model that reproduces the main nonlinear features of the behavior of single piles, as well as the interaction between a pair of piles. A simplified model consisting of coupled, inelastically supported one-dimensional piles was developed that takes into consideration slippage and separation between the piles and the soil, as well as the overall inelastic soil behavior including degradation. A degrading hysteretic model developed by Wen (1976) for the analysis of single and multi-degree oscillators was adapted as the constitutive model for the vertical and horizontal springs of the proposed simplified model. The validity of the proposed model was assessed by an extensive comparison with numerical results from the more accurate three-dimensional study, as well as with results from experimental field tests.

Nogami et al (1992) completed a rational dynamic soil-pile interaction model which was developed adopting Winkler's hypothesis with a special attention to the conditions in which the strong nonlinearity is induced in the vicinity of the pile shaft under dynamic loading. It is formulated in a simple system of frequency independent mass, springs, and dashpots that consists a near-field and a far-field element (**Figure 1.5**). The near-field element, consisting of nonlinear spring and mass, accounts for the nonlinear soil behavior in the vicinity of the pile shaft, and the far-field element, consisting of three parallel spring and dashpot pairs connected in series, reproduces the elastic behavior of the soil outside the region of strong nonlinear behavior. This arrangement enables the model to logically reproduce the nonlinear effects in the dynamic response by transferring the motion through the area of strong nonlinear behavior to the far field. The nonlinear pile-soil interaction model is applicable to both frequency-domain and time-domain dynamic lateral response analyses. The nonlinear condition and dynamic condition are coupled with each other to produce the complex soil action to the pile shaft motion while special consideration of a gap formation at the soil-pile interface is taken.

Kavvadas and Gazetas (1993) studied the kinematic response of free-head piles since such pile deformation was observed to trigger structural damage in many strong earthquakes. In addition, a dynamic Winkler foundation model for two layered deposits was developed and an extensive parametric study on the kinematic response of single free-head piles to vertically propagating harmonic shear waves was conducted showing

that the critical region of pile distress due to kinematic loading is at or near the interface between alternating soft and stiff soil layers.

Duncan et al (1994) developed the characteristic load method (CLM) based on nonlinear p-y analyses for a wide range of flexible free-head and fixed-head piles and drilled shafts in clay and in sand, in which the results are given in the form of relationships among dimensionless variables (**Figure 1.6**). The method can be used to determine: (1) ground-line deflections due to lateral load for free-head conditions, fixed-head conditions, and the flagpole condition, (2) ground-line deflections due to moments applied at the ground line, (3) maximum moments for free-head conditions, fixed-head conditions, and the flagpole condition, and (4) the location of the maximum moment in the pile or drilled shaft. Ooi et al (2004) extended the characteristic load method (CLM) to account for embedment effects for single fixed-head piles and pile groups. A simplified procedure to estimate group deflections and moments was also developed based on the p-multiplier approach. Group amplification factors are introduced to amplify the single pile deflection and bending moment to reflect pile–soil–pile interaction.

Badoni and Makris (1996) proposed a macroscopic model that consists of distributed hysteretic springs and frequency dependent dashpots to compute the nonlinear response of single piles under dynamic lateral loads. The distributed nonlinear spring described by the Bouc-Wen model (Bouc 1971, Wen 1976) is combined with a distributed viscous dashpot placed in parallel. The model is physically motivated, adequate for both cohesive and cohesionless soils, and involves standard geotechnical parameters. Only two parameters have to be calibrated by fitting experimental data. While hysteretic damping is accounted for by the Bouc-Wen model, the distributed damping coefficient that models radiation damping is provided through a realistic frequency dependent expression which has been modified to allow for some reduction when nonlinear behavior prevails. The model was calibrated and validated against five well instrumented full-scale experiments.

El Naggar and Novak (1996) proposed a Winkler model for evaluating the lateral response of piles accounting for nonlinearity. The model includes a hyperbolic stress-strain relationship and slippage and gapping at the pile-soil interface. Springs, sliders and dashpots are combined to approximate the behavior of the pile-soil interface, the 'inner' field and the 'outer' field. The model also accounts for the propagation of waves away

from the pile and energy dissipation through both material and geometric damping. El Naggar and Bentley (2000) modified this model to utilize existing or developed cyclic or static p-y curves to represent nonlinear behavior of the soil adjacent to the pile (**Figure 1.7**).

Wang et al (1998) used several implementations of the beam-on-nonlinear-Winkler-foundation method to predict results of centrifuge model tests of single piles in a soft clay soil profile. By separating the soil into two zones, near field and far field, soil behavior under soil-pile-structure interaction is reasonably modeled. It was found that viscous dashpots in parallel with a hysteretic element (parallel radiation damping) can provide a mechanism for unrealistically large forces transmitted around the hysteretic element. This problem can be avoided by placing the linear viscous dashpot in parallel with only the linear component of the hysteretic element and then in series with the hysteretic component (series radiation damping).

Boulanger et al (1999) proposed a dynamic beam-on-nonlinear-Winkler-foundation (or ‘‘dynamic p-y’’) analysis method for analyzing seismic soil-pile-structure interaction (**Figure 1.8**). The nonlinear behavior consists of elastic, plastic and gap components in series. Important features of the dynamic p-y analyses include the use of series hysteretic/viscous damping to represent radiation damping (as proposed by Wang et al, 1998) and the inclusion of gapping effects (after Matlock et al, 1978) by a nonlinear closure spring in parallel with a nonlinear drag spring. This method was evaluated against the results of a series of dynamic centrifuge model tests. The centrifuge tests included two different single-pile-supported structures subjected to nine different earthquake events with peak accelerations ranging from 0.02 to 0.7g. The soil profile consisted of soft clay overlying dense sand. Reasonably good agreement was obtained between calculated and recorded responses for both structural models in all earthquake events.

Budek et al (2000) used a simple beam-on-Winkler-foundation model to represent the lateral force response of a reinforced concrete (RC) pile in cohesionless soil. An inelastic analysis was performed on the structure, using as the pile constitutive model the section moment-curvature relationship which was based on confined stress-strain relationships for the concrete. The varied parameters included the pile head conditions (free and fixed head), the height of pile head above ground level, and the soil stiffness. Linear, bilinear, and hyperbolic soil models were examined. The analysis

showed that shear would be significantly underpredicted by an elastic analysis, as inelastic behavior moved the point of maximum moment in the pile shaft closer to the surface, thus reducing the shear span. Maximum moment depth in the pile shaft and plastic hinge length were also shown to be strongly dependent on soil stiffness, and in the case of fixed-head piles, on above ground height of the superstructure.

Nikolaou et al (2001) implemented an approximate beam-on-dynamic-Winkler-foundation (BDWF) model for the seismic response of piles in layered soil. After evaluating some existing design methods for kinematic pile loading, a simple approximate formula for estimating the maximum harmonic steady-state bending moment at the interface between two consecutive soil layers under resonant conditions was proposed. The expression is based on a "characteristic" shear stress, τ_c, which is proportional to the actual shear stress that is likely to develop at the interface, as function of the maximum free-field acceleration at surface. Both fixed- and free-head piles, and different boundary conditions at the pile toe, were considered. It was shown that the magnitude of kinematic moments depends mainly on the stiffness contrast between the soil layers, the pile-soil stiffness contrast, the excitation frequency, and the number of excitation cycles.

Hutchinson et al (2004) performed nonlinear static and dynamic analyses to evaluate the inelastic seismic response of bridge and viaduct structures supported on extended cast-in-drilled-hole (CIDH) pile shafts. The nonlinear dynamic analyses used a beam-on-nonlinear-Winkler-foundation model to simulate the soil-pile interaction, nonlinear fiber beam-column elements to model the reinforced concrete sections and one-dimensional site response analyses for the free-field soil profile response. The study included consideration of ground motion characteristics, site response, lateral soil resistance, structural parameters, geometry nonlinearity (P-Δ effects), and performance measures. Results focused on how the ground motion characteristics and variations in structural configurations affect the performance measures that evaluate the inelastic seismic response.

Gerolymos and Gazetas (2005) developed a dynamic nonlinear Winkler spring model to study the seismic response of deep foundations. The model utilizes the phenomenological Winkler-type model for the inelastic response of both the soil and the pile. The constitutive model used for the soil springs, the soil dashpots and the pile is

based on an extension and modification of the Bouc-Wen model, named BWGG. The nonlinear reaction of the soil is modeled realistically by the BWGG interaction springs and dashpots and is able to simulate effects such as separation of the pile from the soil, radiation damping and loss of strength due to pore-water pressure development. The modeling of the pile inelasticity can treat from well-reinforced to poorly-reinforced concrete sections. The proposed model is calibrated through experimental data and is capable of predicting the large amplitude dynamic response of piles up to failure from pile load tests both static and cyclic. Gerolymos et al (2009) applied this model to the analysis of pile-column supported bridge structures, in order to investigate the consequences of pile yielding in the response of such systems.

Allotey and El Naggar (2008) developed a synthesized cyclic normal force-displacement model for the dynamic Beam-on-nonlinear-Winkler-foundation model used in the analysis of shallow and deep foundations. The backbone curve of the model comprises a four-segment adaptable multi-linear curve that can represent both monotonic and post-peak behavior. The approach used for the unloading and reloading curves is an adaptation of Pyke's method (Pyke, 1979) which is modified to account for strength degradation. A soil cave-in modeling approach is developed allowing for the rational modeling of the slack zone formation. A modified version of the rainflow-counting technique of Anthes (1997) is developed for the modeling of cyclic degradation. Radiation damping is modeled using a stiffness-proportional nonlinear damping formulation that comprises a nonlinear dashpot placed in parallel with a nonlinear spring, while the hysteretic damping ratio of the model ranges from zero for a perfectly elastic response to the largest possible amount of energy dissipation per cycle under two-way cyclic loading.

1.4 METHODS BASED ON CONTINUUM MECHANICS

1.4.1 Elastic solutions

Models of this group have analytical or numerical solutions. The elastic continuum analytical method is based on Mindlin's (1936) closed-form solution for the application of point loads within a half-space. Soil nonlinearity is not taken into consideration and the method is applicable to small-strain steady-state vibration problems.

Poulos (1971) used the elastic theory, in which the soil surrounding the pile is modeled as a homogeneous elastic continuum, to study the displacement, rotation and moment in a single floating vertical pile subjected to horizontal load and moment. The effects of local yielding of the soil on the behavior of the pile were also examined. Despite its limitations, the proposed theory enables: (a) quantitative estimates of the effect of pile movements of factors like the pile length and stiffness, (b) an estimate of the relative proportions of immediate and consolidation movement, and (c) a logical analysis of the effects of local soil yielding. Poulos and Davis (1980) extended the elastic theory to analysis and design methods for pile foundations for a wide range of cases.

Kagawa and Kraft (1980) used the results of a 3-D Finite Element analysis to derive spring and dashpot coefficients comparable to those of the plane-strain case. The analyses performed led to dynamic p-y relationships of three heterogeneous soil profiles. Nonlinear stress-strain relationships of soils were approximated by the equivalent linear method. A conventional beam-on-Winkler- foundation method was then used to provide a basis of comparison with the obtained results to gain some insight into the nonlinear discrete soil-pile springs and dashpots for the seismic response analysis of a soil-pile-structure system.

Randolph (1981) conducted a parametric study of the response of laterally loaded cylindrical piles embedded in an elastic soil continuum with: (i) a constant, and (ii) a linearly varying soil modulus, using the finite element method. Based on the results from the analyses, simple algebraic expressions for the active length of the pile, the ground level deformations, and the maximum bending moment along the pile derived. In addition, the patterns of soil movement around a laterally loaded single pile, obtained from the finite element analysis, were used to develop expressions for interaction factors between adjacent piles for fixed-headed and free-headed piles.

Velez et al (1983) utilized an efficient finite-element formulation to study the dynamic response characteristics of single constrained-head piles embedded in a soil stratum having linearly increasing stiffness with depth. The excitation consists of a harmonic horizontal force or moment applied at the pile head and the soil is modeled as a linear hysteretic medium. The results of the study are presented in the form of non-dimensional graphs from which one can estimate static and dynamic stiffnesses and effective damping ratios of piles. The three impedances (swaying, rocking and coupled

swaying-rocking) are expressed in terms of the normalized stiffness and the three corresponding effective damping ratios depend on: (1) the ratio of the Young's modulus of the pile over the Young's modulus of the soil, (2) the slenderness ratio L/d, (3) the dimensionless frequency factor $a_s = \omega d/V_s$, in which V_s the shear wave velocity of the soil, (4) the internal hysteretic damping ratio in the soil β assumed to be either a constant or a decreasing function of depth, (5) the Poisson's ratio v of the soil, and (6) the ratio of mass density of the pile and the soil. In addition, the concept of an effective soil modulus is introduced to elucidate the importance of soil non-homogeneity and it is shown that the effective soil modulus not only depends on the type of loading (force or moment), but also on its frequency of oscillation. Finally, criteria were developed to define when a pile is "flexible" under static and dynamic loads.

Gazetas (1984) presented an extensive parametric study of the dynamic response of end-bearing piles embedded in soils with (a) homogeneous, (b) linear, and (c) parabolic Young's modulus distribution and subjected to propagating harmonic S-waves. The seismic soil-pile-structure interaction was studied as the superposition of two effects: (i) the kinematic interaction effect, and (ii) the inertial interaction effect (**Figure 1.9**). Results from both kinematic and inertial interaction are offered in the form of dimensionless graphs and formulae covering a wide range of excitation frequencies and geometric parameters. The kinematic amplification and interaction factors are given in comparison to the ratio of the excitation frequency to the soil frequency as a function of: the stiffness ratio of the pile and the soil, the soil profile, and the slenderness ratio of the pile length to the pile diameter. Thus, by multiplying a given free-field design response spectrum with the appropriate interaction curve, the design response spectrum that must be input at the base of a structure on piles foundation may derive. The steady state response of piles to lateral dynamic forces from the superstructure is computed as a function of the dynamic impedances $\boldsymbol{K_{HH}}$, $\boldsymbol{K_{MM}}$ and $\boldsymbol{K_{HM}}$ associated with swaying, rocking and coupled swaying-rocking oscillations, respectively. Each impedance is expressed as a product of the static stiffness of the pile with the dynamic stiffness coefficient and the effective damping ratio of the system.

Gazetas and Dobry (1984) developed a procedure for estimating the lateral dynamic stiffness and damping of flexible piles embedded in arbitrarily layered soil deposits. The proposed approximate method involves four steps:

(1) The horizontal displacement profile $y_s(z)$ of the pile subjected to a statically applied horizontal load of magnitude P_o is obtained. The static value K_s of the spring coefficient K is then directly computed.

(2) Two parallel dashpots are assumed attached to the pile at every elevation and their characteristic coefficients c_m and c_r are determined. The first dashpot simulates the material dissipation of energy in the soil, while the second dashpot simulates the radiation of energy by waves spreading geometrically away from the pile-soil interface.

(3) The overall dashpot coefficient C = C(f) at the head of the pile is computed from the values of c_r and c_m distributed along the pile (step 2) in conjunction with the static pile deflection profile $y_s(z)$ (step1).

(4) The variation with frequency of both the spring coefficient K(f) and the damping ration D(f) are estimated from the static stiffness, K_s, and from the results of steps 2 and 3.

In addition, models based on 1-D and 2-D wave propagation idealizations are discussed and a new one is proposed (**Figure 1.10**). This approximate plane-strain model is based on the assumption that compression-extension waves propagate in the two quarter-planes along the direction of loading while shear waves are generated in the two quarter-planes perpendicular to the direction of loading. Only horizontal soil deformations are allowed within each quarter-plane and all straight lines originally normal to the corresponding direction of wave-propagation remain normal during the oscillation. The shear waves are assumed to propagate with velocity V_s in the two quarter-planes, while compression-extension waves propagate with Lysmer's analog velocity V_{La} in the other two quarter-planes.

Nonlinear lateral response solutions from the elastic continuum theory were developed by Budhu and Davies (1987) under the condition that the lateral pile-soil pressure cannot exceed the ultimate lateral pile-soil pressure. Specifically, the cohesionless soil is modeled as en elastic-perfectly plastic material that yields when the normal and shear stresses on the pile exceed those calculated from considerations of limit equilibrium. The analysis takes into account the bearing failure in the compressive soil zone around the pile, the interface slip at the limiting shear stress and the gapping in the tensile soil zone. Similarly for cohesionless soils, Budhu and Davies (1988) proposed

an analysis of laterally loaded piles based on the boundary element method and assuming knowledge of the shear-strength profile of the soil. The shear strength is assumed to increase linearly with depth, a reasonable assumption for soft clays. The analysis encompasses bearing failure in the compressive zones, shear failure along the pile-soil interface, and tension failure in the soil. The solution for a laterally loaded pile using this method requires specification of only one soil parameter, the undrained shear-strength distribution with depth. The elastic loading response and collapse loading conditions are expressed in terms of simple equations, while the effects of soil yielding are presented in convenient dimensionless diagrams and equations in order to facilitate design applications.

Fan et al (1991) studied the kinematic response of groups of vertical floating piles connected through rigid massless caps and subjected to vertically propagating harmonic S-waves. Dimensionless graphs have been presented for dynamic horizontal displacements and rotations developing at the cap level of single piles and pile groups, embedded in three idealized soil profiles: a homogeneous half-space, a half-space with modulus proportional to depth, and a two-layered stratum. These graphs are of practical value in determining the "effective" seismic input motion at the base of structures, if the free-field motion is known (e.g. in the form of a "design" spectrum of the seismic code).

Sun (1994) developed a continuum-based analytical solution for laterally loaded piles based on the Vlasov and Leontiev (1966) method. The proposed method uses variational calculus to obtain the governing differential equations of the soil and pile system. A principal parameter γ is used in this model to present the elastic foundation, and an iterative technique is adopted to obtain a consistent energy solution. Both free and fixed head piles are considered. Two kinds of boundary conditions of practical interest at the pile tip, floating tip and clamped tip, are also considered. The proposed method has been validated by comparison with other available methods based on the elastic continuum and finite element approach. Basu and Salgado (2007) extended this method for laterally loaded piles in homogeneous medium and developed closed-form solutions for piles embedded in multi-layered elastic continua. The analysis takes into account an arbitrary number of soil layers and the 3D interaction of the pile and the surrounding soil.

Tabesh and Poulos (2001) suggested a simple approximate methodology for estimating the maximum internal forces of piles subjected to lateral seismic excitation. The approach assumes that: (i) the soil is an ideal elastic, isotropic material, (ii) the stresses developed between the pile and the soil act normal to the face of the pile, and no account is taken of possible shear stresses developed between the soil and the sides of the pile, and (iii) each pile element is acted upon by a uniform horizontal stress p, which is constant across the width of the pile. The method involves two main steps: (1) computation of the free-field soil movements caused by the earthquake, and (2) the analysis of the response of the pile to the maximum free-field soil movements (considered as static movements) plus a static loading at the pile head, which depends on the computed spectral acceleration of the structure being supported.

Sa'don et al (2007) based on the elastic continuum approach developed an analytical technique for the cyclic response of laterally loaded piles. In this study, the response of the whole pile shaft is represented by a simple set of pile stiffness equations focusing on the pile head. Both linear and nonlinear load−displacement response of the pile are considered and results are verified against the cyclic Winkler calculations and field data.

Maiorano et al (2009) performed an extensive parametric study on single piles and pile groups embedded in a two-layer subsoil profile aiming to evaluate kinematic bending moments developing during earthquakes. A quasi three-dimensional finite element program has been used to perform dynamic analyses in the time domain. Piles have been considered as elastic beams, while the soil has been modeled using a linear elastic constitutive model. Kinematic bending moments in single piles and pile groups with dynamic analyses in the time domain, in different subsoil conditions were evaluated and compared with simplified approaches provided in published literature. On the basis of the obtained results, a modified criterion to evaluate the transient peak bending moments at interfaces between layers is proposed.

Rovithis et al (2009) studied the elasto-dynamic response of soil-pile-structure systems to seismic loading using a rigorous three-dimentional finite element model. The system under investigation comprises of a single pile supporting a single degree of freedom (SDOF) structure founded on a homogeneous visco-elastic soil layer over rigid rock. Parametric analyses are carried out in the frequency domain, focusing on: (a) soil-

pile-structure interaction in terms of the modified dynamic properties of the coupled system, (b) the combined effect of kinematic and inertial interaction on the motion of the pile head, by identifying the fundamental frequencies that dominate the response, and (c) the role of the frequency content of the input motion on the development of pile bending. Furthermore, the notion of a pseudo-natural SSI frequency is introduced, as the frequency where pile-head motion is minimized with respect to free-field surface motion.

Di Laora et al (2012) investigated the behavior of kinematically stressed fixed head and free-head piles in layered soil under the passage of vertically-propagating seismic S waves with three-dimensional finite element analyses. Both pile and soil are idealized as linearly visco-elastic materials, modeled by solid elements and pertinent interpolation functions in the realm of classical elastodynamic theory. The system is analyzed by a time-Fourier approach in conjunction with a modal expansion in space. Constant viscous damping is considered for each natural mode, and a FFT algorithm is employed to switch from frequency to time domain and vice versa in natural or generalized coordinates. Kinematic bending in the vicinity of a layer interface can be viewed as the superposition of two components: (1) a negative contribution imposed by soil curvature in the first (soft) layer, and (2) a positive contribution provided by the restraint effect of the second (stiff) layer. In this context, the interface can be viewed as a bending perturbation agent whose influence vanishes beyond an active pile length above and below that specific elevation. A simplified semi-analytical formula for evaluating pile bending moment at an interface separating two soil layers of different stiffness is proposed. The results of the study offer an interpretation of kinematic pile bending in terms of the interplay between pile and soil, expressed through dimensionless layer thickness, pile-to-soil stiffness ratio and impedance contrast at the layer interface.

1.4.2 Nonlinear solutions

On the second category, the finite element analysis offers the ability to simulate any possible soil profile by applying appropriate constitutive soil models. Regarding dynamic analyses, soil-pile-structure interaction problems are solved efficiently in a fully coupled manner.

Brown and Shie (1990) analyzed the behavior of a pile subjected to lateral loading using a three dimensional finite element model. In order to study parametrically the

effects of pile spacing, pile head fixity, and soil stiffness on the pile response, the model accounts for soil plastic yielding as well as gapping and slippage at the pile-soil interface. Soil constitutive models include a simple elastic-plastic model with a Mises yield surface and associated flow rule and an extended Drucker-Prager model with non-associated flow rule. Frictional interface elements were used to provide for slippage at the pile-soil interface and to allow gapping in the space behind the pile. Bending moment data from the pile were used to obtain p-y curves.

Trochanis et al (1991b) examined the effect of nonlinear soil behavior on the axial and lateral response of piles to monotonic and cyclic loading by means of a three-dimensional finite element model. The soil material, either clay or sand, is idealized as a Drucker-Prager elasto-plastic continuum, and interface elements are used to allow for slipping and separation between the piles and the soil. Neglecting inertia effects, only pseudodynamic loading was considered. A limited parametric study of the response of a single pile and a pair of piles subjected to concentrated loads at their heads was conducted in order to examine the effects of soil plasticity, slippage, and separation between piles and the soil.

Wu and Finn (1997a, b) developed a quasi-3D finite element method of total stress analysis for both: (i) dynamic elastic analysis in frequency domain, and (ii) dynamic nonlinear analysis in time domain of single piles and pile groups. The proposed method is based on a simplified 3D wave equation for describing the dynamic response of foundation soils. The analysis simulates the nonlinear stress-strain response and the hysteretic damping of the soil, as well as soil yielding and potential gapping between the pile and attached soil. The analysis has been incorporated into the computer program PILE-3D and has been validated using data from centrifuge tests. Recently, Thavaraj et al (2010) extended this quasi-3D continuum method of dynamic analysis for the dynamic nonlinear analysis of pile foundation under earthquake excitation. The total stress based method was extended for effective stress analysis by incorporating a model for the pore-water pressure generation due to earthquake shaking. The method was incorporated into computer programs (PILE-PY and PILE3D) and verified against centrifuge tests.

Bentley and El Naggar (2000) developed a 3D finite element model that can accurately model the kinematic soil-pile interaction accounting for the nonlinear behavior of the soil (using the Drucker-Prager model), the discontinuity conditions at the

pile-soil interface, the energy dissipation and the wave propagation. The model was used to investigate the kinematic interaction effects of a free-head pile response with respect to the input ground motion. Overall, the kinematic interaction response for the cases examined resembled the free-field response.

Yang and Jeremic (2003) based on results from a 3D finite element study on the behavior of a single pile in elastic-plastic soils generated p-y curves for pile embedded in uniform sand, clay as well as cases with sand layer in clay deposit and clay layer in sand deposit. Clay was modeled by a simple Von Mises material model which is completely defined with the undrained shear strength, while sand was simulated by a Drucker-Prager material model with a non-associated flow rule.

Maheshwari et al (2004) examined the effects of plasticity and work hardening of soil on the free-field response and the kinematic response of single piles and pile groups using the hierarchical single surface (HiSS) soil model. The analysis extended to include the superstructure in order to evaluate the effects of soil-pile-structure interaction for a fully coupled system taking into account both linear and nonlinear responses.

Zhang et al (2004) examined the effects of slope inclination and sleeving thickness on the behavior of laterally loaded piles based on a series of 3D finite difference analysis in which the soil was simulated with an elastic-perfectly plastic model. Based on the results, empirical relations for estimating the horizontal displacement and the maximum bending moment of a pile in a sloping ground are proposed together with a criterion for selecting suitable sleeving thickness considering both pile response and compressibility of the sleeving material.

Jeremic et al (2009) presented a numerical investigation of the influence of non–uniform soil conditions on a prototype concrete bridge with three bents where soil beneath bridge bents varied between stiff sands and soft clay (**Figure 1.11**). The soil constitutive model used consists of a Drucker–Prager yield surface, Drucker–Prager plastic flow directions (potential surface) and a nonlinear Armstrong–Frederick (rotational) kinematic hardening rule. Eight specific cases representing combinations of different soil conditions beneath each of the bents were simulated. It was shown that variability of soil beneath bridge bents has significant influence on bridge system (soil–foundation–structure) seismic behavior. Furthermore, the obtained results indicate that free-field motions differ from the observed motions under the base of the bridge

columns implying that the use of free-field motions as input for only structural models is not be appropriate. It is also shown that the usually assumed beneficial effect of stiff soils underneath a structure cannot be generalized and that such stiff soils do not necessarily help the seismic performance of structures.

Georgiadis and Georgiadis (2010) proposed p-y curves for flexible free-head piles embedded in sloping cohesive soil based on 3D finite element analyses (**Figure 1.12**). Piles of different diameter and length embedded in sloping cohesive soils, which are modeled as linear elastic–perfectly plastic Tresca material, with various undrained shear strength and several ground slopes were studied. Based on the results of the finite element analyses, analytical formulations for the ultimate load per unit length and the initial stiffness of hyperbolic p-y curves derived. New p-y criteria for static loading of piles in clay are proposed, which take into account the inclination of the slope and the adhesion of the pile-slope interface.

1.5 MACRO-ELEMENT METHOD

Macro-element modeling is a new method for the study of the non-linear effects in the soil-foundation system. The macro-element can be thought of as an advanced finite element, and more precisely a link element, to be used in numerical modeling of structures subjected to seismic loading. This element is placed at the base of the superstructure and aims at reproducing non-linear interaction effects taking place at foundation level. Its main advantages are: (1) computationally expensive 3D non-linear soil-structure interaction analyses can be avoided, since it simplifies drastically the consideration of soil-structure interaction effects in structural analyses by dispensing from the need to model explicitly the soil domain, and (2) foundation response at very small (nearly elastic) and at extremely large deformations are treated within a unified mathematical framework.

At present, the most comprehensive macro-element models for soil-foundation interaction are based on work-hardening plasticity theory. In the non-linear macro-element method, the entire soil-foundation system is replaced by a single element located at the base of the super-structure, described with a suitable yield surface and plastic potential function. Thus, the footing and the soil are considered as a single ‘macro-element’, and a 6 DOF (3D case) or a 3 DOF (2D case) model is formulated

describing the resultant force−displacement behavior of a point of the footing (e.g. the center of a surface foundation or the center of head in the case of a pile foundation) in the vertical, horizontal, and rotational directions (Chatzigogos et al, 2011). The basic assumption beneath this formulation is that the footing is considered as a rigid body. The main advantage with respect to the Beam-on-nonlinear-Winkler-Foundation method is that all degrees of freedom of the macro-element are coupled.

According to Martin and Houlsby (2001) the four basic components needed for the formation of a macro-element are: (1) an expression of the failure envelope of the foundation in three dimensional moment, horizontal and vertical loading M–Q–N space, (2) an expression of the elastic response of the foundation within the yield surface, (3) an expression of a plastic flow rule for the incremental plastic displacements at failure of the reference point of the foundation, and (4) an expression of a hardening law which controls the transition from the elastic (small-strain) response to the yielding (large-strain) response. It is remarked that even though considerable effort has been devoted to the macro-element modeling of shallow foundations (e.g. Nova and Montrasio, 1991; Paolucci, 1997; Cremer et al, 2002; Di Prisco et al, 2003; Chatzigogos et al, 2011 among others), only recently macro-element modeling of deep foundations has been developed.

Gerolymos et al (2012) studied the response of massive square caisson foundations embedded in undrained soil and subjected to combined overturning moment, horizontal and vertical loading M–Q–N through a series of force-controlled and sideswipe 3D finite element analyses. The ultimate limit states are presented by failure envelopes in normalized form with their pure loading capacities. The results emphasized the effects of the embedment depth and the vertical factor of safety on the failure modes of the caisson. Furthermore, analytical expressions for the failure envelope and the associated plastic flow rule, that serve as a basis for a plasticity-based macro-element for caissons in undrained cohesive soils without gap formation were proposed.

Correia et al (2012) extended the macro-element model for shallow foundations by Figini et al (2011) to the design of pile-shafts that support bridges. The lateral response of the entire soil-pile system to seismic actions is condensed at the pile-head, being represented by a joint element located at the base of the columns and subjected to the foundation input motion. A saturated soil deposit is considered with undrained behavior and the Tresca failure criterion. Two undrained shear strength distributions

were studied: (i) a constant one, and (b) a linear one. The main elements of the macro-element consist of: (1) a nonlinear elastic model (small-strain behavior of the system) that accounts for the transition from the initial response (with no gap), to a gap opening on the back of the pile for monotonic response, or to a gap on both sides of the pile when cyclic behavior is considered, (2) a failure mechanism and ultimate loading surface for laterally loaded piles (large-strain behavior of the system) which are determined through optimization procedure of the results of three-dimensional analyses based on the kinematic approach of yield design theory, (3) a gapping behavior which is associated with the evolution of inelastic displacements of the pile-soil system, and (4) a bounding surface plasticity model for the pile-head resultant generalized forces and corresponding displacements that ensures a smooth transition from the initial nonlinear elastic behavior up to large-strain response domains. The resulting macro-element parameters are largely based on fundamental response characteristics and only 4 out of the initial 15 parameters need to be calibrated. The response of the macro-element was calibrated and validated with numerical results and experimental load tests. Additionally, nonlinear incremental dynamic analyses were performed on a reinforced concrete bridge, considering different support conditions and a large set of ground motions, with minor computational effort.

1.6 SCOPE AND STRUCTURE

Even today, the methods of analyses of laterally loaded piles are evaluated and modified, while taking into consideration new experimental data (eg. Curras et al, 2001; Rollins et al, 2005; LeBlanc et al, 2010; Chenaf et al, 2012) and case histories, especially from pile failures during earthquakes (eg. Haiti, 2010 (Green et al, 2011); Chile, 2010 (Villalobos et al, 2011, **Figure 1.13**); Christchurch, 2011 (Tasiopoulou et al, 2011, **Figure 1.14**)). The scope of the present dissertation is the acquisition of knowledge regarding the nonlinear interaction of the pile-soil system under static and dynamic loading. In addition, it contributes to the development of a macro-element for the response of the pile-soil system which takes into consideration the possible nonlinear mechanisms of the response. Finally, the dissertation focuses on the understanding of the influence of key elements, such as the pile-to-pile interaction for nonlinear soil response and the development of plastic hinge at the pile foundation, on the pile-soil interaction.

Chapter 2 presents a simplified constitutive soil model for the static and cyclic response of piles embedded in cohesionless soil under drained conditions. The constitutive model is implemented in a three-dimensional finite element code through a user subroutine. The model predictions are compared with experimental results of three centrifuge experiments on a pile in dry sand from Laboratoire Central des Ponts et Chaussees (LCPC) in Nantes, France. The comparison sheds light on some complicated features of the pile response regarding: (i) the observed plastic shakedown behavior of the pile, (ii) the effect of the so-called "system" densification and the cyclically-induced material (soil) densification that result in the plastic shakedown response of the pile, and (iii) the influence of the number of cycles on the internal structural forces (residual and maximum) and soil reactions of the pile. Appropriately defined performance measure parameters are introduced to evaluate the pile response and to unravel the contribution of soil and "system" densification to the plastic shakedown mechanism. The influence of the π-plane shape of the yield surface of the proposed constitutive model is also investigated. The model is further utilized to the analysis of a case study involving a group of 1x2 piles with similar characteristics to those of the centrifuge tests focusing on: (i) the influence of the shadow effect on the pile group response, and (ii) the efficiency of the pile group.

Chapter 3 deals with components of a macro-element for piles. Closed-form solutions for failure envelopes of flexible single pile under combined Q–M loading for different soil conditions are proposed based on limit equilibrium analysis. The failure envelope is normalized against the pure lateral load and the pure overturning moment capacity of the soil-pile system, thus allowing the shape of the envelope to remain unaffected from any other strength parameter of the soil or the pile. Analytical expressions of the plastic flow rule are also proposed with the assumption of normality.

Chapter 4 verifies the proposed failure envelope and the associated plastic flow rule against force-controlled analyses with an elastoplastic Beam-on-Winkler-foundation model. As expected, the shape of the normalized failure envelope remains unaffected from strength parameters of the soil or the pile such as the soil Young's Modulus, the soil strength and the pile diameter. The assumption of an associated plastic flow rule is verified graphically by the normality of the incremental displacement vectors at failure from the Winkler model on the failure surface. It is also found that the plastic

displacement to rotation ratio at failure equals to the depth of the plastic hinge formation of the rigid body measured from the ground surface. The analytical expressions of both the failure envelope and the associated plastic flow rule are further evaluated against 3D numerical analyses: (i) with different soil constitutive models (including the one developed in **Chapter 2**), and (ii) with and without allowing slippage and separation at the pile-soil interface. Furthermore, the pile response within the proposed normalized failure envelope is examined and separated in four zones of characteristic response. Finally, based on the 3D analyses, a complete failure envelope for M−Q−N loading is proposed without taking into consideration the interaction diagrams of the pile material.

Chapter 5 compares the results from one real-scale pushover test on a vertical pile embedded in clay with the proposed failure envelope and outlines a series of laboratory pushover experiments on single piles embedded in dry sand under lateral force and overturning moment combinations at the pile head conducted at the Laboratory of Soil Mechanics / Dynamics in NTUA. Preliminary tests were performed in order to figure out the influence of parameters such as pile diameter, soil-pile interface, soil density and pile position in the sandbox. The results from the Pushover Tests validate the proposed failure envelope and the assumption of an associated plastic flow rule. Validation of the experiments is achieved through comparisons with results from Class B predictions with a simplified beam-on-nonlinear-Winkler-foundation model. In addition, 3D finite element analyses taking into account the nonlinear behavior of the soil and the pile are undertaken to model the Push-over Tests. For this reason, a fourth parameter is introduced to the proposed constitutive model of **Chapter 2** which accounts for soil softening through the variation of friction angle with octahedral strain.

Chapter 6 investigates the influence of the pile inelastic behavior and soil-structure interaction on structure ductility demand based on the concept proposed by Gerolymos et al (2009), according to which the formation of a plastic hinge in the pile shaft can be beneficial. Hence, a parametric investigation of the nonlinear response of pile-column bridge systems is conducted with the use of two models: (i) a beam-on-nonlinear-Winkler-foundation model, and (ii) a 3-D continuum finite element model utilizing advanced inelastic constitutive laws (including the one developed in **Chapter 2**). Initially, the elastic response of a soil-pile- bridge system is investigated with the two

methods. For the nonlinear response of pile-column bridge systems, a calibration methodology of the "spring" and "dashpot" coefficients of the examined hybrid spring configuration of the Beam-on-nonlinear-Winkler-foundation model is proposed. Regarding the 3D finite element analysis, the constitutive model parameters of **Chapter 2** are calibrated to fit published G-γ and ξ-γ curves by Ishibashi and Zhang (1993) and the dynamic analysis of soil-pile-bridge systems is performed in a fully coupled manner. The role of various key parameters, such as the soil compliance, the aboveground height of the pile-column, the pile diameter and the location of the plastic hinge, is examined on characteristic performance measures of the pile-column bridge system response, namely the local curvature ductility demand μ_ϕ, the global displacement ductility demand μ_δ and the maximum drift ratio γ_{max}. It is clear that the location of the plastic hinge below the ground surface rather than soil compliance has a beneficial influence on the response of the structure.

REFERENCES

Allotey N., El Naggar M.H., 2008, "Generalized dynamic Winkler model for nonlinear soil-structure interaction analysis", *Canadian Geotechnical Journal*, 45, pp 560-573

American Petroleum Institute (API), 2000, Recommended practice for planning, designing and constructing fixed offshore platforms-working stress design, *API Recommended Practice 2A-WSD (RP 2A-WSD)*, 21st edn.

Anthes R.J., 1997, "Modified rainflow counting keeping the load sequence", *International Journal of Fatigue*, 19, pp 529-535

Ashour M., Norris G., 2000, "Modeling lateral soil-pile response based on soil-pile interaction", *Journal of Geotechnical and Geoenvironmental Engineering*, 126 (5), pp 420-428

Badoni D., Makris N., 1996, "Nonlinear response of single piles under lateral inertial and seismic loads", *Soil Dynamics and Earthquake Engineering*, 15, pp 29-43

Basu D., Salgado R., 2007, "Elastic analysis of laterally loaded pile in multi-layered soil", *Geomechanics and Geoengineering: An International Journal*, 2 (3), pp 183-196

Bentley K., El Naggar M.H, 2000, "Numerical analysis of kinematic response of single piles", *Canadian Geotechnical Journal*, 37, pp 1368-1382

Bouc R., 1971, “Modele mathematique d’ hysterisis”, *Acustica*, 21, pp 16-25

Boulanger, R., Curras, C., Kutter, B., Wilson, D., Abghari, A., 1999, ”Seismic soil-pile-structure interaction experiments and analyses”, *Journal of Geotechnical and Geoenvironmental Engineering*, 125 (9), pp 750–759

Broms B., 1964a, “Lateral resistance of piles in cohesive soils”, *Journal of Soil Mechanics and Foundation Division*, ASCE, 90 (2), pp 27-63

Broms B., 1964b, “Lateral resistance of piles in cohesionless soils”, *Journal of Soil Mechanics and Foundation Division*, ASCE, 90 (3), pp 123-156

Broms B., 1965, “Design of laterally loaded piles”, *Journal of Soil Mechanics and Foundation Division*, ASCE, 91 (3), pp 77-99

Brown D.A., Shie C., 1990, “Three dimensional finite element model of laterally loaded piles”, *Computers and Geotechnics*, 10, pp 59-79

Budek A.M., Priestley M.J.N., Benzoni G., 2000, “Inelastic seismic response of bridge drilled-shaft rc pile/columns”, Journal of Structural Engineering, 126 (4), pp 510-517

Budhu M., Davies, T., 1987, ”Nonlinear analysis of laterally loaded piles in cohesionless soils”, *Canadian Geotechnical Journal*, 24 (2), pp 289–296

Budhu M., Davies, T., 1988, ”Analysis of laterally loaded piles in soft clays”, *Journal of Geotechnical Engineering*, 114 (1), pp 21–39

Chatzigogos CT, Figini R, Pecker A, Salençon J., 2011, “A macroelement formulation for shallow foundations on cohesive and frictional soils”, *International Journal for Numerical and Analytical Methods in Geomechanics*, 35, pp. 902–935

Chenaf N., Chazelas J., Escoffier S., Pecker A., 2012, ”Independent experimental observations of kinematic and inertial soil–pile interactions”, *International Journal of Physical Modelling in Geotechnics*, 12 (1), pp 1-14

Correia A.A., Pecker A, Kramer S.L., Pinho R., 2012, “A pile-head macro-element approach to seismic design of extended pile-shaft-supported bridges”, *Second International Conference on performance-based design in earthquake geotechnical engineering*, Taormina, Italy, pp. 862–873

Crémer C, Pecker A, Davenne L., 2002, “Modelling of non-linear dynamic behaviour of a strip foundation with macroelement”, *Journal of Earthquake Engineering*, 6, pp. 175–212

Cubrinovski, M., Kokusho, T., Ishihara, K., 2006, “Interpretation from large-scale shake table tests on piles undergoing lateral spreading in liquefied soils*”, Soil Dynamics and Earthquake Engineering*, 26 (2-4), pp. 275-286

Curras C.J., Boulanger R.W., Kutter B.L., Wilson D.W., 2001, ”Dynamic experiments and analyses of a pile-group-supported structure”, *Journal of Geotechnical and Geoenvironmental Engineering*, 127 (7), pp. 585–596

De Simone P., 2012, “Head embedment in Broms pile lateral capacity theory for cohesionless soils”, *Computers and Geotechnics*, 43, pp 51-60

Di Laora R., Mandolini A., Mylonakis G., 2012, “Insight on kinematic bending of flexible piles in layered soil”, *Soil Dynamics and Earthquake Engineering*, 43, pp 309–322.

Di Prisco C, Nova R, Sibilia A., 2003, “Shallow footings under cyclic loading: experimental behaviour and constitutive modeling”, *Geotechnical Analysis of Seismic Vulnerability of Historical Monuments*, Maugeri M, Nova R (eds), Pàtron: Bologna

Duncan J., Evans L., Ooi P., 1994, ”Lateral load analysis of single piles and drilled shafts”, *Journal of Geotechnical Engineering*, 120 (6), pp 1018–1033

El Naggar M.H., Novak M., 1996, “Nonlinear analysis for dynamic lateral pile response”, *Journal of Soil Dynamics and Earthquake Engineering*, 14 (3), pp 141-157

El Naggar M.H., Bentley K.J., 2000, ”Dynamic analysis for laterally loaded piles and dynamic p-y curves”, *Canadian Geotechnical Journal*, 37, pp 1166-1183

Fan K., Gazetas G., Kaynia A., Kausel E., Ahmad, S., 1991, ”Kinematic seismic response of single piles and pile groups”, *Journal of Geotechnical Engineering*, 117 (12), pp 1860–1879

Figini R., Paolucci R., Chatzigogos C., 2011, “A macro-element model for non-linear soil-shallow foundation-structure interaction under seismic loads: theoretical development and experimental validation on large scale tests”, *Earthquake Engineering and Structural Dynamics*, 41 (3), pp 475-493

Fleming W.G.K., Weltman A.J., Randolph M.F., Elson W. K., 1992, *Piling Engineering*, Surrey University Press, London

Gazetas G., 1984, “Seismic response of end-bearing single piles”, *Soil Dynamics and Earthquake Engineering*, 3 (2), pp 82-93

Gazetas G., Dobry R., 1984, “Horizontal response of piles in layered soils”, *Journal of Geotechnical Engineering*, 110 (1), pp 20-40

Georgiadis M., 1983, “Development of p-y curves for layered soils”, *Proceedings of the Geotechnical Practice in Offshore Engineering*, ASCE, pp 536-545

Georgiadis K., Georgiadis M., 2010, ”Undrained lateral pile response in sloping ground”, *Journal of Geotechnical and Geoenvironmental Engineering*, 136 (11), pp 1489–1500

Gerolymos N., Gazetas G., 2005, “Phenomenological model applied to inelastic response of soil-pile interaction systems”, *Soils and Foundations*, 45 (4), pp 119-132

Gerolymos N., Drosos V., Gazetas G., 2009, “Seismic response of single-column bent on pile: evidence of beneficial role of pile and soil inelasticity”, *BEE*, **7**, pp 547-573

Gerolymos N., Zafeirakos A., Souliotis C., 2012, “Lateral response of caisson foundations: a macroelement approach”, *Proceedings of the 15th World Conference on Earthquake Engineering*, Lisbon, Portugal, September

Green R.A., Olson S.M., Cox B.R., Rix G.J., Rathje E., Bachhuber J., French J., Lasley S., Martin N., 2011, “Geotechnical Aspects of Failures at Port-au-Prince Seaport during the 12 January 2010 Haiti Earthquake”, *Earthquake Spectra*, Vol. 27, No. S1, pp. S43-S65

Hutchinson T.C., Chai Y.H., Boulanger R.W., Idriss I.M., 2004, “Inelastic seismic response of extended pile-shaft-supported bridge structures”, *Earthquake Spectra*, 20 (4), pp 1057-1080

Ishibashi I., Zhang X., 1993, “Unified dynamic shear moduli and damping ratios of sand and clay”, *Soils and Foundations*, Vol. 33 (1), pp 182-191

Jeremic B., Jie G., Preisig M., Tafazzoli N., 2009, “Time domain simulation of soil–foundation–structure interaction in non-uniform soils”, *Earthquake Engineering and Structural Dynamics*, 38, pp 699-718

Kagawa T., Kraft L., 1980, "Seismic p-y response of flexible piles," *Journal of the Geotechnical Engineering Division*, 106 (8), pp 899-918

Kavvadas M., Gazetas G., 1993, “Kinematic seismic response and bending of free-head piles in layered soil”, *Geotechnique*, 43 (2), pp 207–222

LeBlanc C., Houlsby G.T., Byrne B.W., 2010, “Response of stiff piles in sand to long-term cyclic lateral loading”, *Geotechnique*, 60 (2), pp 79–90

Maheshwari B.K., Truman K.Z., El Naggar M.H., Gould P.L., 2004, “Three-dimensional nonlinear analysis for seismic soil-pile-structure interaction”, *Soil Dynamics and Earthquake Engineering*, 24, pp 343-356

Maiorano R.M.S., de Sanctis L., Aversa S., Mandolini A., 2009, "Kinematic response analysis of piled foundations under seismic excitations", *Canadian Geotechnical Journal*, 46 (5), pp 571–84

Martin C.M., Houlsby G.T., 2001, "Combined loading of spudcan foundations on clay: numerical modeling", *Geotechnique*, Vol 51 (8), pp 687-699

Martin C. M., Randolph M. F., 2006, "Upper-bound analysis of lateral pile capacity in cohesive soil", *Geotechnique*, 56 (2), pp 141–145

Matlock H., 1970, "Correlations for design of laterally loaded piles in soft clay", *Proceedings of the 2nd Annual Offshore Technology Conference*, Houston, Texas, pp 577-594

Matlock H., Foo S.H., Bryant L.L., 1978, ''Simulation of lateral pile behavior'', Proc Earthquake Engineering and Soil Dynamics, ASCE, New York, 600–619

Mindlin D., 1936, "Force at a point in the interior of a semi-infinite solid", *Physics*, 7, pp 195-202

Murff J., Hamilton J., 1993, "P-Ultimate for undrained analysis of laterally loaded piles" *Journal of Geotechnical Engineering*, 119 (1), pp 91–107

Nikolaou S., Mylonakis G., Gazetas G., Tazoh T., 2001, "Kinematic pile bending during earthquakes: analysis and field measurements", *Geotechnique*, 51 (5), pp 425-440

Nogami T., Otani J., Konagai K., Chen H., 1992, "Nonlinear soil-pile interaction model for dynamic lateral motion", *Journal of Geotechnical Engineering*, 118 (1), pp 89-106

Nova R., Montrasio L., 1991, "Settlements of shallow foundations on sand", *Geotechnique*, 41(2), pp. 243-256

Novak M., 1974, "Dynamic stiffness and damping of piles", *Canadian Geotechnical Journal*, 11, pp 574-598

O'Neil M.W., Murchison J.M., 1983, "An evaluation of p-y relationships in sands", A report to the American Petroleum Institute, *PRAC 82-41-1*, University of Houston, Texas

Ooi P., Chang B., Wang S., 2004, "Simplified lateral load analyses of fixed-head piles and pile groups", *Journal of Geotechnical Engineering*, 130 (11), pp 1140–1151

Paolucci R., 1997, "Simplified evaluation of earthquake induced permanent displacements of shallow foundations", *Journal of Earthquake Engineering*, 1, pp. 563–579

Poulos H.G., 1971, “Behavior of laterally loaded piles: I - single piles”, *Journal of Soil Mechanics and Foundation Division*, ASCE, 97 (5), pp 711-731

Poulos H.G., Davis E.H., 1980, *Pile Foundation Analysis and Design*, John Wiley and Sons, New York

Pender M.J, 1995, *Aseismic Foundation Design Analysis*, Continuing Education Course, University of Auckland, New Zealand

Penzien J., Scheffy C., Parmelee R., 1964, “Seismic analysis of bridges on long piles”, *Journal Engineering Mechanics Division, ASCE*, Vol 90 (3), pp. 223-254

Pyke R., 1979, “Nonlinear soil models for irregular cyclic loadings”, *Journal of the Geotechnical Engineering Division*, *ASCE*, Vol 105, GMT6, pp 715-726

Randolph M.F., 1981, “The response of flexible piles to lateral loading”, *Geotechnique,* 31 (2), pp 247-259

Randolph M., Houlsby G., 1984, “The limiting pressure on a circular pile loaded laterally in cohesive soil”, *Geotechnique,* 34 (4), pp. 613-623

Reese L.C., Cox W.R., Koop F.D., 1974, “Analysis of laterally loaded piles in sand”, *Proceedings of the VI Annual Offshore Technology Conference*, Houston, Texas, 2: 473-485

Reese L.C., Cox W.R., Koop F.D., 1975, “Field testing and analysis of laterally loaded piles in stiff clay”, *Proceedings of the VII Annual Offshore Technology Conference*, Houston, Texas, 2: 672-690

Reese L.C., Van Impe W.F., 2001, *Single Piles and Pile Groups under Lateral Loading*, A.A.Balkema, Rotterdam

Rollins K., Lane J., Gerber T., 2005, ”Measured and Computed Lateral Response of a Pile Group in Sand”, *Journal of Geotechnical and Geoenvironmental Engineering*, 131 (1), pp 103–114

Rovithis E.N., Pitilakis K.D., Mylonakis G.E., 2009, “Seismic analysis of coupled soil-pile-structure systems leading to the definition of a pseudo-natural SSI frequency”, *Soil Dynamics and Earthquake Engineering*, 29, pp 1005–1015

Sa’don N.M., Pender M.J., Orense R.P., Abdul Karim A.R., 2009, “A macro-element for pile-head response to cyclic lateral loading”, *Proceedings of the 2009 NZSEE Conference*, Paper Number 47

Sun K., 1994, “Laterally loaded piles in elastic media”, *Journal of Geotechnical Engineering*, 120 (8), pp 1324-1344.

Tabesh A., Poulos H.G., 2001, “Pseudostatic Approach for Seismic Analysis of Single Piles”, *Journal of Geotechnical and Geoenvironmental Engineering*, 127 (9), pp 757-765

Tasiopoulou P., Smyrou, E., Bal, İ. E., Gazetas, G., Vintzileou, E., 2011, Geotechnical and Structural Field Observations from Christchurch, February 2011 Earthquake, in New Zealand, *Research Report*, National Technical University of Athens, Greece

Thavaraj T., Finn W.D.L., Wu G., 2010, “Seismic response analysis of pile foundations”, *Geotechnical and Geological Engineering*, 28, pp 275-286

Trochanis A., Bielak J., Christiano P., 1991a, ”Simplified Model for Analysis of One or Two Piles”, *Journal of Geotechnical Engineering*, 117 (3), pp 448–466

Trochanis A., Bielak J., Christiano P., 1991b, ”Three-Dimensional Nonlinear Study of Piles”, *Journal of Geotechnical Engineering*, 117 (3), pp 429–447

Vlasov V.Z., Leontiev N.N., 1966, "Beams, plates and shells on elastic foundations", *NTIS Accession No. N67-14238*, Israel Program for Scientific Translations, Washington, D.C

Velez A., Gazetas G., Krishnan R., 1983, “Lateral dynamic response of constrained-head piles”, *Journal of Geotechnical Engineering*, 109 (8), pp 1063–1081

Villalobos F., Ovando E., Mendoza M., Oróstegui P., 2011, “Damages observed in the 2010 Concepcion earthquake and related soil phenomena”, *Proceedings of the 5th International Conference on Earthquake Geotechnical Engineering*, Santiago, Chile, 10-13 January

Wang S., Kutter B.L., Chacko J.M., Wilson D.W., Boulanger R.W., Abghari A., 1998, “Nonlinear seismic soil-pile-superstructure interaction”, *Earthquake Spectra*, 14(2), pp 377-396.

Wen Y., 1976, "Method for random vibration of hysteretic systems", *Journal of the Engineering Mechanics Division*, 102 (2), pp 249-264

Wu G., Finn W.D.L., 19971, “Dynamic elastic analysis of pile foundations using finite element method in the frequency domain”, *Canadian Geotechnical Journal*, 34, pp 34-43

Wu G., Finn W.D.L., 1997b, “Dynamic nonlinear analysis of pile foundations using finite element method in the time domain”, *Canadian Geotechnical Journal*, 34, pp 44-52

Yang Z., Jeremic B., 2002, “Numerical analysis of pile behavior under lateral loads in layered elastic-plastic soils”, *International Journal for Numerical and Analytical Methods in Geomechanics*, 26, pp 1385-1406

Zhang L.M., Ng C.W.W., Lee, 2004, “Effects of slope and sleeving on the behavior of laterally loaded piles”, *Soils and Foundations*, 44 (4), pp 99-108

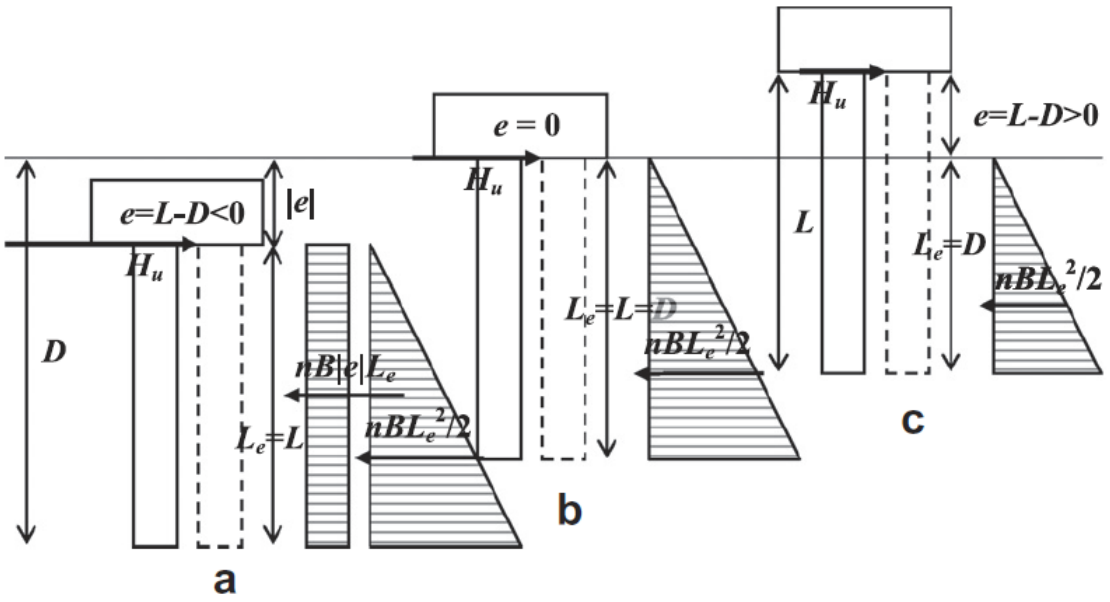

Figure 1.1: Soil reaction for head restrained short piles: (a) e/B<0 embedded cap, (b) e/B<0 (Broms), and (c) e/B>0 cap over-ground (De Simone, 2012)

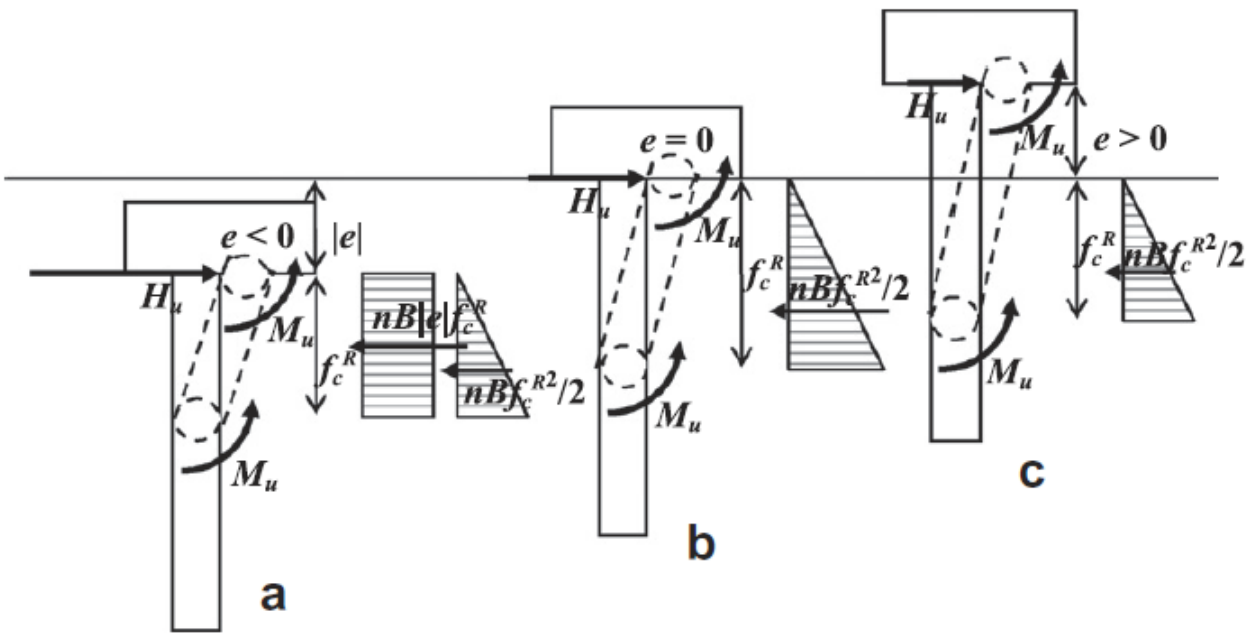

Figure 1.2: Soil reaction for long piles: (a) trapezoidal, (b) triangular (Broms), and (c) e>0 (De Simone, 2012)

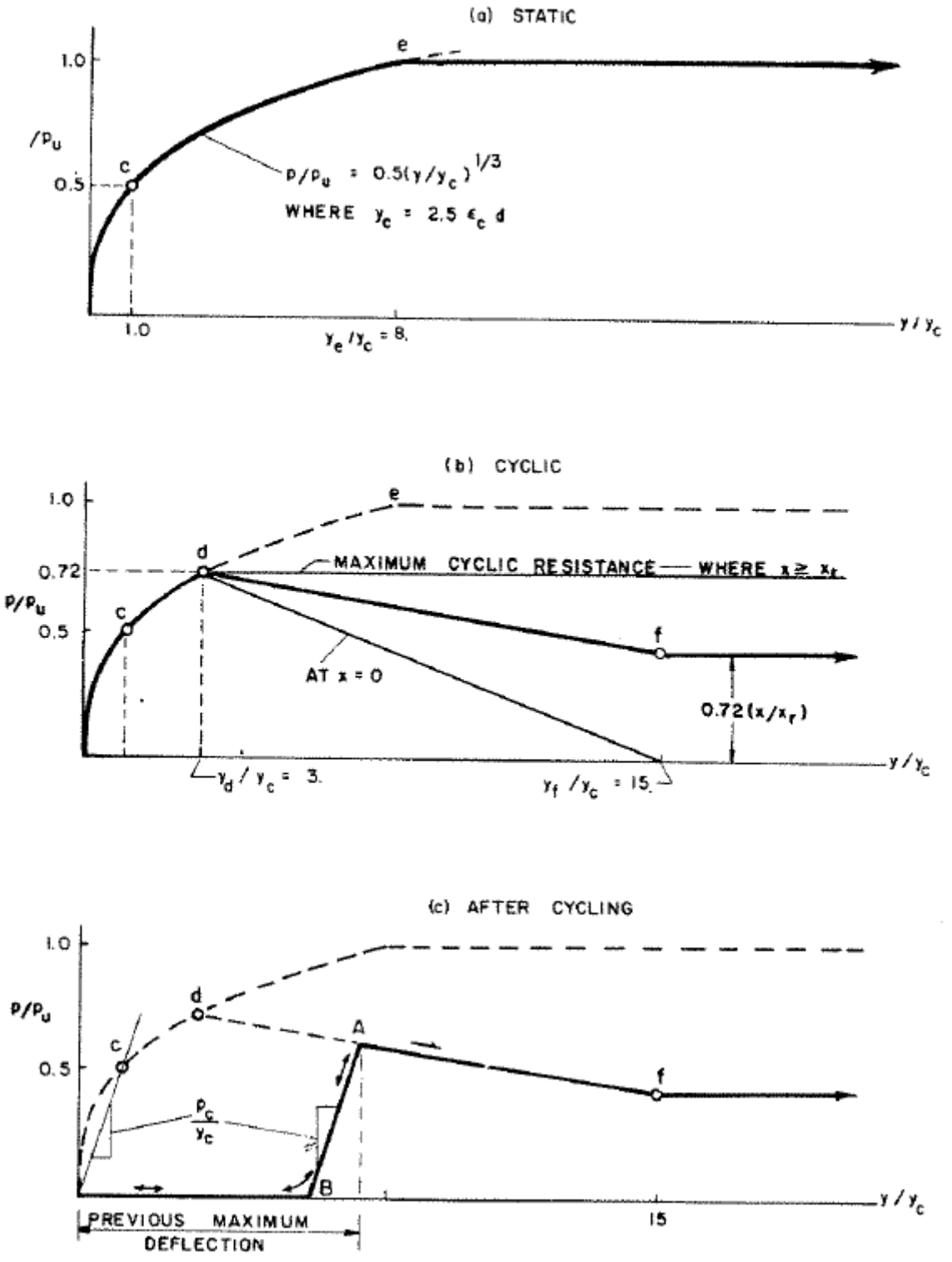

Figure 1.3: P-y curves for: (a) short-time static loading, (b) equilibrium under initial cyclic loading, and (c) reloading after cyclic (Matlock, 1970)

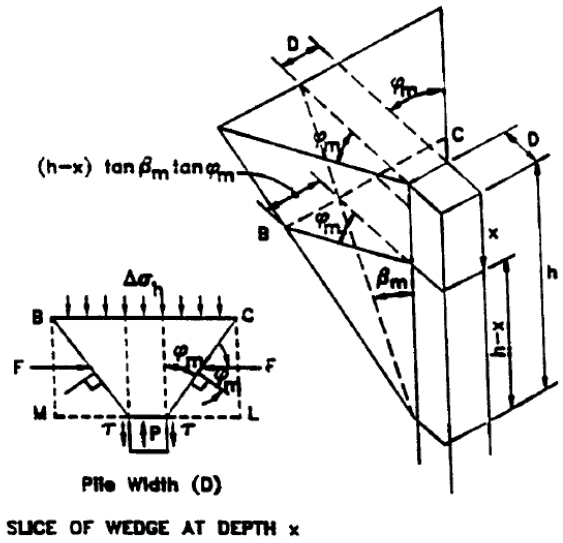

a. Basic Strain Wedge in Uniform Soil

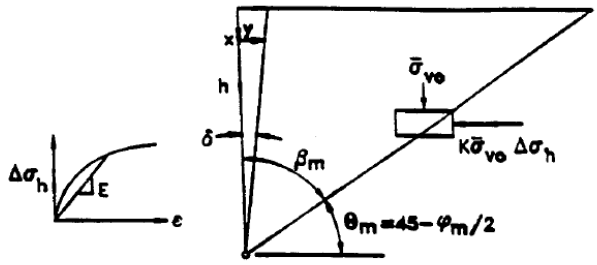

b. Deflection Pattern of a Laterally Loaded Pile and Associated Strain Wedge

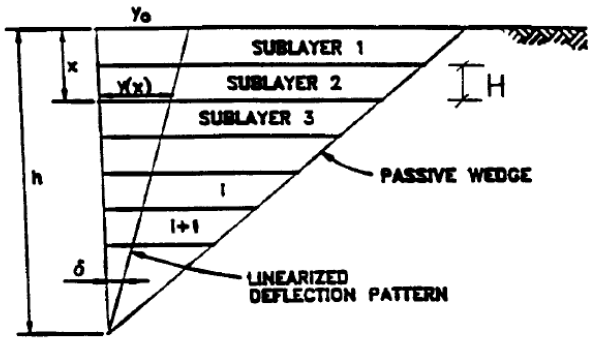

c. Strain Wedge Model Sublayers

Figure 1.4: Basic configuration of the Soil-Wedge model (Ashour and Norris, 2000)

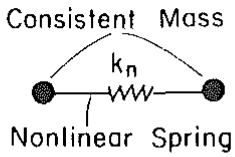

(a)

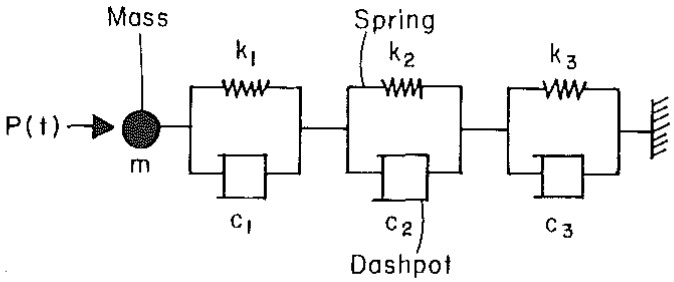

(b)

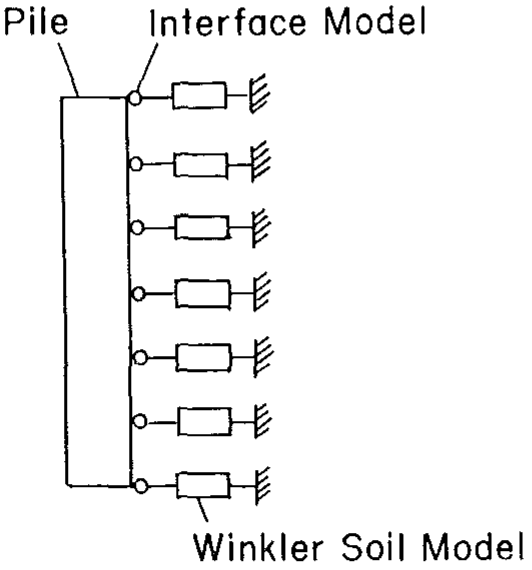

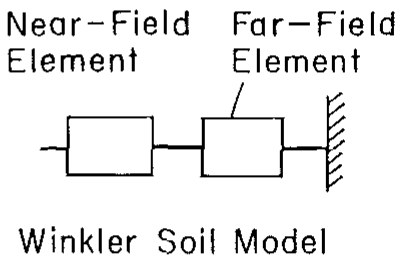

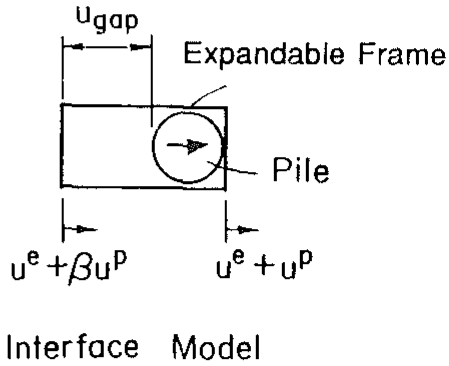

Figure 1.5: (a) Near-Field element model, (b) Far-field element model, (c) Schematic preview of the soil-pile interaction model (Nogami et al, 1992)

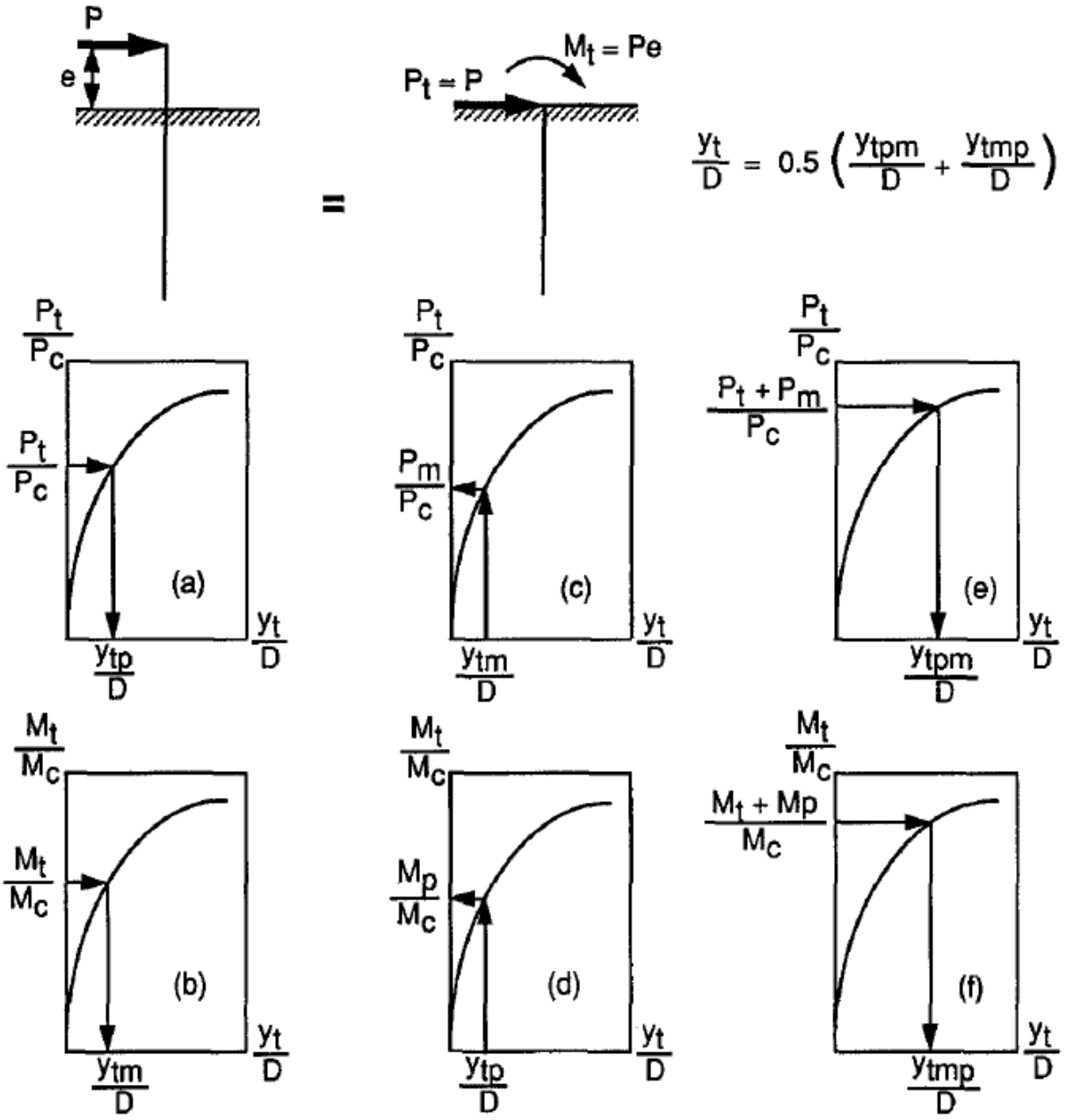

Figure 1.6: Nonlinear superposition of deflections due to load and moment: (a) Step 1, (b) Step2, (c) Step 3, (d) Step 4, (e) Step 5, (f) Step 6 (Duncan et al, 1994)

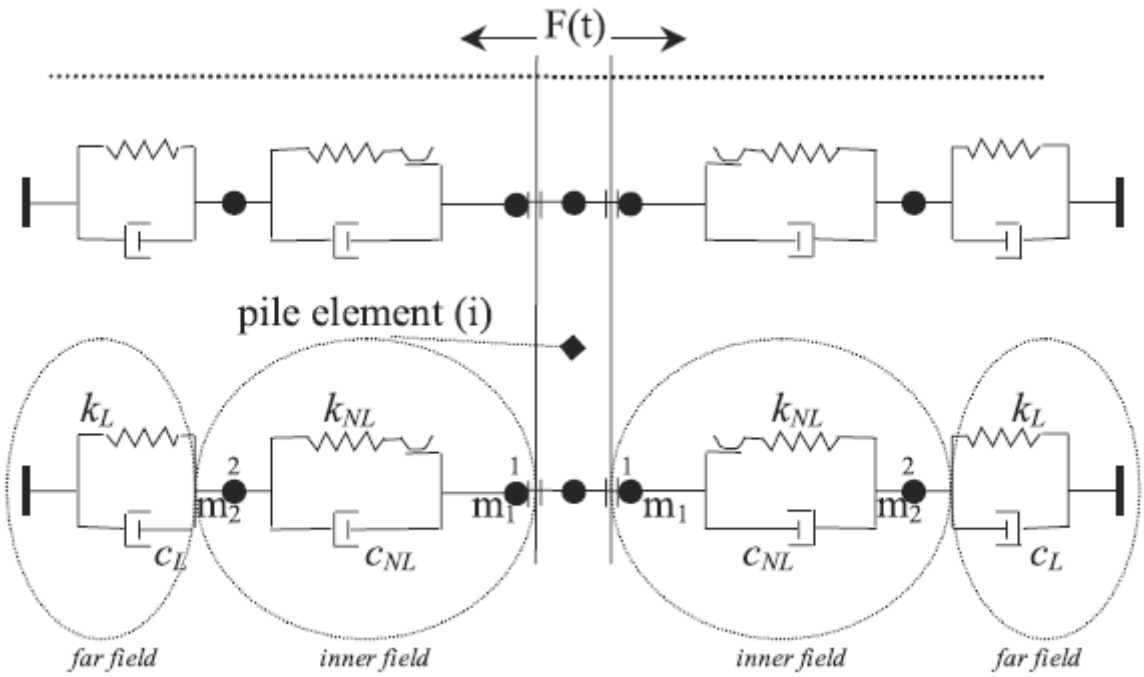

Figure 1.7: Element representation of the proposed model. m_1, m_2 represent the mass of the inner field lumped at two nodes; half (m_1) at the node adjacent to the pile, and the other half (m_2) at the node adjacent to the outer field (El Naggar and Bentley, 2000)

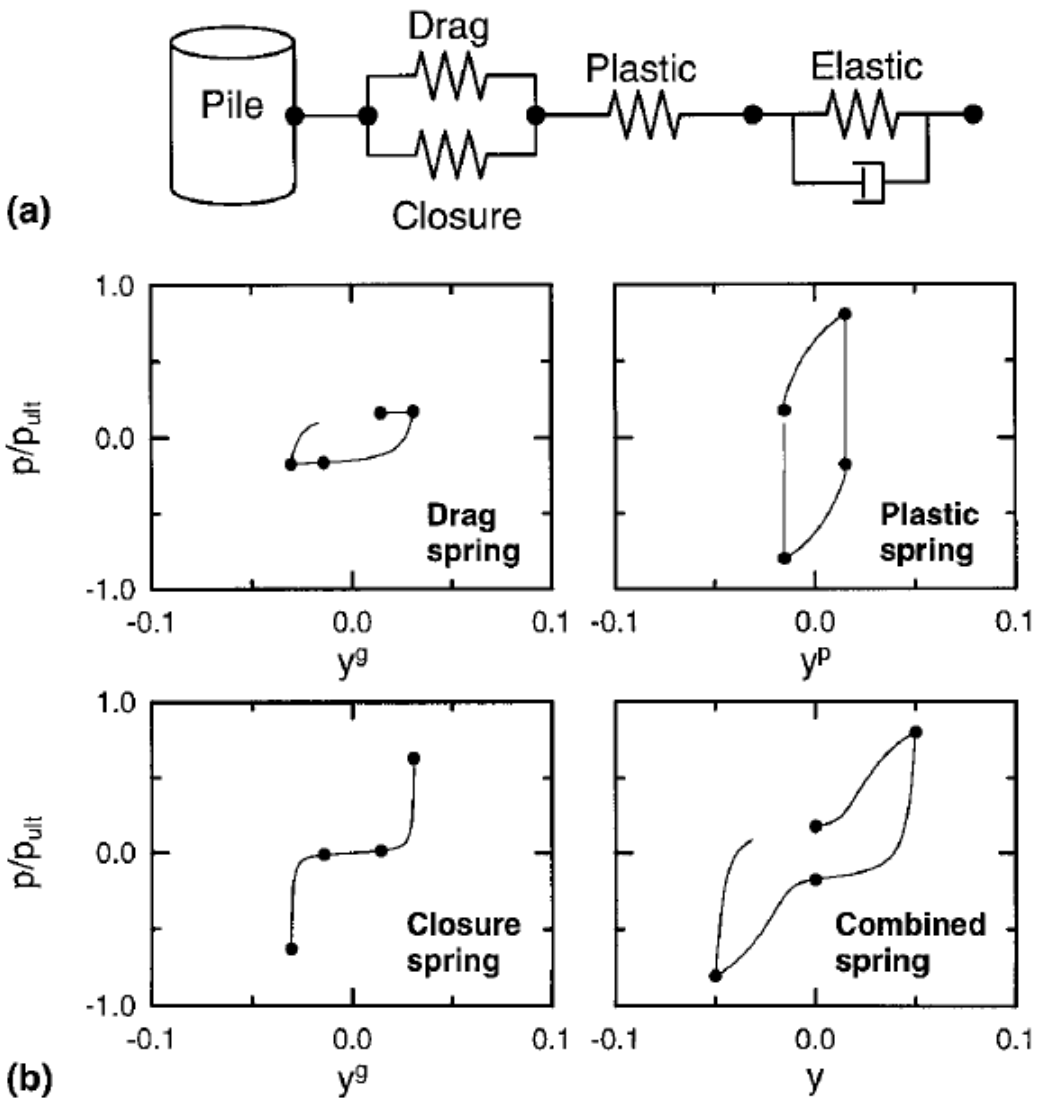

Figure 1.8: Characteristics of Nonlinear p-y element: (a) Components, (b) Behabior of components (Boulanger et al, 1999)

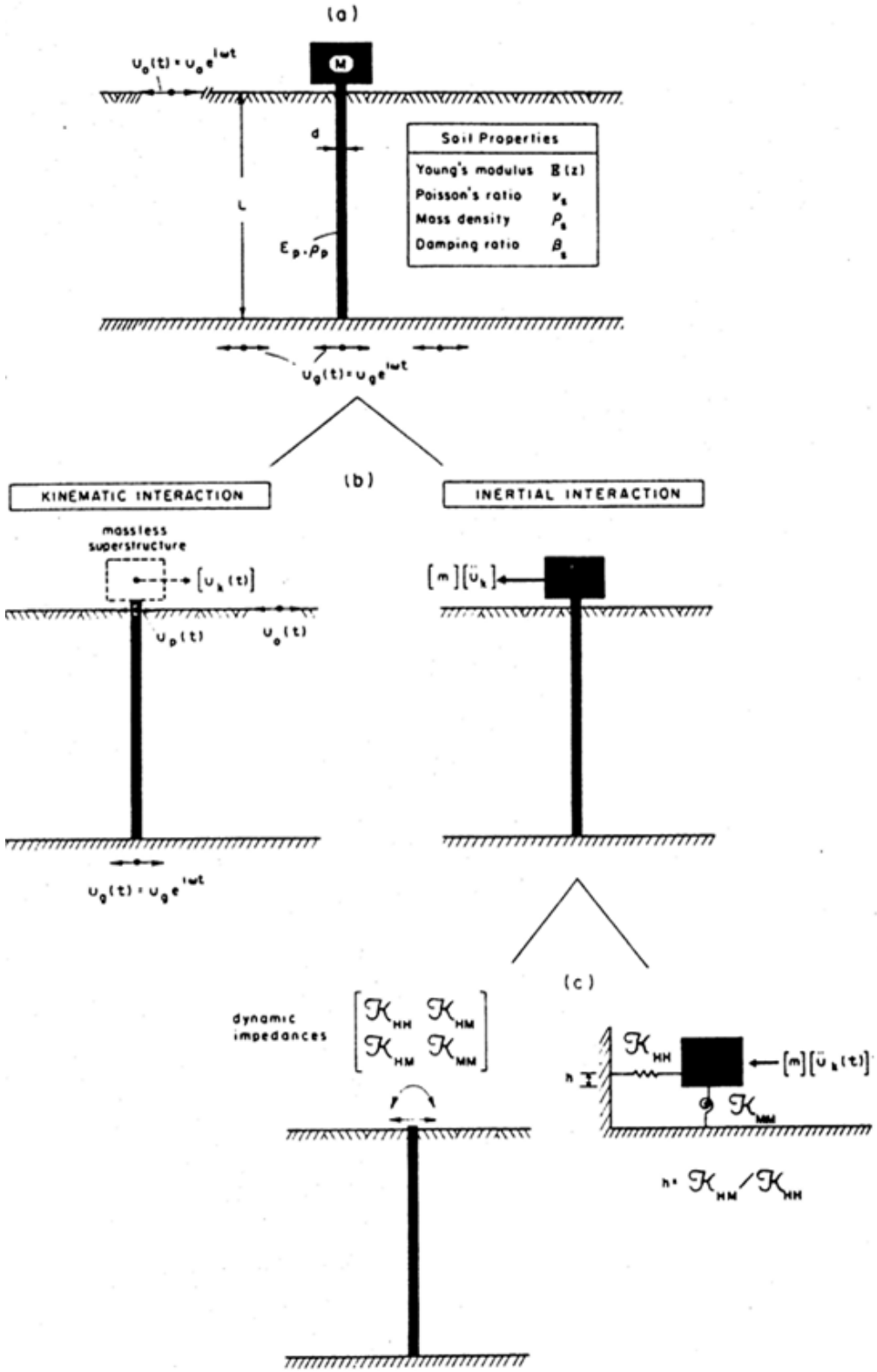

Figure 1.9: (a) Geometry of soil-pile-structure interaction problem, (b) decomposition into kinematic and inertial interaction problems, (c) two-step analysis of inertial interaction (Gazetas, 1984)

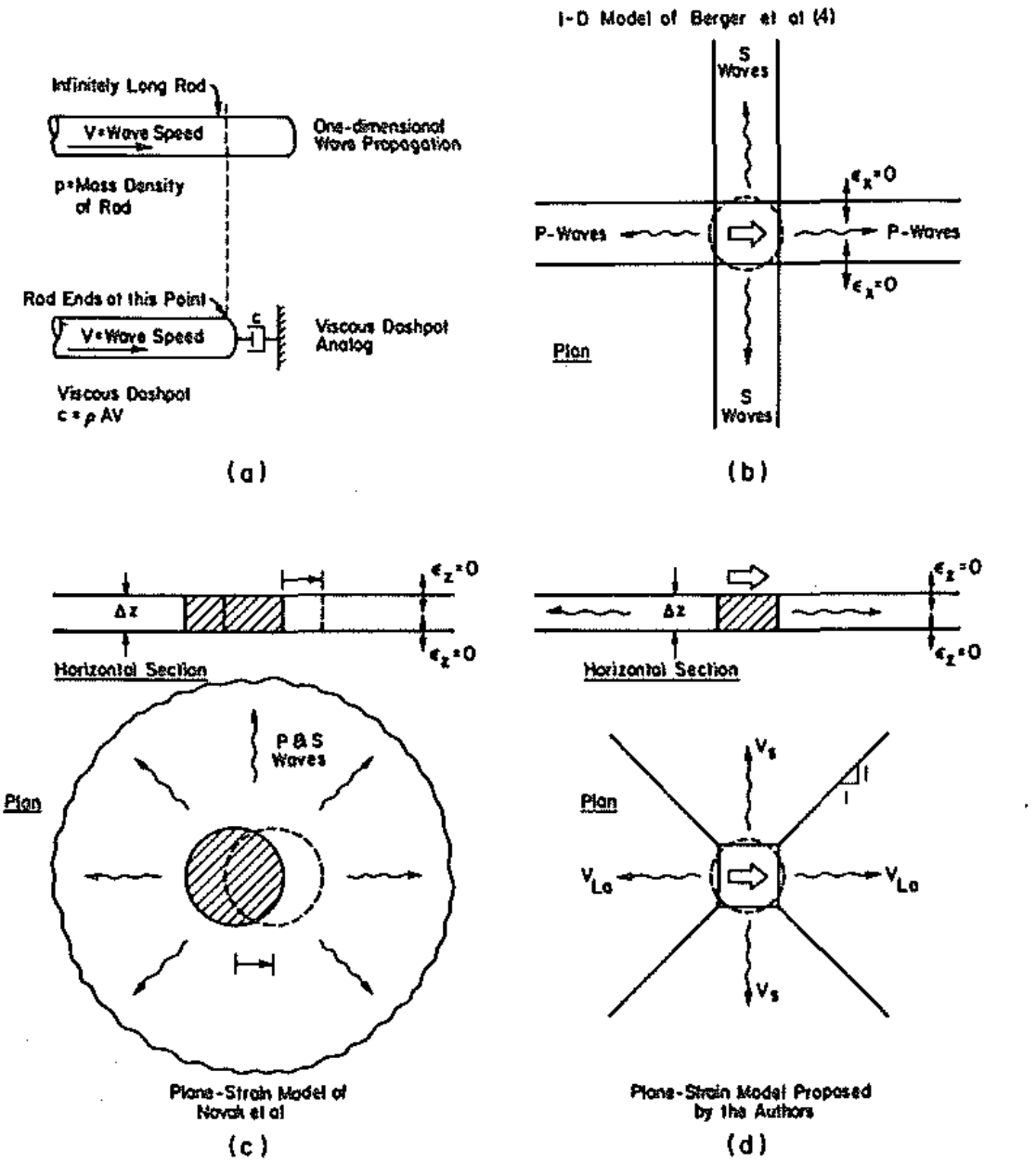

Figure 1.10: 1-D and 2-D radiation damping models (Gazetas and Dobry, 1984)

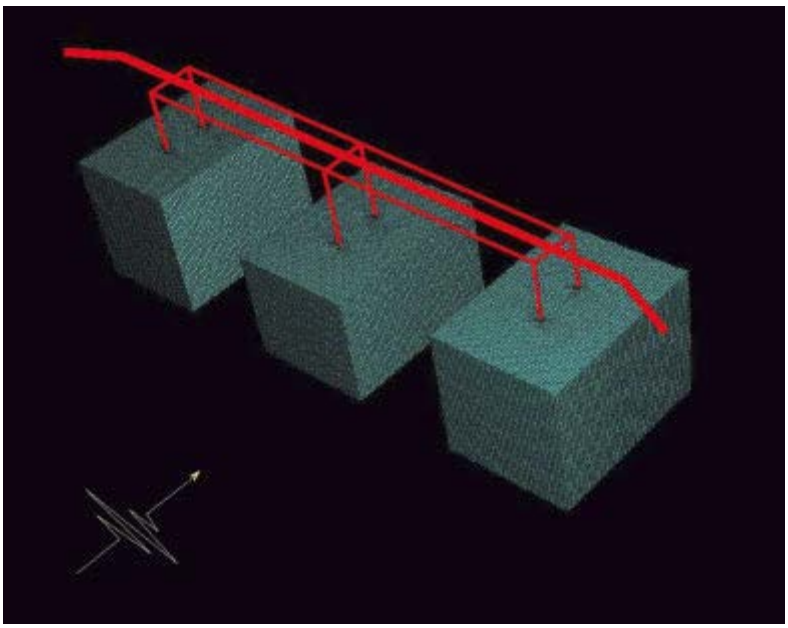

Figure 1.11: Detailed three bent prototype Soil-Foundation-Structure-Interaction Finite Element model (Jeremic et al, 2009)

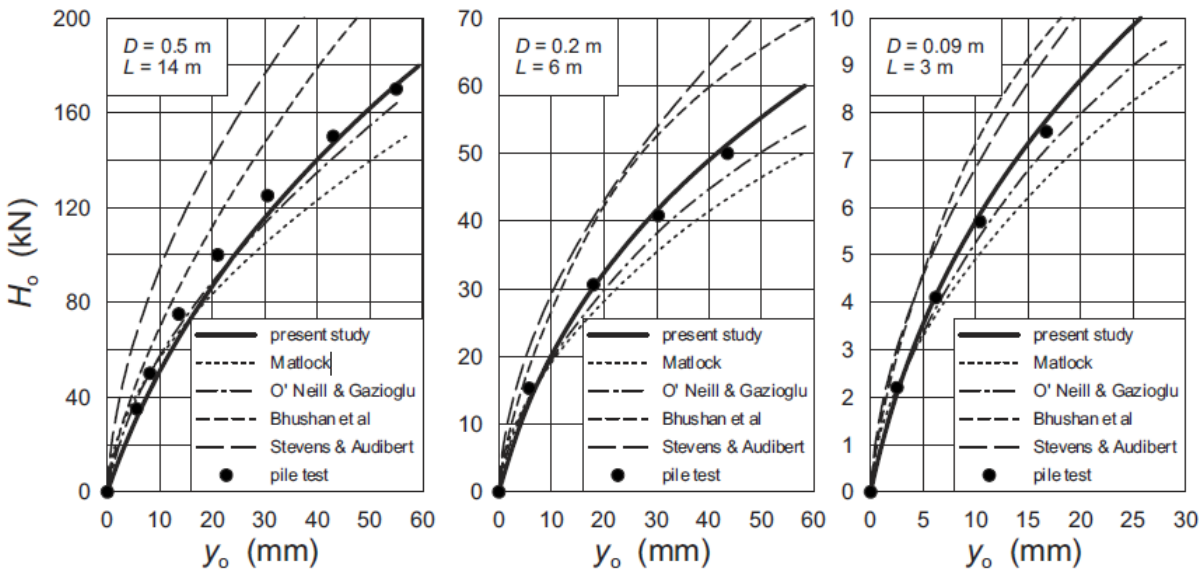

Figure 1.12: Lateral load versus pile head displacement relationships for Shanghai pile tests (Georgiadis and Georgiadis, 2010)

Figure 1.13: Broken pile cap in a wharf extension during the Chile 2010 earthquake (Villalobos et al, 2011)

Figure 1.14: Western abutment of South Bridge Road Bridge after Christchurch earthquake: (a) Concrete spalling exposing the pile reinforcement, (b) Flexural cracks developed at the top of the piles indicating plastic hinging (Tasiopoulou et al, 2011)

CHAPTER 2:
A CONSTITUTIVE MODEL FOR THE CYCLIC RESPONSE OF PILES IN COHESIONLESS SOIL

2.1 PILES UNDER CYCLIC LOADING

The design of piles, such as offshore piles and foundation piles for wind turbines, needs to take into consideration: (i) the necessary depth to which the piles should be driven in order to carry the vertical loads, and (ii) the response of the piles to cyclic lateral forces and moments. There are many simple methods for estimating the required length of the piles to safely carry the vertical loads. On the other hand, more complex methods which account for the nonlinear behavior of the soil are required for the cyclic loading. The behavior of a vertical pile subjected to repetitive lateral loads depends upon the characteristics of the lateral load, the geometrical and structural properties of the pile, the properties of the soil in which the pile is embedded, and the change in soil properties as the pile is loaded repetitively.

The analysis of pile response to cyclic lateral loading can be performed with: (i) an elastic continuum analysis, (ii) a pile connected to nonlinear Winkler springs, p-y analysis, (iii) nonlinear finite element analysis, and (iv) a macro-element analysis. The p-y analysis considers the effects of cyclic loading, usually by extending the static p-y curves in the cyclic domain, but envelopes the response of a pile under cyclic loading without considering the change in pile behavior as the number of cycles increases. On the contrary, a successful implementation of the finite element method depends on the appropriate use of various parameters, such as soil constitutive models, the soil-pile interface and the stiffness degradation in soil during cyclic loading.

The response of piles to lateral loading has been the subject of numerous studies in the last decades. However, only a limited amount of them addresses the effects of cyclic loading on pile response. Different methods of varying degree of accuracy have been used, incorporating simplified (Dawson, 1980; Lin et al, 1999; Long et al, 1994) or

advanced (Grashuis et al, 1990; Hutchinson et al, 2005; Achmus et al, 2009; Zhang et al, 2000; Bourgeois et al, 2010) numerical models. Centrifuge experiments (Verdure et al, 2003) and full-scale tests have also been performed on the cyclic behavior of piles embedded in sand (Brown et al, 1987; Tuladhar et al, 2008; Rollins et al, 2006).

One of the first thorough studies on the lateral response of cyclically loaded piles was carried out by Poulos (1982). According to this study, there are two phenomena that may contribute to the increased deflection of laterally loaded piles with increasing number of cycles:

(1) Structural "shakedown" of the pile-soil system. This phenomenon occurs on every pile embedded in an elastoplastic soil mass whose properties remain unaltered. When the accumulated permanent deformations stabilize "shakedown" will occur. In other words, incremental collapse will result.

(2) Soil stiffness decay and strength degradation.

In general, during cyclic loading it is observed that:

(i) both deflection and moment increase with increasing number of cycles and load magnitude,

(ii) the ultimate lateral load capacity decreases with increasing number of cycles and load magnitude,

(iii) effects of cyclic degradation are more severe for stiff than for soft soils,

(iv) the main features of pile response to cyclic loading are practically unaffected by soil inhomogeneity,

(v) the loading rate has a significant effect on the pile response, with the deflections at a given load decreasing as the loading rate increases,

(vi) the location of the plastic hinge moves deeper when the pile is subjected to fully cyclic loading than to monotonic loading, due to soil stiffness degradation (Tuladhar et al, 2008),

(vii) one-way cyclic lateral loads induce more permanent strains and greater cumulative deformations of the piles than the two-way cyclic lateral loads (Long et al, 1994),

(viii) the effect of group action increases with increasing load. Thus at large deformations, the group capacity appears to be significantly lower than the sum of the capacities of each individual pile (Brown et al, 1987),

(ix) the deflection of the piles in the group is significantly greater than that of a single pile under a load equal to the average load per pile (Brown et al, 1987), and

(x) for a given displacement the leading row piles carry the largest load, while for a given load the maximum bending moment develops at the trailing row (Rollins et al, 2006).

A simplified theory has been developed by Dawson (1980) for predicting the deflection and internal bending moment of piles embedded in sand or clay subjected to cyclic lateral loading. Lin et al (1999) used an empirical approach to calculate the cyclic deformations of laterally loaded piles as a function of the number of cycles. Linear elastic response is assumed and values of a degradation parameter of the soil resistance are estimated from pile test results as a function of the pile length, the soil-pile relative stiffness, the soil density, the installation method and the cyclic load ratio. The developed method is empirical and some differences are justified by the densification of the soil after a number of cycles of loading which is not taken into consideration.

Long et al (1994) observed that the effects of repetitive lateral loads on deflections of two drilled piers in Tampa Bay were significantly greater than predicted by a p-y procedure used in practice outlined by Reese et at (1974). The behavior of an elastic vertical pile, infinitely long, and embedded in cohesionless soil during one cycle of load is described in four phases. During the first phase, the magnitude of the lateral load varies from a value of zero to a maximum horizontal load. The resistance to pile deflection is provided by the soil along the loading side of the pile, while the soil on the opposite side remains in contact with the pile. The soil surrounding the pile may change in volume depending on its initial density and stress state. During the second phase, the load decreases to zero and the soil pressure along the opposite side decreases to an active state. The cohesionless soil flows to prevent the gap formation and maintains contact with the pile. During the third phase, the load reaches a minimum value at the opposite direction. The response of the pile for the fourth phase is similar to the second one but in the opposite direction. It was noted that one-way cyclic lateral loads induce more permanent strains and greater cumulative deformations of the piles than the two-way cyclic lateral loads. Furthermore, the cyclic lateral loads result in deformations that may increase with every cycle. The effect of the cyclic loading is greatest for the first

cycle of loading with the effect of subsequent cycles diminishing. Finally, two methods were developed to model the cyclic lateral load behavior of a pile by degrading soil resistance as a function of the number of cycles of load, the method of pile installation, the soil density and the character of cyclic load. The first method is based upon a closed-form solution for a beam on an elastic foundation with a linearly increasing soil reaction modulus. This is a simple method for predicting the effects of cyclic lateral loading but cannot account for the effects of nonlinear soil response. In the second method, a p-y curve for static loading is modified to a cyclic p-y curve by reducing the static soil resistance p while increasing the static displacement y.

Regarding numerical analysis, Grashuis et al (1990) developed an element that models the gap formation around the pile, the degradation of the soil strength and the backsliding of the soil into the gap taking into account the friction between the pile and the gap walls and the plastic soil behavior at larger depths. Hutchinson et al (2005) performed finite element analyses with computer code FEAP trying to capture the hysteretic behavior of reinforced concrete shafts in sand. For this reason four piles were tested in full-scale combining axial compression and reversed cyclic quasistatic lateral loading in dry sand. This model takes into consideration the gap formation and captures the P-Δ moments together with the post-peak strength degradation and the loading and unloading response of the soil-pile system.

Zhang et al (2000) performed three-dimensional elastoplastic finite element analysis with computer code DGPILE-3D for filed tests of cast-in-place reinforced concrete piles embedded in sand subjected to one way cyclic lateral loading. In the analysis four different constitutive models were compared: (i) the Drucker-Prager model, (ii) a Modified Drucker-Prager model, (iii) the Cam-Clay model, and (iv) the Nekai and Matsuoka sand model. The cracking moment, the yielding moment and the ultimate moment of the pile were taken into account. For small loading stages the load displacement relation from the models had little difference, but as the loading reached the ultimate state, deformation became quite different due to the different shear strength and the stress-strain relation predicted from every model.

Allotey and El Naggar (2008) employed a beam-on-nonlinear-Winkler-foundation model to conduct a numerical assessment of the effects of gapping and soil cave-in and recompression on the lateral cyclic response of soil-pile systems. It was noted that the

effect of soil cave-in and recompression is to decrease pile maximum moment, move its point of occurrence closer to ground surface, and increase hysteretic energy dissipation. For damaged piles that develop plastic hinges at some depth below ground surface, soil cave-in could be beneficial as it helps increase the effective confinement of the plastic hinge which in turn spreads the curvature demand, resulting in an increase of the effective length of the plastic hinge.

Gerolymos et al (2009) simulated numerically the response of a vertical pile embedded in dry sand and subjected to lateral loading in centrifuge tests for both one-way and two-way cyclic loading. The tests were simulated using a cyclic nonlinear Winkler spring model, which describes the full range of inelastic phenomena, including separation and reattachment of the pile from the soil. The model is also able to capture the soil plastification at an early stage of loading, the pinching behavior due to the formation of a relaxation zone around the upper part of the pile and stiffness and strength changes due to cyclic loading. Recently, Bourgeois et al (2010) simulated in 3D the behavior of a pile subjected to one-way cyclic lateral loading with a suitable constitutive model which combined a linear isotropic elastic law with only one deviatoric plastic mechanism and a kinematic hardening law. The model was compared with monotonic triaxial compression tests and a cyclic triaxial compression test and then it was applied to simulate a centrifuge experiment on a model pile subjected to cyclic lateral loading.

Achmus et al (2009) developed design charts independent of the pile bending stiffness for monopole foundations of wind turbines in sandy soil under long-term cyclic lateral load. The calculation of the accumulated displacements is based on cyclic triaxial tests for the stiffness degradation of the soil. An elastoplastic soil model with Mohr-Coulomb failure criterion was used for the analysis. Effects of pile length, diameter, loading state and embedded length were studied. It was found that the soil stiffness decreases along the whole length of a short pile, while it decreases only in the upper part of a longer pile. Additionally, it was shown that the length of the pile rather than its diameter has a significant role on the cyclic performance of the pile. Finally, the displacement accumulation rate is strongly dependent on the ratio of the actual load to the ultimate load and thus on the embedded pile length.

As far as experiments and full-scale tests are concerned, Brown et al (1987) performed a test to a large-scale group of nine steel pipe piles in a closely spaced arrangement subjected to two-way cyclic lateral loading embedded in stiff overconsolidated clay with water above the ground surface. It was found that the effect of group action increases with increasing load. Thus at large deformations, the group capacity appears to be significantly lower than the sum of the capacities of each individual pile. The maximum cyclic soil resistance on a pile in the pile-group is greatly reduced compared to that of the single pile, and this reduction is more significant with depth. Moreover, the deflection of the piles in the group is significantly greater than that of a single pile under a load equal to the average load per pile. It was noted that the greatest portion of shear on the group is distributed as shear to the piles in the front row of the group.

Verdure et al (2003) carried out centrifuge tests of lateral cyclic loading of a single pile in cohesionless soil. It was shown that the global stiffness of the soil-pile system increases dramatically during the first cycle and then varies slowly with the number of cycles. Furthermore, it increases slightly for large cycle amplitude but for small cycle amplitude remains nearly constant. It was also observed that the maximum bending moment and the depth of the maximum bending moment increase with the number of cycles.

Rollins et al (2006) performed full-scale cyclic lateral load tests on pile groups with five rows of piles with free-head conditions embedded in stiff clay. It was shown that group interaction effects decreased as pile spacing increased and that lateral resistance is a function of row location in the group rather than location within a row. Moreover, for a given displacement the leading row piles carry the largest load, while for a given load the maximum bending moment develops at the trailing row.

Tuladhar et al (2008) studied the degradation of the lateral load capacity of piles when subjected to cyclic loading compared to monotonic loading by performing full-scale monotonic and reversed cyclic lateral loading tests on concrete piles embedded in cohesive soil. It was observed that the location of the plastic hinge moves deeper when the pile is subjected to reversed cyclic loading compared to monotonic loading because of the degradation of the soil stiffness. When a pile embedded in cohesive soil is subjected to lateral loading, the soil on the compression side (direction of the loading)

moves with the pile while the soil on the extension side remains stable, thus a gap is being formed. This gap is bigger in the case of reversed cyclic loading. The 3-D analysis showed that for cohesive soils a perfect bond between the soil and the pile highly overestimates the lateral load carrying capacity of the pile, while the use of gap elements in the interface can realistically account for the gap formation.

In practice two-dimensional analyses are conducted for the response of a pile subjected to cyclic lateral loading even though it is a typical three-dimensional problem. Now with the computer progress and the appropriate constitutive model implementation for soils it is possible to conduct three dimensional nonlinear analyses. In the present chapter a simplified constitutive soil model for the cyclic lateral response of piles in cohesionless soil is developed. The plasticity model used in this study for cohesionless soil is an extension of the model used by Gerolymos et al (2005, 2006) for cohesive soils. Despite its simplicity and lack of generality and rigor, for the particular type of problem investigated herein such a constitutive model yields quite reasonable results. Implemented in a three dimensional finite element code, the model is applied to three centrifuge experiments on a pile in dry sand. The first test is used as benchmark for the calibration of model parameters. The model is further utilized to the analysis of a case study involving a group of 1x2 piles with similar characteristics to those of the centrifuge tests. Interesting conclusions are highlighted for the “shadow” effect on soil resistance and pile-to-pile interaction at small and large deformations.

The comparison sheds light on some complicated features of the pile response regarding: (a) the observed plastic shakedown behavior, (b) the effect of the two mechanisms that result in the plastic shakedown response of the pile, that is (b1) soil densification due to voids reduction, and (b2) “system densification” due to the gradual enlargement of the resisting soil mass to greater depths with cyclic loading, (c) the influence of the number of cycles on the internal structural forces (residual and maximum) and soil reactions of the pile, and (d) the efficiency of the pile group: (d1) it presents the efficiency factor as a function of the horizontal pile displacement, (d2) it bridges the gap between pile-to-pile interaction at extremely small (elastic response) and at very large (plastic response) deformations. Finally, appropriately defined performance measure parameters are introduced to evaluate the pile response and to unravel the contribution of soil and “system” densification to the plastic shakedown mechanism.

2.2 REVIEW OF CONSTITUTIVE MODEL FOR COHESIVE SOILS UNDER UNDRAINED CONDITIONS

For the case of a flexible pile embedded in cohesive soil under undrained conditions, Gerolymos et al (2005) described the soil behavior through a constitutive model which is a reformulation of that originally developed by Lemaitre and Chaboche (1990). It belongs to the general category of single surface plasticity models, and it is available in the material library of ABAQUS (Dassault Systèmes Simulia Corp, 2009). According to this model, the evolution of stresses is described by the relation:

$$\sigma = \sigma_0 + \alpha \tag{2.1}$$

where σ_0 is the value of stress at zero plastic strain, assumed to remain constant. The parameter α is the "backstress", which defines the kinematic evolution of the yield surface in the stress space. Integration of the backstress evolution law over a half cycle of a unidirectional load (e.g. tension or compression) yields the following expression:

$$\alpha = \frac{C}{\gamma}\left[1 - \exp\left(-\gamma\,\varepsilon^{pl}\right)\right] \tag{2.2}$$

in which C and γ are hardening parameters that define the maximum transition of the yield surface, and the rate of transition, respectively, and ε^{pl} is the plastic strain. Differentiating α with respect to ε^{pl} and taking the limit at zero, one obtains for parameter C (Gerolymos and Gazetas, 2006):

$$\left.\frac{\partial\alpha}{\partial\varepsilon^{pl}}\right|_{\varepsilon^{pl}\to 0} = C = E \tag{2.3}$$

where E is the modulus of elasticity.

The evolution law of the model consists of two components: (i) a kinematic hardening component, which describes the translation of the yield surface in the stress space (defined through the backstress α), and (ii) an isotropic hardening component, which defines the size of the yield surface σ_0 at zero plastic deformation. The kinematic hardening component is defined as an additive combination of a purely kinematic term (linear Ziegler hardening law) and a relaxation term (the recall term), which introduces the nonlinearity. The evolution of the kinematic component of the yield stress is described as follows:

$$\dot{\alpha} = C\frac{1}{\sigma_0}(\sigma - \alpha)\,\dot{\bar{\varepsilon}}^{pl} - \gamma\,\alpha\,\dot{\bar{\varepsilon}}^{pl} \tag{2.4}$$

where $\dot{\varepsilon}^{pl}$ is the plastic flow rate (obtained through the equivalent plastic work), $\dot{\bar{\varepsilon}}^{pl}$ the equivalent plastic strain rate:

$$\dot{\bar{\varepsilon}}^{pl} = \sqrt{\frac{2}{3}\dot{\varepsilon}^{pl} : \dot{\varepsilon}^{pl}} \tag{2.5}$$

The evolution of the kinematic and the isotropic hardening components of the hardening rule are illustrated in **Figure 2.1** for unidirectional and multiaxial loading. The evolution law for the kinematic hardening component implies that the backstress is contained within a cylinder of radius:

$$\sqrt{\frac{2}{3}}\;\alpha_s = \sqrt{\frac{2}{3}}\;\frac{C}{\gamma} \tag{2.6}$$

where α_s is the magnitude of α at saturation. Since the yield surface remains bounded, this implies that any stress point must lie within a cylinder of radius $\sqrt{(2/3)}\;\sigma_y$. At large plastic strains, any stress point is contained within a cylinder of radius $\sqrt{(2/3)}$ $(\alpha_s + \sigma_s)$ where σ_s is the equivalent stress defining the size of the yield surface at large plastic strain.

The uniaxial yield stress σ_y is given by:

$$\sigma_y = \frac{C}{\gamma} + \sigma_0 \tag{2.7}$$

According to the Von Mises yield criterion this ultimate stress is:

$$\sigma_y = \sqrt{3}\;S_u \tag{2.8}$$

From **Equations 2.3**, **2.7** and **2.8** the hardening parameter γ may be expressed as (Gerolymos and Gazetas 2006):

$$\gamma = \frac{E}{\sqrt{3}S_u - \sigma_0} \tag{2.9}$$

To avoid numerical instability, the stress at zero plastic strain, σ_0 should be expressed as a small fraction of the uniaxial strength σ_y.

$$\sigma_0 = \lambda\sigma_y \tag{2.10}$$

where λ usually 0.1 to 0.3.

This simplified model is appropriate for problems with cohesive soils and rapid application of seismic load where the assumption of undrained behavior is reasonable.

2.3 EXTENSION TO COHESIONLESS SOILS UNDER DRAINED CONDITIONS

The model described in the previous section is extended to account for the behavior of cohesionless soil under drained conditions. Soil behavior is modeled through a constitutive model with nonlinear kinematic hardening and non-associated plastic flow rule because isotropic hardening does not reproduce the plastic strain accumulation under cyclic stress. In this case the Mohr-Coulomb failure criterion is used (**Figure 2.2**). In the Mohr-Coulomb failure criterion σ_y is equal to:

$$\sigma_y = \sqrt{3J_2} \tag{2.11}$$

in which $\sqrt{J_2}$ is the square root of the second deviatoric stress invariant at failure that satisfies the following equation:

$$I_1 \sin\varphi + \frac{1}{2}\left[3(1-\sin\varphi)\sin\theta + \sqrt{3}(3+\sin\varphi)\cos\theta\right]\sqrt{J_2} - 3c\cos\varphi = 0 \tag{2.12}$$

where I_1 is the first principal stress invariant, c cohesion, ϕ friction angle and θ the Lode angle (Chen and Mizuno, 1990) which is given by:

$$\cos(3\theta) = \frac{3\sqrt{3}}{2}\frac{J_3}{J_2^{3/2}} \tag{2.13}$$

where J_2 and J_3 are the second and third deviatoric stress invariants. Combining **Equations 2.3**, **2.7**, with **2.11** one obtains for γ:

$$\gamma = \frac{E}{\sqrt{3J_2} - \sigma_0} \tag{2.14}$$

A user subroutine is imported in ABAQUS, which relates the model parameters to the vertical stress, the principal stresses and the Lode angle at every loading step. Incorporating the Lode angle effect allows for significant accuracy in three-dimensional shear response environments (Yang and Elgamal, 2008). The yield surface of the proposed constitutive model is determined to fit the Mohr-Coulomb failure response in a triaxial loading test for both compression and extension conditions assuming linear interpolation for the intermediate stress states.

For triaxial compression

$$\sigma_y - \sigma_0 = (1-\lambda)\left(\frac{6\sin\varphi}{3-\sin\varphi}p + \frac{6c\cos\varphi}{3-\sin\varphi}\right) \quad (2.15)$$

and for triaxial compression

$$\sigma_y - \sigma_0 = (1-\lambda)\left(\frac{6\sin\varphi}{3+\sin\varphi}p + \frac{6c\cos\varphi}{3+\sin\varphi}\right) \quad (2.16)$$

where ϕ friction angle, c cohesion, and p hydrostatic pressure.

For this reason, the state parameter k is introduced which is a function of Lode angle and takes values from 0 to 1.

$$k = \frac{1}{2} - \frac{\cos(3\theta)}{2} \quad (2.17)$$

k = 0 corresponds to pure triaxial extension conditions, k = 1 to pure triaxial compression conditions, while k = 0.5 corresponds to direct shear test. In summary, the constitutive model parameters are calibrated to match the Coulomb failure criterion on the principal stresses plane for every apex of the hexagon with the smooth envelope of **Figure 2.2**.

The proposed constitutive model is calibrated and validated against three centrifuge experiments of single pile under cyclic lateral load. Obviously, the model in its present form cannot reproduce either dilative response or volume contraction (soil densification) with cyclic loading. Since soil volume reduction dominates the response in a loading with a large number of cycles, the role of the first weakness is usually of insignificant importance. The second drawback of the proposed model will be efficiently used in the sequel as a reference point for evaluating the role of the two hardening mechanisms (“system” and soil densification) responsible for the observed plastic shakedown response of the pile.

2.4 VALIDATION AGAINST CENTRIFUGE EXPERIMENTS

2.4.1 Centrifuge lateral cyclic load pile experiments

Over the past decade, dynamic centrifuge experiments have been widely used to gain insight in the dynamic behavior of geotechnical structures and to calibrate advanced numerical models and procedures. Since cohesionless soils have stress-dependent stiffness and strength characteristics the application of N times the gravitational acceleration to a model with length dimensions 1/N, makes the stresses and mechanical

properties of the model to become similar to those of the prototype. Three such centrifuge tests are used for the calibration and the validation of the proposed model.

Three centrifuge tests on a single pile subjected to cyclic horizontal loading were performed by Rosquoët et al (2004) at Laboratoire Central des Ponts et Chaussées (LCPC). The centrifuge facility of the LCPC in Nantes has a radius of 5.5 m, a maximum model mass of 2000 kg at a centrifuge acceleration of 100 g, and platform dimensions of 1.4 m x 1.15 m (**Figure 2.3**). It is capable of producing 200 g's of centrifugal acceleration, although of course at a much reduced "payload". The acquisition of a servo-hydraulic earthquake actuator has extended the scope of its activities.

The centrifuge models were 1/40 in scale and involved pile head loading with three different force time histories. The loading time histories were: (i) 12 cycles from 960 kN to 480 kN (test P32), (ii) 12 cycles from 960 kN to 0 kN (test P344), (iii) 6 cycles from 960 kN to -960 kN (test P330). The experimental set up and the loading time histories (in prototype scale) are portrayed in **Figure 2.4**.

The cyclic lateral load tests were conducted on a vertical friction pile placed in a sand mass of uniform density. The Fontainebleau sand centrifuge specimens were prepared by the air sand-raining process into a rectangular container (80 cm wide by 120 cm long by 36 cm deep), with the use of a special automatic hopper developed at LCPC (Garnier, 2002). The desired density of the dry sand was obtained by varying three parameters: (a) the flow of sand (opening of the hopper), (b) the automatically maintained drop height, and (c) the scanning rate. The unit weight and the relative density of the specimen were measured to be γ_d = 16.5 ± 0.04 kN/m^3 and D_r = 86%, respectively. Laboratory results from drained and undrained torsional and direct shear tests on Fontainebleau sand reconstituted specimens indicated mean values of peak and critical-state angles of $\phi_p = 41.8^o$ and $\phi_{cv} = 33^o$, respectively. Evidently, in this dense sand the pile used may be considered as flexible.

The model pile at scale 1/40 is a hollow aluminum cylinder of 18 mm external diameter, 3 mm wall thickness, and 365 mm length. The flexural stiffness of the pile is 0.197 kNm^2 and the elastic limit stress of the aluminum is 245 MPa. The centrifuge tests were carried out at 40 g and the characteristics of the model and the prototype pile are presented in **Table 2.1**.

The instrumentation included two displacement sensors, located at the section of the pile above the ground surface, and 20 pairs of strain gauges, positioned along the length of the pile, so that the bending moment profile M(z) could be measured during the tests. The resultant earth pressure p = p(z), per unit length along the pile, was obtained by double differentiation of M(z) as established by Matlock and Reese (Reese and Van Impe, 2001). The strain gauges were spaced at 0.6 m in prototype scale starting from the ground level to the pile tip. This single pile was driven into the sand at 1 g before rotating of the centrifuge. In flight, the single pile was subjected quasi-statically to horizontal cyclic loading through a servo-jack connected to the pile with a cable. With such a configuration the pile head is not submitted to any parasitic bending moment.

The test results were obtained in the form of horizontal force-displacement time histories at the head of the pile, as well as of bending moment along the pile. The bending moment distribution with depth M(z), obtained from the bending strains measured during each test through the strain gauges, was utilized to calculate the shear force, Q(z), and soil reaction, p(z), diagram:

$$Q(z) = \frac{dM(z)}{dz} \tag{2.18}$$

and

$$p(z) = \frac{d^2M(z)}{dz^2} \tag{2.19}$$

High-order spline functions which interpolate between two successive pairs of experimental points (M_i, z_i) and (M_{i+1}, z_{i+1}) were utilized to this end. The experimental M = M(z) curves were also integrated twice to get the pile deflection diagram y = y(z) and the boundary conditions (assuming hinged boundary conditions at the pile tip) were used to determine the two required constants (Gerolymos et al, 2009).

2.4.2 Finite element modeling

The above mentioned centrifuge tests were modeled numerically in 3D using the finite element code ABAQUS. The pile is assumed to be linear elastic, while the cyclic soil behavior is described via the proposed nonlinear constitutive law with kinematic hardening law and non-associated plastic flow rule. **Figure 2.5** depicts the finite element discretization for the centrifuge tests. The distance from the pile tip to the bottom of the

boundaries is 2.4 m (3.3 pile diameters). Approximately 43000 elements were used for each analysis. The soil is modeled with 8-node brick elements, while the pile is replaced by 3D beam elements placed at its center and connected with appropriate kinematic restraints with the nodes at the perimeter of the pile, in order to model the complete geometry of the pile (**Figure 2.6**). The solid elements inside the perimeter of the pile have no stiffness. In this way, each pile section behaves as a rigid disc: rotation is allowed on the condition that the disc remains always perpendicular to the beam axis, but stretching cannot occur.

The element size was small enough (0.3 m in the vertical direction): (a) to capture intense plastic strain concentration at the pile-soil interface, (b) to capture more accurately the pile-to-pile interplay in case of a pile group, and (c) to coincide with the vertical position of the strain gauges along the pile, so as to achieve a direct comparison with the measurements. The mesh is refined up to a distance of 7 diameters around the pile in order to acquire an accurate distribution of soil yielding. When the cohesionless soil reaches the active state as the pile is laterally loaded, it collapses and flows with the pile. Thus no gap is formed and no interface elements are used in the analysis. Finally, the bottom and side boundaries were fixed in order to model the box of the centrifuge tests.

The distribution of Young's Modulus varies parabolically with depth according to:

$$C = E = E_0 \left(\frac{\sigma_v}{P_a} \right)^m \tag{2.20}$$

where E_0 is the reference Young's Modulus, σ_v the vertical stress, P_a the atmospheric pressure (approximately 100 kPa) and m a parameter that defines the distribution of E with depth. E_0 is equal to 192 MPa and m is equal to 0.5 according to the calibration performed by Gerolymos et al, (2009) based on Hardin's formula (Hardin, 1978). The hardening parameter γ of the proposed constitutive model, which is a function of the internal friction angle, was calibrated to correspond to the critical-state friction angle $\phi_{cs} = 33^o$.

2.4.3 Numerical simulation of the centrifuge tests

The model is first calibrated against the results of the one-way cyclic loading test with maximum horizontal force 960 kN and minimum horizontal force 480 kN (designated as P32). Subsequently it is applied to predict the measured data of the other two tests (P330 and P344). The three tests differ by the characteristics of the cyclic loading sequences since one-way and two-way loading at different load amplitudes are used. It should be noted that the applied loads always stay in the domain of service loads.

2.4.3.1 Calibration of model parameters against test P32

As already stated above, the model is calibrated against the one-way cyclic loading test with maximum horizontal force 960 kN and minimum horizontal force 480 kN (test P32). The model parameters C (E_0 = 192 MPa), m (= 0.5), and γ (which is a function of the critical state friction angle ϕ_{cv} = 33^o), were calibrated to match the experimental "force–displacement" loop at the head of the pile (**Figure 2.7**). In one way cyclic loading, the pile displacement increases with every cycle of loading. The model is capable of predicting the plastic shakedown response of the pile. This response is the resultant of the following two mechanisms: (a) Soil densification due to the reduction of voids, and (b) "System densification" due to the gradual extension of the resisting soil mass, towards greater depths with cyclic loading. Only the second mechanism is captured by the proposed model.

Figure 2.8 compares the bending moment profiles at the first and sixth cycle of loading. In general, the agreement between the measured and the computed curves is quite satisfactory. The model predicts well the shape of the moment distribution and the increase of the bending moments with increasing number of cycles. The model is also capable of predicting the depth of the maximum bending moment both for loading and unloading conditions as well as the shift of the maximum bending moment at a higher depth as the number of cycles increases.

Because shear force and soil reaction were calculated indirectly from the measured bending moment during the experiment, a comparison with the calculated bending moment, shear force and soil reaction at different stages of virgin loading is presented in **Figure 2.9**. In general, the agreement between measured and computed

curves is quite satisfactory. Some differences noted at the soil reaction curves are attributed to the fact that the measured values derive from the bending moment distribution with the use of spline interpolation process, while the computed values derive from differentiation of the shear force. But even in this case, the model captures the increase in both (a) the magnitude of the maximum soil reaction, and (b) the depth at which this maximum occurs.

Figure 2.10 shows the comparison between the displacement profiles at the end of the first and twelfth cycle. The difference is attributed to the accumulation of soil plastification with the number of cycles. It should be noted that the displacement profiles have a nearly triangular shape, vanishing at z = 6 m, implying that the effective length of the pile is only a 50% of its total length. **Figure 2.11** depicts the contours of the active and passive stress states in terms of the state parameter k at three different stages of loading: (a) at the 1^{st} cycle at 960 kN, (b) at the 12^{th} cycle at 480 kN, and (c) at the 12^{th} cycle at 960 kN. k = 1 corresponds to pure triaxial compression loading condition (passive state), and k = 0 to pure triaxial extension loading condition (active state) while k ≈ 0.5 corresponds to the response of the soil in direct shear test. Finally, **Figure 2.12 i**llustrates snapshots of contours of the horizontal displacement of the pile subjected to lateral loading at the pile head at three different stages of loading: (a) at the 1^{st} cycle at 960 kN, (b) at the 12^{th} cycle at 480 kN, and (c) at the 12^{th} cycle at 960 kN.

2.4.3.2 Comparison of numerical results with tests P344 (asymmetric cyclic loading) and P330 (symmetric cyclic loading)

The calibrated model (from the P32 test) is utilized to predict the results of the P344 test (cyclic loading without sign reversal) and the P330 test (fully cyclic loading with sign reversal).

Test P344 is a full one-way cyclic loading test with maximum horizontal force 960 kN and minimum horizontal force 0 kN. The computed force-displacement curve at the pile head is compared to the experimental data in **Figure 2.13** for the 12 cycles of loading. Despite the discrepancy in the residual displacement at the pivot point of each unloading phase, the comparison is quite satisfactory. **Figure 2.14** shows comparison between measured and computed bending moment profiles. Although the bending moment profiles from the analysis at the end of the loading phase agree well with the

experimental values, there is a discrepancy during the unloading phase. The discrepancy in the unloading phase is attributed to the developed soil constitutive model not reproducing soil densification and loosening. Hence, the mobilized soil mass behind the pile, which follows the movement of the pile during the loading phase of the analysis, provides higher resistance than the loosened soil of the experiment during the unloading phase when the pile tries to reach its initial position.

Computed shear force distributions are presented in **Figure 2.15**. It is observed that for asymmetric cyclic loading the maximum of the shear force decreases with the number of cycles while the depth of the maximum shear force increases. On the contrary, the maximum of soil reaction (**Figure 2.16**) increases with the number of cycles. The irregular shape of the soil reaction after twelve cycles of loading is attributed to the fact that it is not directly measured but derives from differentiation of the shear force. **Figure 2.17** shows the increase of the horizontal pile displacement in one-way loading as the number of loading cycles increases. As expected, these values are higher than in test P32 because the range of loading–unloading is also higher. It is also observed that the effective length of the pile increases in comparison to test P32, even though the maximum applied load is the same for both tests (960 kN).

Finally, **Figure 2.18** depicts the contours of the active and passive stress states in terms of the state parameter k at three different stages of: (a) at the 1^{st} cycle at 960 kN, (b) at the 12^{th} cycle at 0 kN, and (c) at the 12^{th} cycle at 960 kN. It is interesting to observe that the plastic shakedown effect is reflected by the gradually developing fan-shaped stress bulb, the frontal part of which represents the mobilized soil mass that is in a passive state and expands with increasing cycles of loading, while the trailing part corresponds to the mobilized soil zone that is in an active state and shrinks with increasing number of cycles. The larger the bulb of “passive” stresses the greater the lateral soil reactions that resist the applied load, and finally, the pile reaches a steady state equilibrium of constant plastic strain (plastic shakedown). In **Figure 2.18b** it must be observed that even though there is no lateral force acting on the pile (unloading phase), the pile has not returned to its initial position because of the resistance of the soil that has already moved with the pile during the cyclic loading phase and has now taken the part of the initial position of the pile. This is also verified from the contours of the soil yielding around the pile in **Figure 2.19**.

Test P330 is a two-way cyclic loading test with maximum horizontal force 960 kN and minimum horizontal force -960 kN. The computed force-displacement curve at the pile head is compared to the experimental data for the 6 cycles of loading in **Figure 2.20**. It is observed that the pile displacement at reversal decreases at a decreasing rate as the number of loading cycles increases, in contrast to the previous experiments. This hardening behavior in the pile response is attributed to the extensive soil plastification that takes place around the pile, which leads to an increase of the soil pressure on the pile. In addition, a discrepancy in the displacement of about 1.5 cm is observed at the end of the virgin loading among test P330 and tests P32 and P344. This means that the sand in this experiment was not at the same initial condition as it was in tests P32 and P344. The results in this case are more qualitative than quantitative since no calibration of the proposed model was performed for the new soil condition.

Figure 2.21 depicts bending moment profiles at the first and sixth cycle of loading. For fully cyclic lateral loading, the computed values of bending moment agree well with the experimental ones. It is of interest to note, that the bending moment distributions at 960 kN and -960 kN are not exactly symmetric, but are slightly higher towards the direction of the virgin loading. This effect is attributed to the fact that the trailing part of the soil during the virgin loading flows with the pile and thus, there is an increase of the soil pressure on the pile during the unloading and the loading on the opposite direction. Shear force profiles for the first and sixth cycle (**Figure 2.22**) show that for fully cyclic loading the depth of the maximum shear force moves closer to the ground surface because of the system hardening due to the increased soil pressure on the pile. Similarly, the maximum soil reaction increases and the depth of the maximum soil reaction also shifts closer to the ground surface as depicted in **Figure 2.23. Figure 2.24** depicts the decrease of the horizontal pile displacement in fully cyclic lateral loading as the number of loading cycles increases. It is also observed that the horizontal pile displacement at the end of the loading phase of the sixth cycle is higher (1.44 cm) than the unloading phase of the same cycle (1.3 cm), even though the absolute value of the lateral force is the same in both cases. Finally, **Figure 2.25** depicts the contours of the active and passive stress states in terms of the state parameter k at three different stages of: (a) at the 1^{st} cycle at 960 kN, (b) at the 6^{th} cycle at -960 kN, and (c) at the 6^{th} cycle at 960 kN. k = 1 corresponds to pure triaxial compression loading condition (passive state),

and k = 0 to pure triaxial extension loading condition (active state) while k ≈ 0.5 corresponds to the response of the soil in direct shear test. When the pile reaches a steady state equilibrium of constant plastic strain (plastic shakedown) at the twelfth cycle the developed fan-shaped stress bulbs during unloading and reloading are identical.

2.4.4 Influence of the π-plane shape of the yield surface on pile response

As already stated above, a user subroutine is imported in ABAQUS, which correlates the Young's Modulus of the sand with the vertical stress, the principal stresses and the Lode angle at every step of the loading. The sand behavior is defined for triaxial extension and triaxial compression conditions and linear interpolation is performed for the intermediate states. On the loading side of the pile where compression prevails the soil is in the passive state, while at the back of the pile, where extension dominates the response, the soil is in the active state. For this reason, the predictions of the developed constitutive model (hereafter designated as Model CT) are compared with those from matching the Mohr-Coulomb yield criterion on its π-plane with a circle, in two different ways. In the first case (Model C), the circle circumscribes the Mohr-Coulomb shaped hexagonal pyramid (compressive meridian matching), while in the second case (Model T), the hexagonal pyramid is inscribed by the circle (tensile meridian matching), as illustrated in **Figure 2.26**. The results for all three tests performed are presented herein.

For the case of one-way loading test P32, the computed force-displacement curves at the pile head of the three models are presented in **Figure 2.27**. Obviously, model CT provides the best response. Model C is close to the experimental values but with stiffer response, while Model T leads to a "softer" response. The bending moment profiles at the 1^{st} and 12^{th} cycle of loading are compared in **Figure 2.28**. It is observed that model CT captures well the bending moment distribution while the response of triaxial compression model (Model C) prediction is also close to the measured values, since the passive soil resistance is an order of magnitude greater than the active one. As expected, the triaxial extension model (Model T) overestimates the response. **Figure 2.29** presents the shear force profiles at the end of the first cycle. The proposed model (Model CT) captures better the depth of the maximum shear force in comparison to the triaxial compression model. Again, the triaxial extension model overestimates the response. Finally, **Figure 2.30** depicts the horizontal displacement profiles at two different levels of

cyclic loading, computed from the three models. As expected, the triaxial compression model has a stiffer response than the proposed model, while the triaxial extension model predicts larger displacements and larger effective pile lengths.

For the case of one-way loading test P344, the predictions of the three models are shown comparatively in **Figure 2.31**. Again, Model CT coincides with the experimental values, the model C is close to the experimental values, while Model T has a softer response. Regarding the bending moment profiles in **Figure 2.32** each model exhibits similar behavior to that of test P32. As stated before, some differences noted at the soil reaction curves at **Figure 2.33** are attributed to the fact that the measured values derive from the bending moment distribution, while the computed values derive from differentiation of the shear force. The Model C and Model CT have a response close to the one derived from the experiment with the use of spline interpolation process. On the contrary, the Model T underpredicts the maximum soil reaction near the surface, while it overpredicts the soil reaction at the lower part of the pile. Finally, **Figure 2.34** depicts the increase of the horizontal pile displacement as the number of loading cycles increases for all three models, with the triaxial extension model producing the largest displacement as in test P32. The effective length of the pile increases with the number of cycles for all three models as expected.

For the case of two-way loading test P330 the predictions of the three models are shown comparatively in **Figure 2.35**. As already noted, a discrepancy at the displacement is observed at the end of the virgin loading among test P330 and tests P32 and P344 that indicates that the sand in this experiment is not at the same initial condition as it was in tests P32 and P344. Model C has a stiffer response than Model CT and the force–displacement loops stabilize almost at the second cycle of loading. Bending moment profiles at the 1^{st} and 6^{th} cycle are compared in **Figure 2.36**. In this type of loading the measured values are closer to the response of Model T and Model CT. This is expected, because in two-way loading the role of the active zone during the loading and unloading stage is more important than in the one-way loading. This also underlines that for fully cyclic lateral loading, the proper simulation of both triaxial compression and extension states of the soil are important. Finally, **Figure 2.37** depicts the decrease of the horizontal pile displacement as the number of loading cycles increases for all three models, with

Model T predicting the larger reduction in the displacements and the larger effective pile lengths.

Finally, it should be noted that the same problem of cyclic lateral loading of a pile in nonhomogeneous sand with increasing shear modulus G_0 with depth was attempted to be simulated with two other constitutive models: Mohr-Coulomb and Drucker-Prager. Because of the complicated loading conditions, the above mentioned models were unable to perform the analysis with the existing soil properties. The analyses would fail numerically and unrealistic soil properties should be introduced for the numerical solution of the cyclic loading.

2.4.5 Evaluation of model predictions

Three performance measure parameters are introduced to evaluate the response of the pile-soil system. **Figure 2.38** depicts the tangent stiffness at each unloading-reloading reversal point divided by the tangent stiffness at unloading-reloading reversal point of the first cycle, which is indicative of the elastic response of the pile. It is interesting to observe that the computed tangent stiffness remains constant for the proposed model described above, unaffected by cyclic loading, while the measured tangent stiffness increases in tests P344 and P330. This increase in the measured tangent stiffness is attributed to soil (material) densification during cyclic loading, an effect that is not simulated by the utilized soil constitutive model and which prevails in the elastic response of the pile. In test P32 the measured tangent stiffness shows a small variation without exhibiting a clear trend of hardening response, remaining practically unaffected by cyclic loading, the amplitude of which is too small to trigger soil densification.

Figure 2.39 presents the secant stiffness between two sequential reversal points normalized by the secant stiffness of the first cycle, which is indicative of the overall response of the pile during cyclic loading. It is worthy of note that both the computed and the measured secant stiffnesses increase with the number of cycles. Given that the system densification is captured numerically, the difference between measured and computed response is only attributed to soil densification.

Figure 2.40 presents the relative pile head displacement between two consecutive re-loading–unloading reversal points normalized with the one between the virgin loading-unloading and the first re-loading–unloading reversal points. The pile

displacement at pivot points increases in the asymmetric cyclic loading or decreases in the symmetric two-way cyclic loading with a decreasing rate and the pile finally reaches a zero-plastic strain rate equilibrium. It is observed that the computed versus measured response is in well agreement, implying that the mechanism of “system densification” dominates upon that of soil densification.

2.5 APPLICATION TO 1x2 PILE GROUP

For a pile group, the Winkler model has no interaction between adjacent piles and for this reason p-multipliers are introduced, factors that decrease the soil resistance p in p-y curves. In the elastic continuum model, the deformation of a pile under load is accompanied by deformations of the surrounding soil which decrease with distance from the pile and thus, the application of a load on a pile causes the movement of the adjacent pile. This effect is quantified with the use of interaction factors.

Having compared and validated the developed constitutive model with the analysis of a single free-head pile under lateral cyclic loading in nonhomogeneous sand, its capability for lateral response of piles in sand is further investigated through analysis of a 1x2 pile group. The piles, located at a distance of three diameters, are parallel to the load direction**. Figure 2.41** shows that the pile heads are hinged (zero bending moment) to the pile cap via appropriate kinematic constraints: (a) in order to have the identical pile head displacement as in a pile group, and (b) so that the results could be compared with those from the analyses of the free-head single pile. The pile cap is considered axially incompressible so that the spacing among the pile heads is kept constant. The load is applied at the middle of the pile heads from left to right appointing the left pile the trailing pile and the right pile the leading pile. **Figure 2.42** illustrates the finite element discretization of the pile group.

2.5.1 Test P344 (asymmetric cyclic loading)

The pile group is subjected to an asymmetric cyclic lateral loading similar to that of test P344 but with double amplitude (1920 kN). **Figure 2.43** plots the average force per pile versus group displacement and compares it with the corresponding force−displacement loop of the single isolated pile. For the same average load, the group displacement is greater than that of the solitary pile. Similar results have been derived by

Rollins et al (2006) and Papadopoulou et al (2010). This behavior is attributed to the fact that the passive failure zones of the piles in the group tend to overlap (shadow effect) as the lateral load increases, thus reducing the average soil resistance on the piles in the group. The shadow effect becomes more dominant with decreasing pile-to-pile distance. As in the case of the free-head single pile under asymmetric cyclic loading, the group displacement increases at a decreasing rate with the number of cycles finally reaching a plastic shakedown equilibrium. Interestingly, the force–displacement loop of the pile group is wider than the corresponding of the single isolated pile, implying greater soil plastification.

Figures 2.44 through **2.46** depict the detailed distribution of the bending moments, the shear forces, and the lateral soil reaction with depth along each pile in the group computed for different stages of loading. Comparison is given with the respective results from the analysis of the single isolated pile. The following observations are worthy of note:

- The maximum bending moment increases with the number of cycles and shifts to greater depths following the progressive extension of soil yielding. A similar trend in the behavior is exhibited by both the shear force and the lateral soil reaction.
- The leading pile develops the largest bending moment in comparison to both the trailing and the single pile which shows an intermediate response. The discrepancy in the bending moment distribution between the trailing and the leading pile is attributed to the shadow effect. Similar trends are also observed in the shear force and lateral soil reaction profiles.
- Upon unloading, and for zero applied lateral force, the bending moments, shear forces and lateral soil reactions are not zero. Instead, they retain large values comparable to those for the maximum applied load. Indeed, the reduction in the maximum values is about 40% for the bending moments and shear forces, and rather negligible for the lateral soil reactions. It should be noted that in the case of a linear soil all the aforementioned quantities would vanish to zero, as soil elasticity would act as a restoring force for the pile.

The contours of the state parameter k are presented for the 1^{st} and 12^{th} cycle of loading are shown in **Figure 2.47**. Evidently, the picture is similar to that of **Figure 2.18** for single pile response. The gradual expansion of the compression stress bulb with the

number of cycles signals the plastic shakedown process until the pile group reaches a steady state equilibrium of constant plastic strain. The shadow effect is manifested by the formation of a relaxation zone (k = 0) at the back of the leading pile which softens the response of the trailing one. **Figure 2.47b** shows that even though there is no lateral force acting on the pile (unloading phase), the pile group has not returned at its initial position because of the resistance of the soil that has already flown with the pile group during the cyclic loading phase and has now taken the part of the initial position of the pile group. The evolution of soil yielding around the pile group is depicted in **Figure 2.48**. The plastic strains are plotted on the same scale at each loading phase. It is evident that the plastic strains increase with the number of cycles. Another observation worthy of note is that the soil around the trailing pile yields more than in that around the leading pile.

2.5.2 Test P32 (asymmetric cyclic loading)

Similarly, the pile group is subjected to an asymmetric cyclic lateral loading similar to that of test P32 but with double amplitude (maximum applied load 1920 kN and minimum applied load 960 kN). **Figure 2.49** plots the average force per pile versus group displacement and compares it with the corresponding force–displacement loop of the single isolated pile. For asymmetric cyclic loading, the behavior of the pile group is identical to that of test P344: for the same average load, the group displacement is greater than that of the solitary pile.

Figures 2.50 and **2.51** illustrate the detailed distribution of the bending moments and the shear forces, respectively, with depth along each pile in the group computed for the first and sixth cycle of loading. As in the case of cyclic loading of test P344, the leading pile develops the maximum bending moment and shear force at the same depth with the single pile for both loading and unloading while in the case of the trailing pile they develop at higher depth due to the shadow effect. It is worthy of note that the shear force at the leading pile at the ground surface is about 1.2 times that of the single pile at the end of loading. Equivalently, the shear force at the trailing pile is about 0.8 times that of the single pile at the end of loading.

Finally, **Figure 2.52** presents the contours of the state parameter k for the 1^{st} and 12^{th} cycle of loading. During the loading phase of the first cycle, the soil in front of the

leading pile is at the passive state while behind the trailing pile is at the active state. The soil located between the two piles is in an intermediate state, due to tension near the leading pile and compression near the trailing pile. In general, the soil between the piles provides less resistance to the trailing pile than in the case of a single pile since it tends to flow with the leading pile. On the contrary the soil in front of the leading pile provides similar resistance to the case of a single pile because of the stable soil mass around it. When the direction of the loading changes (unloading) the soil between the piles is not compressed enough in order to change its condition to a complete passive one, so it remains in an intermediate state. This indication of shadow effect is more intense as the number of cycles increases.

2.5.3 Test P330 (symmetric cyclic loading)

Finally, the pile group is subjected to the symmetric cyclic lateral loading of test P330 with double amplitude (maximum applied load 1920 kN and minimum applied load -1920 kN). **Figure 2.53** plots the average force per pile versus group displacement and compares it with the corresponding force−displacement loop of the single isolated pile for the 6 cycles of loading. Even for two-way cyclic loading, the shadow effect causes greater group displacement than that of the solitary pile. As in the case of the single pile, the pile group displacement at reversal decreases with decreasing rate as the number of loading cycles increases due to the extensive soil plastification that takes places around the pile group.

Figures 2.54 and **2.55** present bending moment and shear force profiles of the single pile and the pile group at the first and third cycle of loading. For fully cyclic lateral loading, the maximum bending moment per cycle decreases. Similar behavior is observed for the shear force profile for the first and third cycle. It is also observed that the piles at the end of loading and unloading stage undertake the same percentage of the total load on the pile group depending only on whether they behave as the leading or the trailing pile. Finally, the contours of the state parameter k are presented for the 1^{st} and 6^{th} cycle of loading are shown in **Figure 2.56**. For fully cyclic lateral loading, the fan-shaped stress bulbs developed during loading and unloading are almost identical at the steady state equilibrium (cycle 6).

2.5.4 Efficiency factors

Pushover Tests are performed for the 1x2 pile group with pile diameter d = 0.72 m. **Figure 2.57** compares the efficiency factors, which should not be confused with pile-to-pile interaction factors, for the 1x2 pile group loaded at a height 1.6 meters above the ground surface: (a) calculated with Model CT through complete modeling, and (b) as proposed by Reese and Van Impe (2001):

for the leading pile

$$\eta_L = 0.7\left(\frac{s}{d}\right)^{0.26} \tag{2.21}$$

for the trailing pile

$$\eta_T = 0.48\left(\frac{s}{d}\right)^{0.38} \tag{2.22}$$

with d the pile diameter, and s the pile-to-pile distance. Interestingly, the calculated efficiency factors converge to those of Reese and Van Impe (2001) at very large pile head displacements, with a small discrepancy for the leading pile which shows to recover its initial stiffness ($\eta_L \approx 1$). This hardening response may be attributed to the plastic shakedown effect. On the contrary, the computed efficiency factor for the trailing pile decreases with increasing horizontal displacement, as a result of the shadow effect, but at decreasing rate due to the “plastic shakedown-induced” hardening response of the pile group reaching a minimum value of ($\eta_T \approx 0.7$).

Of equal if not greater interest is that at zero and/or very small pile displacements (elastic response), all three computed efficiency factors (for the leading pile, the trailing pile and the pile group) are very close to 1 (≈ 0.97), implying that pile-to-pile interaction has an insignificant effect on the elastic response of the pile group. This could possibly suggest a “destructive” interference in pile-to-pile interaction rather than that pile-to-pile interaction factors are zero which are certainly not, according to valid published results, e.g. Mylonakis and Gazetas (1998). It is recalled that the efficiency factor for a group of two piles, assuming elastic soil response and neglecting the cross-coupling (displacement/rotation atop the passive pile for a unit rotation/displacement atop the active pile) and rotational (rotation atop the passive pile for a unit rotation atop the active pile) pile-to-pile interaction factors, is expressed by:

$$\eta = \frac{1}{1+\alpha_h} \tag{2.23}$$

in which α_h is the horizontal pile-to-pile interaction factor, approximated by Mylonakis and Gazetas (1998):

$$\alpha_h \approx \sqrt{\frac{d}{2s}} \tag{2.24}$$

with d the pile diameter, and s the pile-to-pile distance. For d = 1 m and s = 3 m, **Equation 2.23** yields η = 0.71 compared to 0.97 from the analysis. The negligible pile-to-pile interaction effect in the elastic response is also evident **in Figures 2.43**, **2.49** and **2.53** which compare the computed force - displacement response of the single pile and the pile group.

Figure 2.58 depicts the average force per pile versus group displacement and compares it with the corresponding force−displacement of the single isolated pile for different soil types: (a) elastic soil with constant Young's modulus with depth, (b) elastic soil with parabolic Young's modulus with depth, and (c) for inelastic soil response. For small displacements (elastic response) the efficiency factor of the pile group is 1 when the pile spacing is three pile diameters. Obviously, the efficiency factor is unaffected by the variation of the soil modulus with depth.

Figure 2.59 illustrates the average force per pile versus group displacement and compares it with the corresponding force−displacement of the single isolated pile for different pile group connections and height of connections. Comparing **Figure 2.59c** and **2.59d** it is verified that the hinged connection of the piles is identical as the case of two free-head piles with load acting at both individual piles. Thus, η = 0.78 is attributed directly to the horizontal pile-to-pile interaction. Comparing **Figure 2.59a** and **2.59b** it is shown that the fixed-head connection leads to even smaller efficiency factor than the hinged-head connection. The comparison of **Figure 2.59a** and **2.59c** proves that the eccentricity of loading greatly affects the efficiency factor (η = 0.97 for e = 1.6 m and η = 0.78 for e = 0 m).

2.6 SUMMARY AND CONCLUSIONS

A simplified constitutive soil model for the static and cyclic response of piles embedded in cohesionless soil under drained conditions is presented. Materialized into a

three-dimensional finite element code, the model predictions were compared with experimental results of a single pile in dry sand, and subsequently the model was utilized in a numerical study. The numerical study addressed the cyclic lateral response of a group of two piles with similar geometric characteristics and soil conditions to those of the experimental tests. The main conclusions are:

- The plastic shakedown response of the single pile is attributed to the so-called "system" densification and the cyclically-induced material (soil) densification.
- During cyclic loading, the mechanism of "system" densification dominates upon soil densification with the contribution of the latter to the macroscopic response of the piles (or pile group) being rather insignificant.
- Upon unloading to zero lateral force, the residual internal structural forces and the lateral soil reactions of the piles are substantial.
- For fully cyclic lateral loading, the proper simulation of both triaxial compression and extension states of the soil are important.
- The formation of a relaxation zone at the back of a leading pile in the pile group significantly reduces the lateral soil resistance on the trailing pile. This behavior, well-known in the literature as "shadow effect", is more prominent at large pile deformations.
- The efficiency factor of the leading pile decreases with increasing pile displacement, but at extremely large deformations recovers if not overpasses its initial (near zero-amplitude-strain) value. On the contrary, the efficiency factor of the trailing pile decreases monotonically with loading, but at a decreasing rate, finally reaching an asymptotic value.
- The asymptotic values of all three efficiency factors (for the leading pile, the trailing pile and the pile group) compare well with those by Reese and Van Impe (2001). But, interestingly, and perhaps surprisingly, all the computed nearly elastic efficiency factors are very close to 1, suggesting that pile-to-pile interaction effects are negligible. This stems mainly from the fact that the load is applied at a height above the soil surface, while the piles are hinged at their top.

REFERENCES

Achmus M., Kuo Y., Abdel-Rahman K., 2009, "Behavior of monopile foundations under cyclic lateral load", *Computers and Geotechnics*, 36, pp 725-735

Allotey N, El Naggar M.H., 2008, "A numerical study into lateral cyclic nonlinear soil-pile response", *Canadian Geotechnical Journal*, 45 (9), pp 1268-1281

Bourgeois E., Rakotonindriana M.H.J., Le Kouby A., Mestat P., Serratrice J.F., 2010, "Three-dimensional numerical modeling of the behaviour of a pile subjected to cyclic lateral loading", *Computers and Geotechnics*, Vol. 37, pp 999-1007

Broms B., 1964, "Lateral resistance of piles in cohesionless soils", *Journal of Soil Mechanics and Foundation Division*, ASCE, 90 (3), pp 123-156

Brown D.A, Reese L.C., O'Neill M.W., 1987, "Cyclic Lateral Loading of a large-scale pile group", *Journal of Geotechnical Engineering*, 113 (11), pp 1326-1343

Chen W.F., Mizuno E., 1990, *Nonlinear Analysis in Soil Mechanics: Theory and Implementation*, Elsevier, New York

Dassault Systèmes Simulia Corp, 2009, *ABAQUS User's Manual, Providence*, RI, USA

Dawson T.H., 1980, "Simplified analysis of offshore piles under cyclic lateral loads", *Ocean Engineering*, Vol 7., pp 553-562

Garnier J., 2002, "Properties of soil samples used in centrifuge models", *Invited Keynote Lecture, International Conference on Physical Modelling in Geotechnics – ICPMG '02*, R. Phillips et al. (Eds), published by A.A. Balkema, Rotterdam, 1, pp 5-19

Gerolymos N., Gazetas G., 2005, "Phenomenological model applied to inelastic response of soil-pile interaction systems", *Soils and Foundations*, 45 (4), pp 119-132

Gerolymos N., Gazetas G., Tazoh T., 2005, "Static and Dynamic Response of Yielding Pile in Nonlinear Soil", *Proceedings of the 1st Greece-Japan Workshop: Seismic Design, Observation and Retrofit of Foundations*, Athens, pp 25-35

Gerolymos N., Gazetas G., 2006, "Static and Dynamic Response of Massive Caisson Foundations with Soil and Interface Nonlinearities–Validation and Results", *Soil Dynamics and Earthquake Engineering*, 26 (5), pp. 377-394

Gerolymos N., Escoffier S., Gazetas G., Garnier J., 2009, "Numerical Modeling of centrifuge cyclic lateral pile load experiments", *Earthquake Engineering and Engineering Vibration*, 8, pp 61-76

Grashuls A.J., Dieterman H.A., Zorn N.F., 1990, “Calculation of Cyclic Response of Laterally Loaded Piles”, *Computers and Geotechnics*, 10, pp 287-305

Hardin B.O., 1978, “Nature of stress-strain behavior of soils”, *Proceedings of the Specialty Conference on Earthquake Engineering and Soil Dynamics*”, ASCE, 1, pp 3-90

Hutchinson T.C., Chai Y.H., Boulanger R.W., 2005, “Simulation of full-scale cyclic lateral load tests on piles”, *Journal of Geotechnical and Geoenvironmental Engineering*, Vol. 131, No. 9, pp 1172-1175

Lemaitre J., Chaboche J., 1990, *Mechanics of Solid Materials*, Cambridge University Press

Lin S., Liao J., 1999, “Permanent strains of piles in sand due to cyclic lateral loads”, *Journal of Geotechnical and Geoenvironmental Engineering*, Vol. 125, No 9., pp 798-802

Long J.H., Vanneste G., 1994, “Effects of cyclic lateral loads on piles in sand”, *Journal of Geotechnical Engineering*, 120(1), pp 33-42

Mylonakis, G. and Gazetas, G. 1998, “Vertical Vibration and Distress of Piles and Pile Groups in Layered Soil”, *Soils and Foundations*, Vol. 38, No 1, pp. 1-14

Papadopoulou M.C., Comodromos E.M., 2010, “On the response prediction of horizontally loaded fixed-head pile groups in sands”, *Computers and Geotechnics*, Vol. 37, Issue 7-8, pp 930-941

Poulos H.G., 1982, “Single pile response to cyclic lateral load”, *Journal of Geotechnical and Geoenvironmental Engineering*, Vol 108, pp 355-375

Reese L.C., Cox W.R., Koop F.D., 1974, “Analysis of laterally loaded piles in sand”, *Proceedings of the VI Annual Offshore Technology Conference*, Houston, Texas, 2: 473-485

Reese L.C., Van Impe W.F., 2001, *Single Piles and Pile Groups under Lateral Loading*, A.A.Balkema, Rotterdam

Rollins K.M., Olsen R.J., Egbert J.J., Jensen D.H., Olsen K.G., Garrett B.H., 2006, “Pile spacing effects on lateral pile group behavior: Load Tests”, *Journal of Geotechnical and Geoenvironmental Engineering*, Vol. 132, No. 10, pp 1262-1271

Rosquoët F., Garnier J., Thorel L., Canepa Y., 2004, “Horizontal cyclic loading of piles installed in sand : Study of the pile head displacement and maximum bending moment”, *Proceedings of the International Conference on Cyclic Behaviour of Soils*

and Liquefaction Phenomena, Bochum, T. Triantafyllidis (Ed.), Taylor & Francis, pp 363-368

Tuladhar R., Maki T., Mutsuyoshi H., 2008, "Cyclic behavior of laterally loaded concrete piles embedded into cohesive soil", *Earthquake Engineering and Structural Dynamics*, 37, pp 43-59

Verdure L., Garnier J., Levacher D., 2003, "Lateral cyclic loading of single piles in sand", *International Journal of Physical Modelling in Geotechnics*, 3, pp17-28

Yang Z., Elgamal A., 2008, "Multi-surface Cyclic Plasticity Sand Model with Lode Angle Effect", *Geotechnical and Geological Engineering*, 26, pp 335-348

Zhang F., Kimura M., Nakai T., Hoshikawa T., 2000, "Mechanical behavior of pile foundations subjected to cyclic lateral loading up to the ultimate state", *Soils and Foundations*, 40 (5), pp 1-17

Table 2.1: Pile characteristics

Name	Symbol	Model scale	Prototype scale (40 g)
Length	L	36.5 cm	14.6 m
Depth of pile tip from ground surface	D	30 cm	12 m
External diameter	B	1.8 cm	0.72 m
Internal diameter		1.5 cm	0.6 m
Young's modulus	E	7.4 x 104 MPa	
Moment of inertia	I	2.67 x 10^{-9} m^4	6.83 x 10^{-3} m^4
Bending stiffness	EI	197 Nm^2	505 MNm^2
Elastic limit	σ_e	245 MPa	

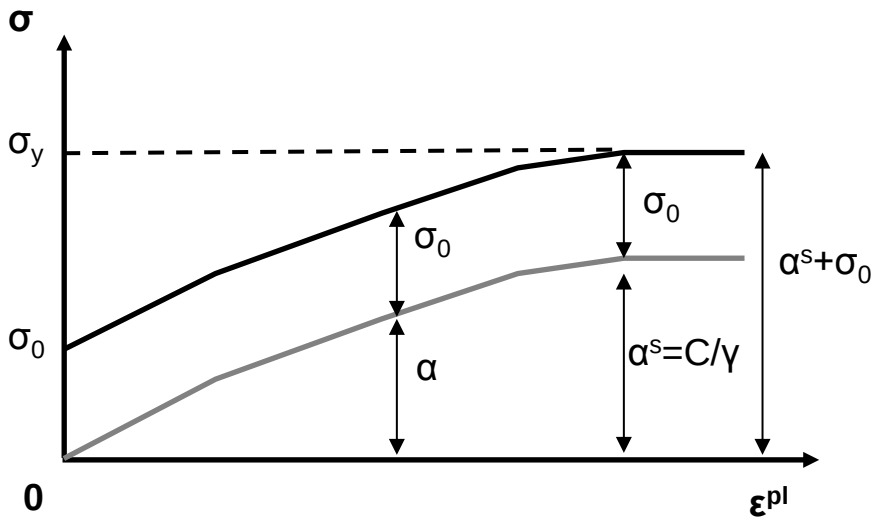

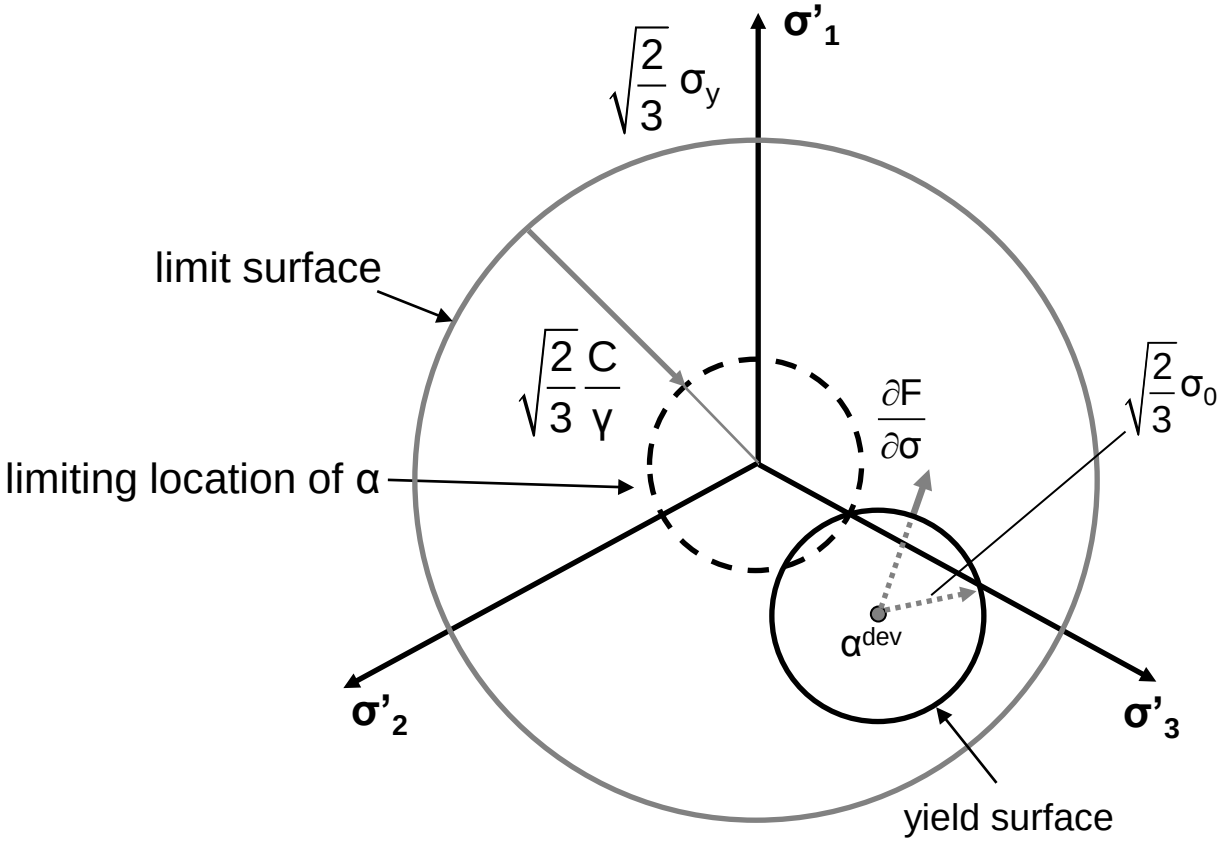

Figure 2.1: (a) Simplified one-dimensional representation of the hardening of the constitutive model for cohesive soils, (b) Three-dimensional representation of the hardening in the nonlinear kinematic model

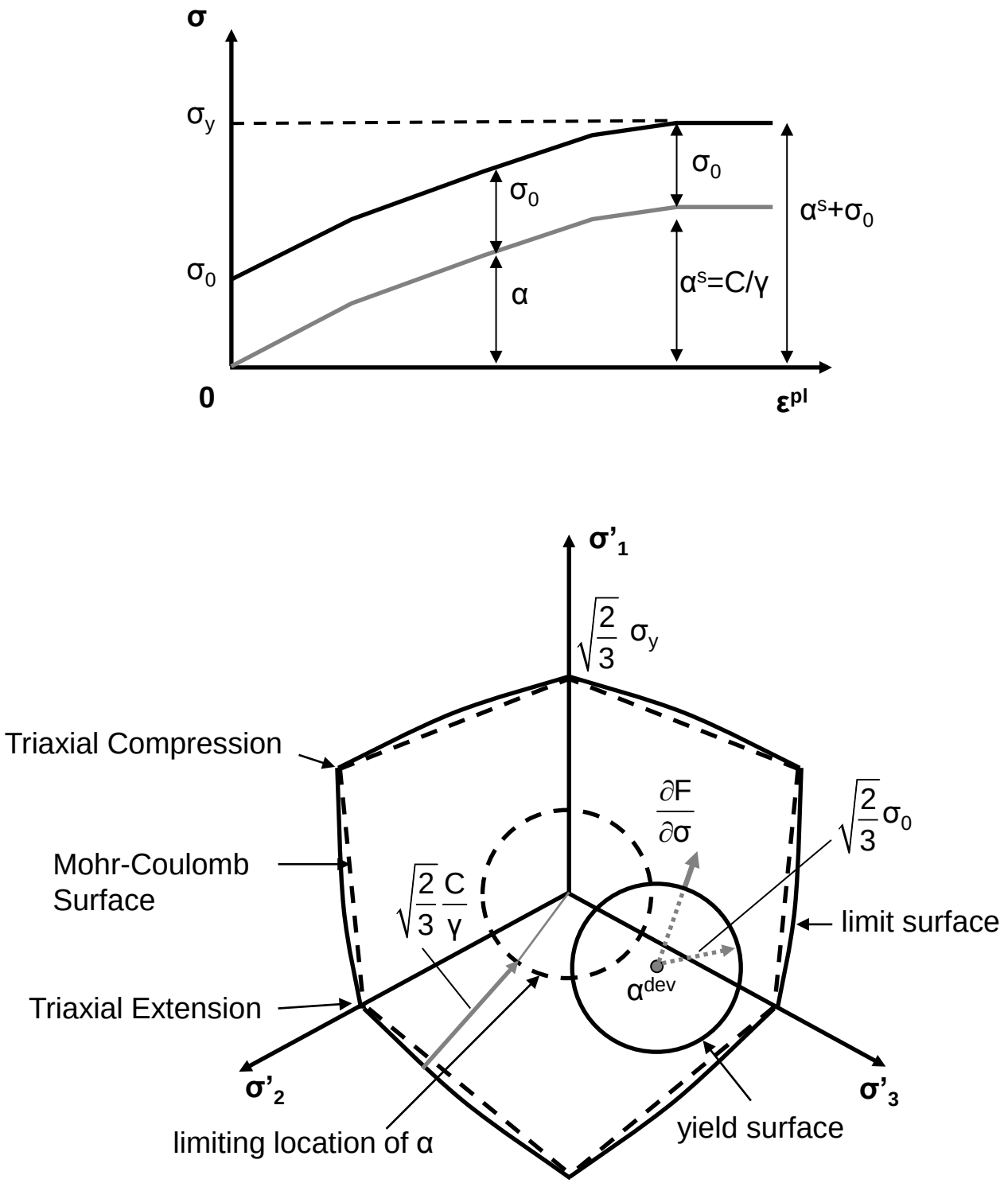

Figure 2.2: (a) Simplified one-dimensional representation of the hardening of the proposed constitutive model for cohesionless soils, (b) Three-dimensional representation of the hardening in the nonlinear kinematic model

Figure 2.3: The centrifuge at LCPC in Nantes, France

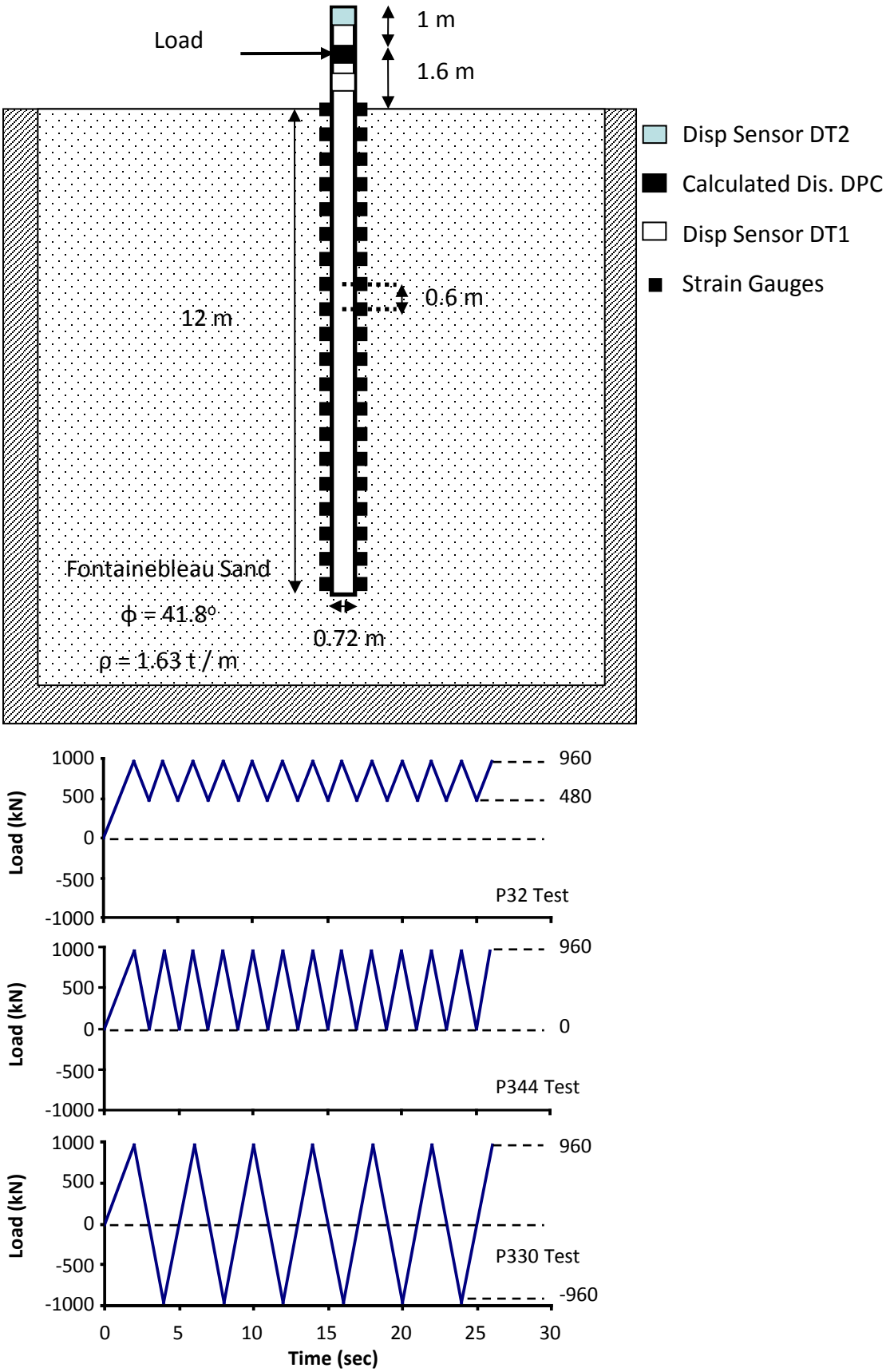

Figure 2.4: (a) Experimental setup of the centrifuge tests conducted in LCPC, (b) Load time histories of the three tests (P32, P344 and P330). All dimensions refer to the modeled prototype

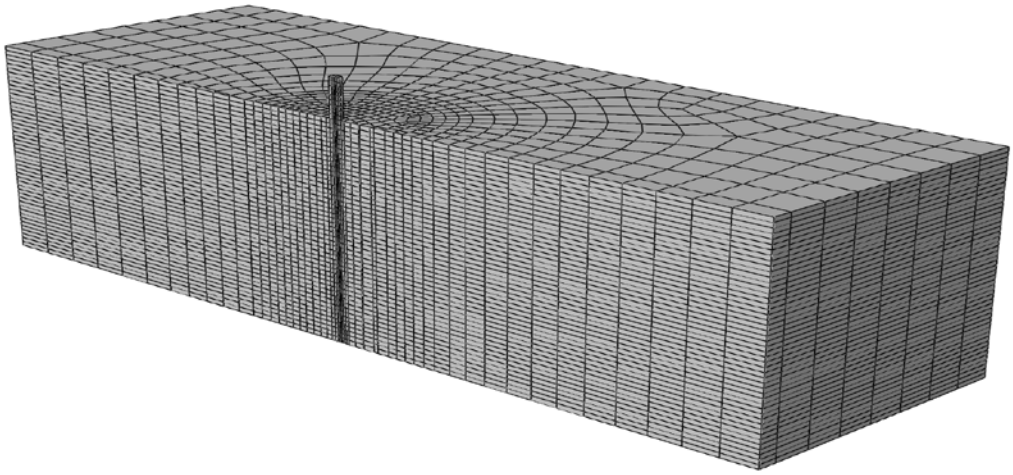

Figure 2.5: Finite element modeling of the centrifuge test

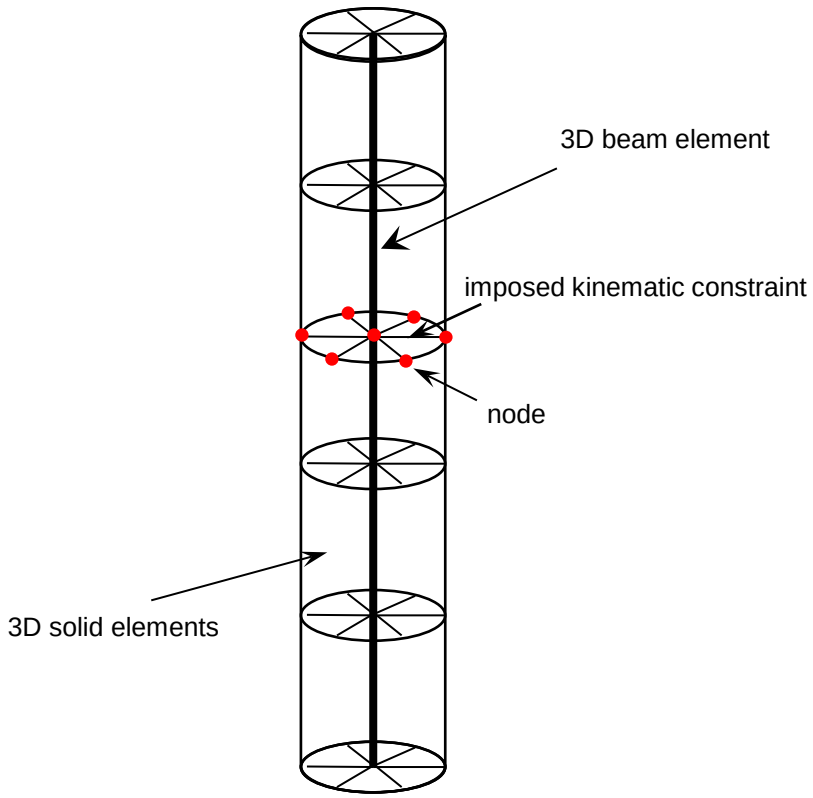

Figure 2.6: Pile modeling

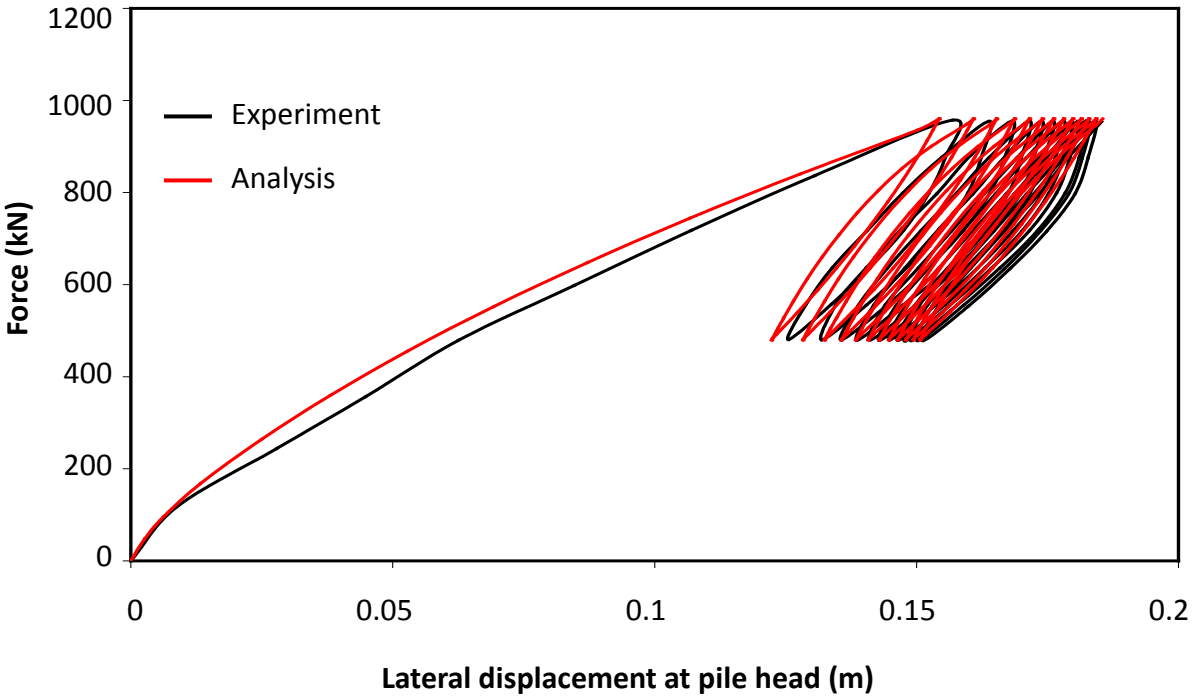

Figure 2.7: Experimental and computed force–displacement curves at pile head for test P32

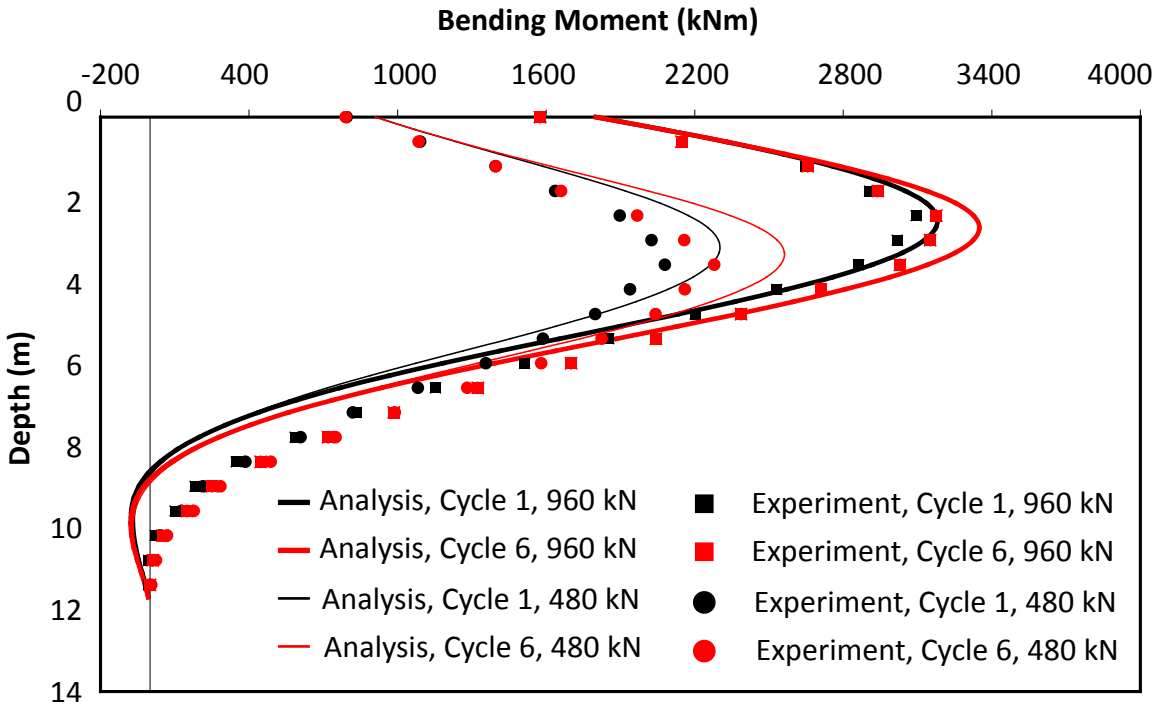

Figure 2.8: Comparison of computed and recorded bending moment distributions for test P32 at two different stages of loading: at 1st and 6th cycles. The maximum applied load is 960 kN and the minimum 480 kN

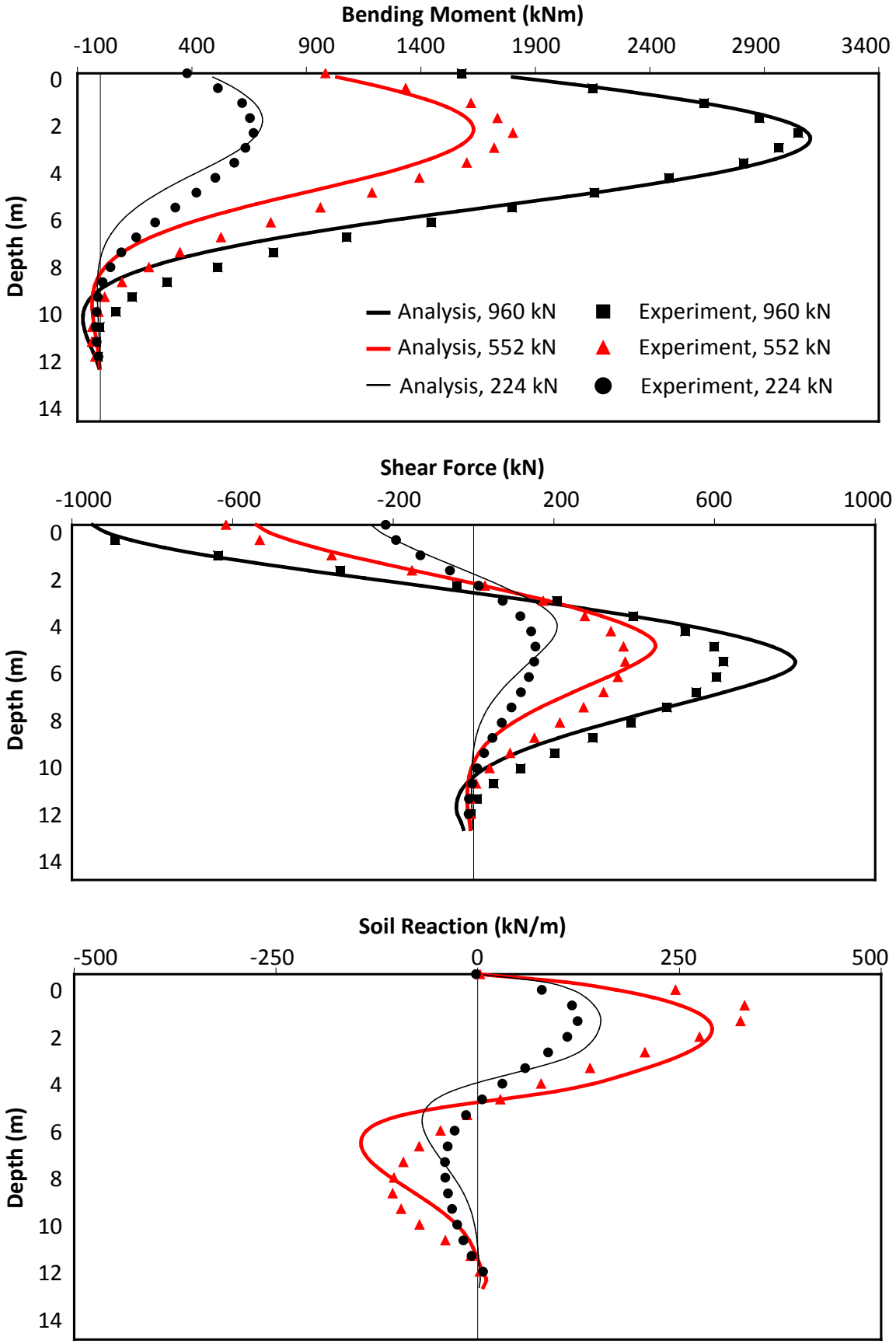

Figure 2.9: Comparison of computed and recorded (a) bending moment, (b) shear force, and (c) soil reaction distributions for virgin loading of test P32 for different loads increments during virgin loading

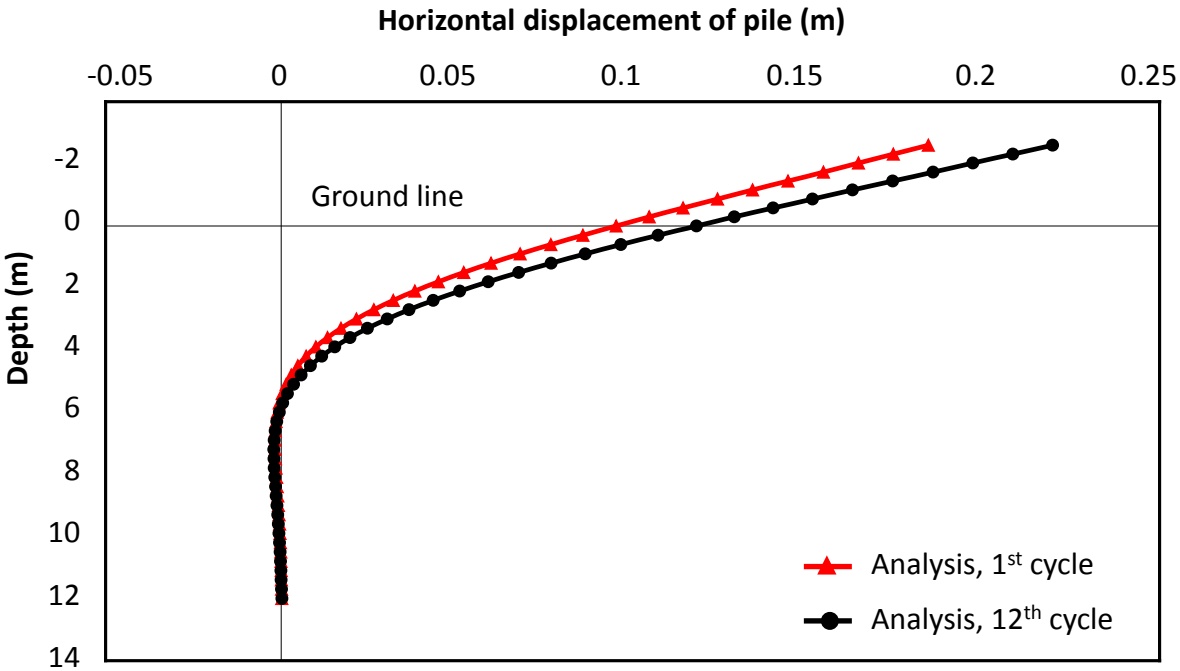

Figure 2.10: Comparison of computed horizontal displacement of the pile for test P32 at two different stages of loading: at the end of the 1st and the 12th cycle. The maximum applied load is 960 kN

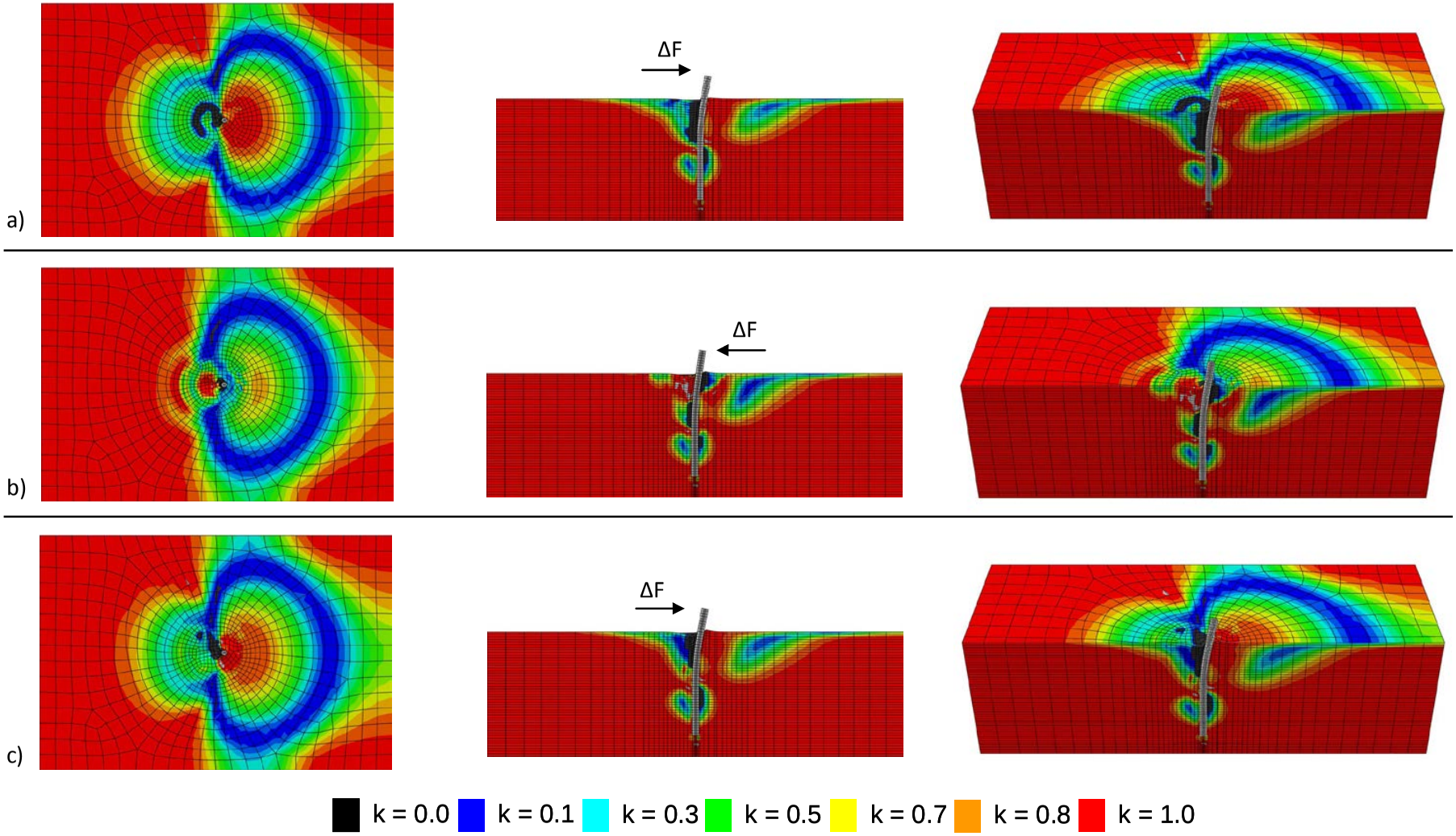

Figure 2.11: Contours of the active and passive stress states in terms of the state parameter k at three different stages of loading of the single pile of test P32: (a) at the 1st cycle at 960 kN, (b) at the 12th cycle at 480 kN, and (c) at the 12th cycle at 960 kN. k = 1 corresponds to pure triaxial compression loading condition (passive state), and k = 0 to pure triaxial extension loading condition (active state) while k ≈ 0.5 sets the boundaries between the active and the passive state. (Deformation Scale Factor = 5)

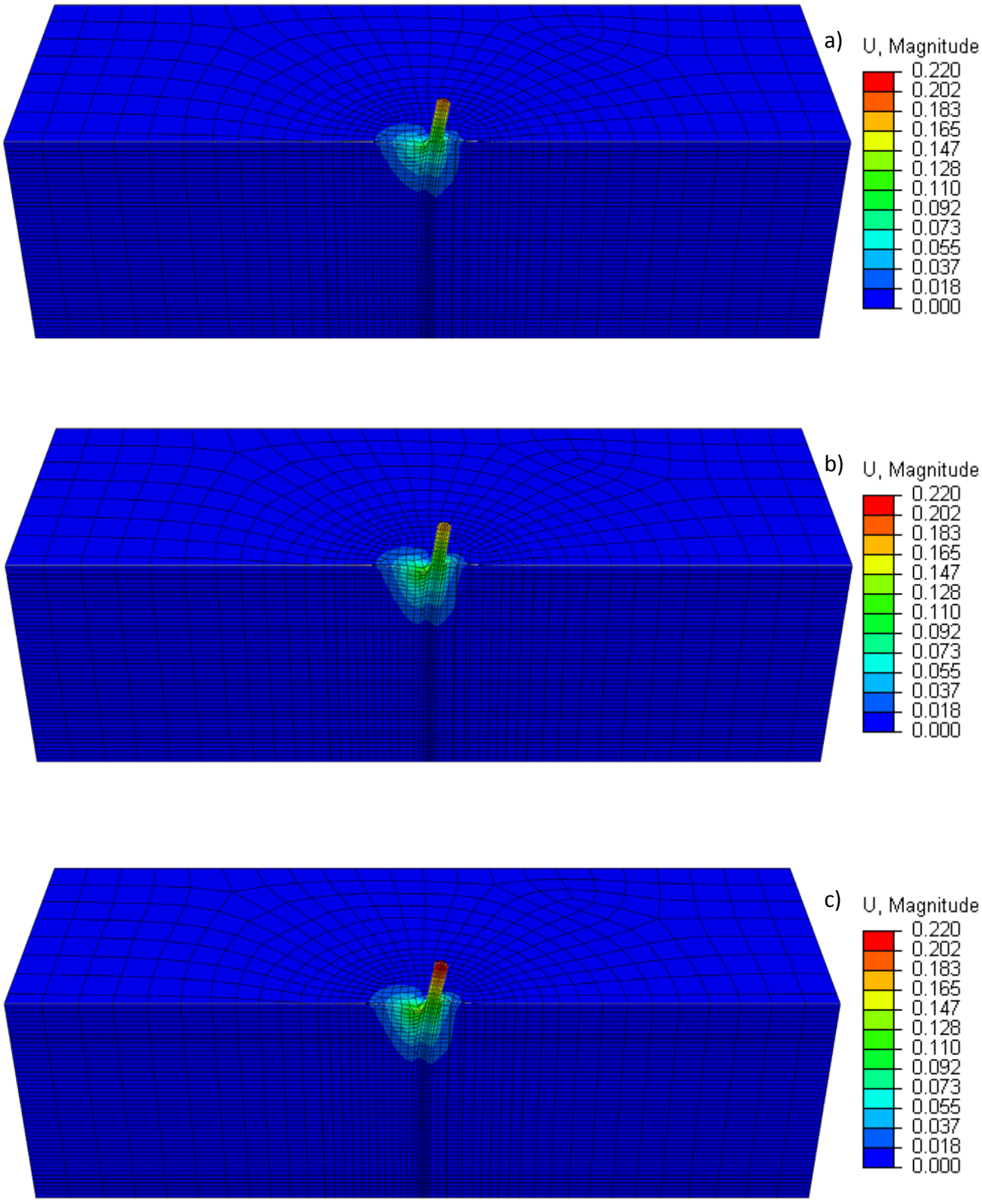

Figure 2.12: Contours of the horizontal displacement, plotted on the deformed mesh, at three different stages of loading of the single pile of test P32: (a) at the 1st cycle at 960 kN, (b) at the 12th cycle at 480 kN, and (c) at the 12th cycle at 960 kN. (Deformation Scale Factor = 5)

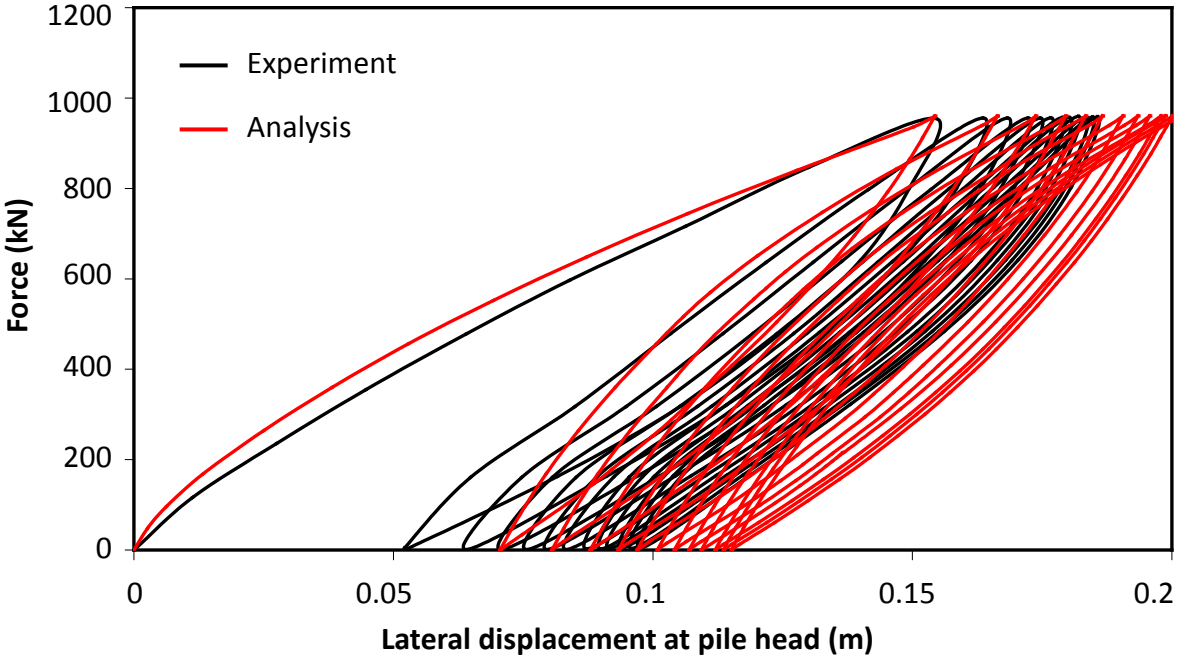

Figure 2.13: Experimental and computed force–displacement curves at pile head for test P344

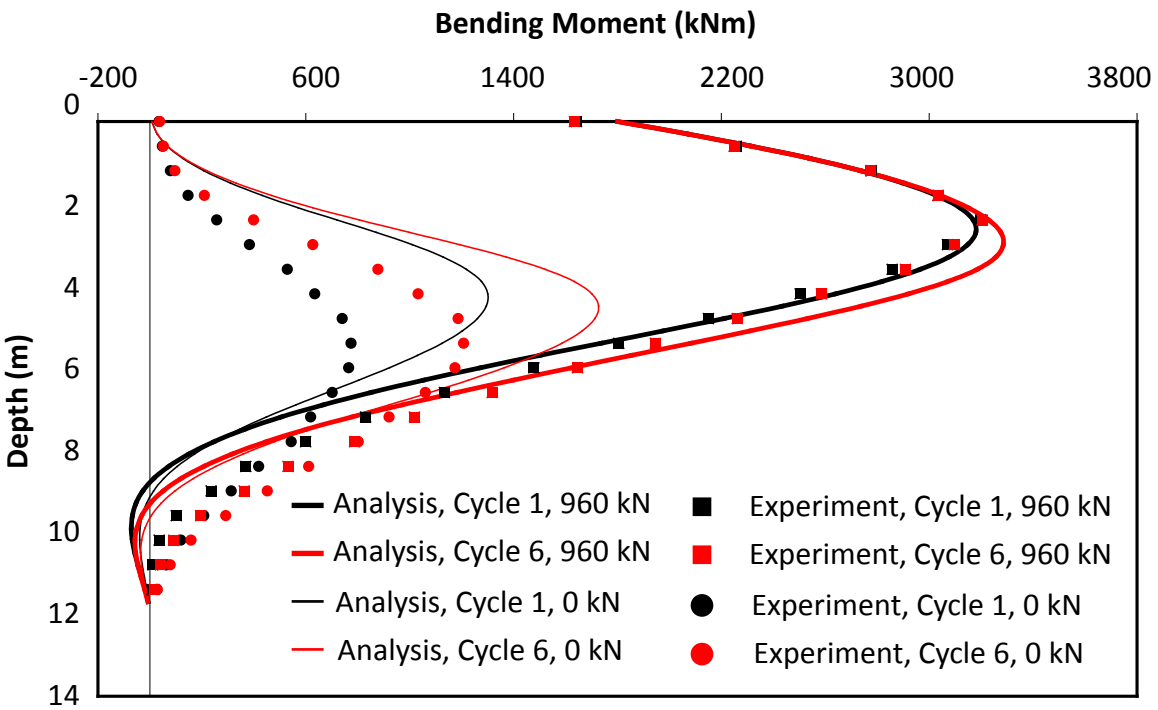

Figure 2.14: Comparison of computed and recorded bending moment distributions for test P344 at two different stages of loading: at 1st and 6th cycle. The maximum applied load is 960 kN and the minimum 0 kN

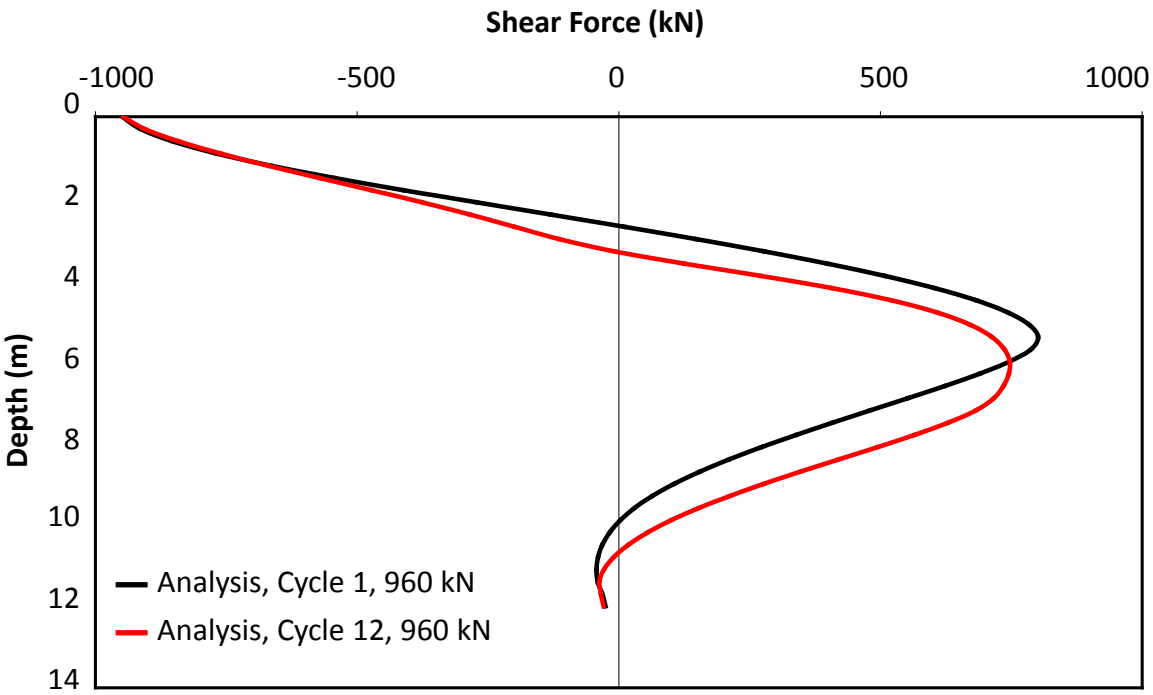

Figure 2.15: Computed shear force distributions for test P344 at 1st and 12th cycle of loading for maximum applied load 960 kN

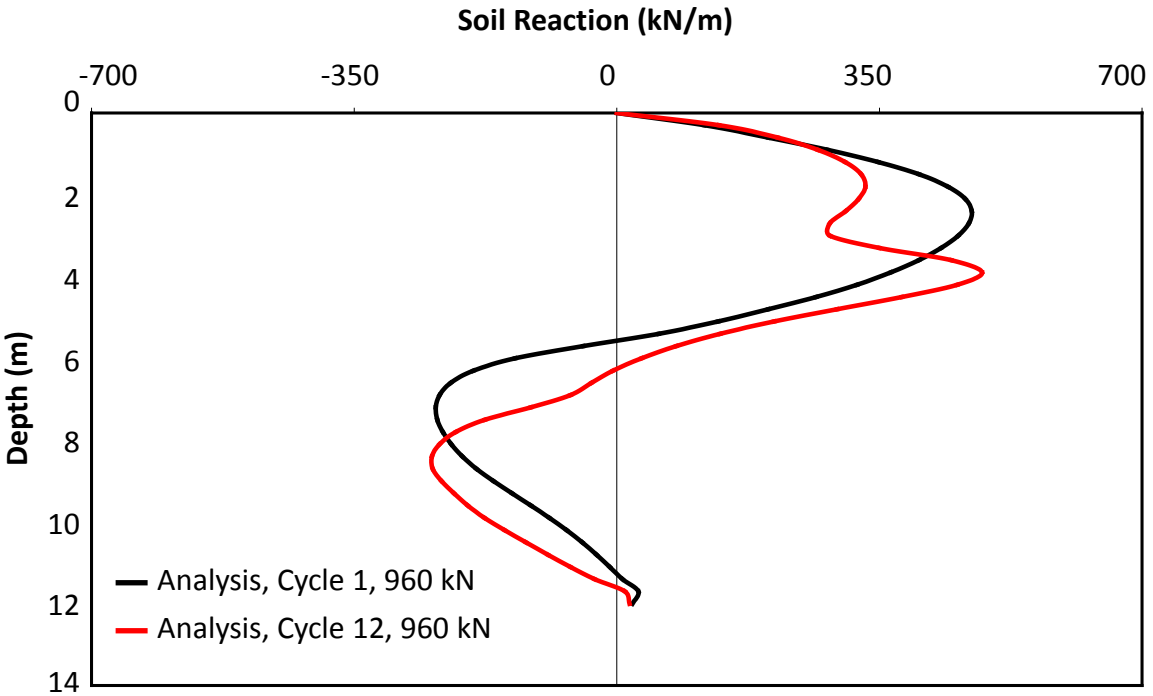

Figure 2.16: Computed soil reaction distributions for test P344 at 1st and 12th cycle of loading for maximum applied load 960 kN

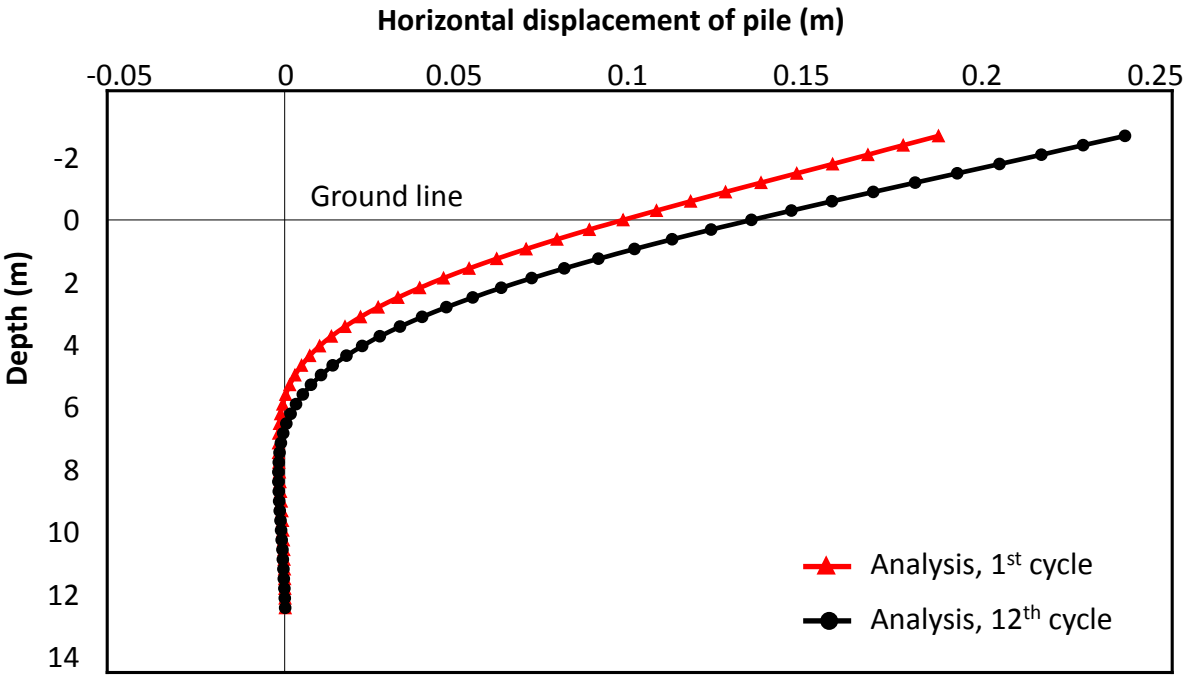

Figure 2.17: Comparison of computed horizontal displacement of the pile for test P344 at two different stages of loading: at the end of the 1st and the 12th cycle. The maximum applied load is 960 kN

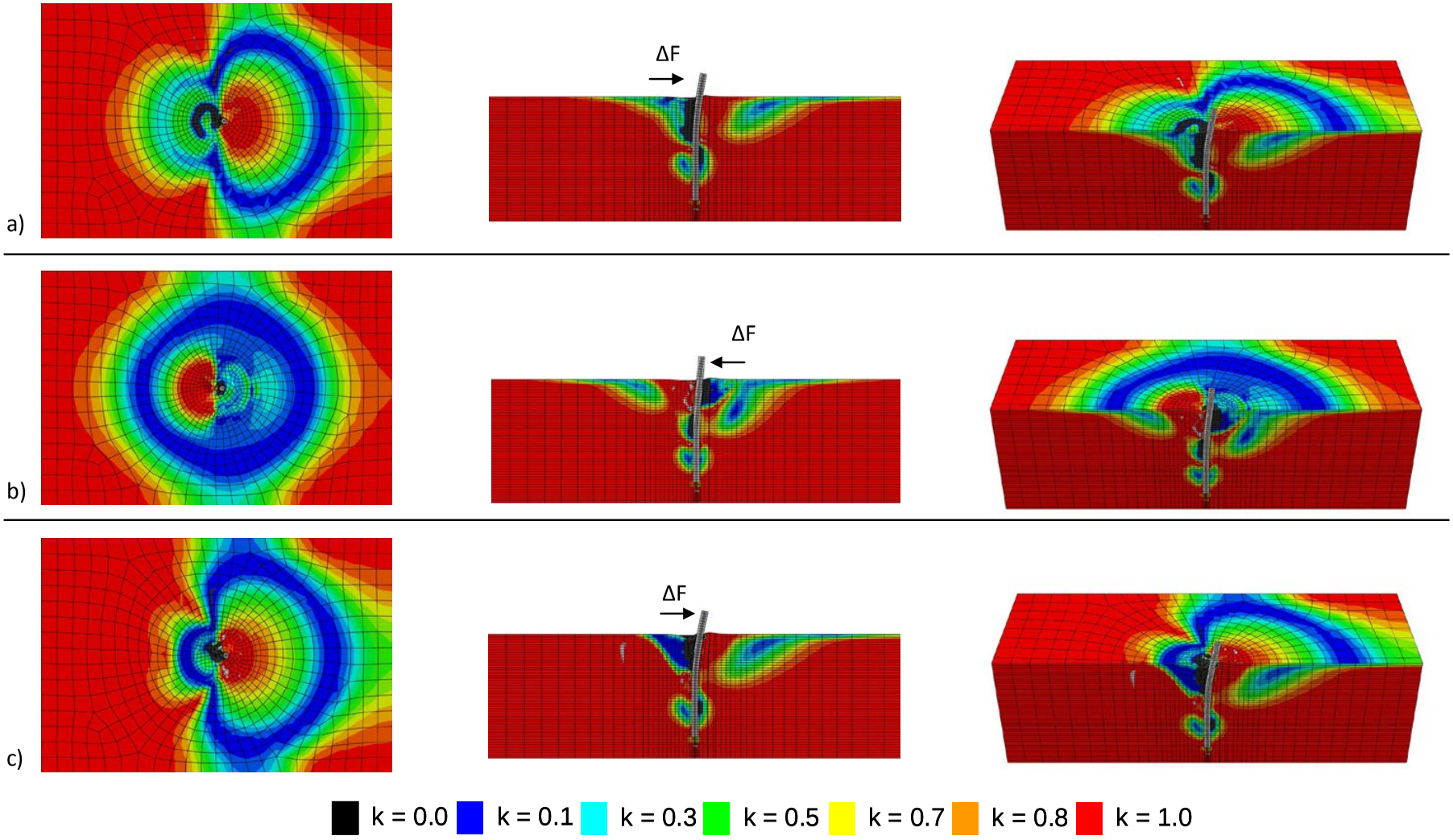

Figure 2.18: Contours of the active and passive stress states in terms of the state parameter k at three different stages of loading of the single pile of test P344: (a) at the 1st cycle at 960 kN, (b) at the 12th cycle at 0 kN, and (c) at the 12th cycle at 960 kN. k = 1 corresponds to pure triaxial compression loading condition (passive state), and k = 0 to pure triaxial extension loading condition (active state) while k ≈ 0.5 sets the boundaries between the active and the passive state. (Deformation Scale Factor = 5)

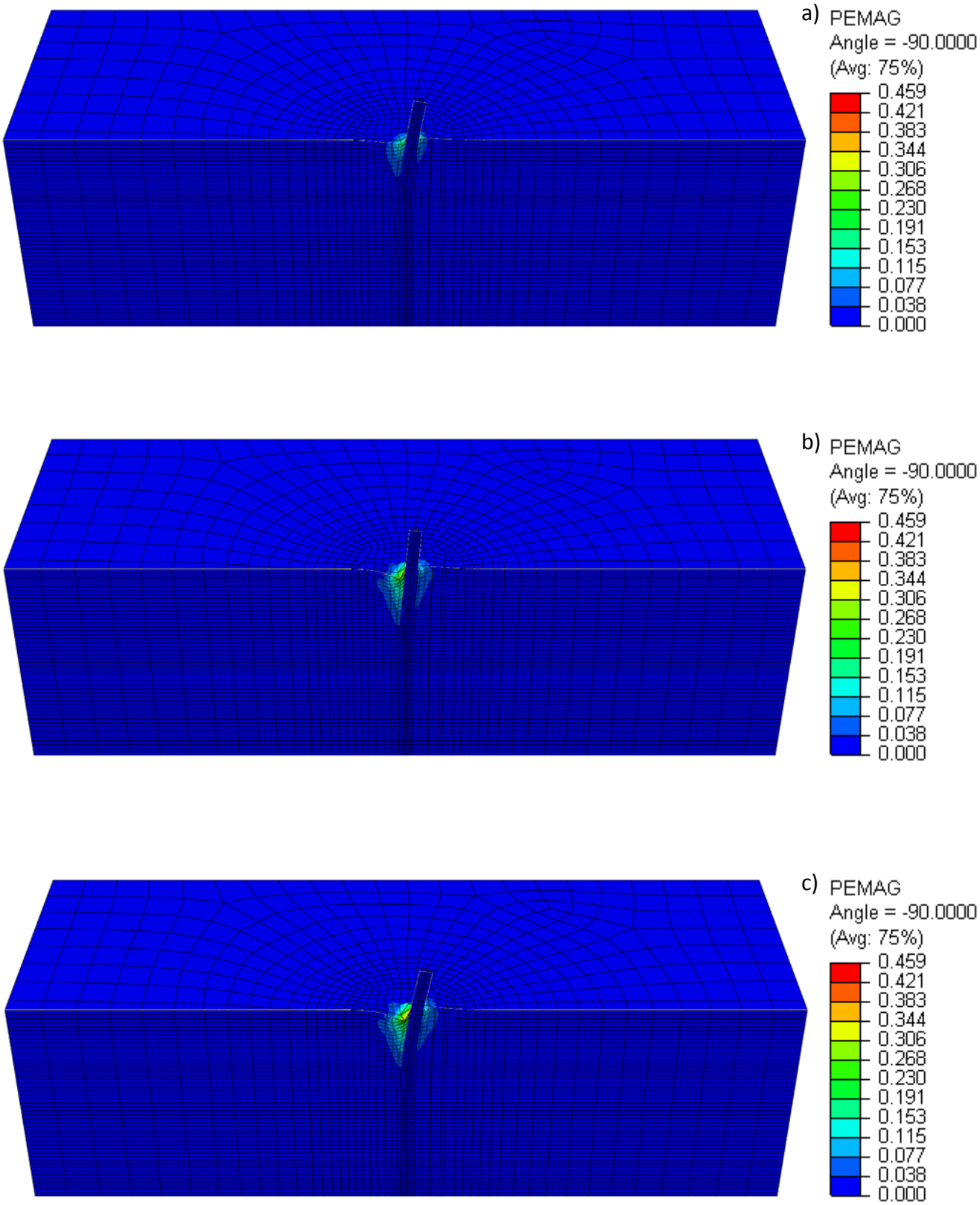

Figure 2.19: Contours of the plastic strain magnitude (plotted on the deformed mesh) at three different stages of loading of the single pile of test P344: (a) at the 1st cycle at 960 kN, (b) at the 12th cycle at 0 kN, and (c) at the 12th cycle at 960 kN. (Deformation Scale Factor = 5)

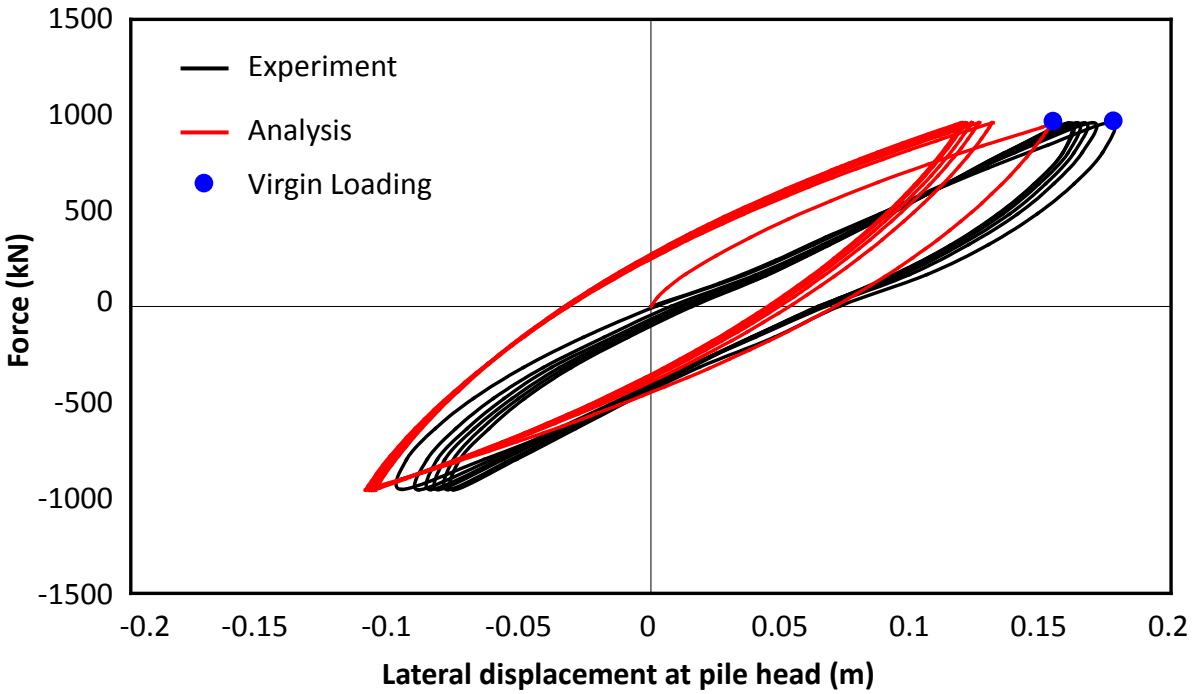

Figure 2.20: Experimental and computed force–displacement curves at pile head for test P330

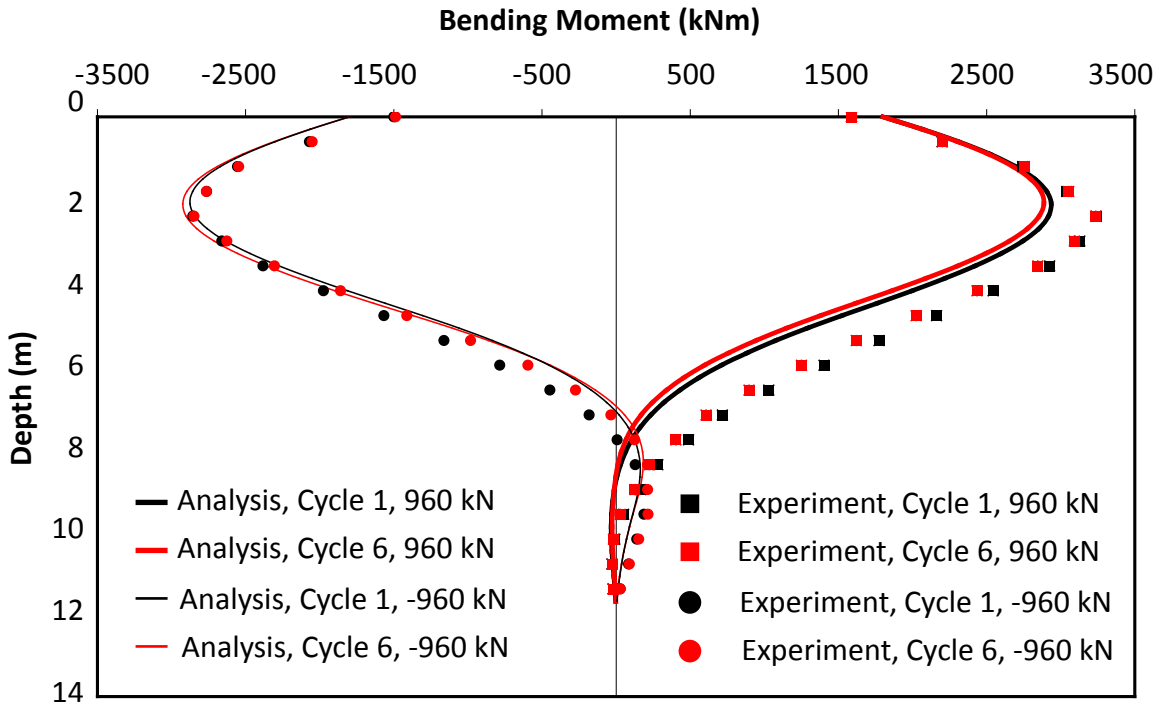

Figure 2.21: Comparison of computed and recorded bending moment distributions for test P330 at two different stages of loading: at 1st and 6th cycle. The maximum applied load is 960 kN and the minimum -960 kN

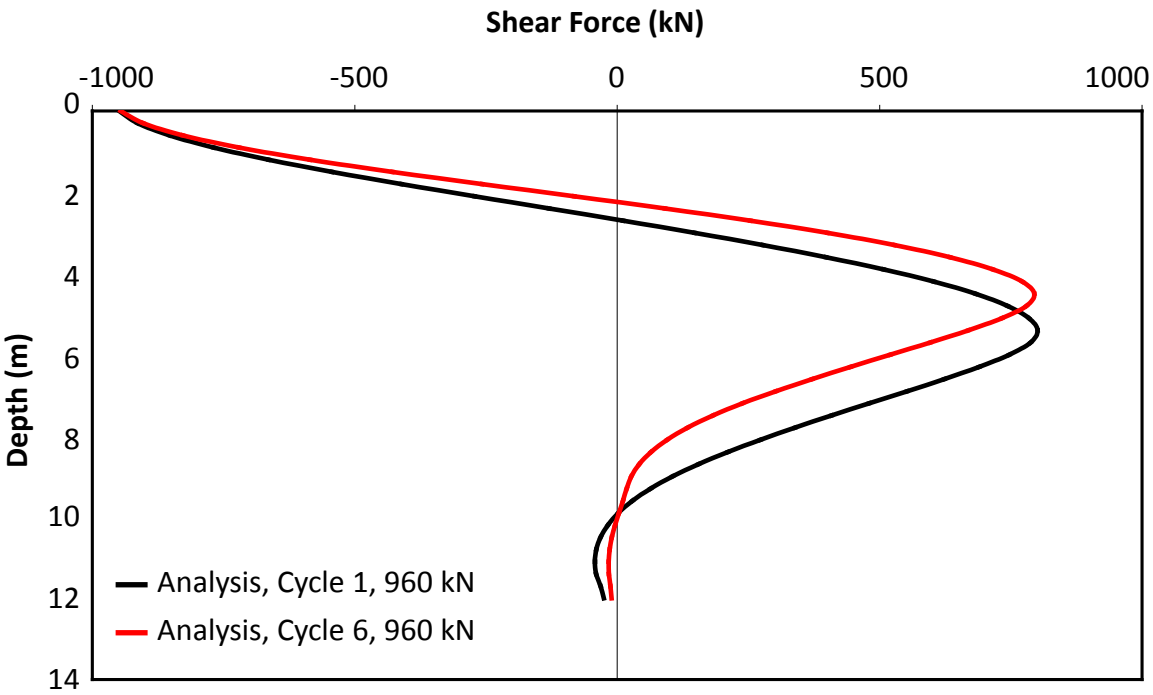

Figure 2.22: Computed shear force distributions for test P330 at 1st and 6th cycle of loading for maximum applied load 960 kN

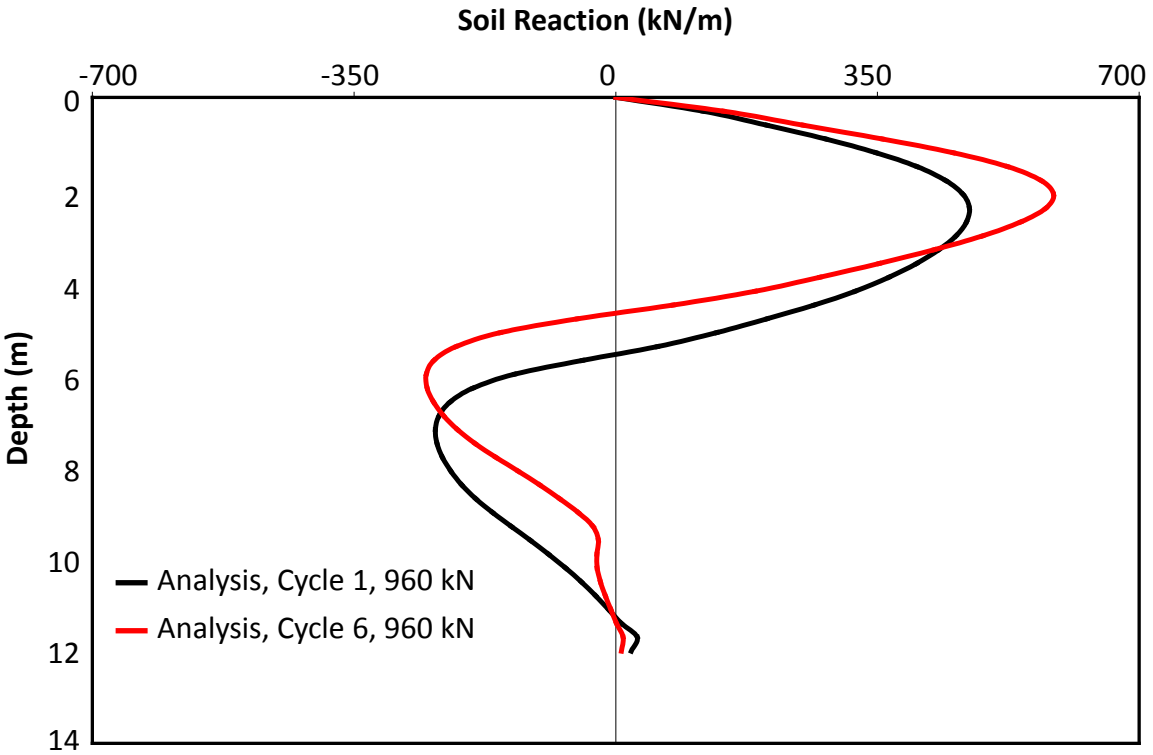

Figure 2.23: Computed soil reaction distributions for test P330 at 1st and 6th cycle of loading for maximum applied load 960 kN

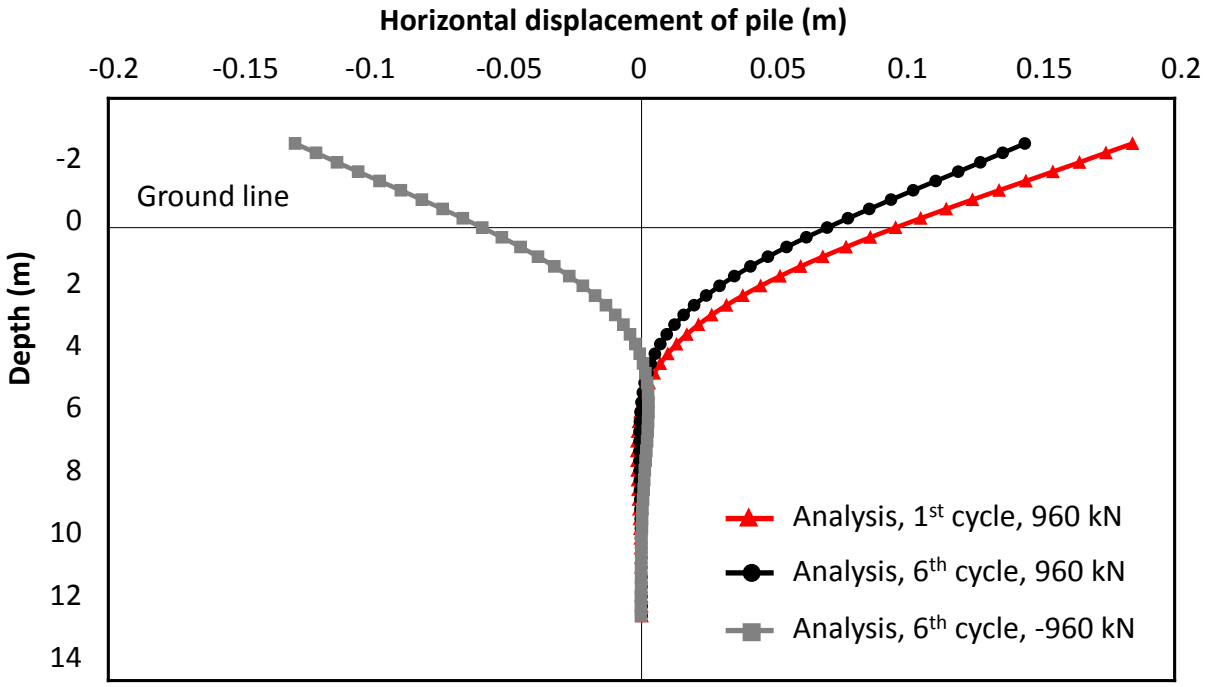

Figure 2.24: Comparison of computed horizontal displacement of the pile for test P330 at two different stages of loading: at the end of the 1st and the 6th cycle. The maximum applied load is 960 kN

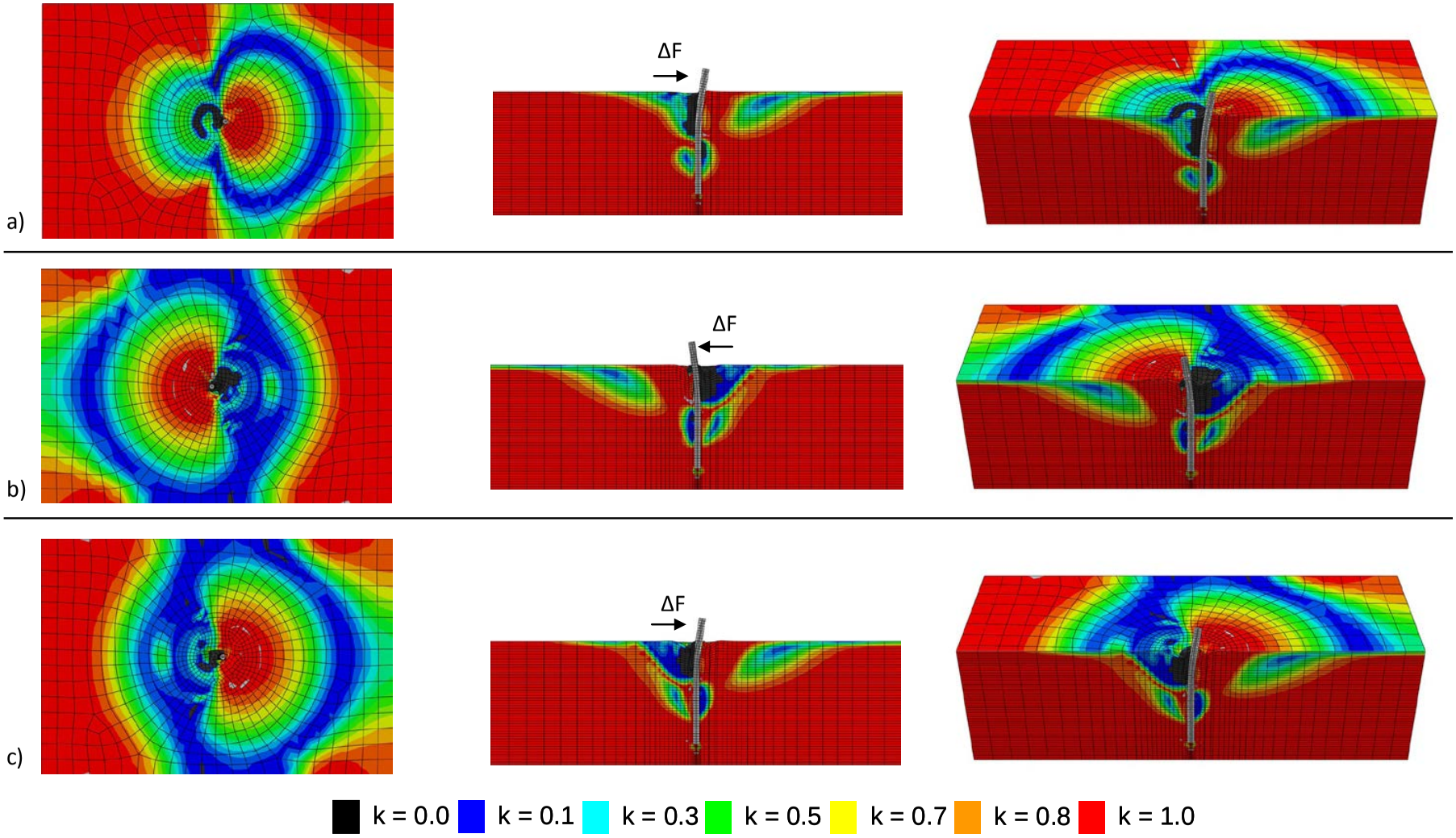

Figure 2.25: Contours of the active and passive stress states in terms of the state parameter k at three different stages of loading of the single pile of test P330: (a) at the 1st cycle at 960 kN, (b) at the 6th cycle at -960 kN, and (c) at the 6th cycle at 960 kN. k = 1 corresponds to pure triaxial compression loading condition (passive state), and k = 0 to pure triaxial extension loading condition (active state) while k ≈ 0.5 sets the boundaries between the active and the passive state. (Deformation Scale Factor = 5)

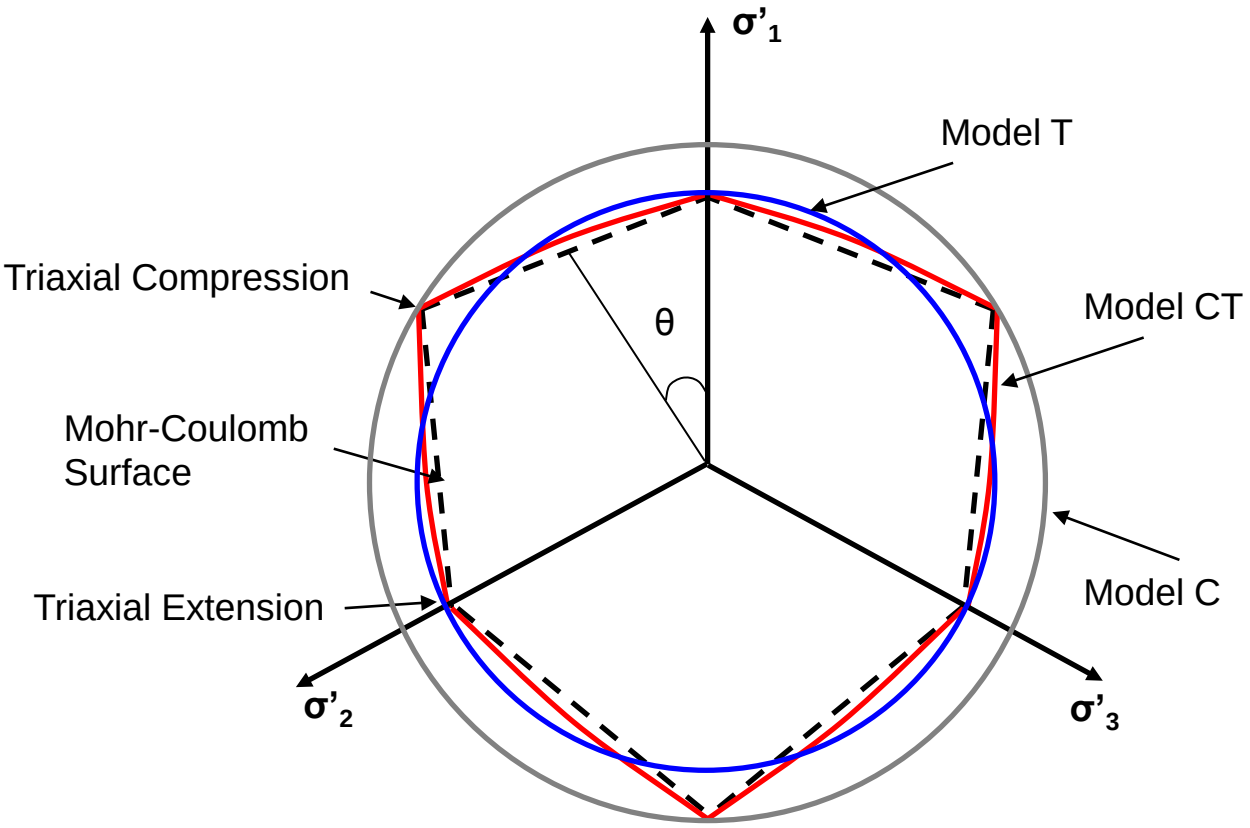

Figure 2.26: Examined yield criteria matching the Mohr-Coulomb yield criterion on the π-plane: (a) the developed constitutive model (Model CT), (b) compressive meridian matching (Model C), and (c) tensile meridian matching (Model T)

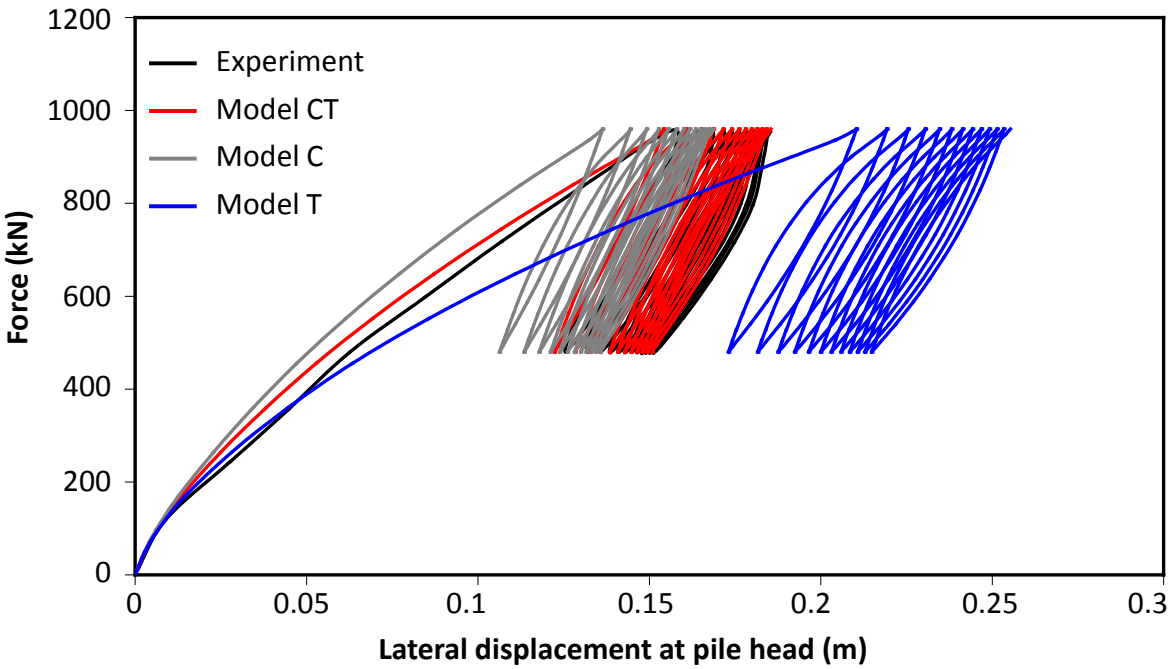

Figure 2.27: Force–displacement curves at pile head for test P32 computed by the three constitutive soil models

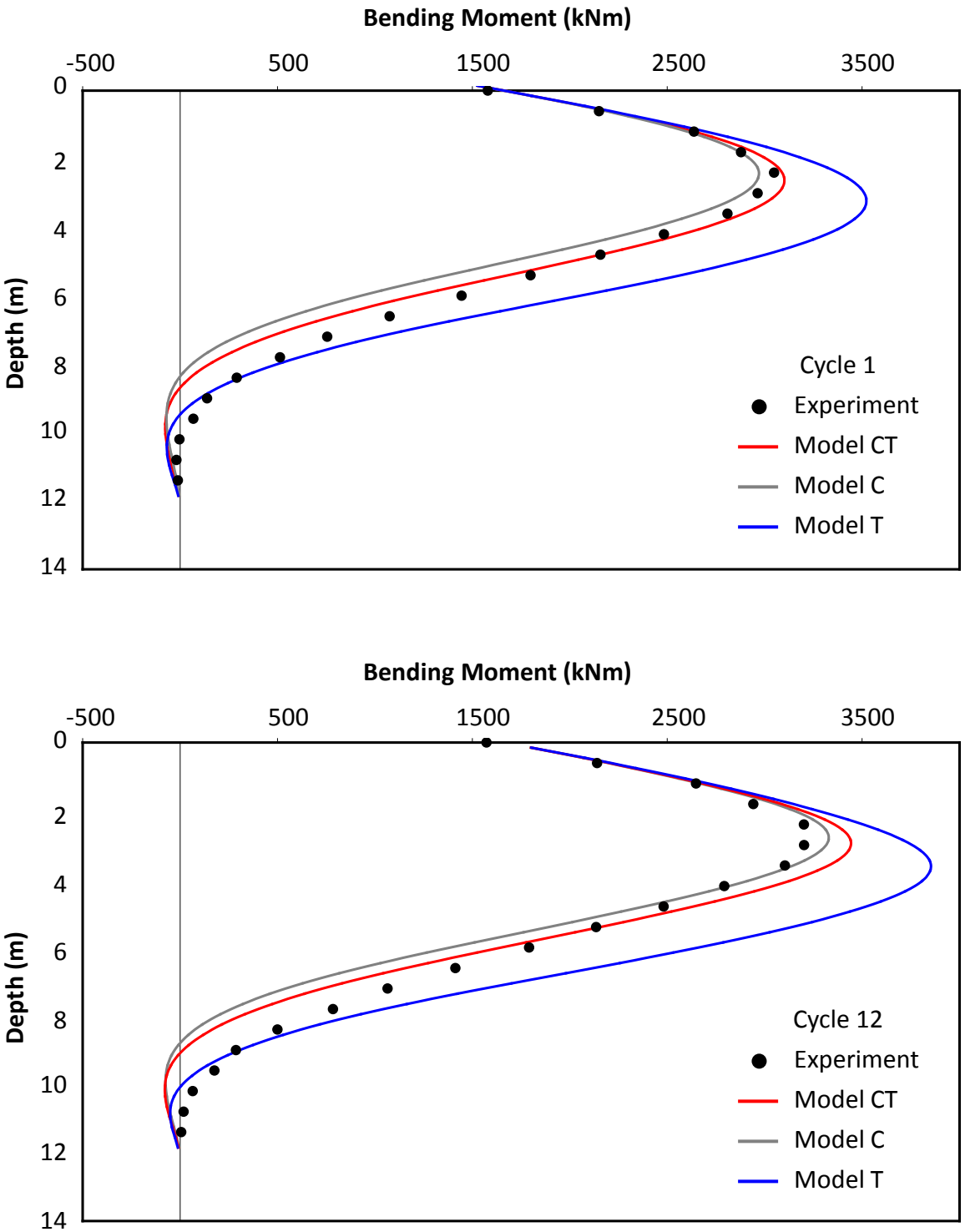

Figure 2.28: Comparison of computed (solid lines) with the three constitutive soil models and recorded (circles) bending moment distributions for test P32, at two different stages of loading: at the end of the 1st and the 12th cycle. The maximum applied load is 960 kN

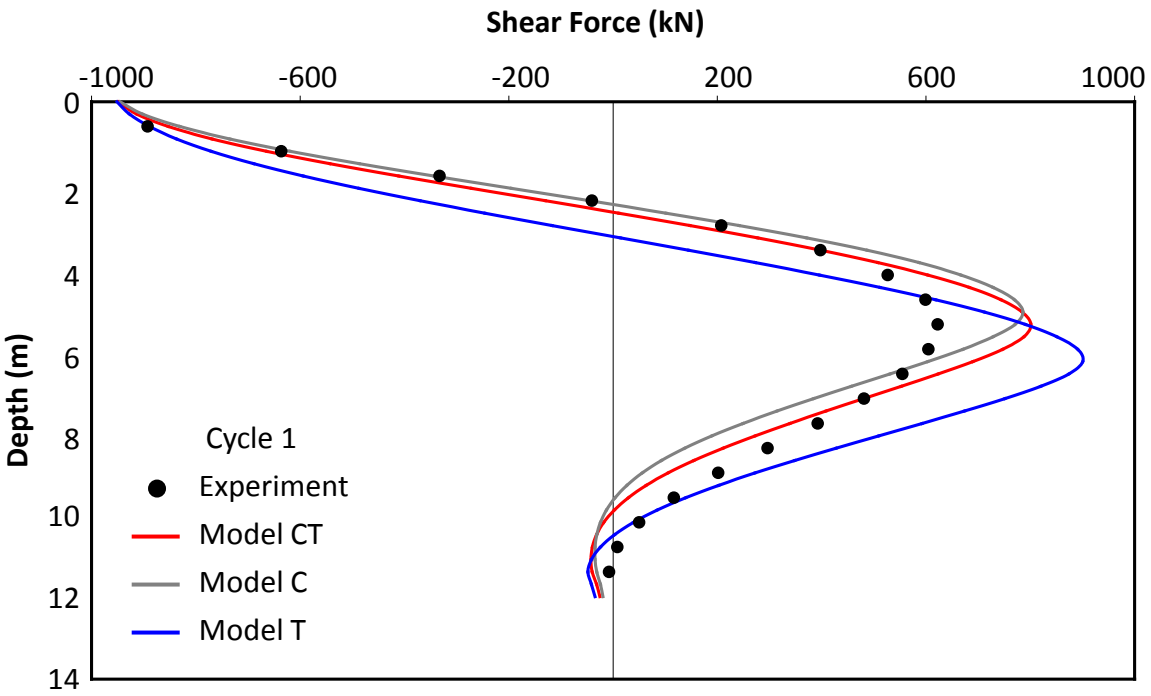

Figure 2.29: Comparison of computed (solid lines) with the three constitutive soil models and recorded (circles) shear force distributions for test P32, at the end of the first cycle. The maximum applied load is 960 kN

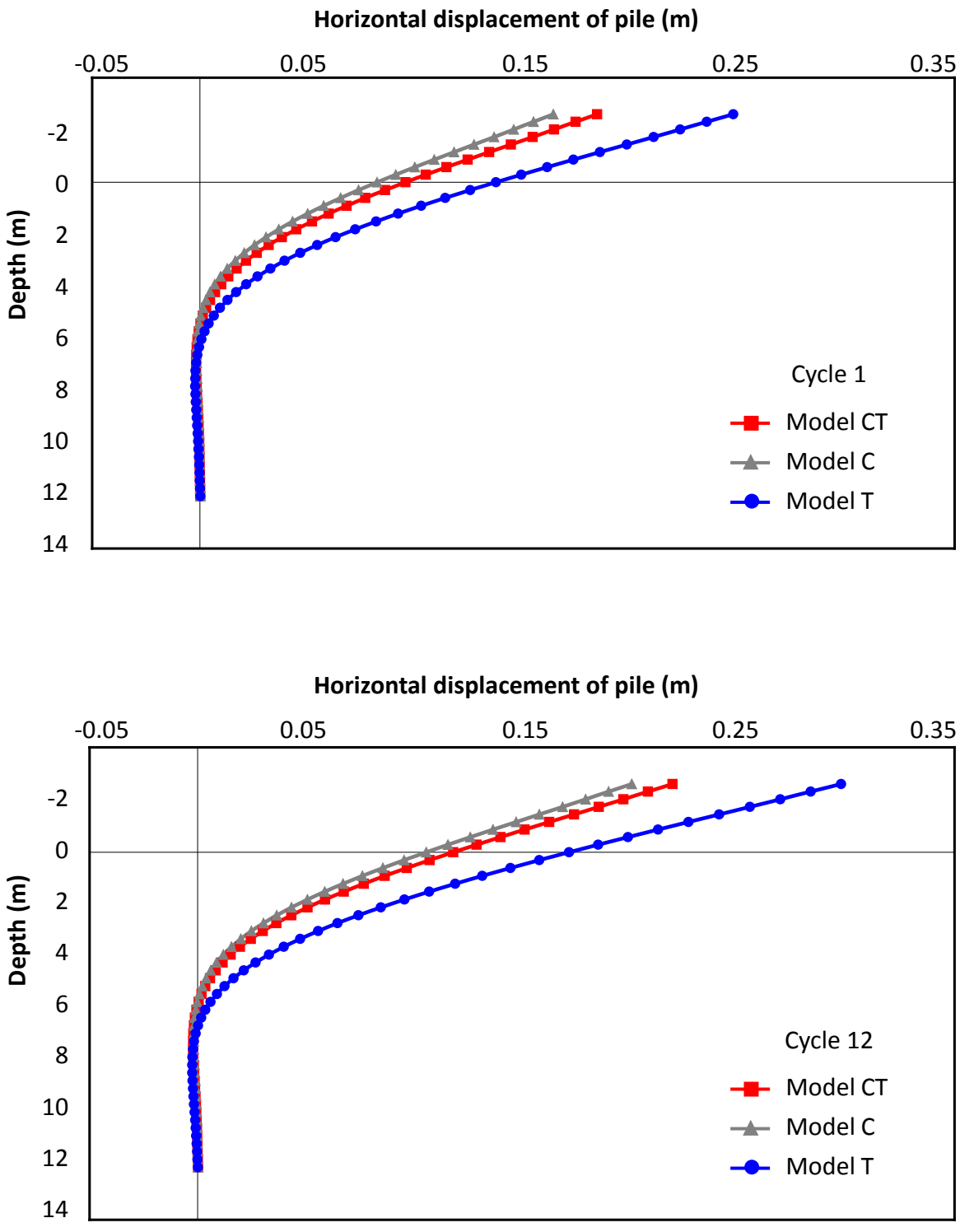

Figure 2.30: Comparison of horizontal displacement distributions for test P32, computed with the three constitutive soil models, at different stages of loading: at the end of the 1st and the 12th cycle. The maximum applied load is 960 kN

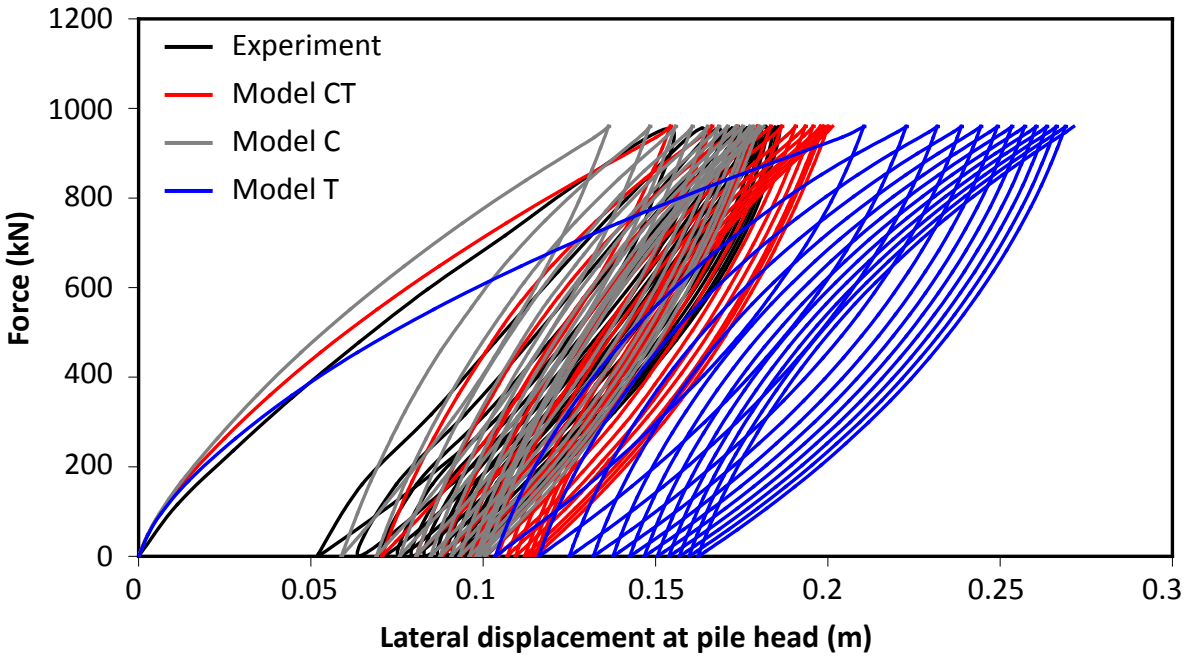

Figure 2.31: Force–displacement curves at pile head for test P344 computed by the three constitutive soil models

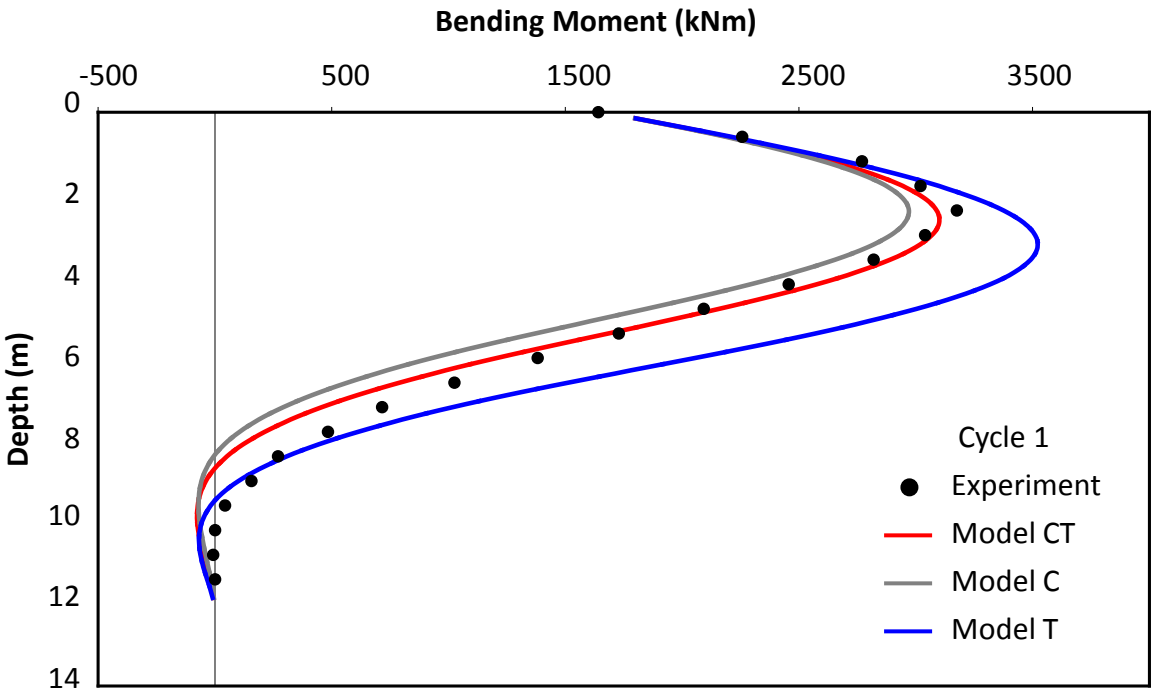

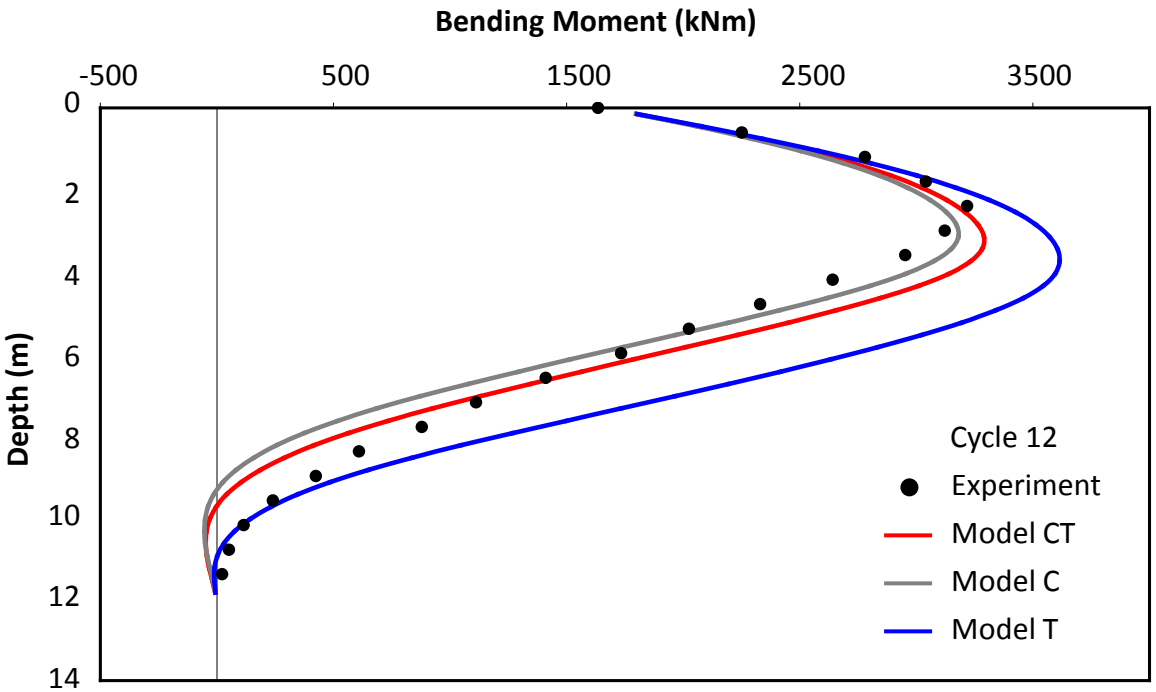

Figure 2.32: Comparison of computed (solid lines) with the three constitutive soil models and recorded (circles) bending moment distributions for test P344, at two different stages of loading: at the end of the 1st and the 12th cycle. The maximum applied load is 960 kN

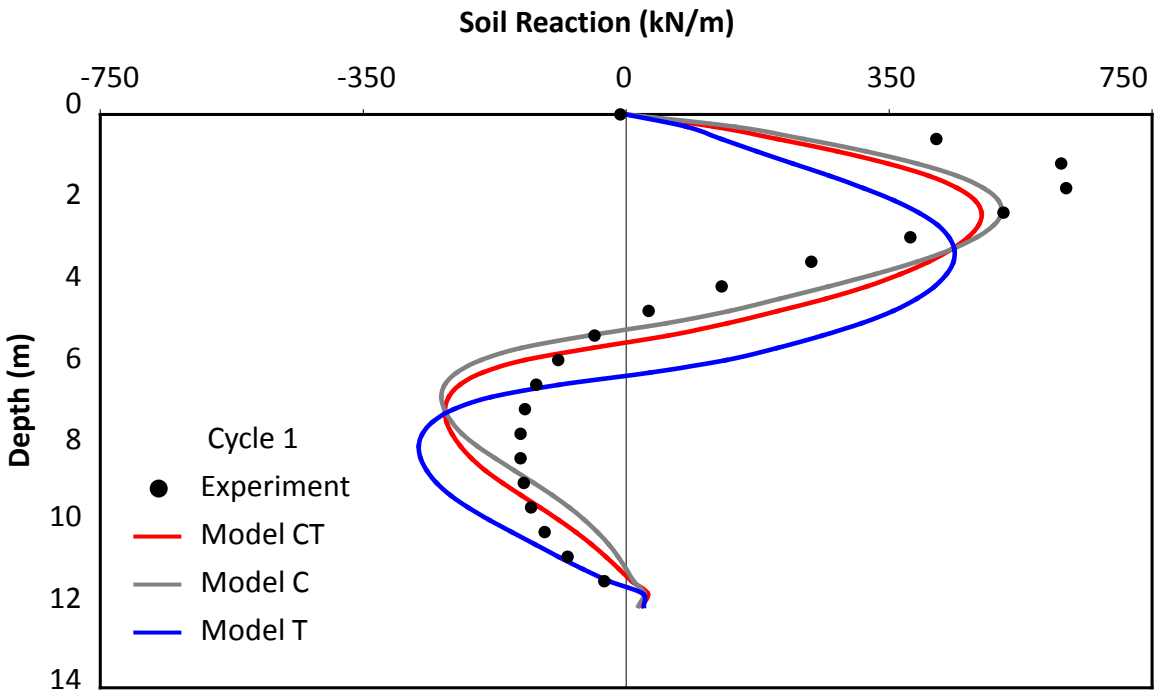

Figure 2.33: Comparison of computed (solid lines) with the three constitutive soil models and recorded (circles) soil reaction distributions for test P344, at the end of the first cycle. The maximum applied load is 960 kN

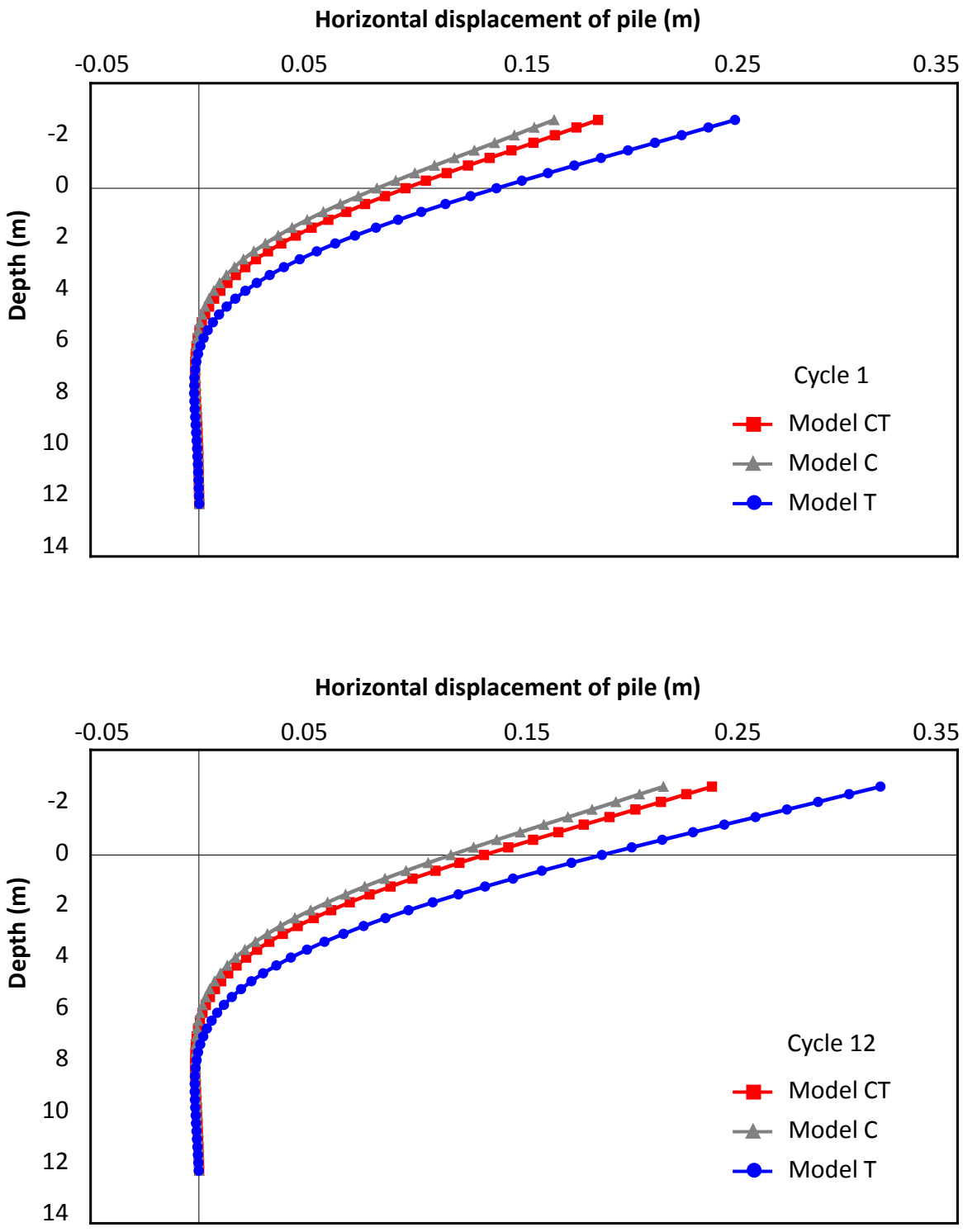

Figure 2.34: Comparison of horizontal displacement distributions for test P344, computed with the three constitutive soil models, at different stages of loading: at the end of the 1st and the 12th cycle. The maximum applied load is 960 kN

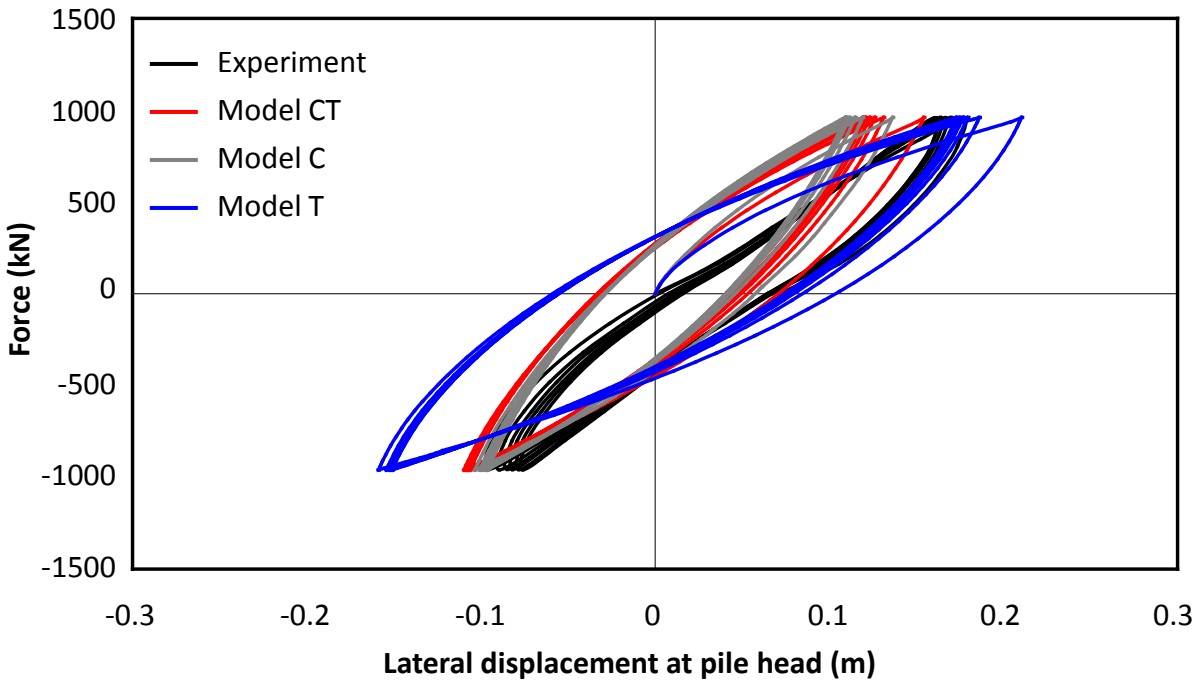

Figure 2.35: Force–displacement curves at pile head for test P330 computed by the three constitutive soil models

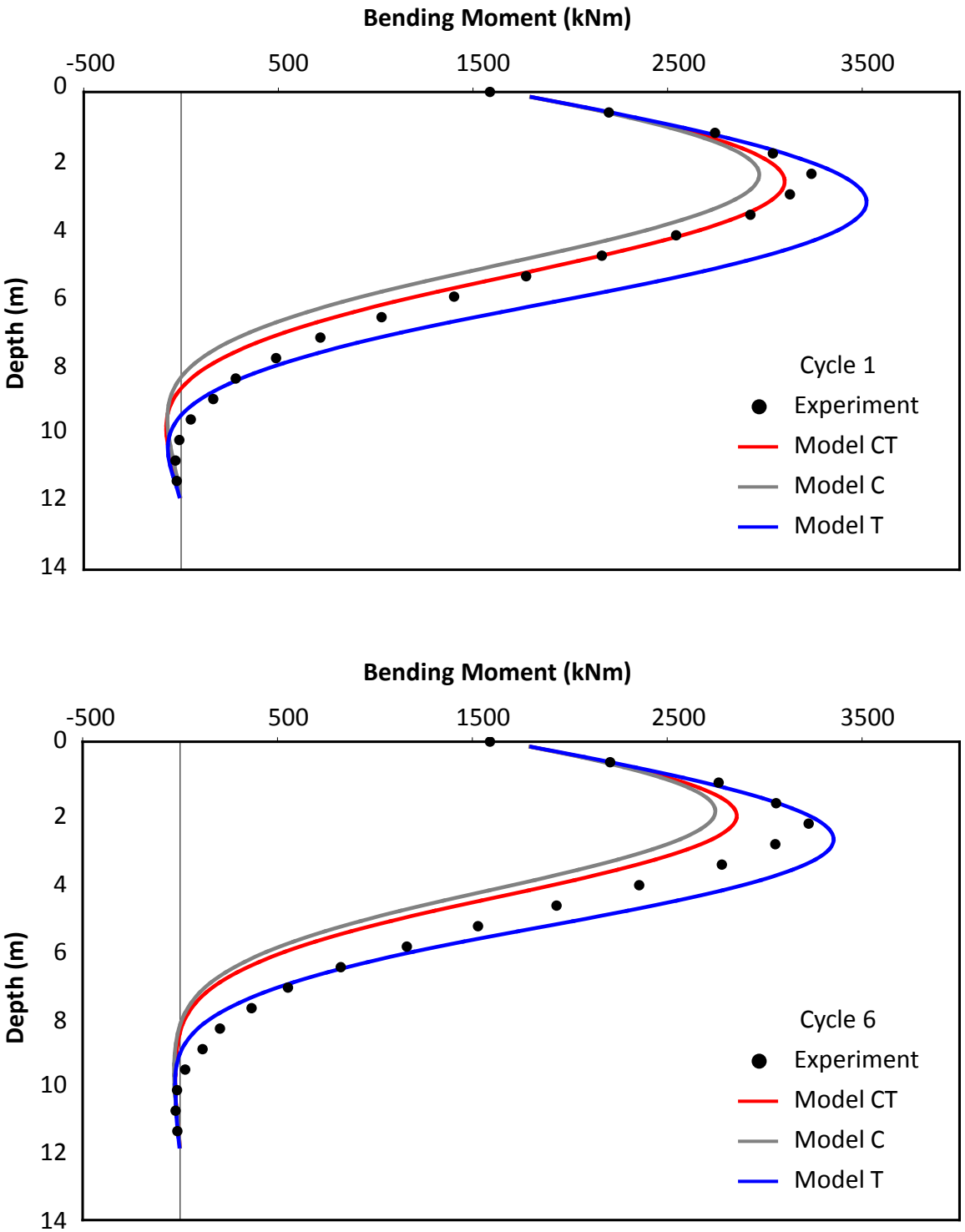

Figure 2.36: Comparison of computed (solid lines) with the three constitutive soil models and recorded (circles) bending moment distributions for test P330, at two different stages of loading: at the end of the 1st and the 6th cycle. The maximum applied load is 960 kN

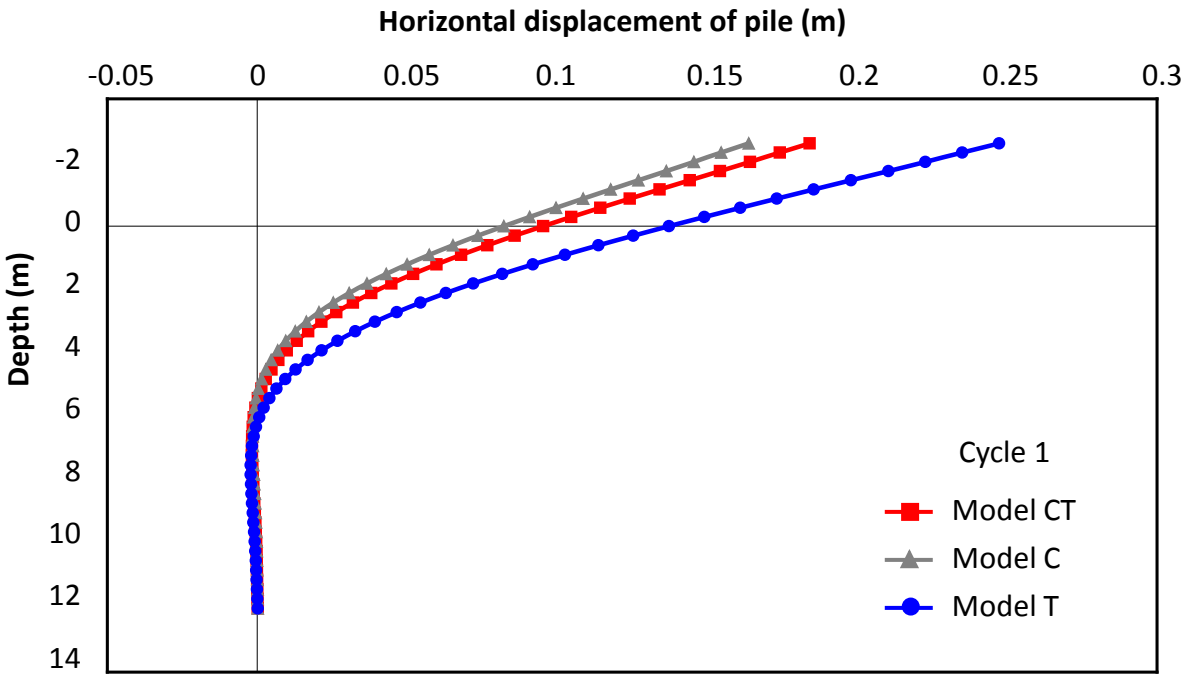

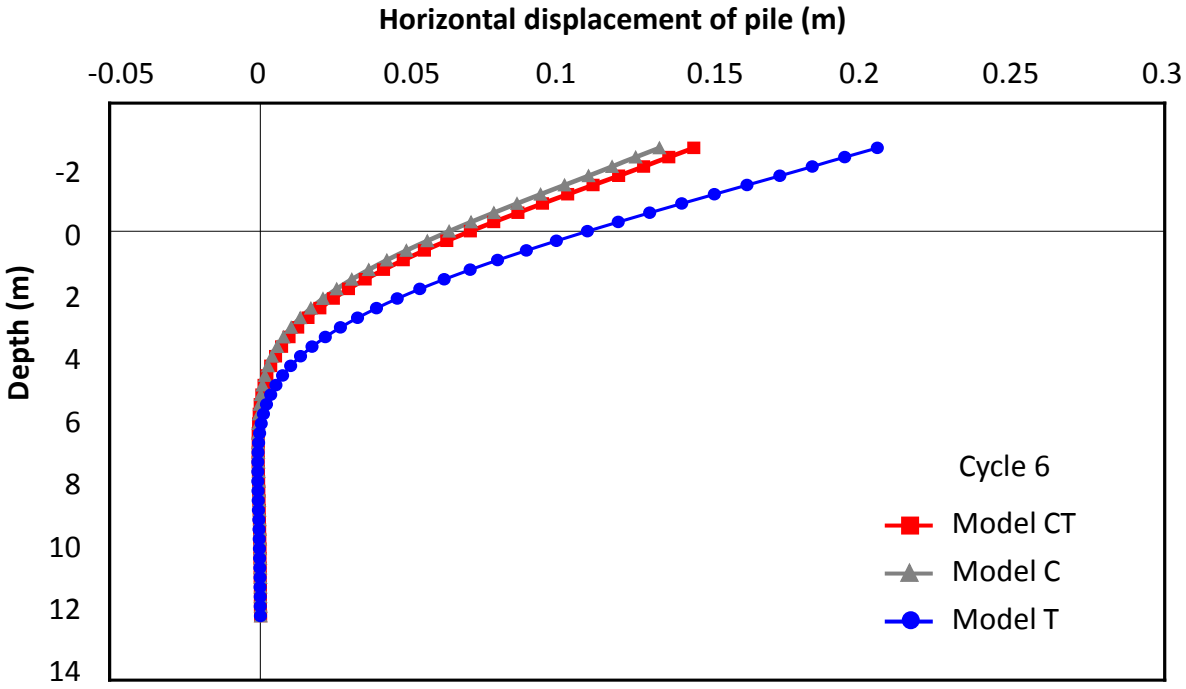

Figure 2.37: Comparison of horizontal displacement distributions for test P330, computed with the three constitutive soil models, at different stages of loading: at the end of the 1st and the 6th cycle. The maximum applied load is 960 kN

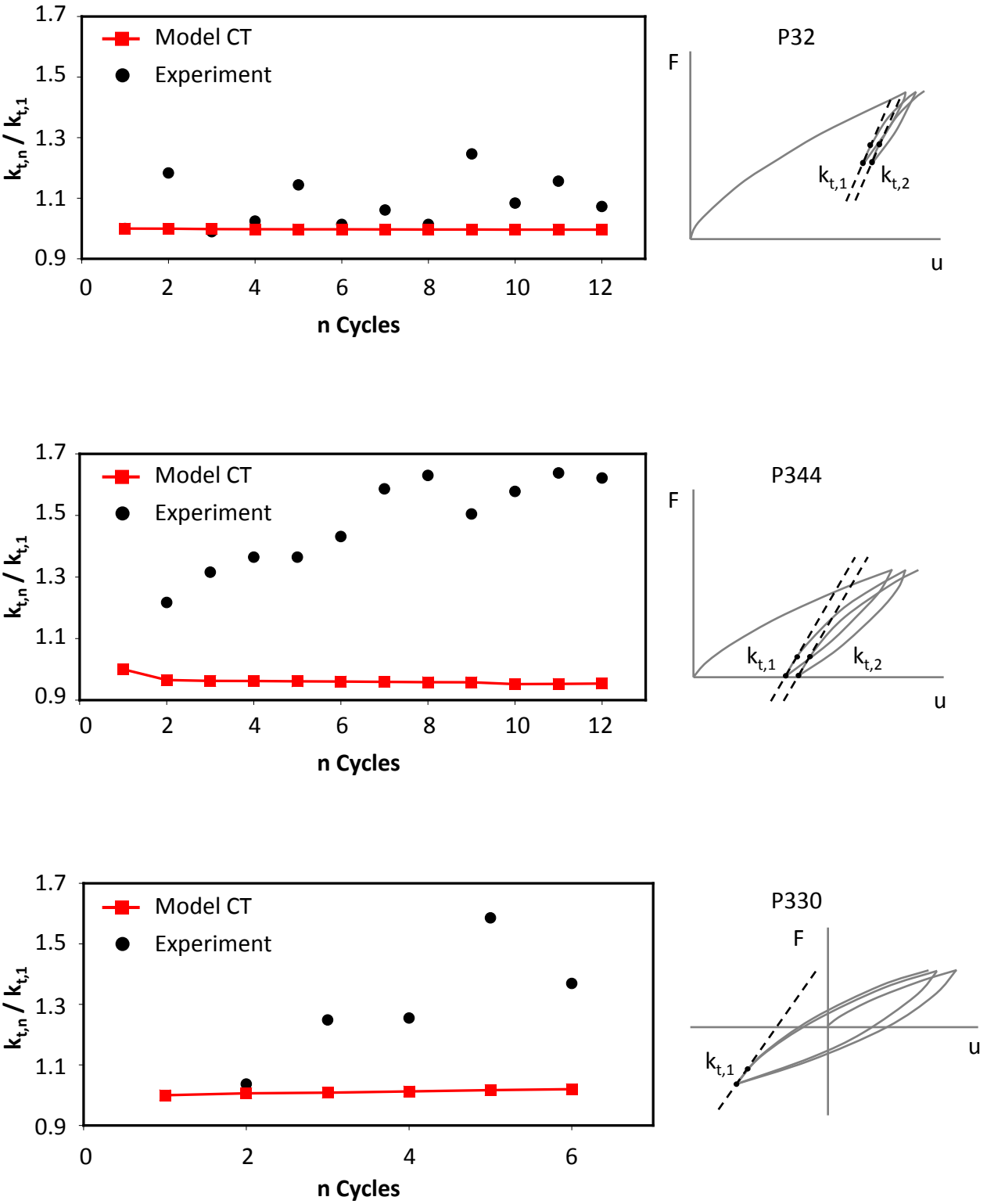

Figure 2.38: Normalized tangent stiffness with respect to the first cycle of loading, for: (a) test P32, (b) test P344, and (c) test P330

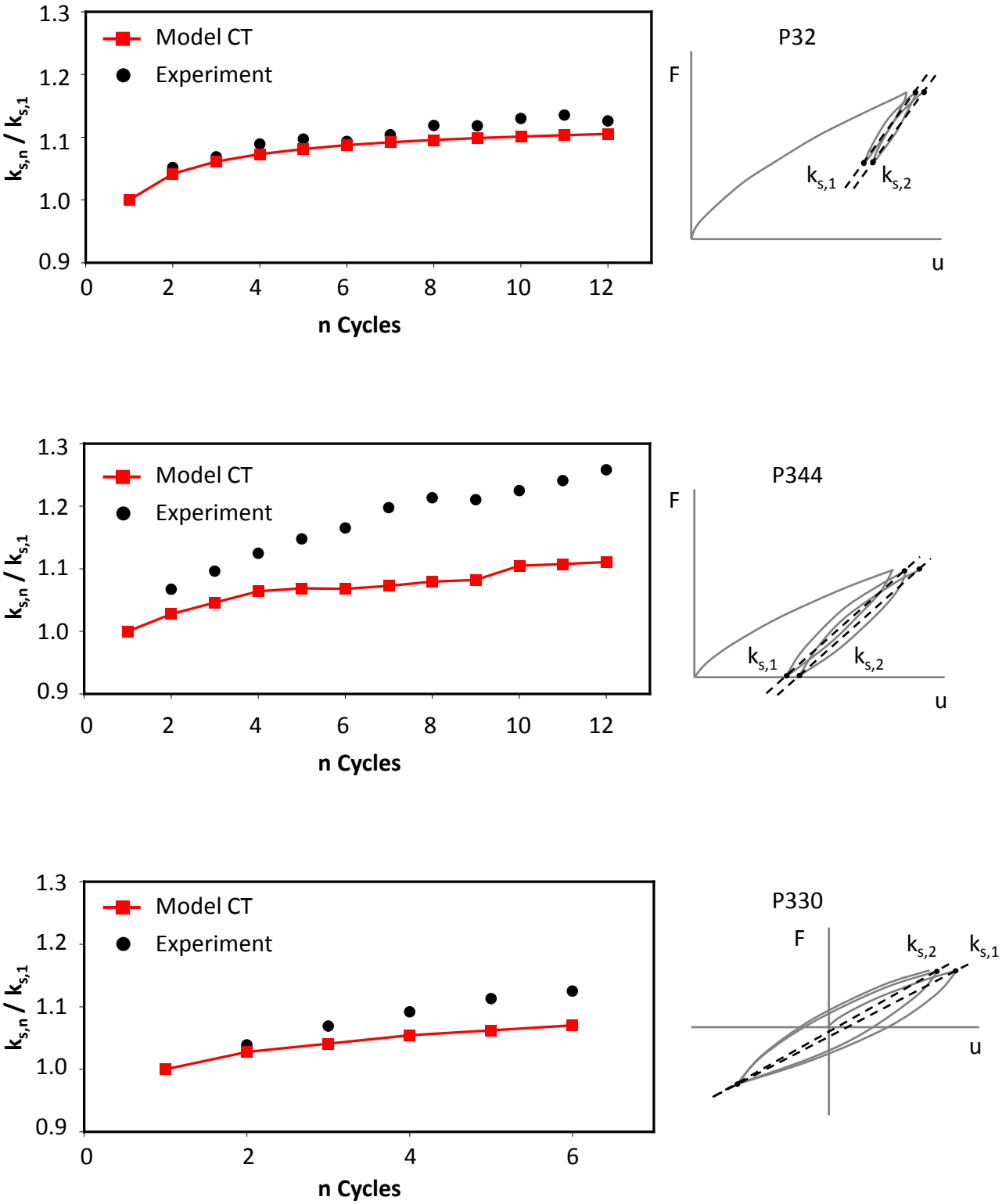

Figure 2.39: Normalized secant horizontal pile stiffness with respect to the first cycle of loading, for: (a) test P32, (b) test P344, and (c) test P330

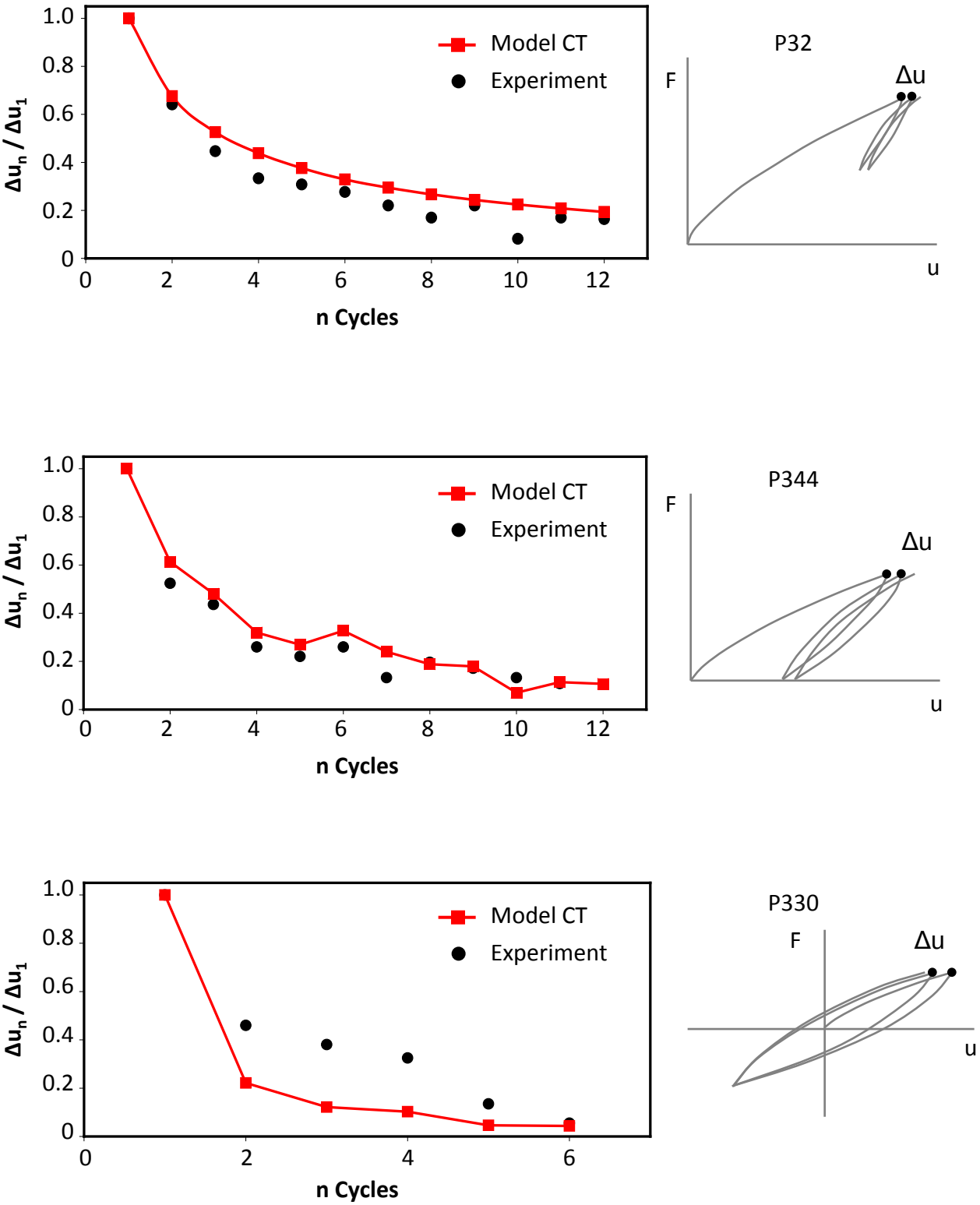

Figure 2.40: Relative pile head displacement between two consecutive re-loading–unloading reversal points normalized with the one between the virgin loading–unloading and the first re-loading–unloading reversal points, for: (a) test P32, (b) test P344, and (c) test P330

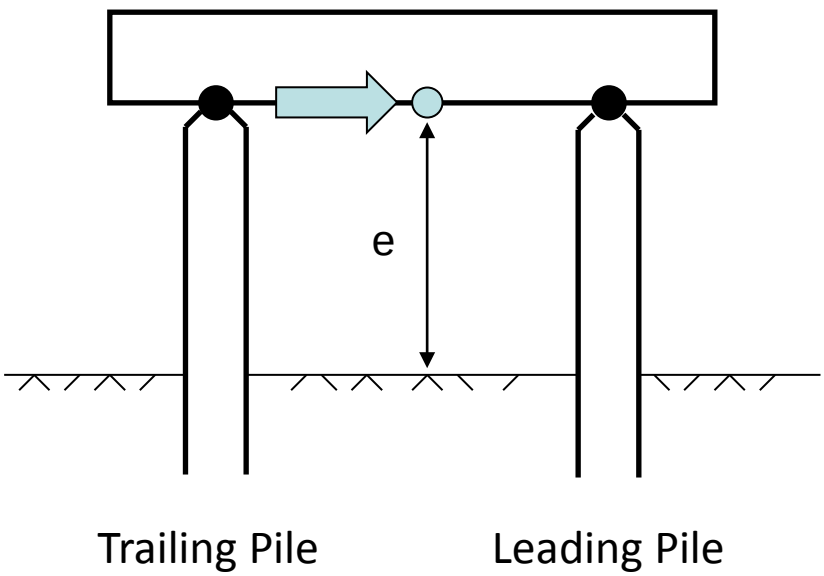

Figure 2.41: Connection of the pile heads in the group and definition of the piles

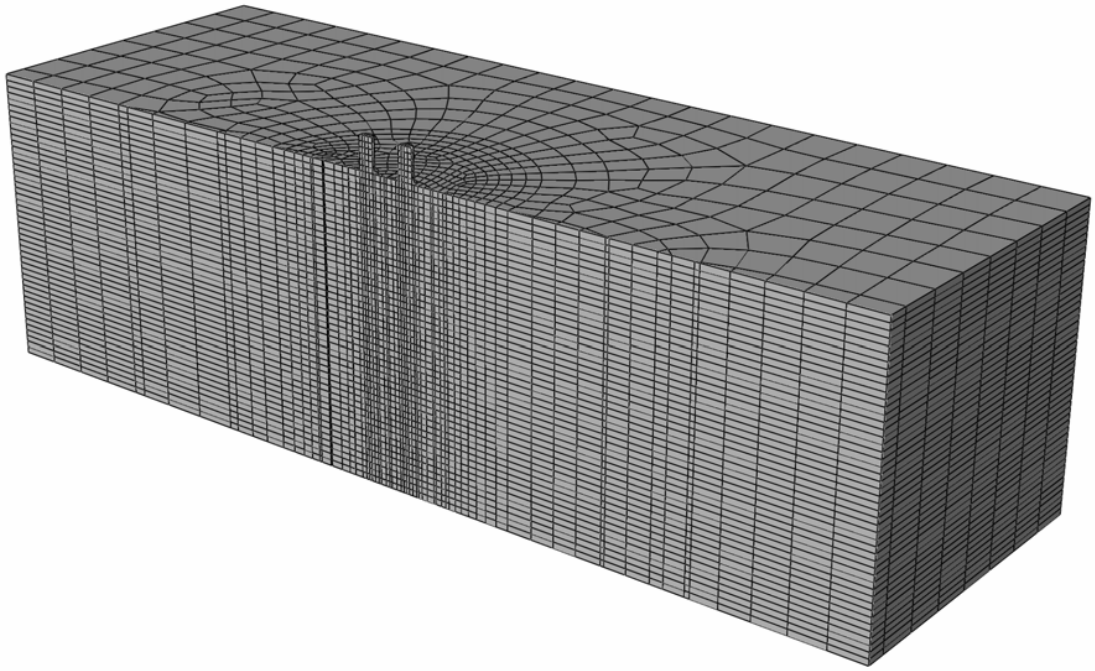

Figure 2.42: Finite element modeling for the pile group

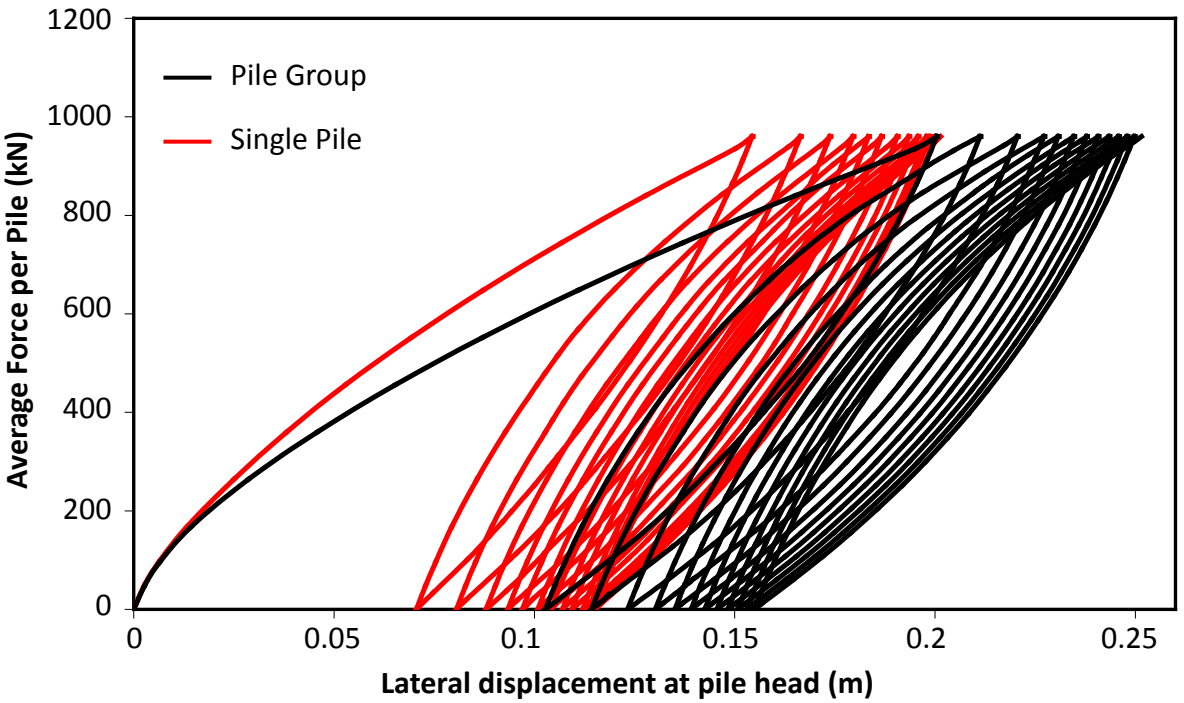

Figure 2.43: Force–displacement curves of the single pile and the pile group for the loading of test P344

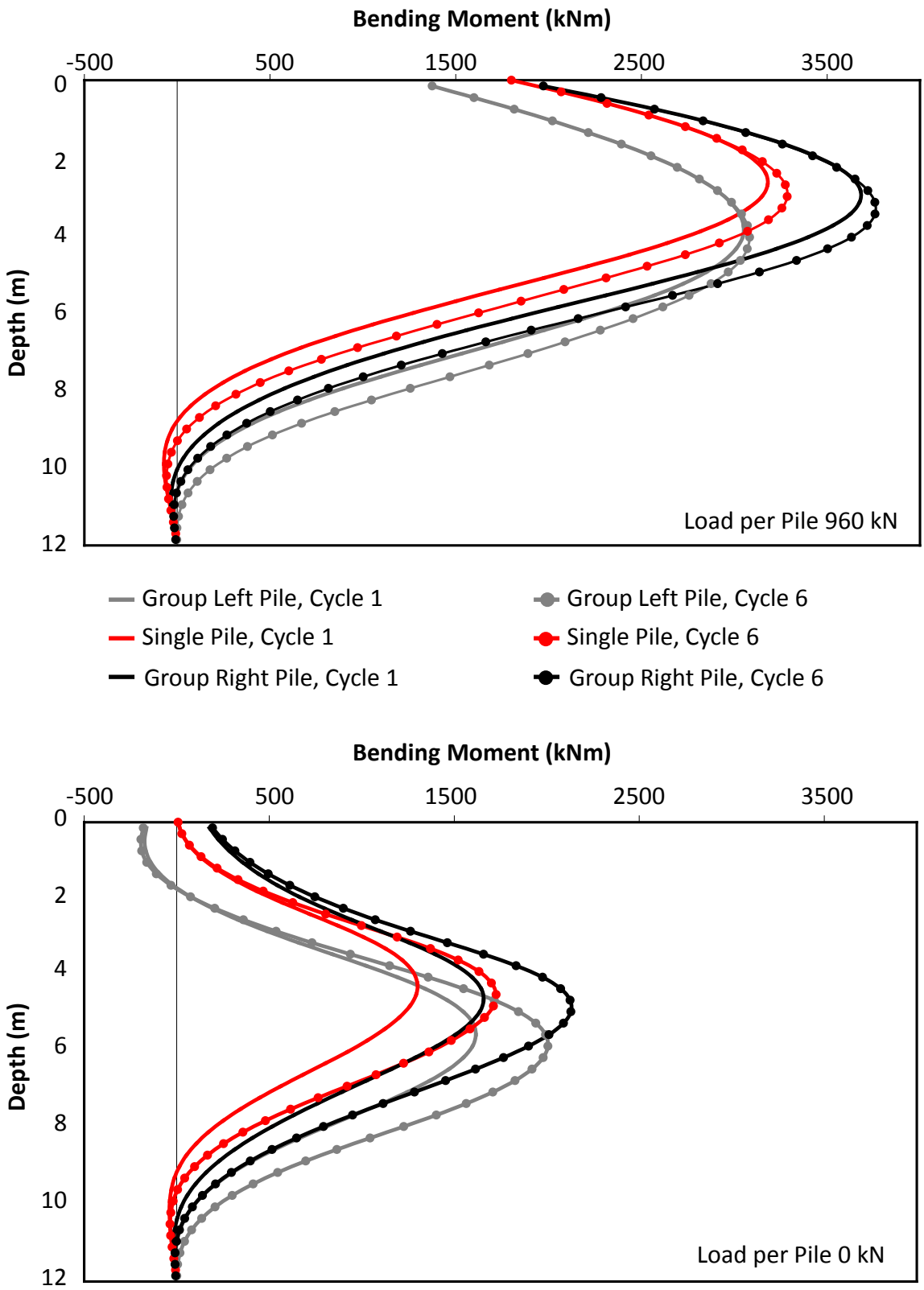

Figure 2.44: Comparison of computed bending moment distributions of the pile group and the single pile for test P344 at two different stages of loading: (atop) at the 1st and 6th cycle and at 960 kN per pile, and (bottom) at the 1st and 6th cycle and at 0 kN per pile. The maximum applied load per pile is 960 kN and the minimum applied one is 0 kN

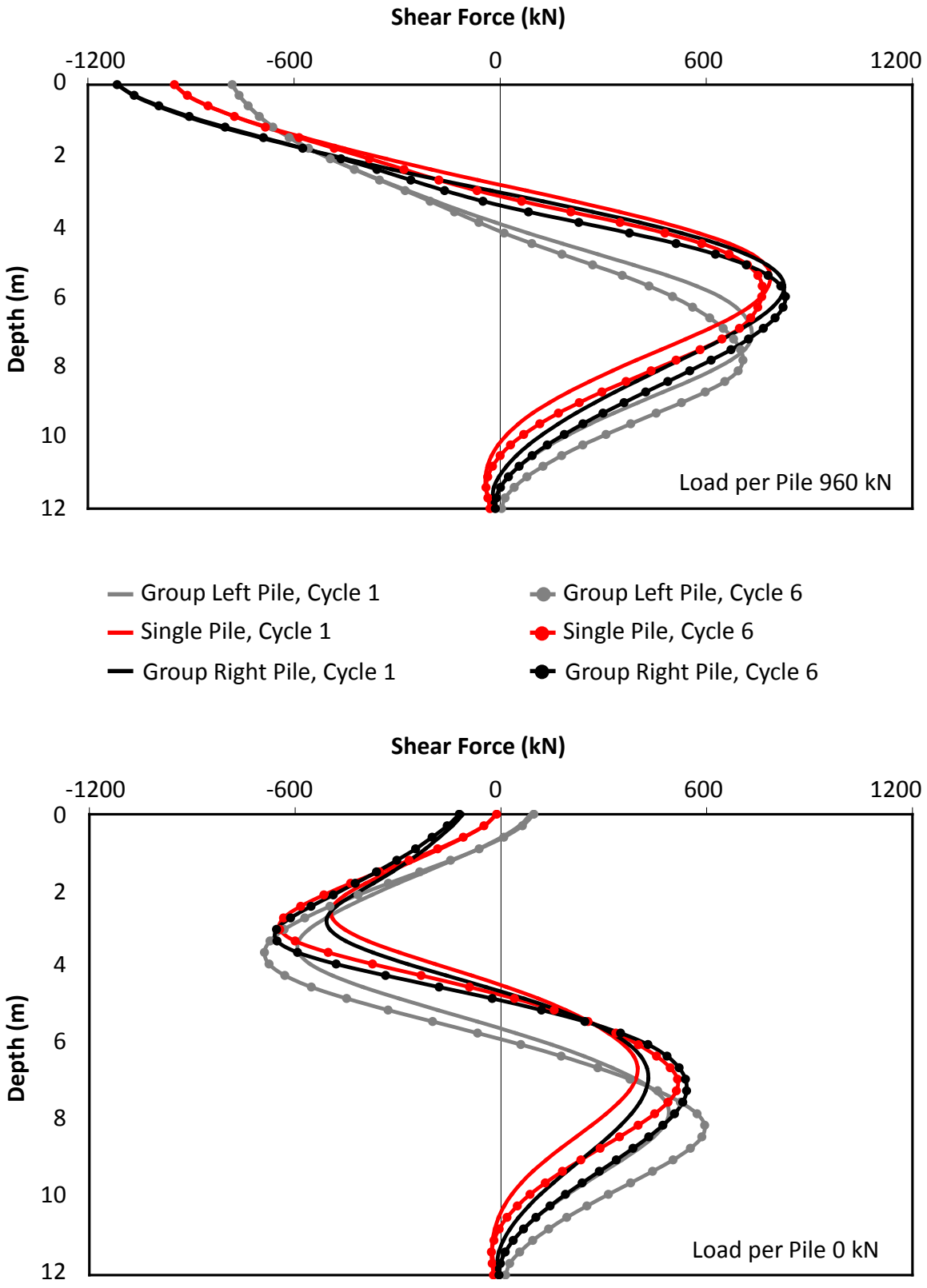

Figure 2.45: Comparison of computed shear force distributions of the pile group and the single pile for test P344 at two different stages of loading: (atop) at the 1st and 6th cycle and at 960 kN, and (bottom) at the 1st and 6th cycle and at 0 kN. The maximum applied load is 960 kN and the minimum applied one is 0 kN

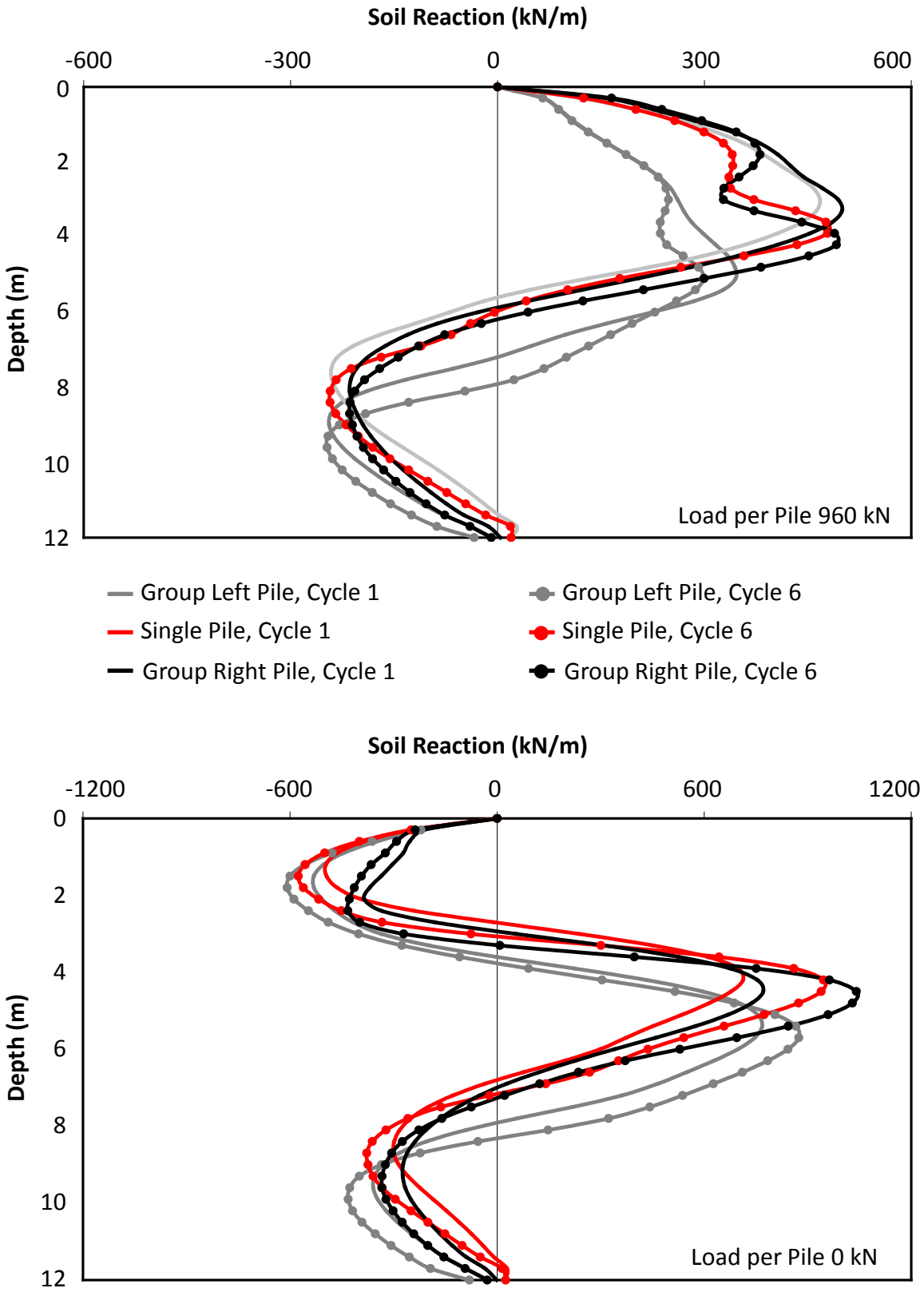

Figure 2.46: Comparison of computed soil reaction distributions of the pile group and the single pile for test P344 at two different stages of loading: (atop) at the 1st and 6th cycle and at 960 kN, and (bottom) at the 1st and 6th cycle and at 0 kN. The maximum applied load is 960 kN and the minimum applied one is 0 kN

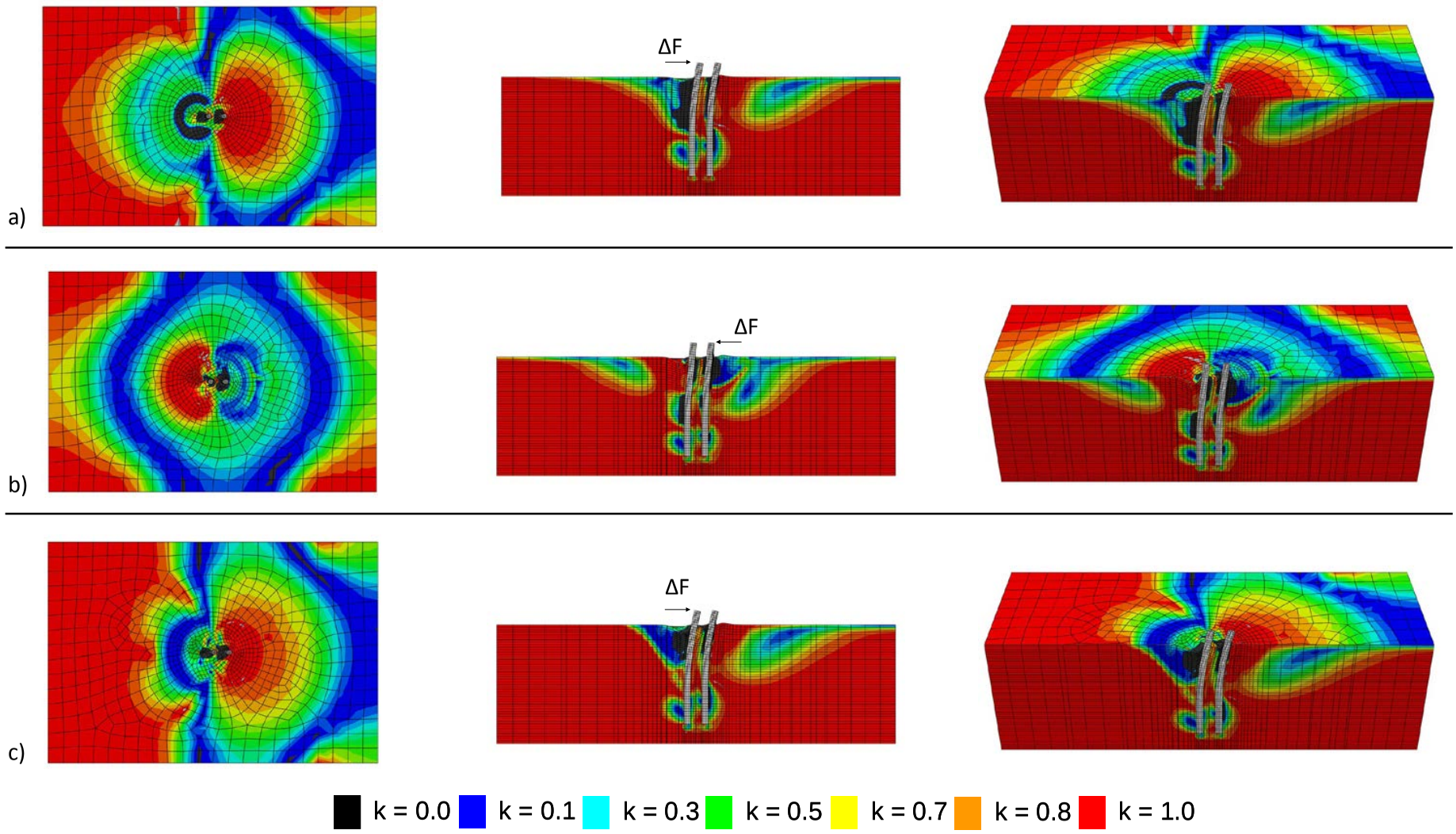

Figure 2.47: Contours of the active and passive stress states in terms of the state parameter k at three different stages of loading of the pile group for the cyclic loading of test P344: (a) at the 1st cycle at 960 kN per pile, (b) at the 12th cycle at 0 kN per pile, and (c) at the 12th cycle at 960 kN per pile. k = 1 corresponds to pure triaxial compression loading condition (passive state), and k = 0 to pure triaxial extension loading condition (active state) while k ≈ 0.5 corresponds to direct shear test. (Deformation Scale Factor = 5)

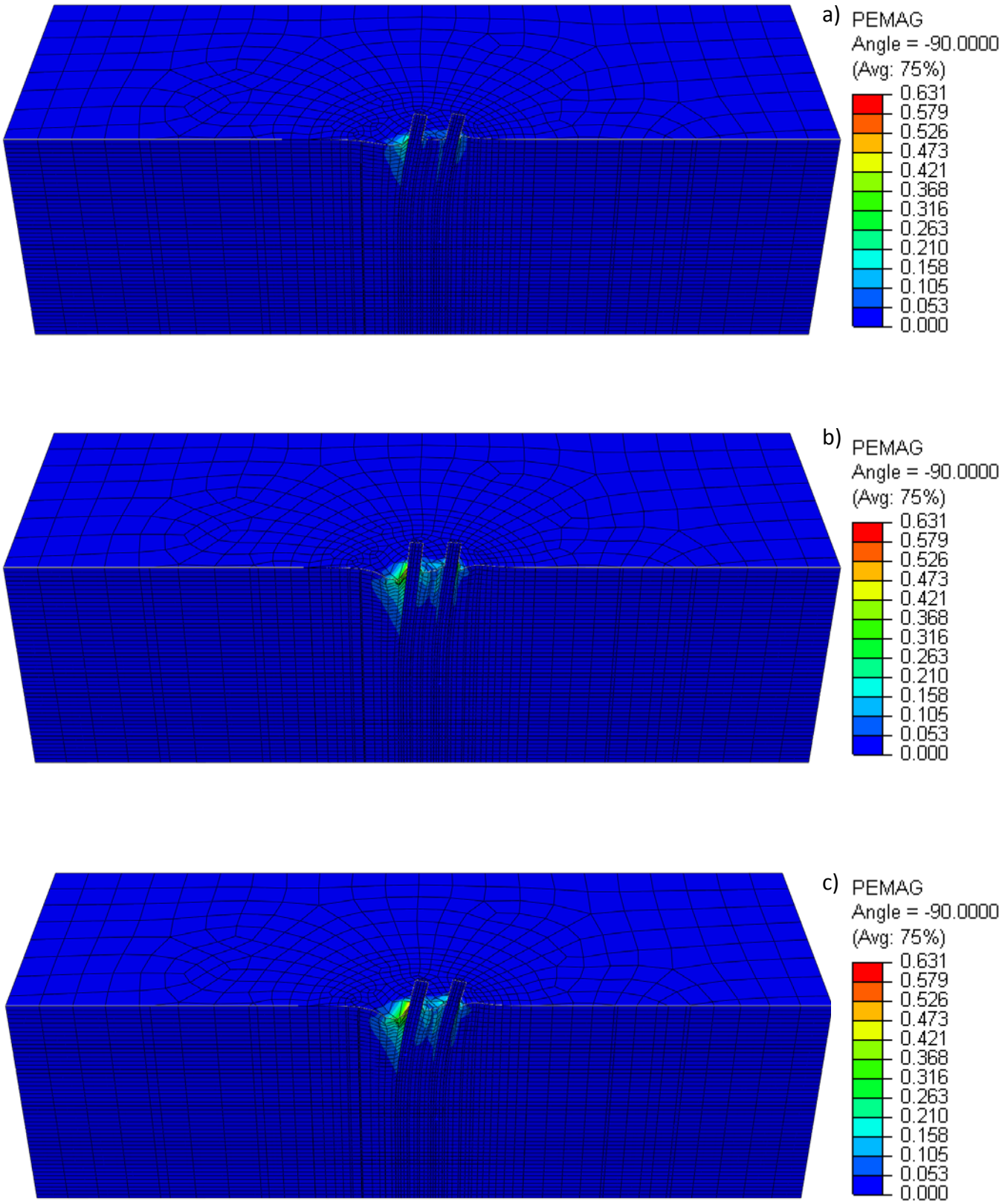

Figure 2.48: Contours of the plastic strain magnitude (plotted on the deformed mesh) at three different stages of loading of the pile group of test P344: (a) at the 1st cycle at 960 kN per pile, (b) at the 12th cycle at 0 kN per pile, and (c) at the 12th cycle at 960 kN per pile. (Deformation Scale Factor = 5)

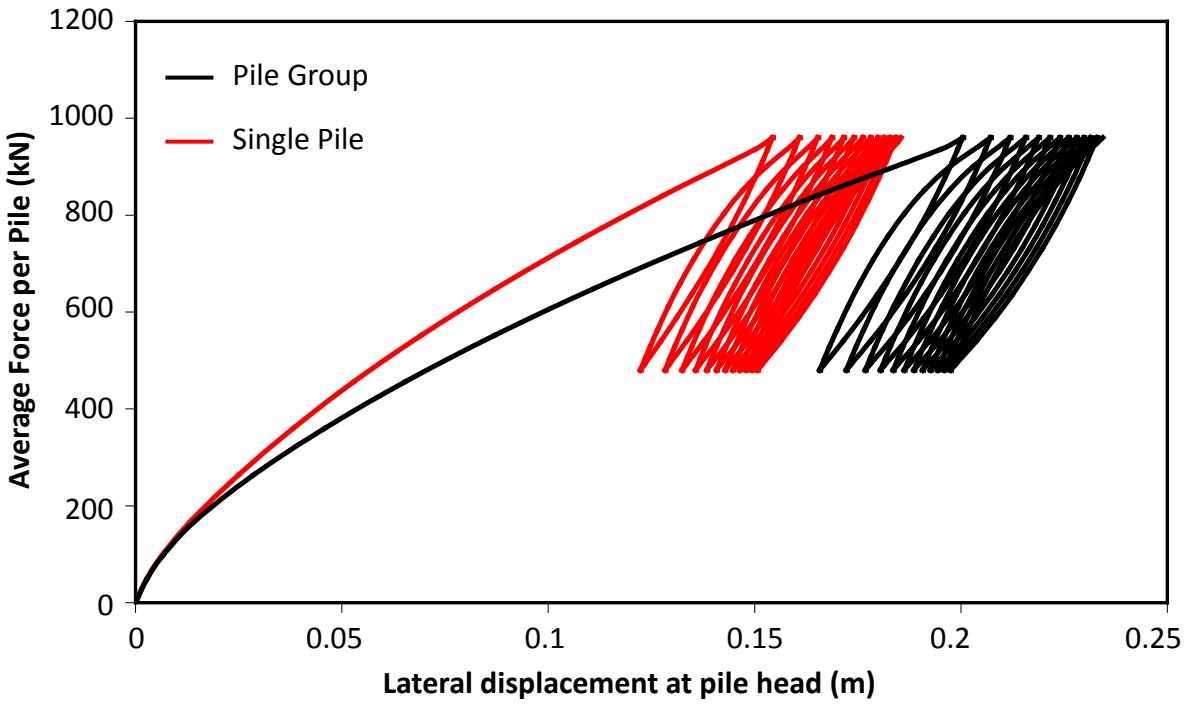

Figure 2.49: Force–displacement curves of the single pile and the pile group for the loading of test P32

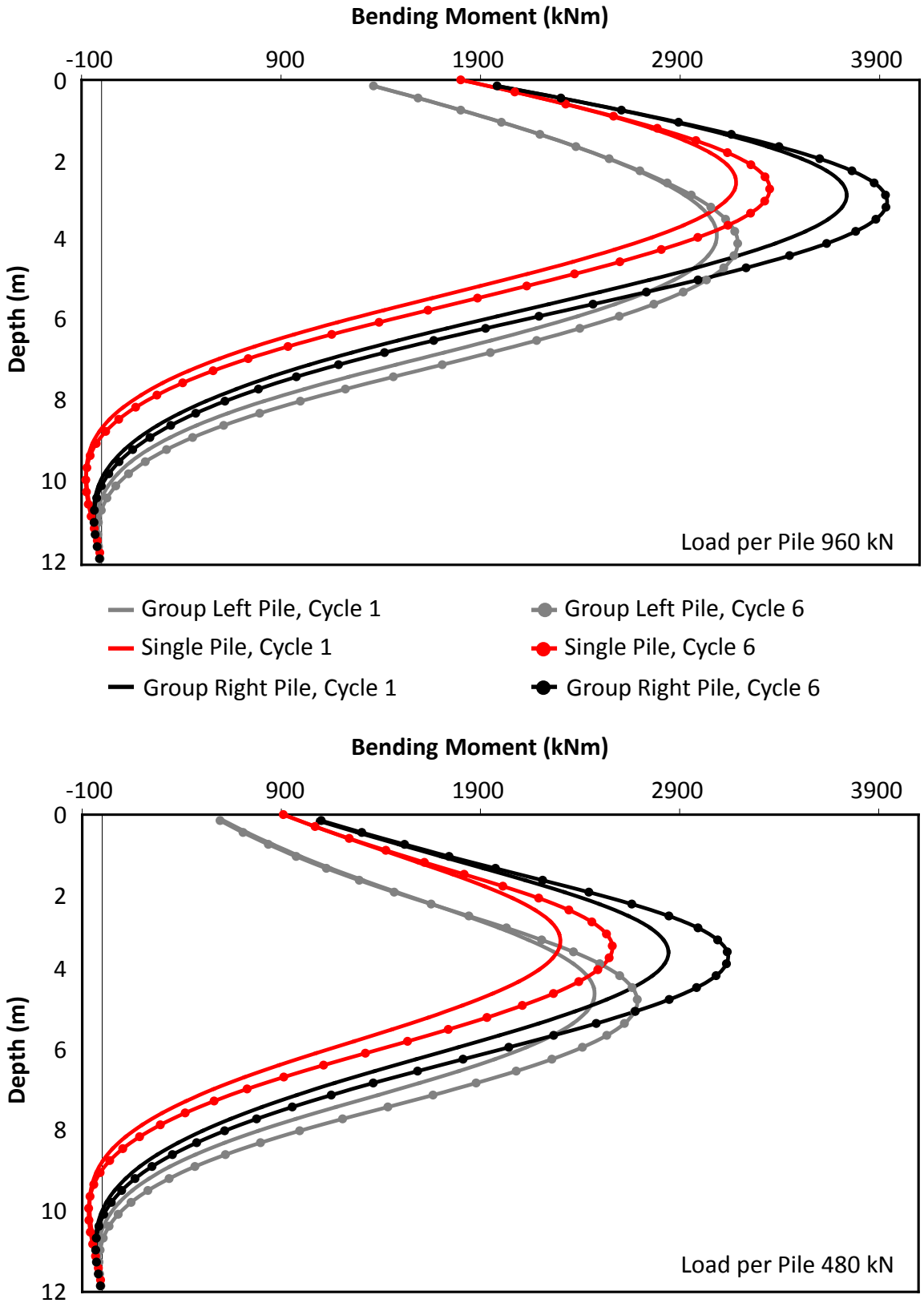

Figure 2.50: Comparison of computed bending moment distributions of the pile group and the single pile for test P32 at two different stages of loading: (atop) at the 1st and 6th cycle and at 960 kN per pile, and (bottom) at the 1st and 6th cycle and at 480 kN per pile. The maximum applied load per pile is 960 kN and the minimum applied one is 480 kN

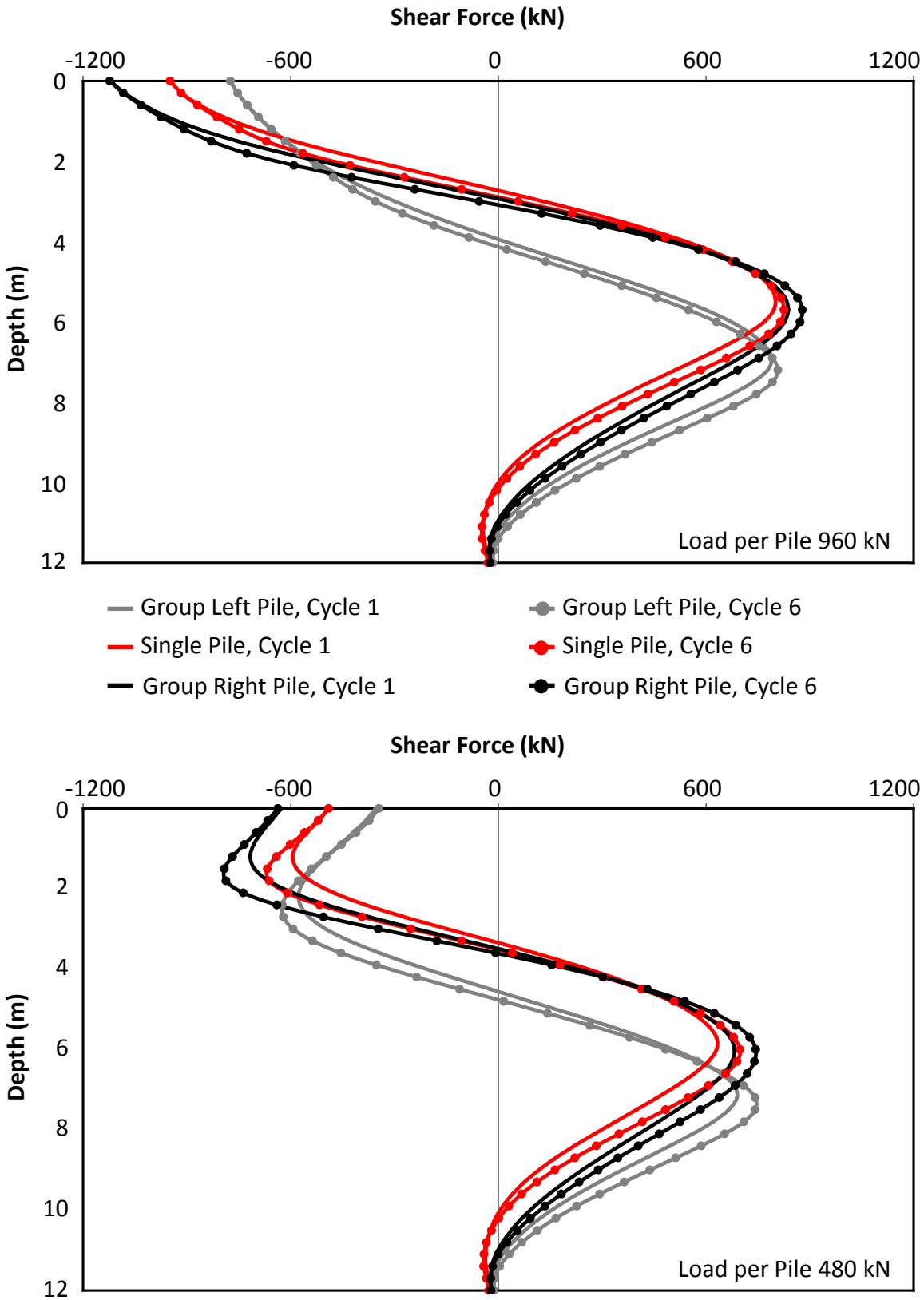

Figure 2.51: Comparison of computed shear force distributions of the pile group and the single pile for test P32 at two different stages of loading: (atop) at the 1st and 6th cycle and at 960 kN, and (bottom) at the 1st and 6th cycle and at 480 kN. The maximum applied load is 960 kN and the minimum applied one is 480 kN

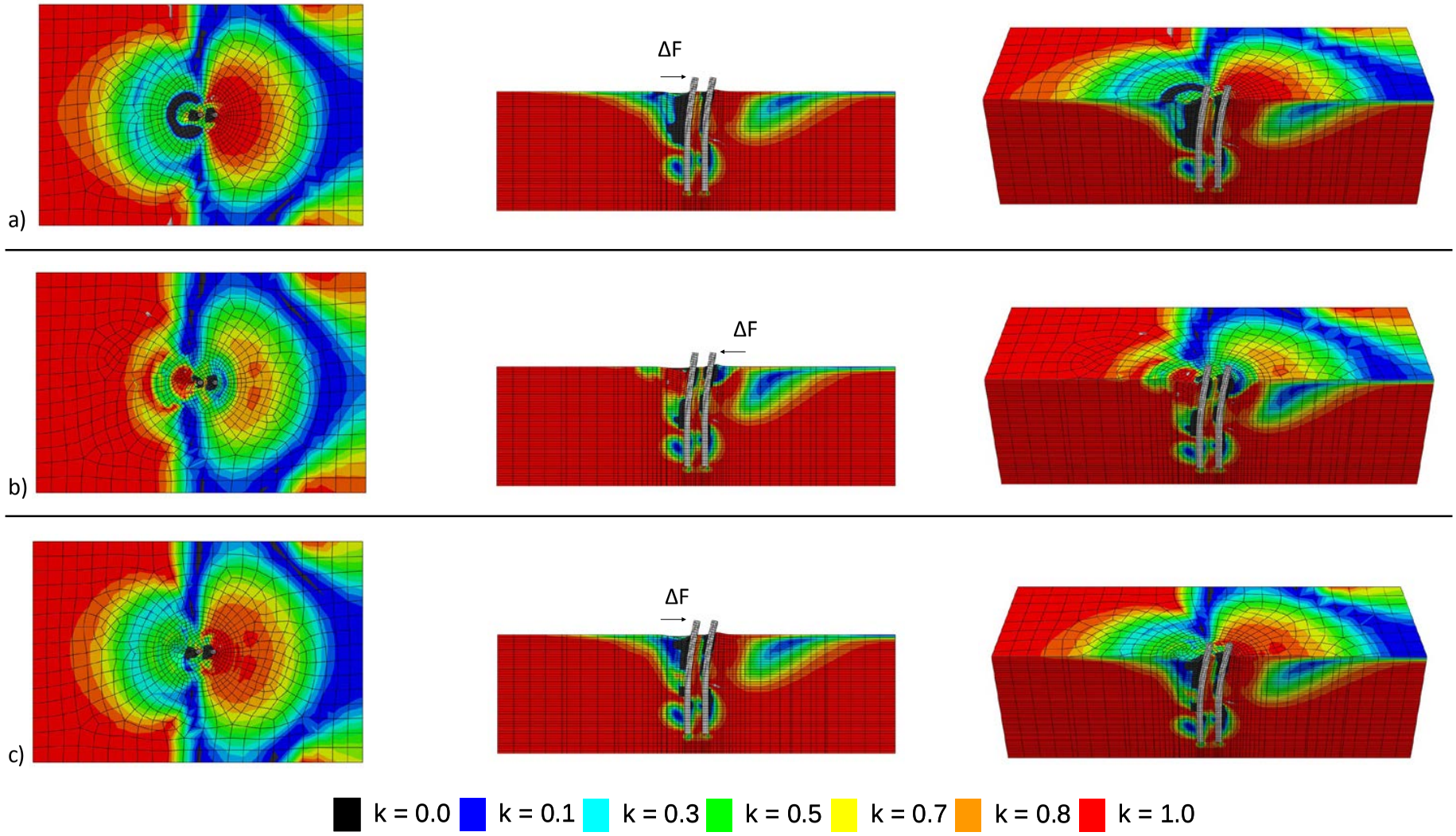

Figure 2.52: Contours of the active and passive stress states in terms of the state parameter k at three different stages of loading of the pile group for the cyclic loading of test P32: (a) at the 1st cycle at 960 kN per pile, (b) at the 12th cycle at 480 kN per pile, and (c) at the 12th cycle at 960 kN per pile. k = 1 corresponds to pure triaxial compression loading condition (passive state), and k = 0 to pure triaxial extension loading condition (active state) while k ≈ 0.5 corresponds to direct shear test. (Deformation Scale Factor = 5)

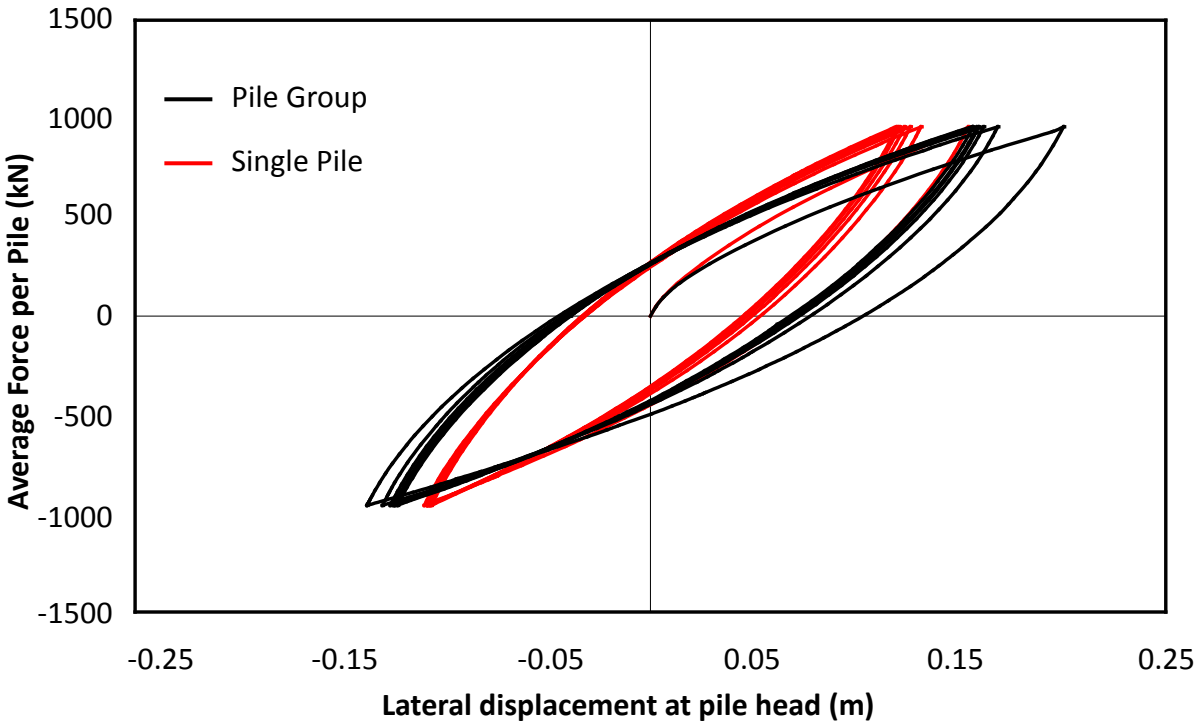

Figure 2.53: Force–displacement curves of the single pile and the pile group for the loading of test P330

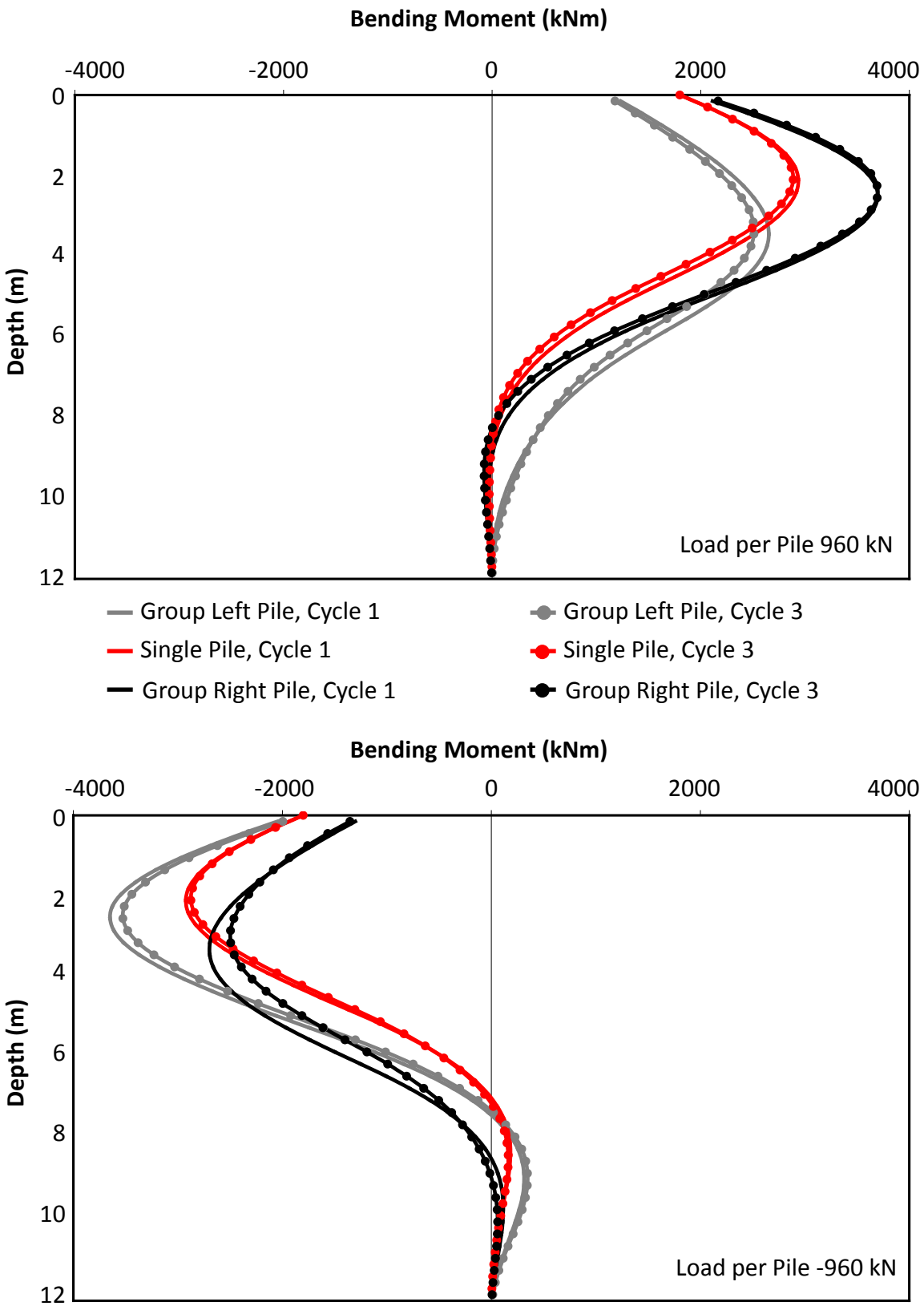

Figure 2.54: Comparison of computed bending moment distributions of the pile group and the single pile for test P330 at two different stages of loading: (atop) at the 1st and 3rd cycle and at 960 kN per pile, and (bottom) at the 1st and 3rd cycle and at -960 kN per pile. The maximum applied load per pile is 960 kN and the minimum applied one is -960 kN

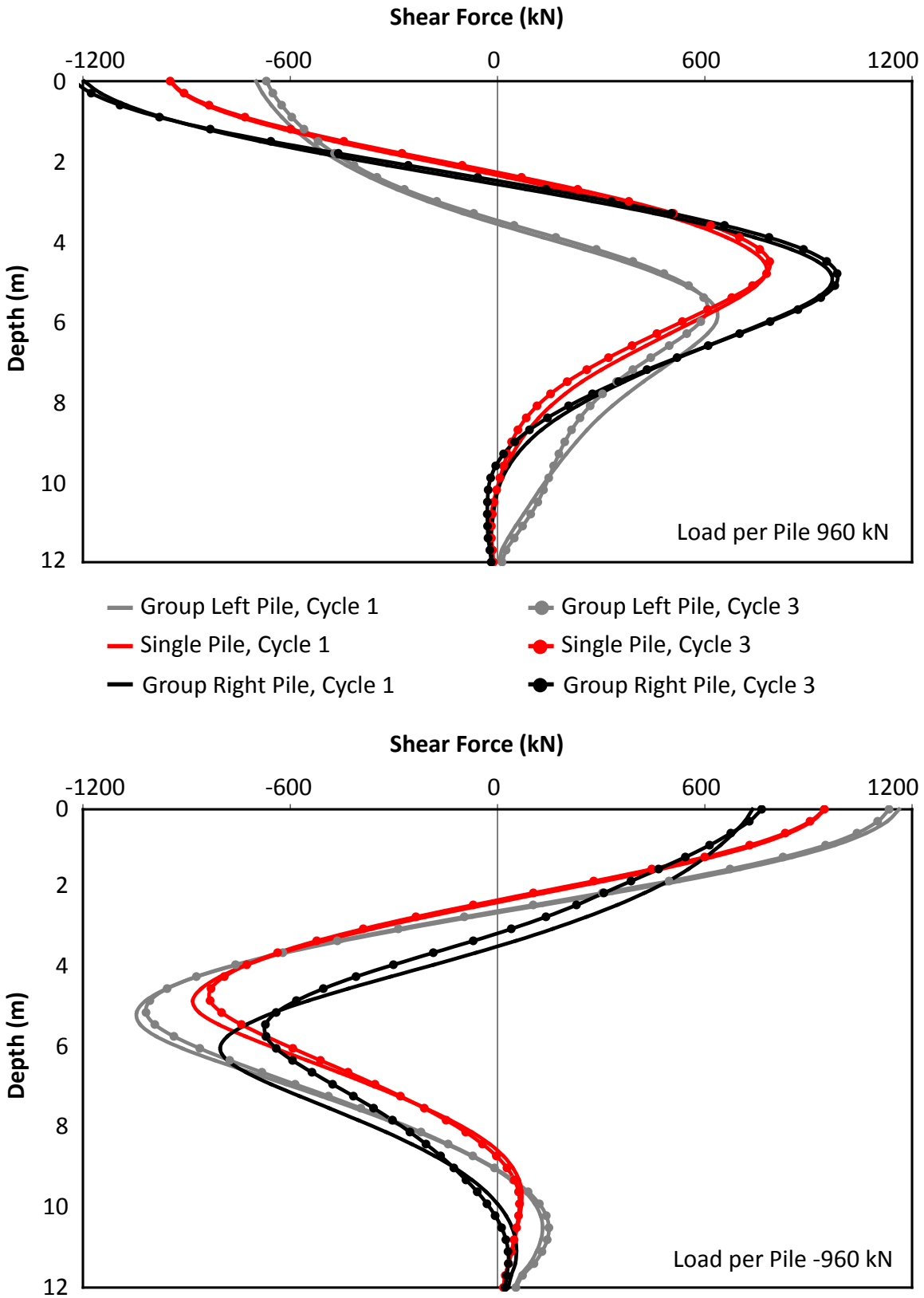

Figure 2.55: Comparison of computed shear force distributions of the pile group and the single pile for test P330 at two different stages of loading: (atop) at the 1st and 3rd cycle and at 960 kN, and (bottom) at the 1st and 3rd cycle and at -960 kN. The maximum applied load is 960 kN and the minimum applied one is -960 kN

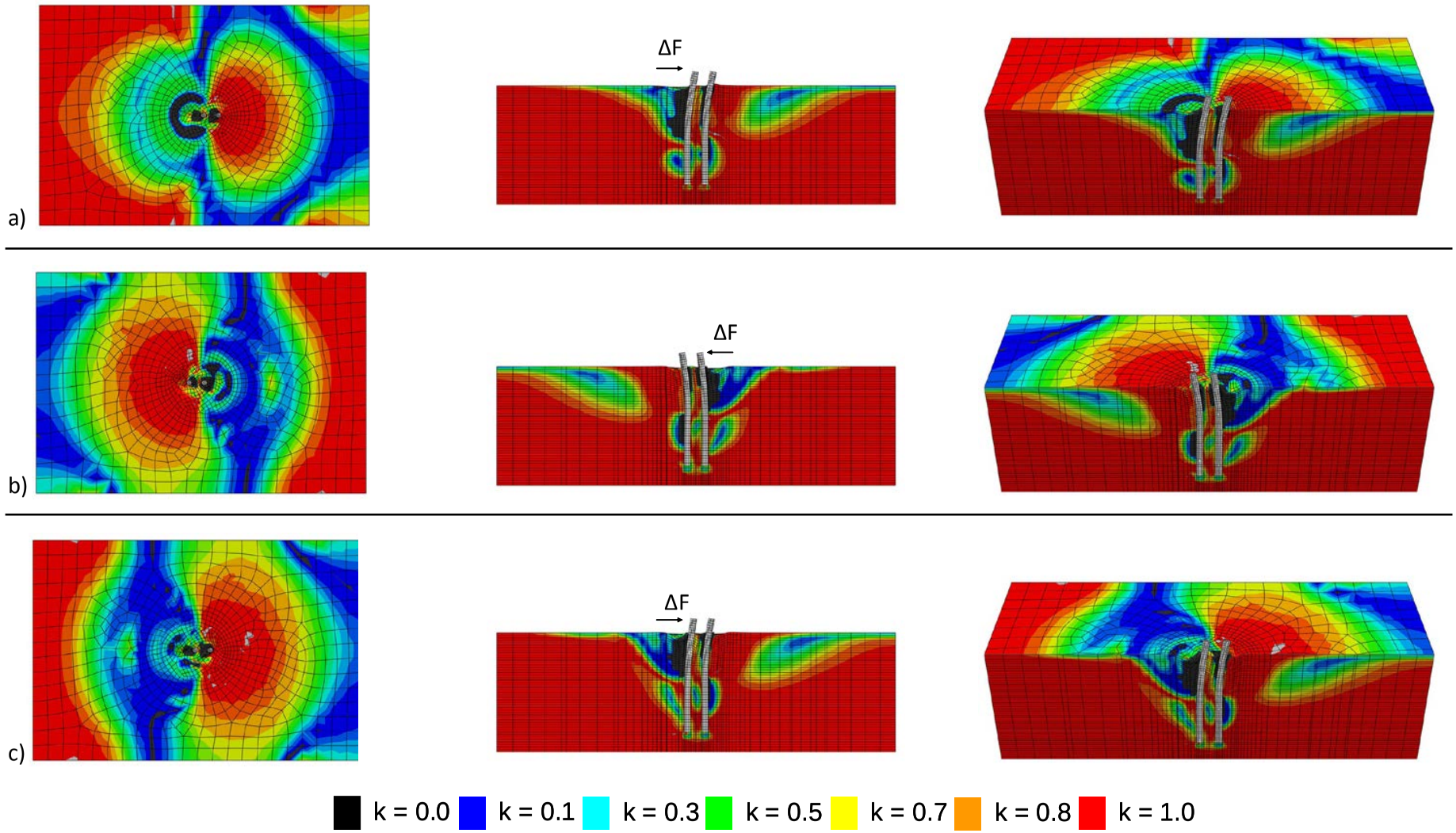

Figure 2.56: Contours of the active and passive stress states in terms of the state parameter k at three different stages of loading of the pile group for the cyclic loading of test P330: (a) at the 1st cycle at 960 kN per pile, (b) at the 6th cycle at -960 kN per pile, and (c) at the 6th cycle at 960 kN per pile. k = 1 corresponds to pure triaxial compression loading condition (passive state), and k = 0 to pure triaxial extension loading condition (active state) while k ≈ 0.5 corresponds to direct shear test. (Deformation Scale Factor = 5)

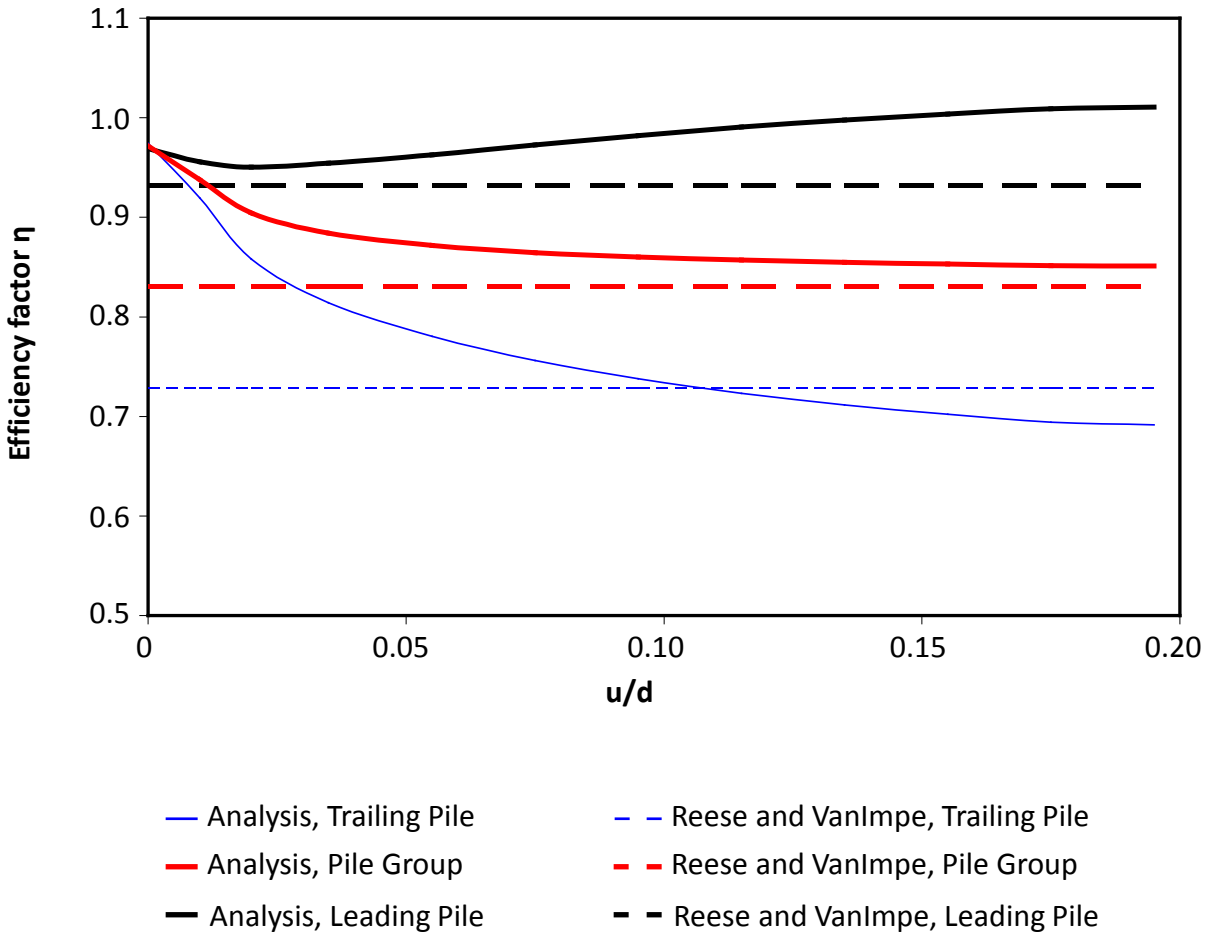

Figure 2.57: Comparison of the calculated efficiency factors for a 1x2 pile group loaded at a height 1.6 meters above the ground surface with those proposed by Reese and Van Impe (2001)

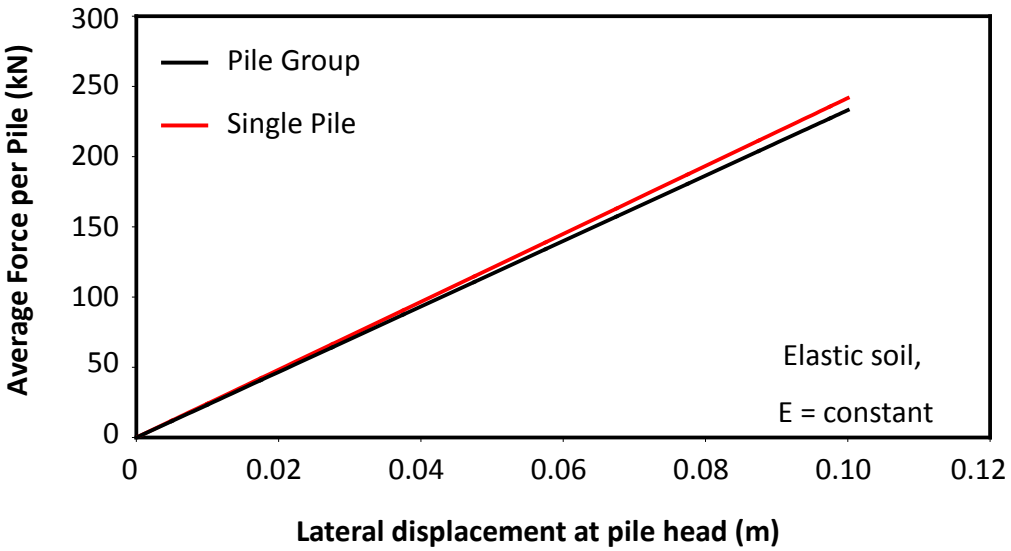

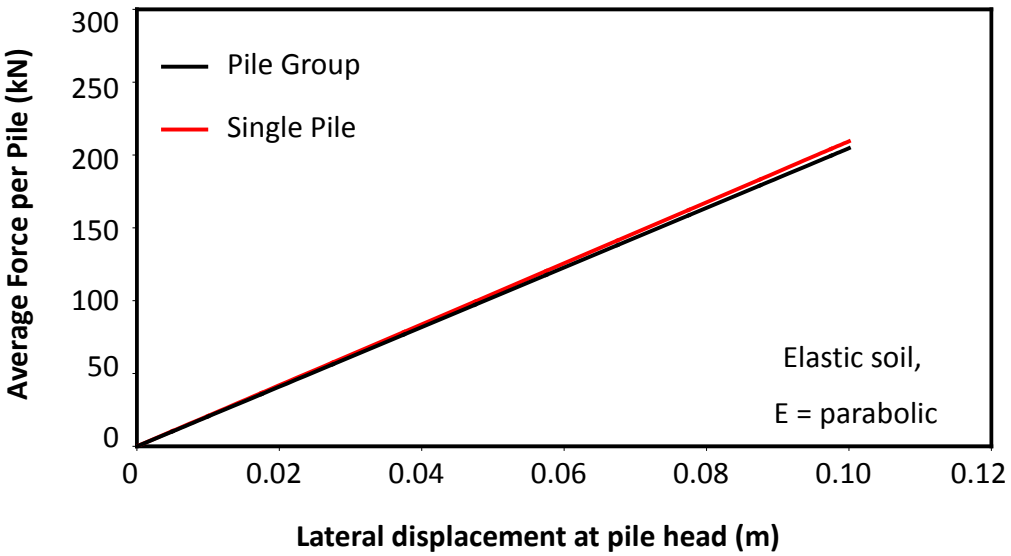

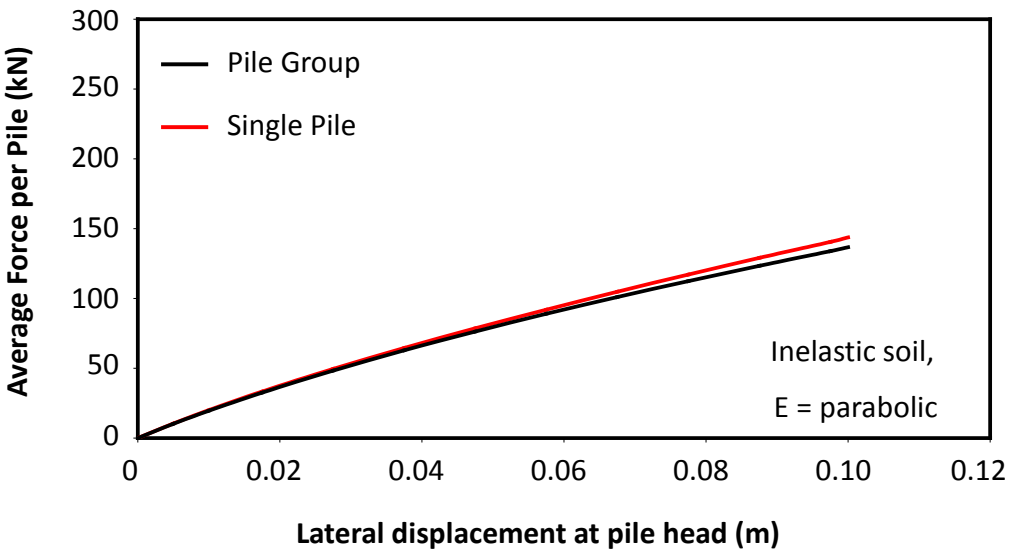

Figure 2.58: Force–displacement curves of the single pile and the pile group for different soil types: (a) elastic soil with constant Young's modulus with depth, (b) elastic soil with parabolic Young's modulus with depth, and (c) for inelastic soil response

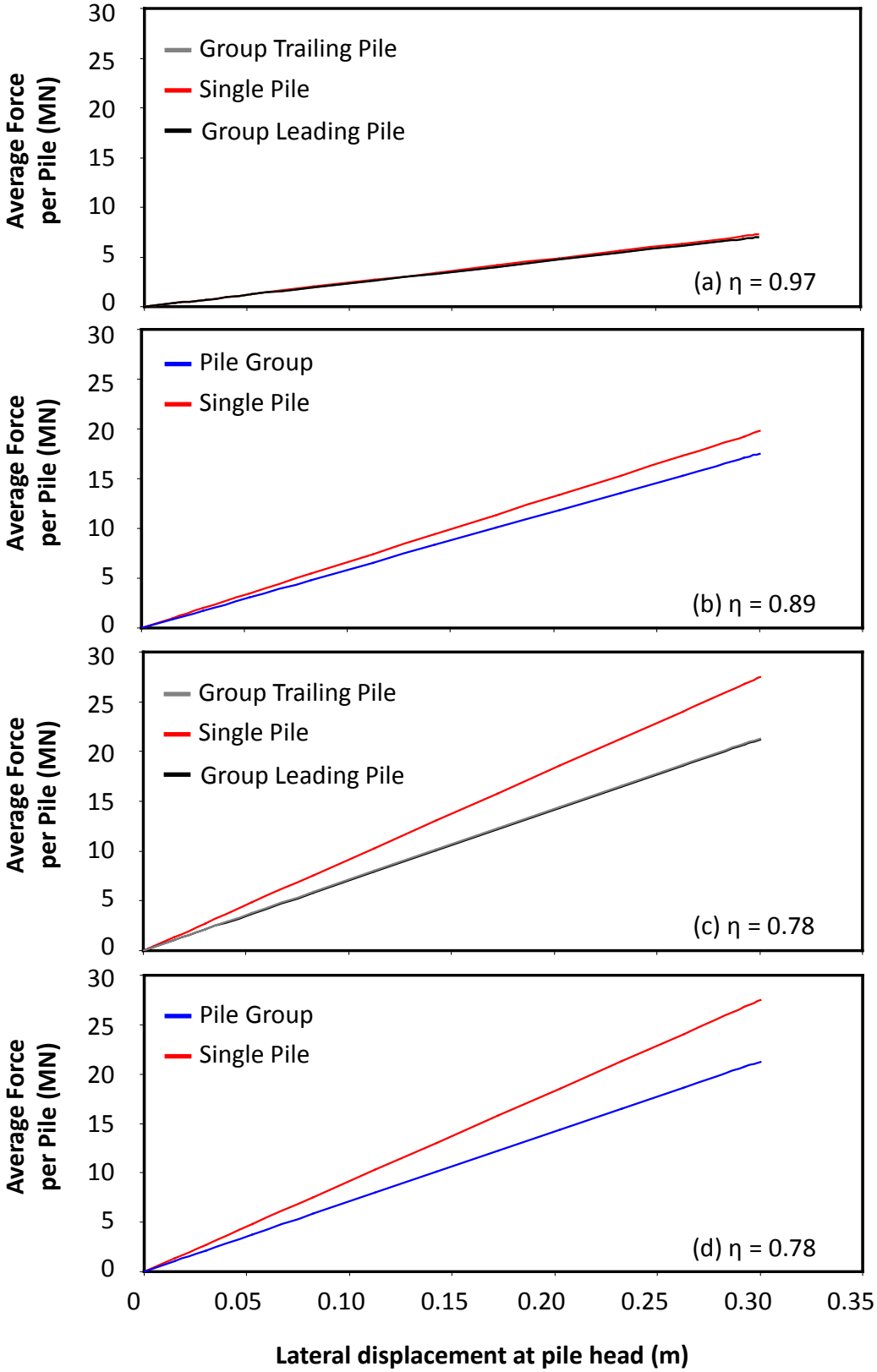

Figure 2.59: Force–displacement curves of the single pile and the pile group for different pile group connections and heights of connections: (a) force acting at 1.6 m above ground surface at both individual free-head piles, (b) force acting at 1.6 m above ground surface for fixed-head piles, (c) force acting at ground surface at both individual free-head piles, and (d) force acting at ground surface at hinged-head piles

CHAPTER 3:

MACRO-ELEMENT MODELING OF THE LATERAL RESPONSE OF FLEXIBLE PILES: FAILURE SURFACE AND PLASTIC FLOW RULE – ANALYTICAL FORMULATION

3.1 MACRO-ELEMENT FORMULATION AND REQUIREMENTS

The macro-element can be thought of as a generalized inelastic stiffness matrix representing the soil-foundation response to applied forces and moments. Placed at the base of the superstructure, it reproduces nonlinear interaction phenomena arising at soil-foundation interface. Thus, instead of executing real-time expensive numerical analyses for the soil, one can alternatively use macro-elements involving minimum calculation effort, as there is no need to model explicitly the soil domain. It exhibits a straightforward and quick calibration procedure, an excellent degree of qualitative insight on foundation dynamic behavior and sufficiently accurate quantitative performance.

In general, macro-element modeling is related to the process of capturing, from the global response of a complex system consisting of the soil and the foundation substructure, only those elements that contribute to the interaction with the superstructure. In order to do so, it is important to investigate and understand in depth the characteristics of soil-foundation response. The basic and realistic modeling assumption is that the foundation is structurally rigid. Thus, one can achieve the condensation of the degrees of freedom of the entire soil-foundation substructure to those of a single point. Accordingly, applied loading on the foundation can be expressed by means of a limited number of force parameters that are work conjugate to the retained degrees of freedom.

According to Martin and Houlsby (2001) the four basic components needed for the formation of a macro-element are (**Figure 3.1**):

(a) Expression of the yield surface (failure envelope) of the foundation in three dimensional moment, horizontal and vertical loading M–Q–N space, that defines the limits of the elastic and inelastic response of the soil-foundation system (large-strain behavior)

(b) Expression of the elastic response of the foundation within the yield surface (small-strain behavior)

(c) Expression of a plastic flow rule for the incremental plastic displacements at failure of the reference point of the foundation

(d) Expression of a hardening law which controls the transition from the elastic (small-strain) response to the yielding (large-strain) response.

Components (b) and (d) can be derived from the literature. For the lateral response of flexible pile, the initial elastic response of the pile-head macro-element (component (b)) can be characterized by approximate expressions for pile-head equivalent-linear impedances such as the ones proposed by Gazetas (1991) or Mylonakis (1995). Hardening and hysteretic behavior (component (d)) can be introduced through a Bouc-Wen type law based on work-hardening plasticity theory such as the one utilized by Gerolymos and Gazetas (2005).

Regarding component (a), the definition of the bearing capacity of the foundation is necessary. In having performed condensation of degrees of freedom and introduced a limited number of force parameters, the definition of bearing capacity may be conceived as the determination of all possible combinations of these force parameters that can be supported by the foundation. Equivalently, bearing capacity of the foundation can be thought of as a surface (failure envelope) in the space of force parameters with the following property: any point in the interior of this surface corresponds to a combination of force parameters that can be supported by the footing. Inversely, any point outside this surface corresponds to a combination of force parameters that cannot be supported by the foundation. One of the advantages of describing bearing capacity as an ultimate surface in the space of force parameters is that it elucidates the existence of different foundation failure mechanisms associated to different combinations of force parameters. In particular, each point or neighborhood in the ultimate surface can be thought of as corresponding to a distinct failure mechanism of the foundation. Inversely, the failure envelope can be determined on the basis of a number of anticipated failure mechanisms,

optimized to yield the most conservative combination of external applied loading. This methodology has been applied successfully for the determination of seismic bearing capacity of strip footings by Salencon and Pecker (1995a, 1995b) and Paolucci and Pecker (1997), and for the seismic bearing capacity of circular footings on cohesive soils by Chatzigogos et al (2007).

Regarding the component (c), the plastic potential expresses the relation of the increments of plastic displacements at failure (v^{pl}, u^{pl}, θ^{pl}) with the loads M–Q–N. In the majority of the studies on embedded foundations, it is assumed that the plastic potential function, *g*, coincides with the yield function (failure envelope), *f*, without further verification of this assumption (associated flow rule, eg. Cremer et al, 2001).

In the present chapter, closed-form solutions for failure envelopes of flexible single piles under combined Q–M loading for different soil conditions are proposed based on limit equilibrium analysis. The plastic flow rule is also investigated analytically and is proposed to be of the associated type. Hence, plastic strains are directly obtained through the analytical expression of the failure envelope.

3.2 FAILURE ENVELOPES: A REVIEW

A failure envelope in the vertical, horizontal, and moment space N–Q–M is a simple tool to estimate the ultimate loading of a foundation. A number of undrained failure envelope analytical formulations can be found in the literature for plane strain and axisymmetric conditions and different interface properties for shallow foundations (Bransby and Randolph, 1998; Taiebat and Carter, 2000; 2010; Cremer et al., 2001; Gourvenec, 2007 among others). For shallow foundations resting on sand, ultimate bearing capacity has been investigated experimentally for strip, rectangular and circular foundations by Ticof (1977), Butterfield and Gottardi (1994), Nova and Montrasio (1991; 1997), Gottardi et al (1999) and Houlsby and Cassidy (2002). Recently, Gerolymos et al (2012) developed failure envelope for caisson foundations in cohesive soils for different embedment ratios.

The shape of the failure envelope is highly influenced by the choice of reference point for footing loads and displacements. Hence, in shallow foundations the reference point is located at their base, in caisson foundations at the centre of their mass (Martin,

1994) or at the centre of their base (Cassidy et al, 2004) or at the centre of the caisson top (Gerolymos et al, 2012) while in pile foundations the obvious point is the pile head.

For pile foundation, the current design practice is to consider axial and lateral loads separately and independently without considering the effect of interaction between the different load directions. Hence, there are limited references in the literature. Poulos and Davis (1980) presented a failure envelope for a perfectly-rigid free-head imbedded vertical plate under moment and horizontal force in a purely cohesive weightless soil for plane-strain conditions. Upper and lower-bound solutions were obtained as shown in **Figure 3.2**. These solutions are only for weightless soil and will tend to be conservative for soil having appreciable weight. Comparisons between the solutions of **Figure 3.2** and those obtained from Broms' theory show that the ultimate lateral resistance calculated from plasticity theory is much less than that from Broms' theory. This difference arises largely from the lower ultimate soil resistances used in the plasticity approach (plasticity theory uses a value of $2S_u$ to $5.14S_u$ while Broms' theory uses a value of $9S_u$). The above plasticity solutions while unduly conservative for normal proportions of pile are relevant to the case of shallow-embedded sheet piling. Also, Murff (1987) has presented an upper bound plasticity method for the plastic collapse analysis of long piles typical of offshore foundations subjected to inclined loading. According to Murff, the assumption of associated plastic flow rule (particularly where the pile yield surface actually represents combined soil-steel behavior) is used primarily for computational convenience, but nevertheless the application of the proposed method to a number of special cases with idealized soil resistance profiles showed that the choice led to excellent results.

Meyerhof (1995) was the first to propose a complete failure envelope formulation for piles by incorporating his previous research results on the ultimate resistance and displacement of rigid piles under lateral loads and moments (Meyerhof and Sastry, 1985) and the general case of eccentric and inclined loads on flexible piles through an equivalent rigid pile method. To this end, a vertical rigid pile of diameter B and fully embedded depth D was subjected at its free-head to the ultimate load Q_u (load height h = 0) with an eccentricity e and inclination α to the vertical (**Figure 3.3a**). The total lateral soil pressures p_1 and p_2 on the shaft were assumed to be trapezoidally distributed: a triangular distribution for the component due to friction and a uniform

distribution for the component due to cohesion. In addition, adhesion forces C_1 and C_2 act on the shaft and the point resistance Q_p at the toe. The net ultimate unit lateral soil pressure p_u on the shaft at any depth z above the critical depth z_c can be expressed by (Hansen, 1961)

$$p_u = \gamma z K_b + c K_c \leq q_u \tag{3.1}$$

where γ is the unit weight of the soil, K_b and K_c are the net lateral soil-pressure coefficients for friction and cohesion with zero shaft friction angle δ and q_u is the ultimate bearing capacity of a vertical strip footing under horizontal load.

The ultimate horizontal load Q_n ($\alpha = 90^o$) was approximately expressed by (Meyerhof and Sastry, 1985):

$$Q_n = \left(0.12\gamma D K_{br} + 0.4\, c K_{cr}\right) BD \leq Q_{nl} \tag{3.2}$$

where

$$Q_{nl} = 0.4\, p_1 BD \tag{3.3}$$

p_1 the limit pressure obtained from pressuremeter tests, and $K_{br} \leq K_b$ and $K_{cr} \leq K_c$ the resultant net lateral soil pressure coefficients for friction and cohesion. Further, for a pile under pure moment M_o at the free head the ultimate moment is given by

$$M_o = \left(0.09\gamma D K_{br} + 0.2\, c K_{cr}\right) BD^2 \leq M_{ol} \tag{3.4}$$

where

$$M_{ol} = 0.2\, p_1 BD^2 \tag{3.5}$$

Under Q_n the maximum bending moment in the pile to prevent structural failure is

$$M_p = m Q_n D \leq M_y \tag{3.6}$$

where m is the bending moment coefficient, which is about 0.35 and 0.22 for piles in sand and clay respectively and M_y is the yield moment of pile section. For a pile under pure moment: $M_o \leq M_y$.

The experimental “interaction diagrams” (failure envelope) for eccentricity e and inclination α of the ultimate load was found based on an ultimate eccentric vertical load Q_{ue} ($\alpha = 0$):

$$\left(\frac{Q_{ue}}{Q_a}\right)^2 + \left(\frac{M_u}{M_o}\right)^2 = 1 \tag{3.7}$$

where Q_a is the ultimate axial pile capacity ($\alpha = 0$), $M_u = Q_{ue}e$ and M_o is the pure moment at the free pile head. Similarly, for an ultimate central inclined load $Q_{u\alpha}$ ($e = 0$) its vertical and horizontal components $Q_{\alpha v}$ and $Q_{\alpha h}$, respectively, can be approximated by the semiempirical relationship:

$$\left(\frac{Q_{\alpha v}}{Q_a}\right)^2 + \left(\frac{Q_{\alpha h}}{Q_n}\right)^2 = 1 \tag{3.8}$$

where Q_n the ultimate horizontal load.

For the case of flexible piles the concept of effective embedment depths of equivalent rigid piles for both ultimate bearing capacity and elastic displacements was used. According to Poulos and Davis (1980), a pile is considered flexible when its relative stiffness K_r compared to that of the soil is less than about 0.01:

$$K_r = \frac{E_p I_p}{E_n D^4} \tag{3.9}$$

where E_pI_p is the flexural rigidity of the pile and E_n is the average normal soil modulus along the embedded depth D. For a laterally loaded flexible pile in the absence of structural pile failure it was suggested that the ultimate horizontal load Q_n and pure moment M_o for soil failure can be estimated from the equations of rigid piles by using a corresponding smaller ultimate effective embedment depth D_{eu} instead of D (**Figure 3.3b**) because of the strength properties of the upper part of the soil mainly govern the lateral resistance of piles. The theoretical relationship between D_{eu} / D and K_r of free-head piles under an ultimate horizontal load Q_n ($\alpha = 90^o$) or pure moment M_o is approximately:

$$\frac{D_{eu}}{D} = f_u K_r^{0.12} \le 1 \tag{3.10}$$

where the factor f_u = 1.65 for sand and f_u = 1.5 for clay. The ratio D_{eu} / D increases roughly parabolically with decreasing α from the above equation for $\alpha = 90^o$ to unity for $\alpha = 0^o$. Accordingly, for the case of flexible piles under eccentric and inclined loads the eccentricity and inclination factors have to be multiplied by a depth factor:

$$i_d = \frac{D_{eu}}{D} + \left(1 - \frac{D_{eu}}{D}\right)\left(1 - \frac{\alpha}{90^o}\right)^2 \tag{3.11}$$

Model tests were performed by Sastry and Meyehoff (1985, 1990) for rigid steel pipe piles in loose sand validated the proposed interaction diagrams and found them somewhat conservative.

Cho and Bang (2002) based on Bransby and Randolph (1998) used the concept of the failure envelope in order to present an analytical solution for the estimation of the ultimate inclined loading capacity of suction rigid piles in clay. The failure envelope was defined on the space V/V_o and H/H_o where V/V_o is the ratio of the vertical load component and the ultimate vertical loading capacity and H/H_o the ratio of the horizontal load component and the ultimate horizontal loading capacity for a given load inclination angle (**Figure 3.4**). The failure envelope labeled as $kD/S_{uo} = 0$ is for piles in a soil with constant undrained soil shear strength whereas the failure envelope labeled as $kD/S_{uo} = 6$ is for piles in a soil whose undrained shear strength increases linearly with a slope of 6 SI units. Recently, Correia et al (2012) proposed a failure envelope for pile foundations in saturated cohesive soils with constant or linearly varying undrained shear strength based on the results from three-dimensional numerical analyses (**Figure 3.5**).

3.3 DERIVATION OF FAILURE ENVELOPES AND PLASTIC FLOW RULE FOR FLEXIBLE PILES: A LIMIT EQUILIBRIUM APPROACH

Broms (1964a,b, 1965) employed a limit analysis solution for laterally loaded pile response. Broms' method addresses both rigid and flexible piles embedded in idealized cohesionless or cohesive soils. In this study, only flexible piles are considered.

For cohesive soils, Broms adopted a constant distribution of soil resistance with depth. The ultimate lateral load can be computed from limit equilibrium. The soil resistance is neglected in the top 1.5 pile diameters because of the lower soil resistance in that zone as the soil wedge can move up and out when the pile is deflected. In general the ultimate soil reaction for cohesive soils can be evaluated from the expression:

$$p_{ult} = aS_u d \tag{3.12}$$

where S_u is the undrained shear strength, d is the diameter of the pile and a an empirical parameter taking values from 9 to 12, depending on the friction ratio f_s / S_u at the pile-soil interface. Usually a value of a = 9 is used for soft clay and a = 11 for stiff clay (Reese and VanImpe, 2001).

For cohesionless soils, Broms adopted a linear distribution of soil resistance with depth. The ultimate soil resistance was assumed to be equal to 3 times the Rankine passive pressure. Thus, at a depth z below the ground surface the soil resistance per unit of length p can be obtained by:

$$p(z) = 3\gamma z K_p d \tag{3.13}$$

where γ is the unit weight of the soil, d the pile diameter, and K_p the Rankine passive earth pressure coefficient given by:

$$K_p = \tan^2(45^o + \phi/2) \tag{3.14}$$

For a free-head long pile when only lateral load is applied, failure will occur with the formation of a plastic hinge ($M_{max} = M_{yield}$) at a depth h. The sign conventions for loads and displacements adopted herein (**Figure 3.6**) obey the right-handed system and clockwise positive convention as proposed by Butterfield et al (1997). The lateral capacities for pure loading are denoted by the subscript "y", whereas the maximum attained loads are subscripted with "max". It should be noted that the reference point for the failure envelopes proposed herein is the pile-head.

3.3.1 Failure envelope for pile in homogeneous cohesive soil

Figure 3.7 shows the problem studied herein. A free-head flexible pile is embedded in cohesive soil with constant undrained shear strength S_u, as in the case of overconsolidated clays. Based on Broms' theory, at the ultimate state (upon the formation of a plastic hinge) the pair of horizontal force Q and overturning moment M that act at the pile head at the soil surface are balanced by the ultimate moment of the pile cross-section M_y (which is also the maximum moment of the pile and a pile cross-section property) and the ultimate soil resistance $p_y h$ (where h is the depth of the plastic hinge formation). For simplicity, the ultimate soil resistance per unit length is considered as $p_y = 10S_u d$ as proposed by Randolph and Houlsby (1984) and the maximum moment of the pile $M_{max} = M_{plastic} = M_{yield}$

From limit equilibrium:

$$p_y h = Q \tag{3.15}$$

$$p_y h \frac{h}{2} = Qh + M - M_y \tag{3.16}$$

From **Equation 3.15** the depth of plastic hinge formation is:

$$h = \frac{Q}{p_y} \tag{3.17}$$

From which:

$$M_y + p_y \left(\frac{Q}{p_y} \right)^2 \frac{1}{2} = Q \frac{Q}{p_y} + M$$

and hence

$$\frac{M}{M_y} + \frac{Q^2}{2 p_y M_y} = 1 \Rightarrow \frac{M}{M_y} + \left(\frac{Q}{\sqrt{2 p_y M_y}} \right)^2 = 1 \tag{3.18}$$

Setting $Q_y = (2 p_y M_y)^{0.5}$ **Equation 3.18** becomes:

$$\frac{M}{M_y} + \left(\frac{Q}{Q_y} \right)^2 = 1 \tag{3.19}$$

In **Equation 3.19** the applied horizontal force Q and overturning moment M are normalized with the respective ultimate capacities. Taking into consideration all possible Q–M combinations at the pile head the failure envelope for a flexible pile embedded in clay with constant S_u is derived:

$$f = \left| \mathrm{sgn}(Q) \left(\frac{Q}{Q_y} \right)^2 + \left| \frac{M}{M_y} \right| \mathrm{sgn}(M) \right| - 1 = 0 \qquad \text{for} \qquad \left| \frac{M}{M_y} \right| < 1 \tag{3.20}$$

and

$$f = \left| \frac{M}{M_y} \right| - 1 = 0 \qquad \text{for} \qquad \left| \frac{M}{M_y} \right| = 1 \tag{3.21}$$

Thus, the failure envelope is normalized against the ultimate lateral load and the ultimate overturning moment of the soil-pile system. The proposed failure envelope is presented in **Figure 3.8** and is symmetric to the beginning of the Q/Q_y–M/M_y axes (zero value). When the overturning moment acts in the same direction with the horizontal force Q, the soil resistance to lateral load decreases in comparison to the ultimate lateral load resistance ($Q / Q_y = 1$, $M / M_y = 0$). What is of great interest is that the maximum horizontal force Q_{max} is sustained with a negative moment loading and is achieved when the pile yields due to that negative moment. This overstrength in the response is obviously attributed to the fact that the overturning moment M acting on the opposite

direction of the horizontal force Q tends to counterbalance a part of that load. When the horizontal load capacity of the soil and the maximum yielding moment of the pile are achieved, the pile-soil system reaches its maximum horizontal capacity. It can be seen that the maximum absolute value of Q / Q_y for the case of a uniform clay layer with constant undrained shear strength is $2^{0.5}$. As already stated, the maximum overturning moment cannot exceed the ultimate moment capacity of the pile (M_{max} / M_y = 1) since the soil does not contribute to the ultimate moment capacity M_y which is a property of the pile cross-section.

The great advantage of the normalized failure envelope with the ultimate values of moment and lateral load is that its shape remains unaffected from any other strength parameter of the soil or the pile. The failure envelope can be defined if the ultimate lateral capacity Q_y and ultimate moment capacity M_y are known.

Assuming an associated plastic flow rule (where the plastic potential function g coincides with the yield function f, g = f) the incremental plastic displacement and the incremental plastic rotation are expressed as:

$$\partial u^{pl} = \lambda \frac{\partial f}{\partial Q} = 2\lambda \frac{Q}{Q_y^2} \tag{3.22}$$

$$\partial \theta^{pl} = \lambda \frac{\partial f}{\partial M} = \lambda \frac{1}{M_y} \tag{3.23}$$

$$\frac{\partial u^{pl}}{\partial \theta^{pl}} = \frac{2QM_y}{Q_y^2} \tag{3.24}$$

where λ a positive factor that defines the magnitude of the plastic displacement and rotation at failure. It can be seen that the plastic flow rule at the Q–M space is independent of the moment M that acts at the pile head and depends only on the horizontal force Q. This equation connects the variations of moment M and horizontal force Q of the failure envelope to the incremental variations of the plastic displacement and rotation at failure. In fact, the vector that starts at a point on the failure envelope and has as inclination the ratio of the plastic incremental displacement to incremental rotation at failure (δu/δθ) is perpendicular at any point to the failure envelope.

According to the assumption of the associated plastic flow rule, at the points of the maximum overturning moment M_{max} the ratio of the displacement increment to the one of rotation will be zero, since only rotation exists at the pile head. Hence,

$$\frac{\partial f}{\partial Q}=0\rightarrow\frac{\partial u^{pl}}{\partial\theta^{pl}}=0 \qquad \text{for} \qquad \left|\frac{M}{M_y}\right|=1 \tag{3.25}$$

On the contrary, at the point of the maximum lateral load Q_{max} apart from displacement there is also rotation at the pile head, since the pile is considered long enough and the failure mechanism is the formation of a plastic hinge at the pile. In the case of a rigid pile, where the soil fails instead of the pile, there would only be a displacement increment and the ratio of the displacement increment to the one of rotation would be infinite.

It must be noted that an associated plastic flow rule implies that the foundation at failure behaves as a rigid body. Thus, the ratio of the plastic displacement to rotation at failure (δu/δθ) equals the depth of the plastic hinge formation of the rigid body measured from the ground surface as will be shown in **Chapter 4**.

3.3.2 Failure envelope for pile in cohesive Gibson soil

In addition to Broms' assumption of a constant soil reaction for clays, a linear distribution of the soil reaction is examined. **Figure 3.9** presents the problem studied herein. A free-head flexible pile is embedded in cohesive soil with linear undrained shear strength S_u distribution with depth, for example $S_u=a\ \sigma'_v$, as in the case of normally consolidated clays. Based on Broms' theory, at the ultimate state the pair of the horizontal load Q and moment M that act at the pile head at the soil surface are balanced by the ultimate moment of the pile $M_{max} = M_{plastic} = M_{yield}$ and the ultimate soil resistance which in this case is:

$$p_y=10\ S_u\ d=10\ \alpha\ \sigma'_v\ d=10\ \alpha\ \gamma\ h\ d \tag{3.26}$$

where α multiplier for σ'_v, γ unit weight of the soil, h depth of the plastic hinge and d pile diameter.

From limit equilibrium:

$$p_y\frac{h}{2}=Q \tag{3.27}$$

$$p_y\frac{h}{2}\frac{h}{3}=Qh+M-M_y \tag{3.28}$$

From **Equations 3.26** and **3.27**:

$$h=\sqrt{\frac{Q}{5a\gamma d}} \tag{3.29}$$

And by applying **Equation 3.29** in **3.28**:

$$\frac{M}{M_y}+\left(\frac{Q}{\left(\frac{45}{4}M_y^2 a\gamma d\right)^{\frac{1}{3}}}\right)^{3/2}=1 \qquad (3.30)$$

Setting $Q_y=\left(\frac{45}{4}M_y^2 a\gamma d\right)^{1/3}$ **Equation 3.30** becomes:

$$\frac{M}{M_y}+\left(\frac{Q}{Q_y}\right)^{3/2}=1 \qquad (3.31)$$

In **Equation 3.31** the applied horizontal force Q and overturning moment M are normalized with the respective ultimate capacities. Taking into consideration all possible Q–M combinations at the pile head the failure envelope for a flexible pile embedded in clay with linear S_u with depth is derived (**Figure 3.10**):

$$f=\left|\mathrm{sgn}(Q)\left|\frac{Q}{Q_y}\right|^{3/2}+\left|\frac{M}{M_y}\right|\mathrm{sgn}(M)\right|-1=0 \qquad \text{for} \quad \left|\frac{M}{M_y}\right|<1 \qquad (3.32)$$

and

$$f=\left|\frac{M}{M_y}\right|-1=0 \qquad \text{for} \quad \left|\frac{M}{M_y}\right|=1 \qquad (3.33)$$

Assuming an associated plastic flow, g = f, the incremental plastic displacement and the incremental plastic rotation are given:

$$\partial u^{pl}=\lambda\frac{\partial f}{\partial Q}=\lambda\frac{3}{2}\frac{Q^{1/2}}{Q_y^{3/2}} \qquad (3.34)$$

$$\partial\theta^{pl}=\lambda\frac{\partial f}{\partial M}=\lambda\frac{1}{M_y} \qquad (3.35)$$

$$\frac{\partial u^{pl}}{\partial\theta^{pl}}=\frac{3}{2}\frac{Q^{1/2}M_y}{Q_y^{3/2}} \qquad (3.36)$$

Again the derived expression for the plastic flow rule which applies at the Q–M space is independent from the moment M that acts at the pile and depends only on the horizontal force Q.

3.3.3 Failure envelope for pile in cohesionless soil

For cohesionless soils, Broms (1964b) adopted a linear distribution of soil resistance with depth and the ultimate soil resistance was assumed to be equal to n = 3 times the Rankine passive pressure, allowing for two dimensional and arching effects. Pender (1995) proposed a value of n = 5 times the Rankine passive pressure because it gave closer match with finite element results. However, the assumption of Broms is adopted here (**Figure 3.11**) for a free-head flexible pile in cohesionless soil. Based on Broms' theory at the ultimate state the pair of horizontal force Q moment M that act at the pile head at the soil surface are balanced by the ultimate soil resistance and the ultimate structural capacity of the pile, $M_{max} = M_{plastic} = M_{yield}$. In this case the soil resistance per unit of length p is obtained:

$$p(z) = n\gamma z K_p d \tag{3.37}$$

where n = 3, γ is the unit weight of the soil, d the pile diameter, z the depth and K_p the Rankine passive earth pressure coefficient.

From limit equilibrium:

$$3K_p\gamma dh\frac{h}{2} = Q \tag{3.38}$$

$$p_y\frac{h}{2}\frac{h}{3} = Qh + M - M_y \tag{3.39}$$

From **Equations 3.38** and **3.39**:

$$h = \sqrt{\frac{2Q}{3K_p\gamma d}} \tag{3.40}$$

from which **Equation 3.39** leads to:

$$\frac{M}{M_y} + \left(\frac{Q}{\left(\frac{27}{8}M_y^2K_p\gamma d\right)^{1/3}}\right)^{3/2} = 1 \tag{3.41}$$

Setting $Q_y = \left(\frac{27}{8}M_y^2K_p\gamma d\right)^{1/3}$ **Equation 3.41** becomes:

$$\frac{M}{M_y} + \left(\frac{Q}{Q_y}\right)^{3/2} = 1 \tag{3.42}$$

In **Equation 3.42** the applied horizontal force Q and overturning moment M are normalized with the respective ultimate capacities. Taking into consideration all possible Q–M combinations at the pile head the failure envelope for a flexible pile embedded in cohesionless soil is derived (**Figure 3.12**):

$$f = \left| \mathrm{sgn}(Q) \left| \frac{Q}{Q_y} \right|^{3/2} + \left| \frac{M}{M_y} \right| \mathrm{sgn}(M) \right| - 1 = 0 \qquad \text{for} \quad \left| \frac{M}{M_y} \right| < 1 \tag{3.43}$$

and

$$f = \left| \frac{M}{M_y} \right| - 1 = 0 \qquad \text{for} \quad \left| \frac{M}{M_y} \right| = 1 \tag{3.44}$$

Assuming an associated plastic flow rule, g = f, the incremental plastic displacement and rotation are:

$$\partial u^{pl} = \lambda \frac{\partial f}{\partial Q} = \lambda \frac{3}{2} \frac{Q^{1/2}}{Q_y^{3/2}} \tag{3.45}$$

$$\partial \theta^{pl} = \lambda \frac{\partial f}{\partial M} = \lambda \frac{1}{M_y} \tag{3.46}$$

$$\frac{\partial u^{pl}}{\partial \theta^{pl}} = \frac{3}{2} \frac{Q^{1/2} M_y}{Q_y^{3/2}} \tag{3.47}$$

As before, the derived expression for the plastic flow rule which applies at the Q–M space is independent from the moment M that acts at the pile and depends only on the horizontal force Q.

3.3.4 Failure envelope for pile in two cohesive layers

For a free-head flexible pile embedded in two clay layers with constant undrained shear strengths S_{u1} and S_{u2} (**Figure 3.13**) the soil resistance is $P_{y1} = 10S_{u1}d$ and $P_{y2} = 10S_{u2}d$. It is assumed that the first layer has thickness b and the plastic hinge is formed in the second layer at a depth h from the surface. For this reason the horizontal force at the pile head Q must be higher than the ultimate resistance of the first layer $Q > P_{y1}b$, otherwise the pile will behave as embedded in one cohesive layer.

From limit equilibrium:

$$p_{y1} b + p_{y2} (h - b) = Q \tag{3.48}$$

$$p_{y1}b\left(h-b+\frac{b}{2}\right)+p_{y2}(h-b)\frac{(h-b)}{2}=M-M_y+Qh \tag{3.49}$$

From **Equation 3.48**:

$$h=\frac{Q-p_{y1}b}{p_{y2}}+b \tag{3.50}$$

And by applying **Equation 3.50** in **3.49**:

$$\frac{M}{M_y\left(1-\frac{p_{y1}b^2\left(p_{y1}-p_{y2}\right)}{2p_{y2}M_y}\right)}+\frac{Q^2+2Qb\left(p_{y2}-p_{y1}\right)}{2p_{y2}M_y\left(1-\frac{p_{y1}b^2\left(p_{y1}-p_{y2}\right)}{2p_{y2}M_y}\right)}=1 \tag{3.51}$$

or

$$\frac{M}{M_y}+\frac{Q^2}{2p_{y2}M_y}+2b\left(p_{y2}-p_{y1}\right)\frac{Q}{2p_{y2}M_y}=1-\frac{p_{y1}b^2\left(p_{y1}-p_{y2}\right)}{2p_{y2}M_y} \tag{3.52}$$

Setting

$$Q_{y2}=\sqrt{2p_{y2}M_y}$$

$$A=\frac{2b\left(p_{y2}-p_{y1}\right)}{\sqrt{2p_{y2}M_y}}$$

And

$$C=\frac{p_{y1}b^2\left(p_{y1}-p_{y2}\right)}{2p_{y2}M_y}$$

Equation 3.52 becomes:

$$\frac{M}{M_y}+\left(\frac{Q}{Q_{y2}}\right)^2+A\frac{Q}{Q_{y2}}+C=1 \tag{3.53}$$

Equations 3.52 and **3.53** are general expressions of failure envelope for a free-head flexible pile embedded in two clay layers. For the case where $S_{u1} < S_{u2}$ **Equation 3.51** leads to:

$$\frac{M}{M_y\left(1-\frac{p_{y1}b^2\left(p_{y1}-p_{y2}\right)}{2p_{y2}M_y}\right)}+\left(\frac{Q}{\sqrt{2p_{y2}M_y\left(1-\frac{p_{y1}b^2\left(p_{y1}-p_{y2}\right)}{2p_{y2}M_y}\right)}}\right)^2$$
$$+\frac{2b\left(p_{y2}-p_{y1}\right)}{\sqrt{2p_{y2}M_y\left(1-\frac{p_{y1}b^2\left(p_{y1}-p_{y2}\right)}{2p_{y2}M_y}\right)}}\frac{Q}{\sqrt{2p_{y2}M_y\left(1-\frac{p_{y1}b^2\left(p_{y1}-p_{y2}\right)}{2p_{y2}M_y}\right)}}=1$$

and setting:

$$M_y^*=M_y\left(1-\frac{p_{y1}b^2\left(p_{y1}-p_{y2}\right)}{2p_{y2}M_y}\right)$$

$$Q_y^*=\sqrt{2p_{y2}M_y\left(1-\frac{p_{y1}b^2\left(p_{y1}-p_{y2}\right)}{2p_{y2}M_y}\right)}$$

and

$$A=\frac{2b\left(p_{y2}-p_{y1}\right)}{\sqrt{2p_{y2}M_y\left(1-\frac{p_{y1}b^2\left(p_{y1}-p_{y2}\right)}{2p_{y2}M_y}\right)}}$$

Equation 3.51 becomes:

$$\frac{M}{M_y^*}+\left(\frac{Q}{Q_y^*}\right)^2+A\frac{Q}{Q_y^*}=1 \qquad (3.54)$$

Taking into consideration all possible Q–M combinations at the pile head for Q > $P_{y1}b$ the failure envelope for a flexible pile embedded in two cohesive layers with constant undrained shear strengths with $Su_1 < Su_2$ is derived:

$$f=\left|\operatorname{sgn}(Q)\left(\frac{Q}{Q_y^*}\right)^2+\operatorname{sgn}(Q)A\left|\frac{Q}{Q_y^*}\right|+\operatorname{sgn}(M)\left|\frac{M}{M_y^*}\right|\right|-1=0 \quad \text{for} \quad \left|\frac{M}{M_y}\right|<1 \qquad (3.55)$$

and

$$f=\left|\frac{M}{M_y}\right|-1=0 \quad \text{for} \quad \left|\frac{M}{M_y}\right|=1 \qquad (3.56)$$

Assuming an associated plastic flow rule, g = f, the incremental plastic displacement and the incremental plastic rotation are:

$$\partial u^{pl} = \lambda \frac{\partial f}{\partial Q} = \lambda 2 \frac{Q}{\left(Q_y^*\right)^2} + A \frac{1}{Q_y^*} \tag{3.57}$$

$$\partial \theta^{pl} = \lambda \frac{\partial f}{\partial M} = \lambda \frac{1}{M_y^*} \tag{3.58}$$

$$\frac{\partial u^{pl}}{\partial \theta^{pl}} = \frac{\left(2Q + AQ_y^*\right) M_y^*}{\left(Q_y^*\right)^2} \tag{3.59}$$

Note that the derived expression for the plastic flow rule at the Q–M space is independent from the moment M that acts at the pile and depends only on the lateral force Q.

3.3.5 Failure envelope for pile-column in cohesionless soil with horizontal force Q and moment M at a distance e from the ground surface

Up to this point, lateral force Q and moment M were applied at the ground surface. Now, the application of Q and M at a distance e above the ground surface is examined, in other words the reference point is considered at distance e from the ground surface, as illustrated in **Figure 3.14** (herein lateral force and moment acting at distance e from the ground surface are noted Q' and M' respectively). A free-head flexible pile-column is embedded in sand.

From limit equilibrium:

$$3K_p \gamma d h \frac{h}{2} = Q' \tag{3.60}$$

$$3K_p \gamma d h \frac{h}{2} \frac{h}{3} = Q'\left(e + h\right) + M' - M_y \tag{3.61}$$

From which:

$$h = \sqrt{\frac{2Q'}{3K_p \gamma d}} \tag{3.62}$$

And by applying **Equation 3.62** in **3.61**:

$$\frac{M'}{M_y}+\left(\frac{Q'}{\left(\frac{27}{8}K_p\gamma dM_y^2\right)^{\frac{1}{3}}}\right)^{3/2}+\frac{e\left(\frac{27}{8}K_p\gamma dM_y^2\right)^{1/3}}{M_y}\frac{Q'}{\left(\frac{27}{8}K_p\gamma dM_y^2\right)^{\frac{1}{3}}}=1 \qquad (3.63)$$

Setting

$$Q_y^*=\left(\frac{27}{8}M_y^2K_p\gamma d\right)^{1/3}$$

and

$$A=\frac{e\left(\frac{27}{8}K_p\gamma dM_y^2\right)^{1/3}}{M_y}$$

Equation 3.63 leads to:

$$\frac{M'}{M_y}+\left(\frac{Q'}{Q_y^*}\right)^{3/2}+A\frac{Q'}{Q_y^*}=1 \qquad (3.64)$$

Hence, the failure envelope for a flexible pile embedded in cohesionless soil with the pile head at a distance e from the ground surface is derived:

$$f=\left|\mathrm{sgn}(Q')\left|\frac{Q'}{Q_y^*}\right|^{3/2}+\mathrm{sgn}(Q')A\left|\frac{Q'}{Q_y^*}\right|+\mathrm{sgn}(M')\left|\frac{M'}{M_y}\right|\right|-1=0 \qquad \text{for} \quad \left|\frac{M'}{M_y}\right|<1 \qquad (3.65)$$

and

$$f=\left|\frac{M'}{M_y}\right|-1=0 \qquad \text{for} \quad \left|\frac{M'}{M_y}\right|=1 \qquad (3.66)$$

Again the associated plastic flow rule, g = f, gives:

$$\partial u^{pl}=\lambda\frac{\partial f}{\partial Q'}=\lambda\left(\frac{3}{2}\frac{Q'^{1/2}}{\left(Q_y^*\right)^{3/2}}+A\frac{1}{Q_y^*}\right) \qquad (3.67)$$

$$\partial\theta^{pl}=\lambda\frac{\partial f}{\partial M}=\lambda\frac{1}{M_y} \qquad (3.68)$$

$$\frac{\partial u^{pl}}{\partial\theta^{pl}}=\frac{\left(\frac{3}{2}Q'^{1/2}+A\left(Q_y^*\right)^{1/2}\right)M_y}{\left(Q_y^*\right)^{3/2}} \qquad (3.69)$$

Once again the plastic flow rule is independent of the moment M' that acts at the pile at a distance e from the ground surface and depends only on the lateral force Q'. It is obvious that in order to transfer the QM pairs at the ground surface (if the pile-head is considered at the ground surface) by setting Q = Q' and M = (M' + Qe) in **Equation 3.61**, **Equations 3.43** and **3.44** for pile in cohesionless soil derive.

3.4 SUMMARY AND CONCLUSIONS

Based on limit equilibrium analysis, failure envelopes in normalized form for flexible single pile in different soil conditions under combined Q–M loading are proposed. The failure envelope is normalized against the ultimate lateral load (lateral load capacity) and the ultimate overturning moment (overturning moment capacity) of the soil-pile system. The great advantage of the normalized failure envelopes with the ultimate values of moment and lateral load is that their shape remains unaffected from any other strength parameter of the soil or the pile.

All the above failure envelopes can be summarized in the following closed-form expression:

$$f = \left| \mathrm{sgn}(Q) \left| \frac{Q}{Q_y^*} \right|^B + \mathrm{sgn}(Q) A \left| \frac{Q}{Q_y^*} \right| + \mathrm{sgn}(M) \left| \frac{M}{M_y^*} \right| \right| - 1 = 0 \quad \text{for} \quad \left| \frac{M}{M_y} \right| < 1 \tag{3.70}$$

and

$$f = \left| \frac{M}{M_y} \right| - 1 = 0 \quad \text{for} \quad \left| \frac{M}{M_y} \right| = 1 \tag{3.71}$$

with A, B, Q_y^* and M_y^* constant values, depending on the problem studied (**Table 3.1**). The same methodology can be used for other cases of piles embedded in soil (eg. pile embedded in three layers).

The plastic flow rule is also investigated analytically and is proposed to be of the associated type, in other words the plastic strains are directly associated with the yield surface. By differentiating **Equations 3.70** and **3.71** the associated plastic flow rule can be derived. An associated plastic flow rule implies that the foundation at failure behaves as a rigid body. Thus, the ratio of the plastic displacement to rotation at failure ($\delta u/\delta\theta$) equals to the depth of the plastic hinge formation of the rigid body measured from the ground surface.

REFERENCES

Bransby M.F., Randolph M.F., 1998, "Combined loading of skirted foundations", *Geotechnique*, 48 (5), pp 637-655

Bransby M.F., Randolph M.F., 1999, "The effect of skirted foundation shape on response to combined V-M-H loadings", *International Journal of Offshore and Polar Engineering*, 9 (3), pp 214-218

Broms B.B., 1964a, "Lateral resistance of piles in cohesive soils", *Journal of Soil Mechanics and Foundation Division*, ASCE 90 (SM2), pp 27-63

Broms B.B., 1964b, "Lateral resistance of piles in cohesionless soils", *Journal of Soil Mechanics and Foundation Division*, ASCE 90 (SM3), pp 123-156

Broms B.B., 1965, "Design of laterally loaded piles", *Journal of Soil Mechanics and Foundation Division*, ASCE 91 (SM3), pp 77-99

Butterfield R., Gottardi G., 1994, "A complete three dimensional failure envelope for shallow footings on sand", *Geotechnique*, 44 (1), pp 181–184

Butterfield R., Houlsby G.T., Gottardi G., 1997, "Standardized sign conventions and notations for generally loaded foundations", *Geotechnique*, 47 (4), pp 1051–1054

Cassidy M.J., Byrne B.W., Randolph M.F., 2004, "A comparison of the combined load behavior of spudcan and caisson foundations on soft normally consolidated clay", *Geotechnique*, 54 (2), pp 91-106

Chatzigogos CT, Pecker A, Salençon J., 2007, "Seismic bearing capacity of a circular footing on a heterogeneous cohesive soil", *Soils and Foundations*, 47 (4), pp 783-797

Cho Y., Bang S., 2002, "Inclined Loading Capacity of Suction Piles", *Proceedings of the 12th International Offshore and Polar Engineering Conference*, Kitakyushu, Japan May 26-31, pp 827-832

Correia A.A., Pecker A., Kramer S.L., Pinho R., 2012, "Nonlinear pile-head macro-element model: SSI effects on seismic response of a monoshaft-supported bridge", *Proceedings of the 15th World Conference on Earthquake Engineering*, Lisbon, Portugal, September

Crémer C., Pecker A., Davenne L., 2001, "Cyclic macro-element for soil structure interaction - Material and geometrical nonlinearities", *Numerical Methods in Geomechanics*, 25, pp 1257–1284

Gazetas G., 1991, “Foundation vibrations”, *Foundation Engineering Handbook*, 2nd edition, editor Fang, H.Y., Van Nostrand Reinhold, New York, USA, pp 553-593

Gerolymos N., Gazetas G., 2005, “Phenomenological model applied to inelastic response of soil–pile interaction systems”, *Soils and Foundations*, 45 (4), pp 119-132

Gerolymos N., Zafeirakos A., Souliotis C., 2012, “Lateral response of caisson foundations: a macroelement approach”, *Proceedings of the 15th World Conference on Earthquake Engineering*, Lisbon, Portugal, September

Gottardi G., Houlsby G.T., Butterfield R., 1999, “Plastic response of circular footings on sand under general planar loading”, *Geotechnique*, 49 (4), pp 453-469

Gourvenec S., 2007, “Shape effects on the capacity of rectangular footings under general loading”, *Geotechnique*, 57 (8), pp 637-646

Hansen J.B., 1961, “The ultimate resistance of rigid piles against transversal forces”, *Bulletin* 12: 5-9, Danish Geotechnical Institute, Copenhagen, Denmark

Houlsby G.T., Cassidy M.J., 2002, “A plasticity model for the behaviour of footings on sand under combined loading”, *Geotechnique*, 52 (2), pp 117-129

Martin C.M., 1994, “*Physical and numerical modeling of offshore foundations under combined loads*”, Doctoral Dissertation, University of Oxford

Martin C.M., Houlsby G.T., 2001, “Combined loading of spudcan foundations on clay: numerical modeling”, *Geotechnique*, Vol 51 (8), pp 687-699

Meyerhof G., 1995, “Behaviour of pile foundations under special loading conditions: 1994 R.M. Hardy keynote address”, *Canadian Geotechnical Journal*, Vol 32 (2), pp 204-222

Meyerhof G., Sastry V.V.R.N., 1985, “Bearing capacity of rigid piles under eccentric and inclined loads”, *Canadian Geotechnical Journal*, Vol 24 (3), pp 471-478

Murff J.D., 1987, “Technical notes on practical applications, plastic collapse of long piles under inclined loading”, *International Journal for Numerical and Analytical Methods in Geomechanics*, Vol 11, pp 185-192

Mylonakis G., 1995, “Contributions to static and seismic analysis of piles and pile-supported bridge piers”, *Doctoral Dissertation*, New York, State University of New York at Buffalo

Nova R., Montrasio L., 1991, “Settlements of shallow foundations on sand”, *Geotechnique*, 41 (2), pp 243-256

Nova R., Montrasio L., 1997, “Settlements of shallow foundations on sand: Geometric effects”, *Geotechnique*, 47 (1), pp 49-60

Paolucci R, Pecker A., 1997, “Seismic bearing capacity of shallow strip foundations on dry soils”, *Soils and Foundations*, 37(3), pp 95-105

Pender M.J, 1995, *Aseismic Foundation Design Analysis*, Continuing Education Course, University of Auckland, New Zealand

Poulos H.G., Davis E.H., 1980, *Pile Foundation Analysis and Design*, John Wiley and Sons, New York

Randolph M.F., Houlsby G.T., 1984, “The limiting pressure on a circular pile loaded laterally in cohesive soil”, *Geotechnique*, 34 (4), pp 613-623

Reese L.C., Van Impe W.F., 2001, *Single Piles and Pile Groups under Lateral Loading*, A.A.Balkema. Rotterdam

Salençon J, Pecker A., 1995a, “Ultimate bearing capacity of shallow foundations under inclined and eccentric loading. Part I: Purely cohesive soil”, *European Journal of Mechanics*, 14 (3), pp 349-375

Salençon J, Pecker A., 1995b, “Ultimate bearing capacity of shallow foundations under inclined and eccentric loading. Part II: Purely cohesive soil without tensile strength”, *European Journal of Mechanics*, 14 (3), pp 377-396

Sastry V.V.R.N., Meyerhof G., 1990, “Behavior of flexible piles under inclined loads”, *Canadian Geotechnical Journal*, 27 (1), pp 19-28

Taiebat H.A., Carter J.P., 2000, “Numerical studies of the bearing capacity of shallow foundations on cohesive soil subjected to combined loading”, *Geotechnique*, 50 (4), pp 409-418

Taiebat H.A., Carter J.P., 2010, “A failure surface for circular footings on cohesive soils”, *Geotechnique*, 60 (4), pp 265-273

Ticof J., 1977, “*Surface footings on sand under general planar loads*”, Doctoral Dissertation, Southampton University, Southampton, U.K.

Table 3.1. Failure envelope constants

Pile embedded in:	A	B	Q_y*	M_y*
Homogeneous cohesive soil	0	2	$\left(2p_yM_y\right)^{1/2}$	M_y
Cohesive Gibson soil	0	3/2	$\left(\frac{45}{4}M_y^2a\gamma d\right)^{1/3}$	M_y
Cohesionless soil	0	3/2	$\left(\frac{27}{8}M_y^2kK_p\gamma d\right)^{1/3}$	M_y
Two cohesive layers with $Su_1 < Su_2$	$\frac{2b\left(p_{y2}-p_{y1}\right)}{\sqrt{2p_{y2}M_y\left(1-\frac{p_{y1}b^2\left(p_{y1}-p_{y2}\right)}{2p_{y2}M_y}\right)}}$	2	$\sqrt{2p_{y2}M_y\left(1-\frac{p_{y1}b^2\left(p_{y1}-p_{y2}\right)}{2p_{y2}M_y}\right)}$	$M_y\left(1-\frac{p_{y1}b^2\left(p_{y1}-p_{y2}\right)}{2p_{y2}M_y}\right)$
Cohesionless soil with horizontal force Q and moment M at a distance e from the ground surface	$\frac{e\left(\frac{27}{8}K_p\gamma dM_y^2\right)^{1/3}}{M_y}$	3/2	$\left(\frac{27}{8}M_y^2K_p\gamma d\right)^{1/3}$	M_y

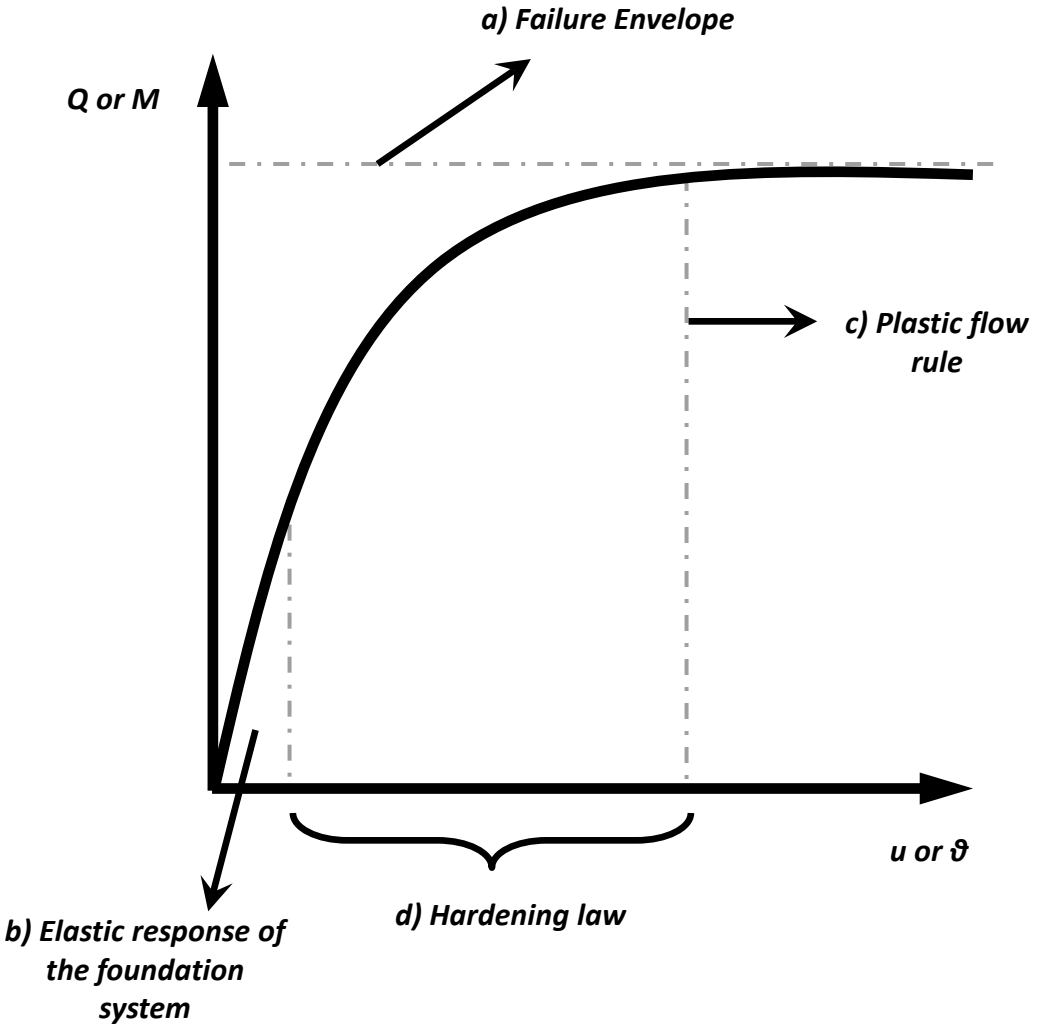

Figure 3.1: Four components needed for a macro-element development and their influence on the force-displacement or moment-rotation curves

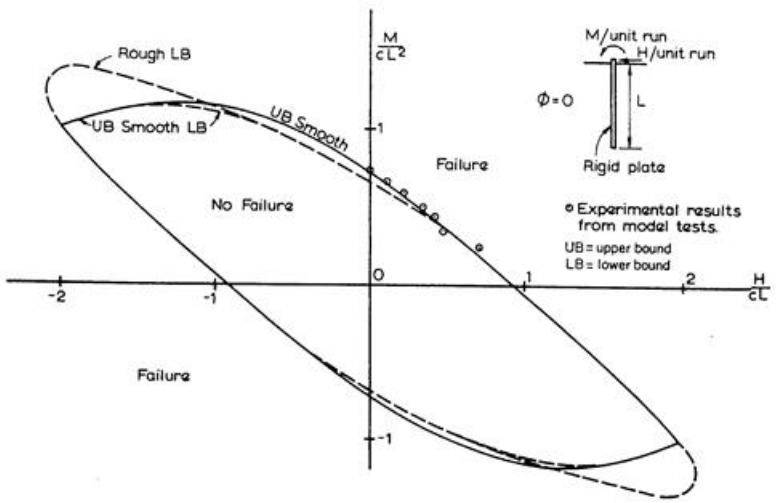

Figure 3.2: Failure of a rigid vertical plate under moment and horizontal load (Poulos and Davis, 1980)

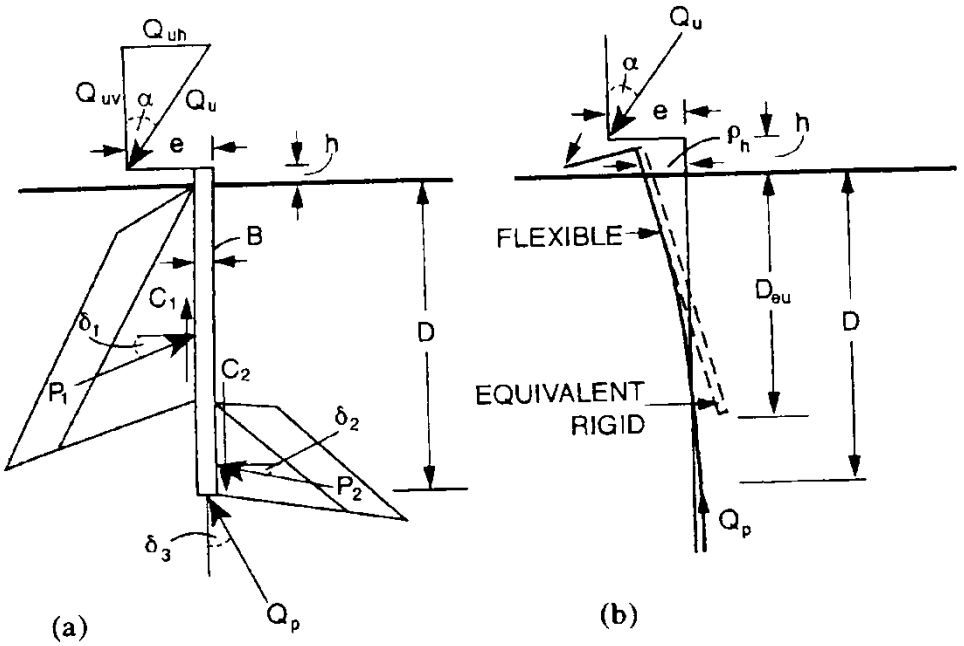

Figure 3.3: (a) Lateral soil pressures and forces on a rigid pile under ultimate eccentric inclined load, (b) Displacements of flexible and equivalent rigid piles (Meyerhof, 1995)

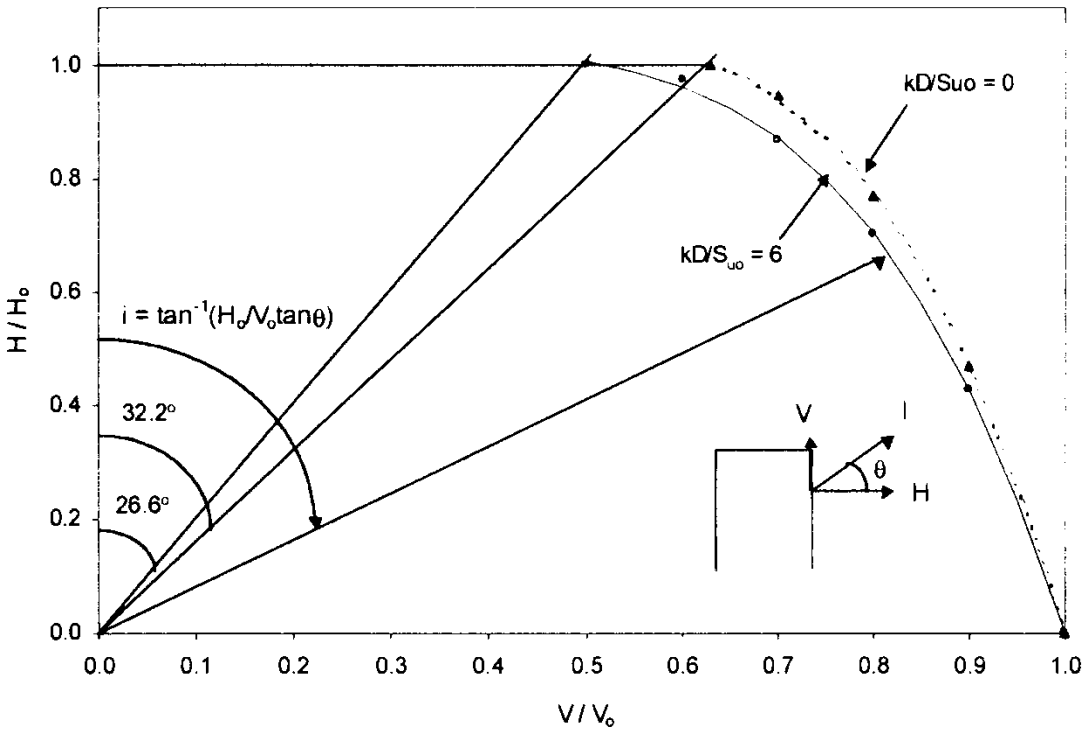

Figure 3.4: Ultimate inclined loading capacity of suction rigid piles in clay (Cho and Bang, 2002)

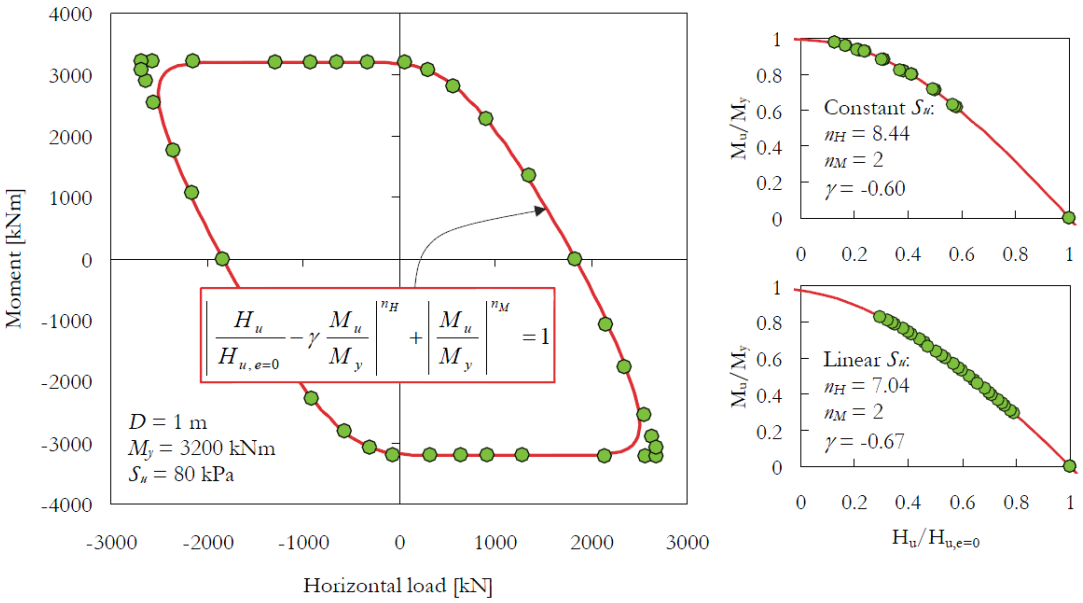

Figure 3.5: Failure surface for flexible piles in cohesive soils (Correia et al, 2012)

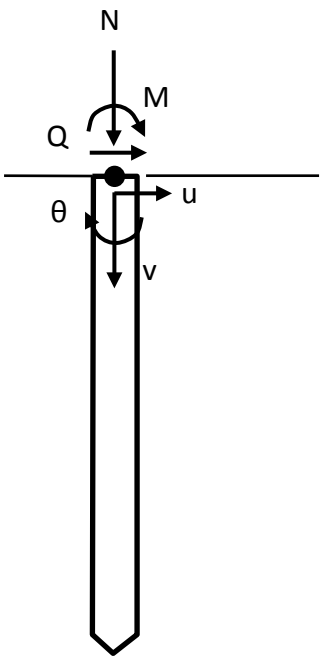

Figure 3.6: Sign convention for loads and displacements

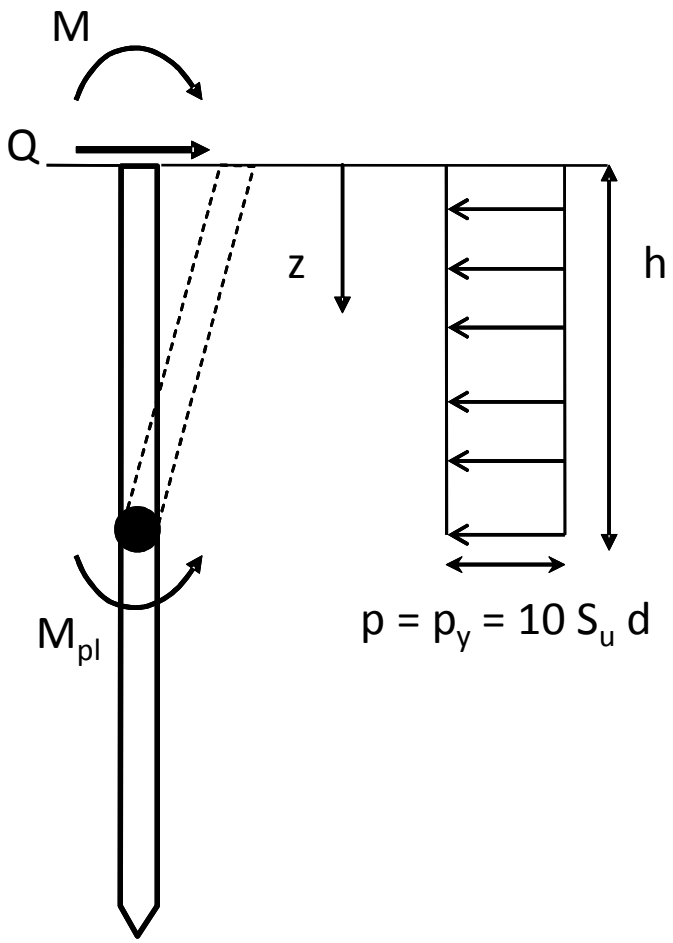

Figure 3.7: Pile embedded in homogenous cohesive soil

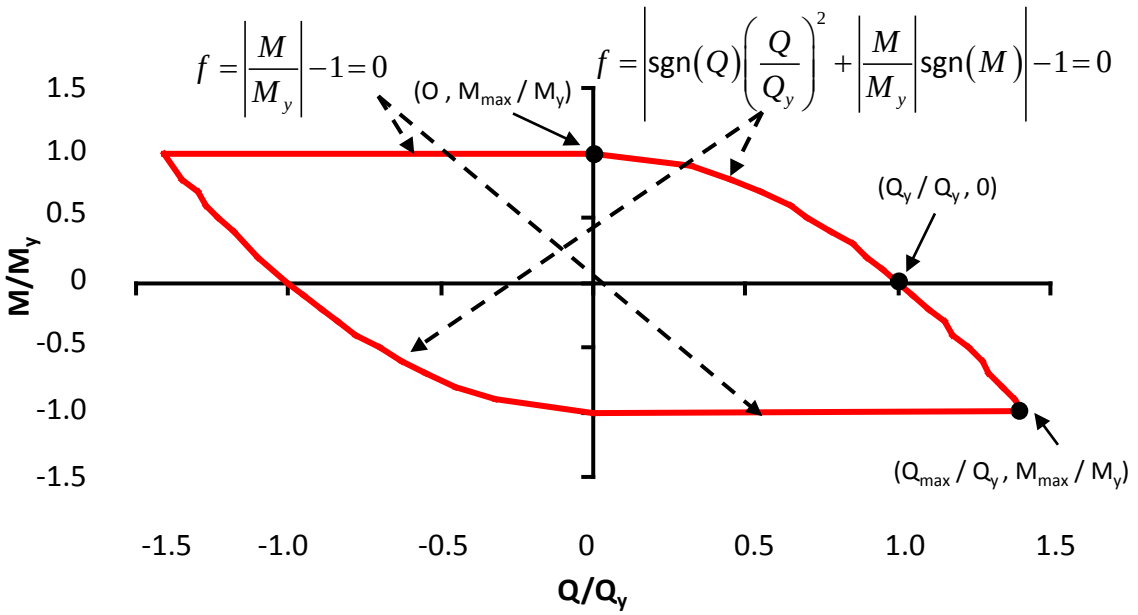

Figure 3.8: Proposed failure envelope for flexible pile in homogeneous cohesive soil

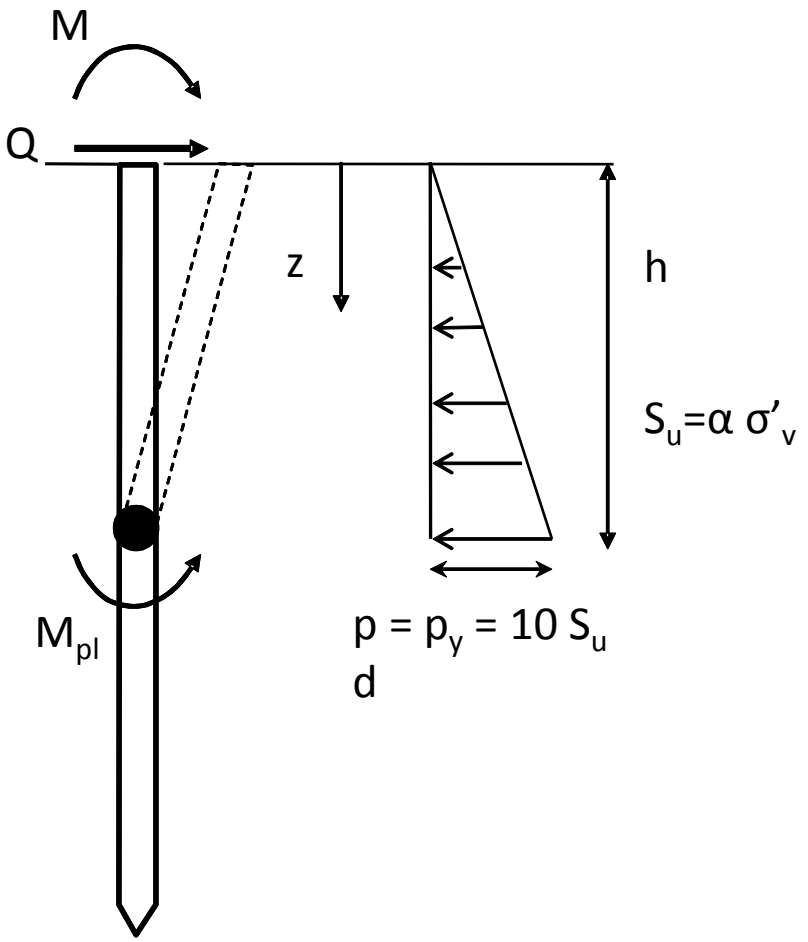

Figure 3.9: Pile embedded in cohesive Gibson soil

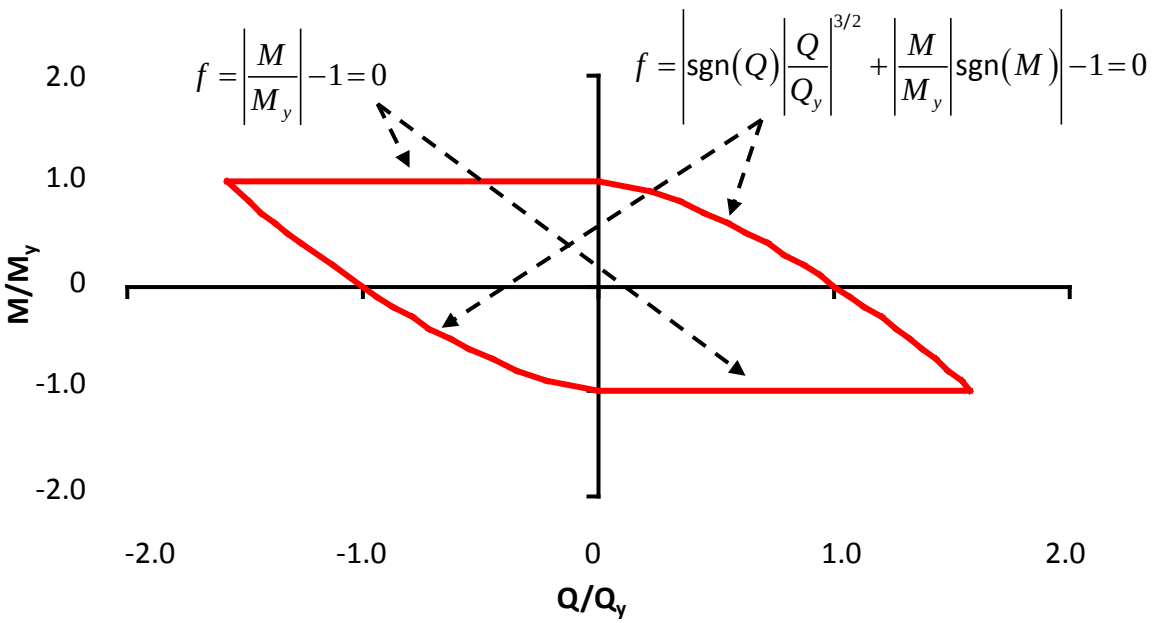

Figure 3.10: Proposed failure envelope for flexible pile in cohesive Gibson soil

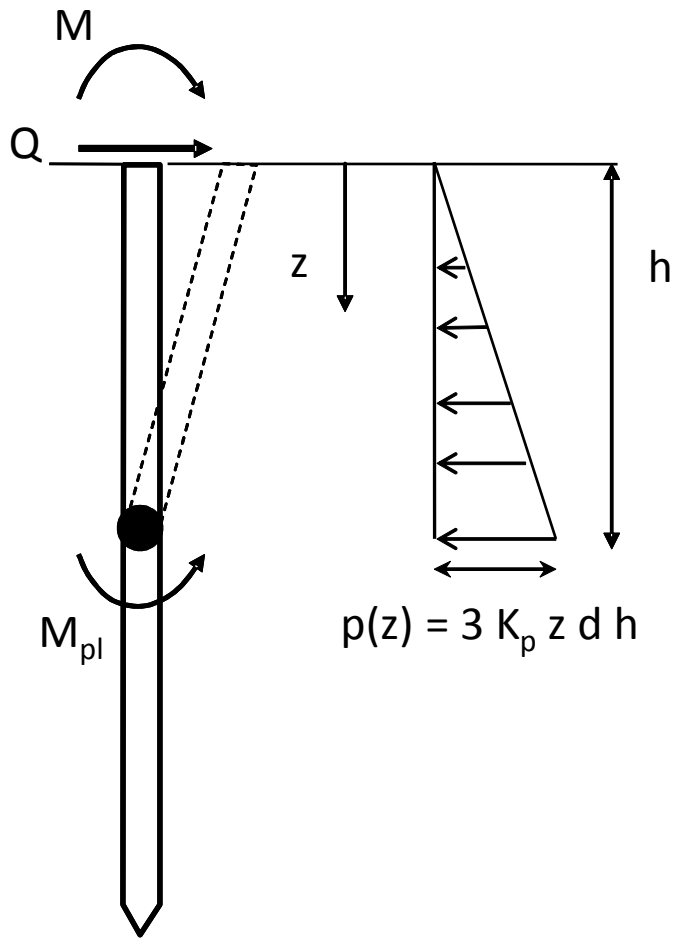

Figure 3.11: Pile embedded in cohesionless soil

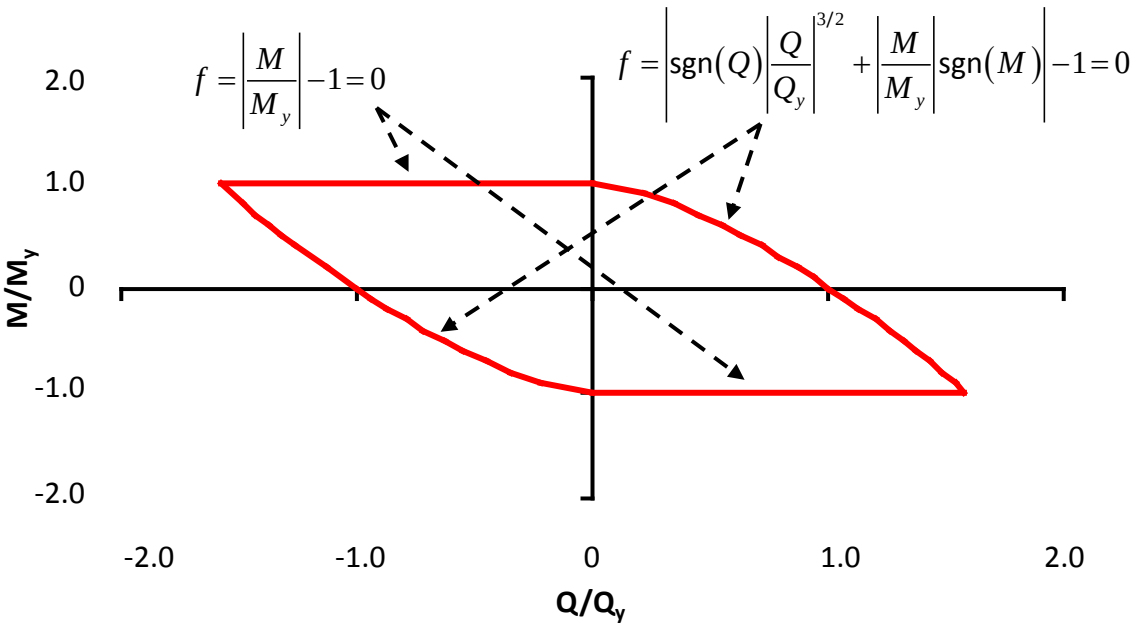

Figure 3.12: Proposed failure envelope for flexible pile in cohesionless soil

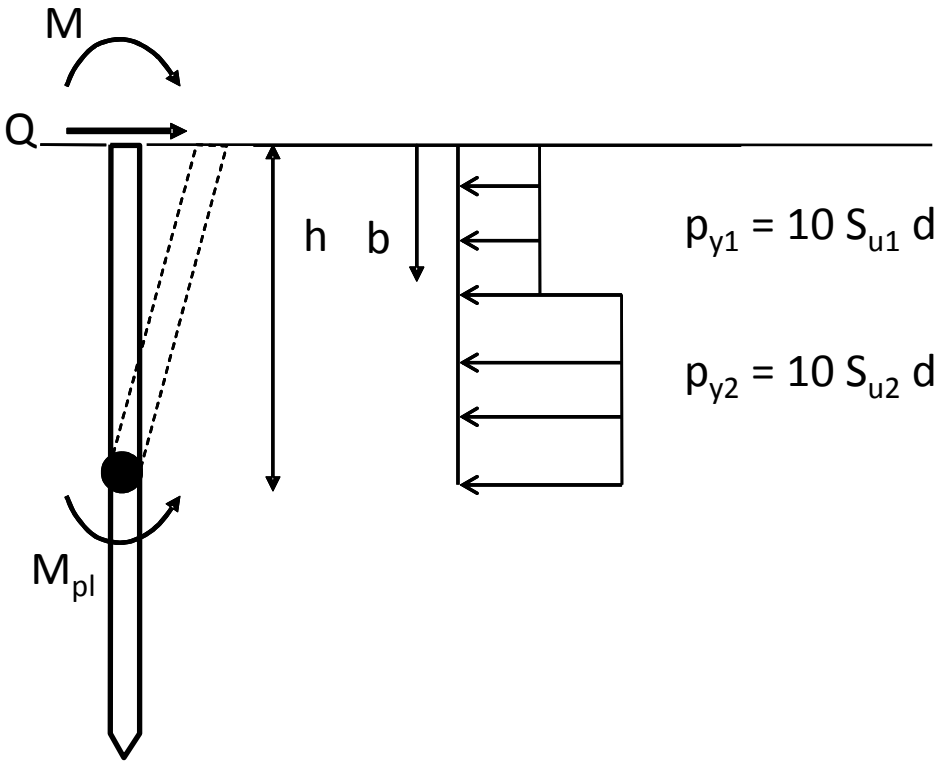

Figure 3.13: Pile embedded in two cohesive layers with $p_{y1} < p_{y2}$

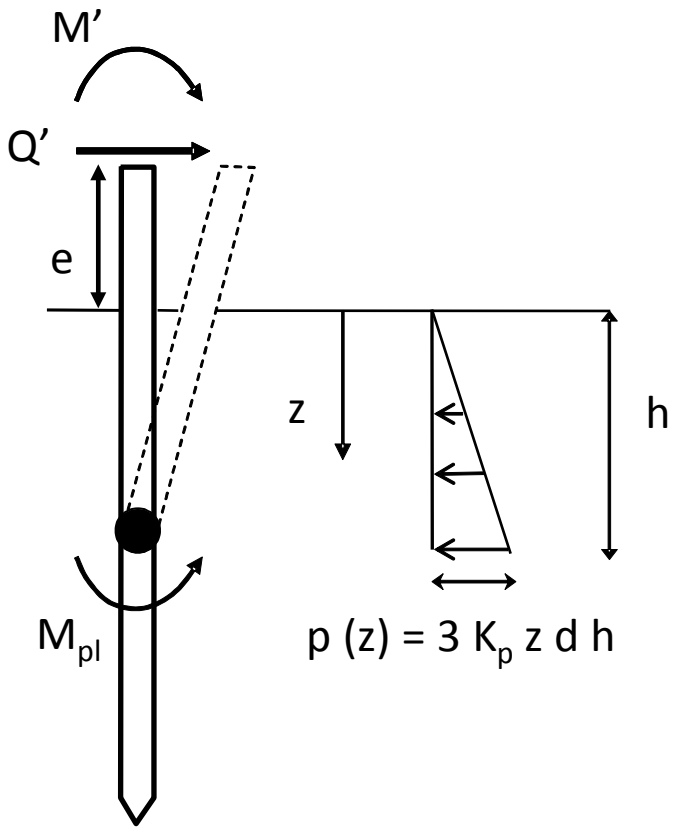

Figure 3.14: Pile-column embedded in cohesionless soil with lateral load Q' and moment M' at a distance e from the ground surface

CHAPTER 4:

MACRO-ELEMENT MODELING OF THE LATERAL RESPONSE OF FLEXIBLE PILES: FAILURE SURFACE AND PLASTIC FLOW RULE – NUMERICAL VERIFICATION

4.1 INTRODUCTION

The failure envelope and associated plastic flow rule developed in **Chapter 3** are verified against numerical analysis. Two methods of analysis are applied: (a) a Beam-on-Winkler-foundation method, and (b) a 3D Finite Element one in which both the pile and the soil are represented by 3D solid elements. In each method of analysis the pile is subjected to a single load path to failure in Q–M space. A combined load of overturning moment and horizontal force is imposed to the pile head under a constant ratio M/Q (radial paths in Q–M space, Gouvernec, 2004) until complete failure of the pile-soil system. **Figure 4.1** illustrates the concept of radial paths in the Q–M space according to Cremer et al (2001). From each individual load path the points at which the pile yields are used to determine a continuous failure envelope in the normalized M/M_y–Q/Q_y space. In addition to assessing the shape of the failure envelope, the force-controlled analyses are used to estimate the displacement increments at yield ($\dot{u}^{pl}$, $\dot{\theta}^{pl}$). Hence, the incremental displacement vectors from the analyses are compared to the analytical expressions under the assumption of an associated plastic flow rule. The validity of each analytical expression for the failure envelopes developed in **Chapter 3** is checked through the results from two different types of analysis: (a) a Beam-on-Winkler-foundation analysis, and (b) a 3D Finite Element analysis.

4.2 WINKLER APPROACH

Numerical static pushover analyses based on the Winkler model for the soil resistance are conducted on the Q–M space in order to verify the analytical expressions

of the failure envelope and the associated plastic flow rules derived in **Chapter 3**. The simple numerical model, shown in **Figure 4.2**, is used for analyzing the responses of the pile-soil system under different specified parameters. The Finite Element Code ABAQUS (Dassault Systèmes Simulia Corp, 2009) is employed to perform pushover analyses. The Beam-on-Winkler-foundation model uses 2D beam elements to simulate the pile and adopts a series of independent springs to model the soil reactions, thus the displacement at any point is directly related to the contact pressure at that point. A free-head pile is embedded 20 m in a homogeneous elastic-perfectly plastic soil of Winkler type. The moment−curvature behavior of the pile cross-section is assumed to be bilinear, determined from point (M_y, κ_y) where M_y is the yield moment and κ_y is the yield curvature and point (M_u, κ_u) where M_u is the ultimate moment and κ_u is the ultimate curvature (**Figure 4.2**).

4.2.1 Failure envelope for pile in homogeneous cohesive soil

A beam-on-Winkler-foundation model is used to verify analytically the failure envelope for a pile embedded in homogeneous cohesive soil (**Equations 3.20** and **3.21**). The ultimate soil resistance is defined as

$$p_{ult} = 10 S_u d \tag{4.1}$$

where S_u is the undrained shear strength and d is the diameter of the pile. The undrained shear strength of the soil is constant with depth. Different pairs of moment M and lateral force Q are applied at the pile head (at the ground level) until the failure of the pile-soil system. The ratio of incremental displacement to incremental rotation at failure is compared with that from **Equation 3.24**.

Initially, the influence of the mesh density on the model response is parametrically examined. For this reason, a pile 20 m long with diameter d = 1 m is considered embedded in a homogeneous clay layer with constant undrained shear strength S_u = 200 kPa. Three different meshes are studied regarding the spatial discretization of piles: 1 m, 0.25 m and 0.1 m. The pairs of moment M and lateral force Q at failure are normalized with the corresponding values for pure moment and lateral force loading conditions, respectively. **Figure 4.3** shows the dependence of the problem on the mesh density. A very coarse mesh gives overstrength to the system for the area of

the failure envelope where the overturning moment M dominates upon the lateral force Q on the response of the pile and has the opposite direction of the lateral force Q. In this area the ratio of the moment to the plastic moment can be higher than 1, as Poulos and Davis (1980) supported based on plasticity theory. However, this behavior is not observed when the mesh is fine, highlighting the importance of a fine mesh for the lateral response of a pile.

Figure 4.4 presents the vectors from the analytical expression with the assumption of an associated plastic flow rule (**Equation 3.24**) along with the incremental displacement vectors at failure from the Winkler model for the three meshes examined (vertical distance z of the Winkler springs (a) z = 1 m, (b) z = 0.25 m, and (c) z = 0.1 m). It can be observed that the assumption of an associated plastic flow rule is in accord with the elasto-plastic Winkler model predictions. A very dense mesh is needed in order to capture this behavior correctly. It is also obvious that the ultimate moment and the ultimate lateral force from the Winkler model coincide with the ones from the analytical expression. Hence, the following results presented herein refer to a mesh with vertical distance z = 0.1 m.

Having investigated the importance of the mesh density, the relative stiffness and the relative strength of the pile and the soil are investigated. The relative stiffness β is defined as:

$$\beta = \left(\frac{k_s}{EI} \right)^{1/4} \tag{4.2}$$

where k_s is the Winkler stiffness according to Makris and Gazetas, (1992) ($k_s = 1.2E_s$, E_s Young's Modulus of the soil) and EI the elastic flexural rigidity of the pile (E the elastic modulus of the pile and I the moment of inertia). The relative strength is defined as:

$$\lambda = \left(\frac{M_{pl}}{S_u} \right)^{1/3} \tag{4.3}$$

where M_{pl} the plastic moment of the pile and S_u the undrained shear strength of the cohesive soil.

A parametric study (1200 analyses) is performed to study the influence of the undrained shear strength S_u, the Young's Modulus of the soil E_s and the diameter of the pile d on the failure envelope and the plastic flow rule. The selected values for the

undrained shear strength S_u are 25, 50, 100, 200 and 400 kPa, for the pile diameter 0.5, 1.0 and 1.5 m and for the Young's Modulus E_s of the soil 10, 50, 100 and 300 MPa. **Figure 4.5** illustrates the influence of the undrained shear strength S_u on the failure envelope for the case of a pile of diameter d = 1 m, embedded in a homogeneous cohesive layer with uniform Young's modulus E_s = 100 MPa. The increase of the undrained shear strength of the soil (and thus the decrease of the relative strength λ) has no influence on the failure envelope on the normalized Q/Q_y–M/M_y space. **Figure 4.6** shows the influence of the undrained shear strength S_u on the plastic flow rule on the Q–M space. It is obvious that as the undrained shear strength increases, the lateral soil resistance increases while the ultimate moment capacity M_y remains constant. The associated plastic flow rule remains unaffected in the Q–M space.

The effect of pile diameter and a corresponding increase of plastic moment are also examined. The pile diameter will change the pile stiffness and the ultimate soil resistance at the same time exhibiting a stiffer response. **Figure 4.7** illustrates the influence of the pile diameter d on the failure envelope on the normalized Q/Q_y–M/M_y space for the case of a pile embedded in a homogeneous cohesive layer with uniform Young's modulus E_s = 50 MPa and undrained shear strength S_u = 50 kPa. The increase in pile diameter (and thus the increase of the relative strength λ and the decrease of the relative stiffness β) has no influence on the failure envelope on the normalized Q/Q_y–M/M_y space. **Figure 4.8** depicts the influence of the pile diameter d on the plastic flow rule on the Q–M space. As the pile diameter d increases both the soil resistance and the ultimate moment increases, but the associativity in plastic flow rule is not violated.

Regarding the effect of the Young's Modulus E_s of the soil, its increase will increase the soil stiffness. **Figure 4.9** presents the influence of Young's Modulus E_s of the soil on the failure envelope for the case of a pile of diameter d = 0.5 m embedded in a homogeneous cohesive layer with undrained shear strength S_u = 100 kPa. Again, the increase of Young's Modulus (and thus the increase of the relative stiffness β) has no influence on the failure envelope on the normalized Q/Q_y–M/M_y space. Even though both the soil resistance and the ultimate moment increase as the Young's Modulus of the soil increases, the variation of Young's Modulus E_s of the soil has no influence on the plastic flow rule on the Q–M space (**Figure 4.10**).

It is thus verified the great advantage of the normalized failure envelopes. When failure envelopes of piles are normalized with their ultimate values, their shape remains unaffected from any other strength parameter of the soil or the pile. In other words, the proposed analytical expressions need no modification. Bransby and Randolph (1999) have also reached a similar conclusion for skirted foundations.

4.2.2 Failure envelope for pile in cohesive Gibson soil

Numerical pushover analyses based on the Winkler model are conducted to verify the failure envelope from **Equations 3.32** and **3.33** using the simple model described before. The problem analyzed is a free-head pile of length 20 m embedded in cohesive Gibson soil. Elastic-perfectly plastic p-y curves are used to define the force-displacement relations of the soil springs. For this problem undrained shear distribution of $S_u = 0.4\ \sigma'_v$, unit weight of $\gamma' = 10\ kN/m^3$, pile plastic moment $M_{pl} = 1.5$ MNm, pile diameter d = 1.0 m and Young's Modulus $E_s = 1800\ S_u$ are assumed while the vertical distance of the soil springs is z = 0.1 m. Different pairs of moment M and lateral force Q are applied at the pile head (at the ground level) until the failure of the pile-soil system. The ratio of incremental displacement to incremental rotation at failure is compared with the one predicted by **Equation 3.36**.

Figure 4.11 depicts the pairs of normalized moment M and lateral force Q at failure. The comparison of the failure envelope calculated by the Winkler model and predicted by the analytical expression is excellent. It can be seen that the maximum absolute value of Q/Q_y for this case is approximately 1.58.

Figure 4.12 shows the vectors from the analytical expression with the assumption of an associated plastic flow rule together with the vectors of incremental displacement failure from the Winkler model. It is logically assumed that the elastic part of the displacements is negligible in comparison to the plastic part of the displacements and thus:

$$u = u^{el} + u^{pl} \approx u^{pl} \tag{4.4}$$

and

$$\theta = \theta^{el} + \theta^{pl} \approx \theta^{pl} \tag{4.5}$$

From geometry, the incremental plastic displacement to rotation ratio equals to the ratio of the plastic displacement to rotation at failure ($\delta u^{pl} / \delta\theta^{pl} = u^{pl} / \theta^{pl}$). The assumption of

an associated plastic flow rule is verified graphically in the figure. Therefore, only the analytical expression for the failure envelope is needed for the definition of the plastic flow rule.

4.2.3 Failure envelope for pile in nonhomogeneous cohesionless soil

Numerical pushover analyses based on the Winkler model are conducted to verify the failure envelope from **Equations 3.43** and **3.44**. A free-head pile of length L = 20 m is embedded in nonhomogeneous cohesionless soil. Elastic-plastic p-y curves are used to define the force-displacement relations of the soil springs. Friction angle $\phi = 32^o$, unit weight of $\gamma = 17$ kN/m^3, pile plastic moment $M_{pl} = 3$ MNm, pile diameter d = 1.0 m and Young's Modulus $E_s = 43700\sqrt{\frac{z}{d}}$ are assumed for this problem while the vertical distance of the soil springs is z = 0.1 m. Different pairs of moment M and lateral force Q are applied at the pile head (at the ground level) until the failure of the pile-soil system. The ratio of displacement to rotation at failure is compared with **Equation 3.47**.

Figure 4.13 presents the pairs of normalized moment M and lateral force Q at failure. Despite the fact that the cohesionless soil is nonhomogeneous, the comparison of the failure envelope calculated by the Winkler model and predicted by the analytical expression is excellent. As in the case of cohesive Gibson soil, the maximum absolute value of Q/Q_y for this case is approximately 1.58. The vectors from the analytical expression with the assumption of an associated plastic flow rule together with the incremental displacement vectors at failure calculated by the Winkler model are compared in **Figure 4.14**. The vectors from both solutions are graphically identical.

As already mentioned, an associated plastic flow rule implies that the foundation at failure behaves as a rigid body. Thus, the plastic displacement to rotation ratio at failure ($\delta u^{pl}/\delta\theta^{pl}$) is equal to the depth of plastic hinge. Defining β as the angle of the pairs QM at failure starting from $\beta = 0^o$ for point $Q = Q_y$ and $M = 0$ and going counterclockwise on the Q/Q_y–M/M_y space, **Figure 4.15** compares the variation of the displacement over rotation ratio at failure for different failure points with the depth of plastic hinge for the same points. It can be seen that apart from the regions where $\left|M/M_y\right| = 1$ (in this case for $\beta = 90^o$ - 145^o and $\beta = 270^o$ - 325^o) where the structural

failure of the pile takes place at the pile head, the plastic displacement to rotation ratio coincides with the depth of plastic hinge. This is an indication of an associated plastic flow rule.

4.2.4 Failure envelope for pile in two cohesive layers with $S_{u1} < S_{u2}$

Numerical pushover analyses based on the Winkler-beam model are conducted to verify the failure envelope from **Equations 3.55** and **3.56**. A free-head pile of length L = 20 m is embedded in two layers of cohesive soils with $S_{u1} < S_{u2}$. The first layer has an undrained shear strength S_{u1} = 40 kPa, Young's Modulus $E_s = 1800\ S_{u1}$ and thickness b = 2 m, the second layer has an undrained shear strength S_{u2} = 100 kPa and Young's Modulus $E_s = 1800\ S_{u2}$ and pile plastic moment M_{pl} = 3 MNm and diameter d = 1.0 m are assumed for this problem. Different pairs of moment M and lateral force Q are applied at the pile head (at the ground level) until the failure of the pile-soil system. The ratio of displacement to rotation at failure is compared with **Equation 3.59**.

Figure 4.16 shows the pairs of normalized moment M and lateral force Q at failure. Again the failure envelope from the Winkler model coincides with the failure envelope from the analytical expression. **Figure 4.17** compares the vectors from the analytical expression with the assumption of an associated plastic flow rule together with the incremental displacement vectors at failure calculated by the Winkler model. The assumption of an associated plastic flow rule is verified also in this case. This result was somehow expected since the macroscopic soil-foundation response is examined. Similar results for the macroscopic response of soil-shallow foundations have been observed (Cremer et al, 2001; Chatzigogos et al, 2011).

4.2.5 Failure envelope for pile in cohesionless soil with horizontal force Q and moment M at a distance e from the ground surface

Numerical pushover analyses based on the Winkler-beam model are conducted to verify the failure envelope from **Equations 3.65** and **3.66**. The case adopted for the analyses is a free-head pile-column with 24 m length, 20 m of which are embedded in nonhomogeneous cohesionless soil. For this problem a friction angle $\phi = 32^o$, unit weight of $\gamma = 17$ kN/m^3, pile plastic moment M_{pl} = 3 MNm, pile diameter d = 1.0 m and Young's

Modulus $E_s = 43700 \sqrt{\frac{z}{d}}$ are assumed. Different pairs of moment M and lateral force Q are applied at the pile head (4 m above the ground level) until the failure of the pile-soil system. The ratio of displacement to rotation at failure is compared with that from **Equation 3.65**.

Figure 4.18 shows the pairs of normalized moment M and lateral force Q at failure. As expected, the failure envelope from the Winkler model coincides with that from the analytical expression. Again, the assumption of an associated plastic flow rule is verified since the vectors from the analytical expression with the assumption of an associated plastic flow rule are parallel to those from the incremental displacements at failure calculated by the Winkler model as shown in **Figure 4.19**.

4.3 3D FINITE ELEMENT APPROACH

The proposed failure envelope and associated plastic flow rule have been confirmed by the Winkler model. The Winkler model is a widespread used tool for the simulation of the pile but it does not take into consideration the exact physics of the problem, especially the geometric nonlinearities. For this reason the proposed failure envelope and the plastic flow rule are further verified against three-dimensional numerical analyses for a flexible pile embedded in cohesive or cohesionless soil using the finite element code ABAQUS. The 3D numerical analyses examine the influence of: (a) different constitutive soil models that consist of non-associated flow rules, (b) geometric nonlinearities, and (c) the vertical load acting at the pile head.

4.3.1 Finite element modeling

A 12 m long pile with 0.72m diameter embedded in the soil is considered. The distance from the pile tip to the bottom of the model is 3.33 diameters. The pile is assumed to be elastoplastic. **Figure 4.20** depicts the cross-section for the finite element discretization of the problem. Approximately 40000 elements were used for each analysis. The soil and the pile are modeled as described in **Chapter 2**.

The vertical distance of the elements is 0.3 m, small enough to avoid mesh sensitivity problems as was observed in the Winkler analysis but also big enough to ensure a reasonable computational time. The mesh is refined up to a distance of 7

diameters around the pile to better capture the intense nonlinearity of this area. Zero-displacement boundary conditions prevent the out-of-plane displacements at the vertical sides of the model, while the base is fixed in all three coordinate directions. Despite the symmetry of the problem the whole model is analyzed. Approximately 40000 elements were used for each analysis.

4.3.2 Flexible pile in cohesionless soil – Verification against different constitutive soil models

For the case of a flexible pile embedded in nonhomogeneous cohesionless soil two different soil constitutive models are concerned: (a) the constitutive model (Model CT) proposed in **Chapter 2** that has nonlinear kinematic hardening and non-associated plastic flow rule, and (b) the Mohr-Coulomb constitutive model that has a non-associated flow rule. No separation at the pile- soil interface is allowed in the analysis, since the cohesionless soil collapses and moves with the pile as the pile is laterally loaded.

A similar problem as in the case of a flexible pile embedded in sand in the Winkler model is studied. A friction angle ϕ = 32^o, unit weight of γ = 17 kN/m^3, and Young's Modulus E_s=43700$\sqrt{\frac{z}{d}}$ are assumed for the soil, while pile has plastic moment M_{pl} = 1.2 MNm and Young's Modulus E_p = 25 GPa.

Initially, the three-dimensional analysis is compared with a beam-on-Winkler-foundation model. Different methods are used in order to calculate the ultimate lateral response of the pile on the Winkler model. For cohesionless soils, Broms (1964) adopted a linear distribution of soil resistance with depth and the ultimate soil resistance was assumed to be equal to n = 3 times the Rankine passive pressure K_p. Pender (1995) proposed a value of n = 5 times the Rankine passive pressure according to his results from finite element programs.

Reese et al (1974) in order to compute the ultimate soil resistance per unit length of a pile embedded in cohesionless soil proposed using the smaller of the values of the following equations:

$$p_{st} = \gamma z\left[\frac{K_0 z\tan\varphi\sin\beta}{\tan(\beta-\varphi)\cos\alpha}+\frac{\tan\beta(b+z\tan\beta\tan\alpha)}{\tan(\beta-\varphi)}+K_0 z\tan\beta(\tan\varphi\sin\beta-\tan\alpha)-K_\alpha b\right] \qquad (4.6)$$

$$p_{sd} = K_{\alpha} b\gamma z\left(\tan^8\beta - 1\right) + K_0 b\gamma z \tan\varphi \tan^4\beta \quad (4.7)$$

where $\alpha = \phi/2$, $\beta = 45+\phi/2$, $K_0 = 0.4$, $K_{\alpha} = \tan^2(45-\phi/2)$, γ the unit weight of the sand, b the diameter of the pile, and z depth.

According to API (2000) the ultimate lateral bearing capacity for sand is the smallest value of the following equations:

$$p_{us} = \left(C_1 H + C_2 D\right)\gamma H \quad (4.8)$$

$$p_{ud} = C_3 D\gamma H \quad (4.9)$$

where p_u ultimate resistance (force/unit length for shallow or deep depths), γ effective soil weight, H depth, C_1, C_2, C_3 coefficients determined from **Figure 4.21** as function of the friction angle of the sand and D average pile diameter from surface to depth.

Reese and Van Impe (2001) proposed the following equation for the ultimate soil resistance per unit length of a pile in c-ϕ soils:

$$p_{ult} = \overline{A} p_{ult\varphi} + p_{ultc} \quad (4.10)$$

where $\overline{A}$ can be taken from **Figure 4.22**, $p_{ult\phi}$ the friction component of the soil resistance taken as the smaller of the values below:

$$p_{ult\varphi} = \gamma z\left[\frac{K_0 z \tan\varphi \sin\beta}{\tan(\beta-\varphi)\cos\alpha} + \frac{\tan\beta\left(b + z\tan\beta\tan\alpha\right)}{\tan(\beta-\varphi)} + K_0 z\tan\beta\left(\tan\varphi\sin\beta - \tan\alpha\right) - K_{\alpha} b\right] \quad (4.11)$$

$$p_{ult\varphi} = K_{\alpha} b\gamma z\left(\tan^8\beta - 1\right) + K_0 b\gamma z \tan\varphi \tan^4\beta \quad (4.12)$$

and p_{ultc} the cohesion component of the soil resistance taken as the smaller of the values below:

$$p_{ultc} = \left(3 + \frac{\gamma}{c} z + \frac{J}{b} z\right) cb \quad (4.13)$$

$$p_{ultc} = 9cb \quad (4.14)$$

where J = 0.25 - 0.5.

Thus, the lateral response of a pile in sand from the aforementioned theoretical expressions and calculated from the Finite Element analysis is compared in **Figure 4.23**. More precisely, the methods of analysis are: (1) the numerical three-dimensional model with the Mohr-Coulomb constitutive model for soil cohesion c = 1 kPa, (2) the numerical three-dimensional model with the Mohr-Coulomb constitutive model for soil cohesion c = 5 kPa, (3) the numerical three-dimensional model with Model CT from **Chapter 2** with

for soil cohesion c = 5 kPa, (4) the Winkler model with Broms' ultimate resistance nK_p for n = 3, (5) the Winkler model with Broms' ultimate resistance nK_p for n = 5, (6) the Winkler model with Broms' ultimate resistance nK_p for n = 8, (7) the Winkler model with Reese's ultimate resistance for sand, (8) Reese's ultimate resistance for c-ϕ soils, and (9) the Winkler model with API's ultimate resistance for sand. It is obvious that all the Winkler model solutions have lower ultimate lateral resistance and stiffness than those derived from three-dimensional analyses which capture better the physics of the problem. To be more precise, the response of the API guidelines is the most flexible and gives the smallest ultimate resistance from the methods examined. Broms' method for n = 3 has the second smallest response, then Reese's method for cohesionless soils and finally Reese's method for c-ϕ soils with cohesion c = 5 kPa. Pender's suggestion (1995) for using Broms' method with n = 5 is closer to the three-dimensional ultimate response having also a similar stiffness. In order for Broms' method to match exactly the ultimate lateral response of the pile with that calculated from the Mohr-Coulomb constitutive model with cohesion c = 1 kPa, n = 8 must be used. As expected, when the soil cohesion in the Mohr-Coulomb constitutive model increases from c = 1 kPa to c = 5 kPa the ultimate lateral response of the pile and the stiffness also increase. Finally, it is noted that the Mohr-Coulomb model has a similar response to Model CT from **Chapter 2**. It is thus evident that the method of analysis influences the predicted pile response.

Figures 4.24 compares the normalized M−Q failure envelope predicted by the analytical expression (**Equations 3.43** and **3.44**) and calculated by the three-dimensional numerical analysis with: (a) the constitutive model CT for cohesionless soil, and (b) the Mohr-Coulomb constitutive model. In general, the comparison is very satisfactory with a minor deviation at the vertices of the envelope. This is attributed to the mesh coarseness, since the vertical thickness of the solid elements is 0.3 m. Denser Finite Element model leads to even more accurate results.

Figure 4.25 illustrates the vectors from the analytical expression with the assumption of an associated plastic flow rule together with the incremental displacement vectors at failure from the three-dimensional numerical analyses with (a) the constitutive model CT, and (b) the Mohr-Coulomb constitutive model for the case of pile embedded in cohesionless soil. It can be observed that the 3D Finite Element results support the assumption of an associated plastic flow rule. This is verified by both constitutive models

with non-associated flow rules. The macroscopic soil-foundation response (in terms of M−Q failure envelope) is practically insensitive to the parameters of the applied constitutive model. From this figure it can also be observed that the ultimate moment of the pile is the same for the analytical expression and both three-dimensional analyses. On the contrary, the ultimate lateral force calculated by the three-dimensional analyses is larger than the predicted one by the analytical expression which is calculated from limit equilibrium analysis. It is noted that the associated flow rule is unaffected by the method of analysis employed.

Figure 4.26 shows the contours of the plastic strain magnitude (plotted on the deformed mesh) for a flexible pile embedded in nonhomogeneous cohesionless soil calculated with the constitutive model proposed in **Chapter 2** for three different angles of loading: (a) $\beta = 0^o$ ($Q / Q_y = 1$, $M / M_y = 0$), (b) $\beta = 70^o$ ($Q / Q_y = 0.28$, $M / M_y = 0.88$), and (c) $\beta = 160^o$ ($Q / Q_y = -1.3$, $M / M_y = 0.47$). The plastic strains are plotted on the same scale. It is evident that larger plastic strains develop around the pile when the moment acts on a different direction than the lateral force. Similarly, when the moment acts on the same direction with the lateral force, the developed plastic strains are less than in the case of the pure lateral loading.

4.3.3 Flexible pile in cohesive soil – Verification against geometric nonlinearities

For the case of a flexible pile embedded in cohesive soil, the soil constitutive model for cohesive soils introduced by Gerolymos et al (2005) which takes into consideration the material nonlinearity of the soil and presented in **Chapter 2** is used. In addition to soil plastification, geometric nonlinearities, such as gapping and slippage, are another important source of nonlinearity for cohesive soils. To simulate this behavior, surface interaction elements are used at the pile-soil interface that allow sliding and detachment of the pile from the soil. When the tensile forces overcome the initial confining pressure, a gap occurs.

For this problem the yield stress at zero plastic strain σ_o is assumed to be equal to 1/3 of the maximum yield stress σ_y. In these FE analyses a homogeneous cohesive soil is considered with constant undrained shear strength S_u = 60 kPa and constant Young's Modulus distribution E_s = 90 MPa with depth. Two cases are studied regarding the pile-soil interface conditions: (a) fully bonded conditions, and (b) displacement-free

conditions (separation and slippage are allowed as shown in **Figure 4.27**). For the latter case, the friction coefficient for the pile-soil interface is considered to be $\mu = 0.7$.

The pairs of moment M and lateral force Q at failure normalized with the values of moment at failure for pure moment conditions M_y and lateral force at failure for pure lateral force conditions Q_y from the three-dimensional numerical analysis with and without the formation of the gap are shown in **Figure 4.28**. The comparison of the failure envelope calculated by the Finite Element models against that predicted by the analytical expression is satisfactory. As in the case of the pile embedded in cohesionless soils, a small discrepancy is observed at the part where the moment on the pile head acts on the opposite direction from the lateral force, at the region where the moment prevails on the behavior of the pile which is attributed to the mesh density of the model. The formation of a gap has no influence on the shape of the failure envelope since in every case the lateral force and the moment at failure are normalized with the corresponding maximum moment and lateral force of each case.

Furthermore, **Figure 4.29** illustrates the characteristic zones of the pile response at the M−Q failure envelope. Due to symmetry only half of the failure envelope is presented. The following four zones can be identified:

(1) Zone of combined positive M–Q loading where the moment prevails in the response of the system. The pile is subjected to small horizontal displacement and large positive rotation. The plastic hinge is developed at the region close to the pile head.

(2) Zone of combined positive M–Q loading where the horizontal force prevails in the response of the system. The pile is subjected to large horizontal displacement and small positive rotation. The plastic hinge is developed at a certain depth.

(3) Zone of combined horizontal force and negative moment where the horizontal force prevails in the response of the system. The pile is subjected to large horizontal displacement and small positive rotation. The plastic hinge is developed at higher depths (compared to zone 2) since the opposite acting moment increases the bending moment capacity of the foundation.

(4) Zone of combined horizontal force and negative moment where the moment prevails in the response of the system. The pile is subjected only to a large negative rotation. The plastic hinge is developed at the pile head.

Figure 4.30 compares the horizontal force−lateral displacement curves at the pile head for pile embedded in cohesive soil with (a) fully bonded conditions, and (b) displacement-free conditions at characteristic points along the failure envelope. As already stated, in the case of pile embedded in homogeneous cohesive soil, the horizontal force capacity increases from point A ($M/M_y = 1$, $Q/Q_y = 0$) up to point ($M/M_y = -1$, $Q/Q_y = 2^{0.5}$). It can be observed the horizontal force calculated from the analysis with fully bonded conditions is always higher than the one from the analysis with displacement-free conditions. For Point D (pure horizontal force at the pile head), the calculated ultimate horizontal force from the analysis with fully bonded conditions is larger than the one predicted by the analytical expression. On the contrary, the ultimate horizontal force calculated by the three-dimensional analysis with displacement-free conditions is about 0.7 times the ultimate lateral response of the pile with fully bonded conditions, which was expected since the soil resistance p_y decreases with the gap formation and the ultimate lateral resistance of the pile-soil system is a function of the square root of the soil resistance. What is of interest is that according to the soil resistance p_y calculated from the analysis with fully bonded conditions, the ultimate soil reaction predicted by Broms' method should have a = 12 rather than a = 10 which was used in this case. For Point F, even though the horizontal force is acting at the pile head, the latter does not move up to the point of failure due to the moment acting towards the opposite direction.

Figure 4.31 presents the computed bending moment distributions at different stages of loading for pile embedded in cohesive soil with fully bonded conditions at characteristic points along the failure envelope. As can be observed, the developed bending moment at failure never exceeds the yielding moment of the pile. Moving from point A to point E, the depth of the maximum bending moment increases, while at points A and F (where the bending moment is the loading that causes the pile failure) the depth of the maximum bending moment is at the ground surface. Similar behavior is observed for the shear force distributions (**Figure 4.32**).

Figures 4.33 illustrates the vectors from the analytical expression with the assumption of an associated plastic flow rule along with the incremental displacement vectors at failure from the three-dimensional numerical analyses with (a) fully bonded conditions, and (b) displacement-free conditions for the case of pile embedded in cohesive soil. Apparently, the vectors of incremental displacements in the three dimensional analysis are vertical to the failure envelope on the Q–M space. From this figure it can also be observed that the ultimate moment of the pile is the same for both the analytical expression from Broms' method and the three-dimensional analysis. For the analysis with fully bonded conditions, the calculated ultimate lateral force is larger than the one predicted by the analytical expression. On the contrary, the ultimate lateral force calculated by the three-dimensional analysis with displacement-free conditions is about 0.7 times the ultimate lateral response of the pile with fully bonded conditions, which was expected since the soil resistance p_y decreases with the pile-soil separation and the ultimate lateral resistance of the pile-soil system is a function of the square root of the soil resistance.

4.3.4 M–Q–N Failure envelope for flexible pile in cohesive soil

The problem of a pile in cohesive soil under undrained conditions is studied further by taking into consideration the effect of vertical loading. In this case, the distance from the pile tip to the bottom of the model is 23.33 diameters ensuring that the boundaries do not affect the response of the pile-soil system. The pile is assumed to behave elastoplasticaly. **Figure 4.34** depicts the finite element discretization for the problem studied. Approximately 80000 elements were used for each analysis. The friction coefficient of the pile-soil interface is considered to be $\mu = 0.5$.

Initially, the tip resistance of the pile is examined under static vertical load. The tip resistance of a pile embedded in cohesive soil is given by:

$$Q_b = f_b A_b = S_u N_c A_b \tag{4.15}$$

where A_b is the cross-sectional area of the pile tip, S_u the undrained shear strength of the soil and N_c a bearing capacity coefficient which equals to $N_c = 13$ from back-calculation of this analysis. The shaft resistance of the pile is given by:

$$Q_f = f_s\left(\text{contact area}\right) = \mu K_0 \sigma_v \left(\text{perimeter}\right)\left(\text{length}\right) \tag{4.16}$$

where K_0 the lateral earth pressure coefficient at rest.

The ultimate resistance from the pile is then calculated as:

$$N_y = Q_b + Q_f \tag{4.17}$$

and the comparison of N_y from the 3D Finite Element analysis with the one from the analytical expression is quite satisfactory ($N_{y,ABQ}$ = 1162kN and $N_{y,Analytical}$ = 1137kN).

Having determined the ultimate vertical load of the pile, the failure envelopes on the Q–M space are examined under the influence of different portion of the ultimate vertical load of the pile, N_y. For this reason, the ultimate lateral force capacity (under pure horizontal force at the pile head, Q_y) and the ultimate moment capacity (under pure moment acting on the pile head, M_y) of the pile are first computed from the 3D Finite Element model. Then, the Q–M failure envelopes are derived by two loading stage analyses. In the first loading stage, a prescribed vertical load, selected as a percentage of the ultimate vertical capacity of the pile, is applied on the pile head. In the second loading stage, the vertical load remains constant, and a combination of overturning moment M and horizontal force Q are applied to the pile head. Both the horizontal force and overturning moment are gradually increased until complete failure of the pile. **Figure 4.35** shows the failure envelope M/M_y–Q/Q_y for four different levels of the ultimate vertical load: 0, $0.25N_y$, $0.5N_y$ and $0.75N_y$. The developed normalized failure envelopes are identical regardless of the magnitude of the vertical load.

Figure 4.36 depicts a representative envelope calculated for $0.25N_y$, $0.5N_y$ and $0.75N_y$ and the plastic strains for characteristic points along the envelope. Due to symmetry, only half of the envelope is presented. As the vertical load increases, the failure mechanism in each point remains unaffected and minor increase of the plastic strains is observed. The six characteristic points along the surface correspond to:

(a) pure overturning moment M_y

(b) combined positive M–Q loading where the moment governs the response of the system

(c) combined positive M–Q loading where the horizontal force governs in the response of the system

(d) pure horizontal force Q_y

(e) combined maximum horizontal force and maximum overturning moment acting on the opposite direction

(f) combined maximum overturning moment and horizontal force where the moment governs the response of the system.

Points (a) and (f) correspond to pure structural failure, while the plastic strain increase when moving from point (b) towards (e).

Furthermore, the plastic flow rule remains also associated, unaffected by the presence of the vertical load (**Figure 4.37**). In other words, all the points with the same inclination angle on the Q/Q_y–M/M_y space (same angle β), regardless the applied vertical load, have the same ratio of incremental displacement to incremental rotation at failure. The above remarks justify the current design practice that considers axial and lateral loads separately and independently without considering the effect of interaction between the different load directions.

The influence of the horizontal force on the action of moment and vertical load on the pile head was studied, as shown in **Figure 4.38** for values of: 0, $0.5Q_y$ and $0.9Q_y$. When no horizontal force acts on the pile head (**Figure 4.38a**), the failure envelope on the M/M_y–N/N_y space is completely symmetric and the maximum vertical force imposed to the pile overexceeds the axial bearing capacity at vertical loading. This increase of the axial bearing capacity is attributed to the increase of shear resistance with increasing passive pressures (Coulomb theory) due to the lateral loading. When the horizontal force acting on the pile head is half of the ultimate horizontal force (**Figure 4.38b**), the symmetry is lost. The overturning moment acting towards the same direction with the horizontal force is less than the ultimate moment, since the horizontal force contributes also to the plasticization of the soil. On the other hand, the maximum vertical load of the pile exceeds the ultimate vertical load of the pile, since passive pressures increase due to the lateral loading. When the overturning moment and the horizontal force are of the same sign the increase of the maximum vertical load is higher than in the case of the negative sign. This Behavior increases further when the horizontal force is close to its ultimate value (**Figure 4.38c**). However, in this case the increase of the maximum vertical load takes place when the moment is applied towards the opposite direction of the horizontal force, since the moment acts beneficially to the plasticized soil which is close to failure under the action of the horizontal force.

Figure 4.39 presents the failure envelope of a single pile embedded in cohesive soil on the three-dimensional space M/M_y–Q/Q_y–N/N_y with the simplification that the maximum vertical load of a flexible pile cannot exceed its ultimate vertical load. It should be noted that this failure envelope refers to pile-soil system failure for constant values of plastic moment of the pile material (its lowest value) under any loading combination. A more precise failure envelope should also take into consideration the interaction diagrams of the pile material.

4.4 SUMMARY AND CONCLUSIONS

The failure envelope of flexible single pile under combine Q–M loading for different soil conditions derived from the analytical expressions of **Chapter 3** as well as the assumption of an associated plastic flow rule are verified through force-controlled Winkler model analyses. The shape of the failure envelope in the normalized Q/Q_y–M/M_y space remains unaffected from any other strength parameter of the soil or the pile such as the soil Young's Modulus, the soil strength and the pile diameter. The failure envelope can be determined when the ultimate horizontal capacity Q_y (from pure horizontal loading) and the ultimate moment capacity M_y (from pure overturning moment loading) of the soil-pile system are known.

The assumption of an associated plastic flow rule is graphically verified by the normality of the incremental displacement vectors at failure from the Winkler model. It is also found that the plastic displacement to rotation ratio at failure ($\delta u^{pl}/\delta\theta^{pl}$) is equal to the depth of the plastic hinge. Since the plastic flow rule is confirmed to be of associated type, only the analytical expression for the failure envelope is needed for its determination.

Both the theoretical expression of the failure envelope and the associated plastic flow rule are further evaluated against 3D numerical analyses with two different constitutive models comprised of non-associated flow rules. It is shown that the macroscopic soil-foundation response is insensitive to the features of the constitutive model used in the analyses. The effect of slippage and separation at the pile-soil interface is also examined and proven to have no influence on the shape of the normalized failure envelope and on the associated plastic flow rule.

The M−Q failure envelope is characterized by the following four zones:

(1) Zone of combined positive M–Q loading where the moment prevails in the response of the system. The pile is subjected to small horizontal displacement and large positive rotation. The plastic hinge is developed at the region close to the pile head.

(2) Zone of combined positive M–Q loading where the horizontal force prevails in the response of the system. The pile is subjected to large horizontal displacement and small positive rotation. The plastic hinge is developed at a certain depth.

(3) Zone of combined horizontal force and negative moment where the horizontal force prevails in the response of the system. The pile is subjected to large horizontal displacement and small positive rotation. The plastic hinge is developed at higher depths (compared to zone 2) since the opposite acting moment increases the bending moment capacity of the foundation.

(4) Zone of combined horizontal force and negative moment where the moment prevails in the response of the system. The pile is subjected only to a large negative rotation. The plastic hinge is developed at the pile head.

Based on the 3-D analyses, analytical expression of the failure envelope for M–Q–N loading is proposed without taking into consideration the interaction diagrams of the pile material. This envelope is an extension of the proposed failure envelopes for the Q–M space being insensitive to the vertical load. The general expression of the yield surface of a flexible pile (with reference to its top) in M–Q–N space could be approximated by:

$$f = \left| \mathrm{sgn}(Q) \left| \frac{Q}{Q_y^*} \right|^B + \mathrm{sgn}(Q) A \left| \frac{Q}{Q_y^*} \right| + \mathrm{sgn}(M) \left| \frac{M}{M_y^*} \right| \right| - 1 = 0 \quad \text{for} \quad \left| \frac{M}{M_y} \right| < 1 \tag{4.18}$$

$$f = \left| \frac{M}{M_y} \right| - 1 = 0 \quad \text{for} \quad \left| \frac{M}{M_y} \right| = 1 \tag{4.19}$$

$$f = \left| \frac{N}{N_y} \right| - 1 = 0 \quad \text{for} \quad \left| \frac{N}{N_y} \right| = 1 \tag{4.20}$$

with A, B, Q_y^* and M_y^* constant values, depending on the problem studied (**Table 3.1**).

REFERENCES

American Petroleum Institute (API), 2000, Recommended practice for planning, designing and constructing fixed offshore platforms-working stress design, *API Recommended Practice 2A-WSD (RP 2A-WSD)*, 21st edn

Bransby M.F., Randolph M.F., 1999, "The effects of embedment on the undrained response of caisson foundations to combined loadings", *Soils and Foundations*, 39 (4), pp 19-34

Broms B.B., 1964, "Lateral resistance of piles in cohesionless soils", *Journal of Soil Mechanics and Foundation Division*, ASCE 90 (SM3), pp 123-156

Chatzigogos CT, Pecker A, Salençon J., 2007, "Seismic bearing capacity of a circular footing on a heterogeneous cohesive soil", *Soils and Foundations*, 47(4), pp. 783-797

Crémer C., Figini R., Pecker A., Salençon J, 2011, "A macroelement formulation for shallow foundations on cohesive and frictional soils", *International Journal for Numerical and Analytical Methods in Geomechanics*, 35, pp 902-931

Dassault Systèmes Simulia Corp, 2009, *ABAQUS User's Manual*, Providence, RI, USA

Gerolymos N., Gazetas G., 2005, "Phenomenological model applied to inelastic response of soil-pile interaction systems", *Soils and Foundations*, **45** (4), pp 119-132

Gourvenec S., 2004, "Bearing capacity under combined loading – a study of the effect of shear strength heterogeneity", *9th Australian and New Zealand Conference on Geomechanics*, Auckland, New Zealand, pp 527-533

Makris N., Gazetas G., 1992, "Dynamic pile-soil-pile interaction. Part II: Lateral and seismic response", *Earthquake Engineering and Structural Dynamics*, 21, pp 145-162

Pender M.J, 1995, *Aseismic Foundation Design Analysis*, Continuing Education Course, University of Auckland, New Zealand

Poulos H.G., Davis E.H., 1980, *Pile Foundation Analysis and Design*, John Wiley and Sons, New York

Reese L.C., Cox W.R., Koop F.D., 1974, Analysis of laterally loaded piles in sand, *Proceedings of the VI Annual Offshore Technology Conference*, Houston, Texas, 2: 473-485

Reese L.C., Van Impe W.F., 2001, *Single Piles and Pile Groups under Lateral Loading*, A.A.Balkema, Rotterdam

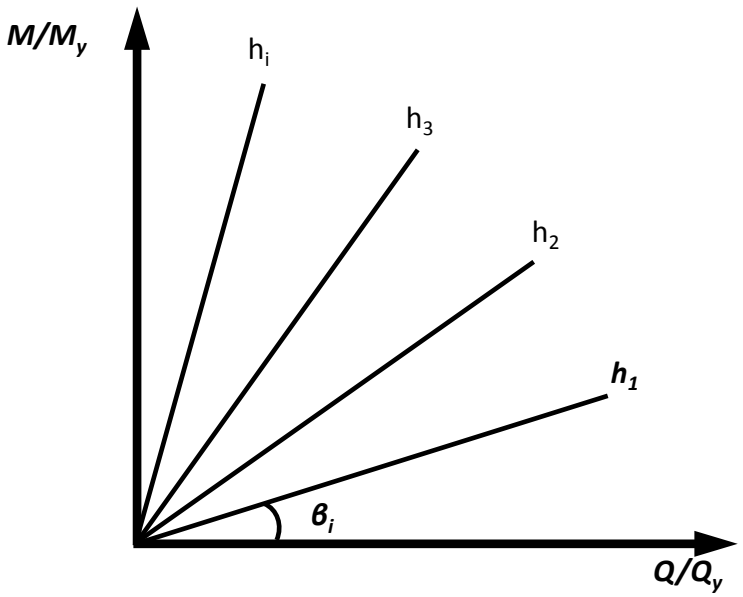

$\tan\beta_i = MQ_y / QM_y$

Figure 4.1: The concept of radial paths of loading which is used in the force-controlled analyses for the lateral response of pile foundations

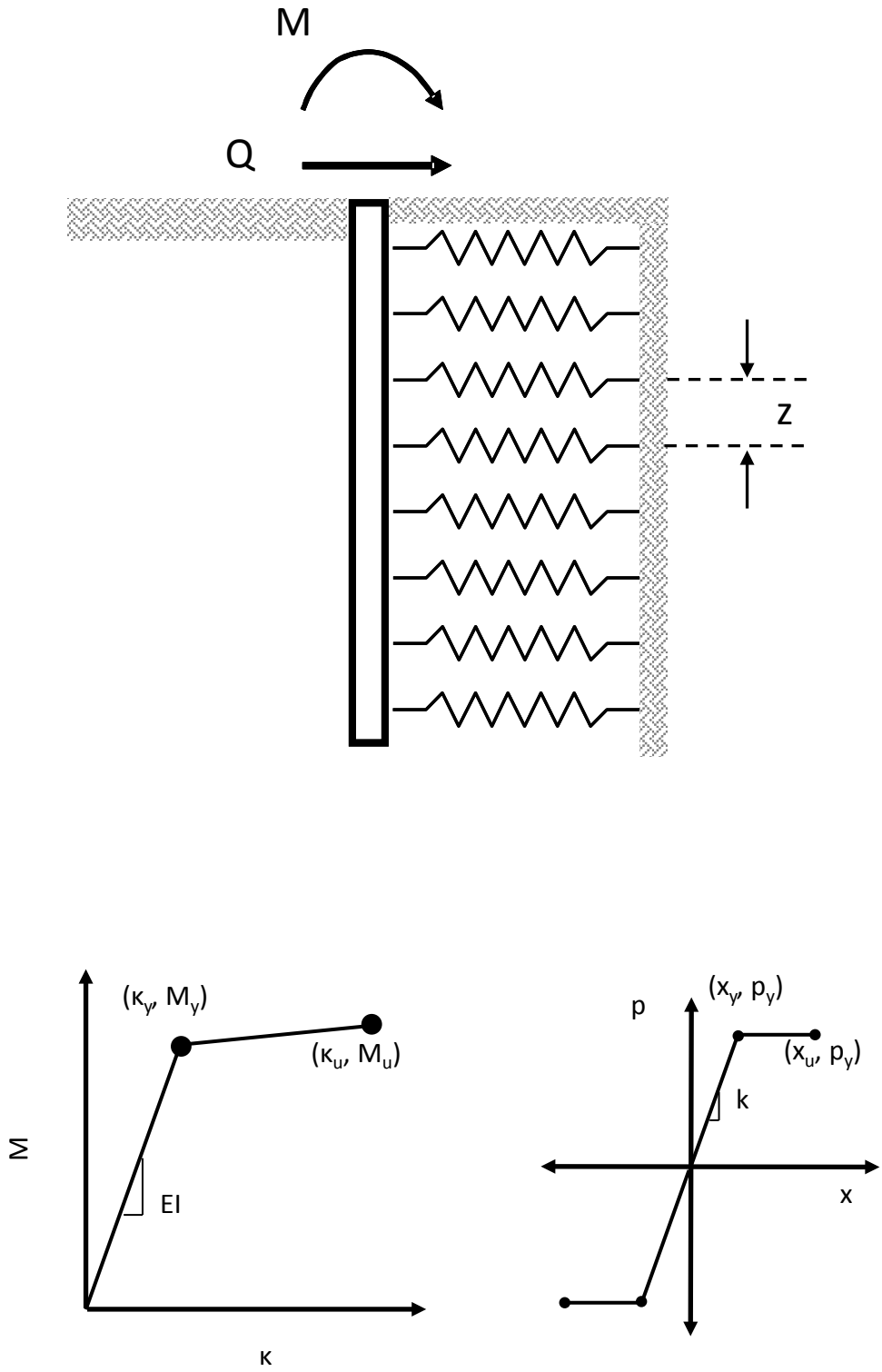

Figure 4.2: Ideal analytical Winkler model: (a) Free-head pile in homogeneous Winkler soil, (b) moment–curvature relationship, and (c) soil reaction–displacement relationship

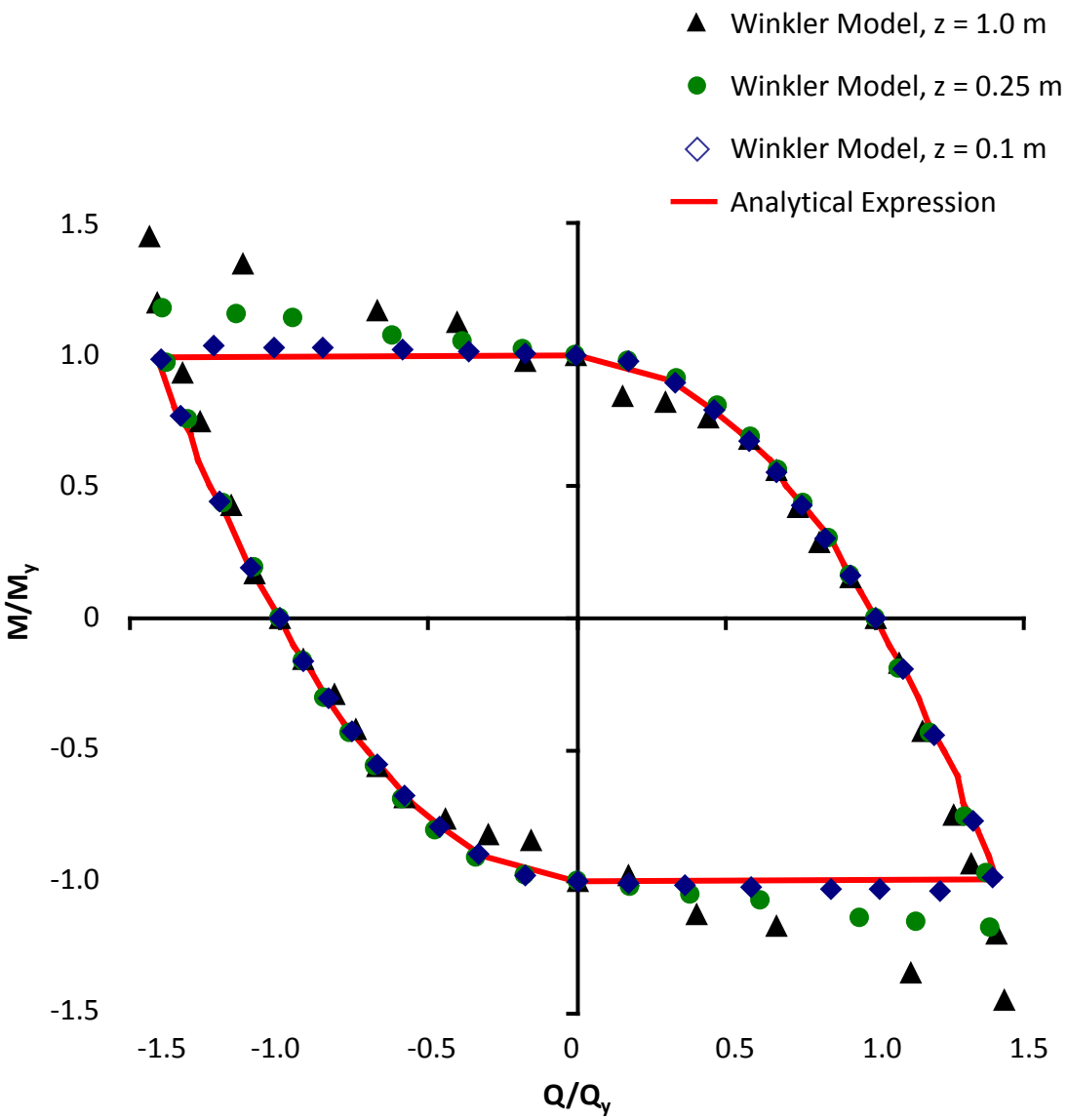

Figure 4.3: Influence of the vertical distance z of the Winkler springs on the failure envelope

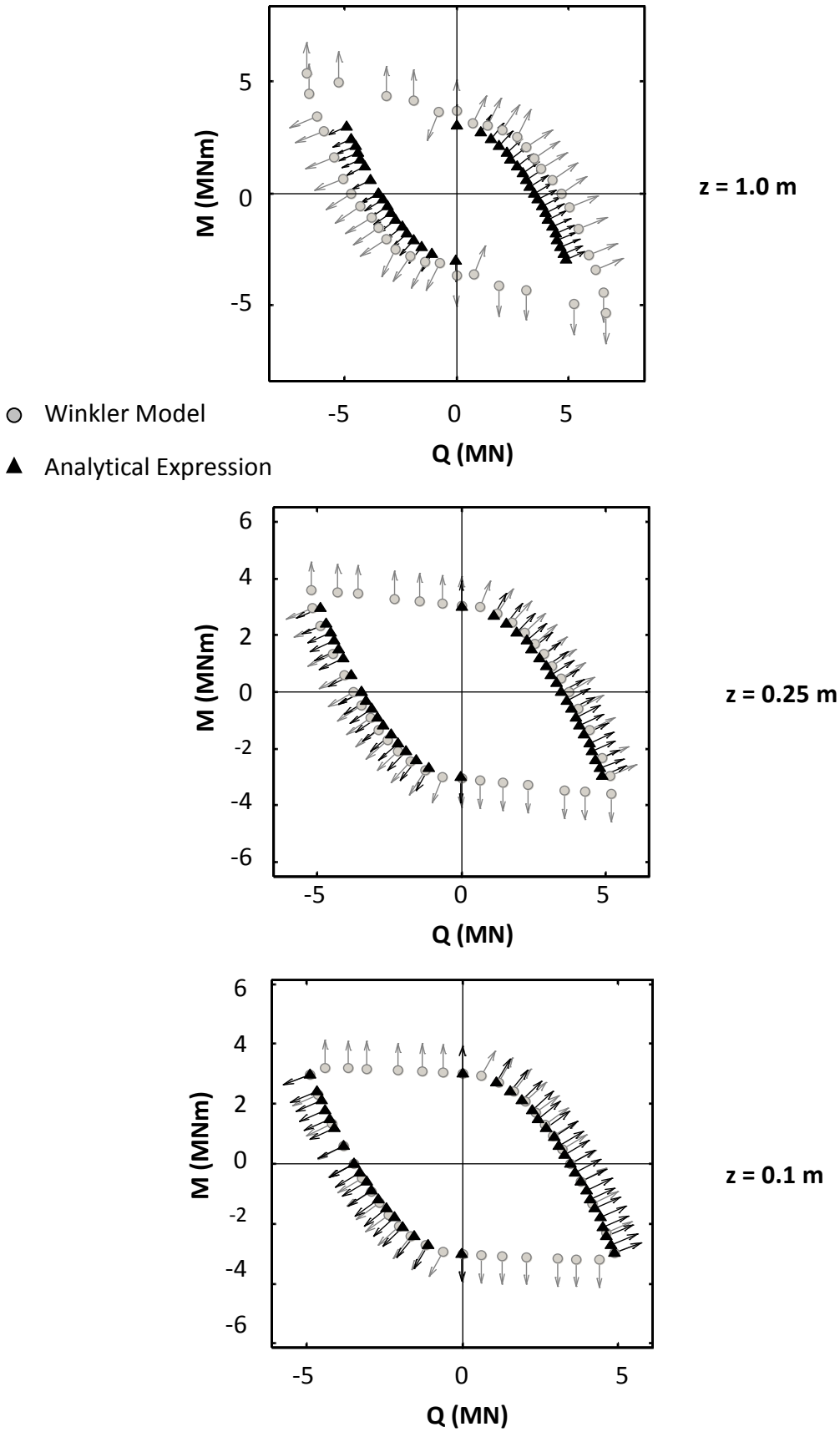

Figure 4.4: Influence of the vertical distance z of the Winkler springs on the flow rule on the Q–M space

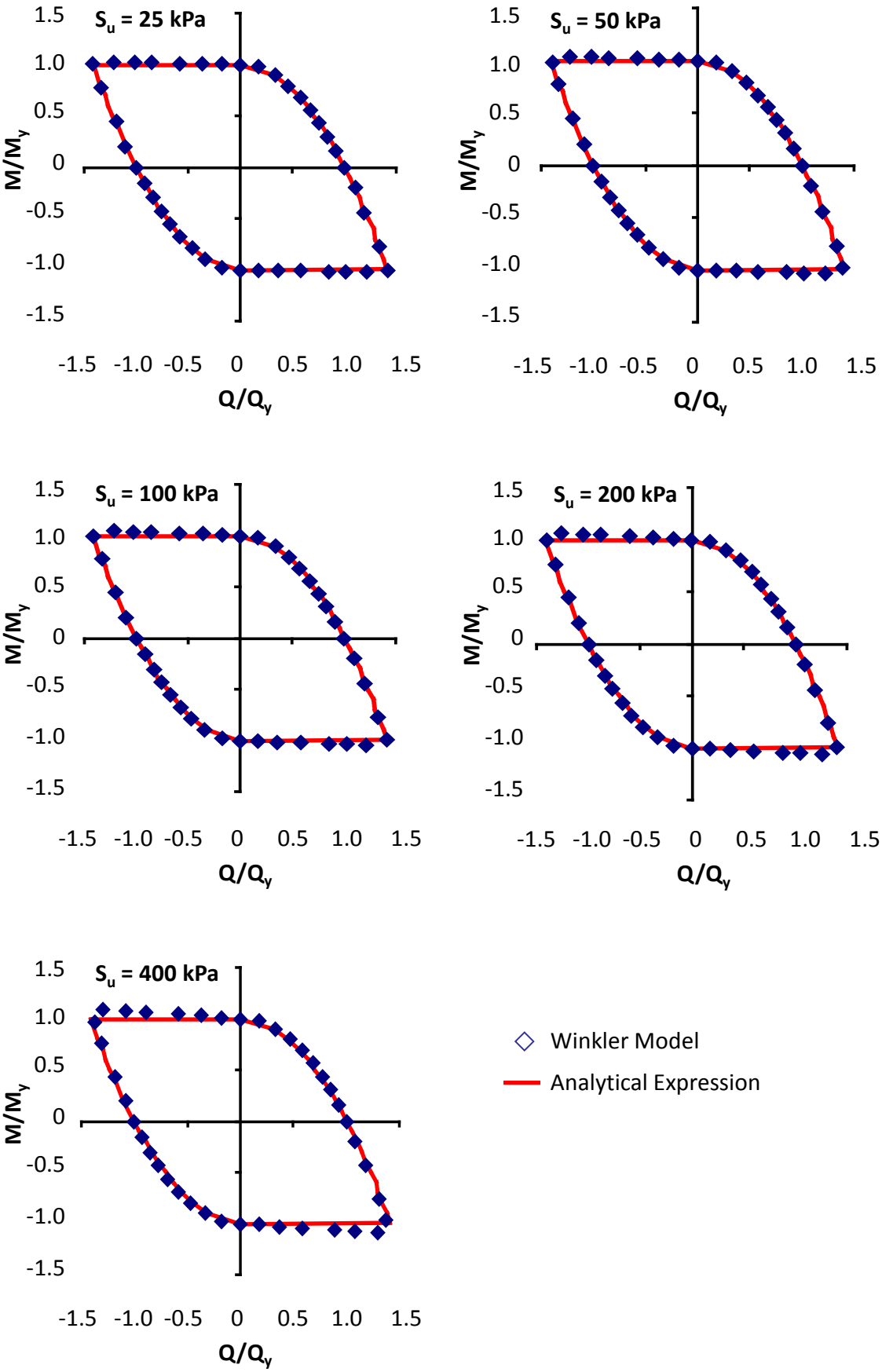

Figure 4.5: Influence of the undrained shear strength S_u on the failure envelope from the analytical expression for the case of a pile of diameter d = 1 m, embedded in a homogeneous cohesive layer with uniform Young's modulus E_s = 100 MPa

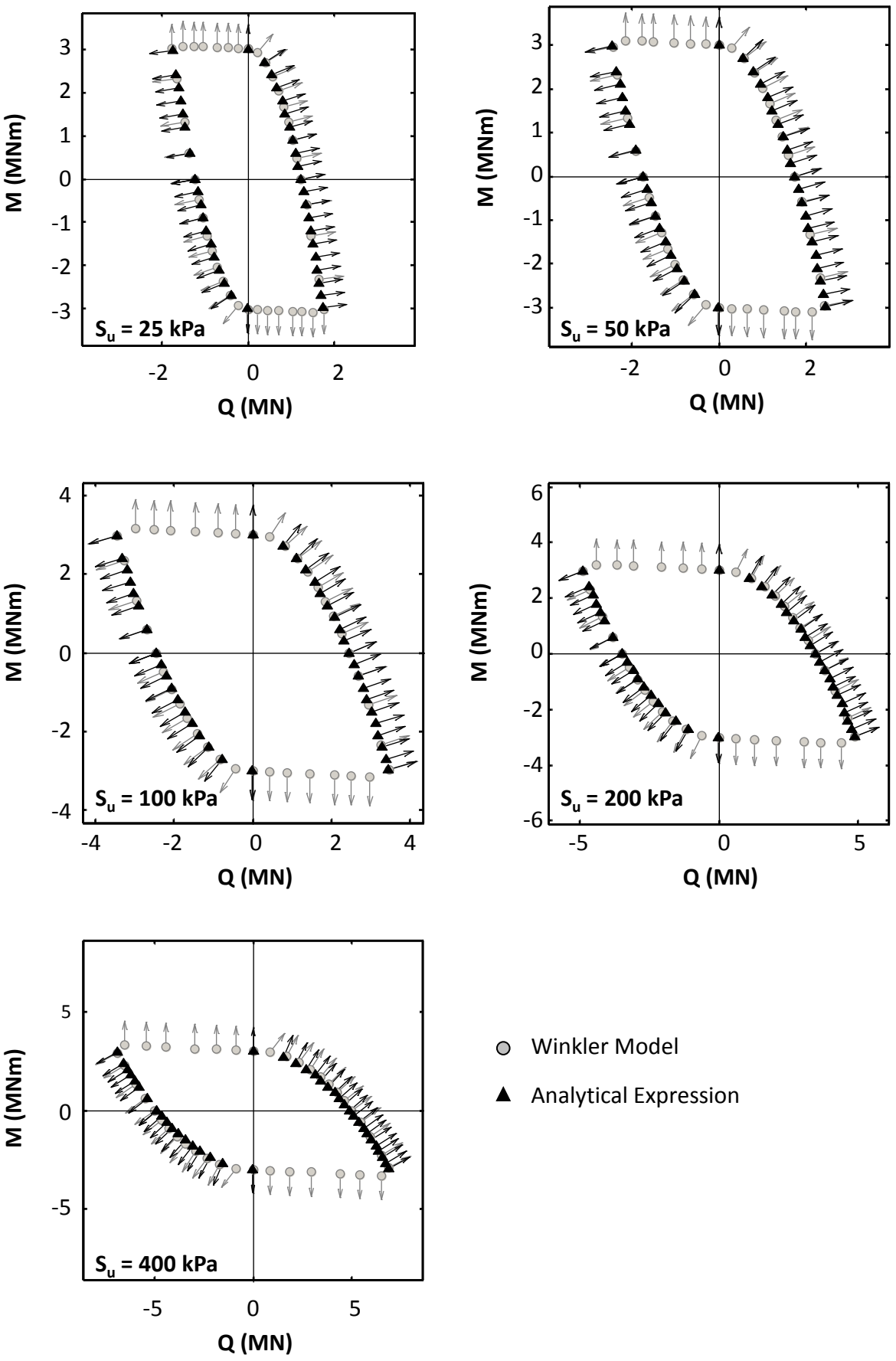

Figure 4.6: Influence of the undrained shear strength S_u on the flow rule on the Q–M space

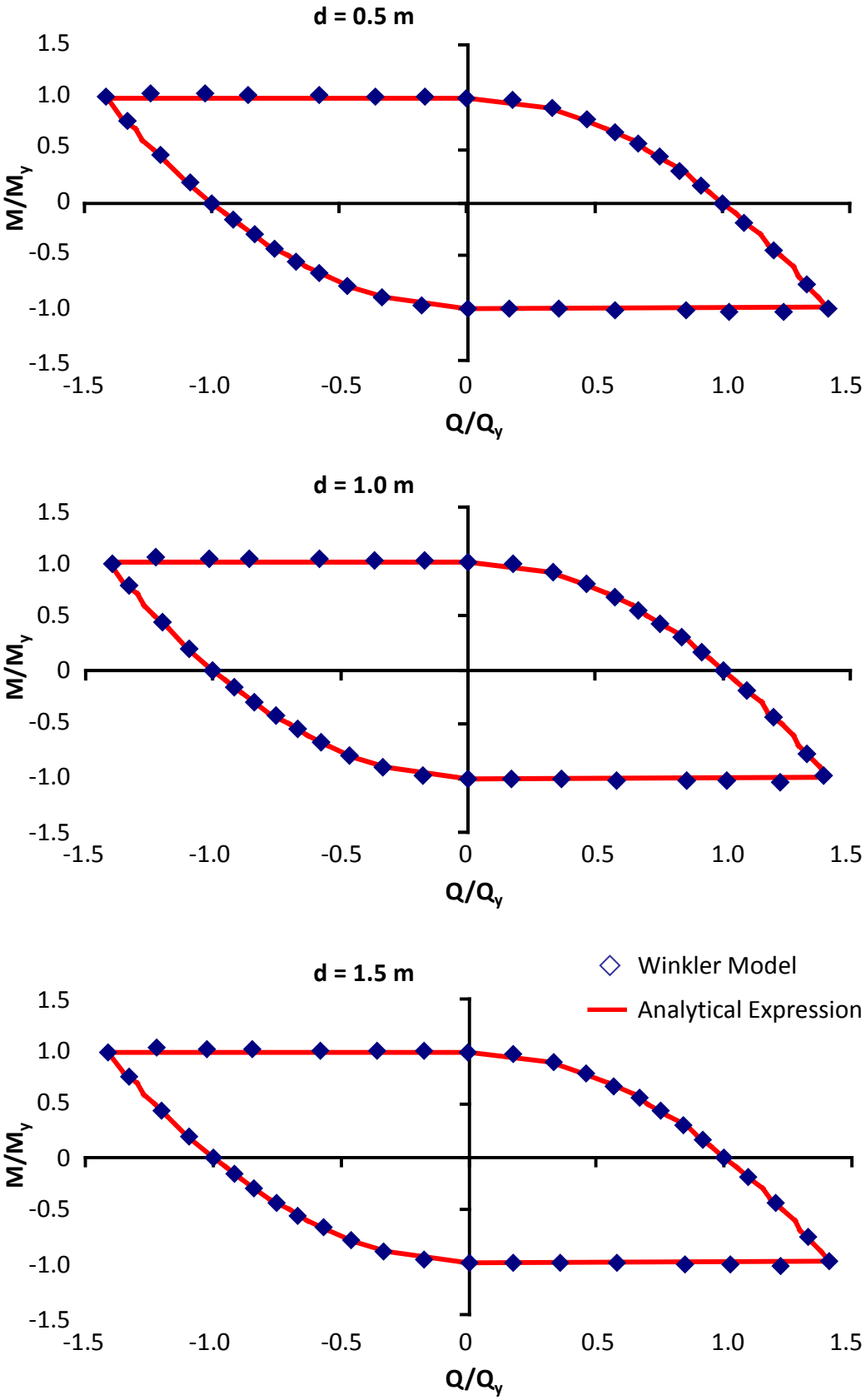

Figure 4.7: Influence of the pile diameter d on the failure envelope from the analytical expression for the case of a pile embedded in a homogeneous cohesive layer with uniform Young's modulus E_s = 50 MPa and undrained shear strength S_u = 50 kPa

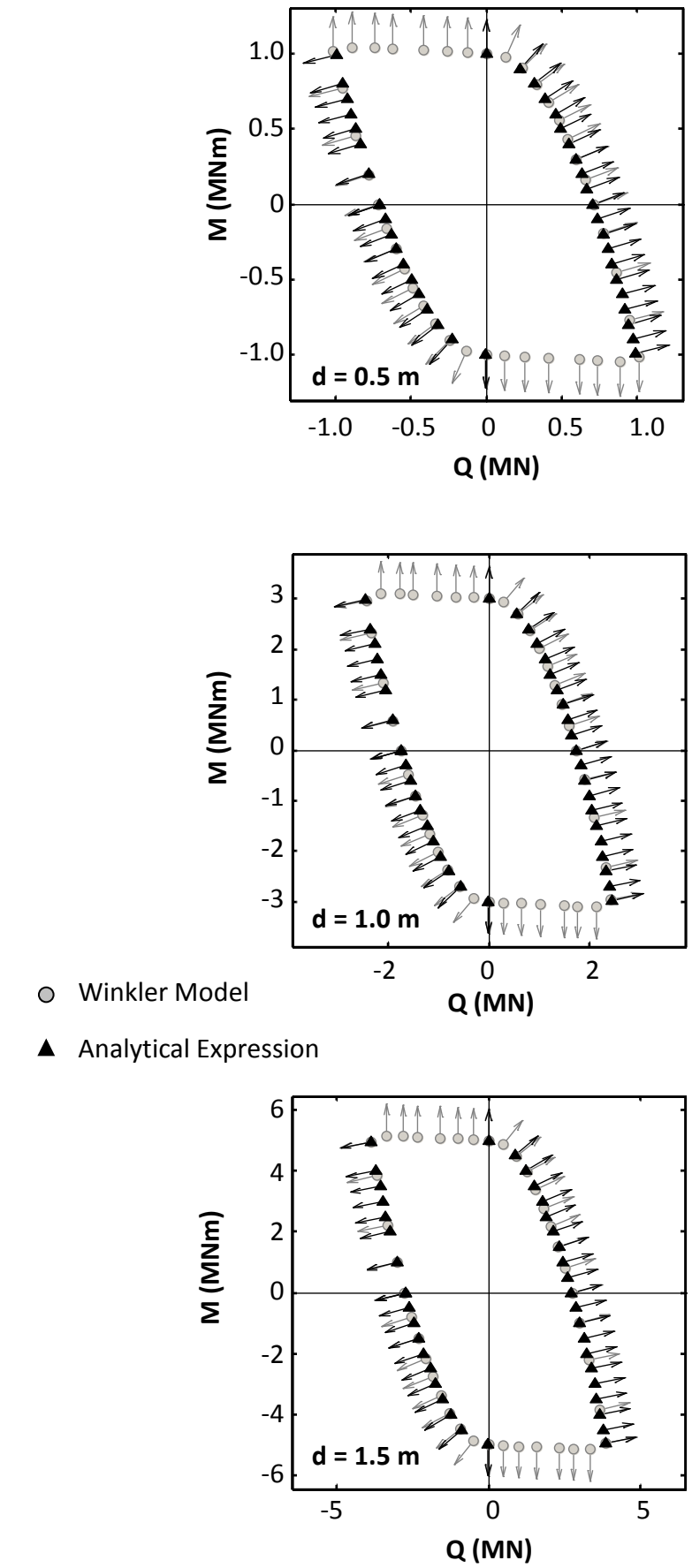

Figure 4.8: Influence of the pile diameter d on the flow rule on the Q–M space

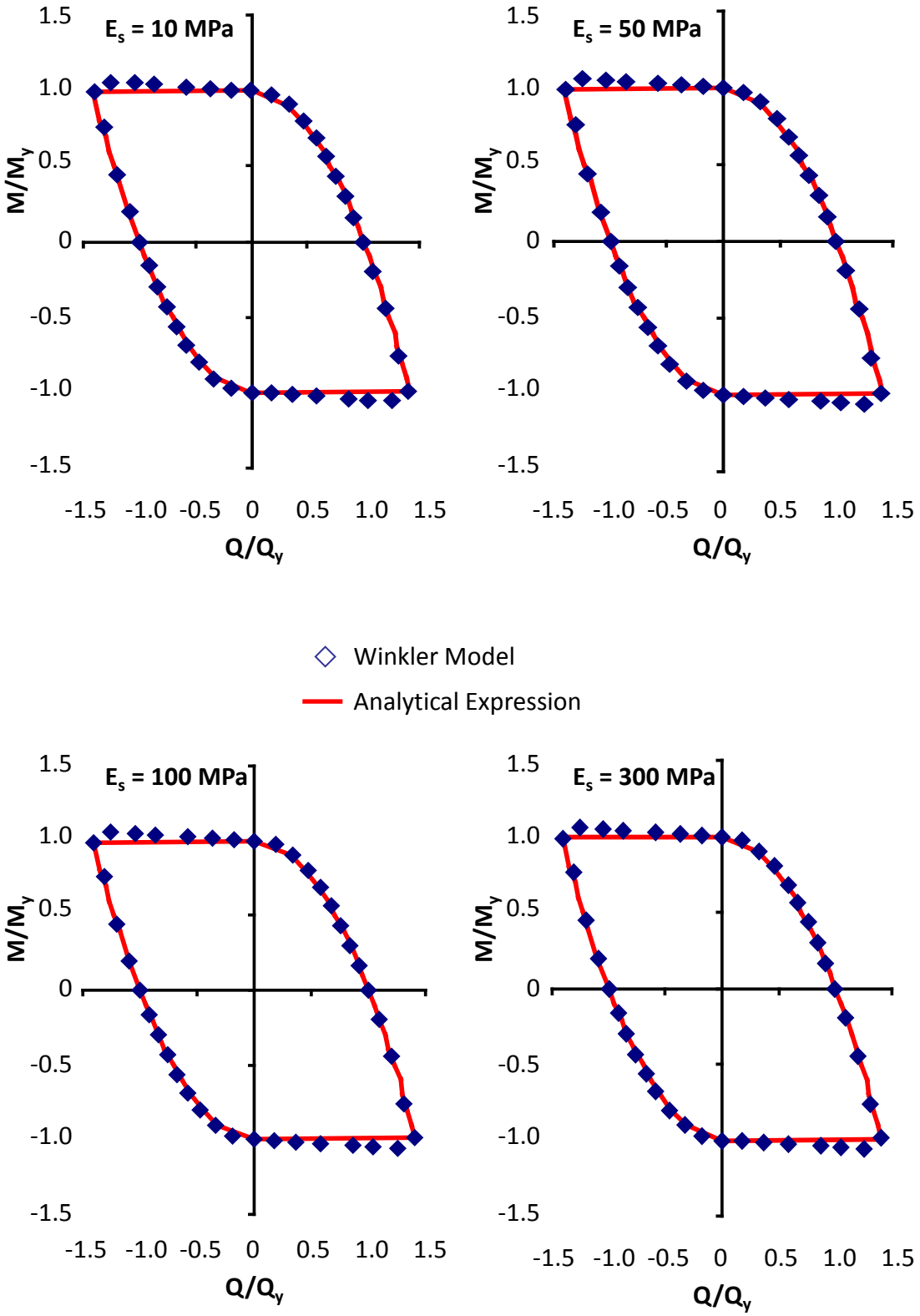

Figure 4.9: Influence of Young's Modulus E_s of the soil on the failure envelope from the analytical expression for the case of a pile of diameter d = 0.5 m embedded in a homogeneous cohesive layer with undrained shear strength S_u = 100 kPa

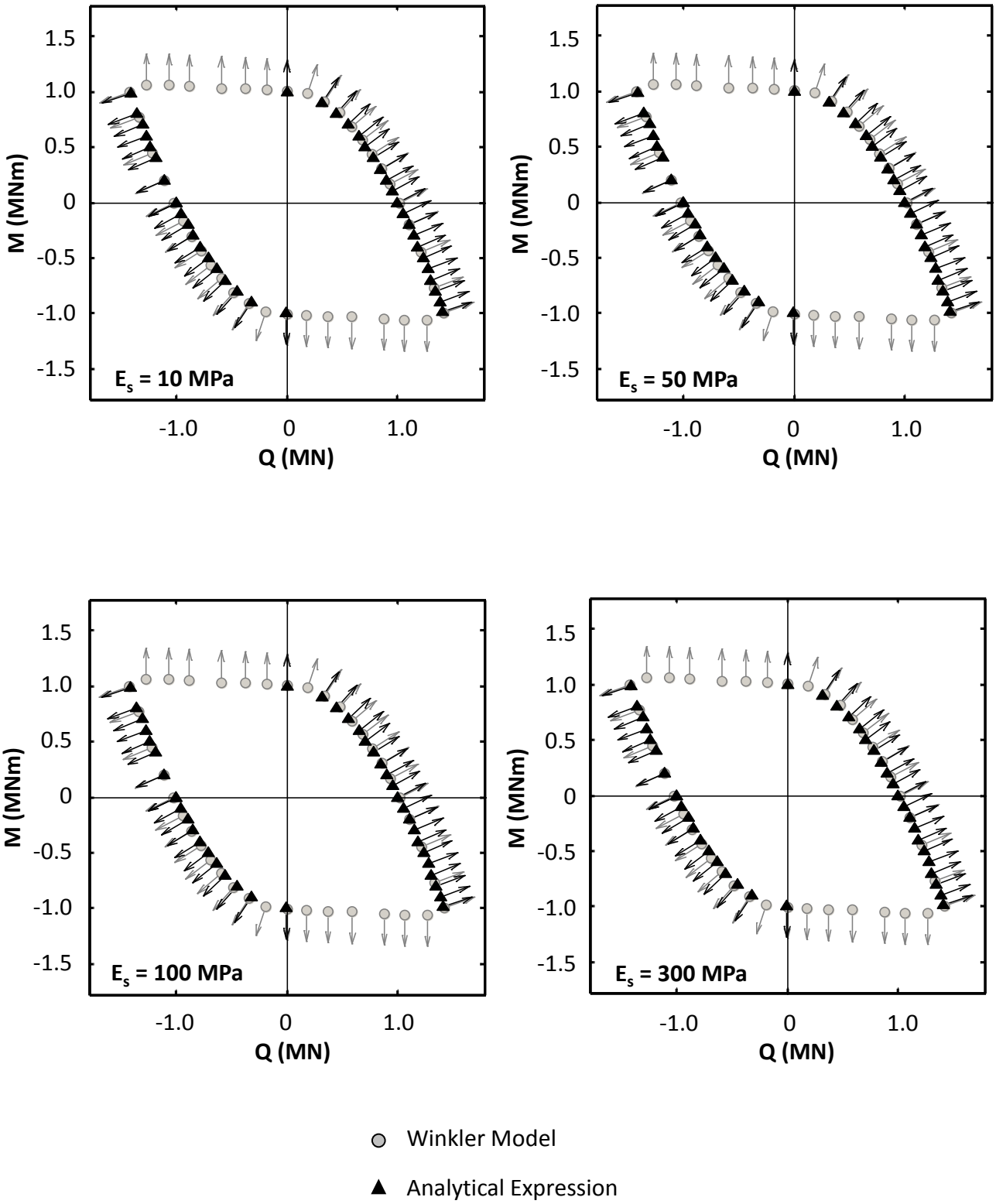

Figure 4.10: Influence of Young's Modulus E_s of the soil on the flow rule on the Q–M space

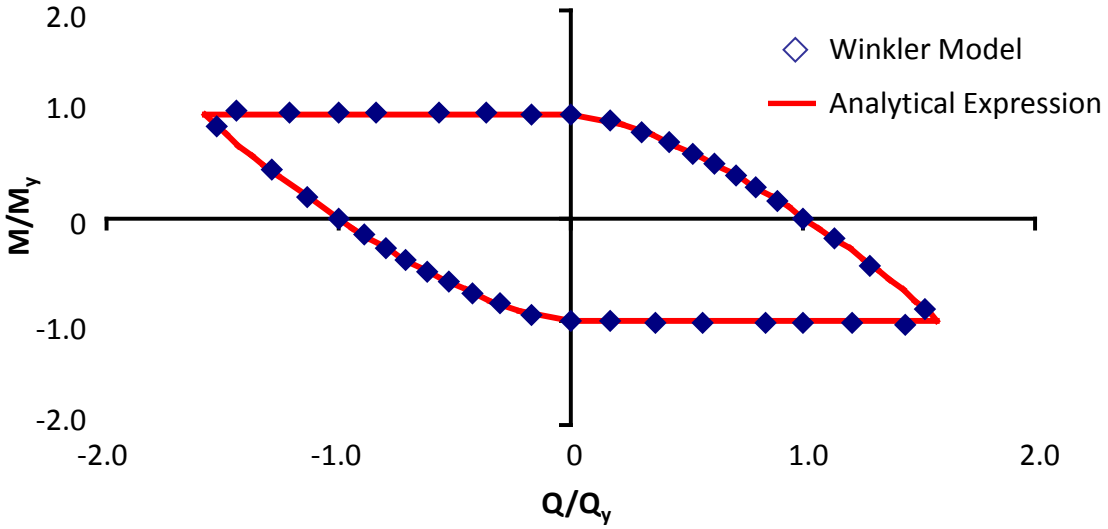

Figure 4.11: Comparison of the failure envelope calculated by the Winkler model and predicted by the analytical expression. The pile is embedded in cohesive Gibson soil

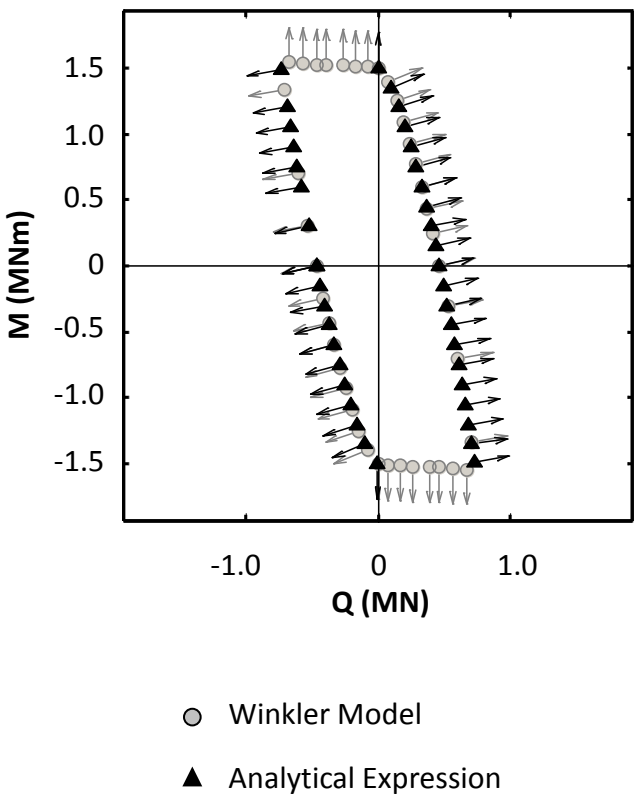

Figure 4.12: Comparison of the vectors from the analytical expression with the assumption of an associated flow rule with those from the incremental displacements at failure from the Winkler model for pile in cohesive Gibson soil

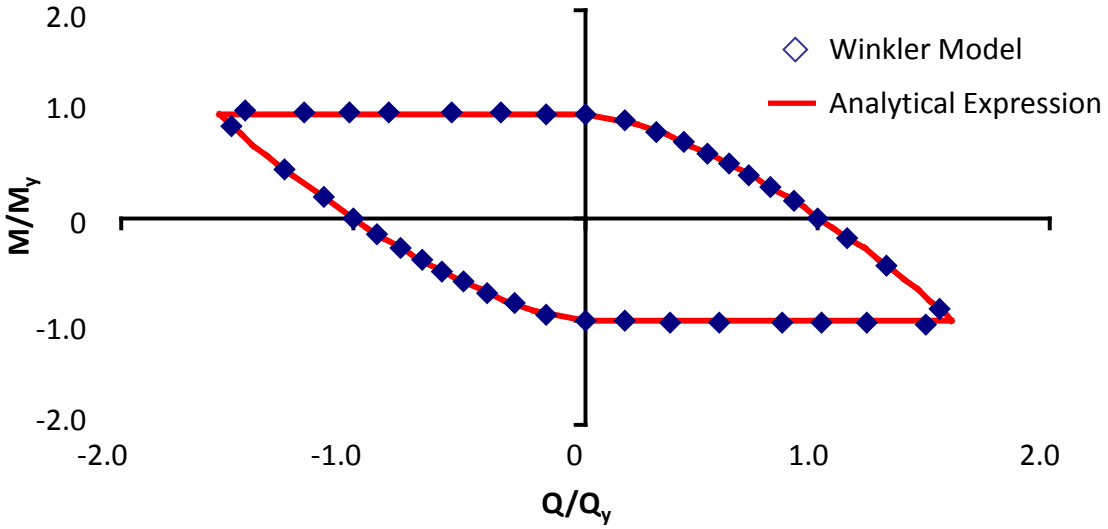

Figure 4.13: Comparison of the failure envelope calculated by the Winkler model and predicted by the analytical expression. The pile is embedded in nonhomogeneous cohesionless soil

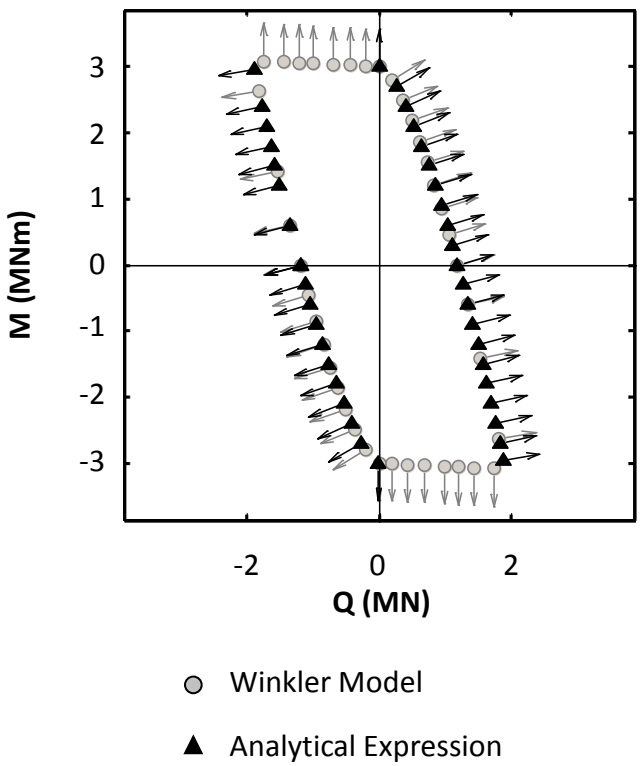

Figure 4.14: Comparison of the vectors from the analytical expression with the assumption of an associated flow rule with those from the incremental displacements at failure from the Winkler model for pile in nonhomogeneous cohesionless soil

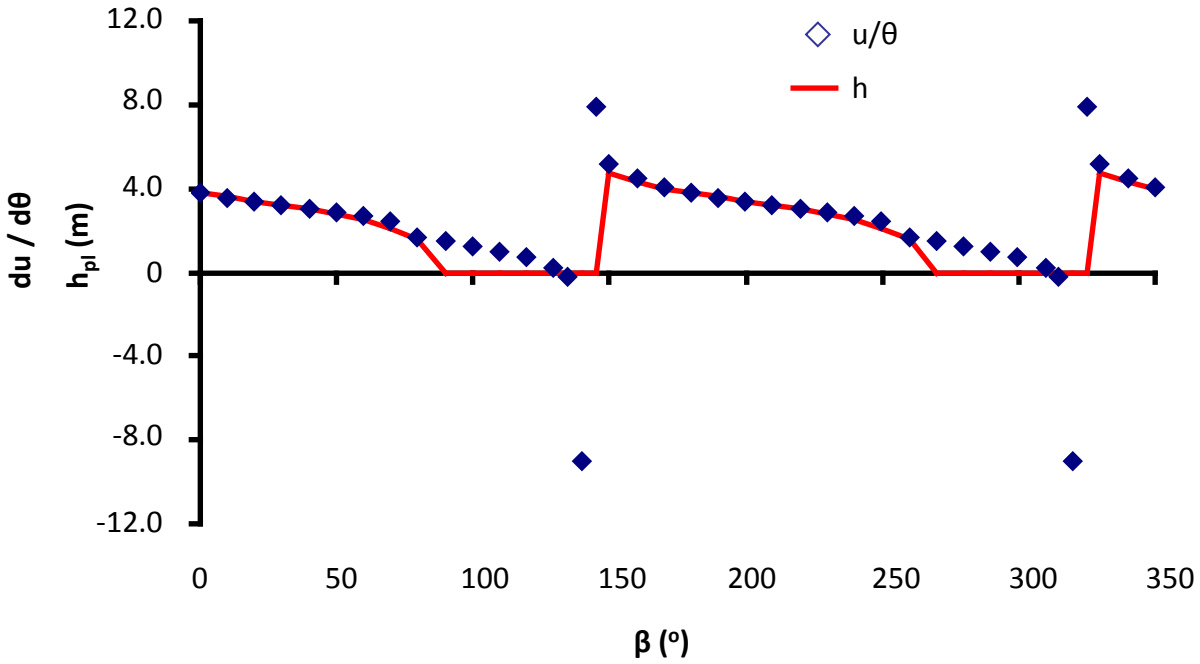

Figure 4.15: Comparison of the computed displacement over rotation ratio at failure for different failure points with the depth h of plastic hinge for the same points

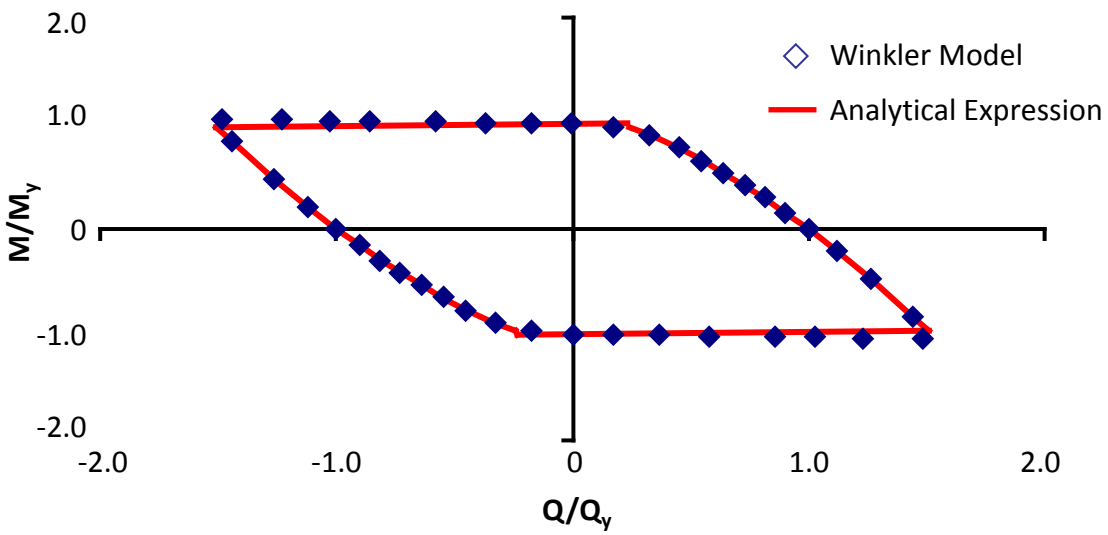

Figure 4.16: Comparison of the failure envelope calculated by the Winkler model and predicted by the analytical expression. The pile is embedded in two cohesive layers with $p_{y1} < p_{y2}$

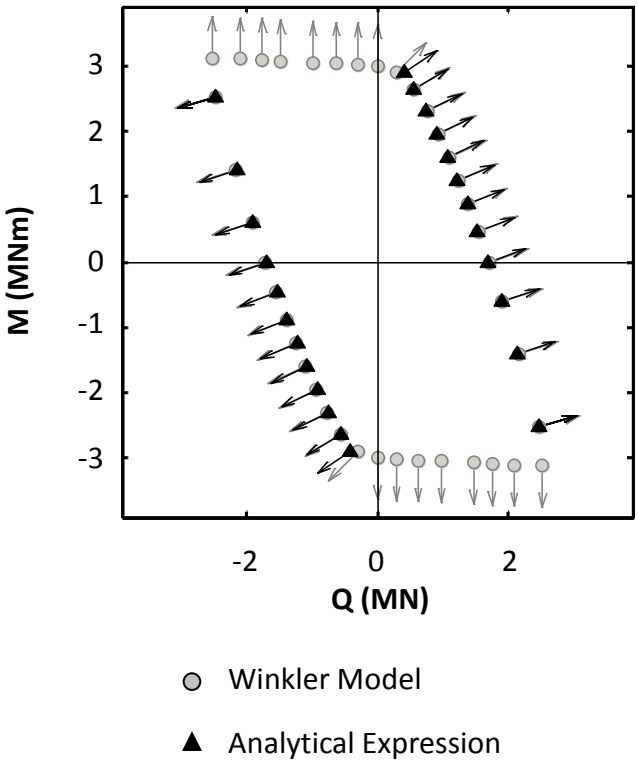

Figure 4.17: Comparison of the vectors from the analytical expression with the assumption of an associated flow rule with those from the incremental displacements at failure from the Winkler model for pile embedded in two cohesive layers with $p_{y1} < p_{y2}$

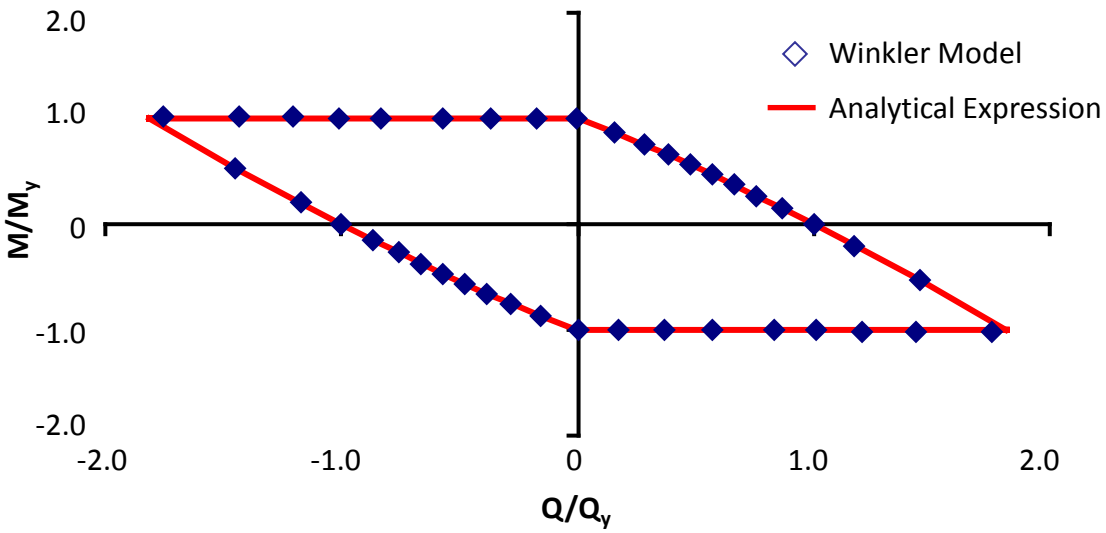

Figure 4.18: Comparison of the failure envelope calculated by the Winkler model and predicted by the analytical expression. The pile-column is embedded in cohesionless soil with pile head at a distance e from the ground surface

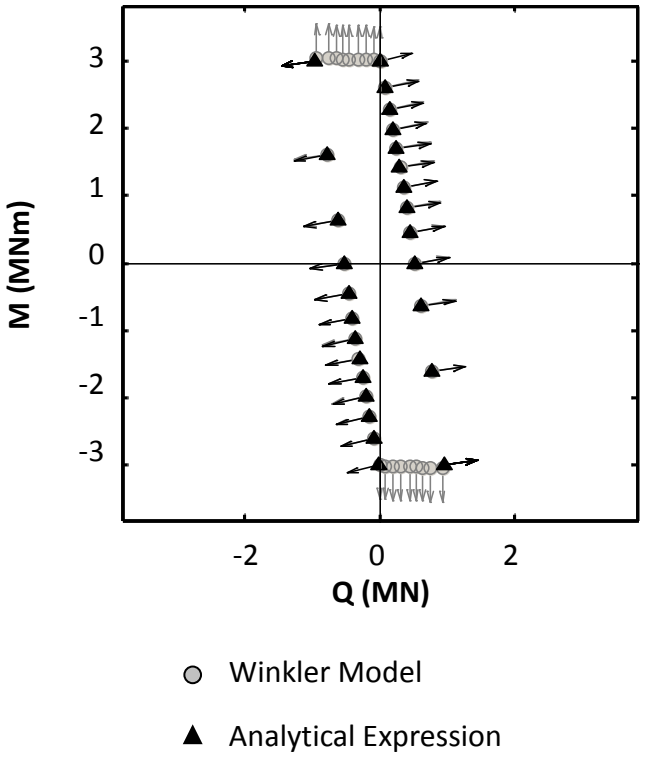

Figure 4.19: Comparison of the vectors from the analytical expression with the assumption of an associated flow rule with those from the incremental displacements at failure from the Winkler model for pile-column embedded in cohesionless soil with pile head at a distance e from the ground surface

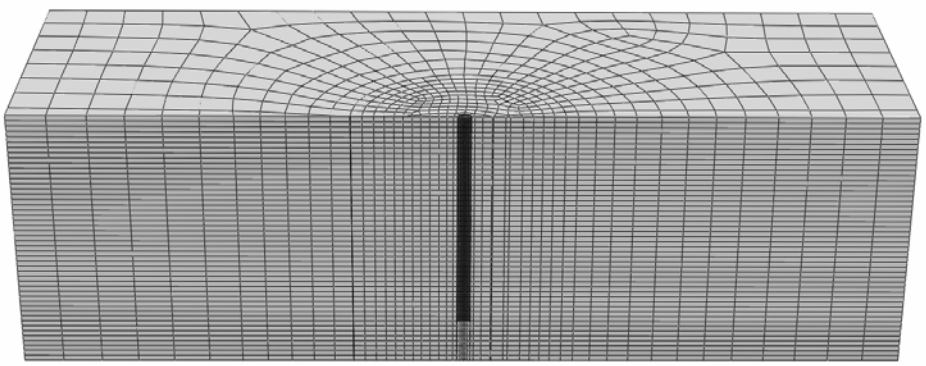

Figure 4.20: Cross section of the finite element discretization

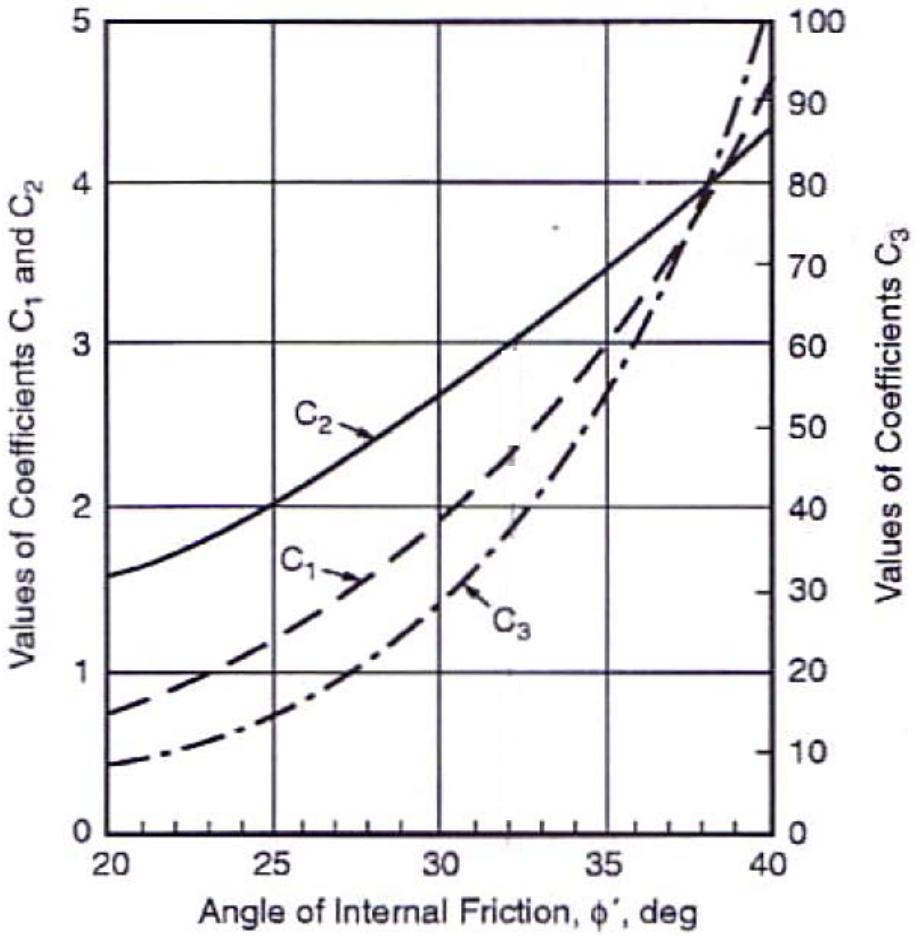

Figure 4.21: Values of coefficients C1, C2, C3 for soil resistance versus depth (API, 2000)

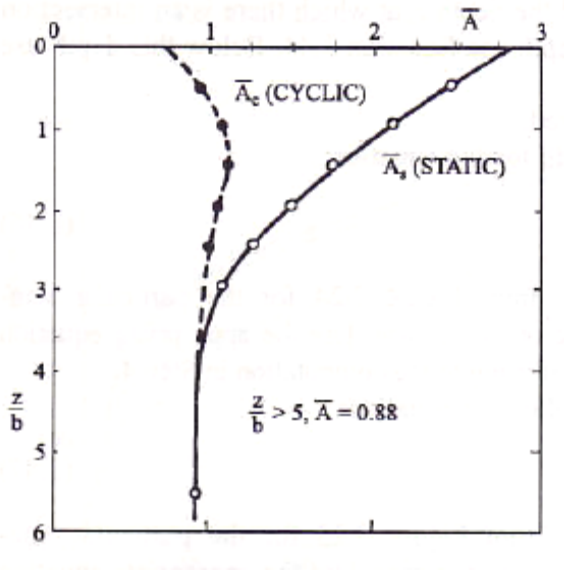

Figure 4.22: Values of coefficients for soil resistance versus depth (Reese and Van Impe, 2001)

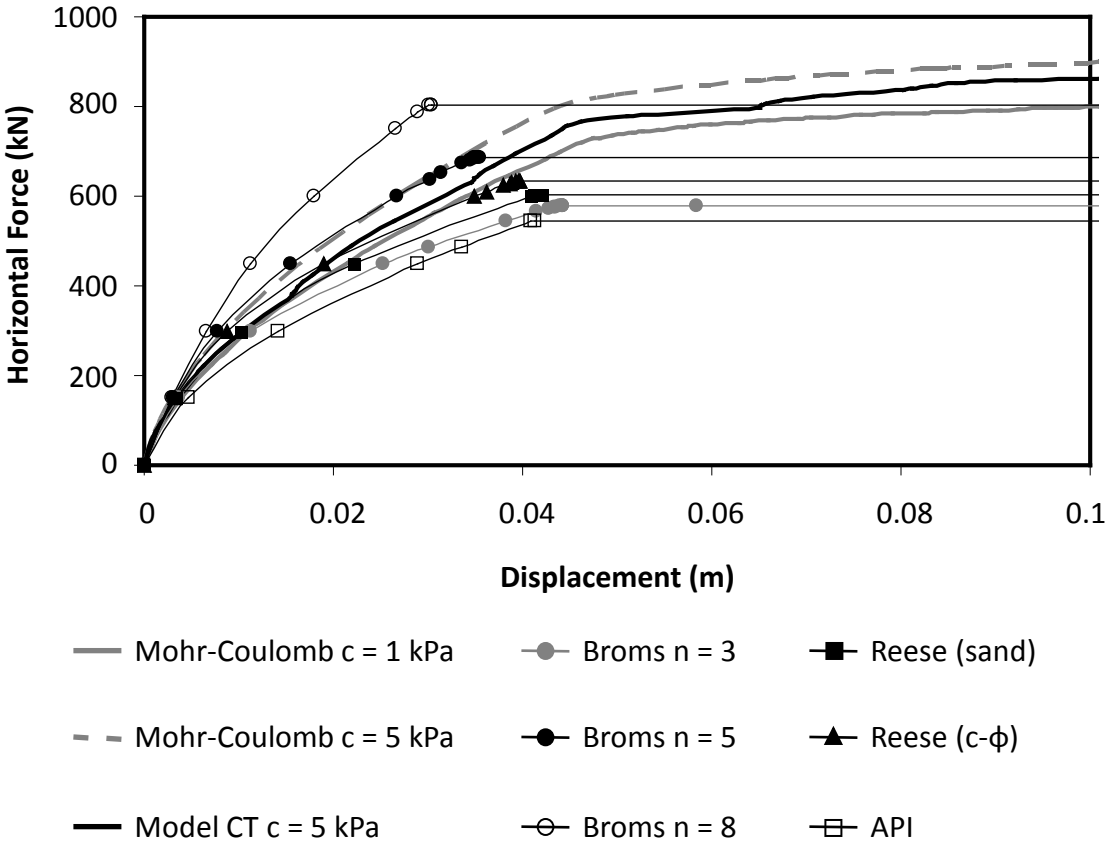

Figure 4.23: Comparison of the lateral response of a flexible pile embedded in sand computed by different methods of analysis

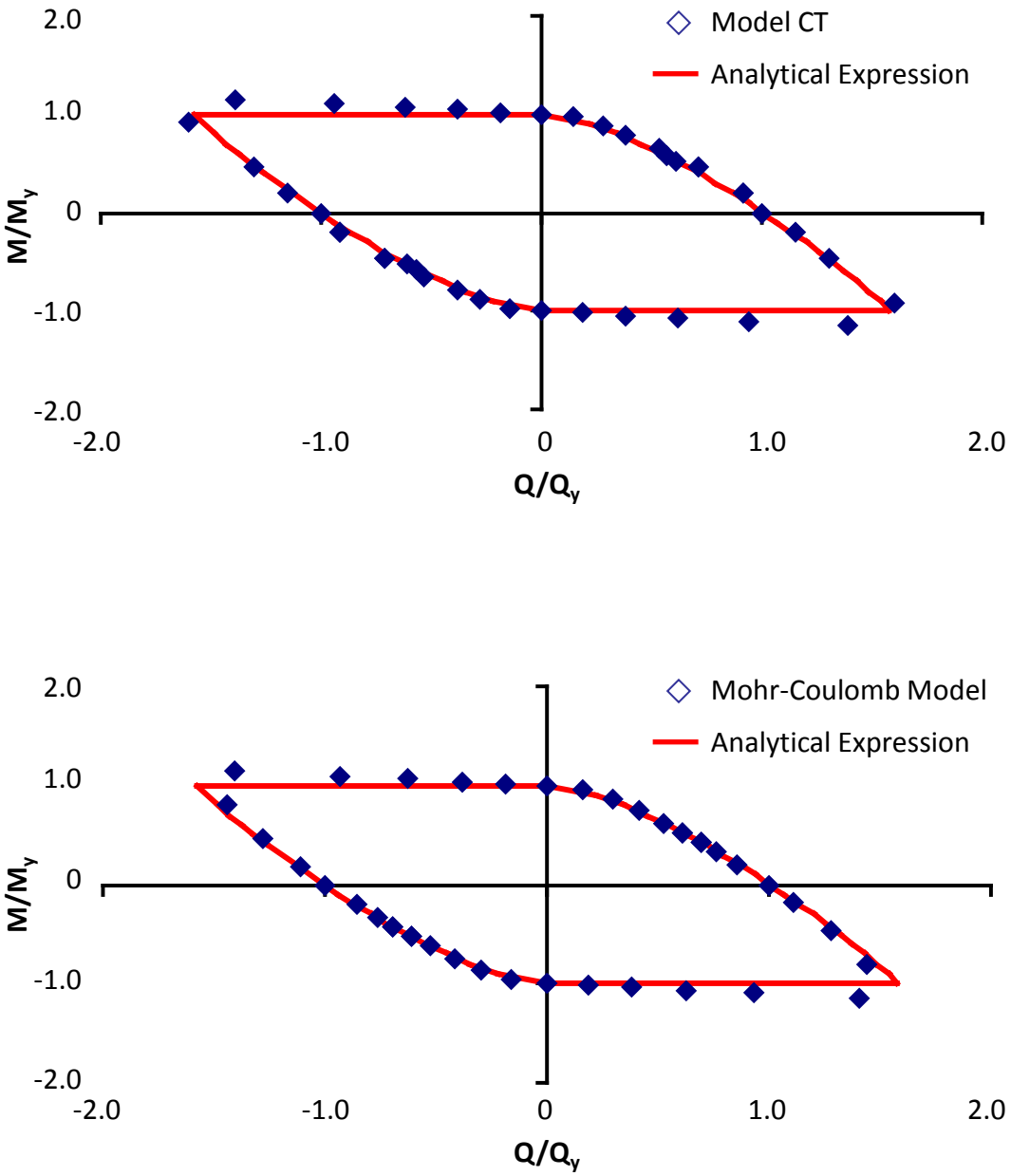

Figure 4.24: Comparison of the failure envelope calculated by three-dimensional numerical analysis with (a) the constitutive model CT, and (b) the Mohr-Coulomb constitutive model and predicted by the analytical expression for pile in cohesionless soil

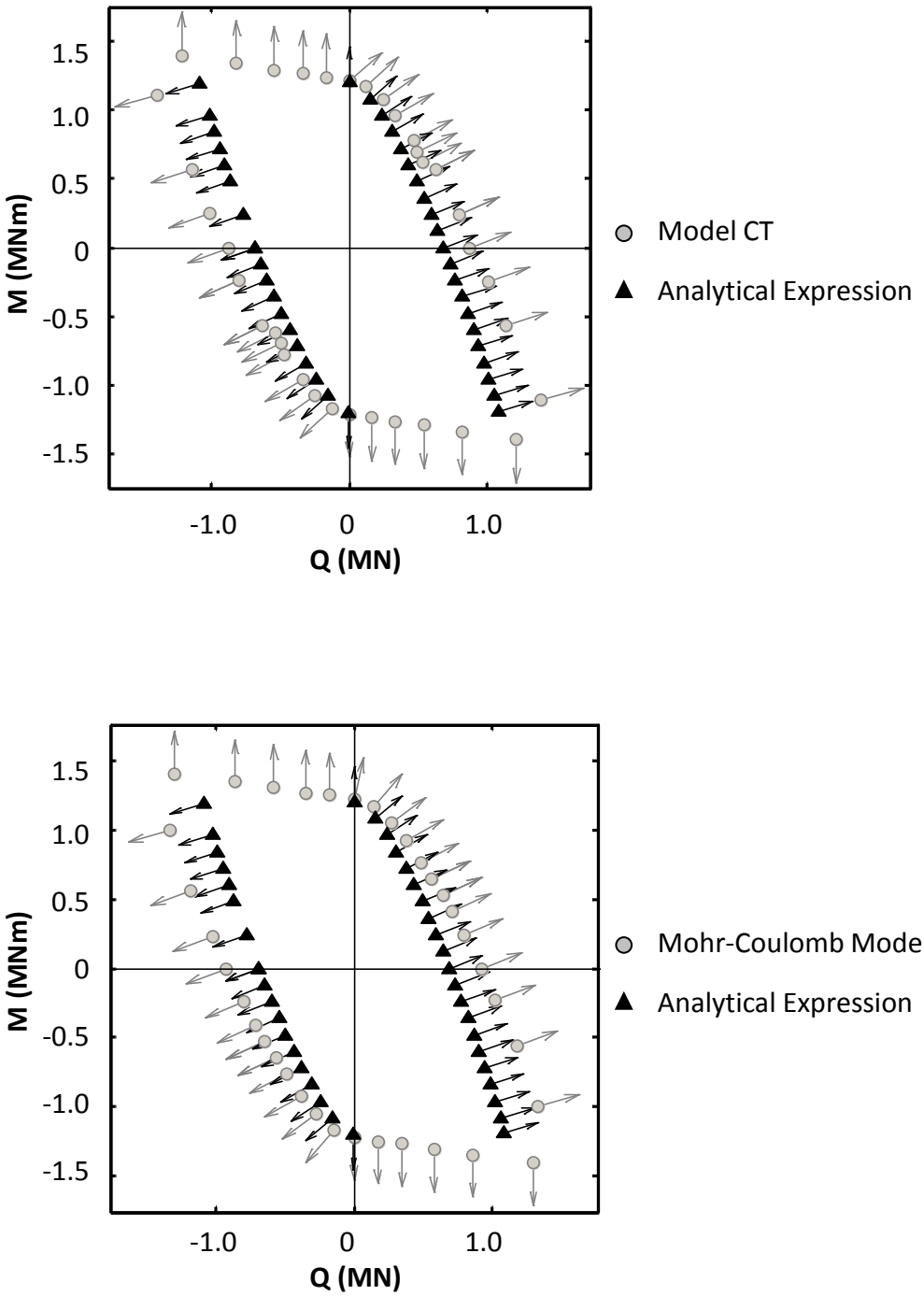

Figure 4.25: Comparison of the vectors from the analytical expression with the assumption of an associated flow rule with those from the incremental displacements at failure from the three-dimensional numerical analysis with (a) the constitutive model CT, and (b) the Mohr-Coulomb constitutive model for pile in cohesionless soil

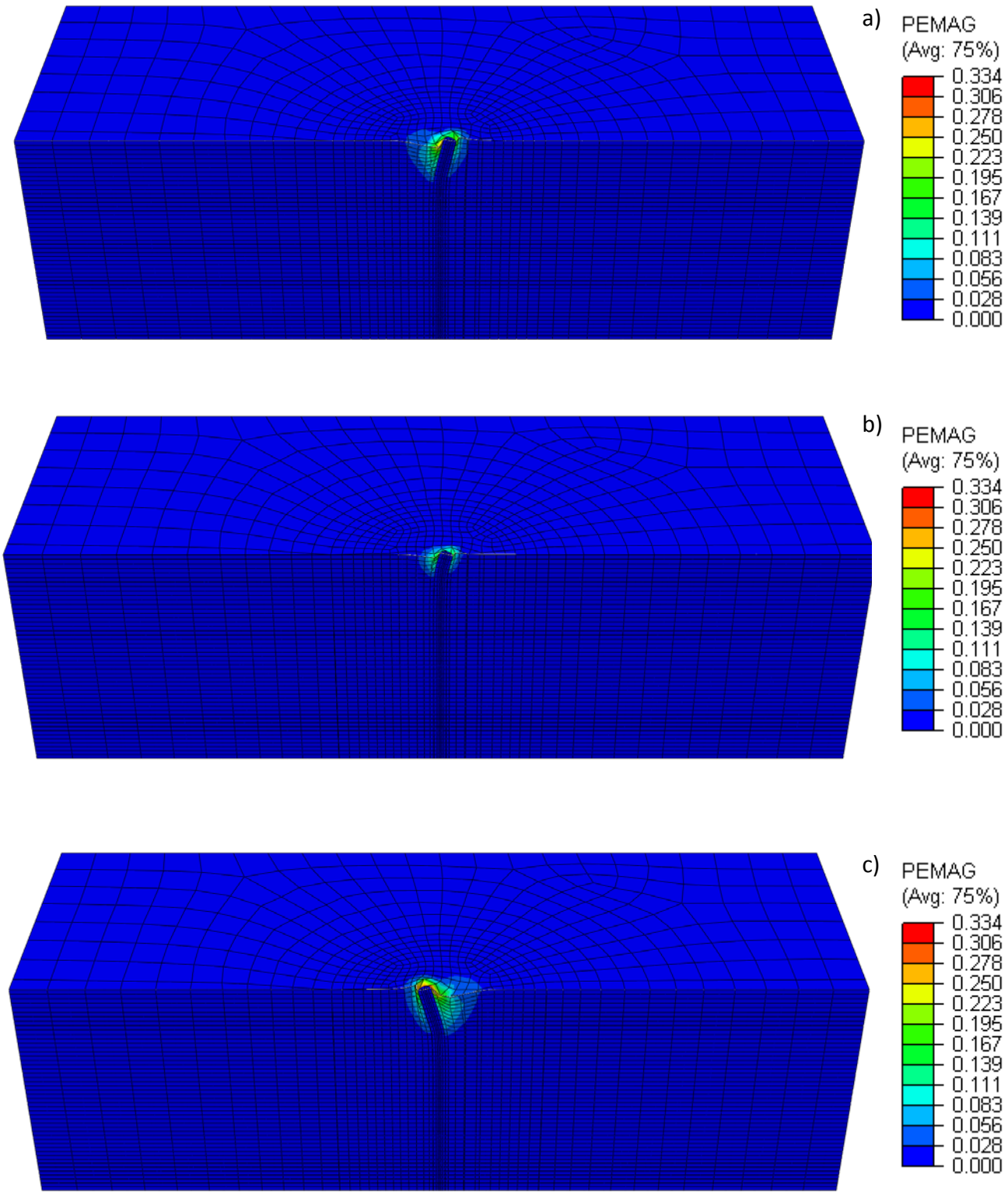

Figure 4.26: Contours of the plastic strain magnitude (plotted on the deformed mesh) for a flexible pile embedded in nonhomogeneous cohesionless soil calculated with the constitutive model CT for three different angles of loading: (a) $\beta = 0^o$ ($Q / Q_y = 1$, $M / M_y = 0$), (b) $\beta = 70^o$ ($Q / Q_y = 0.28$, $M / M_y = 0.88$), and (c) $\beta = 160^o$ ($Q / Q_y = -1.3$, $M / M_y = 0.47$). (Deformation Scale Factor = 5)

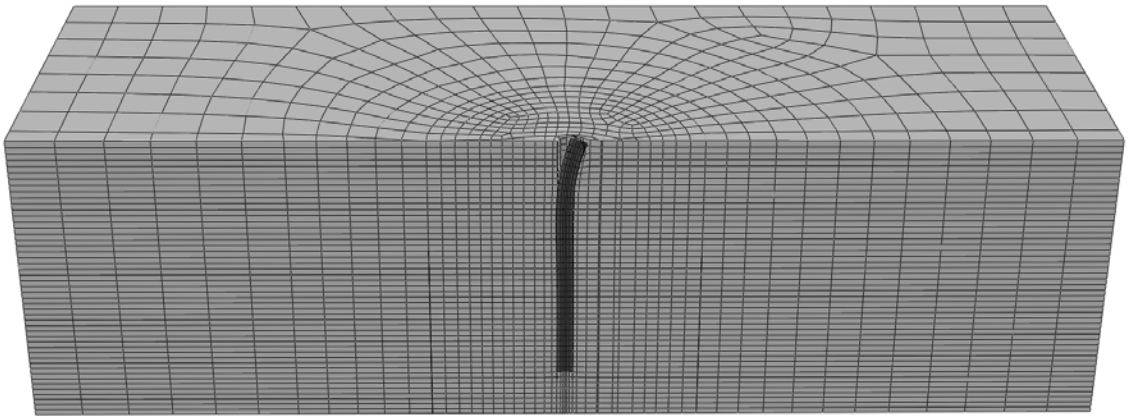

Figure 4.27: Gap formation from the action of the ultimate moment at the pile head. (Deformation Scale Factor = 40)

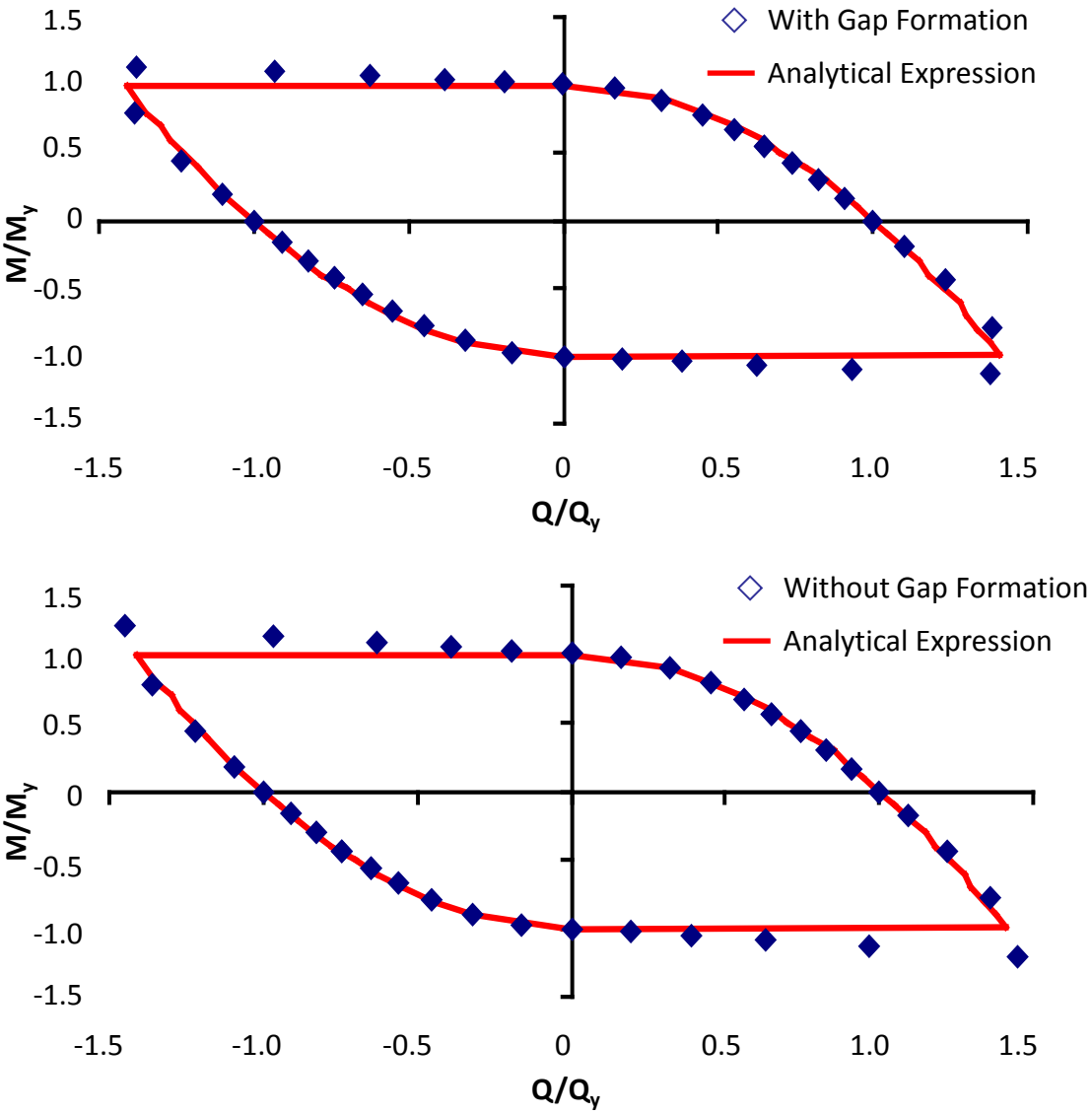

Figure 4.28: Comparison of the failure envelope predicted by the analytical expression for pile in cohesive soil and calculated by three-dimensional numerical analysis with (a) displacement-free conditions, and (b) fully bonded conditions

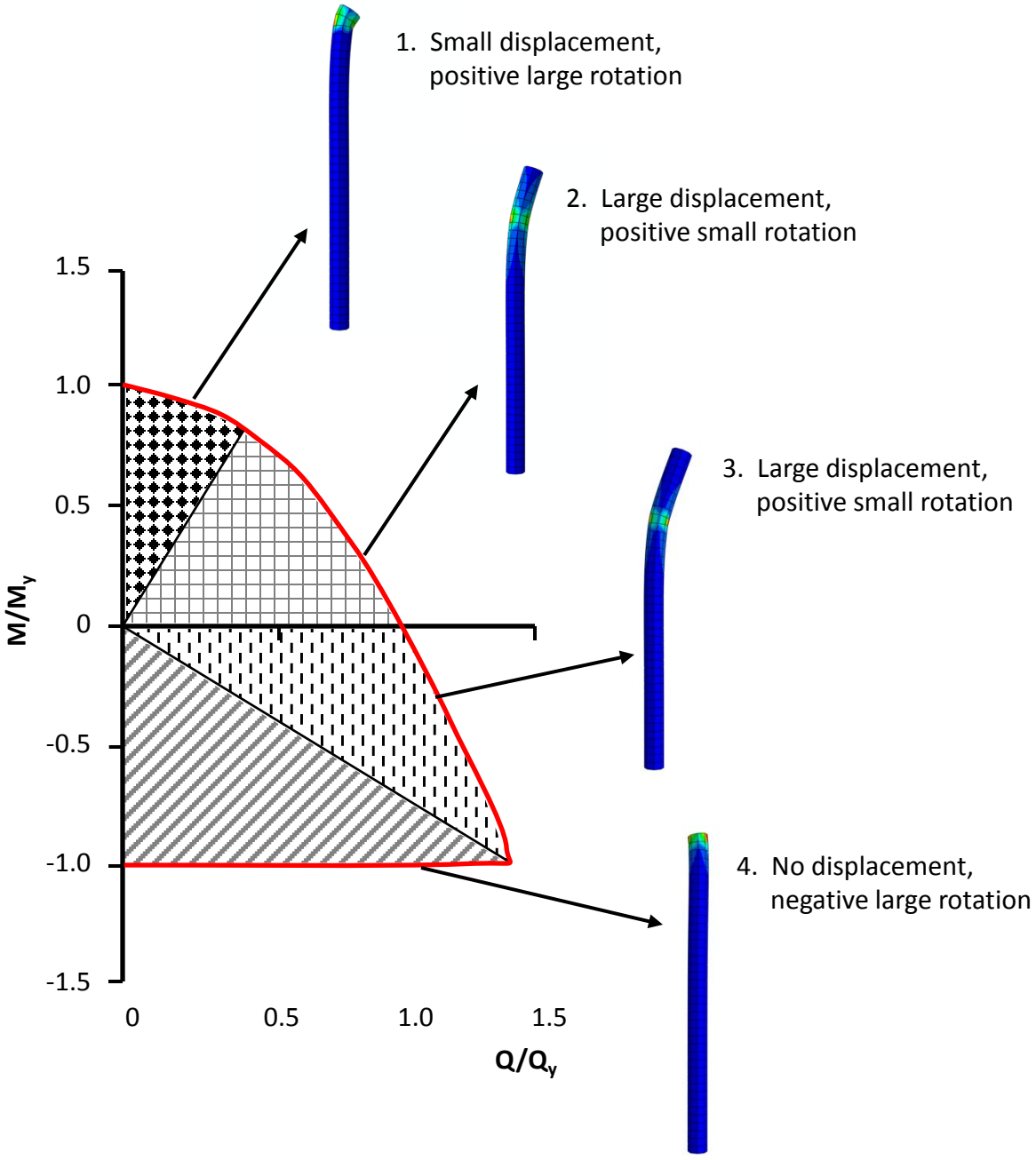

Figure 4.29: Characteristic zones of the pile response at the M−Q failure envelope

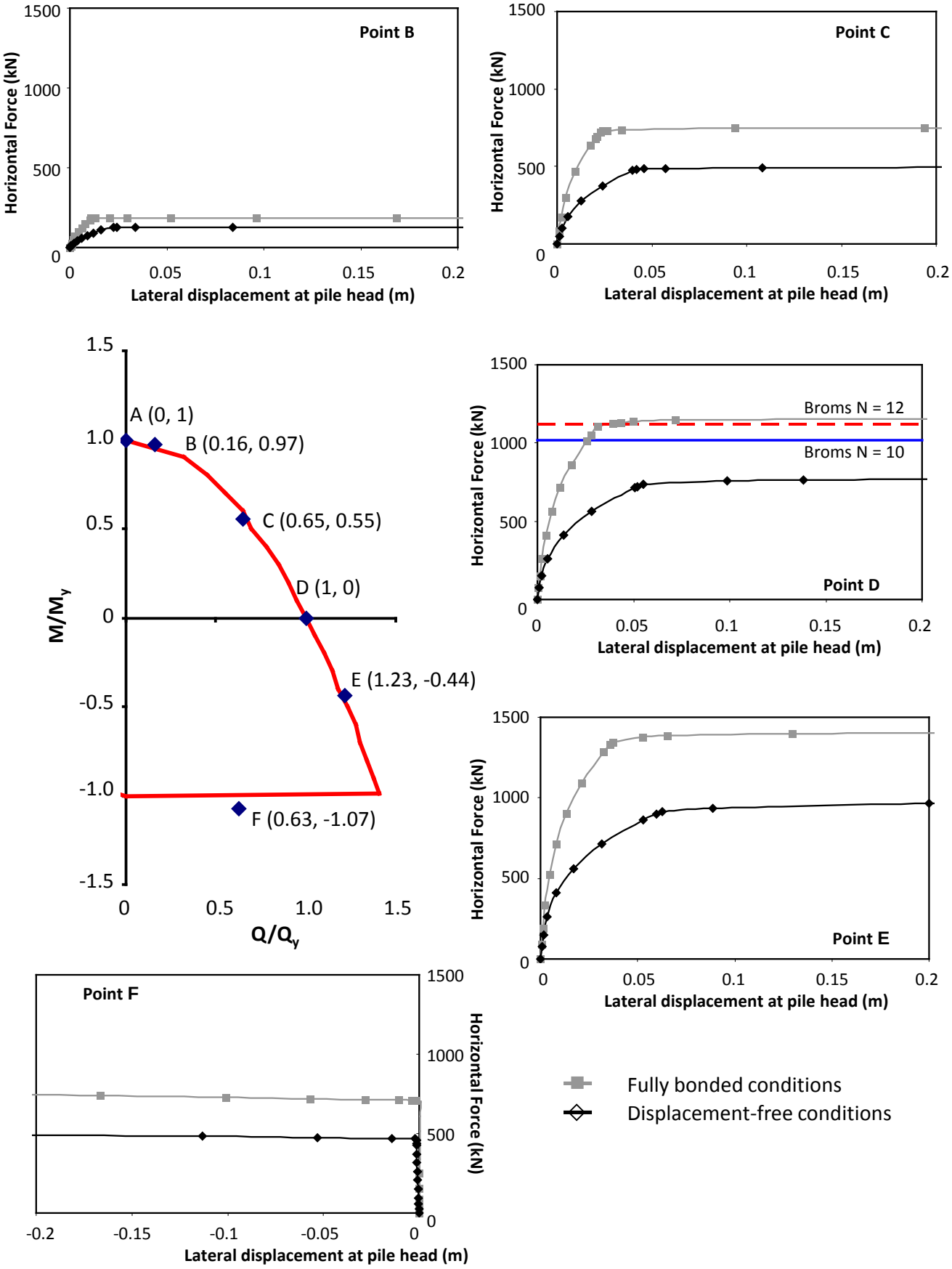

Figure 4.30: Comparison of the horizontal force–lateral displacement curves at the pile head for pile embedded in cohesive soil with (a) fully bonded conditions, and (b) displacement-free conditions at characteristic points along the failure envelope

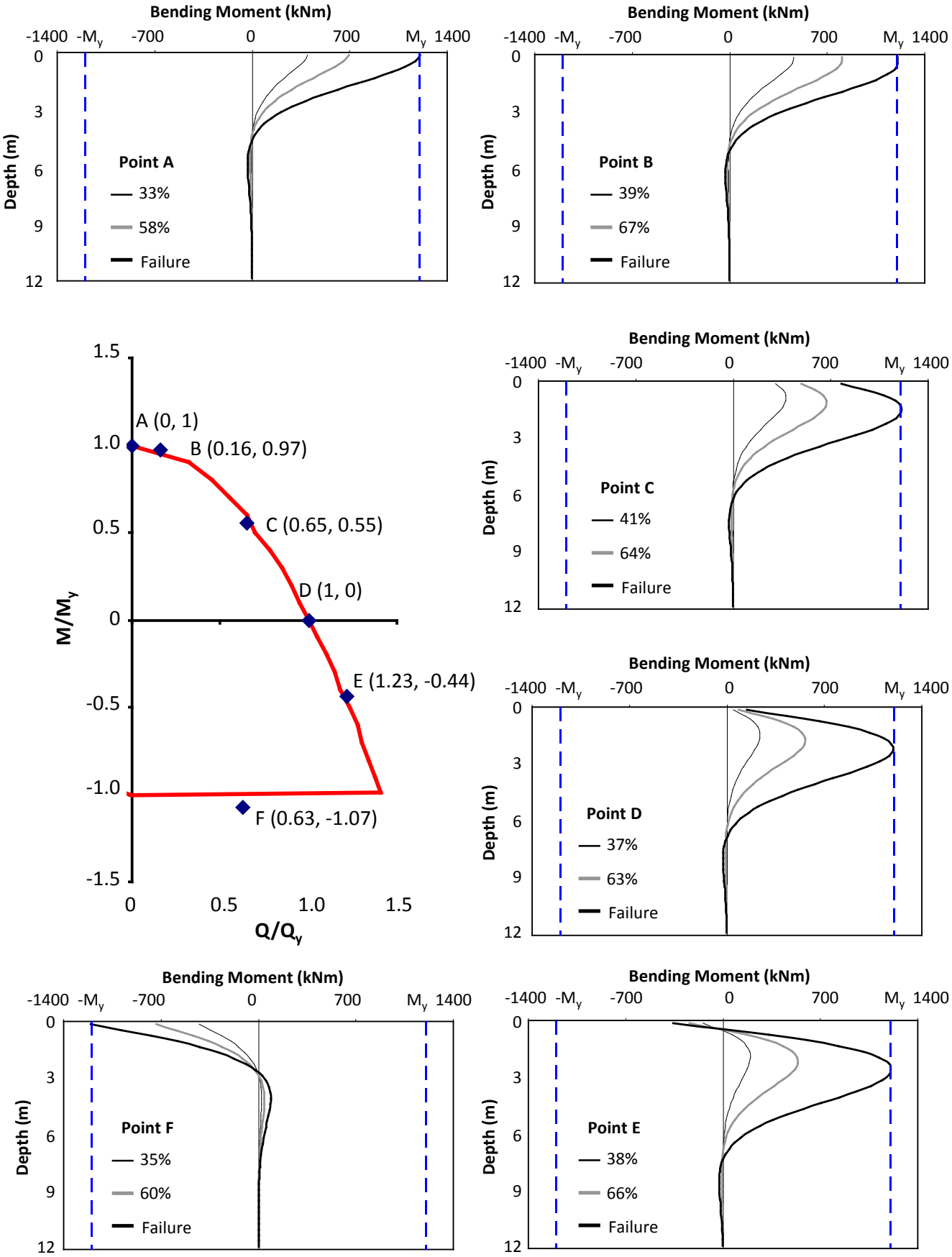

Figure 4.31: Computed bending moment distributions at different stages of loading for pile embedded in cohesive soil with fully bonded conditions at characteristic points along the failure envelope

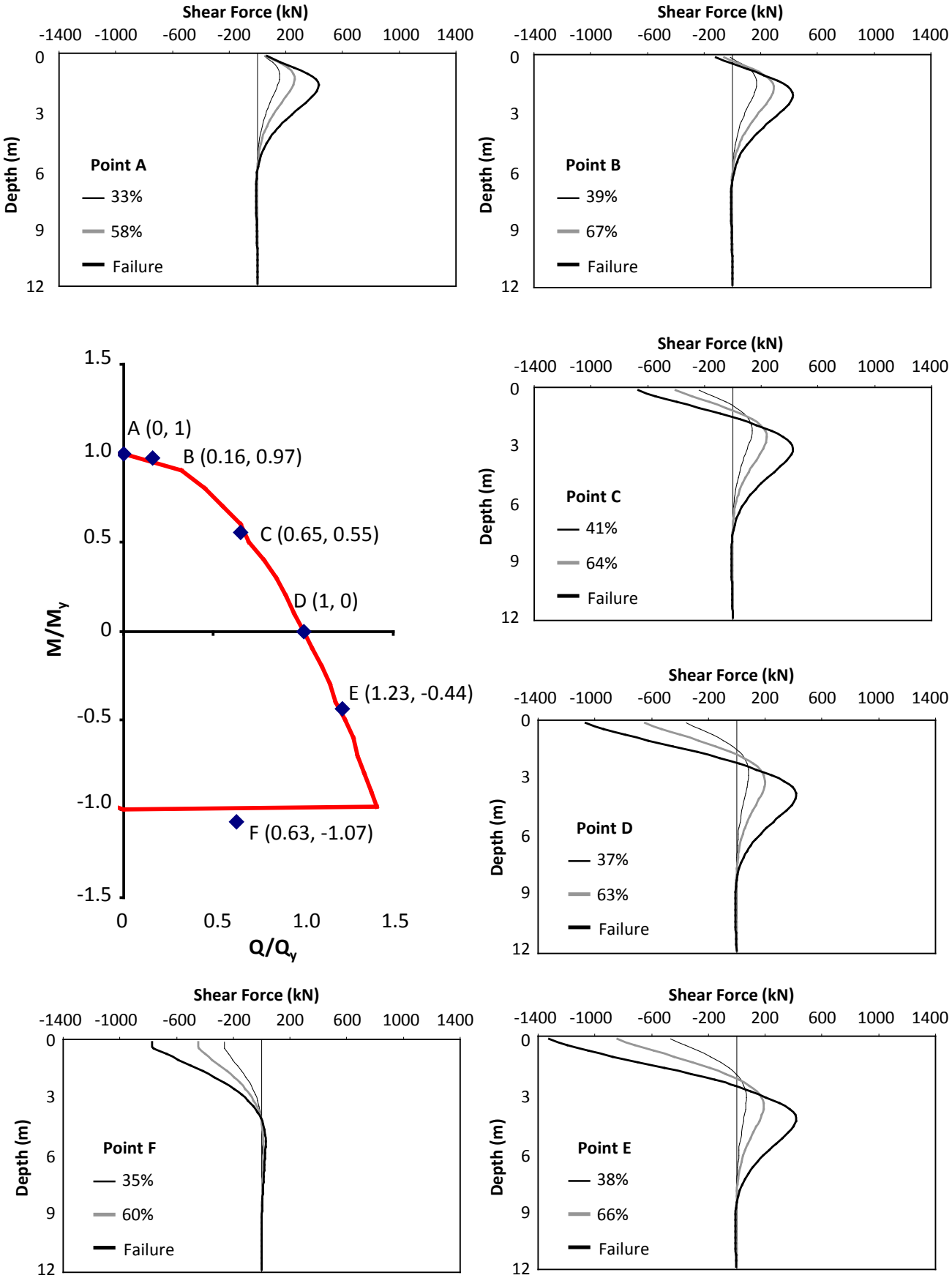

Figure 4.32: Computed shear force distributions at different stages of loading for pile embedded in cohesive soil with fully bonded conditions at characteristic points along the failure envelope

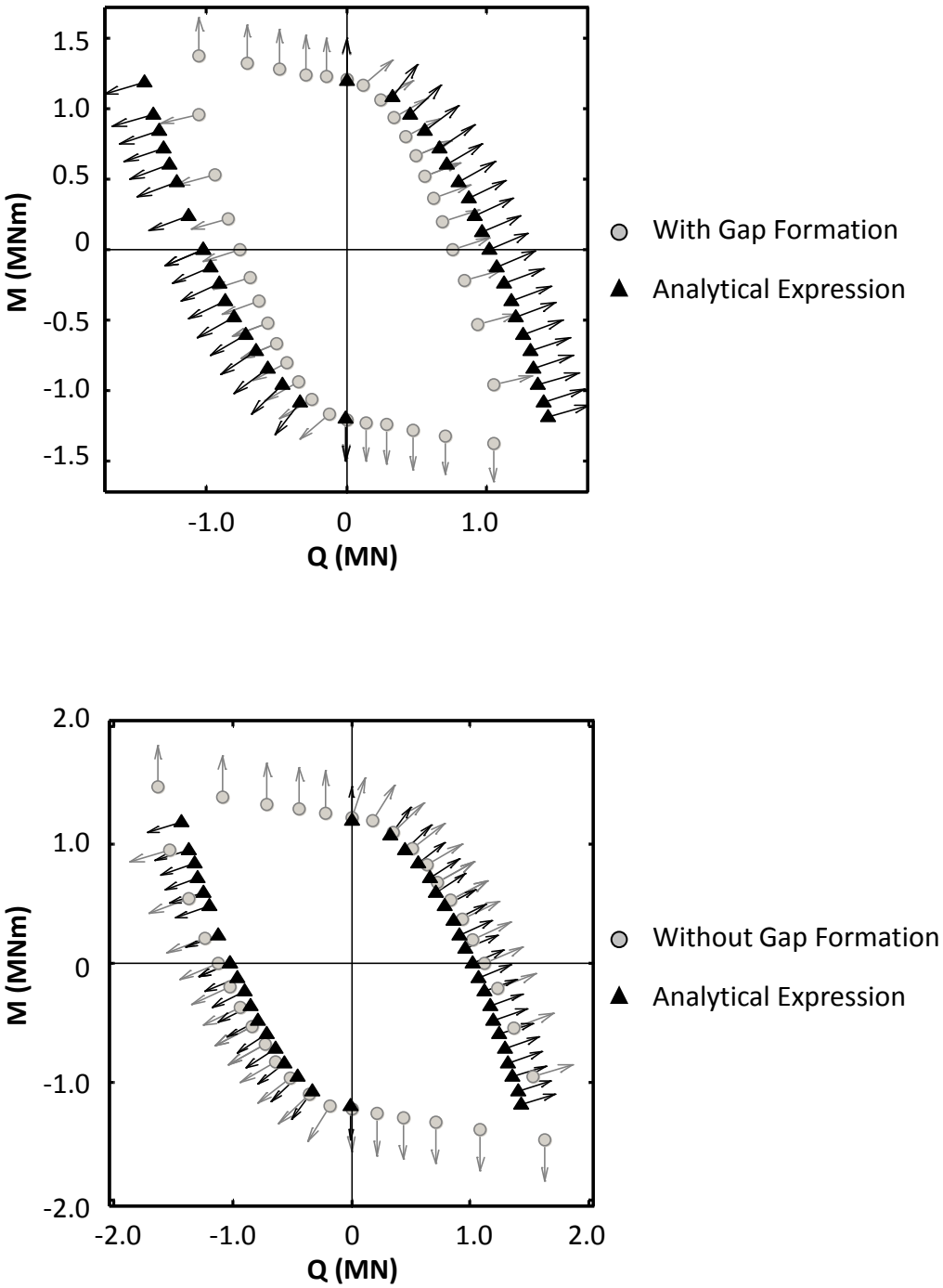

Figure 4.33: Comparison of the vectors from the analytical expression with the assumption of an associated flow rule with those from the incremental displacements at failure from the three-dimensional numerical analysis with (a) displacement-free conditions, and (b) fully bonded conditions for pile in cohesive soil

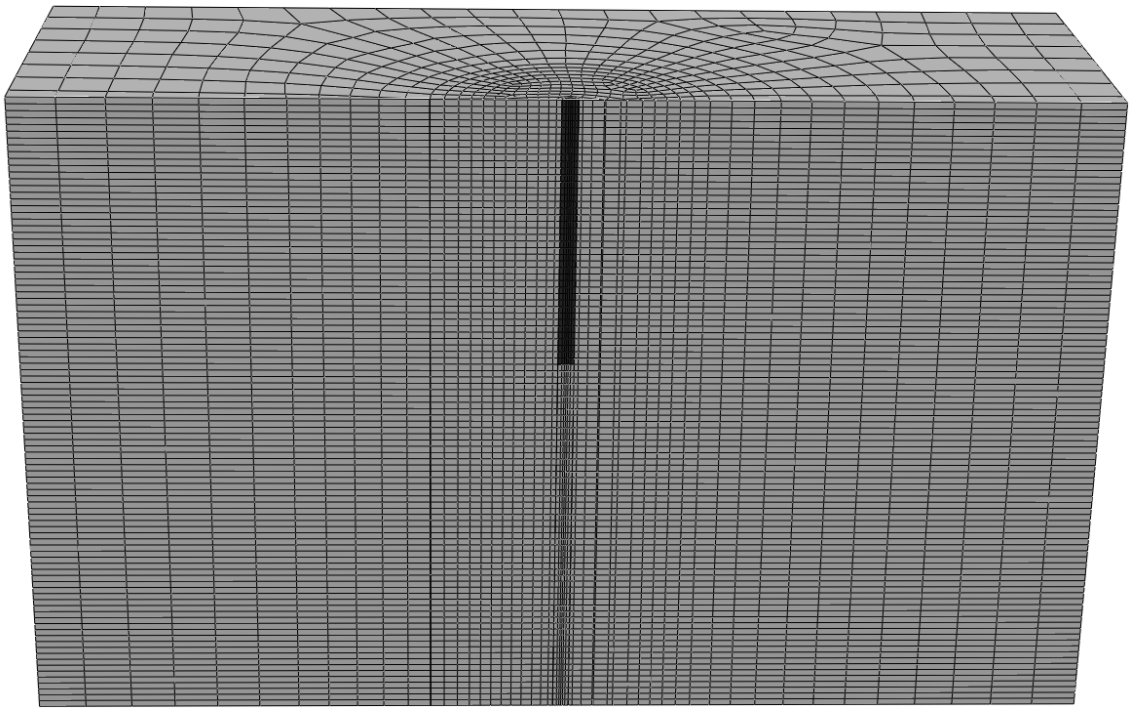

Figure 4.34: Cross section of the finite element discretization for case of vertical load acting on the head of the pile

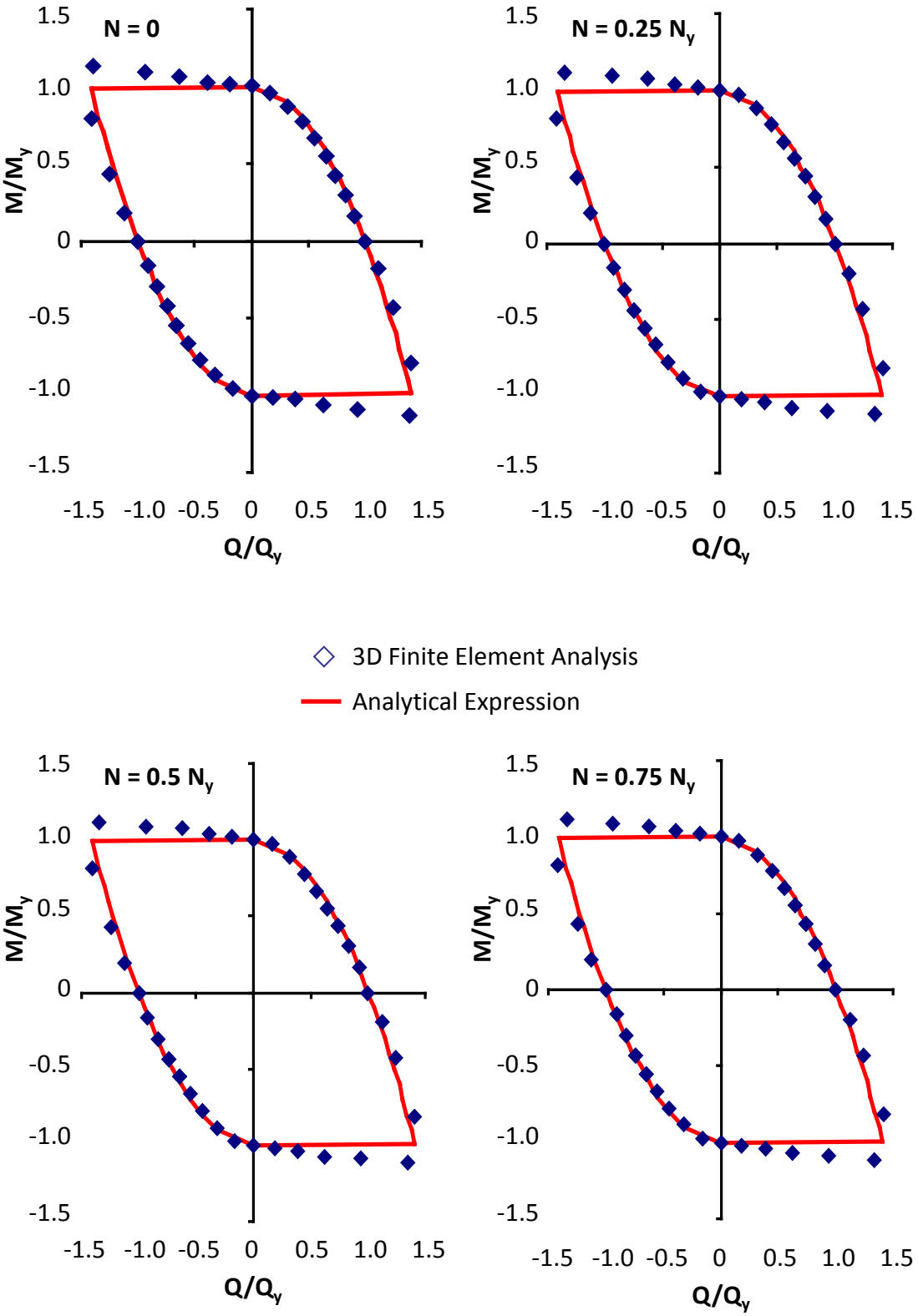

Figure 4.35: Comparison of the failure envelope calculated by three-dimensional numerical analyses for different vertical loads: (a) 0, (b) $0.25N_y$, (c) $0.5N_y$, and (d) $0.75N_y$ and predicted by the analytical expression for cohesive soil

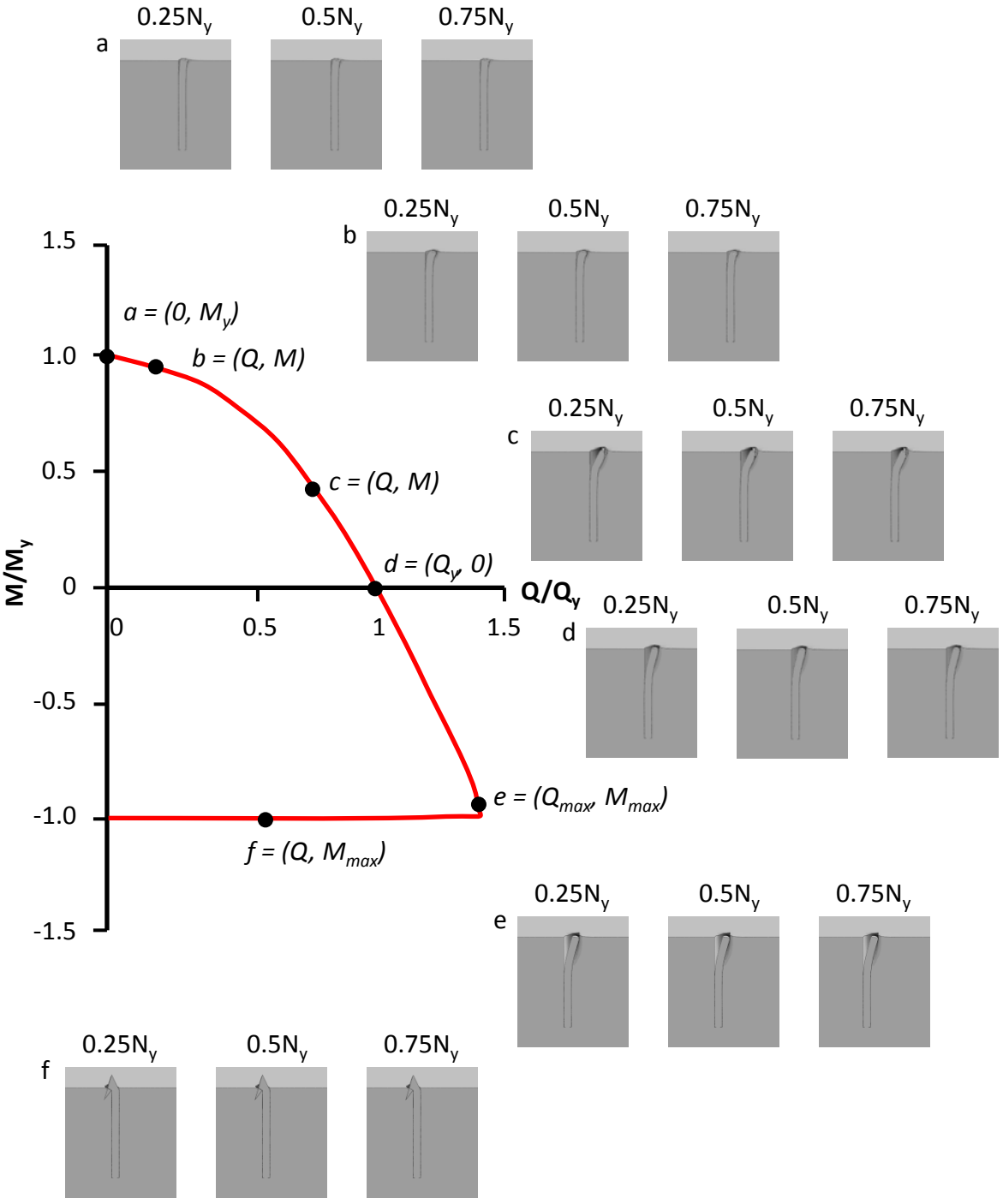

Figure 4.36: Q–M failure envelopes normalized by the respective lateral capacities Q_y and M_y when N = 0. Snapshots of the contours of plastic shear strain at failure are provided for characteristic points of the failure envelope and for three different vertical loads: (a) 0.25 N_y, (b) 0.5 N_y, and (c) 0.75 N_y

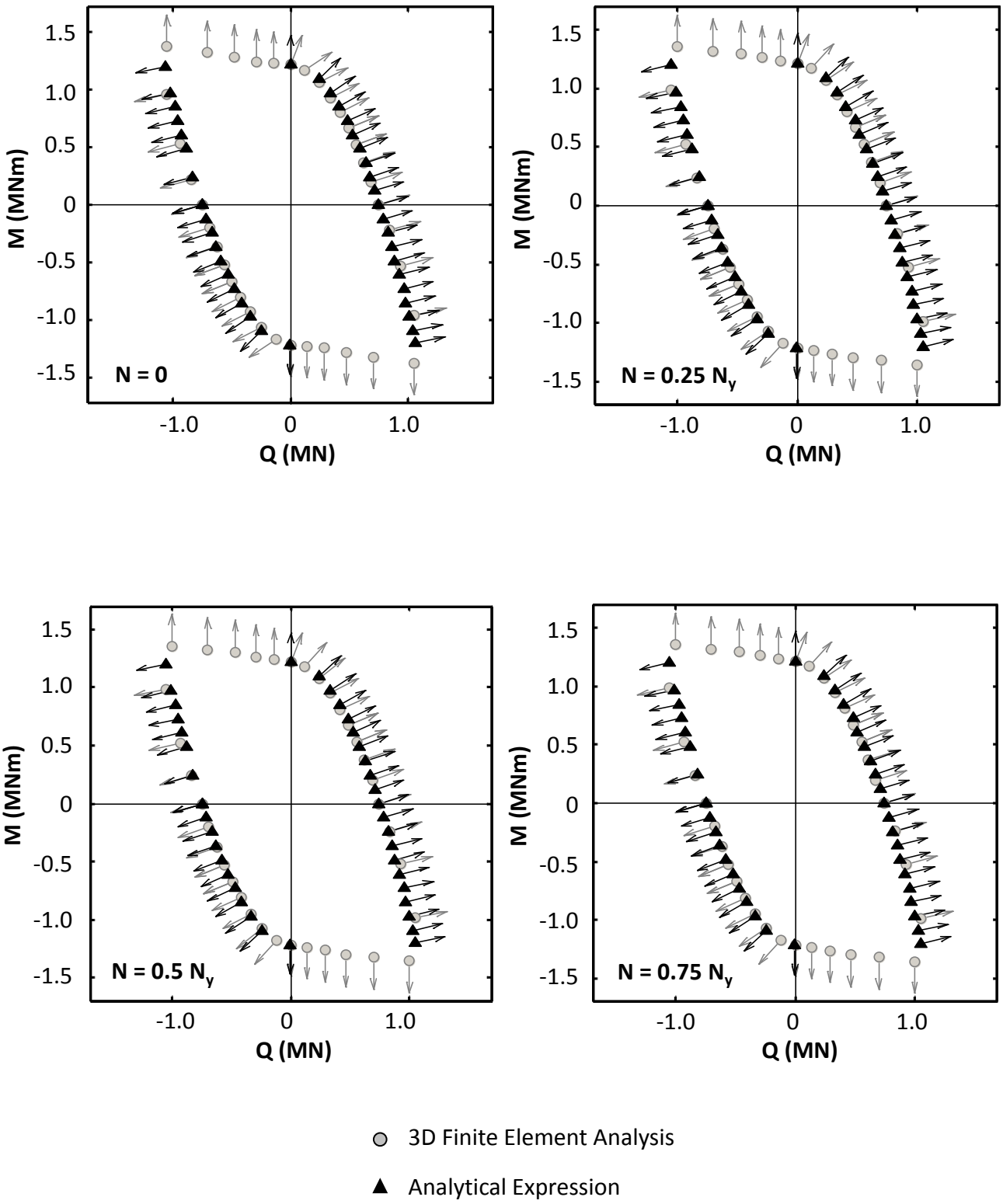

Figure 4.37: Comparison of the vectors from the analytical expression with the assumption of an associated flow rule with those from the incremental displacements at failure from the three-dimensional numerical analyses for cohesive soils with displacement-free conditions for different vertical loads: (a) 0, (b) $0.25N_y$, (c) $0.5N_y$, and (d) $0.75N_y$

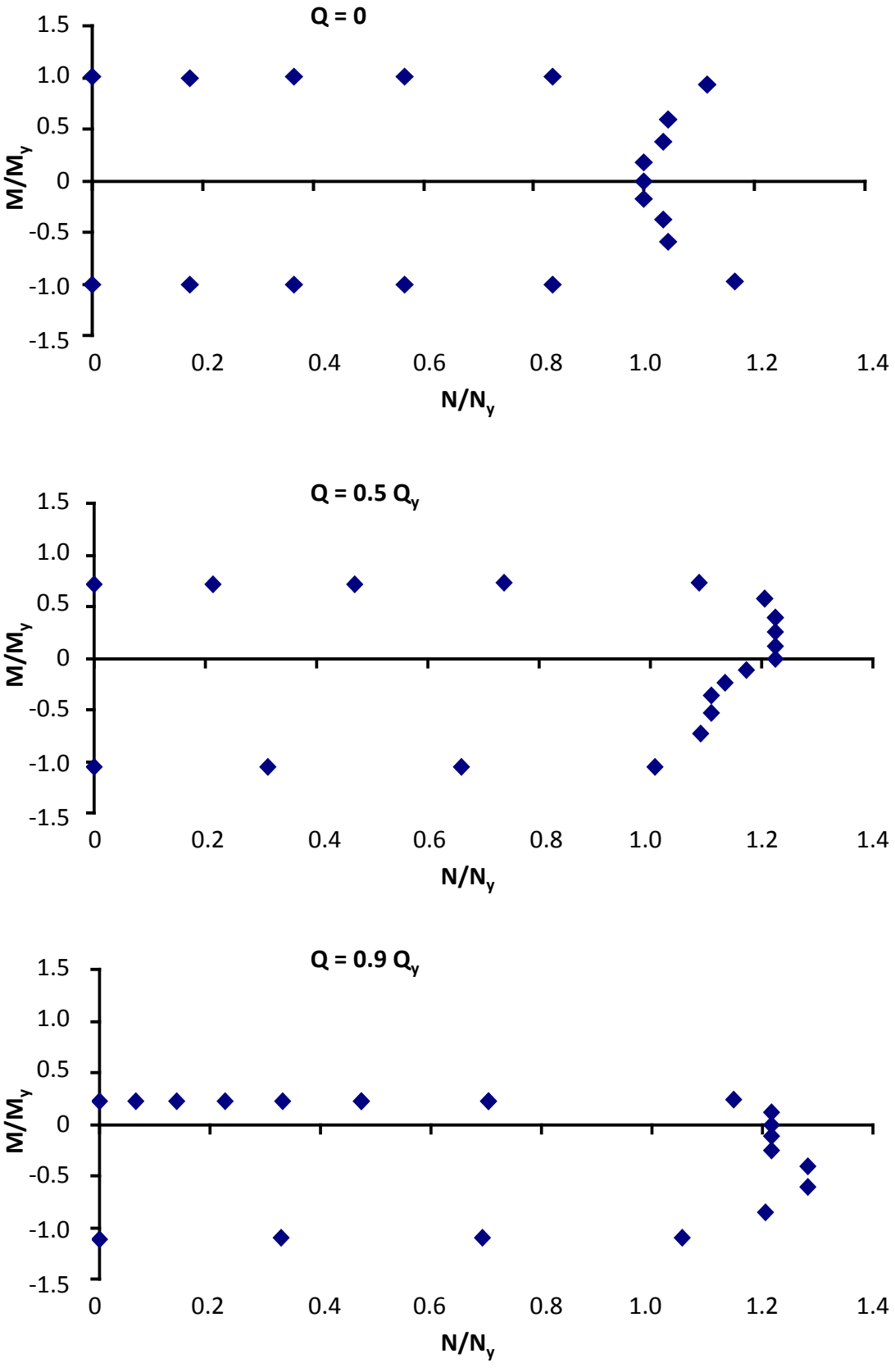

Figure 4.38: M/M_y–N/N_y failure envelope calculated by the three-dimensional numerical analyses for cohesive soils for constant lateral load: (a) 0, (b) $0.5Q_y$, and (c) $0.9Q_y$

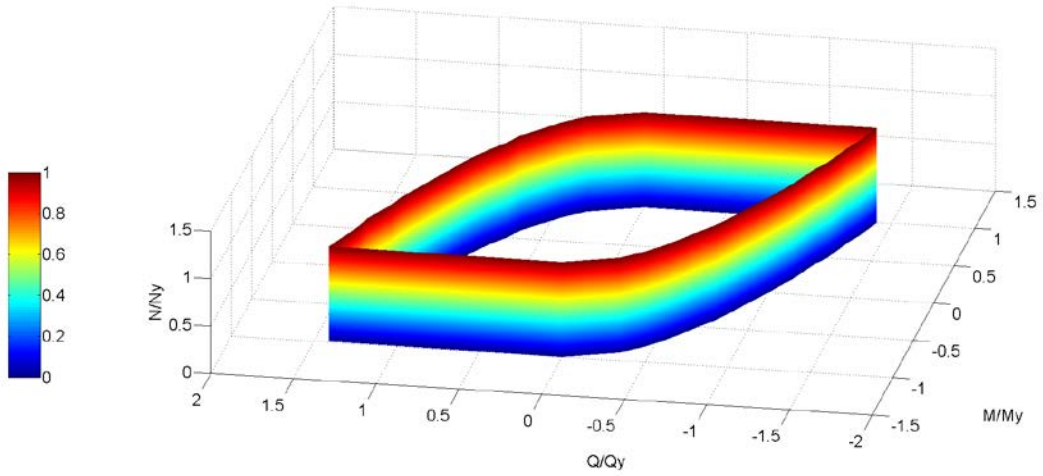

Figure 4.39: Proposed failure envelope of a single pile embedded in cohesive soil on the three dimensional plane M/M_y–Q/Q_y–N/N_y

CHAPTER 5:

MACRO-ELEMENT MODELING OF THE LATERAL RESPONSE OF FLEXIBLE PILES: FAILURE SURFACE AND PLASTIC FLOW RULE – EXPERIMENTAL VALIDATION

5.1 INTRODUCTION

Failure envelopes are a simple tool to estimate the ultimate loading of foundations. In order to validate the adequacy of the proposed failure envelope described in the previous chapters, results from a real-scale pushover test on a vertical flexible pile are compared with the analytical expression. The result of the real-scale pile is expressed as a single point at the failure envelope. A series of pushover tests on a vertical single pile embedded in dry sand under different load paths to failure in Q–M space was conducted in the Laboratory of Soil Mechanics / Dynamics in NTUA, thus providing several points on a failure envelope. The reference point is at the ground surface and the pile was modeled to behave as a flexible pile. To avoid reduced-scale testing problems, the model was tested in true scale (micro-pile).

5.2 VALIDATION AGAINST FULL-SCALE TEST

In this paragraph the proposed failure envelope is evaluated by comparing the prediction from the analytical expression against measured response of a pile at a test site in Iraq (Gerolymos, 2013).

A reinforced concrete pile with an overall length L = 25 m, diameter d = 0.8 m, and plastic moment M_{pl} = 800 kNm was installed in a construction site and was laterally loaded. The load was applied at 19 cm above the ground surface. The top 11 m of soil consist of soft homogeneous clay. The soil layers together with the SPT data are depicted in **Figure 5.1**.

Figure 5.2 presents the experimental setup. The loading frame was designed to apply a maximum lateral load of more than 37 tons in order to accommodate the

required load increments of the loading stages as instructed by ASTM D3966 – 07. Lateral loads and movements were recorded at various time points throughout the testing along one cycle of loading and unloading. The hydraulic cylinder and load cell were set against the test plate to the pile head in a horizontal position. The lateral movements were measured by two displacement gages attached to the pile head from the opposite side of the applied load.

The test was intended to determine whether the pile capacity was adequate throughout one cycle of loading and unloading under the applied lateral loads. During the loading stage a force equal to twice the working load is applied through 8 loading increments. After completing the loading stage, the unloading stage is conducted by unloading the total applied load through 4 loading decrements. The force–displacement curve of the loading stage is depicted in **Figure 5.3**.

The undrained shear strength of the clay deposit used for the comparison of the experiment with the proposed failure envelope was obtained from the SPT results according to Stroud and Butler (1975) with reasonable assumptions. Thus, a uniform undrained shear strength of S_u = 18 kPa was selected. According to Fleming et al (1992), the limiting lateral pressures for a pile in cohesive soils are given by:

$$p_u = \frac{P_u}{d} = 2S_u + \sigma'_v + \alpha S_u \frac{z}{d} \qquad (5.1)$$

where the factor α lies between 0.5 and 3. Thus, a uniform limiting lateral pressure was calculated with p_u = 5 S_u. The corresponding point at failure from the experiment in comparison to the proposed failure envelope is shown in **Figure 5.4**. The comparison is really satisfactory, but only one point on the failure envelope is determined. In addition, no data are available for the verification of the associated plastic flow rule. For this reason, a series of pushover tests on a vertical single pile embedded in dry sand under different loading paths was conducted in the Laboratory of Soil Mechanics / Dynamics in NTUA.

5.3 VALIDATION AGAINST LABORATORY TESTS

For most applications in civil engineering, the major and fundamental difference between soil and concrete is that the behavior of the former is strongly dependent on the stress state and stress path, whereas the latter is generally not. This implies that any

laboratory or field test which fails to correctly model the stress state and stress path will likely produce incorrect results. The main shortcoming of small-scale testing, which is alleviated by centrifuge model testing, is that generally involves low stresses. The significantly lower levels of effective stress in the model result in overestimating ϕ', as the latter is in fact a function of confining stress (Bolton, 1986) rather than a constant value, and as a result the soil appears to have larger strength and dilatancy in comparison to real-scale conditions. Nevertheless, 1 g testing is a valid method, provided that the scale effects and the stress-dependent soil behavior are considered in the design of the experiments and results are interpreted appropriately (Drosos et al, 2012). Although reduced−scale testing generally involves low stresses, this is not quite the case here owing to the significant load conditions of the pile and the normalized nature of the proposed failure envelope.

5.3.1 Experimental equipment

The response of a tubular single vertical pile (d_{out} = 3.0 cm, d_{in} = 2.8 cm, l = 60 cm) embedded in dry sand under different load paths to failure in Q–M space is studied experimentally. The pile head, considered as the reference point at the ground surface, is subjected to a combined load of overturning moment and horizontal force under a constant ratio M/Q (radial paths in Q–M space, Gouvernec, 2004) until the pile failure. The piles used are tubular made of aluminum alloy 6063 – F25 whose characteristics are given in **Table 5.1**. Each pile is instrumented with wire displacements transducers in order to measure the displacement and rotation at the pile-head. The length of the pile embedded in the sand is long enough to ensure that the pile will behave as flexible, in other words the plastic moment of the material will be lower than the maximum moment that the soil can sustain in the case of a short pile. **Figure 5.5** presents the experimental setup. In order to ensure repeatability of the test results, floating piles were abandoned and the piles tested are resting on the bottom of the sandbox. For no vertical load N, the ultimate lateral load Q_y and overturning moment M_y are determined. Different combinations of moment and lateral force at the ground surface can be produced by changing the height e of application of the horizontal load Q (hence M = Qe).

Longstone sand, an industrially produced fine and uniform quartz sand with D_{50} = 0.15 mm and uniformity coefficient $C_u = D_{60}/D_{10}$ = 1.42, is used in the experiments. The void ratios at the loosest and densest state have been measured as e_{max} = 0.995 and e_{min} = 0.614, and the specific weight of the solids as G_s = 2.64. The grain size distribution curve for the sand is shown in **Figure 5.6**. The material and strength characteristics of the sand, as derived through a series of laboratory tests, have been documented in Anastasopoulos et al (2010). In the present study, the initial soil sample was chosen to be of high density, $D_r \approx 94\%$ for all tests, to avoid soil densification during loading.

The sandbox is of internal dimensions, (length x width x height) 1.48 m x 0.78 m x 0.645 m, respectively. Transparent barriers have been placed at the two opposite larger sides of the box, in order to better observe the experimental procedure. These barriers are a combination of Plexiglas and glass. Plexiglas has been placed at the external side so that rigidity and durability are achieved, whereas glass has been put at the internal side, in order to minimize friction and simultaneously avoid scratching of the Plexiglas from the sand particles.

The Pushover Test apparatus, designed and constructed in the Laboratory of Soil Mechanics / Dynamics in NTUA, is used for monotonic and slow-cyclic pushover testing of soil-foundation-structure systems. The Pushover Test apparatus is equipped with an electronically controlled screw-jack actuator, having a capacity of 1 ton and producing a stroke of +/- 500 mm, with a maximum velocity of 50 mm/sec. The apparatus is rigidly attached to a reaction wall, while its free end is connected to the model through a linear guideway and a hinged connection in series, allowing the system to freely settle, slide, and rotate as horizontal displacement is imposed (**Figure 5.7**). A device capable of measuring the applied load on the pile (load cell) is connected at the edge of the actuator.

The wire displacement transducers (Space Age Series 6) were installed after completion of the model. The body of each transducer was fixed on the rigid walls of the sandbox, and the sensing wires were connected to the pile model. All sensors were connected to the data acquisition system.

5.3.2 Model preparation

The pile is first installed in the empty sandbox with its tip resting at the bottom. The vertical position of the pile is checked and wires from the rigid walls of the sandbox are connected to the pile head to maintain its vertical position during the raining process of the sand (**Figure 5.8**).

The sand specimens are prepared by an air sand raining process into the rectangular sandbox. The raining system, shown in **Figure 5.9**, consists of a bucket hanged from a steel beam, which is fixed on the roof of the laboratory. An electric motor moves the bucket horizontally along the length of the roof beam with a controllable speed. Moreover, another motor makes the bucket move in the vertical direction, sliding along the two vertical support beams. The bucket movement in both directions is operated by an electronic system, which allows remotely controlling of the pluviation speed and height during the sample preparation.

The bucket is filled with sand, which is poured through an opening of controllable aperture. After the bucket is fixed at a certain height above the sandbox, the shutter is removed and sand flows through the opening (**Figure 5.10**). Pluviation is conducted in steps of about 5 cm of soil layer. At each step the pluviation height (height of the bucket) is increased proportionally to achieve uniform distribution of the density with depth.

The achieved soil sample density during raining pluviation depends on the drop height and the discharge rate of the sand. The drop height is specified by the vertical position of the soil bucket whereas the sand discharge rate is controlled by the bucket opening and the velocity of its movement in the horizontal direction (pluviation speed). Hence, the calibration of the raining system focused on these three variables: (a) the bucket opening aperture, (b) the pluviation height, and (c) the pluviation speed.

The procedure followed for the preparation of the model is as follows:

(i) The aluminum model pile is covered with an artificial in-house interface consisting of glue-paper and sand, aiming to produce realistically rough soil–foundation interfaces

(ii) The model pile is installed in the empty sandbox in a vertical position and a cap is placed on its top to prevent sand from entering through the open tube while raining.

(iii) The sand is rained in layers until the edges of the sandbox.

(iv) When the sand reaches the desired height the surface is leveled and the cap removed.

After the sand raining is completed, a crane is used to position the sandbox from the sand raining room to the Pushover Test apparatus. When the sandbox is placed in position, the wire displacement transducers (Space Age Series 6) and the load cell that measures the impact load are installed and connected to the data acquisition system. When all connections are made the model is ready to be tested (**Figure 5.11**).

5.3.3 Experimental results

5.3.3.1 Results of preliminary tests

The pile is subjected to displacement control lateral loading. Preliminary tests were performed in order to figure out the influence of parameters such as pile diameter, soil-pile interface, soil density and pile position in the sandbox.

Initially, three very thin tubular piles of different diameter (6x4 mm, 8x6 mm and 10x8 mm) were tested in loose sand (D_r = 45%) under pure lateral loading conditions. The embedded length of the pile was 53 cm. No special interface was used between the soil and the pile. The experimental results are presented in terms of lateral load with respect to horizontal displacement at the ground surface. **Figure 5.12** depicts the influence of the pile diameter on the system response. As expected, the increase of the pile diameter increases the maximum soil reaction. The spikes observed in the load–displacement diagram are attributed to the sliding of the Pushover Test apparatus on the aluminum pile surface. The maximum system response is almost two times higher than the one predicted by Broms' method for friction angle of the sand at critical state, a fact that can be attributed to several factors such as the change of the friction angle, the high dilatancy, the small-scale effects and the stress-dependent soil behavior. But since the proposed failure envelope is normalized and the measured ultimate lateral load is used for the definition of the failure envelope, this difference is eliminated. Another important point is that the depth of plastic hinge from the ground surface increases with the pile diameter from 16 cm for the 6x4 mm pile to 18 cm for the 8x6 mm pile and 19 cm for the 10x8 mm pile.

The next test took place in dense sand of D_r = 94% and the embedded pile length reached 60 cm. Because the ultimate lateral loads for the previous pile tests were low

compared to the capacity of the utilized equipment, piles of larger diameters were also tested. In this experiment the influence of the relative density of the sand as well as the influence of the existence of different interfaces was tested. Thus, the piles tested were (i) a 8x6 mm pile with no interface, (ii) a 10x8 mm pile with no interface, (iii) a 10x8 mm pile with an in-house made soil-pile interface consisting of glue-paper and sand, (iv) a 30x28 mm pile with no interface, (v) a 30x28 mm pile with an in-house made soil-pile interface consisting of glue-paper and sand, and (vi) a 30x28 mm pile with sandpaper N 120 as soil-pile interface. **Figure 5.13** demonstrates the increase in soil resistance with increasing soil density from D_r = 45% (loose sand) to D_r = 94% (dense sand). It is observed that after reaching a maximum loading for the case of dense sand, the system exhibits a softening-like behavior. The piles examined are the ones with diameter 8x6 mm and 10x8 mm (outer and inner diameter, respectively) without the use of extra soil-pile interface. In the case of the dense sand the depth of plastic hinge from the surface of the pile decreased compared to the loose sand from 18 cm to 13 cm and from 19 cm to 15 cm for the 8x6 mm and the 10x8 mm pile, respectively.

Figure 5.14 depicts the influence of the soil-pile interface on the soil reaction. In **Figure 5.14a** the response to lateral loading of a 10x8 mm pile with no interface (smooth interface) is compared to the one of a 10x8 mm pile with an in-house made soil-pile interface consisting of glue-paper and sand (rough interface). It is observed that the existence of an interface smoothes the load−displacement curve since the developed friction on the new interface prevents the Pushover Test apparatus from sliding on the pile as the latter bends. The diameter of the pile is very small though, and no difference is observed on the lateral system capacity. For this reason, piles of bigger diameter were also checked (30x28 mm) with three different soil-pile interfaces: (1) no interface (smooth), (2) the in-house made (rough) interface, and (3) a (very rough) interface with N 120 sandpaper (**Figure 14b**). It is observed that in the case of the pile with no interface, the Pushover Test apparatus slides in the beginning of the test and the load is acting in a higher point on the pile, thus changing the loading conditions. The measured soil resistance is almost 30% less than in the case of the rough interfaces. The difference in the lateral response of the piles with the rough and the very rough interface is minor and thus, the in-house made (rough) interface was selected for the subsequent pile tests. It

has to be noted that the plastic hinge was developed at 20 cm for the pile without interface and at 23 cm at the other two piles.

The influence of pile position on the measured response for the same experimental conditions was checked by testing a 30x28 mm pile with rough interface at two different locations: (i) at the center of the sandbox (**Figure 5.15**), and (ii) at a position of 1/3 of the length of the sandbox. **Figure 5.16** compares the two alternative pile locations in the sandbox through the monotonic loading response curves. For the same experimental conditions, no significant differences are observed in terms of stiffness and ultimate lateral load capacity. The maximum lateral capacity was measured 102 kg and 98 kg for the first and the second experiment, respectively, while in both experiments the depth of plastic hinge was 24 cm from the surface. Moreover, upon reaching a peak value, the pile exhibits a softening - like response.

5.3.3.2 Results of the pushover test series

Having figured out the influence of parameters such as pile diameter, soil-pile interface, soil density and pile position in the sandbox, it was decided to test a tubular pile of 30x28 mm diameter with rough in-house made soil-pile interface consisting of glue-paper and sand embedded in dense sand (D_r = 94%) at the center of the sandbox for the whole series of tests performed. As already mentioned, the piles studied are subjected to displacement control lateral loading. Monotonic loading is imposed either at the pile head considered to be at the ground surface, or at a specified distance from ground surface in order to produce a moment acting at the ground surface. The sequence of the experiments performed was:

(1) lateral load at the ground surface level in order to determine Q_y (97.15kg; Point 1,0)
(2) pure moment conditions in order to validate the plastic yield moment M_y of the pile (18.19 kgm; Point 0, 1)
(3) lateral load applied at 32 cm above the ground surface (Point 0.47, 0.80)
(4) lateral load applied at 20 cm above the ground surface (Point 0.59, 0.63)
(5) retest of the pile under lateral load applied at 32 cm above the ground surface in order to check the repeatability of the experiments (Point 0.46, 0.79)
(6) lateral load applied at 10 cm above the ground surface (Point 0.75, 0.40)

(7) lateral load applied at 6 cm above the ground surface (Point 0.88, 0.28)

(8) first test of pile under lateral load applied at the ground surface and moment acting on the opposite direction (Point 1.27, -0.47)

(9) second test of pile under lateral load applied at the ground surface and moment acting on the opposite direction (Point 1.44, -0.62)

(10) lateral load applied at 56 cm above the ground surface (Point 0.28, 0.84)

Aiming to ensure the validity and repeatability of the testing procedure and gain confidence in the presented data, the lateral pushover test for the pile subjected to lateral load at 32 cm above the ground surface (Test 3) was repeated (Test 5) and, indeed, the results were very consistent. In **Figure 5.17** the comparison of the lateral force−horizontal displacement at the pile head curves shows quite satisfactory agreement between the results of the original and repeated test, indicating that the experimental conditions are repeated with accuracy in every experiment.

Figure 5.18 compares the failure envelope of the analytical expression for piles embedded in cohesionless soil with the points of the pairs of overturning moment M and lateral force Q at failure normalized with the values of pure moment capacity M_y and pure lateral loading capacity Q_y, respectively, as derived from the laboratory experiments. Despite small-scale effects, it is observed that the points almost coincide with the proposed failure envelope, since the methodology used eliminates the possible errors. The red triangle on the figure corresponds to the repeated test performed in order to check the repeatability of the experiments for pile under lateral load applied at 32 cm above the ground surface.

Figure 5.19 illustrates the vectors from the analytical expression with the assumption of an associated plastic flow rule along with those from the measured incremental displacements at failure. Rotation was not measured for the two experiments of a pile subjected to lateral load applied at the ground surface and moment acting on the opposite direction because the deflected shape of the pile prevented precise measurements. However, when the moment and lateral load act on the same direction, the vectors from both approaches are graphically identical. Therefore, the assumption of an associated plastic flow rule for the macroscopic behavior of a flexible pile is justified. Thus, the analytical expression for the failure envelope is only needed for the definition of the plastic flow rule.

5.4 NUMERICAL MODELING OF THE PUSHOVER TESTS

The pushover tests described in the previous section are modeled numerically with three different numerical models:

- A simplified beam-on-nonlinear-Winkler-foundation model (Model 1) for static analysis. The soil is modeled with spring elements while the pile is modeled with 2-node beam elements (in plane). Model 1 is used for the validation of the experiments through Class B predictions (Lambe, 1973).
- A fully 3D Finite Element model taking into account material nonlinearities (Model 2) for static analysis. The soil is modeled with 8-node brick elements while the pile is modeled with 2-node beam elements (in space) and 8-node brick elements with appropriate kinematic restraints. Model 2 is used as a tool to reproduce the experimental results by introducing a fourth parameter to the proposed constitutive model of **Chapter 2** which accounts for soil softening through the variation of friction angle with octahedral strain.
- A 3D Finite Element model of the pile without the soil (Model 3) for static analysis with Riks method. The pile is modeled with 4-node shell elements. Model 3 is used to validate the moment−displacement response of the tested pile.

All models are created using the finite element code ABAQUS (Dassault Systèmes Simulia Corp, 2009).

The beam-on-nonlinear-Winkler-foundation model (Model 1) was created after Test 2 was performed, having defined the lateral capacities for pure lateral loading Q_y and moment M_y. As in **Chapter 4**, a simple ideal model is applied to construct the numerical model shown in **Figure 4.2** for analyzing the responses of the pile-soil model system under different load conditions. Model 1 uses 2D beam elements to simulate the pile and adopts a series of independent springs to model the soil reaction. A free-head pile is embedded 60 cm in uniform elastic-perfectly plastic soil of Winkler type. The structural moment−curvature response of the pile cross-section is assumed to be bilinear, defined with the yield point (M_y, κ_y) where M_y is the yield moment and κ_y is the yield curvature and an ultimate point (M_u, κ_u) where M_u is the ultimate moment and κ_u is the ultimate curvature. The stiffness coefficients of the soil springs are calculated according to Makris and Gazetas (1992). The distribution of Young's Modulus for the

Longstone Sand varies parabolically with depth according to the empirical equation of Loli et al (2011):

$$E = 2000p^{0.4} \quad (5.2)$$

where p the hydrostatic pressure. Based on Broms' method for flexible piles in cohesionless soils (Broms, 1964), an equivalent constant friction angle of $\phi = 64^{o}$ was found for the sand through back analysis of Test 1 and was used for the calculation of ultimate soil resistance of the springs. Having calibrated the model to match the values of the moment capacity and the lateral load capacity of the pile, Class B (Lambe, 1973) predictions of Tests 3 – 7 and 10 were performed (M and Q act on the same direction) in order to gain insight on the selection of the appropriate height of the load application.

After the completion of the experiments, the tests were simulated in 3D. The pile and soil are analyzed at model scale, assuming model parameters appropriate for very small confining pressures. The cross-section of the Finite Element mesh of the pile with the sandbox is depicted in **Figure 5.20**. Approximately 45000 elements were used for each analysis. The pile in Model 2 is modeled as elastic-perfectly plastic with 3D beam elements placed at its center and connected with appropriate kinematic restraints with the nodes at the perimeter of the pile in order to model the complete geometry of the pile.

The behavior of the soil-pile system under pure moment depends only upon the pile characteristics. Thus, the numerical behavior of the pile is validated against Test 2 which was performed in order to verify the ultimate moment capacity of the pile as derived from the alloy specifications. In this test, the pile was fixed to the sandbox through an aluminum plate and a lateral load was applied at 32 cm above the fixity point (**Figure 5.21**). Due to the existence of initial gaps between the plate and the pile and to the flexibility of the equipment used for this measurement, only the value of the ultimate moment capacity was verified. For the flexural stiffness, a model of the pile alone (Model 3) consisting of 4-node shell elements was created (**Figure 5.22**) in ABAQUS which captured the shape of the yielding pile and the force–displacement curve for a load acting at 32 cm from the fixed points of the pile. Model 3 uses the Riks method of analysis which is suitable for unstable collapse and postbuckling analysis (Riks, 1979). As observed, the deformed shape of the pile of Model 3 is remarkably similar to the

deformed shape of the tested pile. Thus, the flexural stiffness from Model 3 was used as the flexural stiffness of the pile in Models 1 and 2 (**Figure 5.23**). It can be observed that Model 3 with Riks method of analysis captures satisfactorily the experimental response. The same figure depicts the elasto-plastic behavior of Models 1 and 2.

Having calibrated the pile structural behavior, the soil-pile system behavior of Models 1 and 2 are calibrated against Test 1 (lateral load at the ground surface). The constitutive model for cohesionless soils developed in **Chapter 2** is encoded in ABAQUS through a user subroutine. Isotropic strain softening is also implemented as a fourth parameter in the model. As depicted in **Figure 5.24**, strain softening is introduced by reducing the mobilized friction angle ϕ with the increase of the octahedral plastic shear strain. Initially, from 0 to 5 % strain, the friction angle of the soil equals to the peak friction angle ϕ_{peak} which varies with the vertical stress σ_v according to Anastastasopoulos et al (2010):

$$\varphi_{peak} = 53.1 - 2.8\ln\left(\sigma_v\right) \tag{5.3}$$

From 15 % strain and onwards, the friction angle of the soil equals to the friction angle at critical state $\phi_{cs} = 32^o$ and from 5 to 15 % strain linear interpolation is performed for the values of the friction angle. It must be noted that the proposed constitutive model cannot reproduce dilative response. The remaining model parameters are calibrated through the experimental data for small confining pressures. The empirical correlation of the Young's modulus distribution with depth for the Longstone Sand of Loli et al (2011) is utilized for the calibration of model parameter C, leading to:

$$C = 17000\sqrt{\frac{\sigma_v^{0.8}}{P_a}} \tag{5.4}$$

where σ_v the vertical stress and P_a the atmospheric pressure (approximately 100 kPa), while soil cohesion is c = 0.7 kPa. **Figure 5.25** presents the force–lateral displacement curve at the pile head derived from the experiment and the calibration of Model 2. It is observed that both the stiffness and the maximum lateral capacity of the pile of the calibrated 3D model match the experimental values. On the contrary, Model 1 was calibrated to match only the maximum lateral capacity of the pile.

Figure 5.26 shows the contours of the plastic strain magnitude of Model 2, plotted on the undeformed mesh, for the experimental setup of: (a) Test 1 (lateral load

at the ground surface), (b) Test 4 (lateral load at 20 cm above the ground surface), and (c) Test 10 (lateral force at 56 cm above the ground surface). The plastic strains are plotted on the same scale. It is obvious that larger plastic strains develop around the pile for the case of the pure lateral loading. Similarly, **Figure 5.27** depicts the contours of the active and passive stress states in terms of the state parameter k at the maximum measured lateral loading of the single pile in Test 1. k = 1 corresponds to pure triaxial compression loading condition (passive state) and k = 0 to pure triaxial extension loading condition (active state), while k ≈ 0.5 corresponds to the response of the soil in direct shear test. The calculated depth of plastic hinge formation coincides with the measured depth in the experiment.

Having calibrated Model 2 to match the measured lateral capacities M_y and Q_y, the behavior of the pile-soil system in the other tests was investigated. **Figures 5.28** to **5.34** compare the measured with the computed lateral force acting at various heights on the pile with the pile displacement at the ground surface. Both the stiffness and maximum force values from the numerical analysis compare well with the measured ones from the experiment. Some small differences that are observed can be attributed to the small soil variation from test to test and the soil dilatancy that is not captured by the proposed constitutive model. On **Figures 5.28** to **5.32** the predicted behavior of the pile-soil system with Model 1 is also plotted. Given the simplicity of the beam-on-nonlinear-Winkler-foundation model the results are quite satisfactory and the predicted radial paths in Q−M space compare well with the experimental ones.

5.5 SUMMARY AND CONCLUSIONS

In order to validate the analytically derived failure envelope presented in **Chapter 3**, the derived analytical expression is compared with results from a real-scale pushover test on a vertical flexible pile. Since the failure of the real-scale pile provides only a single point at the failure envelope, a series of pushover tests on a vertical single pile embedded in dry sand under lateral force and overturning moment combinations at the pile head were performed. Preliminary tests were carried out in order to examine the influence of parameters such as pile diameter, soil-pile interface, soil density and pile position in the sandbox. It was found that:

- In general, the maximum lateral soil reaction is higher than the one predicted by Broms' method for friction angle of the sand at critical state, a fact that could be attributed to several factors the most important of which is the strain dependency of the soil properties. However, the normalized failure envelope is not particularly affected by the aforementioned factors.
- The depth of plastic hinge from the ground surface and the maximum soil reaction increase with the pile diameter.
- The lateral pile resistance increases with increasing soil density from D_r = 45% (loose state) to D_r = 94% (dense state), while it remains almost unaffected by the pile position in the sandbox.
- Piles with three different soil-pile interfaces were tested: (1) no interface, (2) an in-house made (rough) interface, and (3) a (very rough) interface with N 120 sandpaper. In the case of the pile with no interface, the Pushover Test apparatus slides easily at pile surface as the pile deflects and the load is acting in a higher point on the pile, thus changing the loading conditions. Furthermore, the soil resistance is almost 30% less than in the case of the rough interface. The difference in the lateral response of the piles with the other two interfaces is minor.

The results from the Pushover Tests validate the proposed failure envelope and connect theory and numerical analysis from **Chapters 3** and **4** with practical applications, strengthening the accuracy of the analytical expression. From the perspective of a macro-element approach of the pile response the results encourage the hypothesis of normality rule for plastic flow.

Validation of the experiments was achieved through comparisons with results from Class B predictions from a simplified beam-on-nonlinear-Winkler-foundation model.

The Pushover Tests were modeled in 3D using the Finite Element method taking into account the nonlinear behavior of both the soil and the pile. A fourth parameter is introduced to the proposed constitutive model of **Chapter 2** which accounts for soil softening through the variation of friction angle with octahedral strain. The 3D Finite Element analysis yielded results that compare well with the measured pile response in terms of lateral load–lateral displacement at pile head, and is capable of reproducing the

failure modes observed in the experiments. The easy implementation of the Finite Element model provides a useful tool that captures the key parameters that influence the lateral response of piles.

REFERENCES

Anastasopoulos, I., Georgarakos, P., Georgiannou, V., Drosos, V., Kourkoulis, R., 2010, "Seismic performance of bar-mat reinforced-soil retaining wall: Shaking table testing versus numerical analysis with modified kinematic hardening constitutive model", *Soil Dynamics and Earthquake Engineering*, 30, pp 1089–1105

ASTM D3966 – 07, *Standard Test Methods for Deep Foundations under Lateral Load*

Bolton M.D., 1986, "The strength and dilatency of sands", *Geotechnique*, 36 (2), pp 65-78

Broms B.B., 1964, "Lateral resistance of piles in cohesionless soils", *Journal of Soil Mechanics and Foundation Division*, ASCE 90 (SM3), pp 123-156

Dassault Systèmes Simulia Corp, 2009, *ABAQUS User's Manual*, Providence, RI, USA

Drosos, V., Georgarakos, T., Loli, M., Anastasopoulos, I., Zarzouras, O., Gazetas, G., 2012, "Soil-Foundation-Structure interaction with mobilization of bearing capacity: Experimental study on sand", *Journal of Geotechnical and Geoenvironmental Engineering*, 138 (11), pp 1369–1386

Fleming W.G.K., Weltman A.J., Randolph M.F., Elson W.K., 1992, *Piling Engineering*, 2nd Edition, John Wiley and Sons Inc., New York

Gerolymos N., 2013, *Geotechnical Report for METKA S.A: Geotechnical calculation for pile lateral pushover test*, Al-Basra Power Plant Project, Iraq

Gourvenec S., 2004, "Bearing capacity under combined loading – a study of the effect of shear strength heterogeneity", *9th Australian and New Zealand Conference on Geomechanics*, Auckland, New Zealand, pp 527-533

Lambe, T.W., 1973, "Predictions in soil engineering", *Geotechnique*, 23 (2), pp 149-202

Loli M., Anastasopoulos I., Gelagoti F., Kourkoulis R., Gazetas G., 2011, "Inelastic response of footings: Numerical analysis against experimental simulation", *Research Report*, Laboratory of Soil Mechanics, NTUA

Makris N., Gazetas G., 1992, "Dynamic pile-soil-pile interaction. Part II: Lateral and seismic response", *Earthquake Engineering and Structural Dynamics*, 21, pp 145-162

Riks E., 1979, “An incremental approach to the solution of snapping and buckling problems”, *International Journal of Solids and Structures*, 15, pp 524-551

Stroud M.A., Butler F.G., 1975, “The standard penetration test and the engineering properties of glacial materials”, *Proceedings of the Symposium on Engineering Properties of Glacial Materials*, Birmingham, pp 117-128

Table 5.1: Pile characteristics

Name	Symbol	Model scale
Embedded Length	L	60 cm
External diameter	d_{out}	3 cm
Internal diameter	d_{in}	2.8 cm
Young's modulus	E	7. x 10^4 MPa
Yield Stress	σ_y	215 MPa

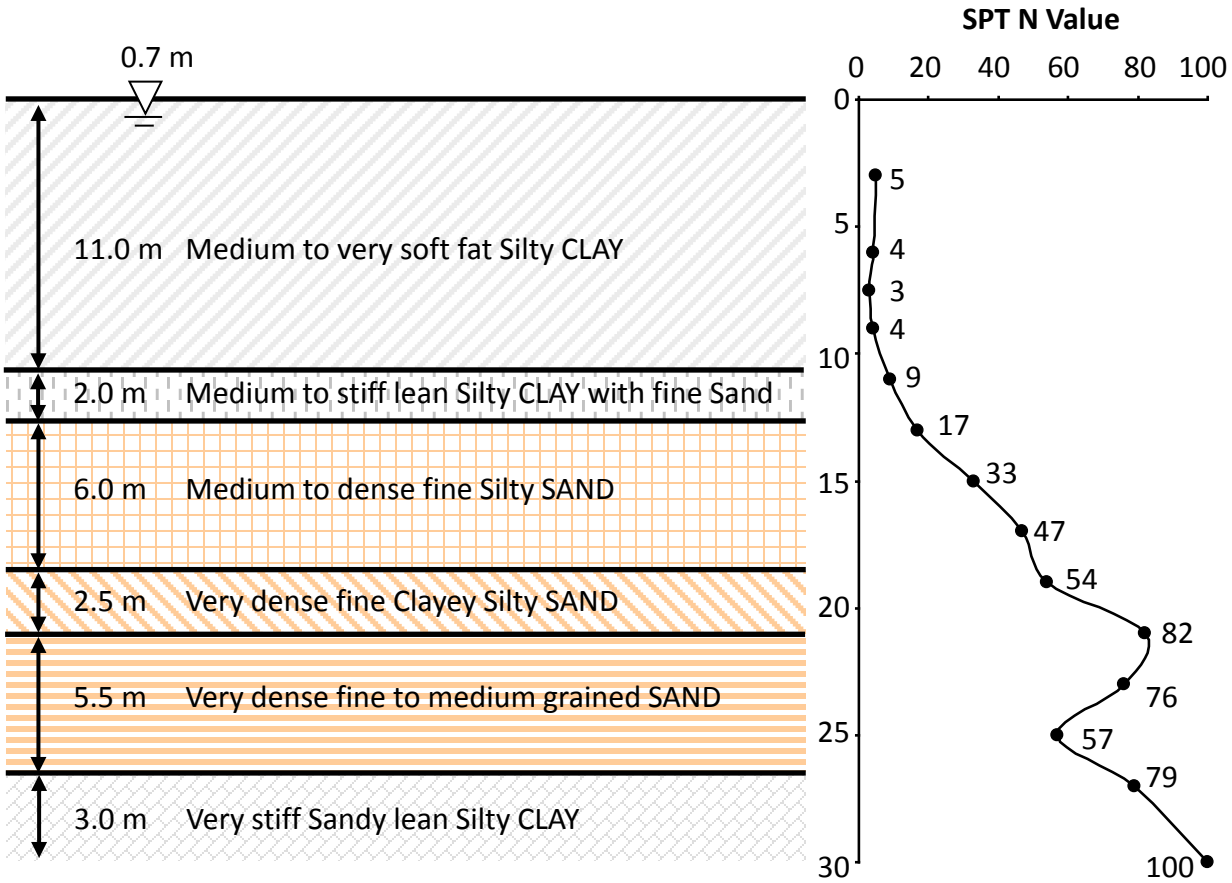

Figure 5.1: Soil layers and the SPT N values at the test site

Figure 5.2: Experimental setup (Gerolymos, 2013)

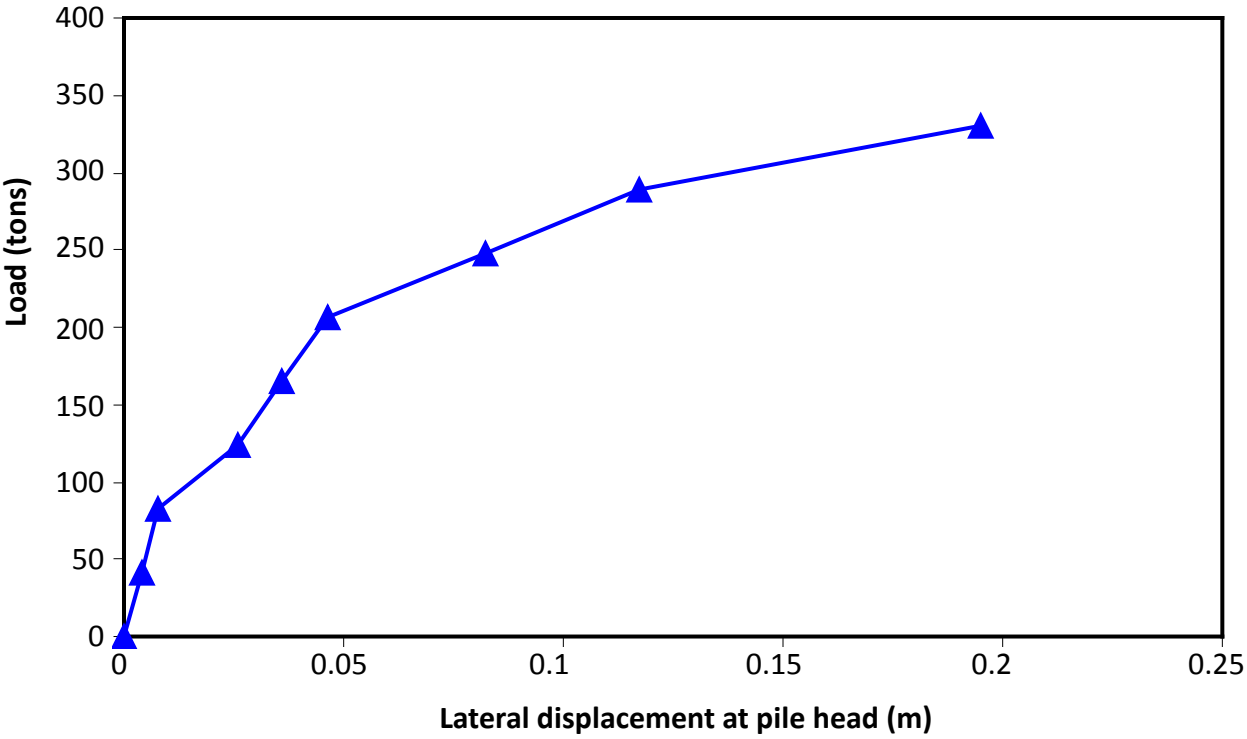

Figure 5.3: Experimental force–displacement curve at pile head for test

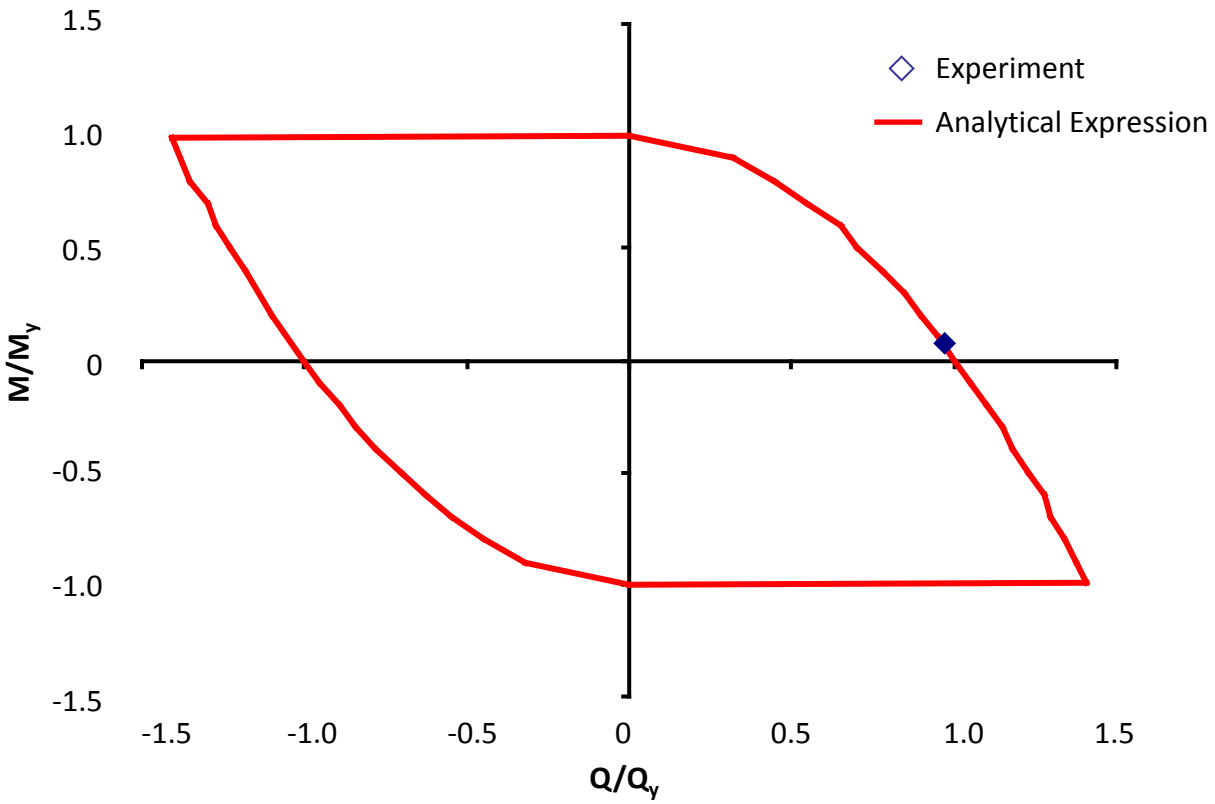

Figure 5.4: Comparison of the result of the real-scale experiment with the failure envelope from the analytical expression for pile in embedded in cohesive soil

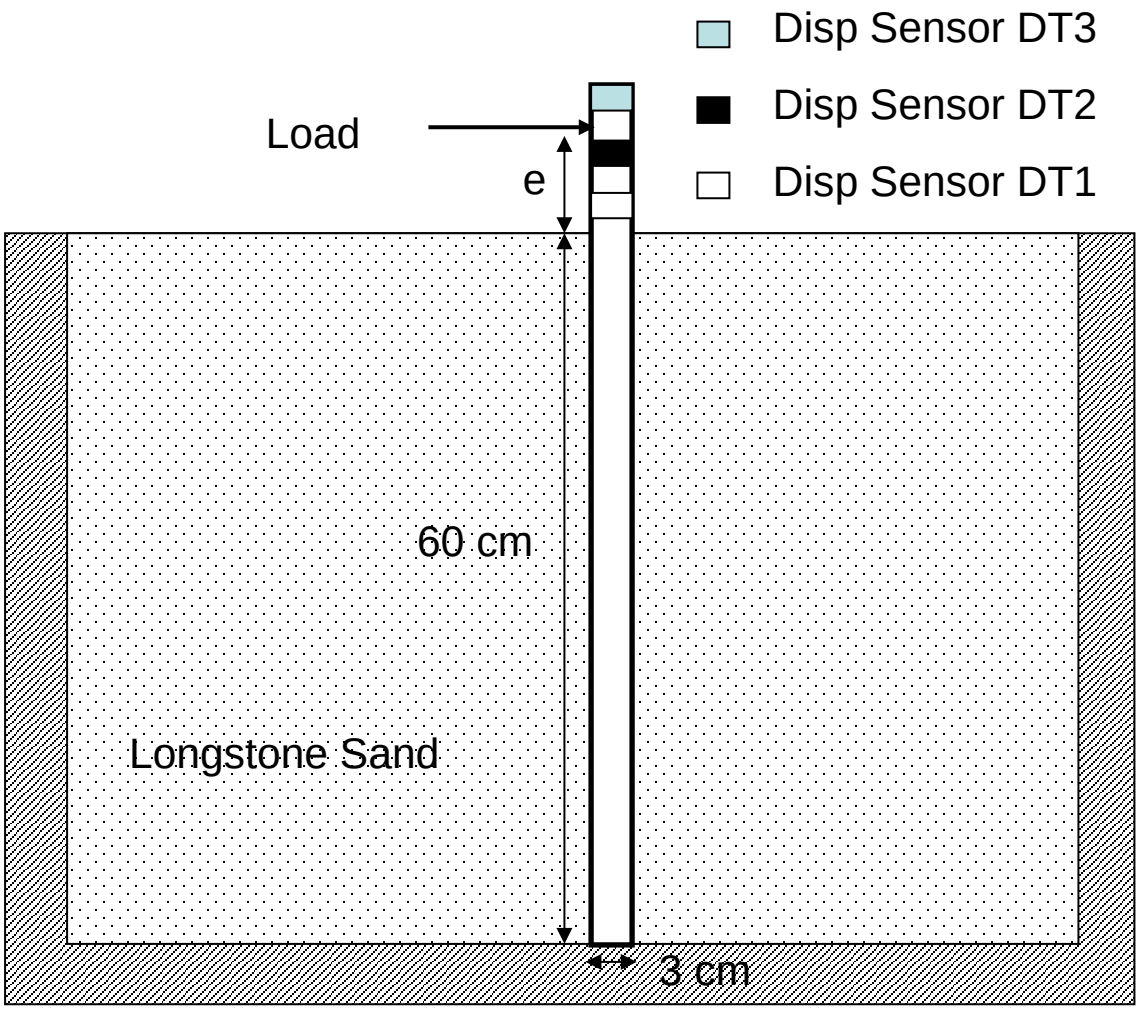

Figure 5.5: Pushover model setup: geometry and instrumentation

Figure 5.6: Grain size distribution of the "Longstone" sand used in the experiments, a fine uniform sand with d_{50} = 0.15 mm and uniformity coefficient C_u = 1.42

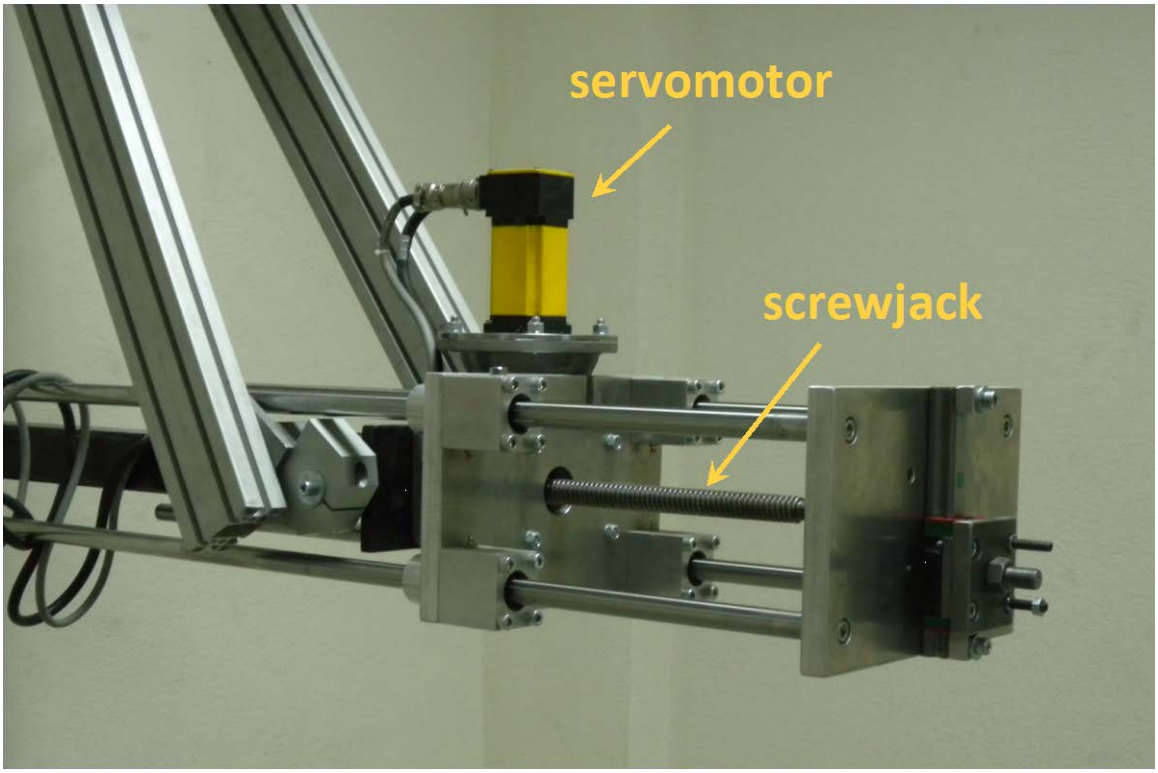

Figure 5.7: Push-over Test Apparatus

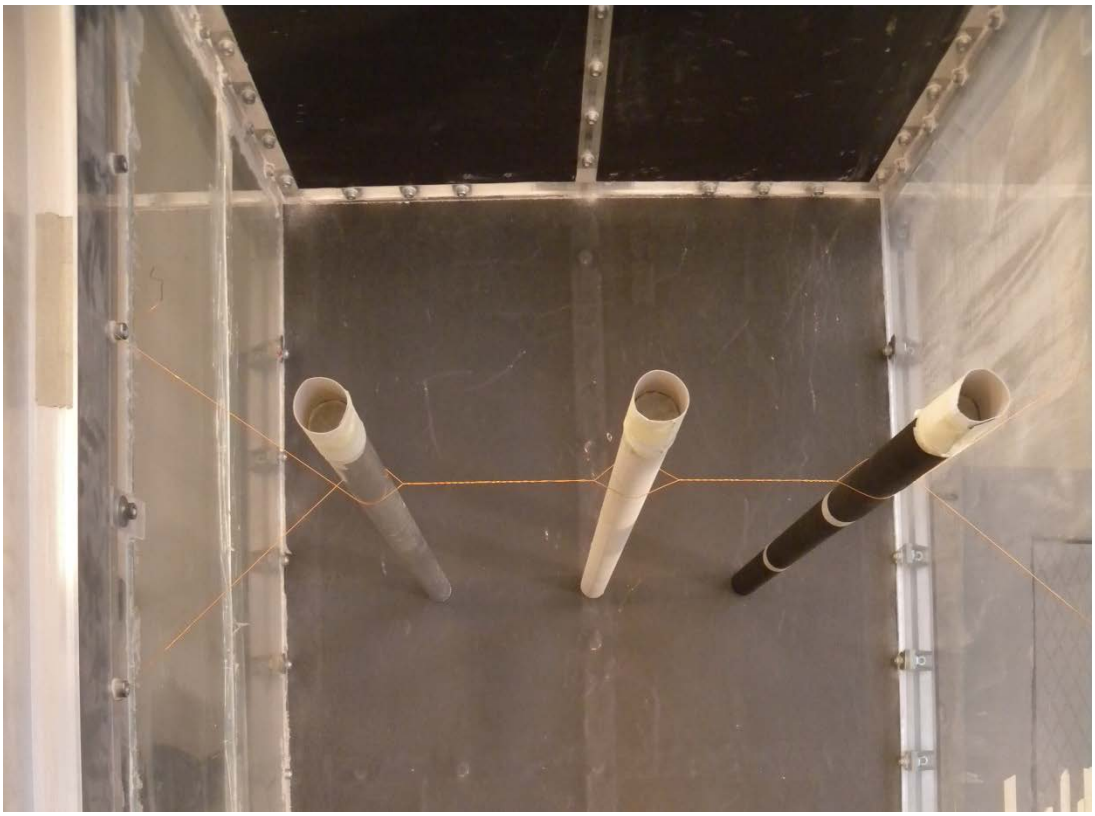

Figure 5.8: Position of the piles with different surface in the sandbox before the sand installation

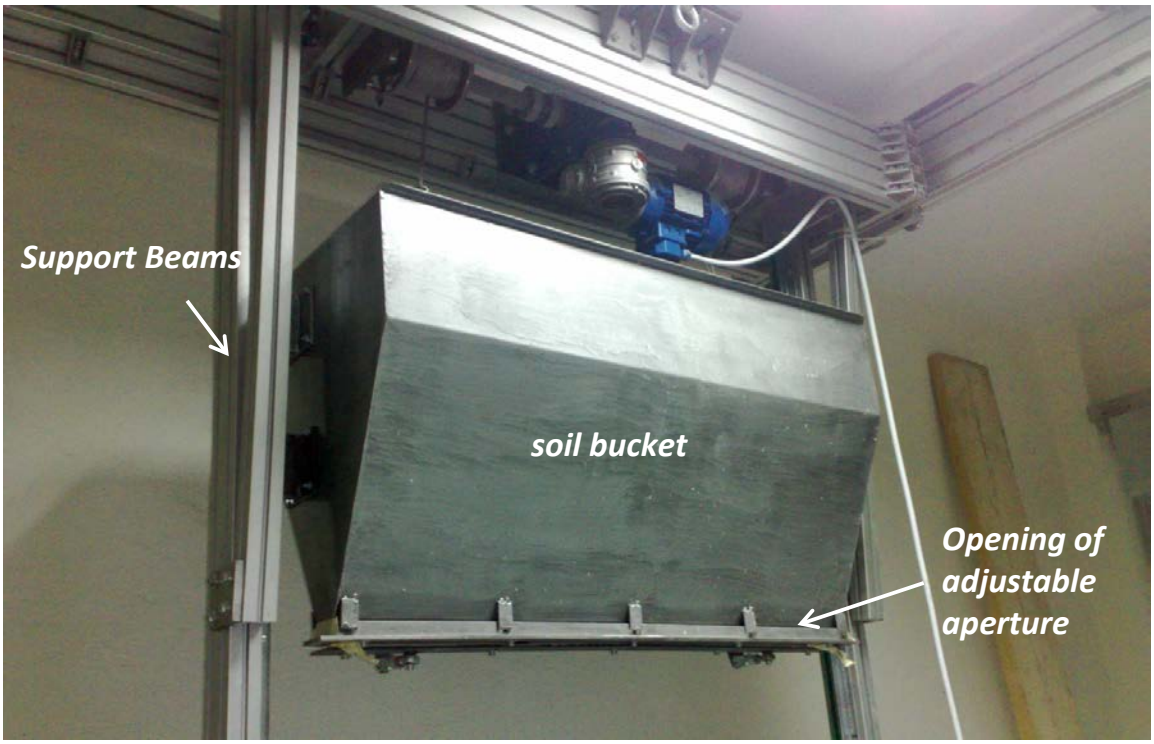

Figure 5.9: Electronically controlled raining system used for soil samples preparation in the Laboratory of Soil Mechanics / Dynamics in NTUA

Figure 5.10: Raining of sand in the sandbox

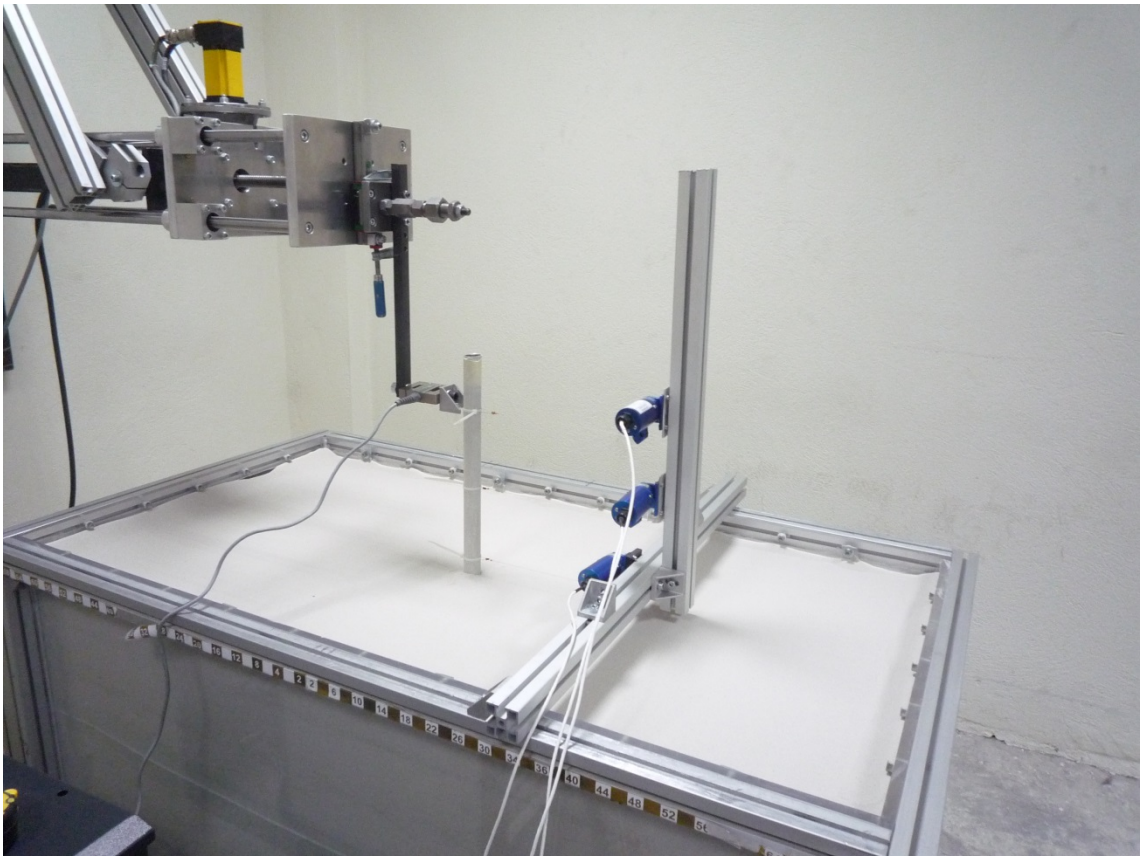

Figure 5.11: Pile model ready to be tested

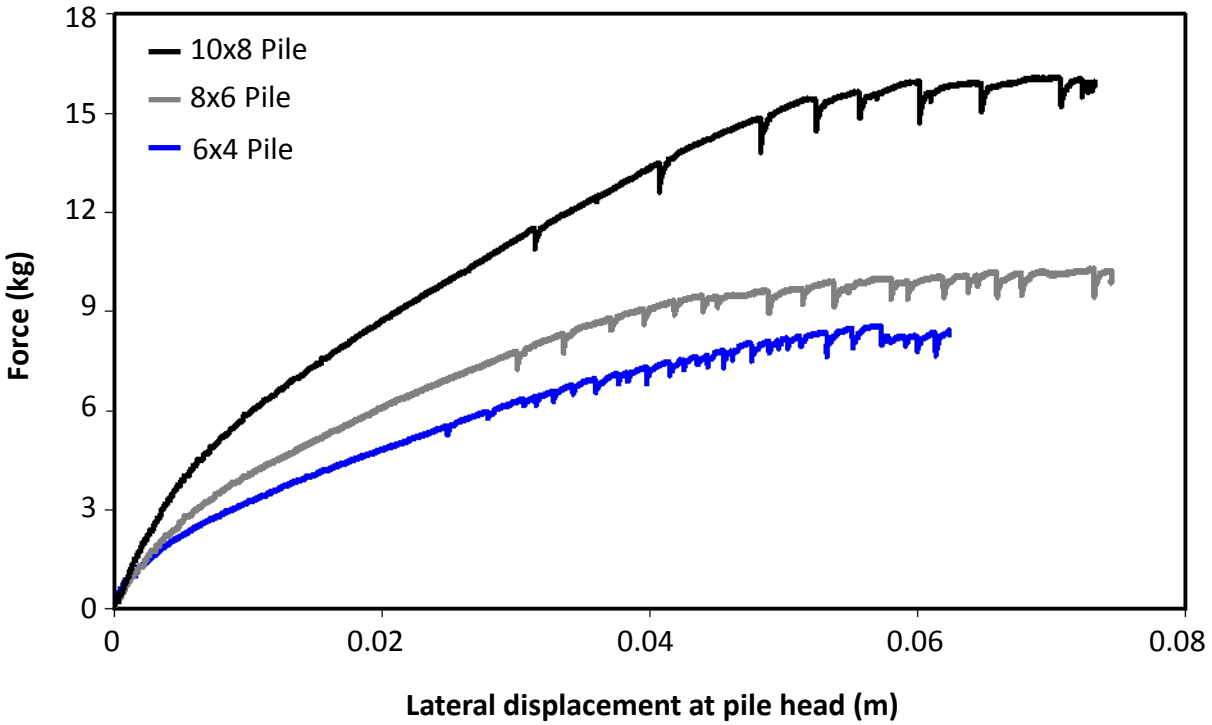

Figure 5.12: Influence of the pile diameter on the system response

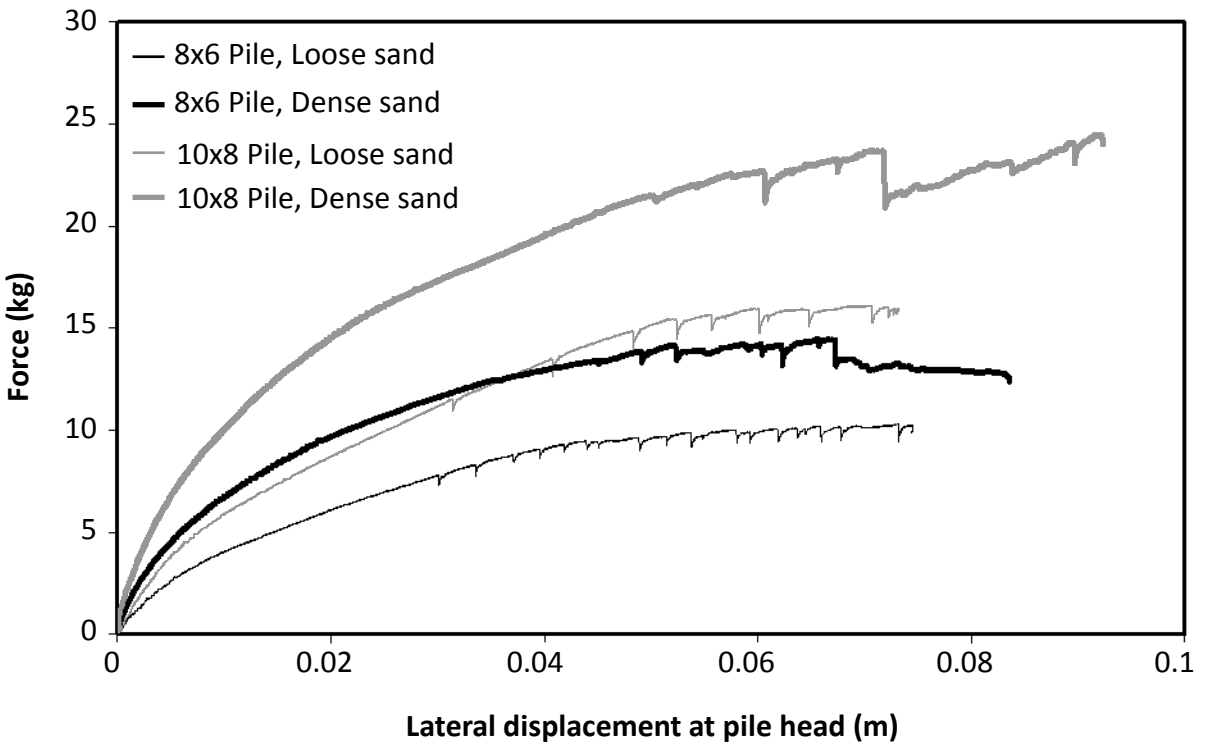

Figure 5.13: Influence of the soil density on the system response

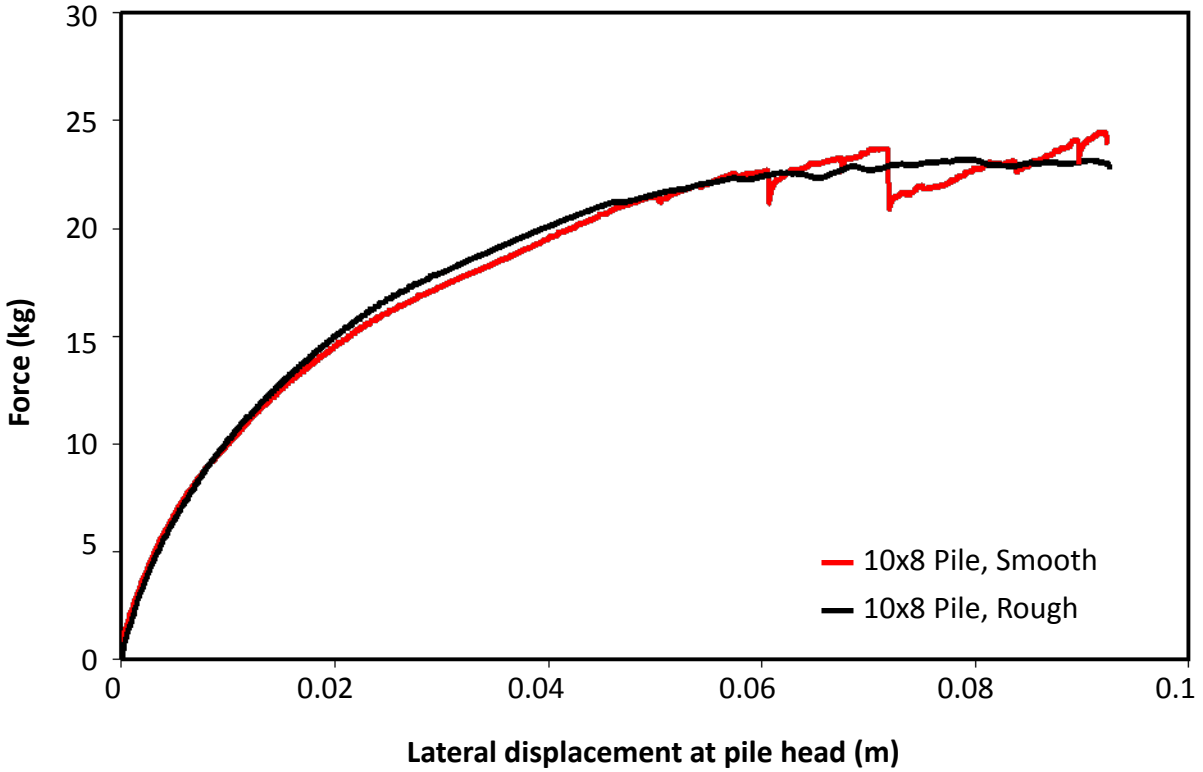

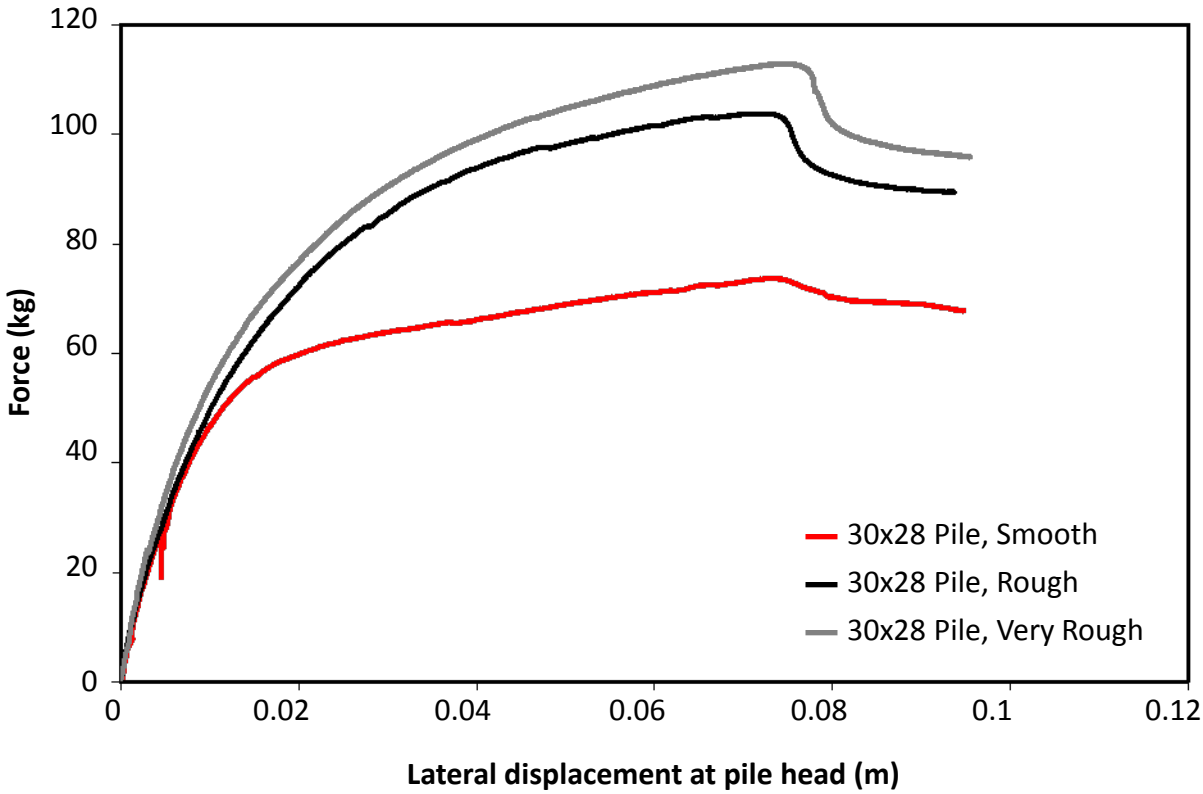

Figure 5.14: Influence of the soil-pile interface on the system response (a) on 10x8 mm (small) diameter pile, and (b) on 30x28 mm (big) diameter pile

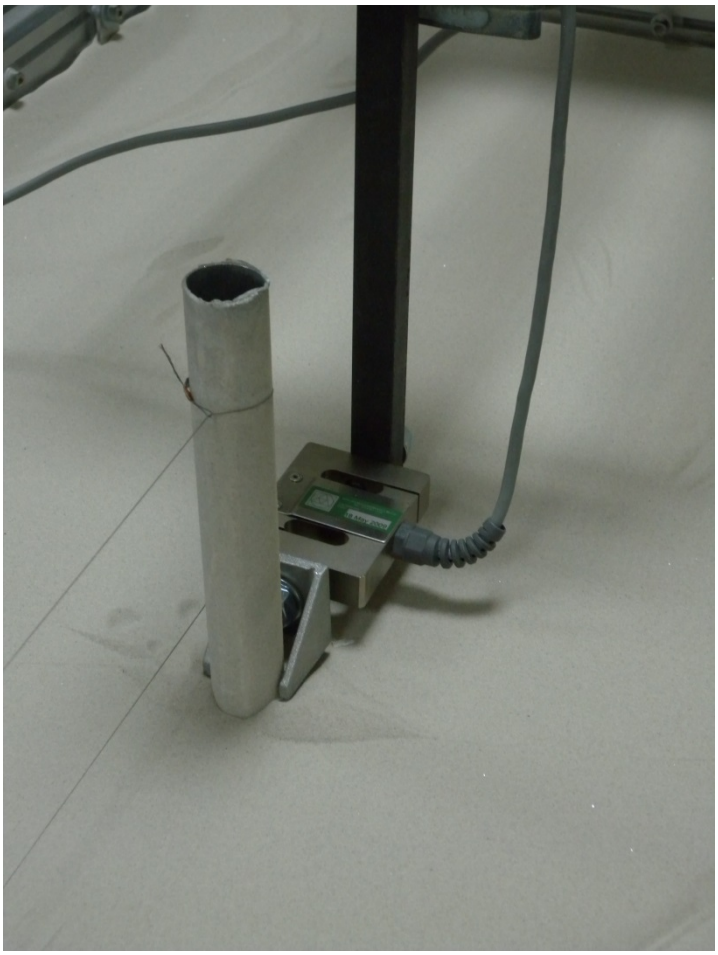

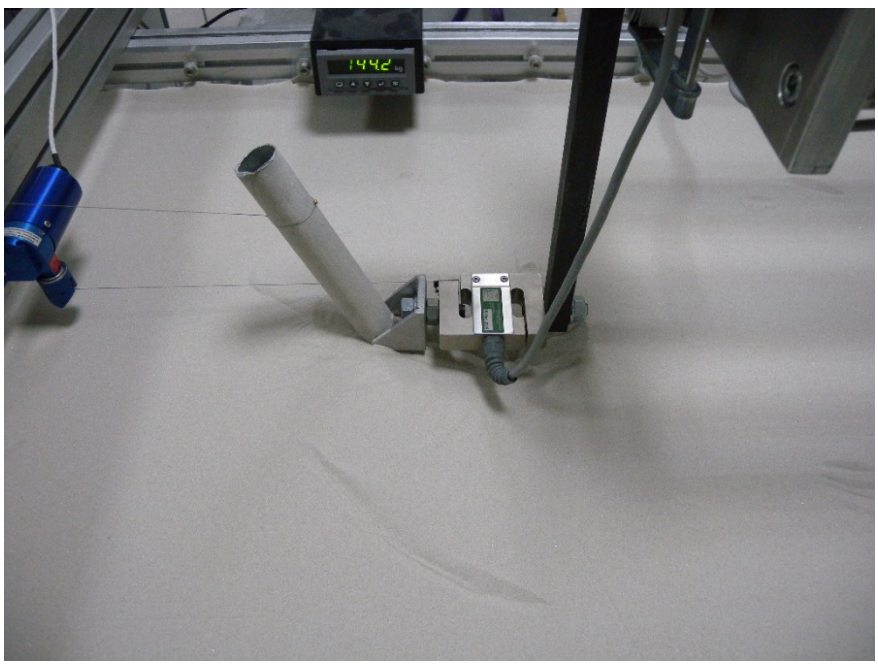

Figure 5.15: Lateral Push-Over test on the 30x28mm pile: (a) before the test, and (b) after the test

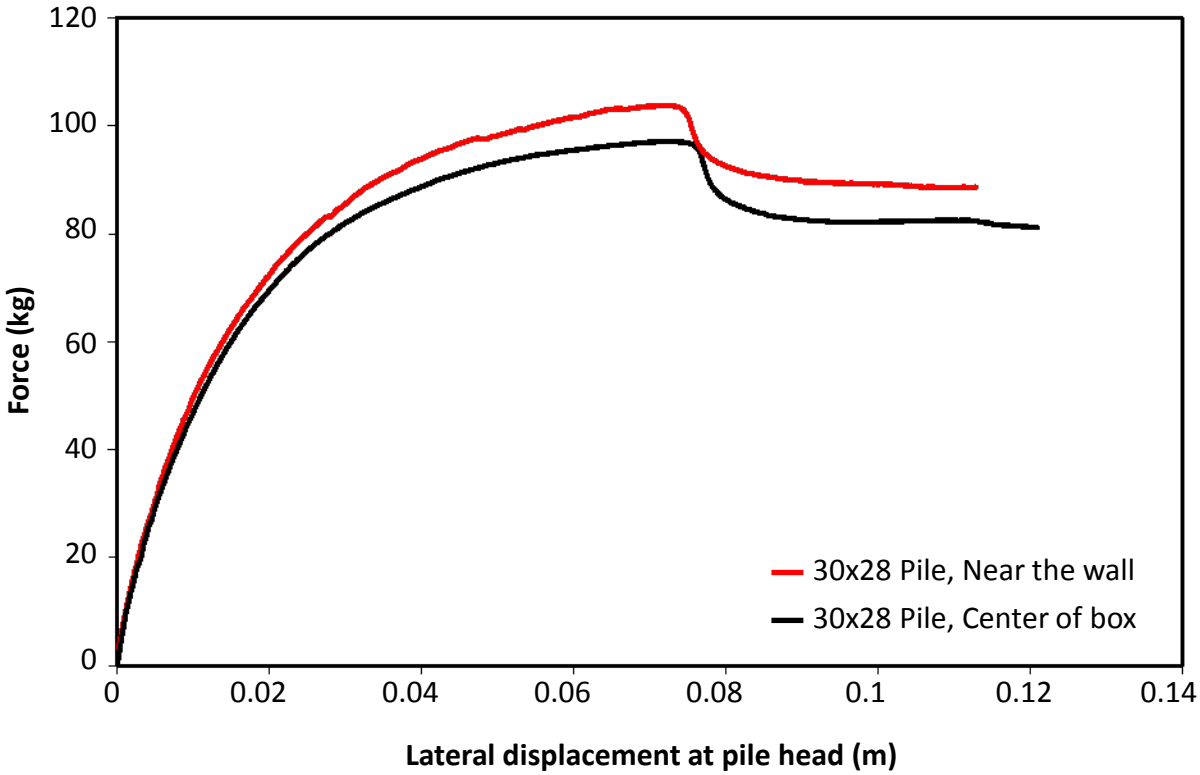

Figure 5.16: Influence of the position of the pile in the sandbox on the system response

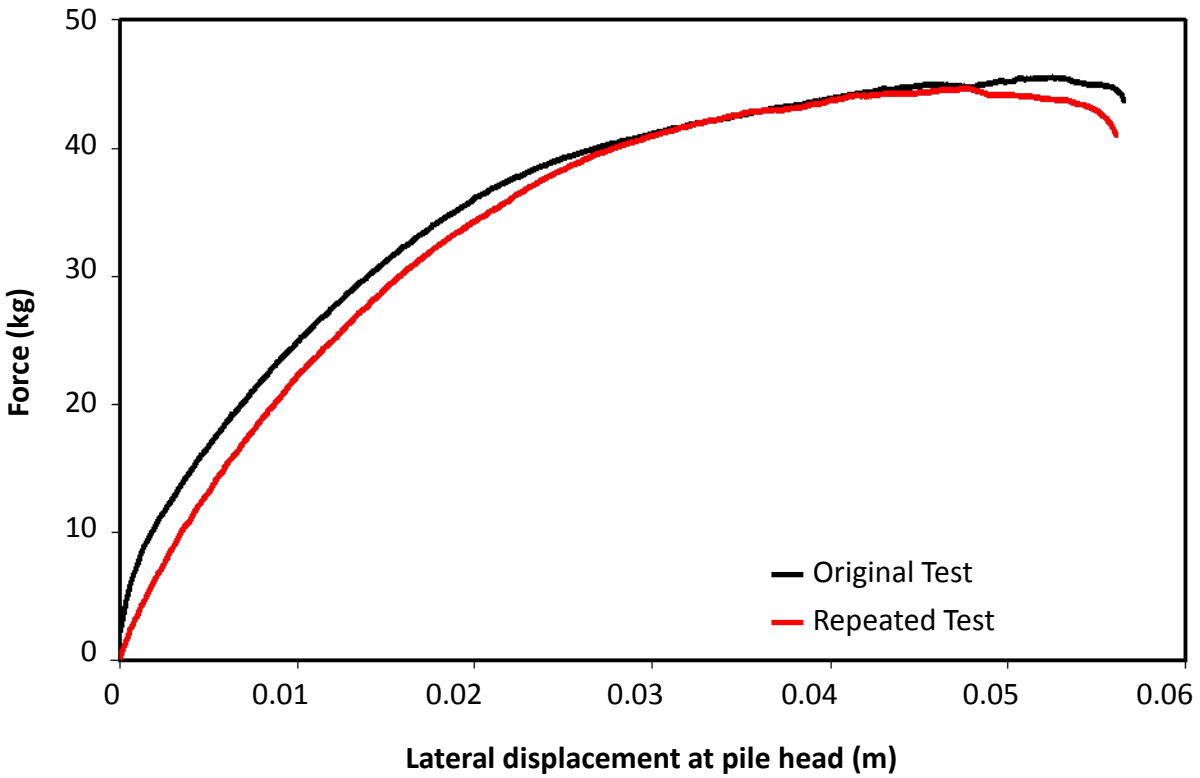

Figure 5.17: Comparison of the lateral load versus lateral displacement curves of two identical tests (Test 3 and 5) for pile under lateral load applied at 32 cm above the ground surface

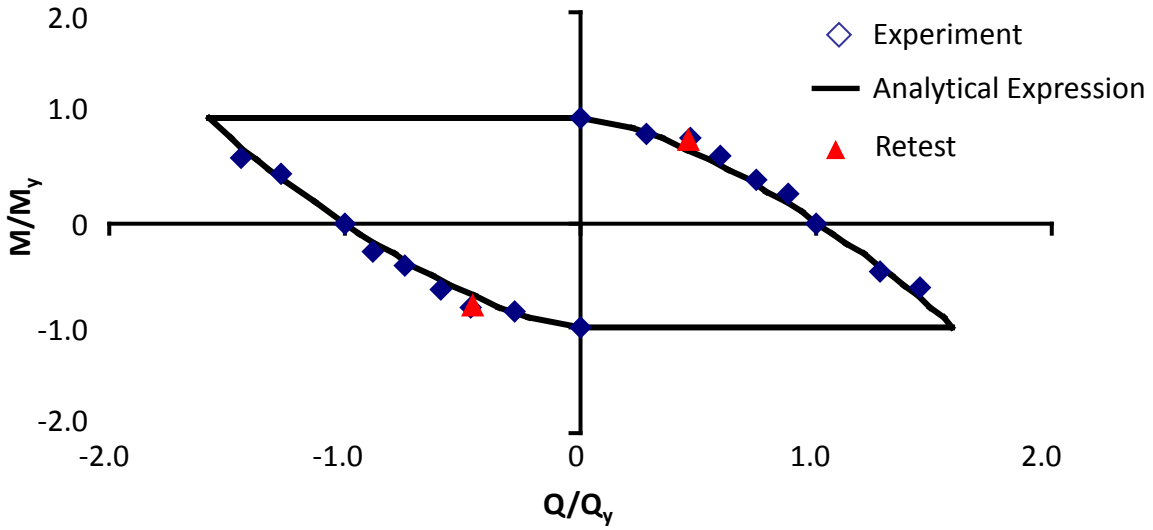

Figure 5.18: Comparison of the experimental results with the failure envelope from the analytical expression for pile embedded in cohesionless soil

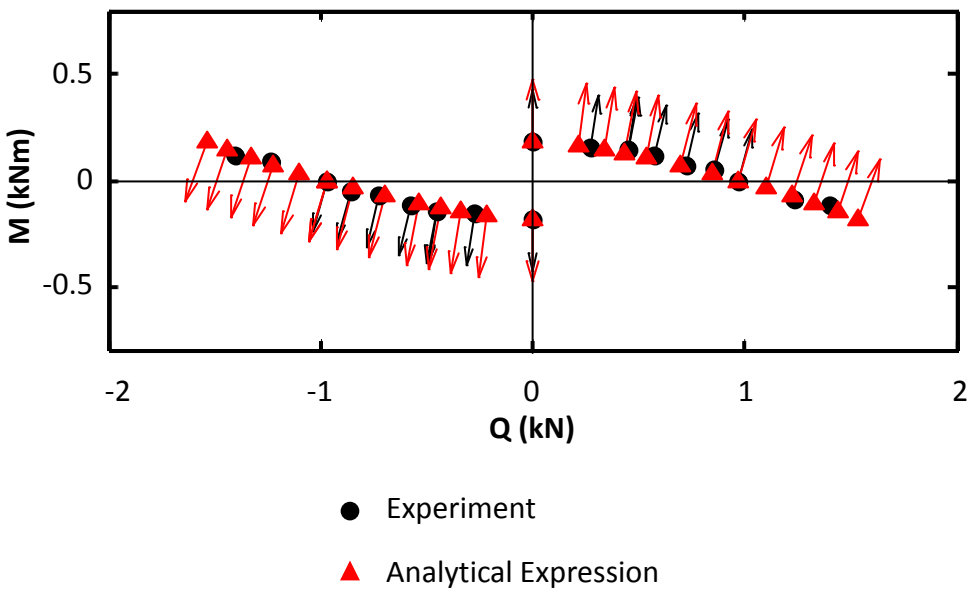

Figure 5.19: Comparison of the vectors from the analytical expression with the assumption of an associated flow rule with those from the measured incremental displacements at failure for pile embedded in cohesionless soil

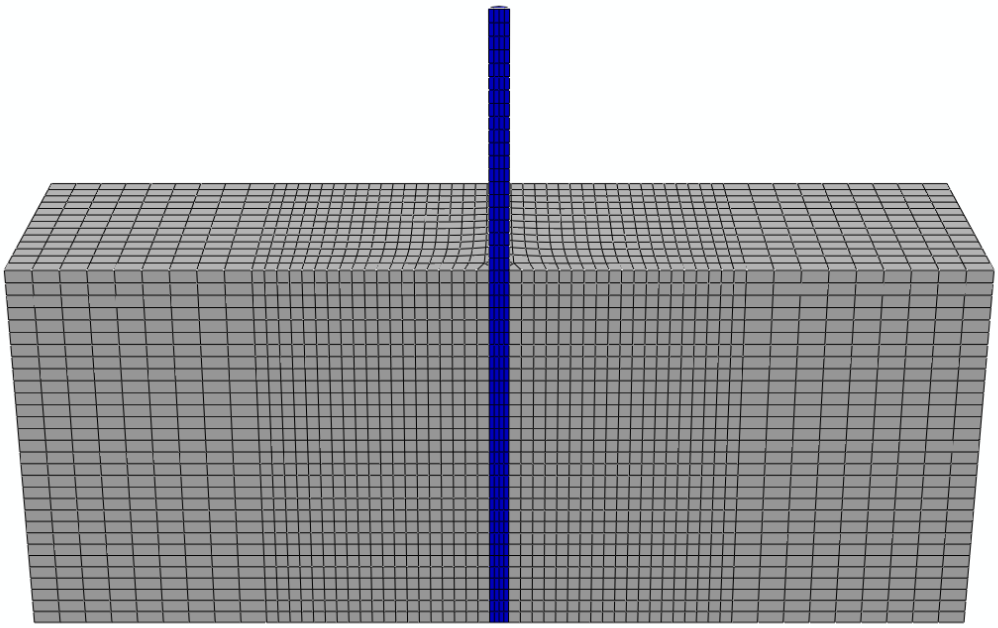

Figure 5.20: Cross-section of the 3D Finite Element mesh of Model 2 for the Pushover Tests

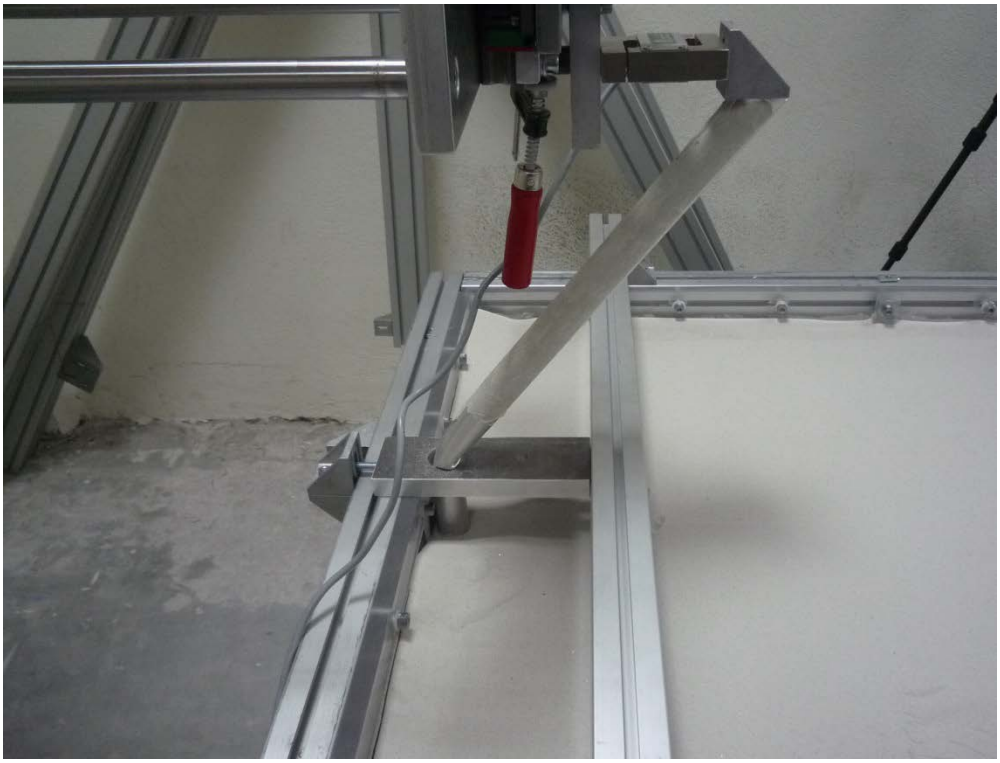

Figure 5.21: Pile under pure moment conditions (Test 2) in order to validate the yield moment M_y of the pile

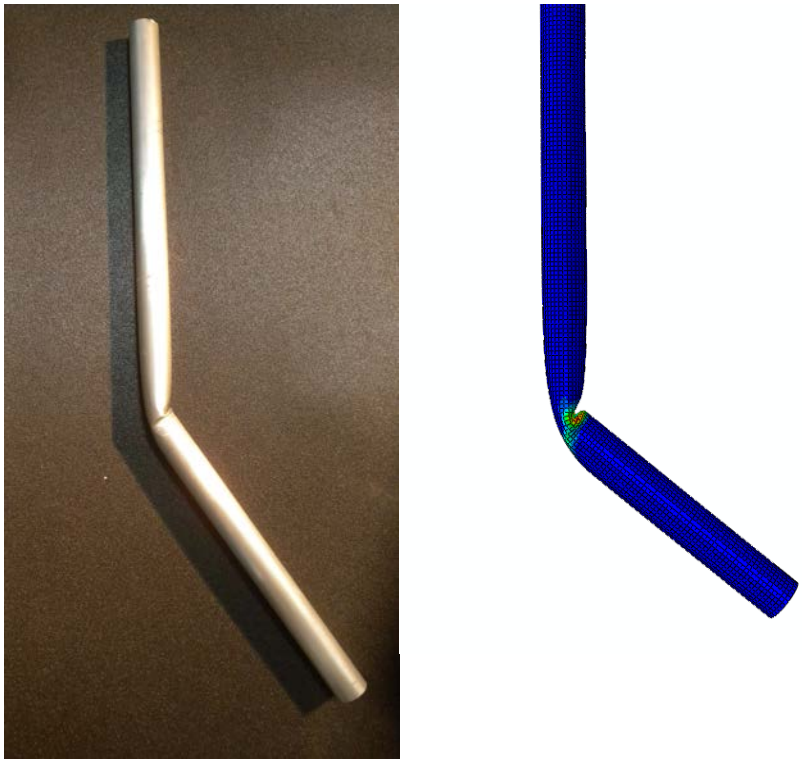

Figure 5.22: Comparison of the tested pile with the pile of Model 3 for load acting at 32 cm from the yielding surface (Test 2)

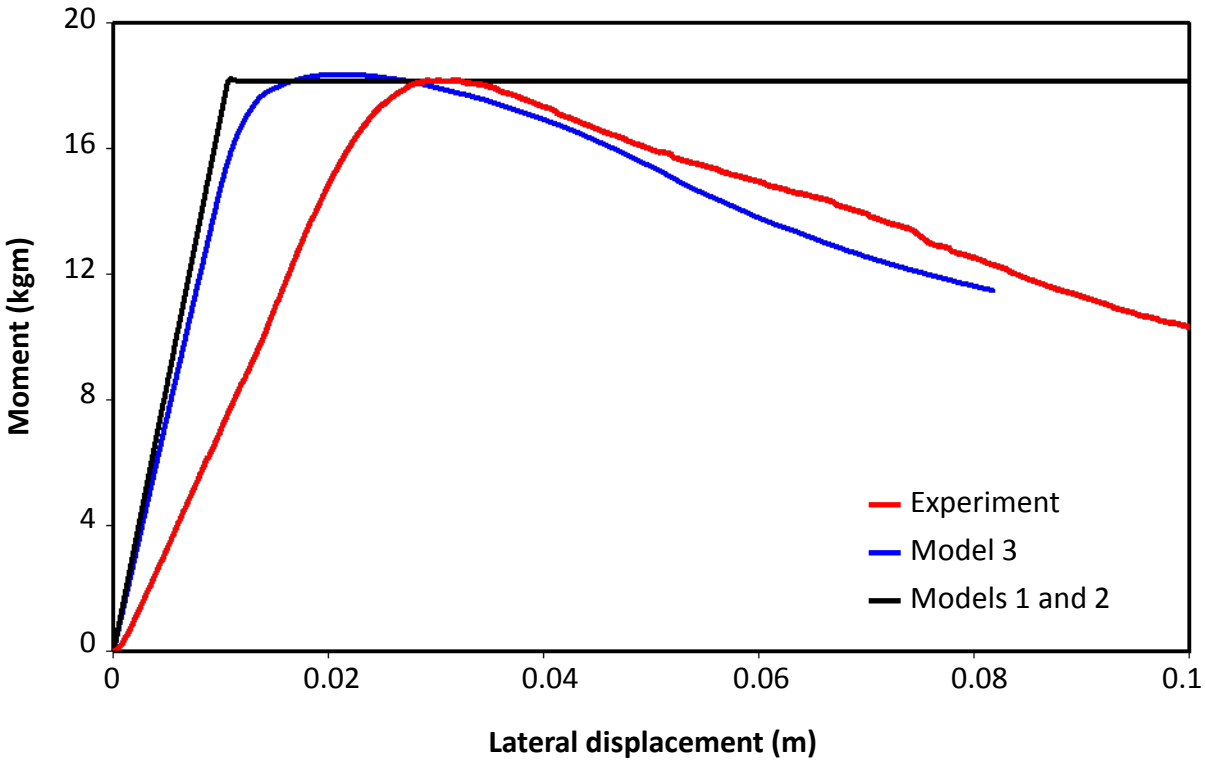

Figure 5.23: Experimental and numerical moment–displacement curves at pile head for Test 2 (pure moment conditions) in order to validate the pile response

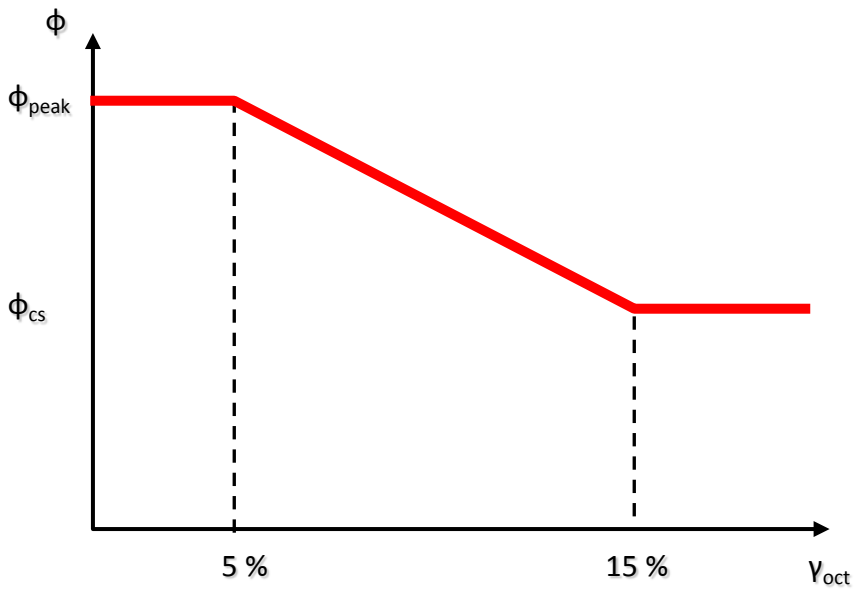

Figure 5.24: Variation of the friction angle ϕ with the octahedral plastic shear strain γ_{oct}

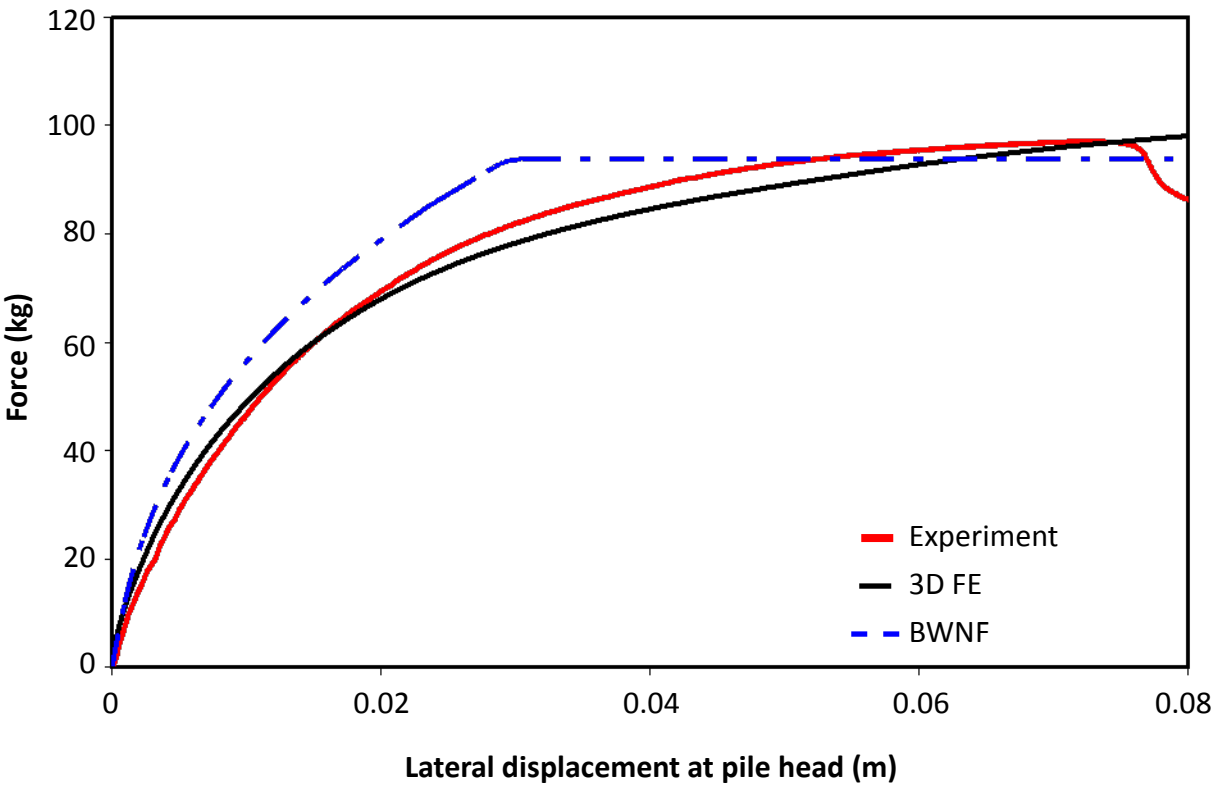

Figure 5.25: Experimental and calibrated (Models 1 and 2) force–displacement curves at pile head for Test 1 (lateral loading acting at the pile head at the ground surface)

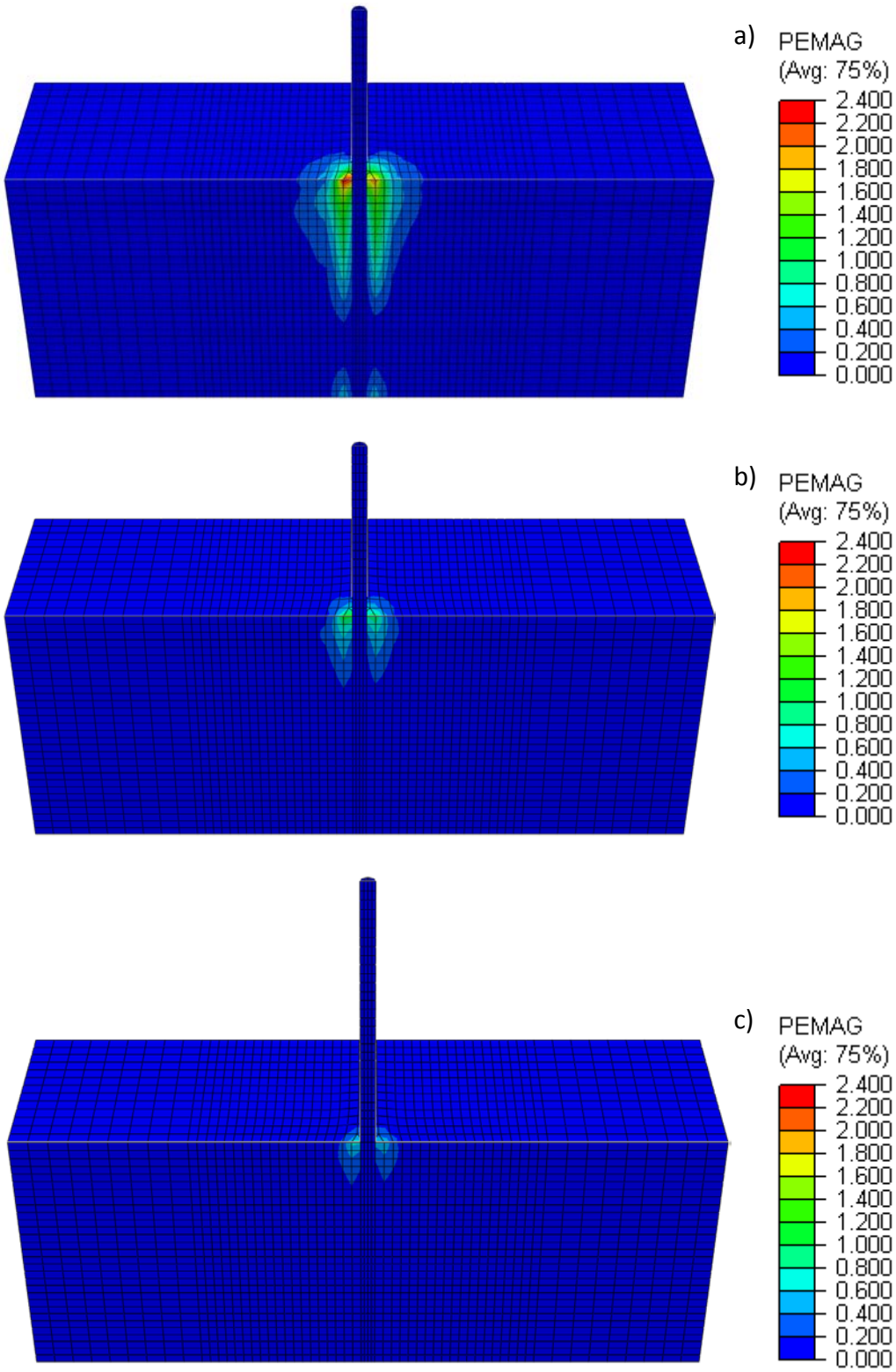

Figure 5.26: Contours of the plastic strain magnitude (plotted on the undeformed mesh) for the experimental setup of: (a) Test 1 (pure lateral load), (b) Test 4 (lateral load at 20 cm above the ground surface), and (c) Test 10 (lateral force at 56 cm above the ground surface)

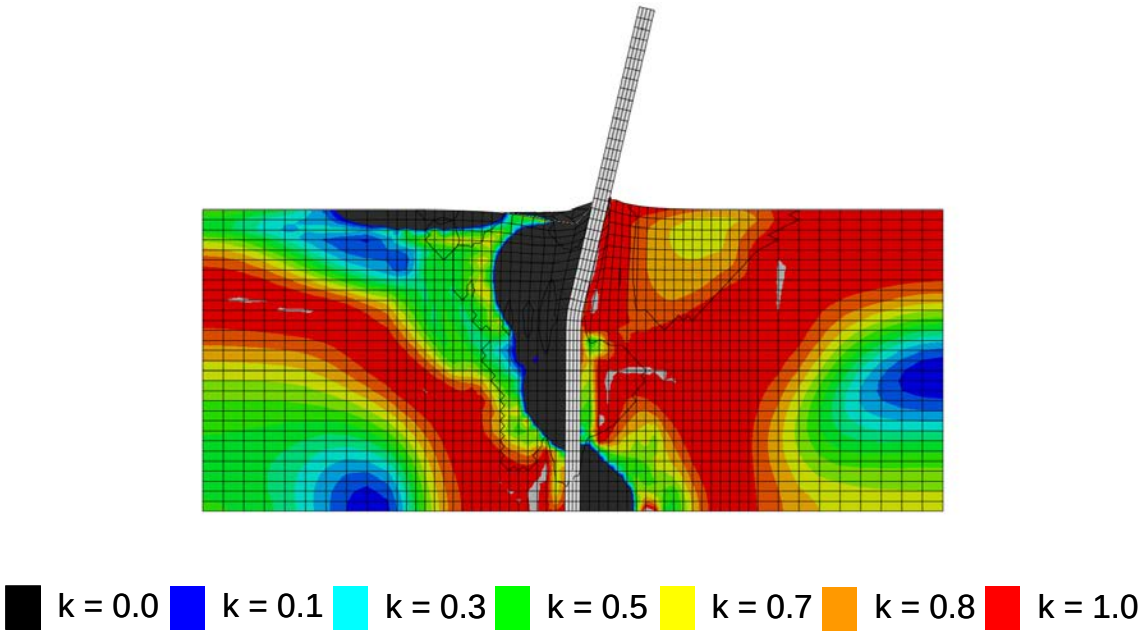

Figure 5.27: Cross-section with the contours of the active and passive stress states in terms of the state parameter k at the maximum measured lateral loading of the single pile in Test 1: k = 1 corresponds to pure triaxial compression loading condition (passive state) and k = 0 to pure triaxial extension loading condition (active state), while k ≈ 0.5 sets the boundaries between the active and the passive state.

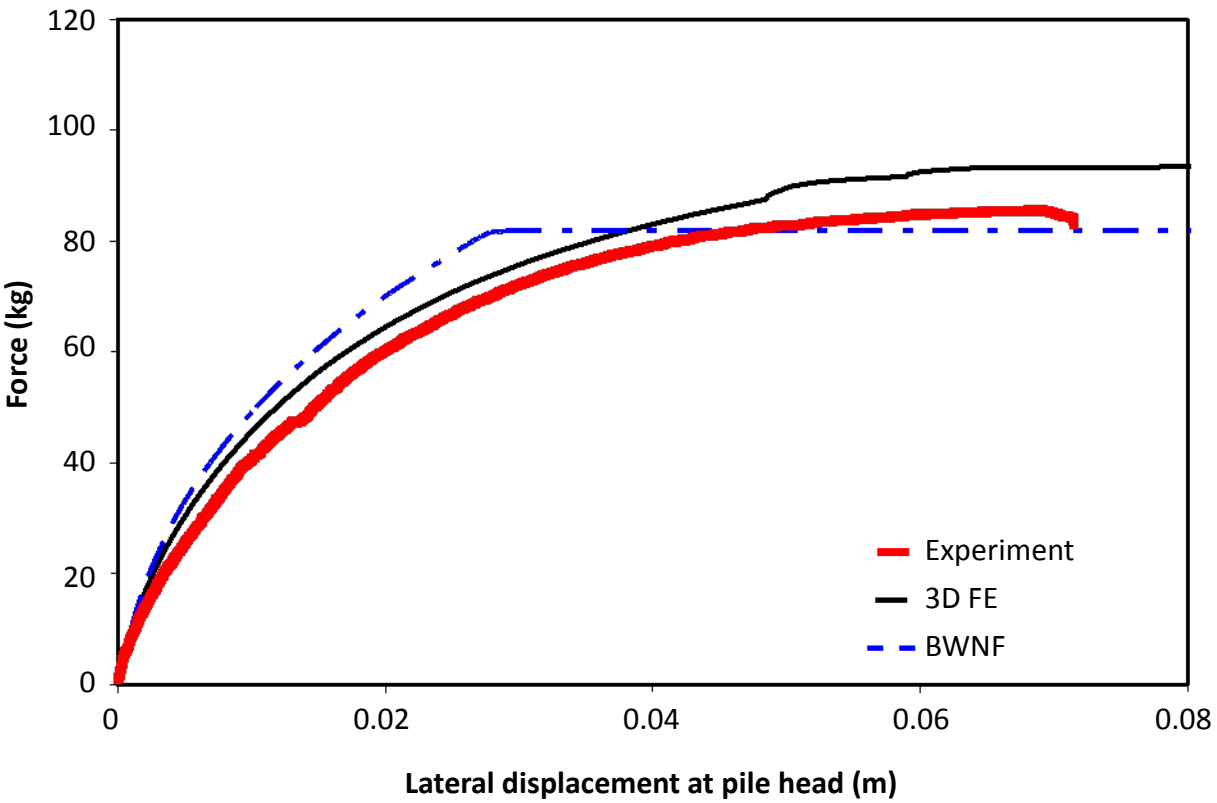

Figure 5.28: Experimental and computed force–displacement curves at pile head for Test 7 (lateral force at 6 cm above the ground surface). The dashed line is Class B prediction

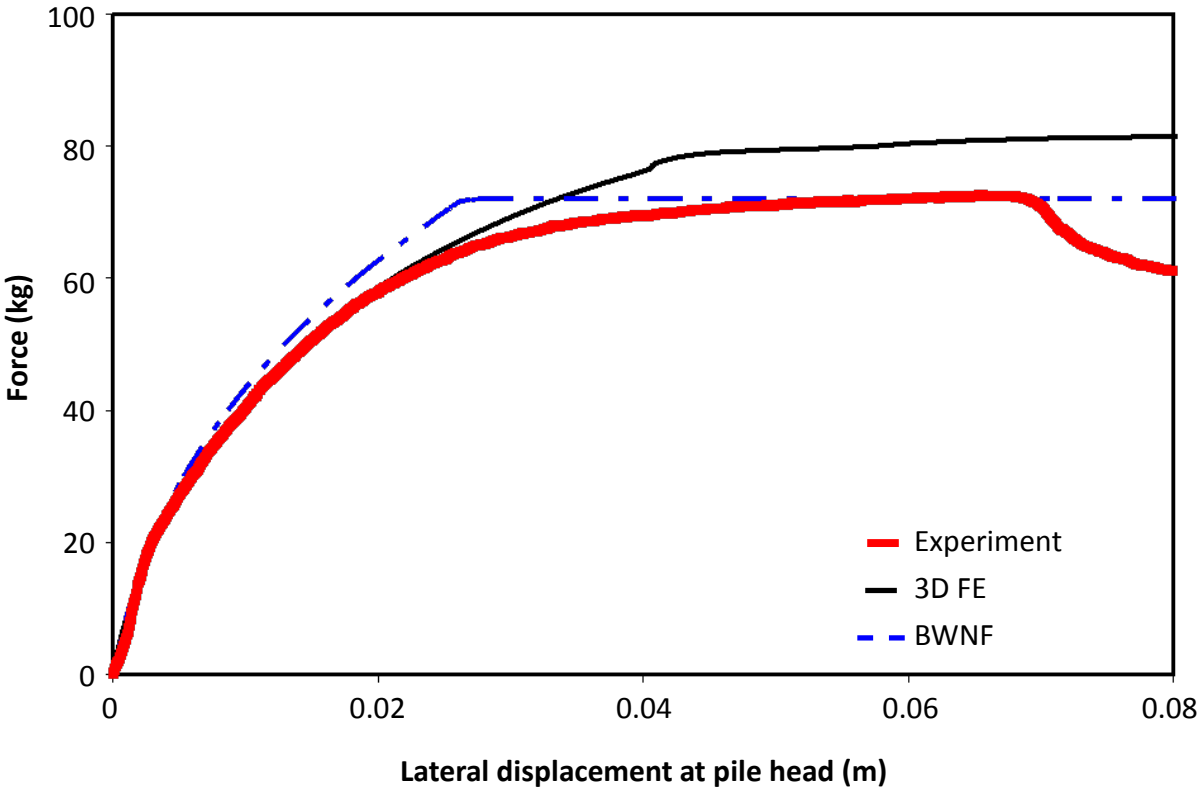

Figure 5.29: Experimental and computed force–displacement curves at pile head for Test 6 (lateral force at 10 cm above the ground surface). The dashed line is Class B prediction

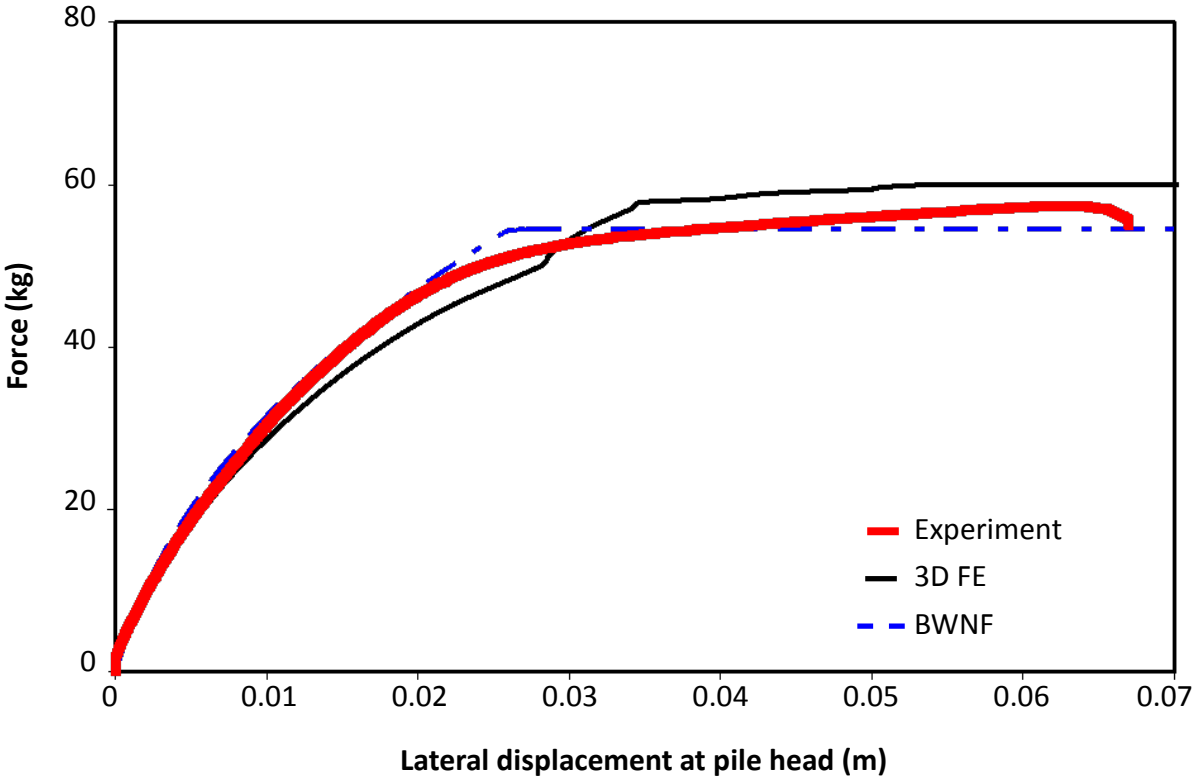

Figure 5.30: Experimental and computed force–displacement curves at pile head for Test 4 (lateral force at 20 cm above the ground surface). The dashed line is Class B prediction

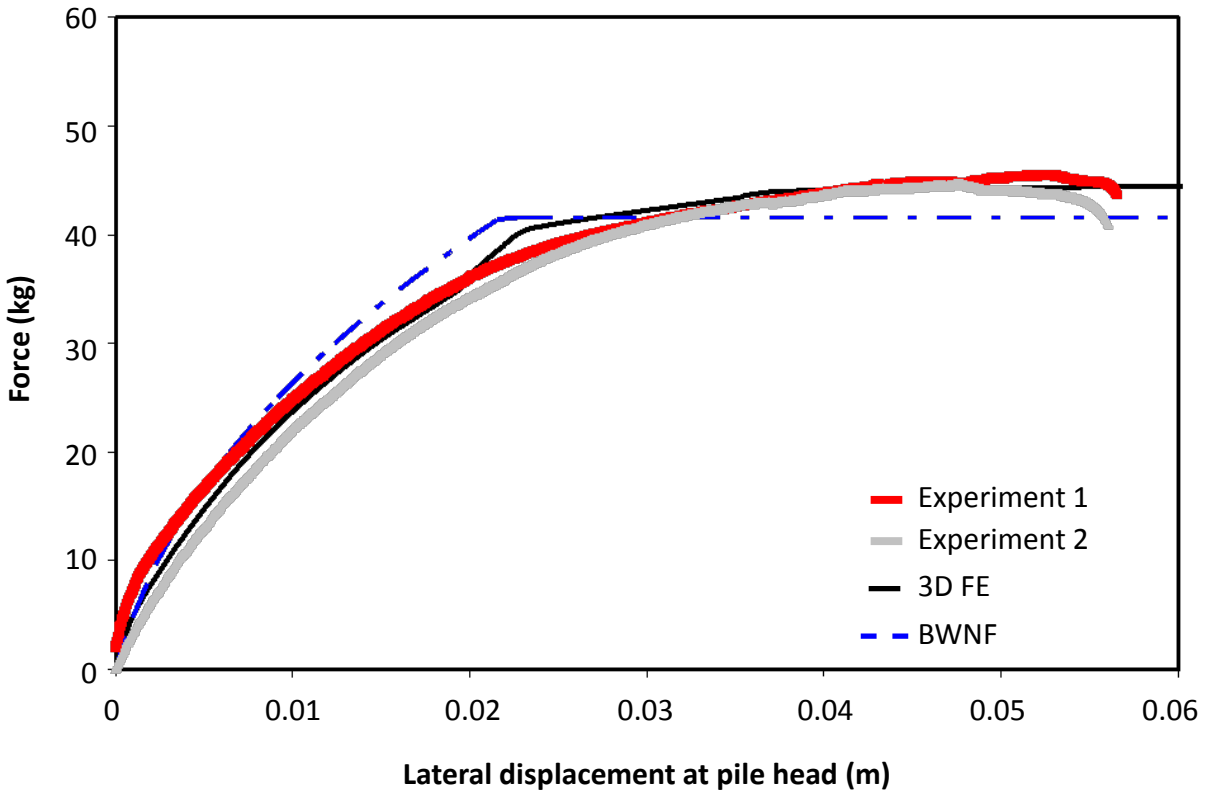

Figure 5.31: Experimental and computed force–displacement curves at pile head for Tests 3 and 5 (lateral force at 32 cm above the ground surface). The dashed line is Class B prediction

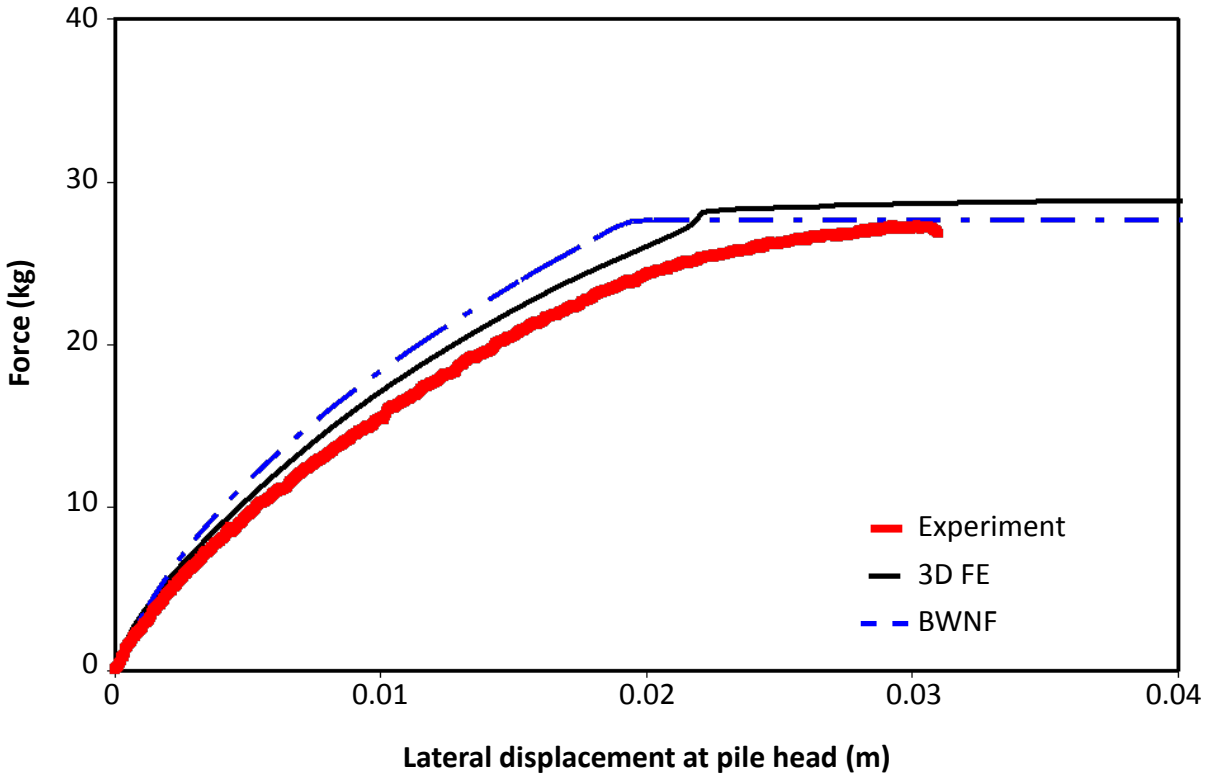

Figure 5.32: Experimental and computed force–displacement curves at pile head for Test 10 (lateral force at 56 cm above the ground surface). The dashed line is Class B prediction

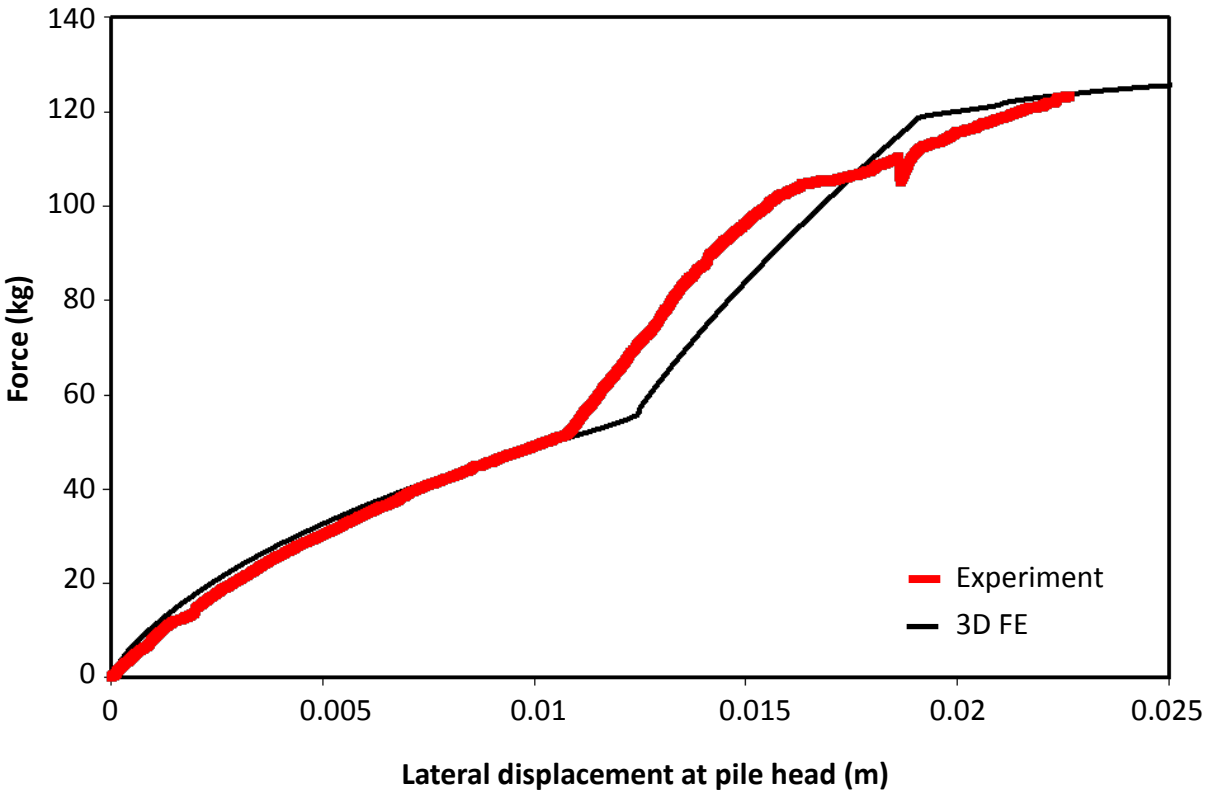

Figure 5.33: Experimental and computed force–displacement curves at pile head for Test 8 (first test of pile under lateral load applied at the ground surface and moment acting on the opposite direction)

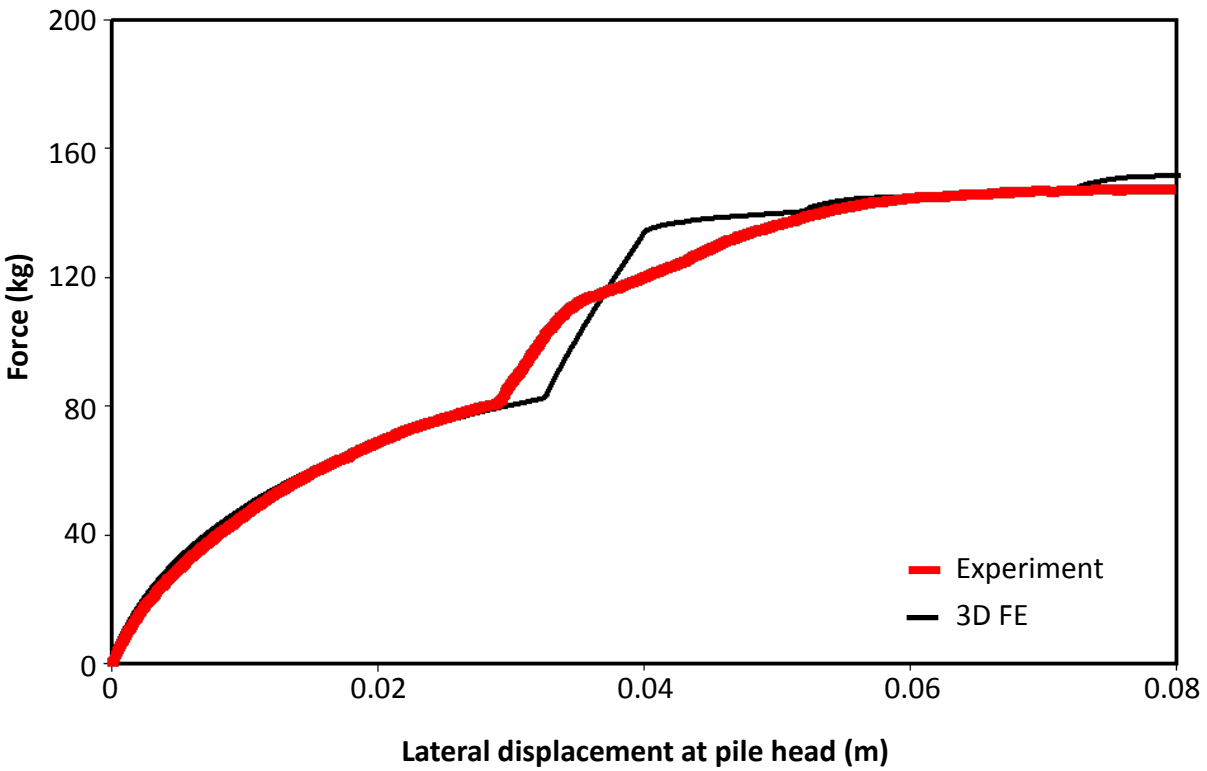

Figure 5.34: Experimental and computed force–displacement curves at pile head for Test 9 (second test of pile under lateral load applied at the ground surface and moment acting on the opposite direction)

CHAPTER 6:

APPLICATION TO THE SEISMIC RESPONSE OF BRIDGE PILE-COLUMNS

6.1 INTRODUCTION

In current practice, structures are designed so that their foundation system will behave elastically for every type of loading, and the damage is concentrated on the aboveground structural elements. Contrary to this belief, many researchers have proved that allowing plastic hinging at the soil-foundation system can be beneficial, especially in shallow foundations (Pecker, 1998; Makris and Roussos, 2000; Apostolou et al., 2007; Chatzigogos et al., 2009; Gerolymos et al., 2009, Anastasopoulos et al., 2010 among others).

In the present chapter, a parametric investigation of the nonlinear inelastic response of pile-column bridge systems is conducted with a fully 3D finite element model with the constitutive models described in **Chapter 2** and the results are compared against those from a nonlinear Winkler model. The influence of the pile inelastic behavior and soil-structure interaction on structure ductility demand is examined based on the concept proposed by Gerolymos et al. (2009). According to this concept the formation of a plastic hinge in the pile shaft can be beneficial. Current seismic design of bridge structures is based on the restriction of nonlinear response on the aboveground elements of the bridge. For most bridges, the foundation system is designed to remain structurally elastic while the pier dissipates energy and deforms inelastic. This approach is intended to avoid: (a) the difficulty of post-earthquake inspection and repair of a plastic hinge inside the soil, (b) the high cost which is associated to the repair of a severely damaged foundation, and (c) the failure due to pile yielding prior to the soil capacity mobilization. The elastic response of the foundation is ensured by increasing the strength of the foundation above that of the bridge pier so that the plastic hinge forms at the pier instead of the foundation. However, several case-histories have shown that: (a) pile integrity checking after an earthquake is a cumbersome, yet feasible task, as proven

by the Kobe 1995 earthquake, (b) the lateral confinement provided by the soil helps in retarding the development of high levels of localized plastic rotation, thereby providing an increase in ductility capacity, and (c) pile yielding under strong shaking cannot be avoided, especially with piles embedded in soft soil. In the latter argument belong structures like the pile-column foundation where plastic hinging of the foundation cannot be avoided during a severe earthquake. In the case of a free-head pile-column the plastic hinge that controls the inelastic response will form in the shaft below grade level (Budek et al., 2000). If plastic hinging in the foundation system is prevented, then high ductility demands might be imposed to the structure. On the contrary, if soil–foundation yielding is allowed it can effectively limit the transmitted accelerations.

For these reasons, a parametric investigation of the nonlinear response of pile-column bridge systems is conducted with the use of both beam-on-nonlinear-Winkler-foundation model and 3D continuum finite element model utilizing advanced inelastic constitutive laws. The influence of the inelastic behavior of the pile and the soil-structure interaction on the ductility demand of the structure are investigated. The role of various key parameters, such as the soil compliance, the aboveground height of the pile-column, the pile diameter and the location of the plastic hinge, is examined on characteristic performance measures of the pile-column bridge system response and precisely the local curvature ductility demand μ_ϕ, the global displacement ductility demand μ_δ and the maximum drift ratio γ_{max}.

6.2 ELASTIC ANALYSIS: EVALUATION OF THE METHODS USED

6.2.1 Problem investigated

Initially, the two numerical methods that will be used for the parametric investigation of the nonlinear response of pile-column bridge systems, are evaluated in the elastic response of the system. The studied problem is presented in **Figure 6.1**. A pile-column monolithically connected to the bridge deck is embedded in two layers of clay and is excited by a seismic motion. It is assumed that the transverse response of the bridge structure may be characterized by the response of a single bent, as would be the case for a regular bridge with coherent ground shaking applied to all bents.

The concentrated mass at the centre of the deck is 60 tons, the height of the pier H is 10 m, the embedment length of the pile L is 30 m while the diameter d of the pile-

column equals to 1.5 m. The pile-column is assumed to be linear elastic while the idealized soil profile from the Agios Stefanos bay depicted in **Figure 6.1** was used for the ground response analyses. A soft to medium normally consolidated clay sets on top of a stiff clay. The bedrock is assumed at 50 m depth. The soft clay has a thickness of 18 m and a plasticity index PI (%) = 35. The second layer is 32 m thick and has constant undrained shear strength of 100 kPa. The maximum shear modulus is calculated by the empirical equations of Seed and Idriss (1970).

The influence of shaking on the seismic response is investigated by selecting three real acceleration records as seismic excitations:

- the record from Aegion earthquake (1995)
- the record from Lefkada earthquake (2003)
- the JMA record from Kobe earthquake (1995)

The first two records were chosen as two strong motions of the seismic environment of Greece, with one and many cycles, respectively. JMA record is used to investigate the dynamic response of the soil-pile-structure system to a quite unfavorable incident. All the records were first scaled to a PGA of 0.5 g at the ground surface. Then, through deconvolution analyses conducted with SHAKE91 (Idriss and Sun, 1991), the bedrock motion as well as the motion at various depths along the pile were estimated. The acceleration time histories at the surface scaled to a_g = 0.5 g and the corresponding elastic response spectra for 5% damping are presented in **Figure 6.2**.

6.2.2 Numerical models

The elastic seismic response of the soil-pile-structure system is investigated with two different methods: (1) with a simplified method based on the beam-on-Winkler-foundation model, and (2) with method based on the 3D Finite Element Model.

Generally, in the beam-on-Winkler-foundation model a beam supported in discrete springs is used to model the lateral static and dynamic response of a pile. In this method, the soil-pile contact is discretized into combinations of springs and dashpots. Soil can also have nonlinear behavior modeled with p-y curves which derive from field tests. Such curves have the advantage of including pile installation effects on the surrounding soil. In advanced applications, capabilities for soil-pile gapping, cyclic degradation and rate dependency are also provided. For seismic loadings, free-field soil

response is calculated in separate site response analysis and the obtained displacement time histories are applied externally to the ends of the soil-pile springs. This multi-staged uncoupled approach has the disadvantage of potentially introducing numerical errors in the presence of soil nonlinearities and artificially separating the overall soil-pile system response. Another drawback of this method is that each soil spring responds independently from the adjacent ones, thus ignoring the shear transfer between the soil layers.

The advantages of a 3D finite element model include the capability of performing the analysis of a pile in a fully coupled manner, without resorting to the independent calculations of site or superstructure response. This method allows the use of more complicated soil constitutive models that account for the nonlinear behavior and the use of suitable transmitting boundaries for avoiding spurious wave reflections. Its main disadvantage lies in the excessive computational time required.

6.2.2.1 Beam-on-Winkler-foundation model

The first method consists of two stages: (i) seismic analysis of the site response without the presence of the structure with the computer program SHAKE91 and (ii) analysis of the soil-pile-structure system (under the excitations derived from stage (i)) with the use of the beam-on-nonlinear-Winkler-foundation model in Finite Element Program OpenSees.

The site response program SHAKE91 (Idriss and Sun, 1991) is a computer code that computes the response of a semi-infinite horizontally layered soil deposit overlying a uniform half-space subjected to vertically propagating shear waves. The soil profile is idealized as a system of homogeneous visco-elastic sublayers of infinite horizontal extend. An equivalent linear method models the nonlinear variation of soil shear modulus and damping as a function of shear strain.

OpenSees (Mazzoni et al, 2005) is an open-source object-oriented software framework for simulation of applications in earthquake engineering using the finite element method. It has been developed in the Pacific Earthquake Engineering Center (PEER) at University of California, Berkeley. OpenSees can simulate linear and nonlinear structural and geotechnical models under static, cyclic and dynamic loading. It contains a

large material library which is ever-growing as researchers have the permission to create new material models and incorporate them into the platform.

For the second stage in OpenSees, the pile-column is discretized into linear elastic beam elements with length of 1 m. The mass of the deck is simulated as a concentrated mass at the top node of the pile-column, while the distributed mass of the extended pile is simulated by lumped masses on the beam-element nodes.

Soil springs and dashpots elements are connected in parallel. The soil springs are assumed to be linear elastic and the dashpots are calculated according to Makris and Gazetas (1992). The free extremities of the soil springs were excited by the displacement time histories obtained at each depth from the free-field seismic response analysis. Rayleigh damping which represents material damping was taken equal to 5% in order to avoid spurious oscillations at very small deformations. **Figure 6.3** presents the model used for the analyses.

6.2.2.2 3D finite element model

In this method, the site response and the soil-pile-structure interaction are performed in a fully coupled manner with the Finite Element Code ABAQUS (Dassault Systèmes Simulia Corp, 2009).

The pile-column is modeled with 3D beam elements placed at its center and connected with appropriate kinematic restraints with the nodes at the perimeter of the pile in order to model the complete geometry of the pile. The solid elements inside the perimeter of the pile have no stiffness. In this way, each pile section behaves as a rigid disc: rotation is allowed on the condition that the disc remains always perpendicular to the beam axis, but stretching cannot occur. The pile-column and the soil behavior are assumed to be elastic. The soil is modeled with 8-node brick elements. The vertical length of the elements is identical to the beam-on-Winkler-foundation model in order to avoid mesh sensitivity differences. Appropriate kinematic constraints are imposed to the lateral edges of the model, allowing it to move as the free-field.

The acceleration time histories derived from the site response analysis with SHAKE91 at 30 m depth are used as the input excitation motion in the 3D finite element model. Due to symmetry, only half of the problem is analyzed, thus significantly reducing computational demands, leading to approximately 15000 elements for each analysis. The

model used for the analyses is depicted in **Figure 6.4**. It must be noted that even though both the developed models have the capability to reproduce higher order phenomena like P-Δ effects, such phenomena were ignored.

6.2.3 Results of elastic analyses

In order to construct a rigorous and precise 3D Finite Element model and avoid the "box effect" (Kramer, 1996), the free-field boundaries were first investigated by two different types of boundaries: (1) three dashpots (one in each direction) on each node on the boundaries of the 3D model were employed, while the soil motion at each depth from the free-field seismic response analysis was imposed on every node on the boundaries, and (2) appropriate kinematic constraints were used, imposed to the lateral edges of the model, allowing it to move as the free-field, namely Multi-Point Constrains (MPC) boundaries, and the soil motion at 30 m depth from the free-field seismic response analysis was imposed only on the nodes of the bottom boundaries of the model. **Figure 6.5** presents the comparison of the acceleration, displacement and rotation time histories at the deck of the 3D Finite Element Model with the boundary types studied for the JMA record scaled at a_g = 0.5. It is obvious that both types of boundaries produce identical results. This behavior was expected since the effective period of the soil was $T_{effsoil}$ = 0.45 sec from Fast Fourier Transform Analysis while the effective period of the soil-foundation-structure system was $T_{effsyst}$ = 0.63 sec, as shown in **Figure 6.6** and, thus no radiation of waves from the system to the soil takes place. Hence, the MPC boundaries were selected for the analyses conducted.

An additional factor that had to be investigated in order to perform the 3–D analysis was the damping of the soil elements. Rayleigh damping of 5% was initially selected for the soil elements of the 3D Finite Element Model. As illustrated in **Figure 6.7** this resulted in an overestimation of the computed acceleration, displacement and rotation time histories in comparison to the Beam-on-Winkler-foundation Model. Hence, the Rayleigh damping of the 3D soil elements was taken equal to the equivalent damping from the dampers of the beam-on-Winkler-foundation Model according to:

$$\xi = \frac{\omega C}{2K} \tag{6.1}$$

where ω soil circular frequency, C damping coefficient of the damper, and K soil stiffness. **Figure 6.8** illustrates the improvement of the response of the 3D Finite Element Model in comparison to the Beam-on-Winkler-foundation Model.

Figures 6.9 and **6.10** present the acceleration time histories and the corresponding (ξ = 5%) response spectra. The acceleration time histories from the 3D Finite Element Model compare well with the Beam-on-Winkler-foundation Model, but are slightly higher. As expected, the response spectra of the 3D Finite Element Model produce higher peak acceleration values, due to the fact that the damping in this model is less than in the Beam-on-Winkler-foundation Model, as shown before. Nevertheless, the response spectra from both models produce the maximum acceleration values at the same periods.

Figure 6.11 compares the displacement time histories of the two models used. As in the case of the acceleration time histories, the peak displacement values calculated with the 3D Finite Element Model are higher than those from the Beam-on-Winkler-foundation Model. What is of interest is the case of Aegion (1995) where a great difference in the response of the system is observed, even though the acceleration time histories are similar. In order to verify the correctness of the Beam-on-Winkler-foundation Model in the Finite Element code OpenSees, the same model was created in the Finite Element code ABAQUS which provides a graphical interface. **Figure 6.12** compares the displacement time histories from the two models. It is apparent that the results are similar. Hence, the observed difference in the displacement time histories of **Figure 6.11** is attributed to the sequence of significant pulses of the Aegion (1995) record. The response of the deck calculated by the Beam-on-Winkler-foundation Model exhibits greater displacement at the first peak displacement (positive direction) than that by the 3D Finite Element model. As the deck starts to move towards the opposite direction, it does not pass far from its initial position in the Beam-on-Winkler-foundation Model, while it moves greater towards the negative direction in the 3D Finite Element Model. By the end of second positive peak displacement, the deck moves even further towards the positive direction in both models. The distance covered until the second negative peak displacement is smaller than the previous stages. Thus, in the 3D Finite Element the deck moves to the left, while in the Beam-on-Winkler-foundation Model the deck remains to the right side. As the distance covered among each peak displacement

value decreases, the deck oscillates in the side that was before until the end of the oscillation. The difference in the responses became greater when the peak ground acceleration was increased from 0.5 to 0.8 g. However, this is a unique case, since analyses with other records that contain asymmetric loading (e.g. Lefkada 1973) showed no differences in the response of the system. **Figure 6.13** illustrates snapshots of the deformed pile-column for the Aegion (1995) excitation scaled to a_g = 0.5 g at (a) t = 1.75 sec, (b) t = 2.65 sec, and (c) t = 4.5 sec in comparison to the undeformed state (deformation scale factor = 50) from the 3D and the Winkler models in FE code ABAQUS, verifying the aforementioned justification.

Finally, **Figure 6.14** presents the comparison of the maximum bending moment distributions calculated by the two models examined. In general, the agreement between the computed curves is quite satisfactory. Both models predict similar shapes of the moment distribution as well as the increase of the bending moment at the interface of the two soil layers. The models also predict the same depth of the maximum bending moment. The maximum bending moment predicted by the 3D Finite Element Model is attributed to the higher predicted acceleration values at the deck level.

The results calculated with the 3D Finite Element Model and the Beam-on-Winkler-foundation Model compare well for all cases. The sequence of significant pulses of the Aegion (1995) record influences the response of the models examined for the case of displacement time histories. Having compared the elastic response of the soil-pile-structure system by two different methods, a parametric investigation of the nonlinear response of pile-column bridge systems is conducted with the use of both nonlinear Winkler and 3D continuum finite element models utilizing advanced inelastic constitutive laws. In this study, the influence of the inelastic behavior of the pile and the soil-structure interaction on the ductility demand of the structure are investigated.

6.3. INELASTIC ANALYSIS

6.3.1 Problem investigated

The problem studied herein is presented in **Figure 6.15**. A pile-column monolithically connected to the bridge deck is embedded in clay or sand deposit and is excited by a seismic motion. Initially the two soil profiles selected were: (a) sand with friction angle $\phi = 40^o$ and cohesion c = 5 kPa constant with depth, and (b) clay with

undrained shear strength S_u with parabolic distribution with depth. Again, it is assumed that the transverse response of the bridge structure may be characterized by the response of a single bent, as would be the case for a regular bridge with coherent ground shaking applied to all bents.

The height of the pier H is given parametrically the values of 5 and 10 m, so that a typical urban bridge and a rather short viaduct are analyzed. The diameter b of the pile-column aboveground takes values of 1.5 and 3.0 m. In order to investigate the influence of the plastic hinge position on the system response, two more cases are examined: the belowground pile-column diameter d is increased by 33% relatively to the aboveground diameter b. Thus, for pile diameters d = 1.5, 2.0, 3.0 and 4.0 m the pier diameter equals to b = 1.5, 1.5, 3.0 and 3.0 m, respectively. **Table 6.1** shows the pile-column characteristics for each of the eight structural configurations analyzed. The pile-columns with constant diameter will inevitable lead to a belowground plastic hinge formation while the variable-diameter pile-columns will appear a plastic hinge at the base of the pier (SDC, 2010). The embedment length of the pile L is considered in every case equal to 30 m.

The mass of the deck is calculated so that the fundamental period of the fixed-base pier would be T = 0.3 sec. The nonlinear behavior of the pile-column is characterized through the predefined moment−curvature relations illustrated in **Figure 6.16**. These curves have been obtained with the BWGG model (Gerolymos N. and Gazetas G., 2005a) for n = 1, initial stiffness equal to the uncracked flexural stiffness EI of the pile-column, and ultimate strength equal to the conventionally calculated moment at the ground surface considering that a critical acceleration of 0.2 g is applied on the deck mass. This critical acceleration was selected in order to ensure that the system will enter the inelastic regime under the used seismic excitations. It is noted that the objective of the parametric study is to investigate the seismic response of the system in the inelastic regime and not to design the structure.

A single soil profile is selected for the ground response analysis as depicted in **Figure 6.17** in order to avoid the differences in the free-field motions from the soil response analysis of the different soil profiles that would complicate the results. The bedrock was assumed at 50 m depth. The influence of shaking on the seismic response is investigated by selecting the same seismic excitations used in the elastic analysis:

i) the record from Aegion earthquake (1995)

ii) the record from Lefkada earthquake (2003)

iii) the JMA record from Kobe earthquake (1995)

The dominant periods of the acceleration time histories for the aforementioned earthquake records range from 0.2 to 0.8 sec. For the inelastic analysis, all the records were first scaled to a PGA value of 0.5 g and 0.8 g at the ground surface. Then through deconvolution analyses conducted with SHAKE91, the bedrock motion as well as the motion at various depths along the pile were estimated and used as input motions for the Beam-on-nonlinear-Winkler-foundation model, while the acceleration time histories at 30 m depth was used as the input excitation motion in the fully 3D finite element model.

6.3.2 Numerical modeling

The inelastic seismic response of the soil-pile-structure system is investigated parametrically with the same methods used in the elastic analysis: (1) a simplified multiple method based on the Beam-on-nonlinear-Winkler-foundation Model, and (2) a direct method based on the 3D Finite Element Model.

6.3.2.1 Beam-on-nonlinear-Winkler-foundation model

For the first stage, curves of shear modulus reduction G and damping ratio ξ increase with shear strain γ developed by Ishibashi and Zhang (1993) are used for the analysis of the nonlinear seismic site response without the presence of the structure.

For the second stage, the pile-column is discretized into nonlinear beam elements with length of 1 m, whose bending behavior is governed by the macroscopic constitutive BWGG model (Gerolymos, 2002, Gerolymos and Gazetas, 2005a) as shown in **Figure 6.16**. The BWGG model is an extension of the hysteretic Bouc-Wen model, a one-dimensional action-reaction relationship suitable for the estimation of the nonlinear response of (i) soil-pile interface, and (ii) moment−curvature behavior of a beam element in order to simulate an inelastic pile. The relation between the pile bending moment M_p and the pile curvature κ can be expressed as the sum of an elastic and an inelastic component:

$$M_p(t) = a_p E_p I_p \kappa(t) + (1 - a_p) M_{p,y} \zeta_p(t) \tag{6.2}$$

where E_p is the Young's modulus of the pile, I_p is the pile section moment of inertia, a_p is the post yielding stiffness ratio of the pile, $M_{p,y}$ is the yielding bending moment of the pile idealized by an elastic-perfectly plastic behavior (ultimate bending moment), and ζ_p is the hysteretic dimensionless parameter that controls the nonlinear structural response given by

$$\frac{d\zeta_p}{dt} = \frac{1}{\kappa_y}\left(A_p \frac{d\kappa}{dt} - b_p \frac{d\kappa}{dt}\left|\zeta_p\right|^{n_p} - g_p \left|\frac{d\kappa}{dt}\right|\left|\zeta_p\right|^{n_p-1}\zeta_p \right) \tag{6.3}$$

in which A_p, b_p, g_p and n_p are the dimensionless parameters of the original Bouc-Wen model that control the shape of the moment−curvature loop and κ_y is the yielding curvature ($\kappa_y = M_{p,y} / E_p I_p$). The mass of the deck is simulated as a concentrated mass at the top node of the pile-column, while the distributed mass of the extended pile is simulated by lumped masses on the beam-element nodes.

Soil nonlinearity is taken into consideration by means of a hybrid spring configuration consisting of a nonlinear (p-y) spring connected in series to an elastic spring–damper model as proposed by Wang et al (1998). The nonlinear spring captures the near-field plastification of the soil while the spring–damper system (Kelvin–Voigt element) represents the far-field visco-elastic character of the soil. Otherwise, having the dashpot in parallel with the entire nonlinear element can result in excessive dashpot forces when the element is loaded into the highly nonlinear range. The far-field soil springs are assumed to be linear elastic while the near field soil-pile interface is simulated with nonlinear p-y spring elements, the behavior of which is described also by BWGG model. The lateral soil reaction against a deflecting pile is expressed as the sum of an elastic and an inelastic component according to:

$$F_s(t) = a_s k_s u(t) + (1 - a_s) F_{s,y} \zeta_s(t) \tag{6.4}$$

where k_s is the horizontal stiffness coefficient of the soil spring, a_s is a parameter the controls the post yielding stiffness ratio of the soil spring, $F_{s,y}$ is the force of an elastic-perfectly plastic soil spring on yielding (ultimate soil reaction), and ζ_p is the hysteretic dimensionless parameter that controls the nonlinear structural response given by

$$\frac{d\zeta_s}{dt} = \frac{1}{u_y}\left(A_s \frac{du}{dt} - b_s \frac{du}{dt}\left|\zeta_s\right|^{n_s} - g_s \left|\frac{du}{dt}\right|\left|\zeta_s\right|^{n_s-1}\zeta_s \right) \tag{6.5}$$

in which A_s, b_s, g_s and n_s are the dimensionless parameters of the original Bouc-Wen model that control the shape of the force-displacement loop and u_y is the horizontal yielding displacement. BWGG parameters of the soil springs have been calibrated by Drosos (2007) in order to predict sufficiently the p-y curves of Reese et al (1974) and Matlock (1970) for the sand and clay, respectively.

A calibration methodology of the "spring" and "dashpot" coefficients of the examined hybrid spring configuration is proposed. The lateral soil reaction against a deflecting pile is expressed as the sum of a hysteretic elastic–perfectly plastic and a visco-plastic component, according to the lumped parameter model, as depicted in **Figure 6.18**. In this way, the frequency–dependent characteristics of the subgrade reaction are realistically captured through a series–parallel assembly of frequency–independent springs and dashpots. In the elastic regime, the small–amplitude frequency–dependent "spring" and "dashpot" coefficients for the lateral soil reaction are approximated by:

$$k_x = \mathrm{Re}\left(\frac{k_{el} k_{nl} + i\omega c_{el} k_{nl}}{k_{el} + k_{nl} + i\omega c_{el}} \right) \tag{6.6}$$

and

$$c_x = \frac{1}{\omega} \mathrm{Im}\left(\frac{k_{el} k_{nl} + i\omega c_{el} k_{nl}}{k_{el} + k_{nl} + i\omega c_{el}} \right) \tag{6.7}$$

in which ω is the circular frequency. The parameters c_{el}, k_{el}, and k_{nl} are appropriately calibrated through an optimization procedure to match the stiffness and dashpot coefficients (**Figure 6.19**) proposed by Makris and Gazetas (1992)

$$k_x = 1.2E_s \tag{6.8}$$

$$c_x = 6a_0^{-1/4} \rho_s V_s d \tag{6.9}$$

in which E_s, V_s and ρ_s are the Young's modulus, shear wave velocity and mass density of the supporting soil, and a_0 is a dimensionless frequency parameter defined as:

$$\alpha_0 = \frac{\omega d}{V_s} \tag{6.10}$$

Having calibrated the stiffness k_x and dashpot coefficient c_x according to **Equations 6.8** and **6.9**, plastic behavior is then introduced by imposing a threshold value for the reaction force of spring "k_{nl}" equal to the ultimate soil resistance per unit length of the

pile, p_{ult}, as determined by Broms (1964) for clay and Reese and Van Impe (2001) for c-ϕ soils under cyclic loading, respectively (**Figure 6.20**). Obviously, when p_{ult} is reached the arranged in-parallel spring and dashpot unit is deactivated and the radiation damping vanishes.

The free extremities of the soil springs were excited by the displacement time histories obtained at each depth from the free-field seismic response analysis. To avoid spurious oscillations at very small deformations (nearly elastic response), Rayleigh damping that represents material damping, was introduced and taken equal to 3% between period T = 0.1 and 1 sec. **Figure 6.21** presents the model used for the analyses.

6.3.2.2 3D finite element model

The pile-column is modeled with 3D beam elements placed at its center and connected with appropriate kinematic restraints with the nodes at the perimeter of the pile in order to model the complete geometry of the pile. The solid elements inside the perimeter of the pile have zero stiffness. In this way, each pile section behaves as a rigid disc: rotation is allowed on the condition that the disc remains always perpendicular to the beam axis, but stretching cannot occur (Bernoulli hypothesis). The nonlinear behavior of the pile-column is described by an elasto-plastic law that matches the predefined moment−curvature relations illustrated in **Figure 6.16**.

The soil is modeled with 8-node brick elements. The vertical length of the elements is identical to the Beam-on-nonlinear-Winkler-foundation model in order to avoid mesh sensitivity differences. Soil behavior is modeled with the constitutive model for cohesive soils proposed by Gerolymos et al (2005b) and with the constitutive model of **Chapter 2** for cohesionless soils that both take into consideration the nonlinear cyclic response of the soil through a user subroutine.

For clay, the shear modulus reduction G with shear strain γ of the constitutive model of Gerolymos et al (2005b) through simple shear test is given by:

$$\frac{G}{G_0}=\begin{cases}1, & \gamma<\gamma_y\\ \dfrac{\left(S_u\left(1-\dfrac{1}{a}\right)\right)}{\left(\gamma-\dfrac{S_u}{aG_0}\right)}\left(1-e^{\dfrac{-G_0\left(\gamma-\frac{S_u}{aG_0}\right)}{S_u\left(1-\frac{1}{a}\right)}}\right) & \gamma>\gamma_y\end{cases} \tag{6.11}$$

and the damping ratio ξ increase with shear strain γ:

$$\xi=\begin{cases}0, & \gamma<\gamma_y\\ \dfrac{2}{\pi}\left[\dfrac{1+e^{\dfrac{-\gamma+\frac{S_u}{aG_0}}{\left(\frac{\sqrt{3}S_u\left(1-\frac{1}{a}\right)}{\sqrt{3}G_0}\right)}}}{1-e^{\dfrac{-\gamma+\frac{S_u}{aG_0}}{\left(\frac{S_u\left(1-\frac{1}{a}\right)}{G_0}\right)}}}-\dfrac{2\dfrac{S_u\left(1-\dfrac{1}{a}\right)}{G_0}}{\gamma-\dfrac{S_u}{aG_0}}\right] & \gamma>\gamma_y\end{cases} \tag{6.12}$$

where

$$\gamma_y=\frac{S_u}{aG_0} \tag{6.13}$$

is the shear strain at incipient yielding, G_0 is the maximum shear modulus and a = 3.

For sand, the shear modulus reduction G with shear strain γ of the constitutive model of **Chapter 2** at a simple shear test is given by:

$$\frac{G}{G_0}=\begin{cases}1, & \gamma<\gamma_y\\ \dfrac{\left(\left(c+p\tan\varphi\right)\cos\varphi\left(1-\dfrac{1}{a}\right)\right)}{\left(\gamma-\dfrac{\left(c+p\tan\varphi\right)\cos\varphi}{aG_0}\right)}\left(1-e^{\dfrac{-\gamma G_0+\frac{\left(c+p\tan\varphi\right)\cos\varphi}{a}}{\left(c+p\tan\varphi\right)\cos\varphi\left(1-\frac{1}{a}\right)}}\right) & \gamma>\gamma_y\end{cases} \tag{6.14}$$

and the damping ratio ξ increase with shear strain γ:

$$\xi = \begin{cases} 0, & \gamma < \gamma_y \\ \dfrac{2}{\pi}\left[\dfrac{1+e^{\left(\frac{-\gamma+\frac{(c+p\tan\varphi)\cos\varphi}{aG_0}}{\left(\frac{\sqrt{3}(c+p\tan\varphi)\cos\varphi\left(1-\frac{1}{a}\right)}{\sqrt{3}G_0}\right)}\right)}}{1-e^{\left(\frac{-\gamma+\frac{(c+p\tan\varphi)\cos\varphi}{aG_0}}{\left(\frac{(c+p\tan\varphi)\cos\varphi\left(1-\frac{1}{a}\right)}{G_0}\right)}\right)}} - \dfrac{2\dfrac{(c+p\tan\varphi)\cos\varphi\left(1-\dfrac{1}{a}\right)}{G_0}}{\gamma - \dfrac{(c+p\tan\varphi)\cos\varphi}{aG_0}}\right] & \gamma > \gamma_y \end{cases} \quad (6.15)$$

where

$$\gamma_y = \frac{(c+p\tan\varphi)\cos\varphi}{aG_0} \quad (6.16)$$

is the shear strain at incipient yielding, G_0 is the maximum shear modulus, p is the mean pressure, ϕ is the friction angle, c is the cohesion and a = 5. Based on **Equations 6.11** to **6.16** the model parameters are calibrated to fit published G-γ and ξ-γ curves by Ishibashi and Zhang (1993) (**Figure 6.22**). Appropriate kinematic constraints are imposed to the lateral edges of the model, allowing it to move as the free-field. The acceleration time histories derived from the site response analysis with SHAKE91 at 30 m depth were used as the input excitation motion in the fully 3D finite element model. Thus, the 1D equivalent linear site response analysis is compared to the 3D nonlinear site response analysis. To avoid spurious oscillations at very small deformations (nearly elastic response), Rayleigh damping that represents material damping, was introduced and taken equal to 3% between period T = 0.1 and 1 sec.

Initially, the fully 3D finite element model consisted of 60000 elements and the computational time required for a seismic motion of 20 sec lasted 15 days. Due to symmetry, only half of the problem was analyzed, thus significantly reducing computational demands. **Figure 6.23** proves that the results of the half model were not influenced quantitatively. The final model used for the analyses is depicted in **Figure 6.24.**

6.3.3 Results of parametric analysis

Prior to the dynamic parametric analysis, Pushover Tests took place with both models used. A horizontal force is gradually applied at the center of the mass of the

superstructure. At first, the pier of the bridge is fixed in order to verify the similar structural behavior of the models. At the next phase, Pushover Test was performed for the whole soil-pile-bridge system response in order to verify the similar response of the system under static loading (**Figure 6.25**).

Typical results of the nonlinear parametric analyses referring to the JMA (1995) record are presented herein. **Figures 6.26** to **6.29** present the acceleration time histories at the ground surface of the free-field for the JMA (1995) record scaled at 0.5 and 0.8 g and the corresponding elastic response spectra (ξ = 5 %) derived from the Equivalent Linear Analysis and the 3D Nonlinear Analysis for both clay and sandy soil. The following conclusions derive:

- There is a difference observed at the acceleration time histories due to the different damping of the two methods. Apparently the Rayleigh damping in the fully 3D Finite Element Model should be slightly increased. In addition, the decreased acceleration amplitude at high frequencies in the Equivalent Linear Analysis is attributed to the fact that SHAKE overdamps the soil response at high frequencies and also does not take into consideration surface waves (1D Analysis).
- In all cases, the 3D Nonlinear Analysis leads to equal or smaller values of the peak ground acceleration (PGA) in comparison to the Equivalent Linear Analysis, showing the importance of the actual nonlinear soil behavior in the site response.
- As expected, apart from the site response in high frequencies, the 3D Nonlinear Analysis reduces the spectral accelerations, while the predominant period is the same for both methods of Analysis
- In the 3D Nonlinear Analysis, the plastification of the soil increases as the peak ground acceleration (PGA) increases. Thus, the amplification of the seismic motion is less than in the Equivalent Linear Analysis.

The evolution of soil yielding around a pile-column of constant diameter d = 3 m with tall (H= 10 m) and short pier (H= 5 m) embedded in cohesionless soil is depicted in **Figure 6.30**. The plastic strains from both systems are plotted on the same scale at each time step. It is evident that the larger plastic strains develop around the system with the shorter pier (H = 5 m). **Figure 6.31** illustrates the contours of the active and the passive

stress state of the sand around the pile in terms of the state parameter k. Results are presented for the same times step as in **Figure 6.30**. The red color stands for k = 1 (triaxial compression state, passive state), dark blue for k = 0 (triaxial extension state, active state), while green sets the boundaries for the active or the passive zone k = 0.5 (simple shear state). From the distribution of the colors around the pile-column the deformed shape of the pile-column can easily be recognized. The pile pushes the soil (red color) towards the direction it tends to move, while the soil reaches an active state (blue color) in the opposite side of the pile. The initial state of the soil in the analyses was the passive state. As shown from the plastic strain contours, the extension of the active and passive zone around the pile-column is greater for the case of the short pier (H = 5 m).

The influence of the pile diameter on soil yielding around a pile-column with aboveground height H = 5 m embedded in cohesionless soil is depicted in **Figure 6.32**. The plastic strains from both systems are plotted on the same scale at each time step. As expected, larger plastic strains develop around the system with the smaller diameter d = 1.5 m (e.g maximum plastic strain 5.2 % at time step 8.25) in comparison to the pile-column with diameter d = 2.0 (e.g maximum plastic strain 3.7 % at time step 8.25). **Figure 6.33** illustrates the contours of the active and the passive stress state of the sand around the pile in terms of the state parameter k. Results are presented for the same times step as in **Figure 6.32**. The red color stands for k = 1 (triaxial compression state, passive state), dark blue for k = 0 (triaxial extension state, active state), while green sets the boundaries for the active or the passive zone k = 0.5 (simple shear state). From the distribution of the colors around the pile-column the deformed shape of the pile-column can easily be recognized. The pile pushes the soil (red color) towards the direction it tends to move, while the soil reaches an active state (blue color) in the opposite side of the pile. As shown from the plastic strain contours, the extension of the active and passive zone around the pile-column is greater for the case of the constant diameter pile-column (d = 1.5 m).

Figure 6.34 depicts the acceleration time histories of a 5 m high pier embedded in cohesive soil for different pile diameters. Smaller pile diameter leads to higher deck acceleration. As can be seen, at t = 15 sec of the acceleration time histories (almost free response of the soil-pile-bridge system) the effective period of the small diameter soil-pile-bridge system (approximately 1 sec) is less that of the large diameter soil-pile-bridge

system (> 1.5 sec). This can be attributed to the fact that the small pile-column diameters (d = 1.5, 2.0 m) correspond to a much smaller deck mass (**Table 6.1**) than that of the larger pile-column diameters (d = 3.0, 4.0 m). Furthermore, a small decrease in peak acceleration values is observed in constant-diameter pile-columns (d = 1.5, 3.0 m) compared to those from variable-diameter systems (d = 2.0, 4.0 m). The soil plastification in the former case increases the hysteretic damping and thus decreases the deck response. These trends are evident with both methods of analysis used. Significant differences on the response are observed between pile-columns of different aboveground height as shown in **Figure 6.35**. For a pile-column embedded in cohesionless soil with diameter d = 3 m and aboveground height H = 5 m the peak acceleration is 0.14 g and 0.12 g calculated with the 3D Finite Element Model and the Beam-on-nonlinear-Winkler-foundation model respectively, while for pier height H = 10 m the peak acceleration is 0.22 g and 0.21 g. Even though both pile-columns have been designed to have the same fixed base fundamental natural periods T = 0.3 sec, the effective period of the short soil-pile-bridge system from Fast Fourier Transform analysis is higher (T = 1.5 sec for this case) than the corresponding value of the soil-pile-bridge system (T = 0.9 sec for this case). Thus, higher accelerations are developed at the mass of the longer pier. The calculated response spectra verify the above comments. **Figures 6.36** and **6.37** show the lower response of the pile-columns with large diameter and short piers.

Figures 6.38 and **6.39** depict the influence of the pile diameter and the height of the pier on the maximum distributions of bending moments. The increase of pile diameter results in shifting the maximum moment depth to greater depths. It should be noticed that the maximum bending moment depth does not always coincide with the plastic hinge position, due to the differences in pile and pier diameters. Both the 3D Finite Element Model and the Beam-on-nonlinear-Winkler-foundation Model agree well on the distributions of the maximum moment with depth while the maximum bending moment depth is identical or slightly larger for the Beam-on-nonlinear-Winkler-foundation Model.

The position of the plastic hinge is assessed via distributions of pile curvature with depth. **Figures 6.40** and **6.41** show the influence of the pile diameter and the height of the pier on the distributions of pile curvature with depth. In the case of pile-columns with

pier smaller than the pile (d = 2.0, 4.0 m) the pier is stressed more than the pile and the plastic hinge is formed just above the ground surface. Curvature values decrease rapidly below the ground surface. On the contrary, constant diameter pile-columns (d = 1.5, 3.0 m) develop the plastic hinge below the ground surface and plastic rotations are distributed at greater length, thus decreasing the maximum curvature. Furthermore, as the height of the pier increases the position of the plastic hinge moves closer to the ground surface. Again, both the 3D Finite Element Model and the Beam-on-nonlinear-Winkler-foundation Model agree well on the shape distributions of the pile curvature with depth. The greater maximum curvature calculated with the 3D Finite Element Model is attributed to the higher maximum acceleration values calculated at the deck with this method. Finally, **Figure 6.42** illustrates the hysteretic moment–rotation loops for pile-columns with diameter d = 2 m and aboveground height H = 5 m embedded in cohesive soil calculated with both numerical models examined. It is evident that the hysteretic loops of the 3D Finite Element Model are slightly larger and thus, the energy destruction in this analysis is greater. On the other hand, the shape of the loops from the Beam-on-nonlinear-Winkler-foundation Model produced by the BWGG constitutive model is closer to reality.

In general, the results from the 3D Finite Element Model and the Beam-on-nonlinear-Winkler-foundation Model compare well. A similar conclusion has been derived by Wang et al (1998) who compared several implementations of the dynamic p-y method and showed that calculations can be sensitive to the details of the nonlinear springs and dashpots but the different codes did produce similar results when similar modeling details were used.

6.3.4 Local and global ductility demands

Besides the fundamental response amounts that describe the behaviour of a structure under dynamic loading, other important seismic performance measures are the local and global ductility demand μ_ϕ and μ_δ and the drift ratio γ. The local curvature ductility demand μ_ϕ is defined as the maximum curvature κ_{max} imposed on the structure by an earthquake, divided by the yield curvature κ_y which is a pile-column cross-section property.

$$\mu_{\varphi} = \frac{\kappa_{max}}{\kappa_{y}} \tag{6.17}$$

For bridge supported on extended piles, the local ductility demand imposed on the pile shaft might govern the design of the system, because damage to pile (such as buckling of reinforcement) is related to the local curvature ductility.

Figure 6.43 presents the procedure followed for the assessment of local curvature ductility demand in the analyses conducted. The moment–curvature curve of each pile column cross section is approximated by a bilinear elastic-perfectly plastic relation, in which the first (linear) section is defined as the secant stiffness through the first yield point κ_{fy} (yielding of first longitudinal reinforcement bar) and the second section by the tangent line on the post-yielding section of the actual moment-curvature curve. The intersection of these two lines defines the cross-section yield curvature κ_y.

Similarly, the global displacement ductility demand μ_{δ} is the ratio of the maximum displacement of the system u_{max} imposed by an earthquake to the yield displacement u_y, which is a soil-pile-structure system property.

$$\mu_{\delta} = \frac{u_{max}}{u_{y}} \tag{6.18}$$

The yield displacement u_y is assessed through static nonlinear analyses (pushover analyses) according to the procedure depicted in **Figure 6.44**. A horizontal force is gradually applied at the center of the mass of the superstructure, while the maximum displacement and the curvature along the pile-column are continuously monitored. The measured displacement when the pile curvature reaches the first yield point κ_{fy} is defined as the first yield displacement u_{fy}. Then, similarly to the procedure followed for the determination of the yield curvature, the load–displacement curve is approximated by a bilinear elastic-perfectly plastic relation, in which the first (linear) section is defined as the secant stiffness through the first yield point u_{fy} and the second section by the tangent line on the post-yielding section of the load–displacement curve. The intersection of these two lines defines the system yield displacement u_y.

The maximum displacement of the system u_{max} refers to the part of structure that is above the ground surface and is defined as

$$u_{max} = \max(u_{deck} - u_{pier-base} - \theta_{el} H) \tag{6.19}$$

where u_{mass} the displacement of the deck, $u_{pier\text{-}base}$ the displacement of the pier at the ground surface, θ_{el} the rotation of the pile below the depth of the plastic hinge and H the aboveground height of the pile-column (**Figure 6.45**). The maximum elastic rotation of the soil θ_{el} is defined with a procedure similar to the one used for the yield displacement u_y.

The drift ratio γ is defined as the maximum displacement of the deck imposed by an earthquake relative to the pier base displacement divided by the height of the pier

$$\gamma = \frac{\max\left(u_{deck} - u_{pier-base}\right)}{H} \tag{6.20}$$

Correlations between the performance measures are presented below. **Figure 6.46** demonstrates the correlation of (a) the local curvature ductility μ_ϕ, (b) the global curvature ductility μ_δ, and (c) the drift ratio γ% calculated with the 3D Finite Element Model and the Beam-on-nonlinear-Winkler-foundation Model. The correlation of all three parameters to the two methods examined show a stiffer average response of the 3D Finite Element Model in comparison to the Beam-on-nonlinear-Winkler-foundation Model. This is also verified by the correlation of local curvature ductility demand to the global displacement ductility demand shown in **Figure 6.47**. All the analyses resulted in nonlinear behaviour of the pile-column are categorised according to the method of analysis used. For a given seismic imposed global ductility demand, the local curvature ductility demand from the 3D Finite Element Model is higher than the one from the Beam-on-nonlinear-Winkler-foundation Model.

Figure 6.48 presents the correlation of local curvature ductility demand to the global displacement ductility demand according to the potential plastic location of the plastic hinge. For constant diameter pile-columns the plastic hinge is likely developed below the ground surface whereas for variable diameter pile-columns plastic hinges are developed at the base of the pier. The average ratio $(\mu_\phi - 1) / (\mu_\delta - 1)$ takes a value of 1.9 or 1.0 for plastic hinge below ground surface (according to the 3D Finite Element Model and the Beam-on-nonlinear-Winkler-foundation Model, respectively) and 2.7 or 2.6 for plastic hinge above the ground surface. The results encourage the inelastic design of the pile.

The influence of the pier diameter on the correlation of local curvature ductility demand to the global displacement ductility demand is illustrated in **Figure 6.49**. No

significant influence is observed by the 3D Finite Element Model as the diameter of the pier increases (($\mu_\phi - 1$) / ($\mu_\delta - 1$) ≈ 2.4 for both diameters). In the case of the Beam-on-nonlinear-Winkler-foundation Model the ratio changes from 1.8 (pier diameter d = 1.5 m) to 2.2 (pier diameter d = 3.0 m).

The correlation of local curvature ductility demand to the global displacement ductility demand according to the pier height is depicted in **Figure 6.50**. According to Eurocode 8 (CEN, 2005) the local curvature ductility demand μ_ϕ is correlated to the global displacement ductility demand μ_δ by:

$$\mu_\varphi = 1 + \frac{(\mu_\delta - 1)H^2}{3L_p\left(H - \frac{1}{2}L_p\right)} \tag{6.21}$$

where L_p the length of the plastic hinge and H the height of the pier. As expected, taller piers (H = 10 m) exhibit greater local curvature ductility demand for a given displacement ductility level, since for tall piers (H = 10 m) the ($\mu_\phi - 1$) / ($\mu_\delta - 1$) ratio equals to 2.7 and 2.1 according to the 3D Finite Element Model and the Beam-on-nonlinear-Winkler-foundation Model, respectively, while for short piers (H = 5 m) the ratio equals to 1.3 and 1.1. This is attributed to the higher effective period of the column pile with the short pier in comparison to the one with the tall pier, as derived from Fast Fourier Transform Analysis. Furthermore, the ductility demand from Eurocode 8 is conservative in comparison to both methods of analysis used.

The correlation of local curvature ductility demand to the maximum drift ratio derived from the two methods examined is presented in **Figure 6.51**. For a given maximum drift ratio, the required curvature ductility is slightly greater with the 3D Finite Element Model.

The effect of the plastic hinge location on the correlation of local curvature ductility demand to the maximum drift ratio is presented in **Figure 6.52**. The local curvature ductility demand for a given maximum drift ratio for both methods examined is higher when the pier is plasticized. For the aboveground failure case, the two methods examined have similar correlation of the local curvature ductility demand to the maximum drift ratio. For belowground failure, the Beam-on-nonlinear-Winkler-foundation Model has a higher local curvature ductility demand for a given maximum drift ratio than 3D Finite Element Model.

The correlation of local curvature ductility demand to the maximum drift ratio according to the pier diameter is depicted in **Figure 6.53**. It is evident that as the pier diameter increases, for a given maximum drift ratio, the local curvature ductility demand also increases. The increase of this demand is smaller in the 3D Finite Element Model since, as already mentioned, it has a stiffer response than the Beam-on-nonlinear-Winkler-foundation Model. Similar is the influence of the pier height shown in **Figure 6.54**. Taller piers exhibit greater local curvature ductility demand for a given drift ratio. Indeed, for a given maximum drift ratio the differential horizontal displacement between the deck and the pier base decreases with decreasing aboveground height of the pier, thus leading to smaller pier distress and ductility demand.

In **Figures 6.55** to **6.57**, the mean and peak values of the factors μ_ϕ, μ_δ, γ_{max} are illustrated for the various parameters examined. It is clearly observed that the mean and maximum values of both μ_ϕ and μ_δ are lower for plasticized piles. These figures together with **Figure 6.48** reveal the beneficial influence of belowground failure on the response of the structure. The increase of the aboveground height H and the pier diameter cause the increase in the mean and maximum values of μ_δ and μ_ϕ and decrease in the mean and maximum value of γ_{max}. There is no certain trend regarding the method of analysis used, nevertheless it is noted that their results agree qualitatively.

6.3.5 Effect of soil compliance

The influence of near-field soil compliance on the seismic response of the soil-pile-superstructure system is investigated parametrically considering four different soil profiles: (a) sand with friction angle $\phi = 40^o$ and cohesion c = 5 kPa constant with depth (thereinafter called dense), (b) sand with friction angle $\phi = 28^o$ and cohesion c = 5 kPa constant with depth (thereinafter called loose), (c) clay with undrained shear strength S_u with parabolic distribution with depth (thereinafter called stiff), and (d) clay with undrained shear strength $S_u/5$ with parabolic distribution with depth (thereinafter called soft, as shown in **Figure 6.58**). Because the decrease of the soil strength in the 3D Finite Element model also affects the dynamic properties of the soil (**Equations 6.11** to **6.16**) and thus the peak ground acceleration at the ground surface is less than the target acceleration, the soil compliance is studied only with the Beam-on-nonlinear-Winkler-foundation Model.

Figures 6.59 and **6.60** present the acceleration time histories at the deck for pile-columns with diameter d = 3 m and aboveground height H = 5 m for the different soil profiles examined. The amplitude of the acceleration at the deck decreases for the softer soils. However, the decrease of the response in the case of the loose sand is not as obvious as in the case of soft clay. This can be attributed to the lateral confinement of the soil which might be considerable even for smaller values of internal friction angles, leading to stiffer soil-pile-structure response. In every case, the spectral accelerations are lower for the case of softer soils, as expected.

The influence of the soil type on the maximum bending moment distribution is shown in **Figure 6.61**. As expected, soft soils result in increasing the effective length of the pile and the depth of the maximum bending moment. The difference of the maximum bending moments among the four cases is attributed to the difference of the plastic hinge position on the pile. Similarly, **Figure 6.62** illustrates the influence of the soil type on the position of the plastic hinge. The amplitude of the curvature increases significantly in stiffer soils.

Figure 6.63 demonstrates the correlation of the local curvature ductility demand to the global displacement ductility demand. It is obvious that the decrease of the soil strength for the same soil dynamic properties has no influence on the ductility demand parameters which are structurally defined. Thus the mean ratio $(\mu_\phi - 1) / (\mu_\delta - 1)$ is insensitive to the soil conditions. For this reason, all four lines would be expected to coincide. The small difference among the behaviour of the sand and clay is attributed to the definition of the elastic rotation of the soil and the assumption of an equivalent linear elastic–perfectly plastic response of the system for the determination of parameters μ_ϕ and μ_δ. **Figures 6.64** and **6.65** depict the correlation of the local curvature ductility demand to the global displacement ductility demand for different soil types for aboveground and belowground failure. It is observed that the previous trend remains for the aboveground failure. When the failure is below ground the $(\mu_\phi - 1) / (\mu_\delta - 1)$ ratio for the stiff clay and the dense sand coincide. The correlation of the local curvature ductility demand to the maximum drift ratio for different soil profiles is shown in **Figure 6.66**. For a given maximum drift ratio, the required curvature ductility is greater for the soft clay.

In **Figures 6.67** to **6.69**, the mean and peak values of the factors μ_ϕ, μ_δ, γ_{max} are illustrated for the different soil profiles examined. In general, the mean and maximum

values of all factors examined decrease slightly when the soil becomes softer. It should be noted that no great differences are observed in the two sandy deposits examined, since, even though the sand with friction angle $\phi = 28^o$ and cohesion c = 5 kPa is looser than the other sand deposit, it is still dense enough in its response. Hence, the soil stiffness has a slight beneficial influence on the response of the structure, but the more beneficial influence derives from the location of the plastic hinge below the ground surface. This is further shown in **Figure 6.70** where the mean and peak values of the local curvature ductility demand μ_δ are illustrated for different soil types for aboveground and belowground failure. Even though for a given displacement ductility demand the curvature ductility capacity of a pile-column is insensitive to the soil type, for a given seismic excitation the absolute values of the local ductility demand μ_ϕ for soft soils and below ground failure are smaller than for stiff soils and aboveground failure.

6.4 SUMMARY AND CONCLUSIONS

The seismic response of a soil-pile-structure system is investigated with two numerical methods: (1) with a simplified method based on the Beam-on-nonlinear-Winkler-foundation Model, and (2) with a 3D Finite Element Model.

Initially, the elastic response of the soil-pile-bridge system embedded in two layers of clay under different seismic excitations is examined. The influence of the boundaries on the response of the soil-pile-bridge system on the 3D finite element Model is investigated. Equivalent damping is also used on the 3D finite element Model in order to match the damping from the Beam-on-Winkler-foundation Model. Three different seismic motions are used for the analysis. The results from the two models examined compare well for all cases. The sequence of significant pulses of the Aegion (1995) record influences the response of the models examined for the case of displacement time histories.

Having compared the elastic response of the soil-pile-structure system by two different methods, a parametric investigation of the nonlinear response of pile-column bridge systems is conducted with the use of both nonlinear Winkler and 3D continuum finite element models utilizing advanced inelastic constitutive laws.

- A calibration methodology of the “spring” and “dashpot” coefficients of the examined hybrid spring configuration of the Beam-on Winkler-foundation Model is proposed.

Regarding the seismic site response derived from the Equivalent Linear Analysis and the 3D Nonlinear Analysis:

- There is a difference observed at the acceleration time histories due to the different damping of the two methods. Apparently the Rayleigh damping in the fully 3D Finite Element Model should be slightly increased. In addition, the decreased acceleration amplitude at high frequencies in the Equivalent Linear Analysis is attributed to the fact that SHAKE overdamps the soil response at high frequencies and also does not take into consideration surface waves (1D Analysis).
- In all cases, the 3D Nonlinear Analysis leads to equal or smaller values of the peak ground acceleration (PGA) in comparison to the Equivalent Linear Analysis, showing the importance of the actual nonlinear soil behavior in the site response.
- As expected, apart from the site response in high frequencies, the 3D Nonlinear Analysis reduces the spectral accelerations, while the predominant period is the same for both methods of Analysis
- In the 3D Nonlinear Analysis, the plastification of the soil increases as the peak ground acceleration (PGA) increases. Thus, the amplification of the seismic motion is less than in the Equivalent Linear Analysis.

From the parametric analyses, both models examined agree that:

- For a given global displacement ductility demand μ_δ, the potential formation of plastic hinge belowground surface decreases the local curvature ductility demand μ_ϕ highlighting the inelastic design of the pile.
- The pier diameter has no apparent influence on the correlation of local curvature ductility demand to the global displacement ductility demand.
- As expected, taller piers exhibit greater local curvature ductility demand for a given displacement ductility level. In addition, the ductility demand according to Eurocode 8 is conservative in comparison to both methods of analysis used.

- Similarly, the local curvature ductility demand for a given maximum drift ratio is higher when diameter and height of the pier increase and when the pier is plasticized.
- Regarding the peak values of the factors μ_ϕ, μ_δ, and γ_{max} that are reached during an earthquake, it is observed that the mean and maximum values of both μ_ϕ and μ_δ are lower for plasticized piles while the increase of the aboveground height H and the pier diameter cause the increase in the mean and maximum values of μ_δ and μ_ϕ and decrease in the mean and maximum value of γ_{max}.
- The correlation of the local curvature ductility demand to the global displacement ductility demand is slightly sensitive to the soil compliance.
- On the contrary, for a given maximum drift ratio, the required curvature ductility is greater for softer soils.

It is clear that the soil stiffness has a slight beneficial influence on the response of the structure, but the more beneficial influence derives from the location of the plastic hinge below the ground surface.

REFERENCES

Anastasopoulos I., Gazetas G., Loli M., Apostolou M., Gerolymos N., 2010, "Soil failure can be used for seismic protection of structures", *BEE*, 8, pp 309-326

Apostolou M., Gazetas G., Garini E., 2007, "Seismic response of slender rigid structures with foundation uplifting", *Soil Dynamics and Earthquake Engineering*, 27(7), pp 642-654

Broms B.B., 1964, "Lateral resistance of piles in cohesive soils", *Journal of Soil Mechanics and Foundation Division*, ASCE 90 (SM2), pp 27-63

Budek A.M., Priestley M.J.N., Benzoni G., 2000, "Inelastic seismic response of bridge drilled-shaft RC pile/columns", *Journal of Geotechnical and Geoenvironmental Engineering*, 126 (4), pp 510-517

CEN, "Eurocode 8: Design of structures for earthquake resistance. Part 2: Bridges", Final Draft prEN 1998-2, Brussels, Belgium: European Committee for Standardization, 2005

Chatzigogos C.T., Pecker A., Salencon J., 2009, “Macroelement modeling of shallow foundations”, *Soil Dynamics and Earthquake Engineering*, 29 (6), pp 765-781

Dassault Systèmes Simulia Corp, 2009, *ABAQUS User’s Manual*, Providence, RI, USA

Drosos V., 2007, “*Inelastic dynamic soil-structure interaction*”, Doctoral Dissertation, National Technical University of Athens

Gerolymos N., 2002, “*Constitutive model for the static and dynamic response of soil, soi-pile and soil-caissonl*”, Doctoral Dissertation, National Technical University of Athens

Gerolymos N., Gazetas G., 2005a, “Phenomenological model applied to inelastic response of soil-pile interaction systems”, *Soils and Foundations*, 45 (4), pp 119-132

Gerolymos N., Gazetas G., 2005b, “Constitutive model for 1-D cyclic soil behavior applied to seismic analysis of layered deposits”, *Soils and Foundations*, 45 (3), pp 147-159

Gerolymos N., Drosos V., Gazetas G., 2009, “Seismic response of single-column bent on pile: evidence of beneficial role of pile and soil inelasticity”, *BEE*, 7, pp 547-573

Idriss I.M.., Sun J.I., 1991, “SHAKE91: A computer program for conducting equivalent linear seismic response analyses of horizontally layered soil deposits”, *Center for Geotechnical Modeling Report*, Department of Civil and Environmental Engineering, University of California, Davis

Ishibashi I., Zhang X., 1993, “Unified dynamic shear moduli and damping ratios of sand and clay”, *Soils and Foundations*, Vol. 33 (1), pp 182-191

Kramer S.L., 1996, *Geotechnical Earthquake Engineering*, Prentice Hall, Upper Saddle River, NJ

Makris N., Gazetas G., 1992, “Dynamic pile-soil-pile interaction. Part II: Lateral and seismic response”, *Earthquake Engineering and Structural Dynamics*, 21, pp 145-162

Makris N., Roussos Y.S., 2000, “Rocking response of rigid blocks under near-source ground motions”, *Geotechnique*, 50 (3), pp 243-262

Matlock H., 1970, “Correlations for design of laterally loaded piles in soft clay”, *Proceedings of the 2nd Annual Offshore Technology Conference*, Houston, Texas, pp 577-594

Mazzoni S., McKenna F., Fenves G.L., 2005, “OpenSees command language manual”, The Regents of the University of California

Pecker A., 1998, “Capacity design principles for shallow foundations in seismic areas”, P*roceedings of the 11th European Conference on Earthquake Engineering*, Paris

Reese L.C., Cox W.R., Koop F.D., 1974, “Analysis of laterally loaded piles in sand”, *Proceedings of the VI Annual Offshore Technology Conference*, Houston, Texas, 2: 473-485

Reese L.C., Van Impe W.F., 2001, *Single Piles and Pile Groups under Lateral Loading*, A.A. Balkema, Rotterdam

SDC, 2010, *Seismic Design Criteria – Version 1.6*, California Department of Transportation (Caltrans), USA

Seed H.B., Idriss I.M., 1970, “Soil modulii and damping factors for dynamic response analysis”, *Report No. UCB/EERC-70/10*, University of California, Berkeley

Wang S., Kutter B.L., Chacko J.M., Wilson D.W., Boulanger R.W., Abghari A., 1998, “Nonlinear seismic soil-pile-superstructure interaction”, *Earthquake Spectra*, 14 (2), pp 377-396

Table 6.1 Pile-column characteristics

Height (m)	Pile / Pier Diameter (m)	Deck mass (tons)
5	1.5 / 1.5	450
5	2.0 / 1.5	450
5	3.0 / 3.0	6960
5	4.0 / 3.0	6960
10	1.5 / 1.5	60
10	2.0 / 1.5	60
10	3.0 / 3.0	900
10	4.0 / 3.0	900

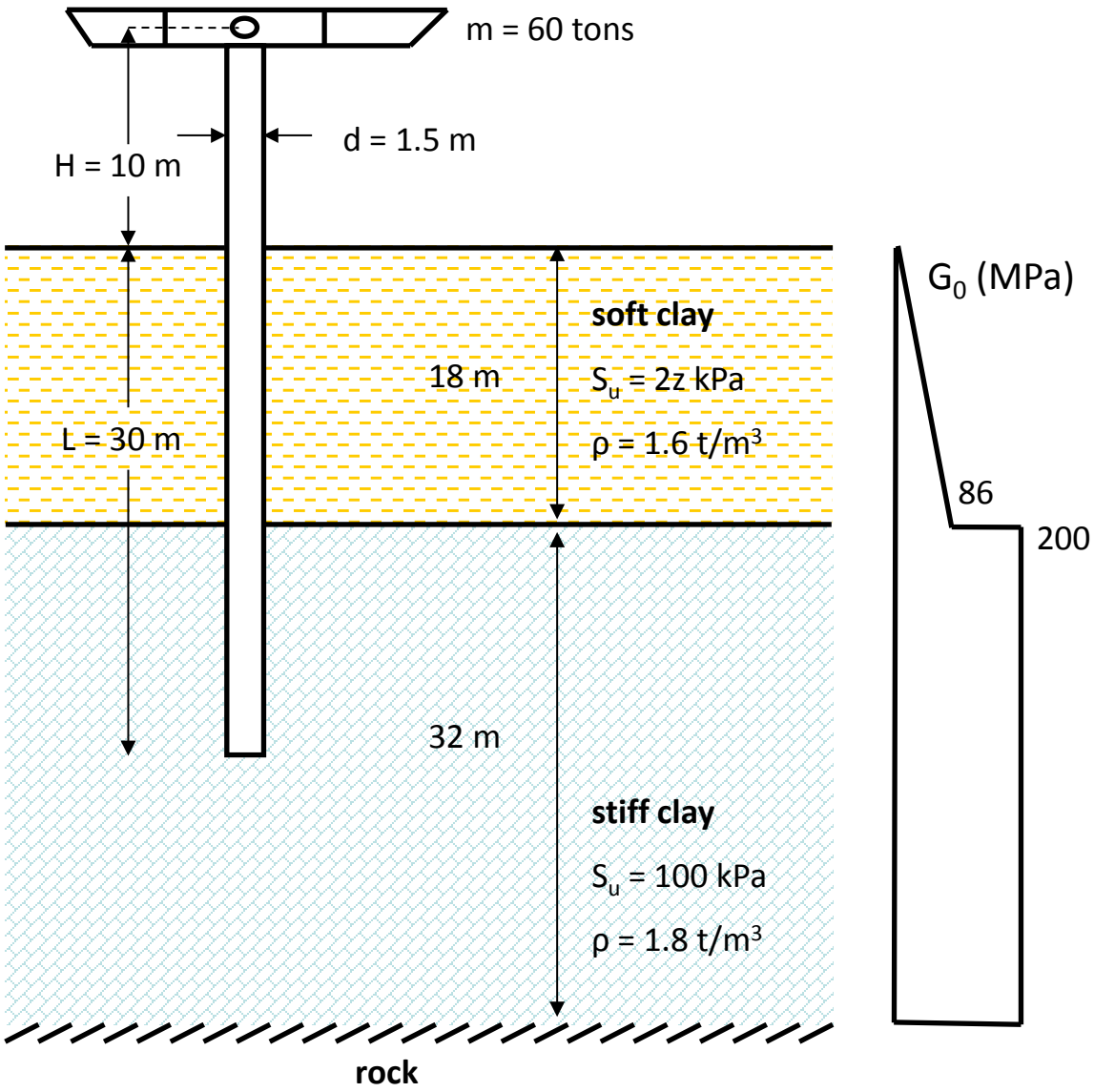

Figure 6.1: The problem investigated

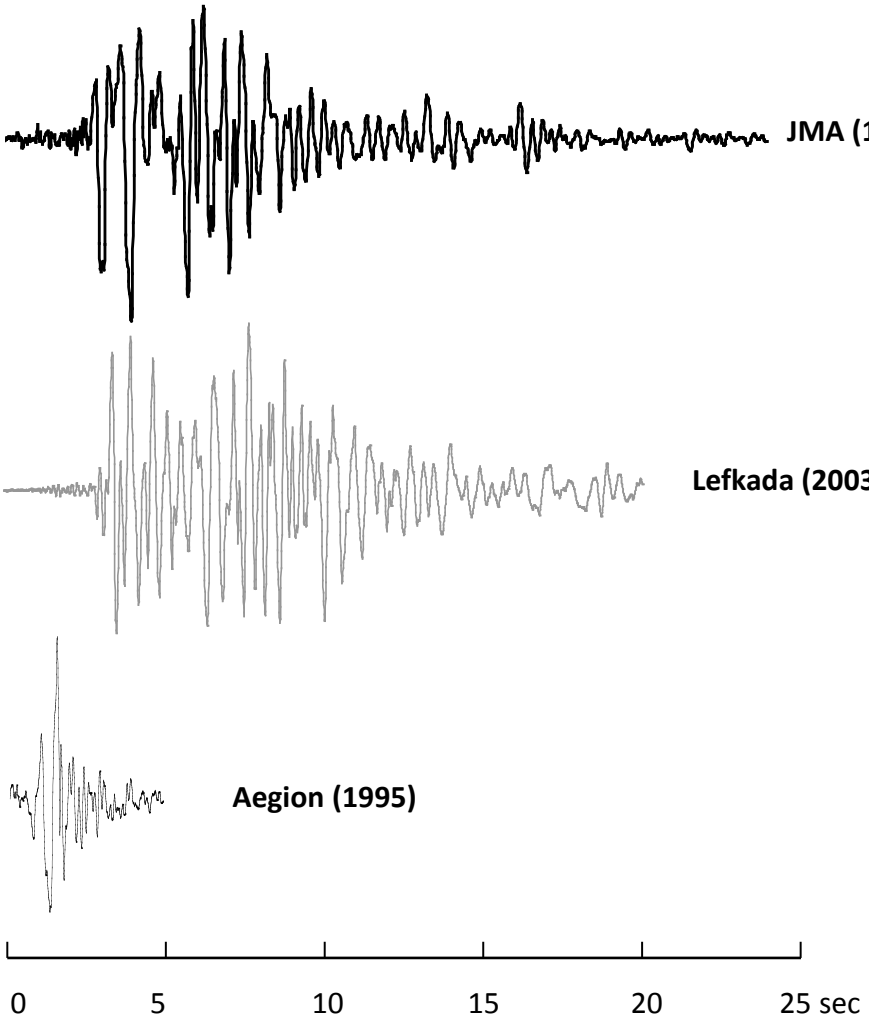

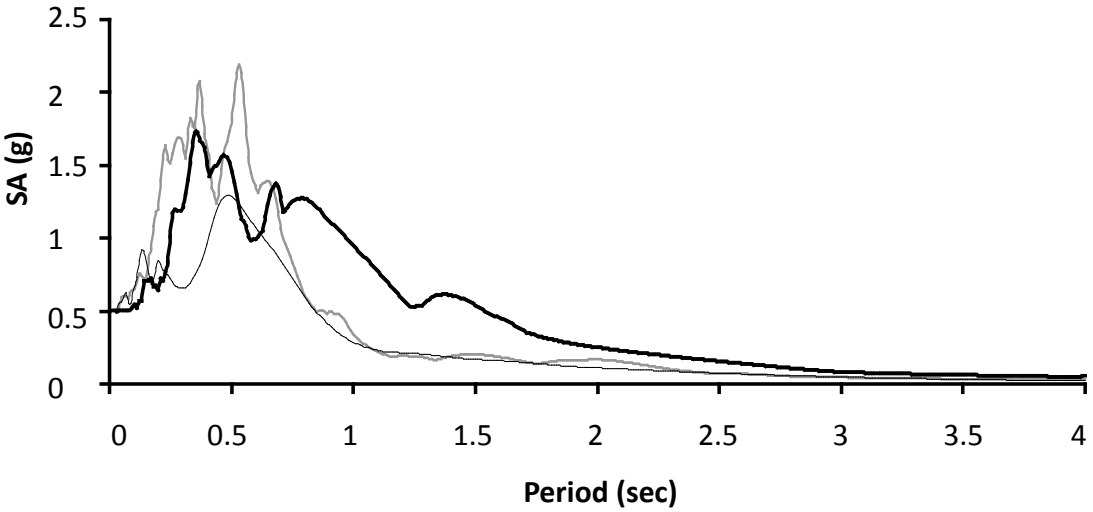

Figure 6.2: Accelerograms scaled to a_g = 0.5 used as excitation and corresponding 5 % damped response spectra

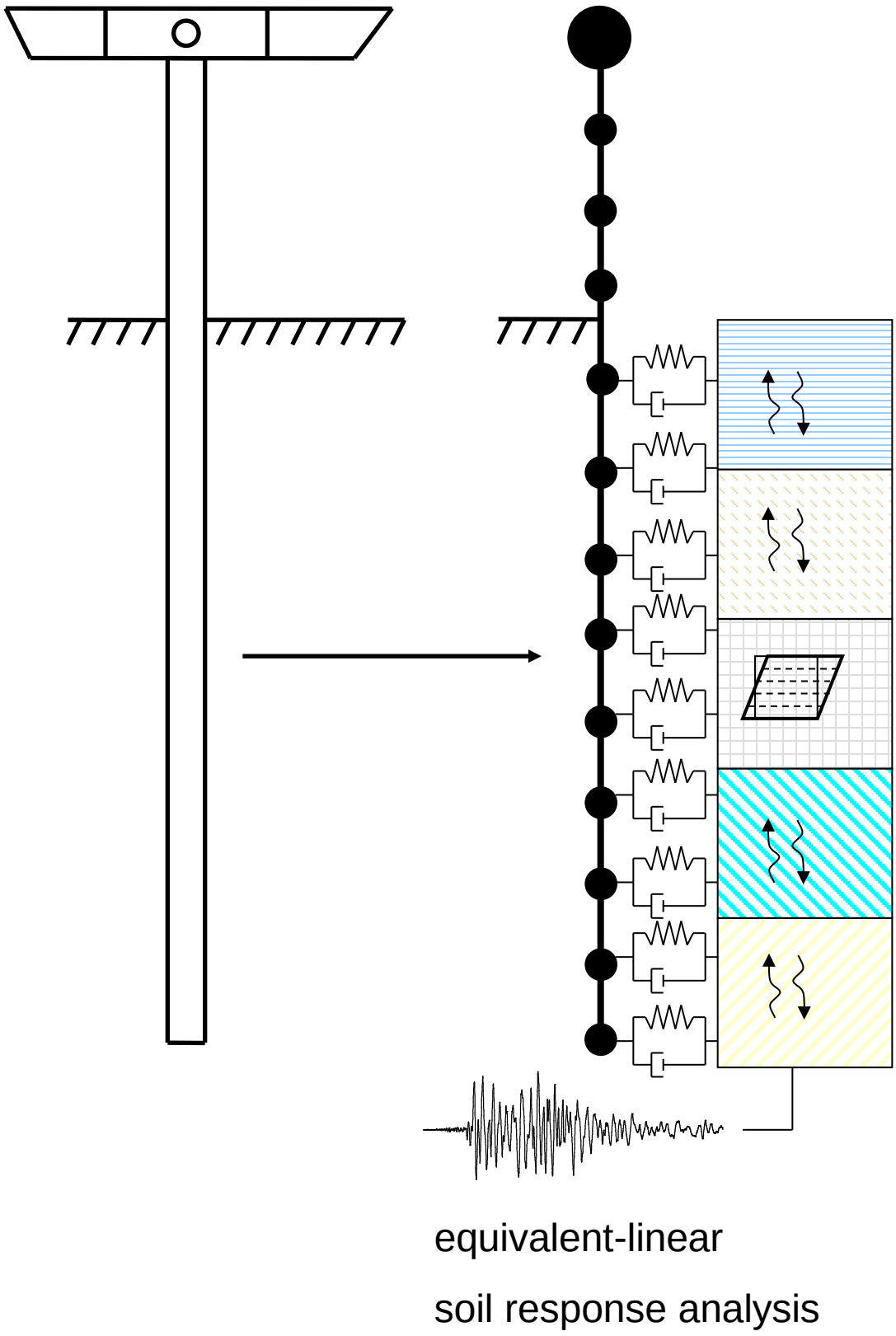

Figure 6.3: Schematic illustration of the beam-on-Winkler-foundation model used for the elastic analyses

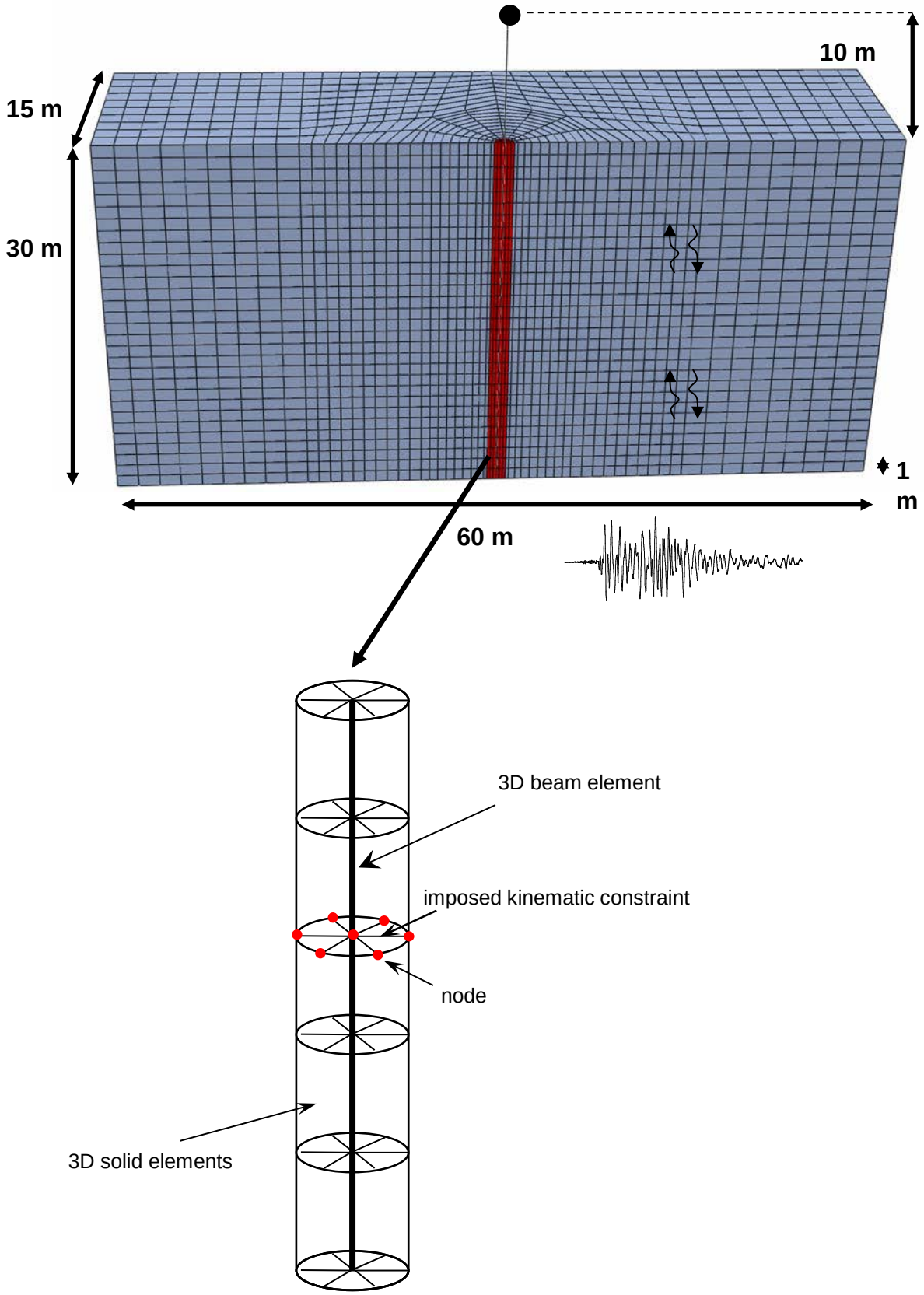

Figure 6.4: Mesh discretization of the 3D Finite Element Model used for the elastic analyses

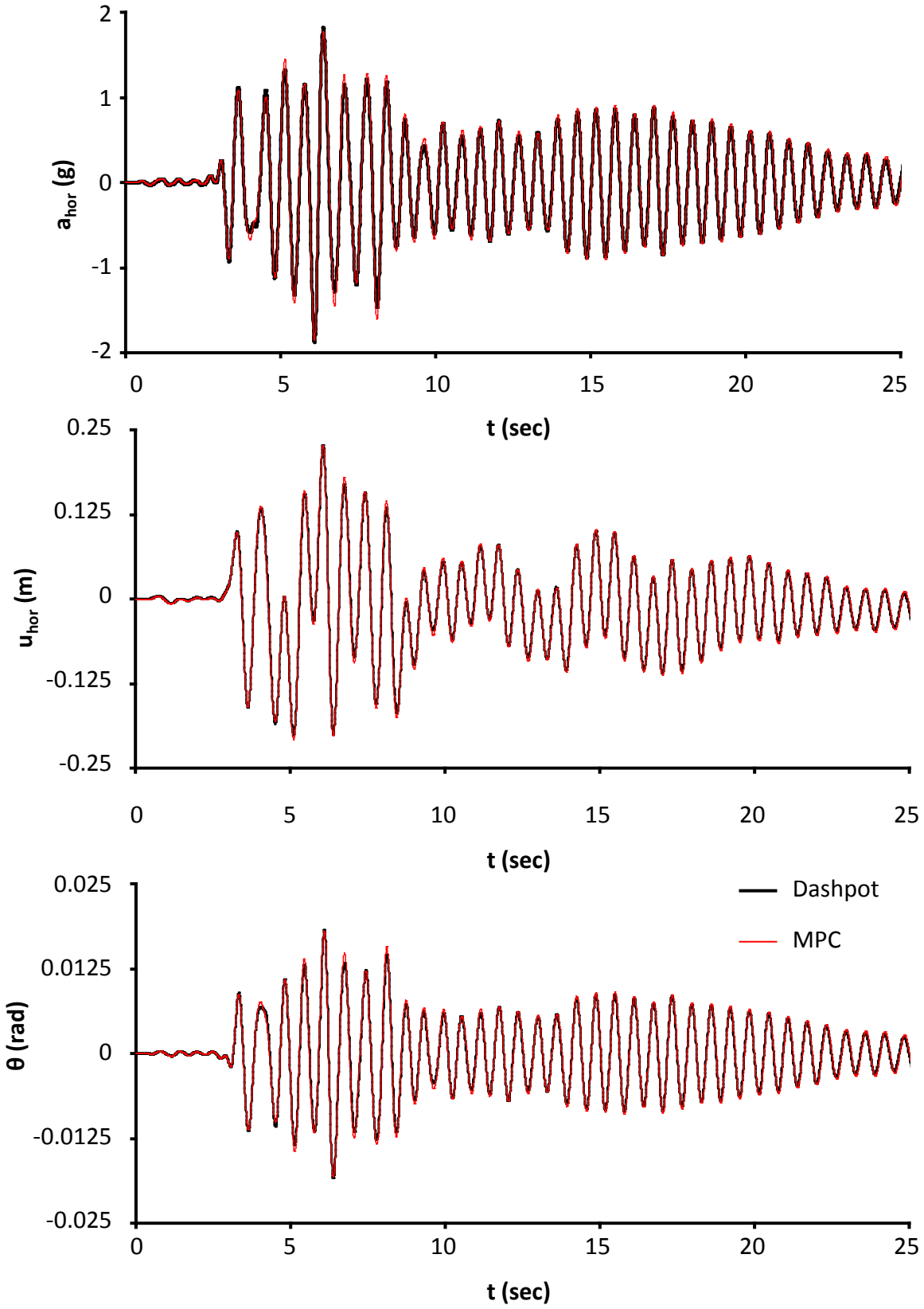

Figure 6.5: Comparison of the acceleration, displacement and rotation time histories at the deck of the 3D Finite Element Model with dashpot and mpc boundaries for the JMA record scaled at a_g = 0.5 g

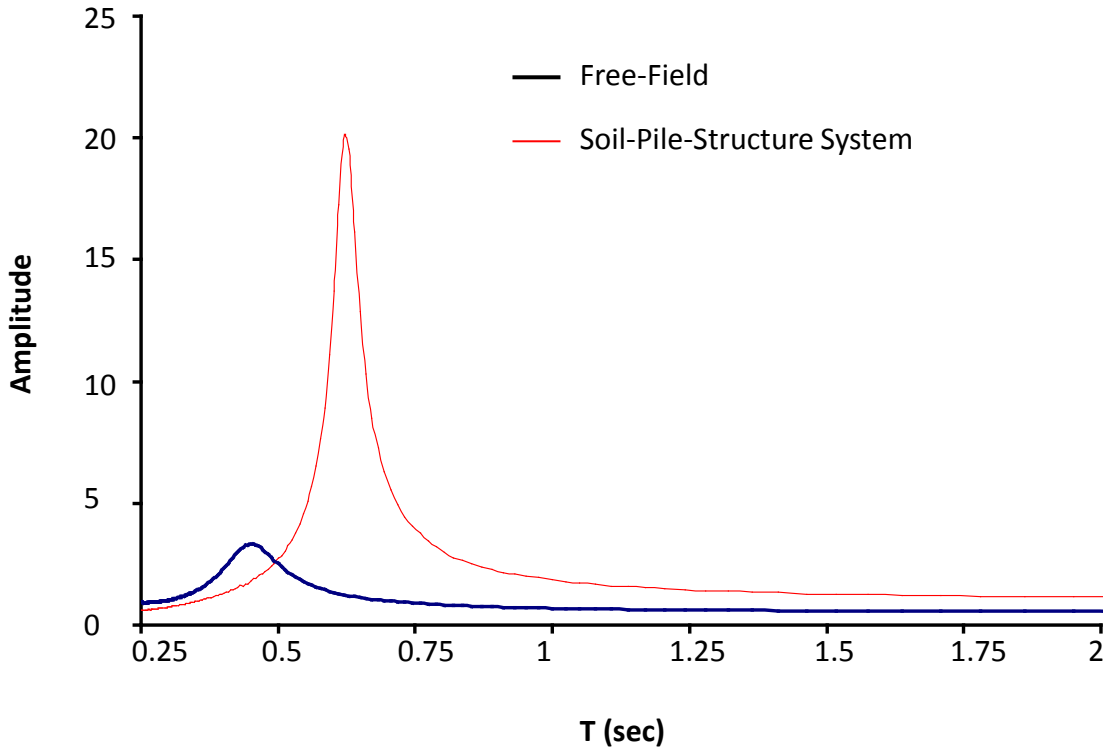

Figure 6.6: Fast Fourier Transform Analysis for the free-field and soil-pile-structure system response

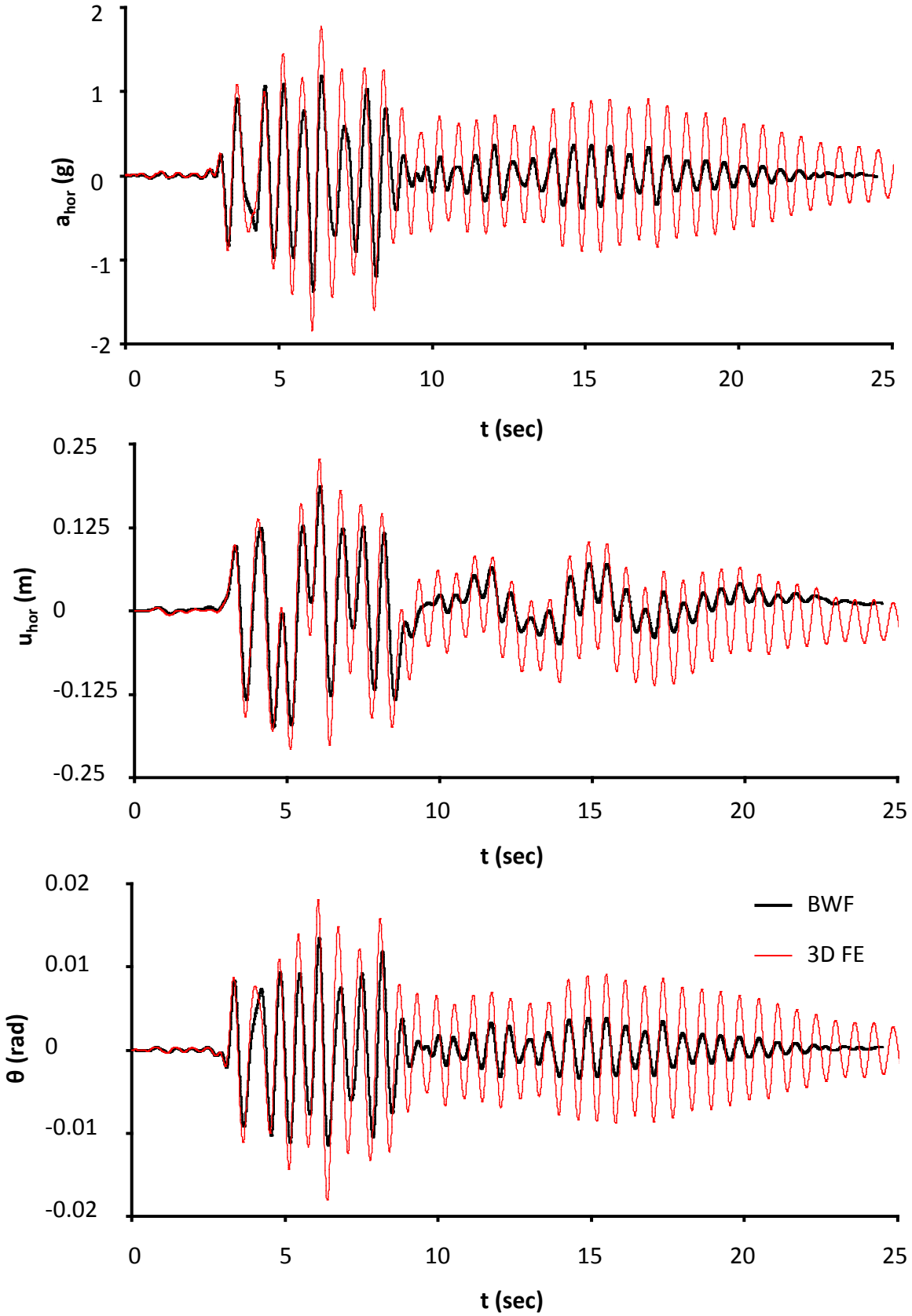

Figure 6.7: Comparison of the acceleration, displacement and rotation time histories at the deck of the 3D Finite Element Model and the Beam-on-Winkler-foundation Model for the JMA record scaled at a_g = 0.5 g

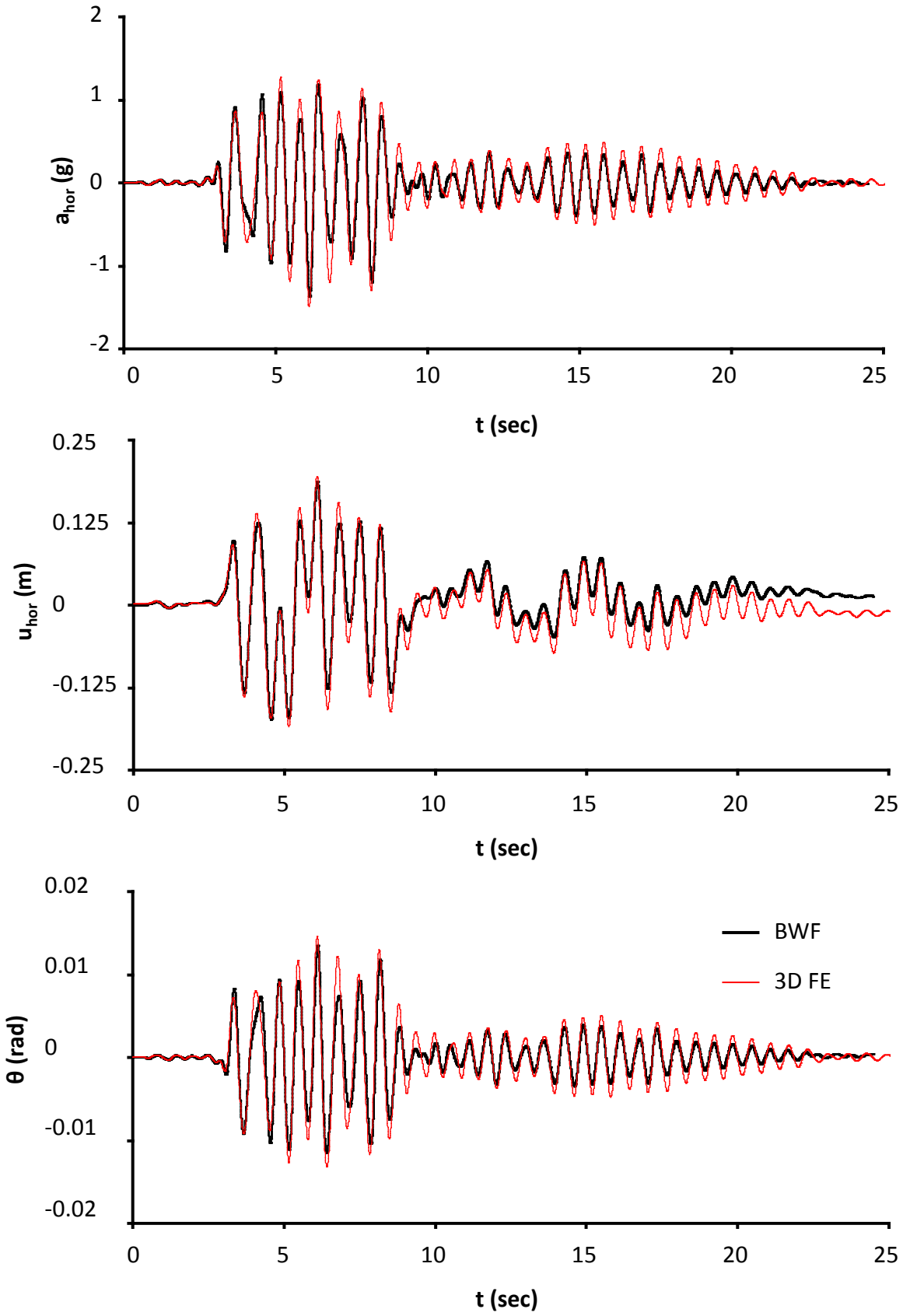

Figure 6.8: Comparison of the acceleration, displacement and rotation time histories at the deck of the 3D Finite Element Model with equivalent damping to the Beam-on-Winkler-foundation Model for the JMA record scaled at a_g = 0.5 g

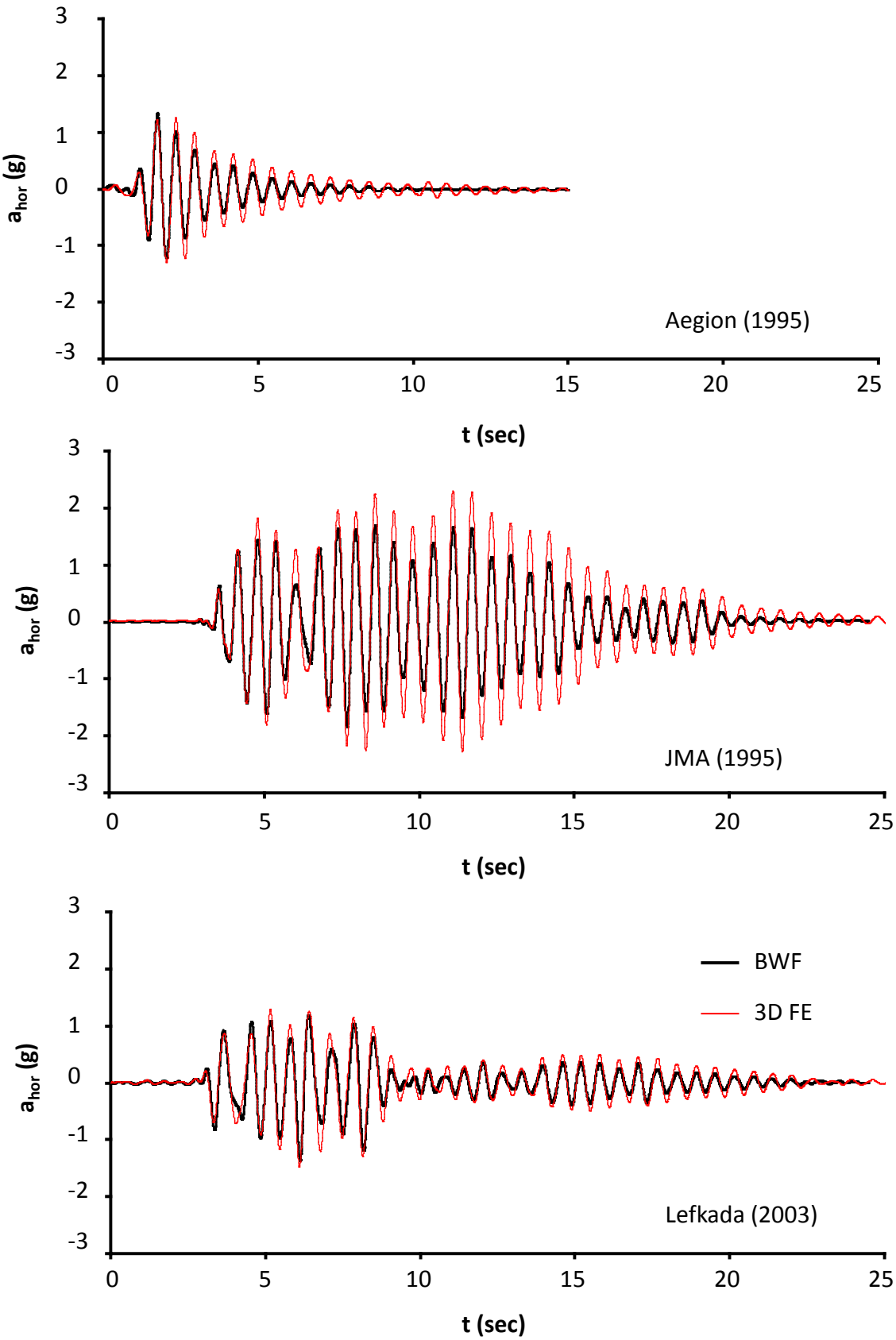

Figure 6.9: Comparison of the acceleration time histories at the deck of the 3D Finite Element Model with the Beam-on-Winkler-foundation Model

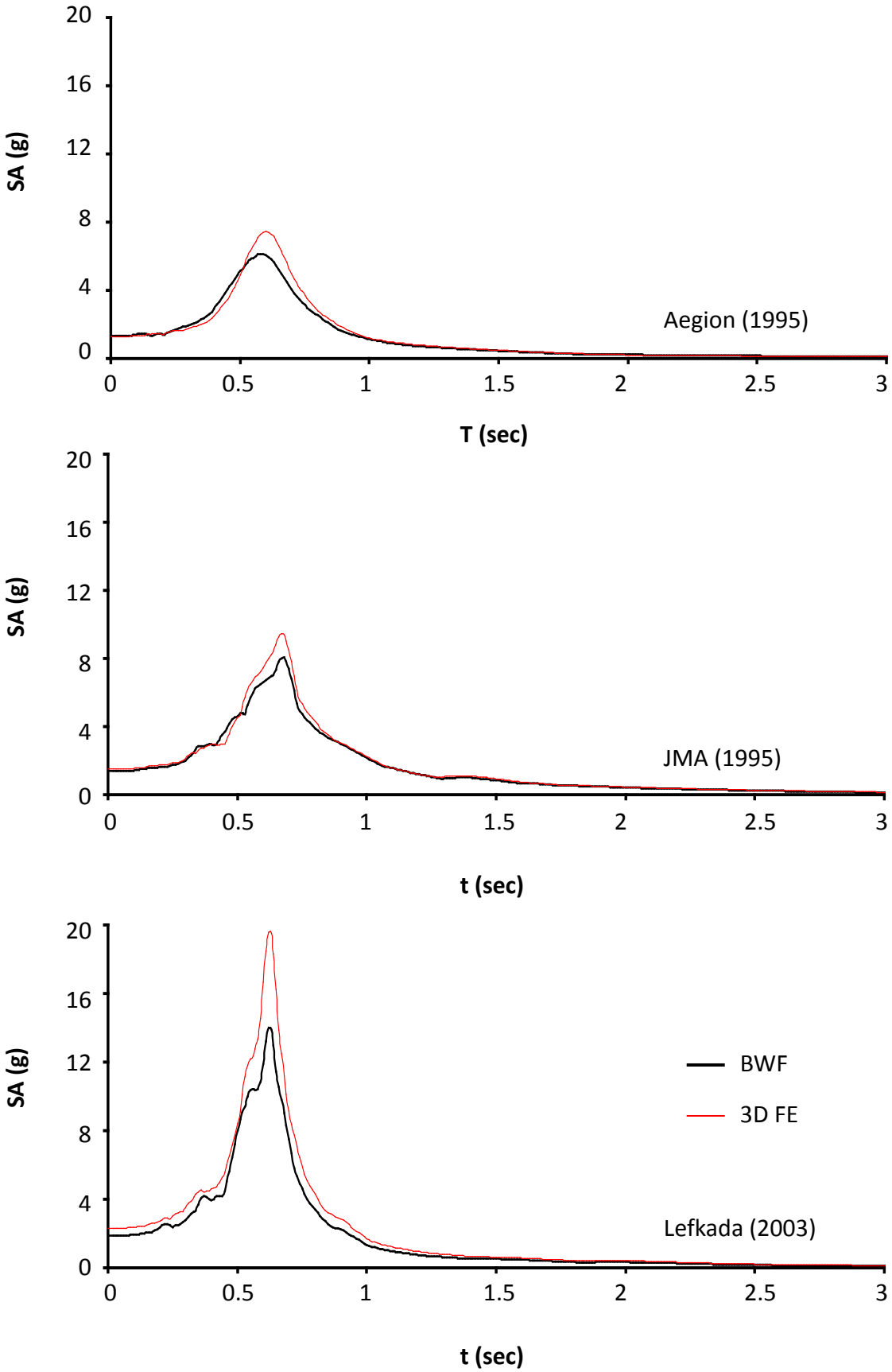

Figure 6.10: Comparison of the (ξ = 5 %) response spectra at the deck of the 3D Finite Element Model with the Beam-on-Winkler-foundation Model

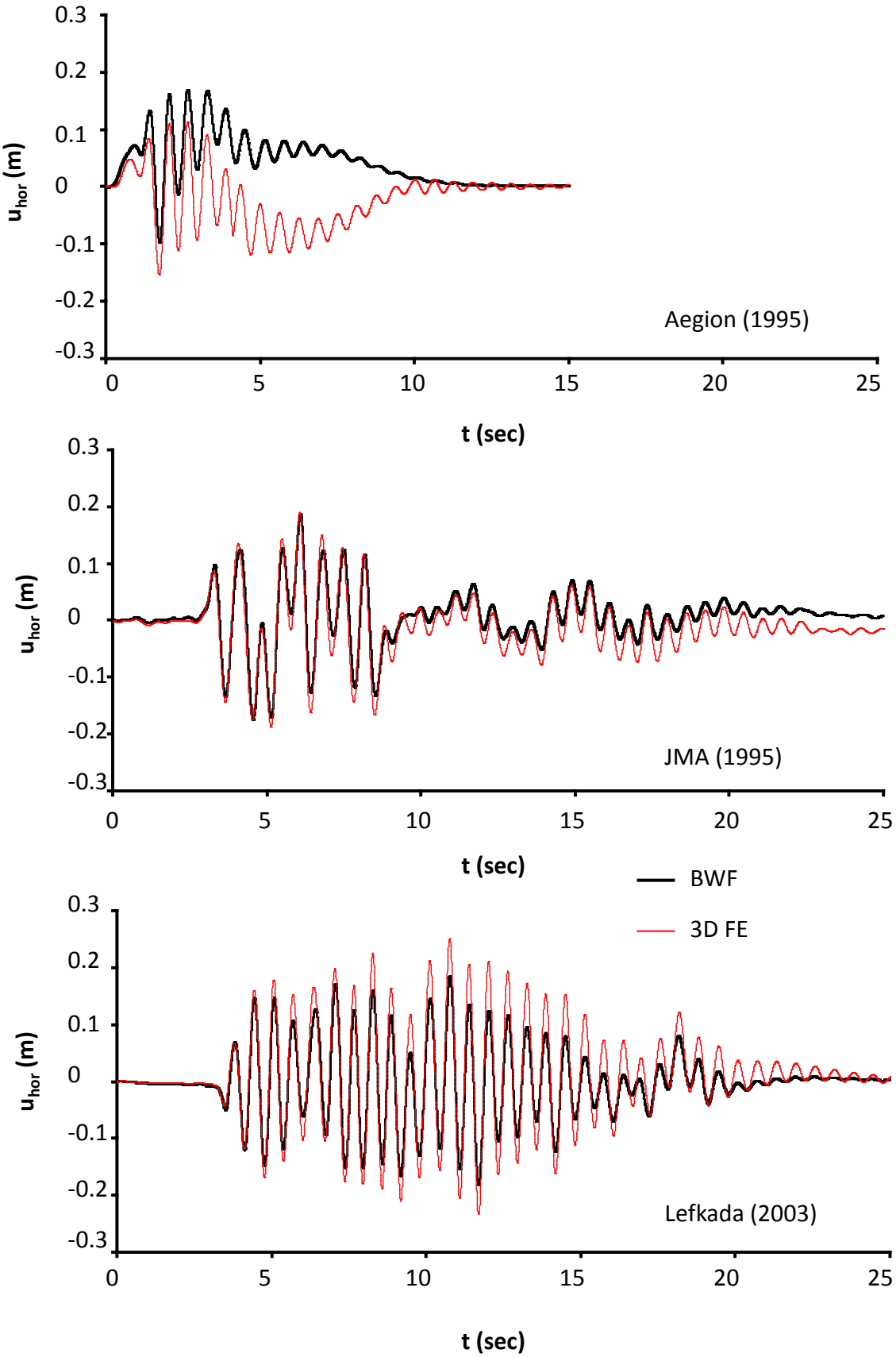

Figure 6.11: Comparison of the displacement time histories at the deck of the 3D Finite Element Model with the Beam-on-Winkler-foundation Model

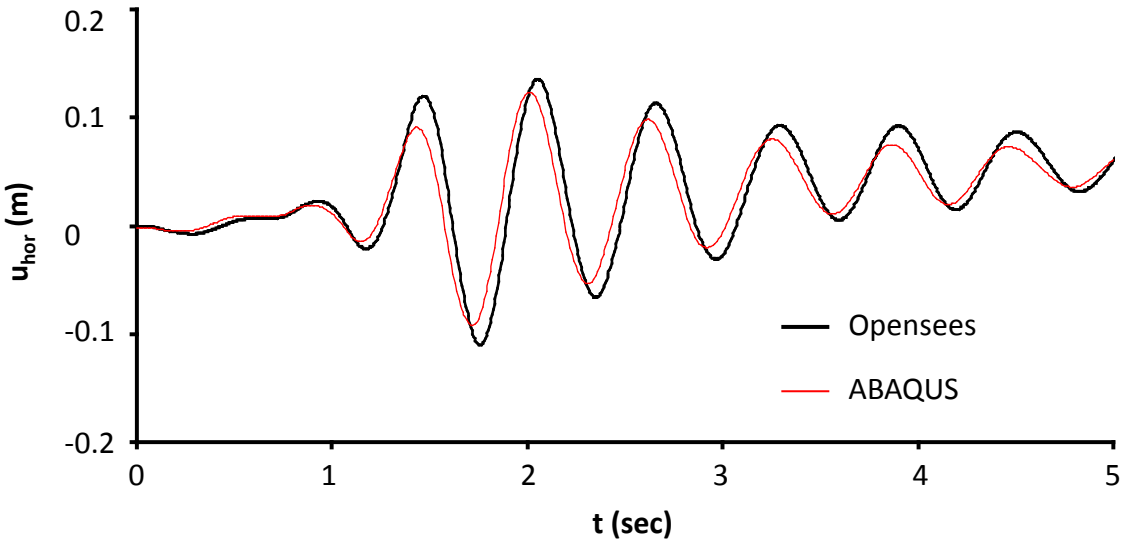

Figure 6.12: Comparison of the displacement time histories at the deck of the two Beam-on-Winkler-foundation Models with Finite Element Codes OpenSees and ABAQUS

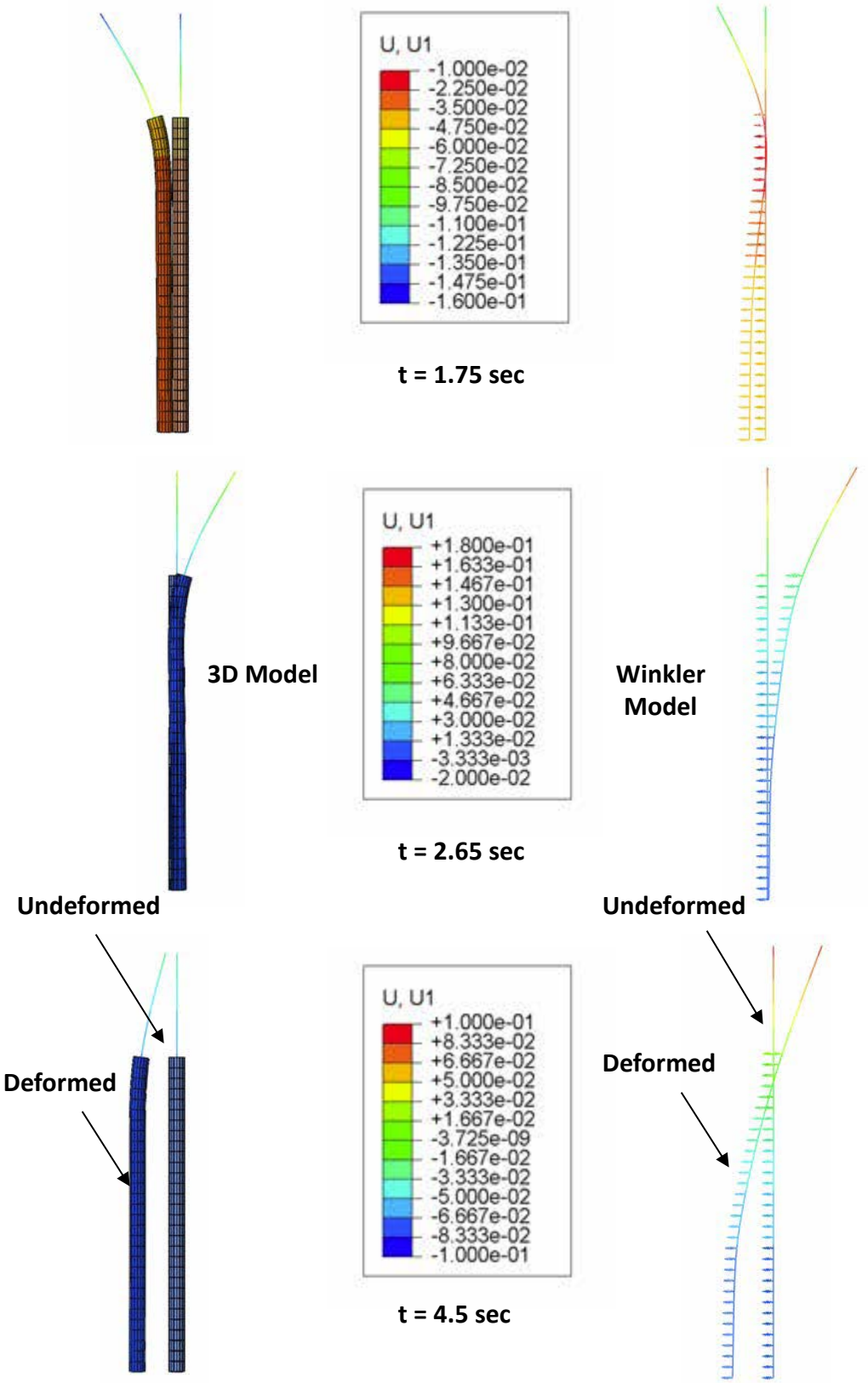

Figure 6.13: Snapshots of the deformed pile-column for the Aegion (1995) excitation scaled to a_g = 0.5 g at: (a) t = 1.75 sec, (b) t = 2.65 sec, and (c) t = 4.5 sec in comparison to the undeformed state. (Deformation Scale Factor = 50)

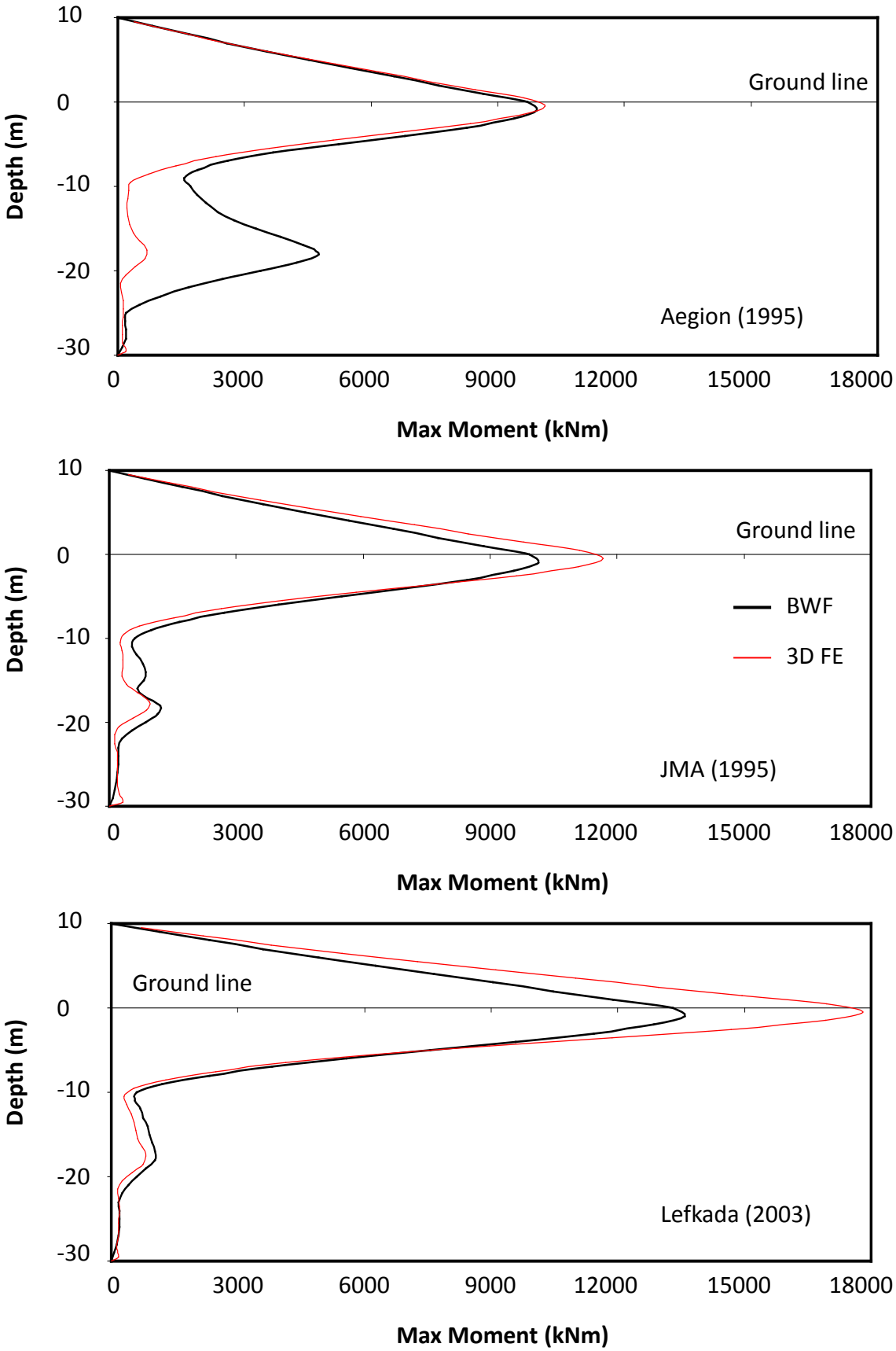

Figure 6.14: Comparison of the maximum bending moment distributions calculated from the 3D Finite Element Model and the Beam-on-Winkler-foundation Model

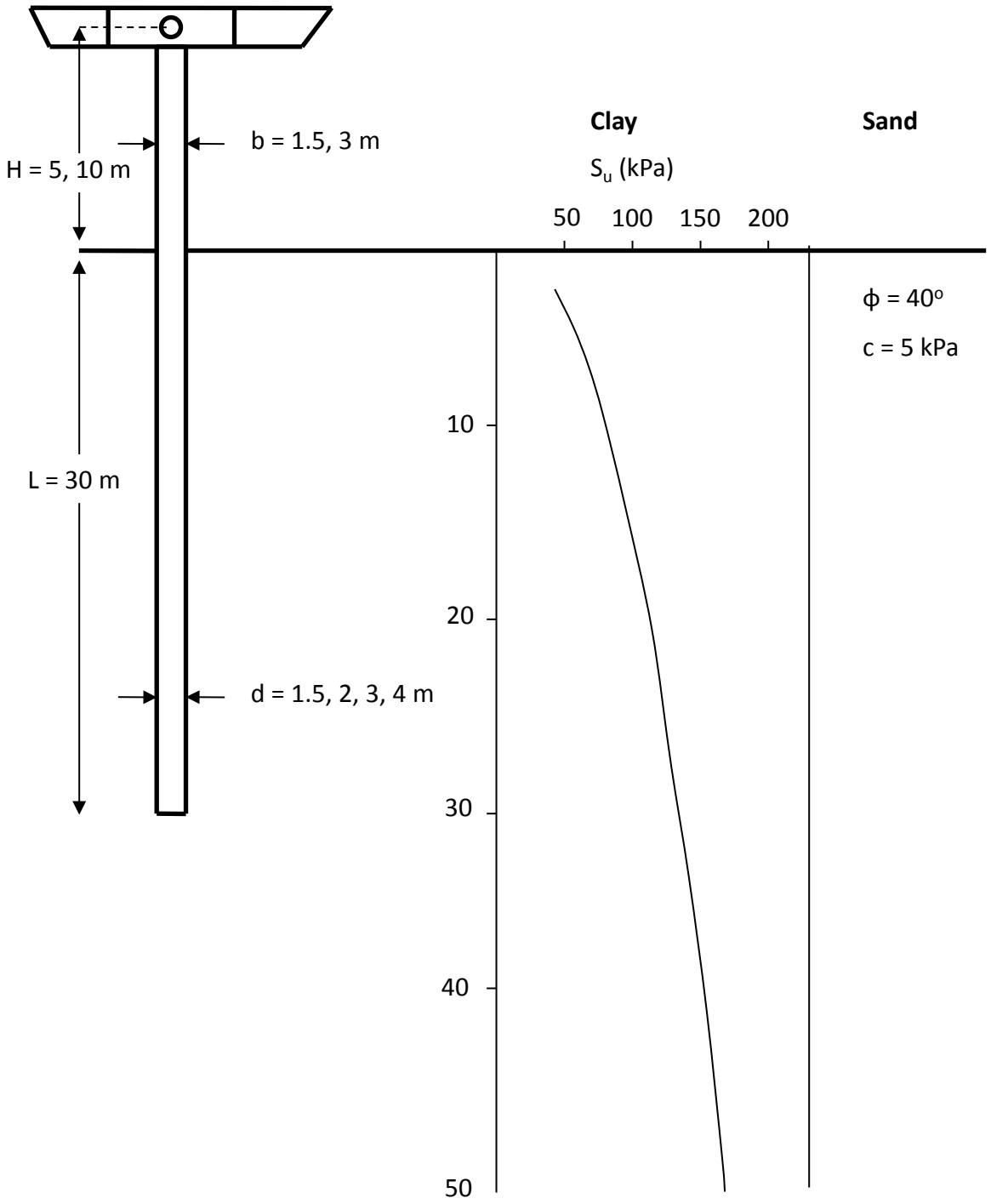

Figure 6.15: The problem investigated

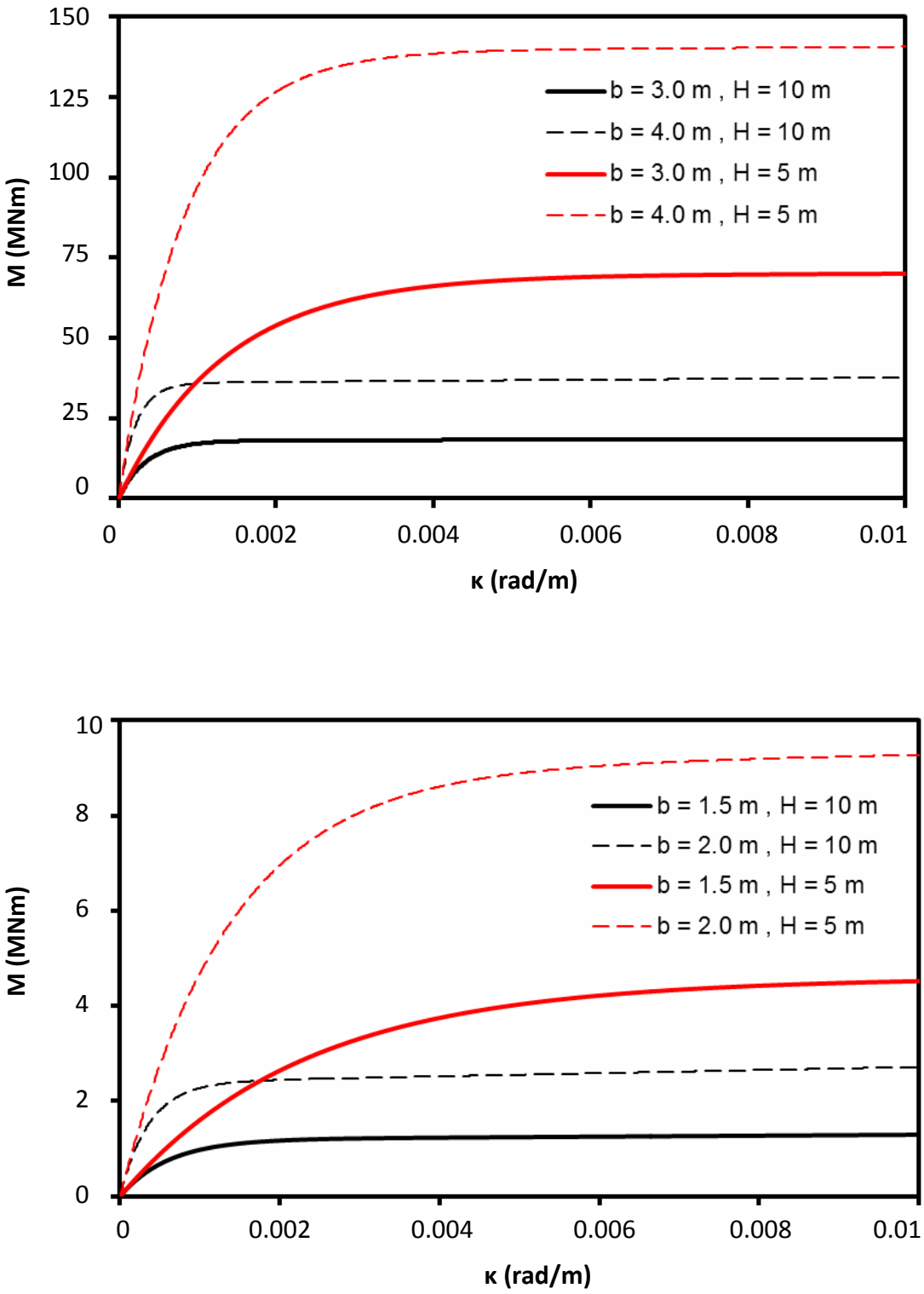

Figure 6.16: Predefined moment-curvature relations used for the analyses

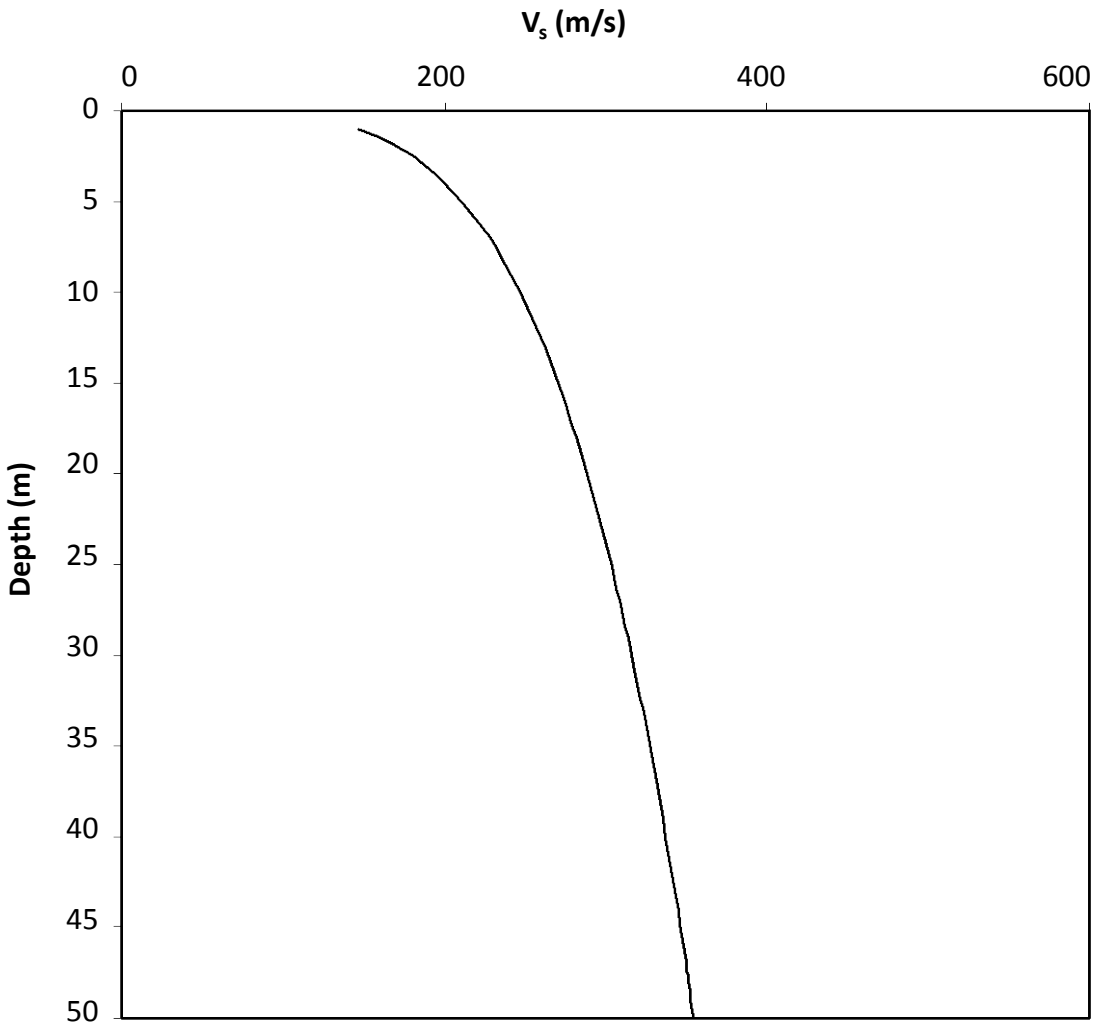

Figure 6.17: Shear wave velocity distribution of the adopted soil deposit used for the wave propagation analyses

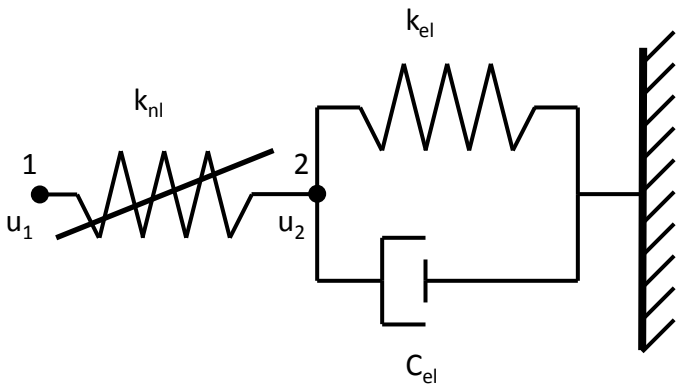

Figure 6.18: The examined configuration of springs and dashpots

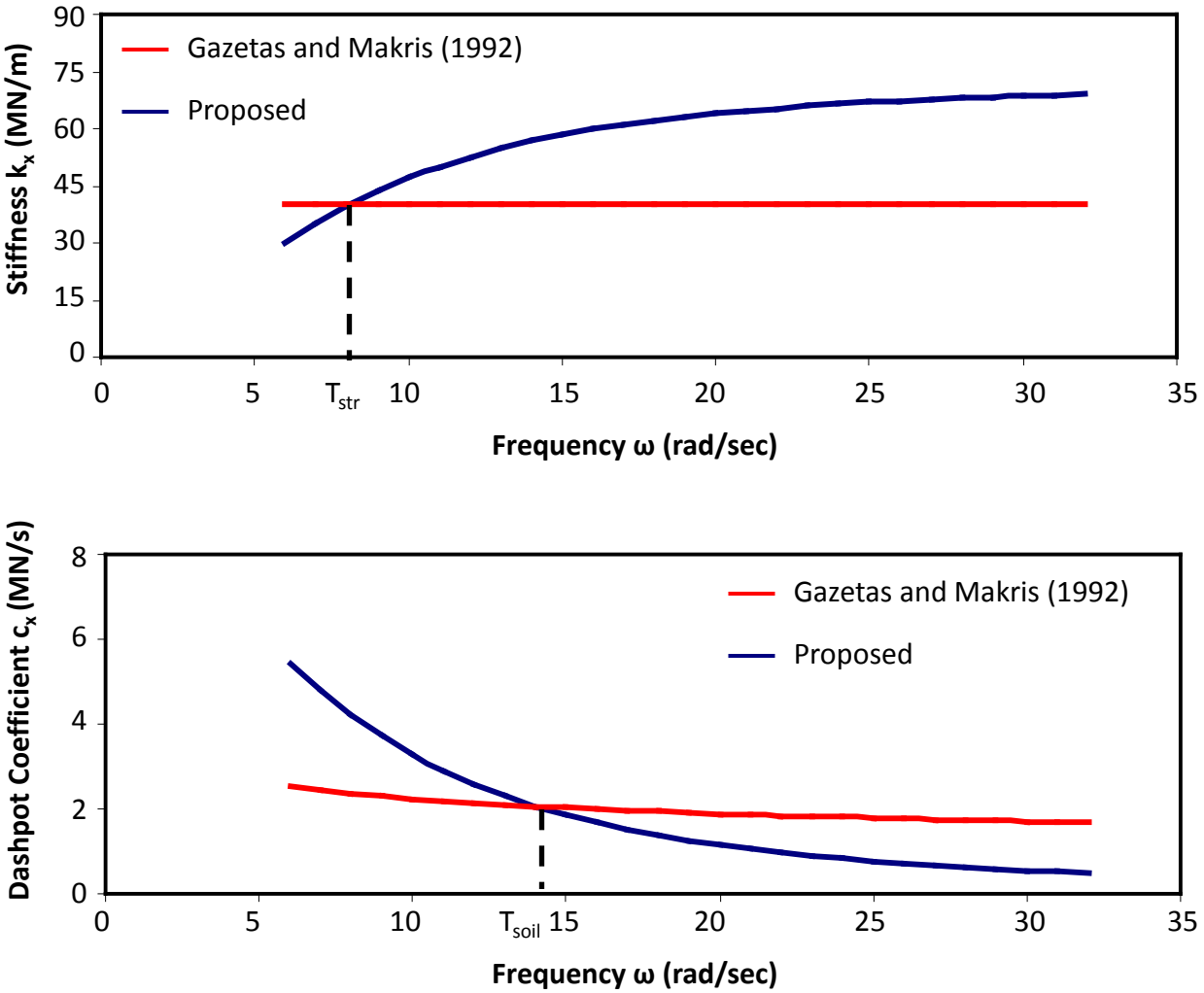

Figure 6.19: Calibration of stiffness k_x and damping coefficient c_x for the examined configuration

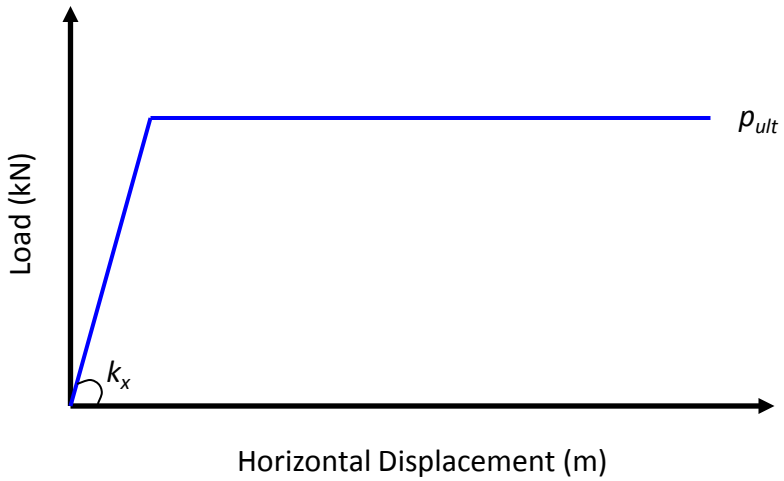

Figure 6.20: Load–displacement curve for the examined configuration

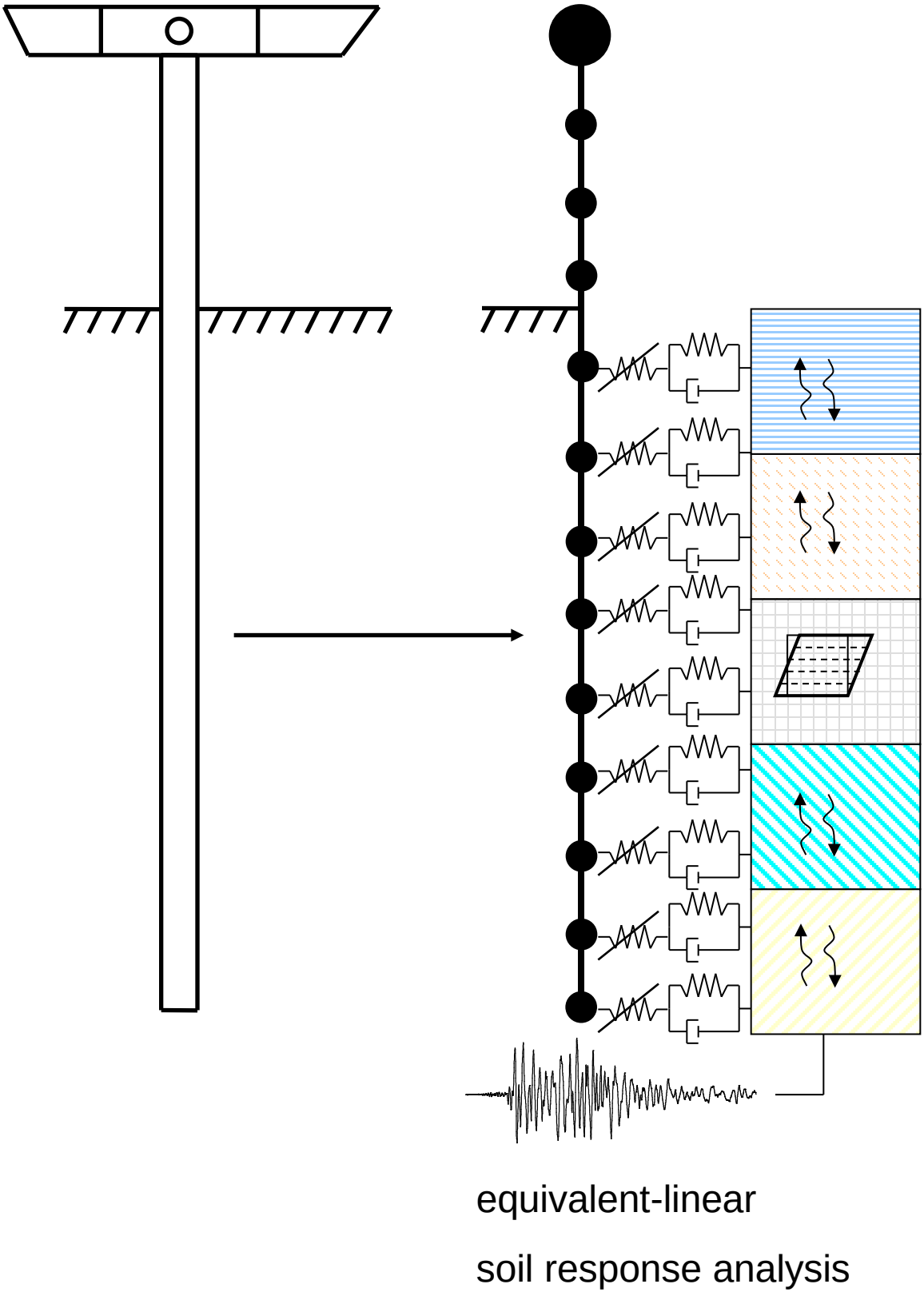

Figure 6.21: Schematic illustration of the Beam-on-nonlinear-Winkler-foundation model used for the inelastic analyses

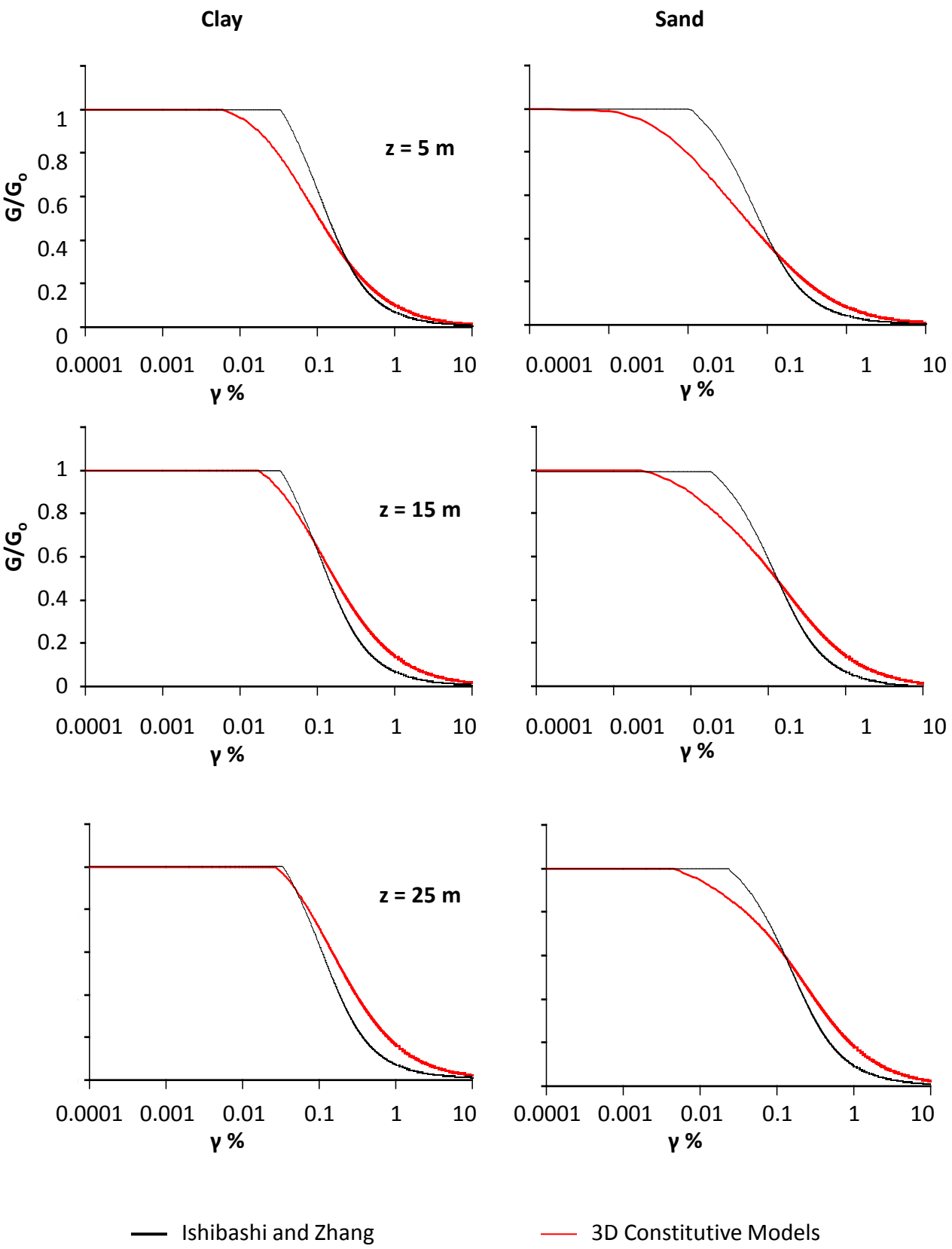

Figure 6.22: Calibration of soil models against published G-γ curves (Ishibashi and Zhang, 1993) for depth: (a) 5 m, (b) 15 m, and (c) 25 m

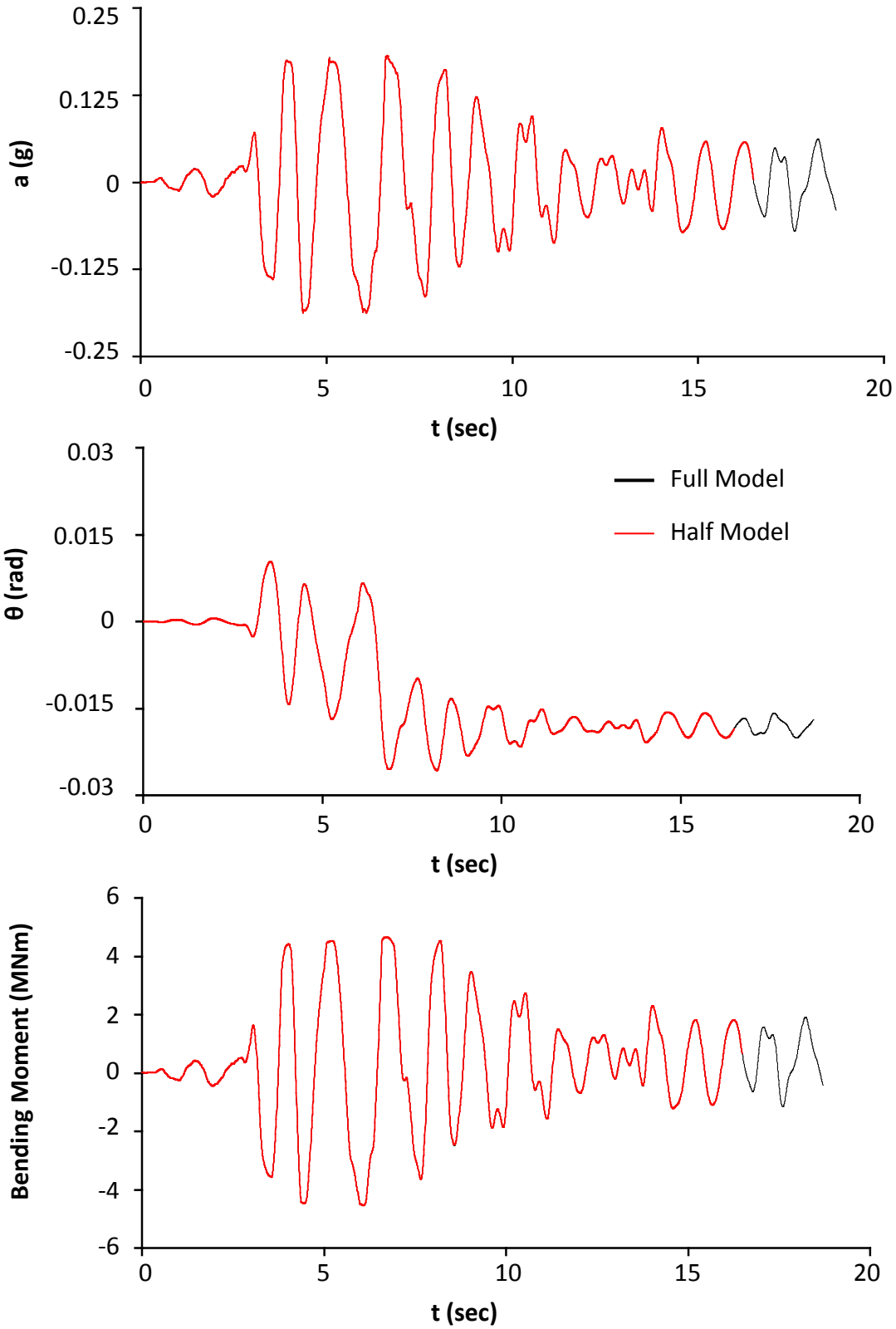

Figure 6.23: Comparison of the (a) acceleration time histories, (b) rotation time histories, and (c) bending moment time histories at the deck calculated with the half and full 3D Finite Element Model for the case of pile-columns with diameter d = 1.5 m, aboveground height H = 5 m founded in clay (excitation at ground surface: Lefkada 2003 scaled at a_g = 0.5 g)

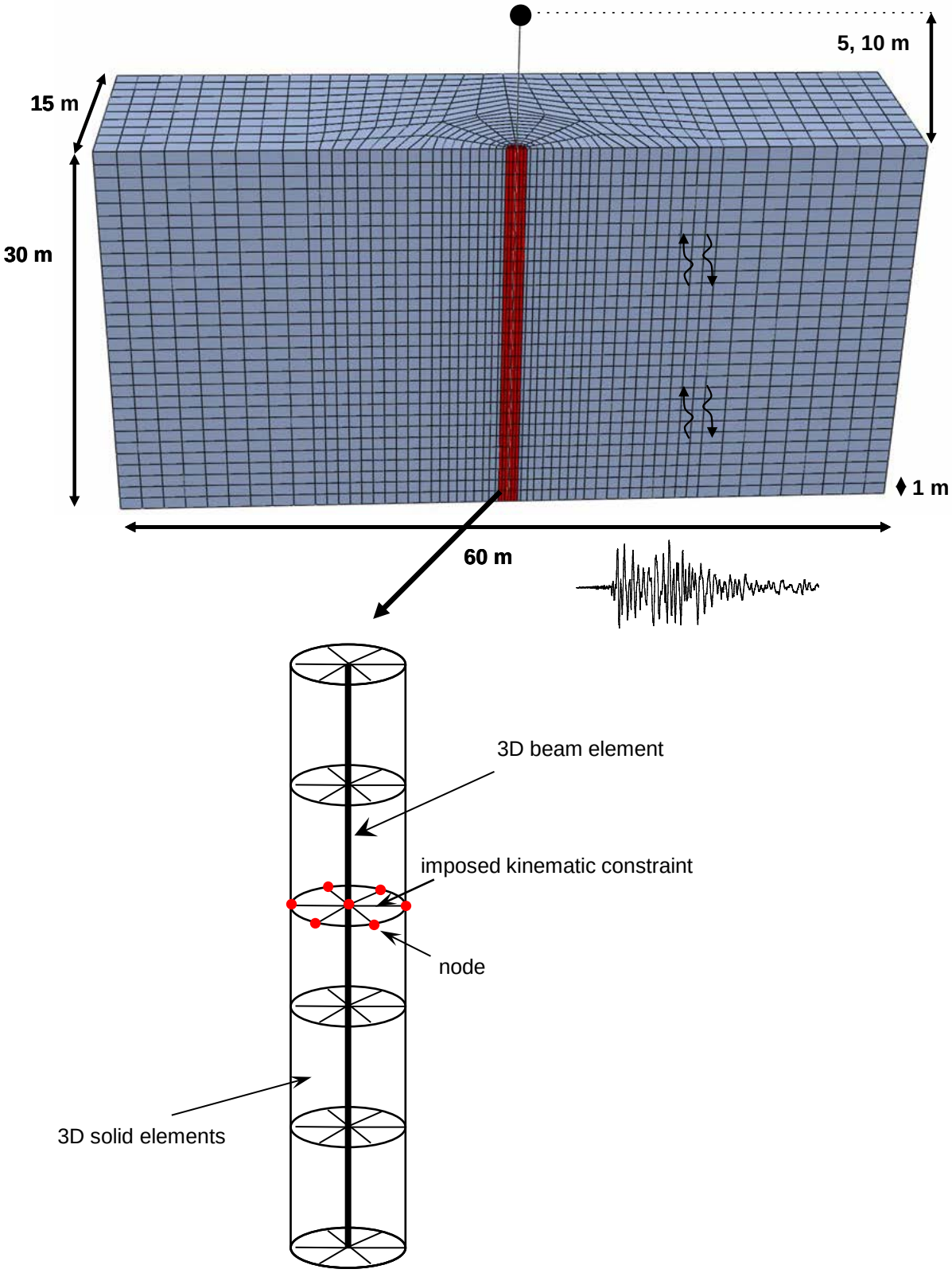

Figure 6.24: Mesh discretization of the 3D Finite Element Model used for the inelastic analyses

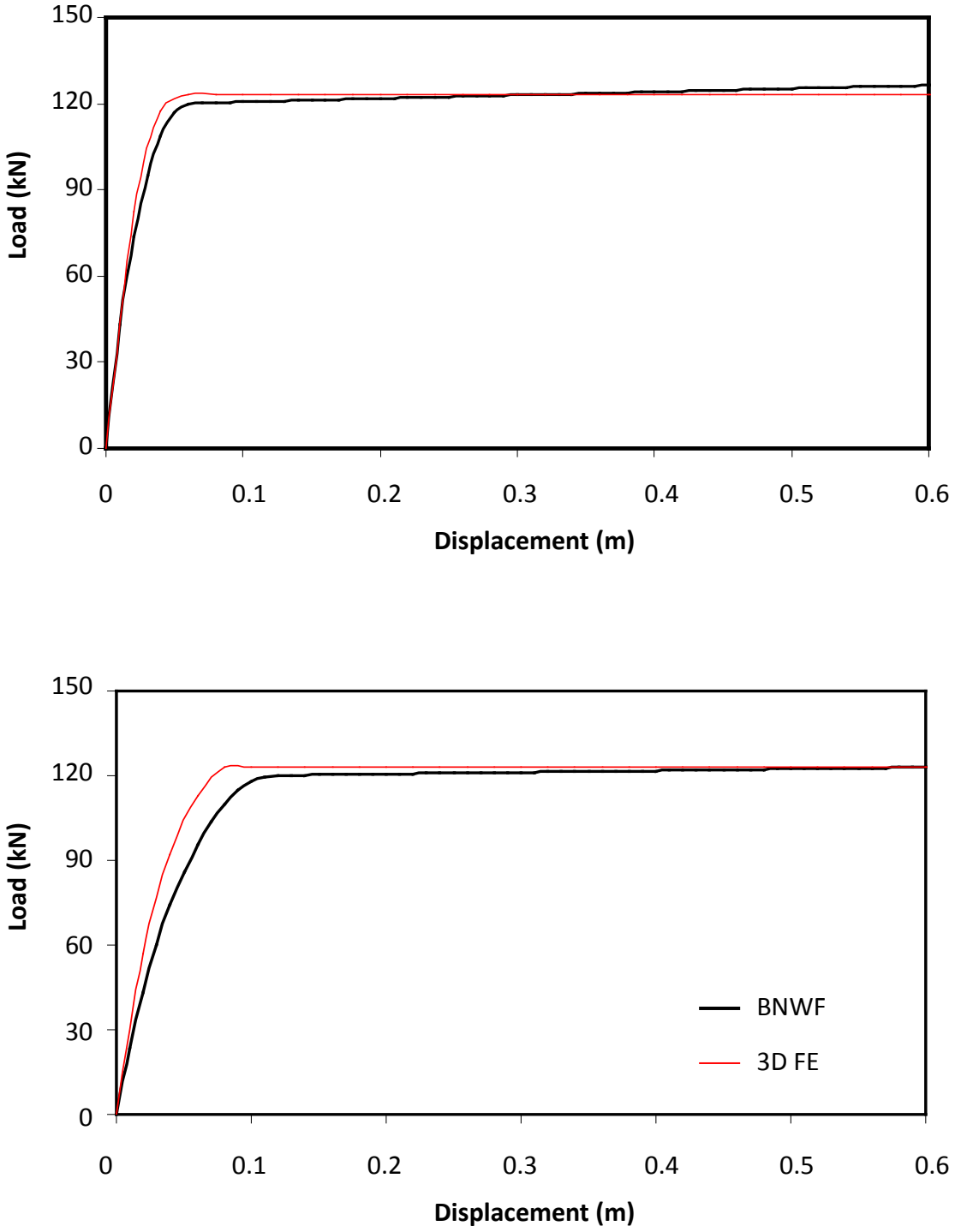

Figure 6.25: Pushover Tests (a) for the case of the fixed pier-bridge system, and (b) for the case of the soil-pile-bridge system

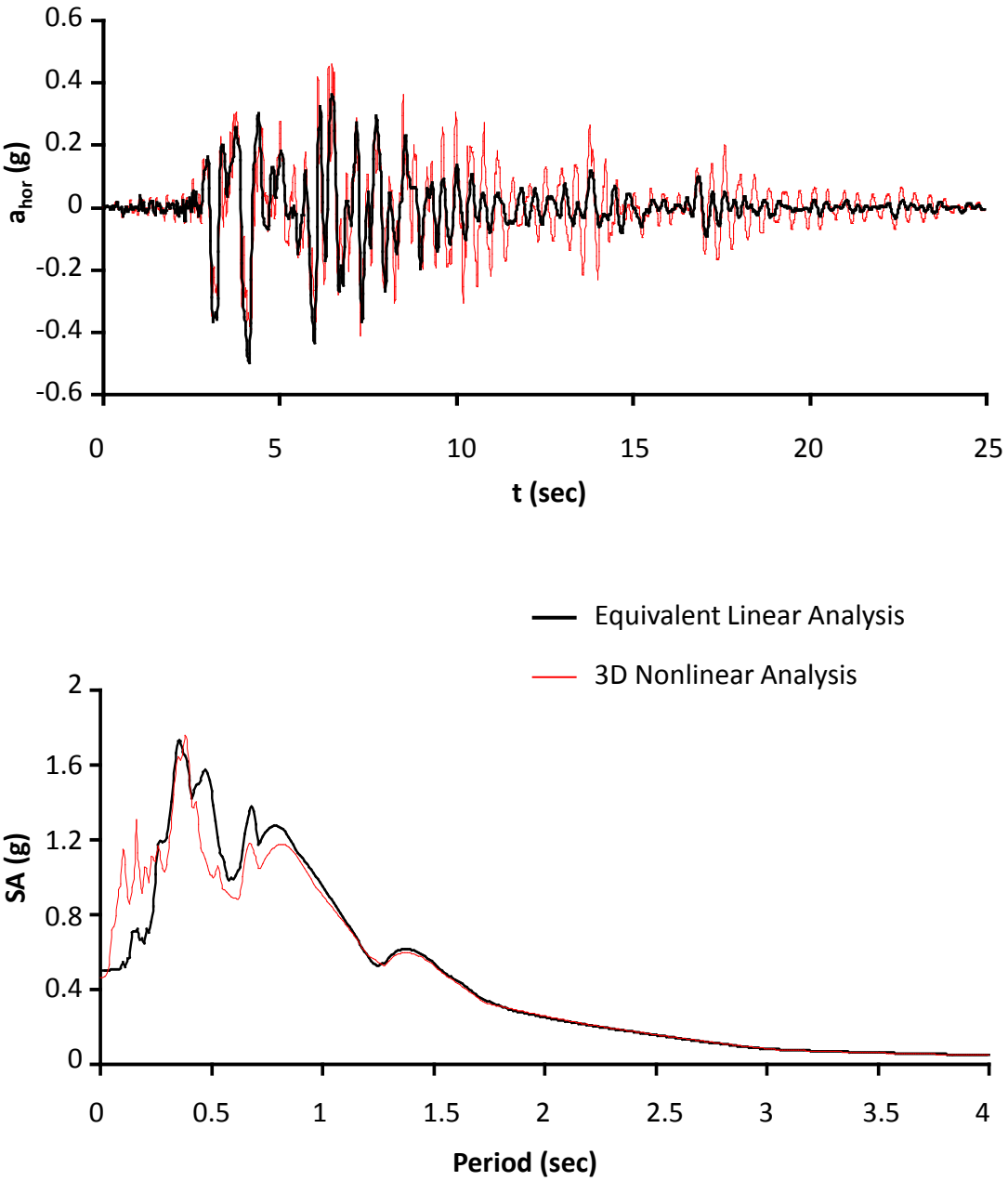

Figure 6.26: (a) Free-field acceleration time histories for the JMA (1995) record scaled at 0.5 g, and (b) corresponding (ξ = 5 %) response spectrum derived from the Equivalent Linear Analysis and the 3D Nonlinear Analysis for clay soil

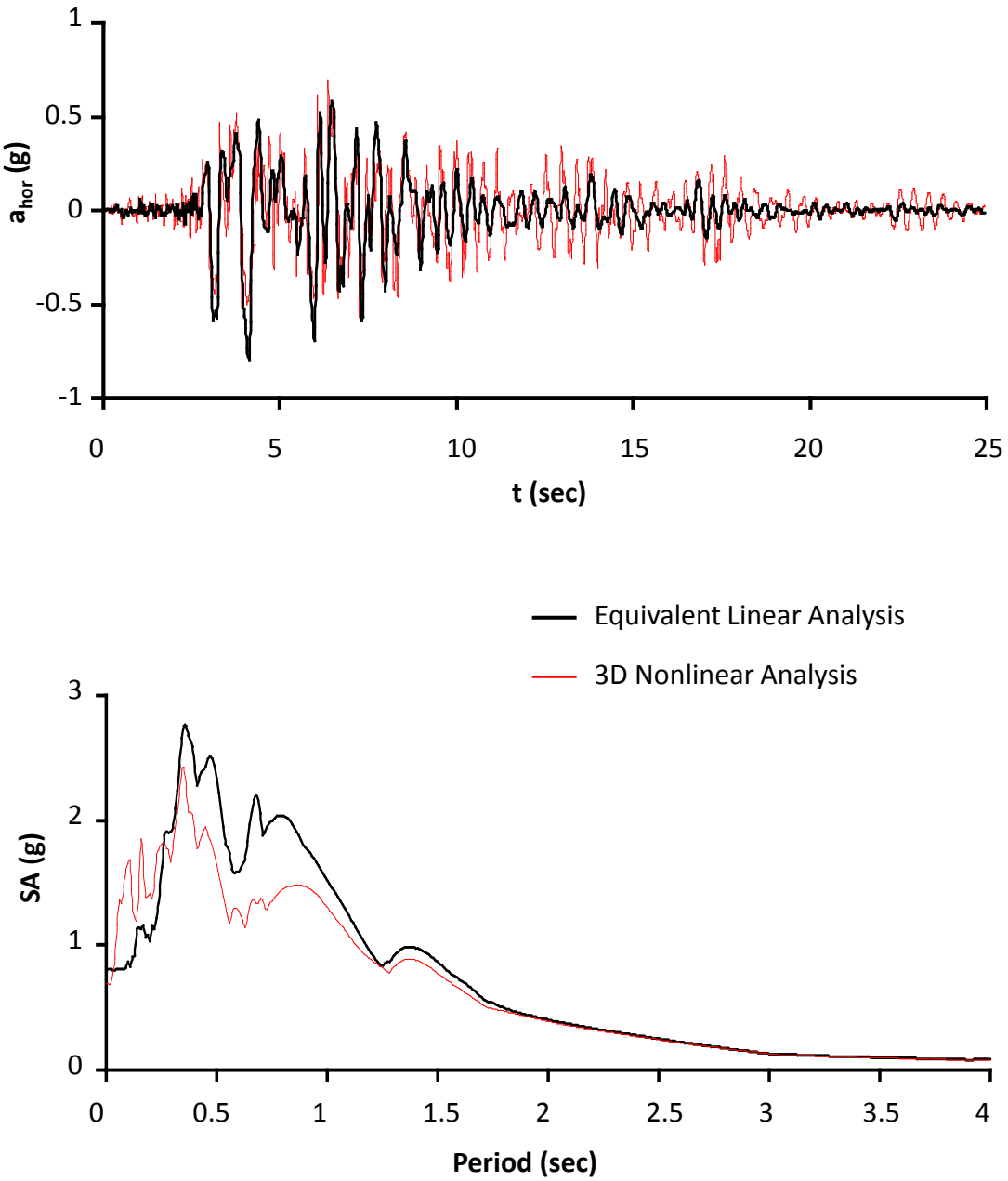

Figure 6.27: (a) Free-field acceleration time histories for the JMA (1995) record scaled at 0.8 g, and (b) corresponding (ξ = 5 %) response spectrum derived from the Equivalent Linear Analysis and the 3D Nonlinear Analysis for clay soil

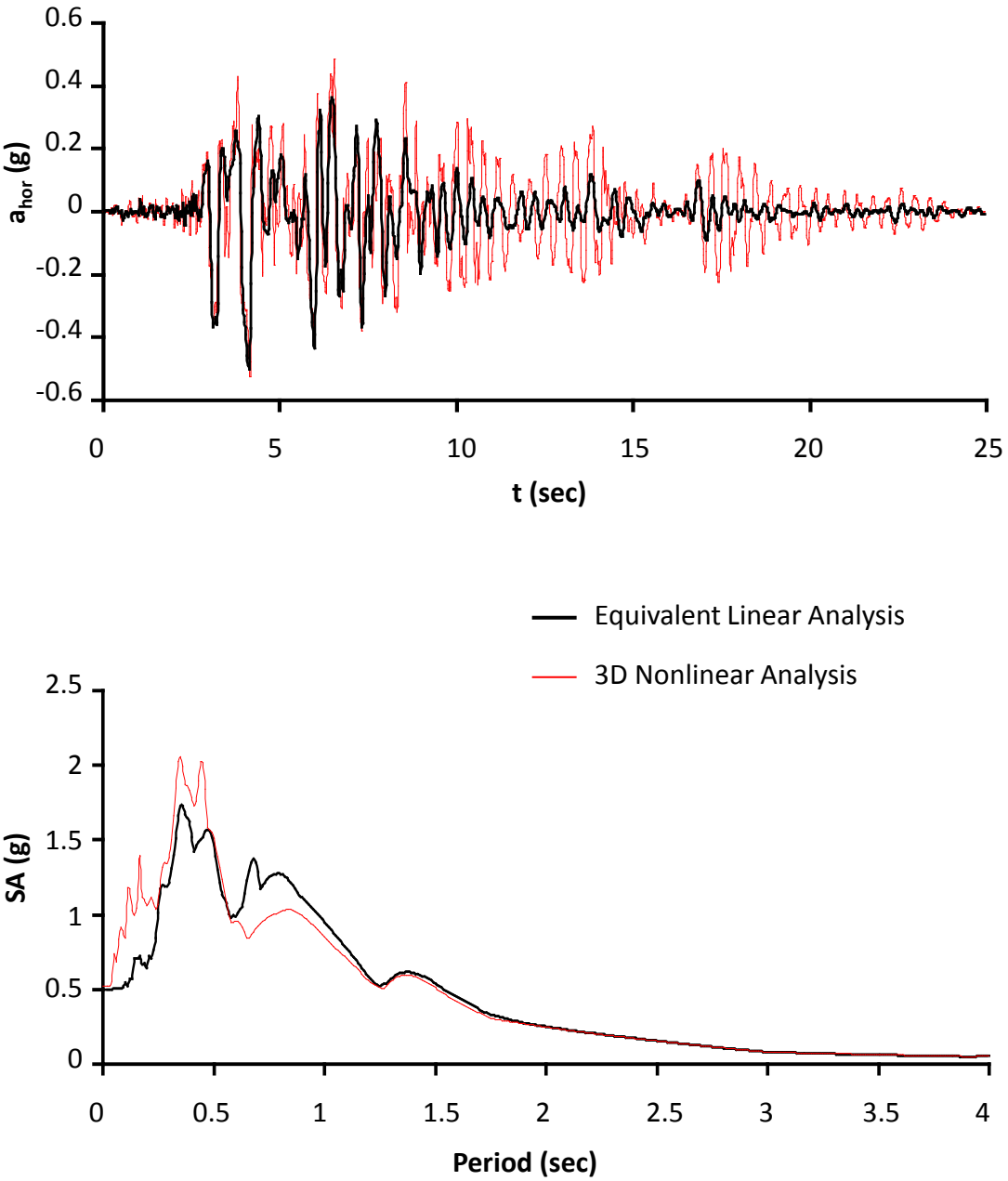

Figure 6.28: (a) Free-field acceleration time histories for the JMA (1995) record scaled at 0.5 g, and (b) corresponding (ξ = 5 %) response spectrum derived from the Equivalent Linear Analysis and the 3D Nonlinear Analysis for sandy soil

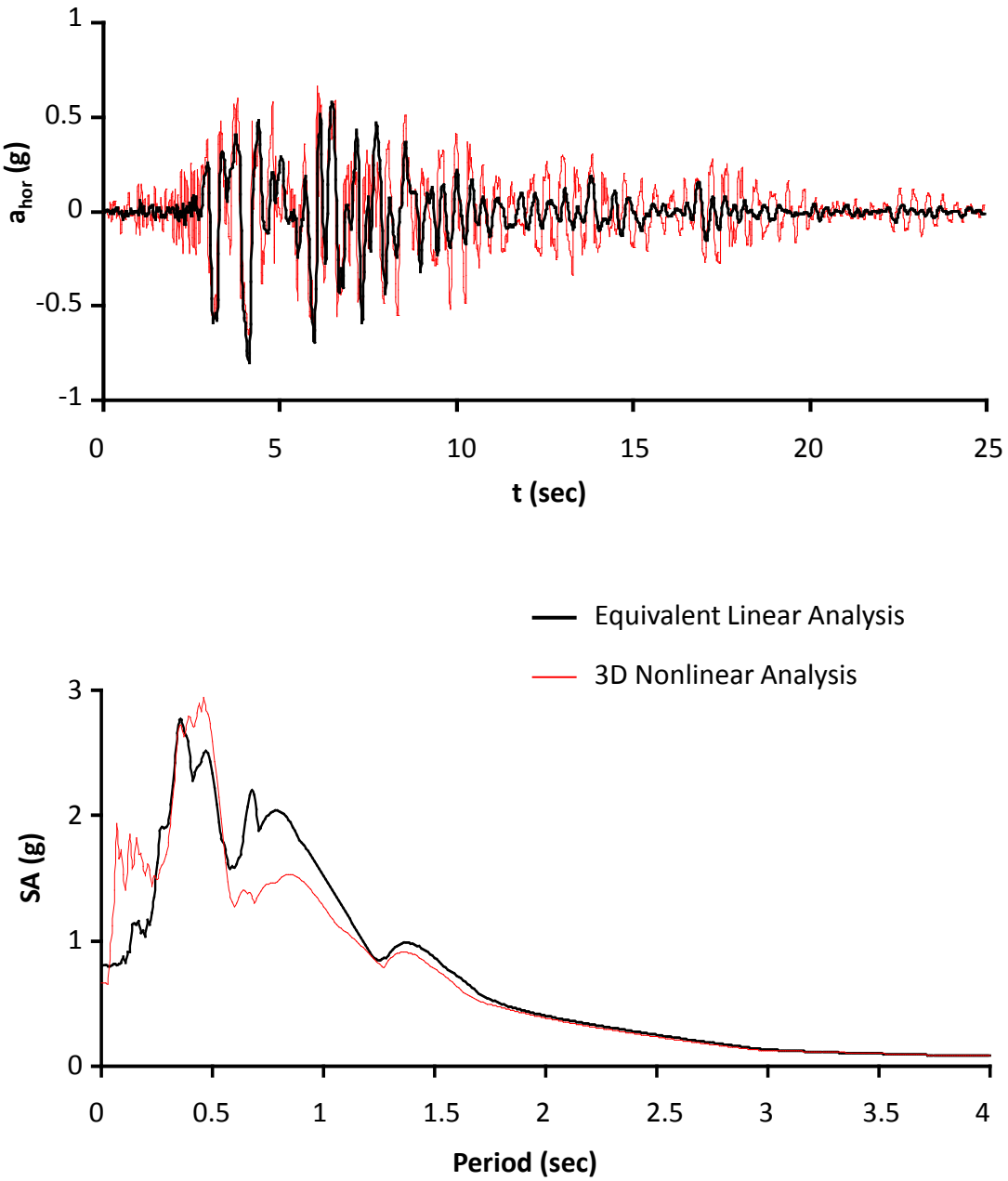

Figure 6.29: (a) Free-field acceleration time histories for the JMA (1995) record scaled at 0.8 g, and (b) corresponding (ξ = 5 %) response spectrum derived from the Equivalent Linear Analysis and the 3D Nonlinear Analysis for sandy soil

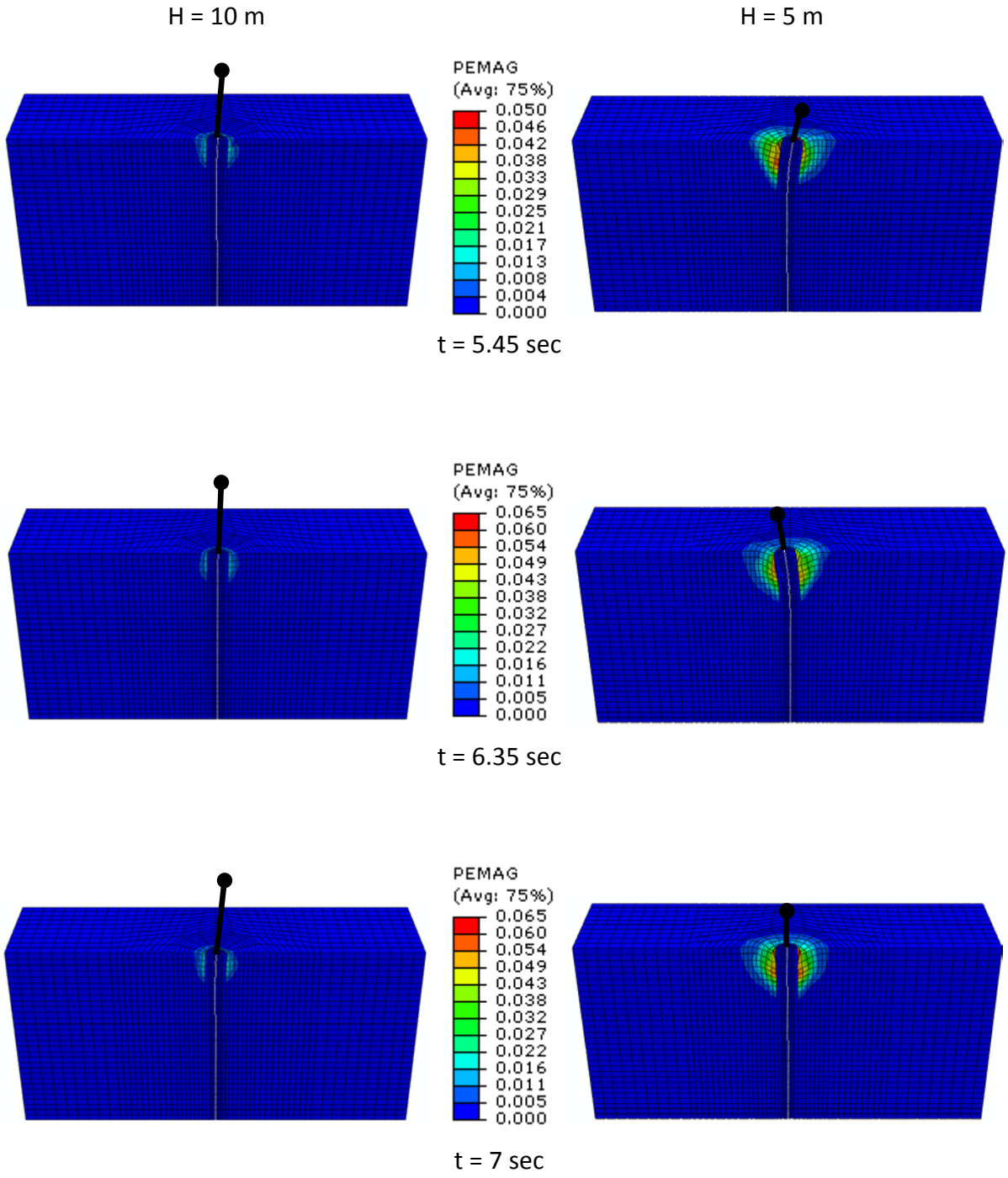

Figure 6.30: Contours of plastic strain magnitude (plotted on the deformed mesh) at different time steps for pile-columns with constant diameter d = 3.0 m founded in sandy soil. The plastic strains of both systems are plotted on the same scale at each time step. (Excitation JMA (1995) motion scaled at a_g = 0.5 g, deformation scale factor = 10)

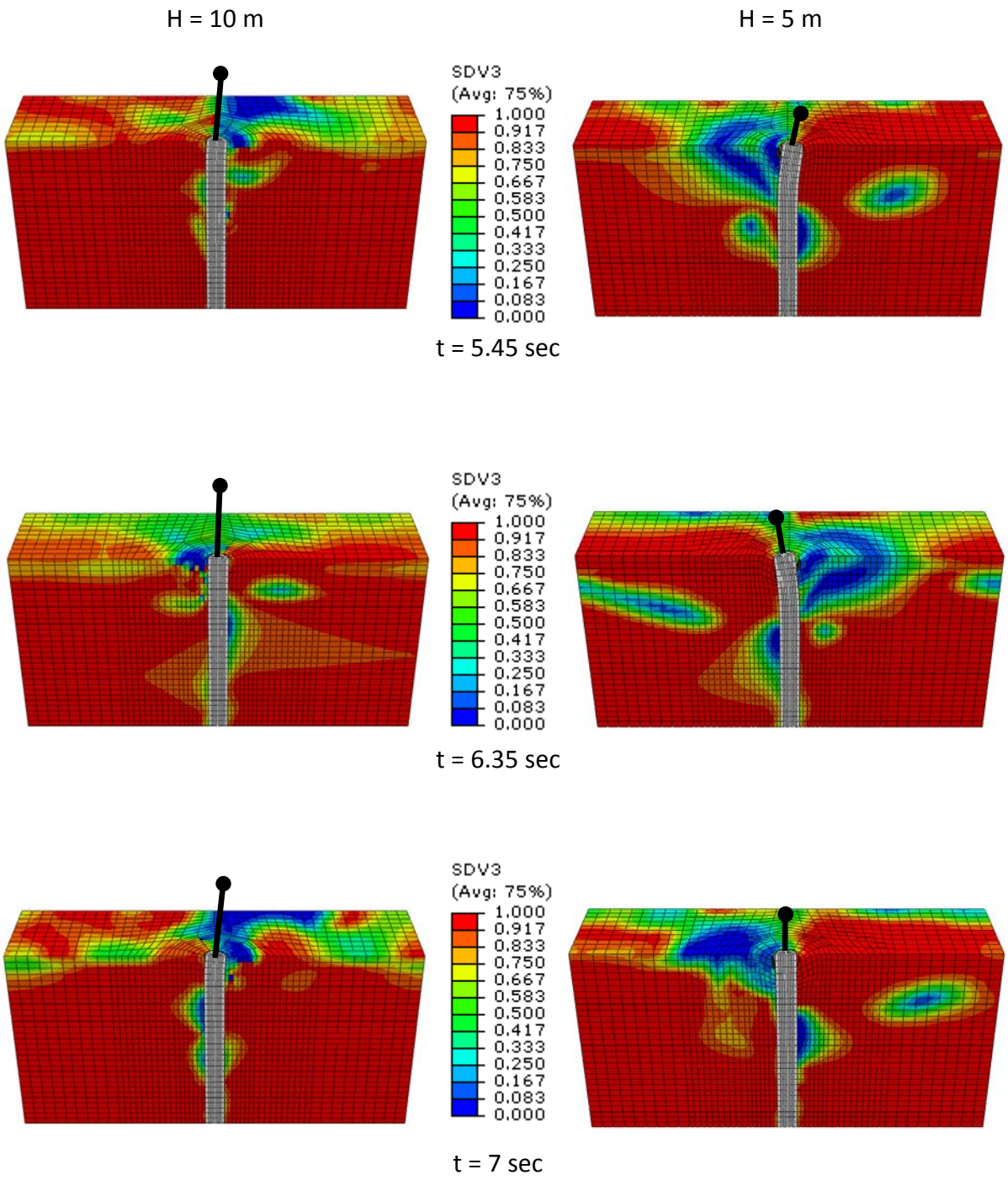

Figure 6.31: Contours of the active and the passive stress states in terms of the state parameter k (plotted on the deformed mesh) at different time steps for pile-columns with constant diameter d = 3.0 m founded in sandy soil. k = 1 corresponds to pure triaxial compression loading condition (passive state), and k = 0 to pure triaxial extension loading condition (active state) while k ≈ 0.5 to simple shear state. (Excitation JMA (1995) motion scaled at a_g = 0.5 g, deformation scale factor = 10)

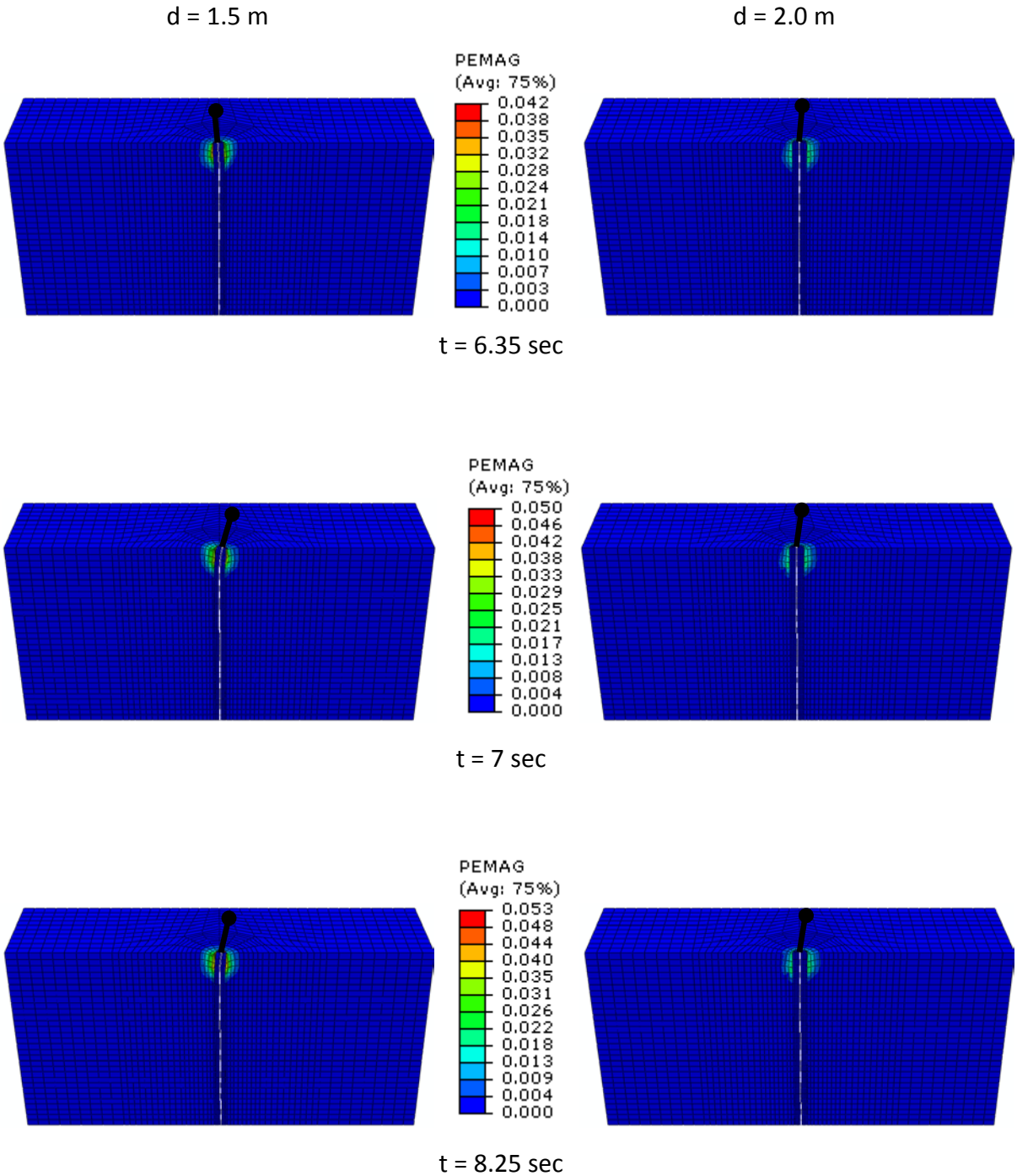

Figure 6.32: Contours of plastic strain magnitude (plotted on the deformed mesh) at different time steps for pile-columns with aboveground height H = 5 m founded in sandy soil. The plastic strains of both systems are plotted on the same scale at each time step. (Excitation JMA (1995) motion scaled at a_g = 0.5 g, deformation scale factor = 10)

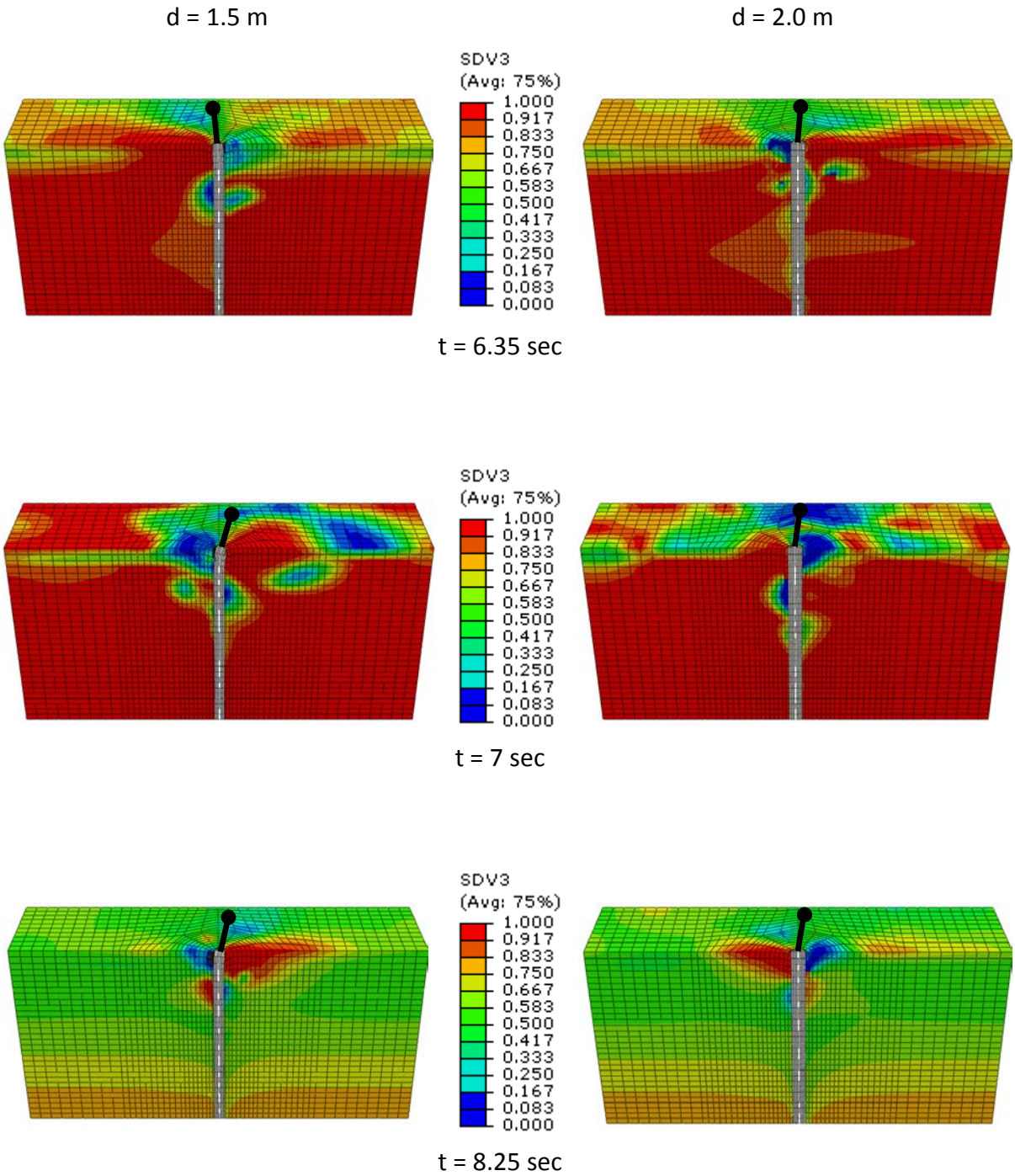

Figure 6.33: Contours of the active and the passive stress states in terms of the state parameter k (plotted on the deformed mesh) at different time steps for pile-columns with aboveground height H = 5 m founded in sandy soil. k = 1 corresponds to pure triaxial compression loading condition (passive state), and k = 0 to pure triaxial extension loading condition (active state) while k ≈ 0.5 to simple shear state. (Excitation JMA (1995) motion scaled at a_g = 0.5 g, deformation scale factor = 10)

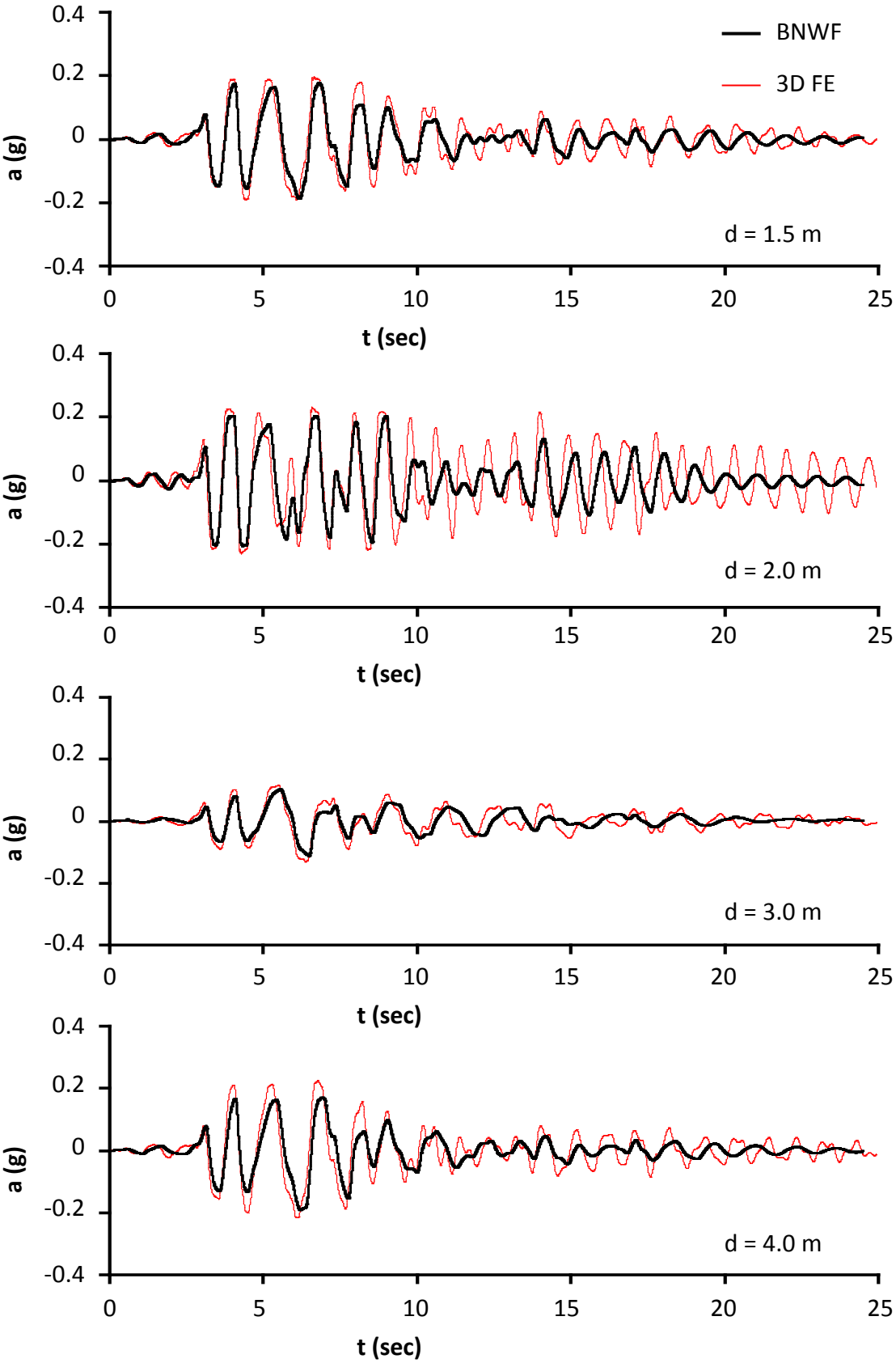

Figure 6.34: Acceleration time histories at the deck for pile-columns with aboveground height H = 5 m founded in cohesive soil (excitation at ground surface: JMA 1995 scaled at a_g = 0.5 g)

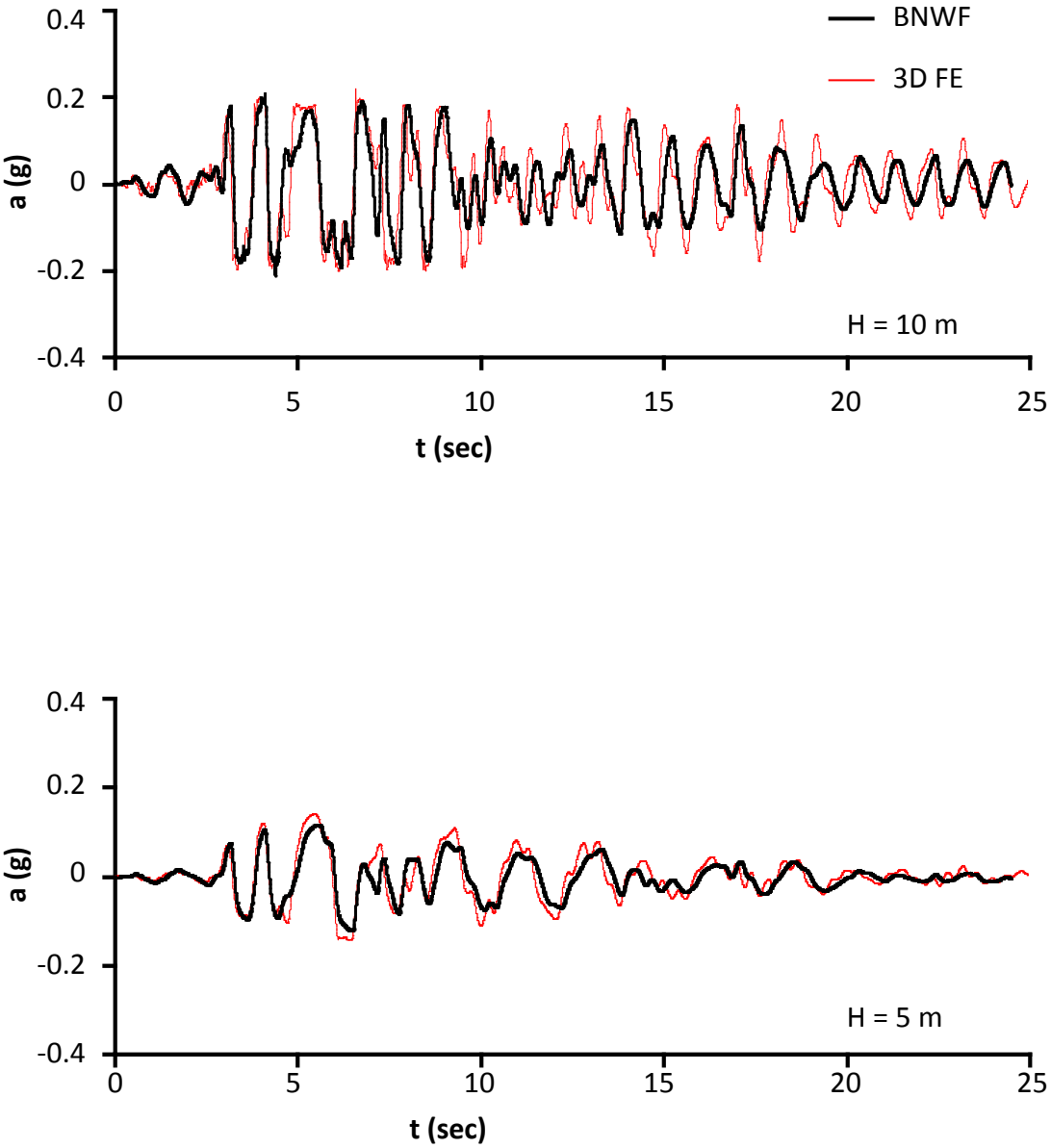

Figure 6.35: Acceleration time histories at the deck for pile-columns with diameter d = 3 m founded in cohesionless soil (excitation at ground surface: JMA 1995 scaled at a_g = 0.8 g)

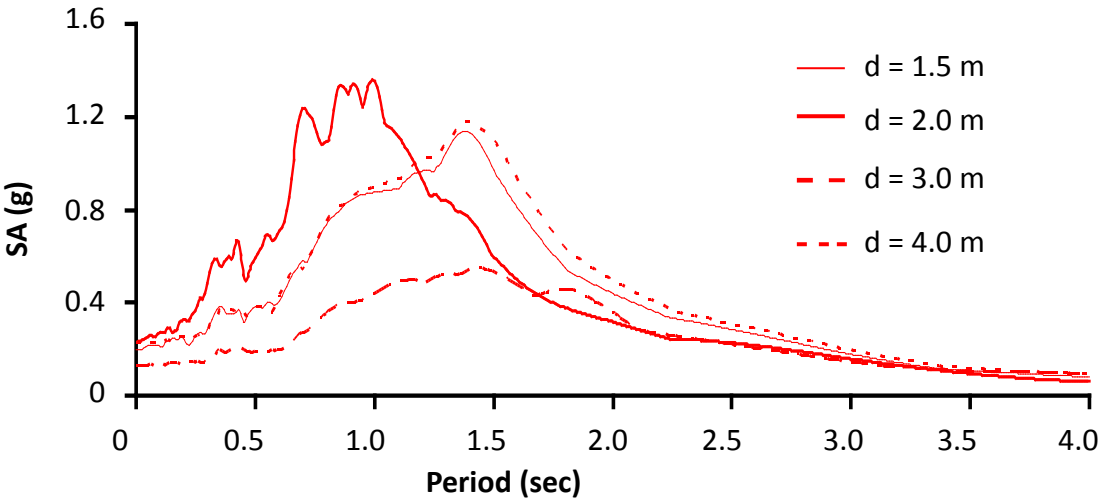

3D Finite Element Model

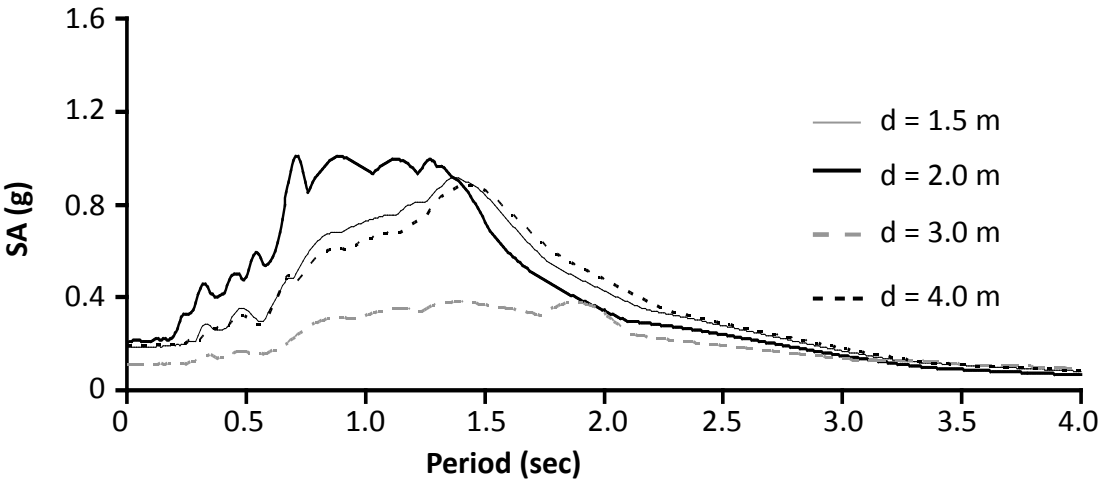

Beam-on-nonlinear-Winkler-foundation Model

Figure 6.36: Response spectra at the deck (ξ = 5%) for pile-columns with aboveground height H = 5 m founded in cohesive soil (excitation at ground surface: JMA 1995 scaled at a_g = 0.5 g) calculated with (a) the 3D Finite Element model, and (b) the Beam-on-nonlinear-Winkler-foundation model

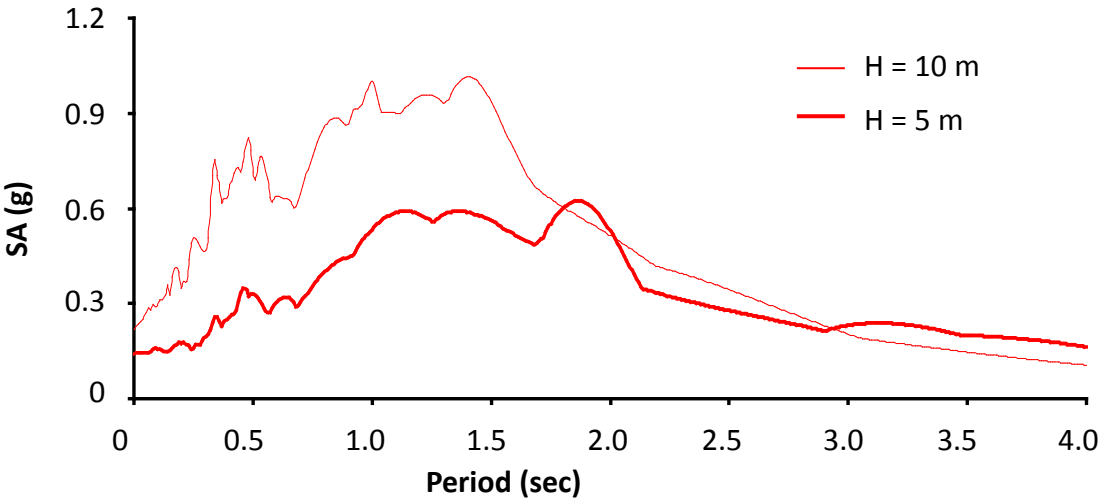

3D Finite Element Model

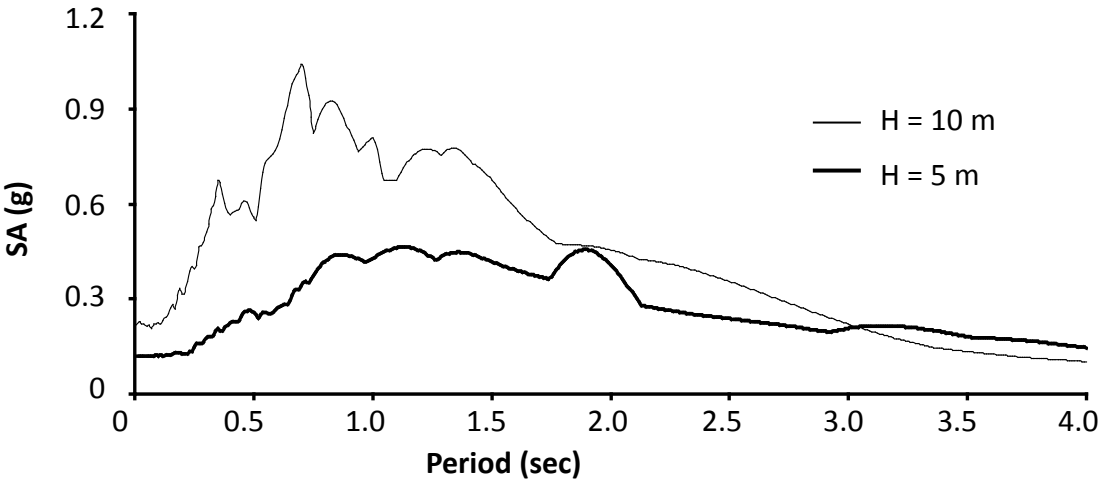

Beam-on-nonlinear-Winkler-foundation Model

Figure 6.37: Response spectra at the deck (ξ = 5%) at the deck for pile-columns with diameter d = 3 m founded in cohesionless soil (excitation at ground surface: JMA 1995 scaled at a_g = 0.8 g) calculated with (a) the 3D Finite Element Model, and (b) the Beam-on-nonlinear-Winkler-foundation Model

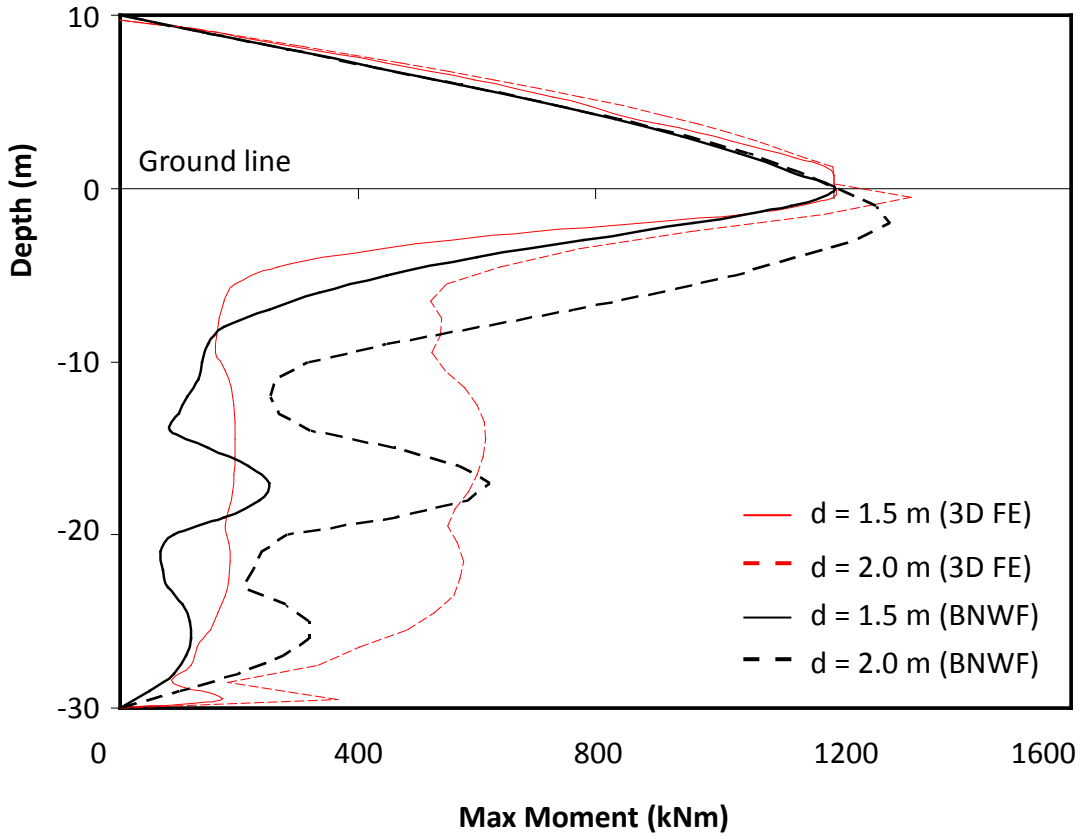

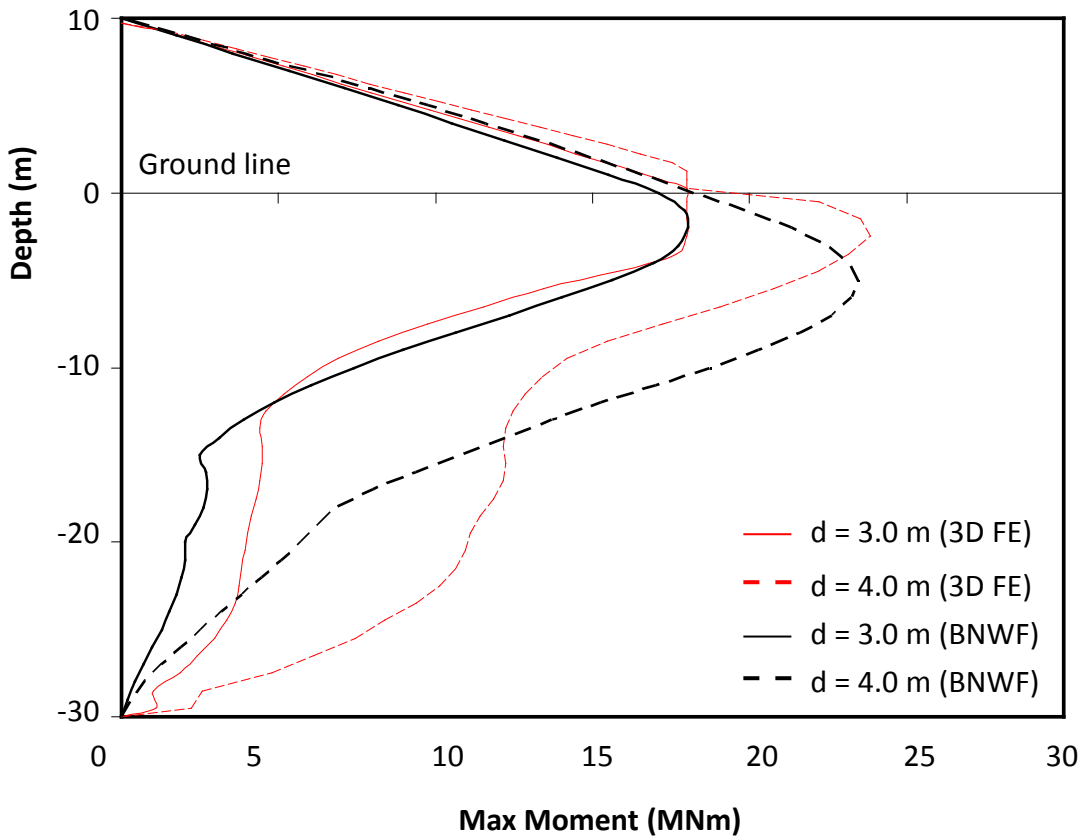

Figure 6.38: Maximum bending moment distributions for pile-columns with aboveground height H = 10 m embedded in cohesive soil (excitation at ground surface: JMA 1995 scaled at a_g = 0.5 g)

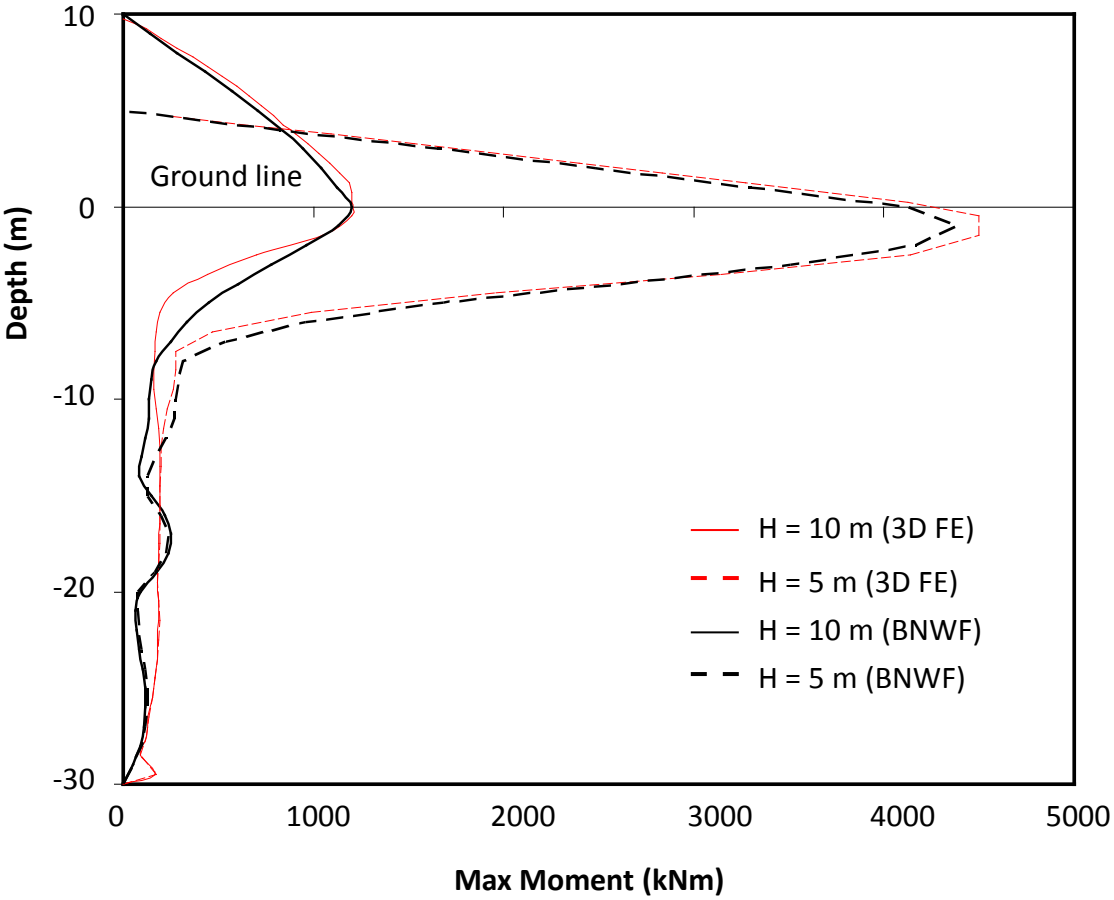

Figure 6.39: Maximum bending moment distributions for pile-columns with diameter d = 3 m embedded in cohesive soil (excitation at ground surface: JMA 1995 scaled at a_g = 0.5 g)

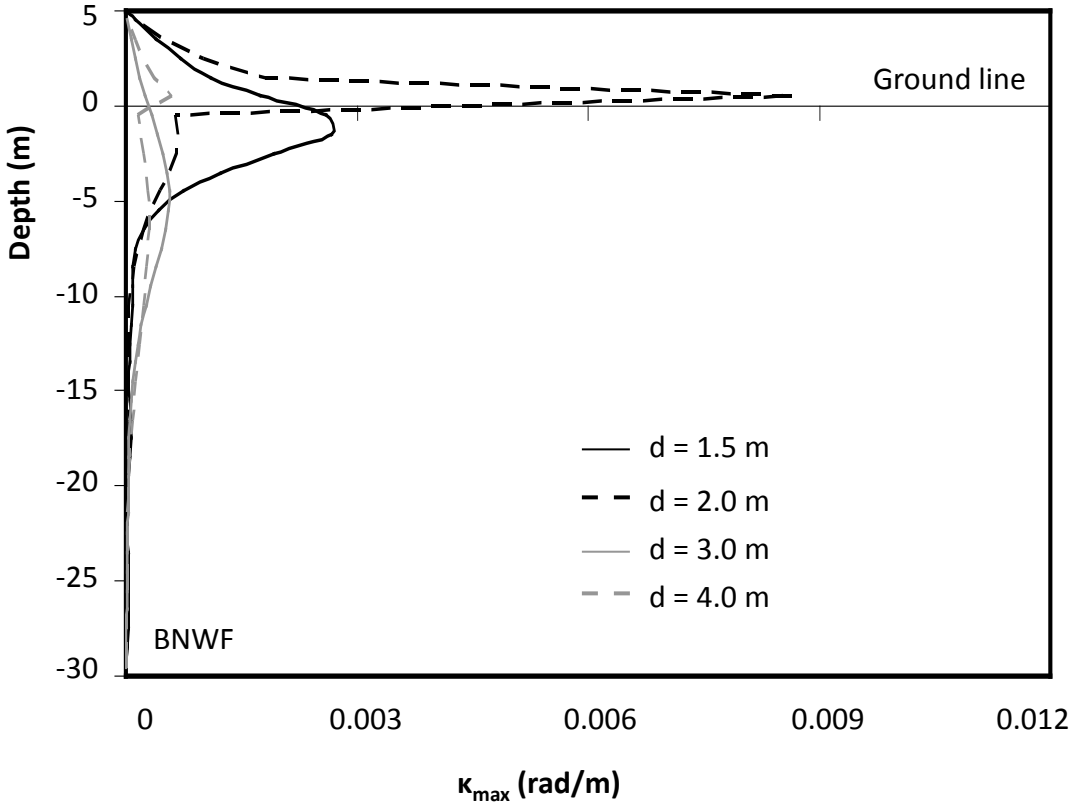

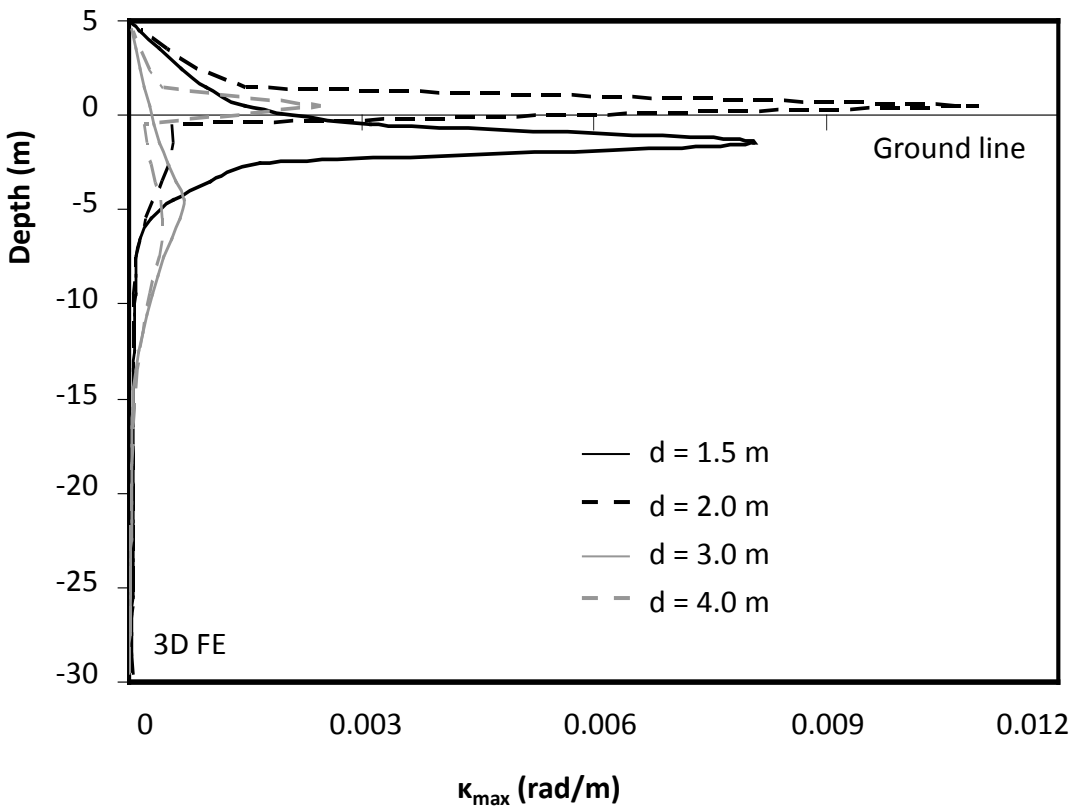

Figure 6.40: Maximum curvature distributions for pile-columns with aboveground height H = 5 m embedded in cohesive soil (excitation at ground surface: JMA 1995 scaled at a_g = 0.5 g)

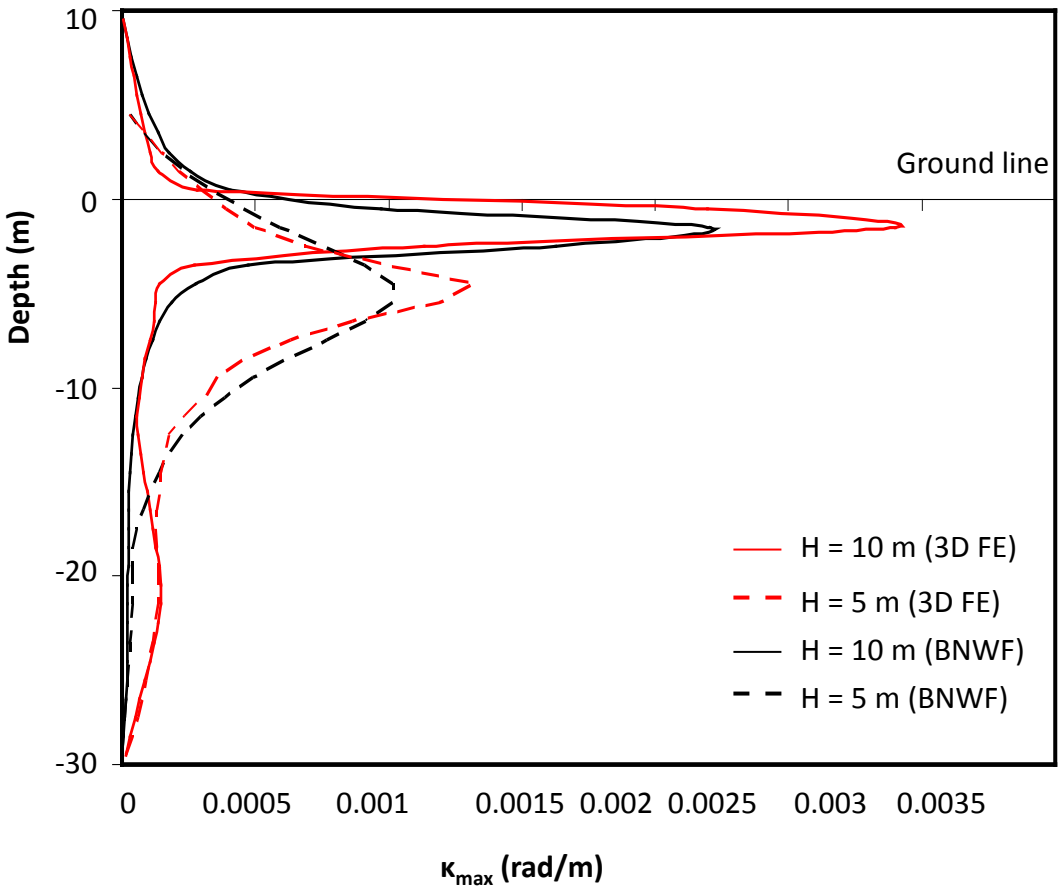

Figure 6.41: Maximum curvature distributions for pile-columns with diameter d = 3 m embedded in cohesive soil (excitation at ground surface: JMA 1995 scaled at a_g = 0.8 g)

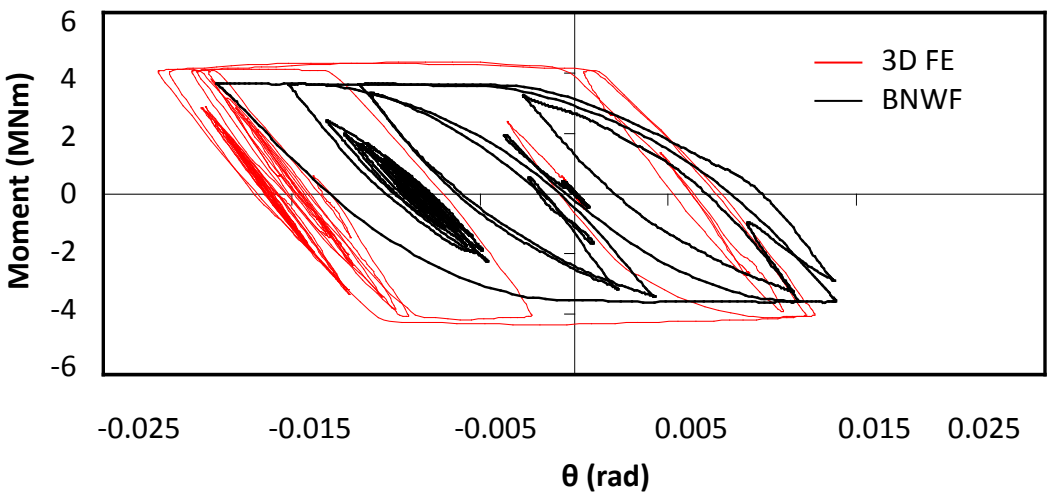

Figure 6.42: Moment – rotation loops for pile-columns with diameter d = 2 m and aboveground height H = 5 m embedded in cohesive soil (excitation at ground surface: JMA 1995 scaled at a_g = 0.5 g) calculated with the 3D Finite Element Model, and the Beam-on-nonlinear-Winkler-foundation Model

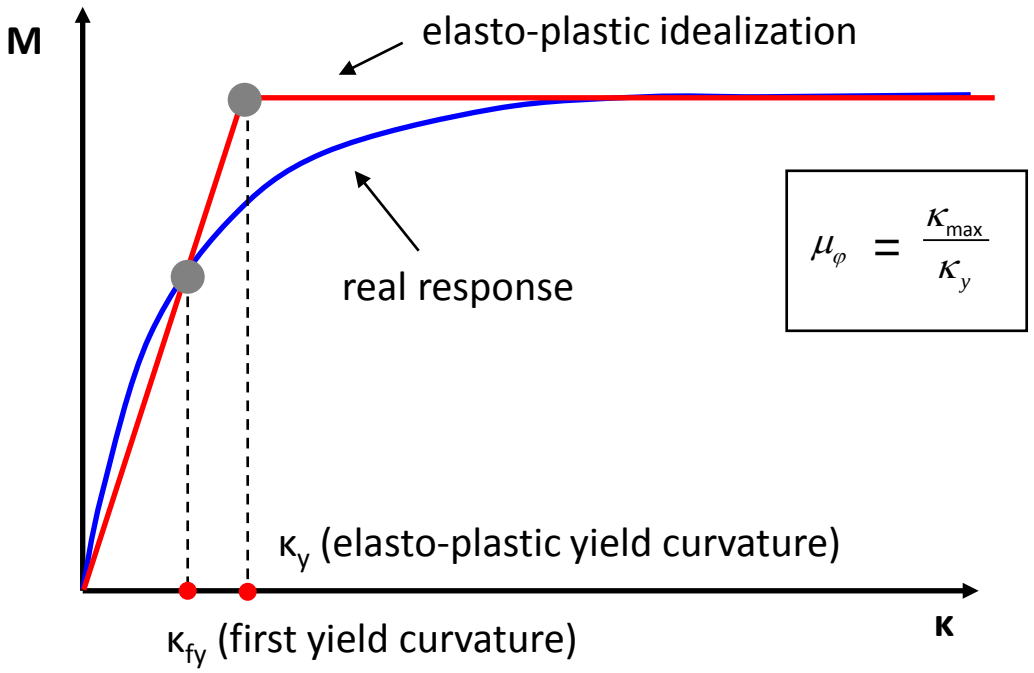

Figure 6.43: Definition of the yield curvature of the soil-pile-structure system

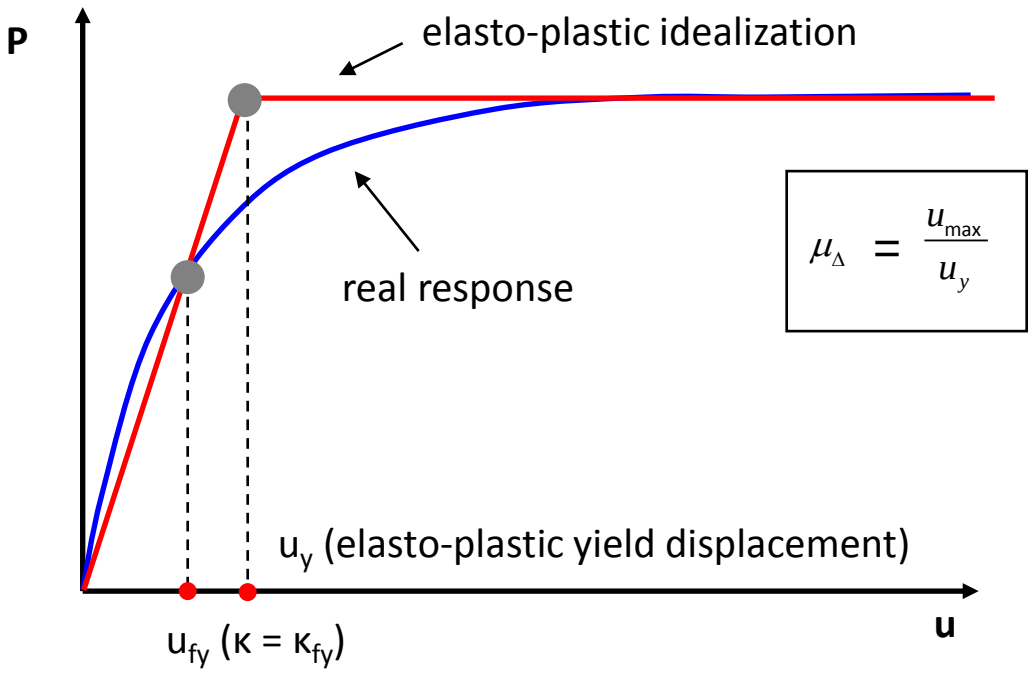

Figure 6.44: Definition of the yield displacement of the soil-pile-structure system

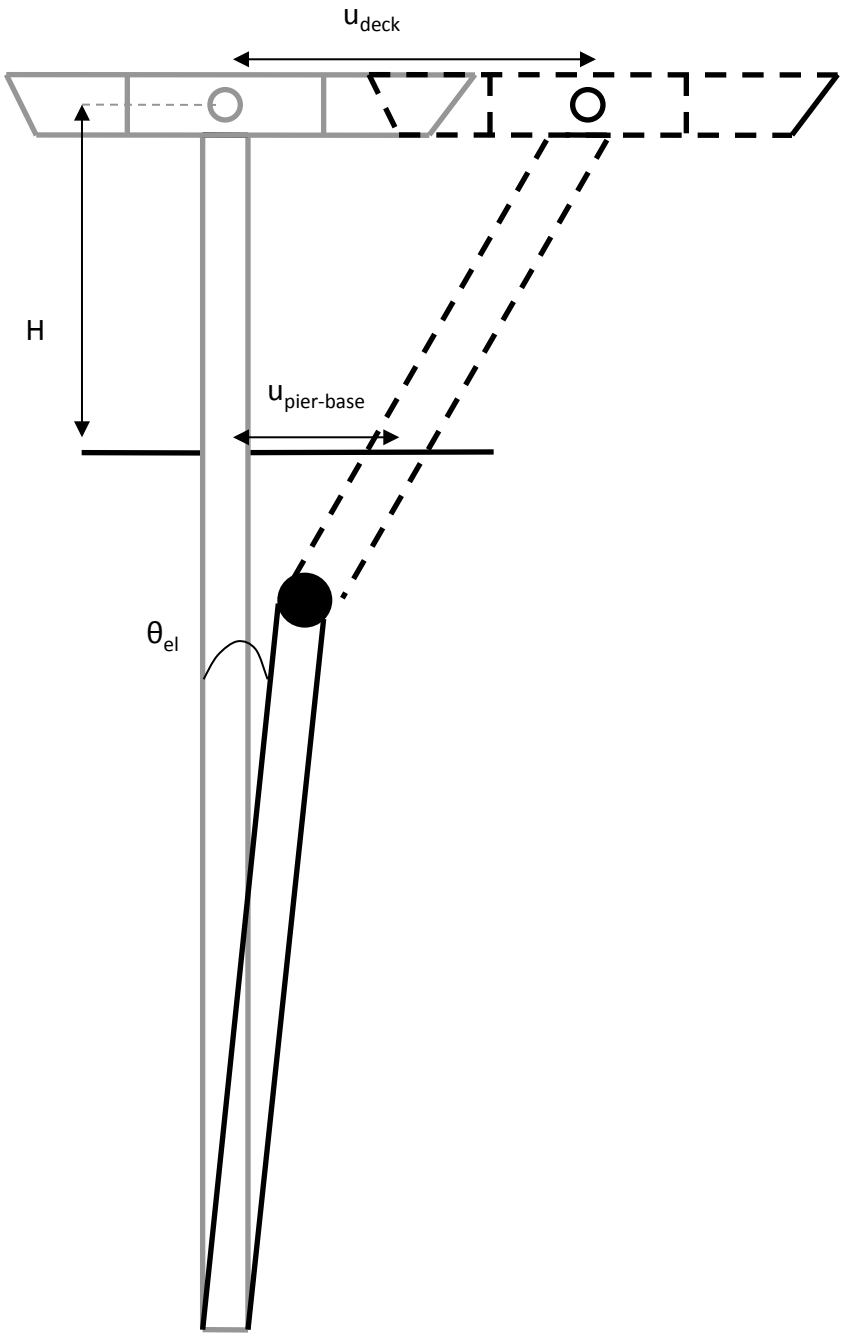

Figure 6.45: Definition of the maximum displacement of the soil-pile-structure system

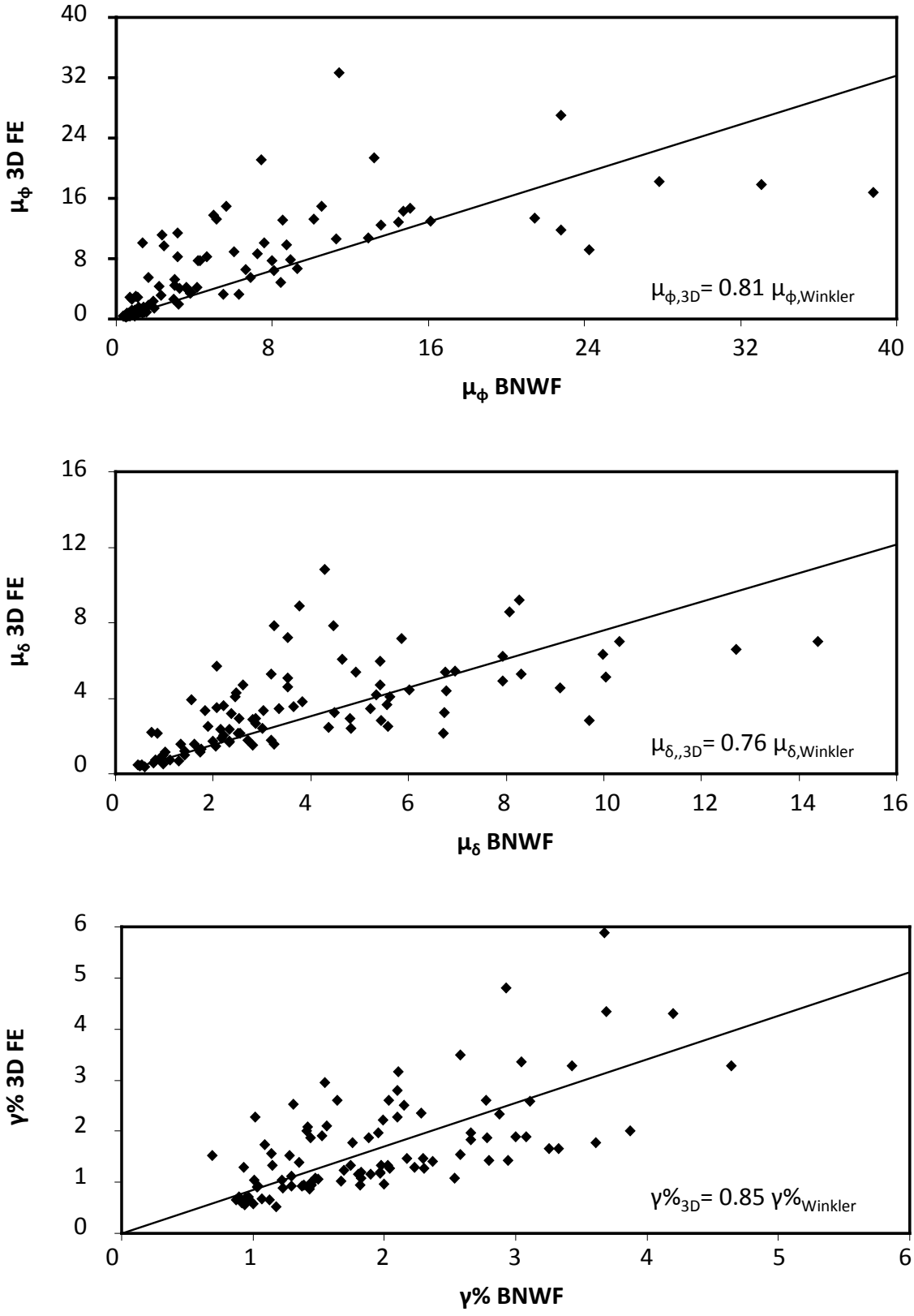

Figure 6.46: Correlation of the (a) local curvature ductility μ_ϕ, (b) global curvature ductility μ_δ, and (c) drift ratio γ% calculated with the 3D Finite Element Model and the Beam-on-nonlinear-Winkler-foundation Model

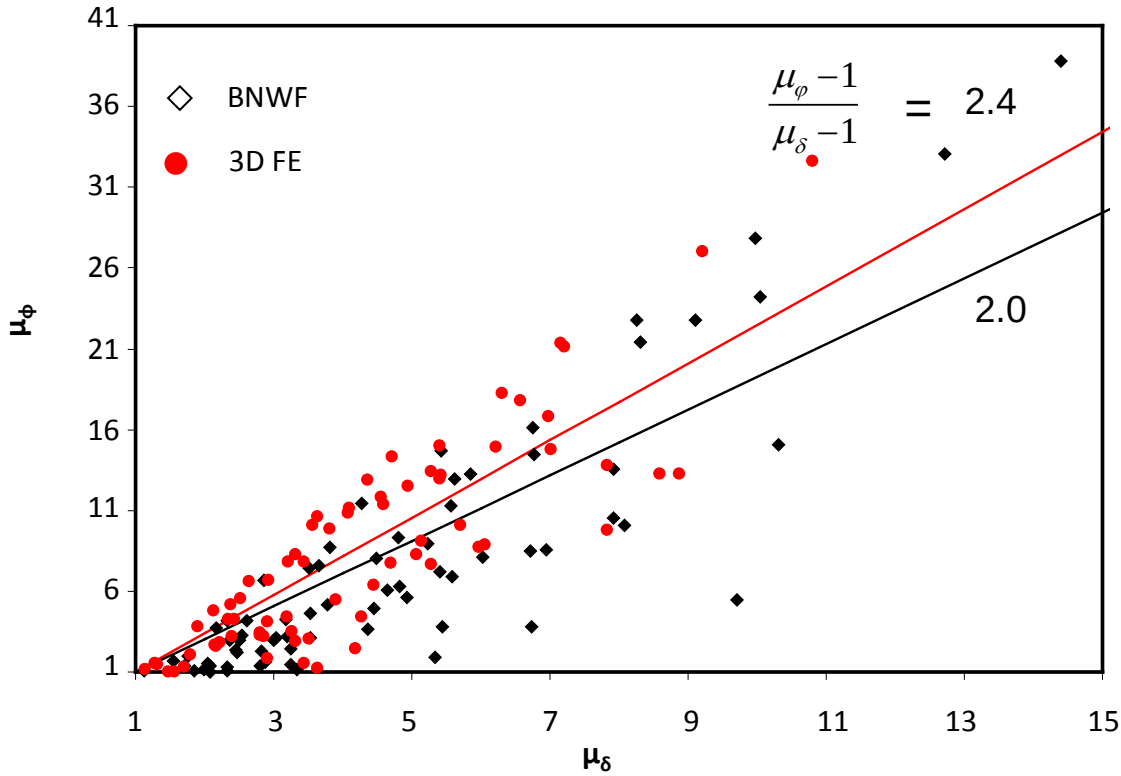

Figure 6.47: Correlation of local and global ductility demands calculated with the 3D Finite Element Model and the Beam-on-nonlinear-Winkler-foundation Model

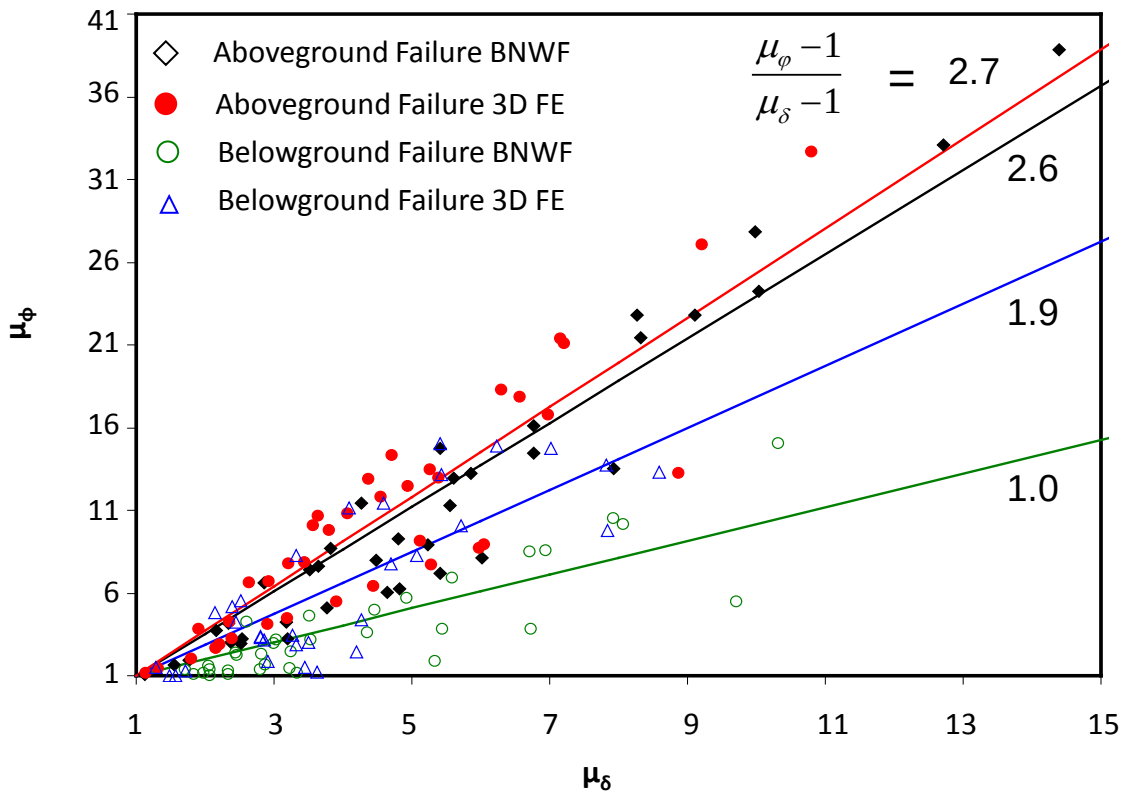

Figure 6.48: Correlation of local and global ductility demands for different plastic hinge locations

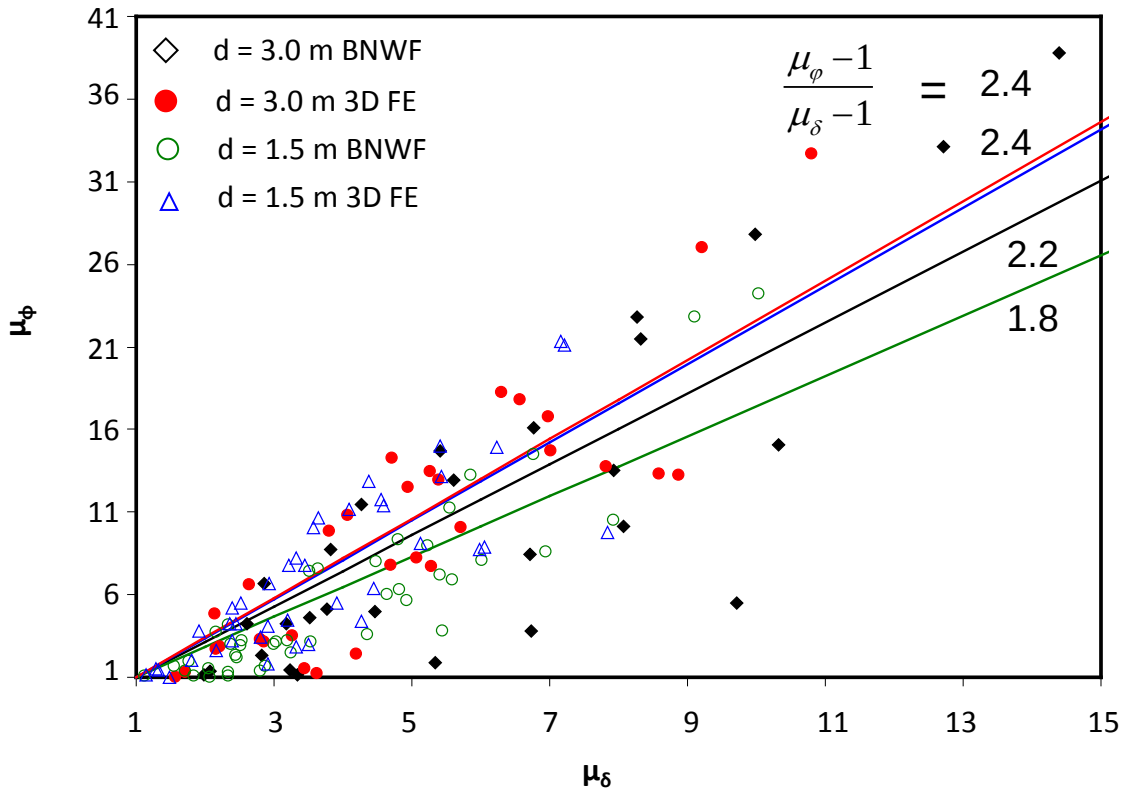

Figure 6.49: Correlation of local and global ductility demands for different pier diameters

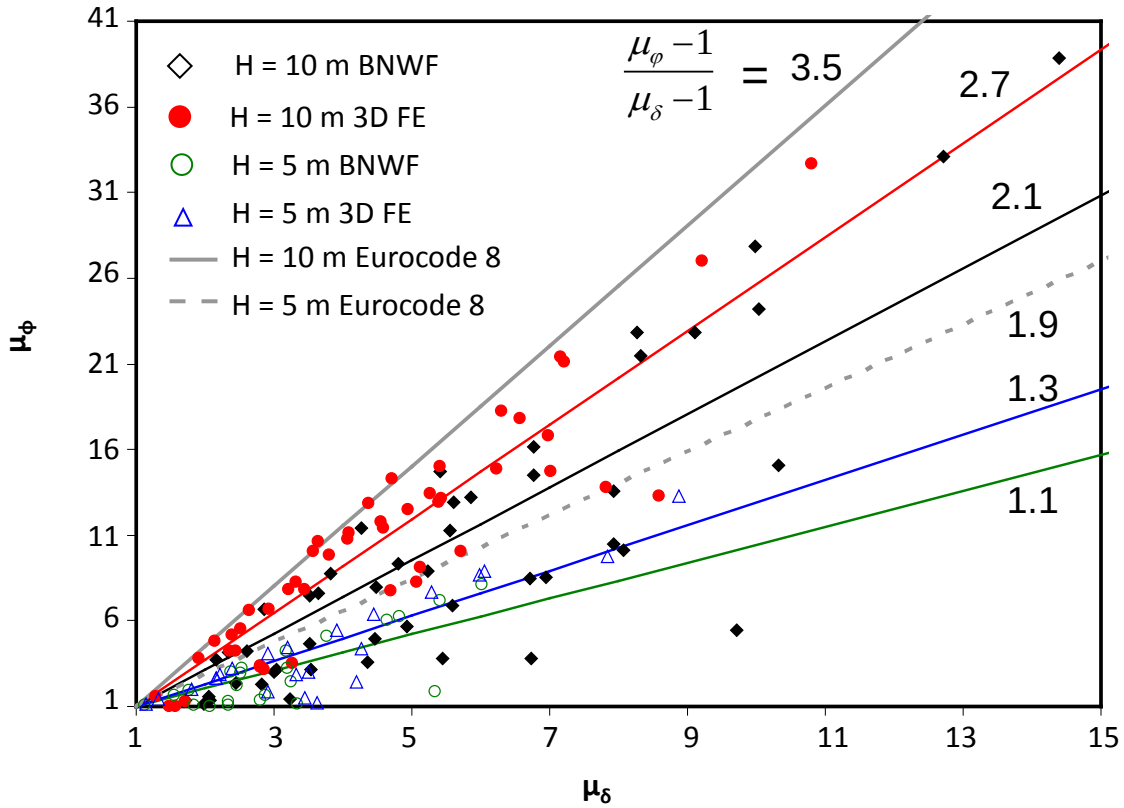

Figure 6.50: Correlation of local and global ductility demands for different pier heights

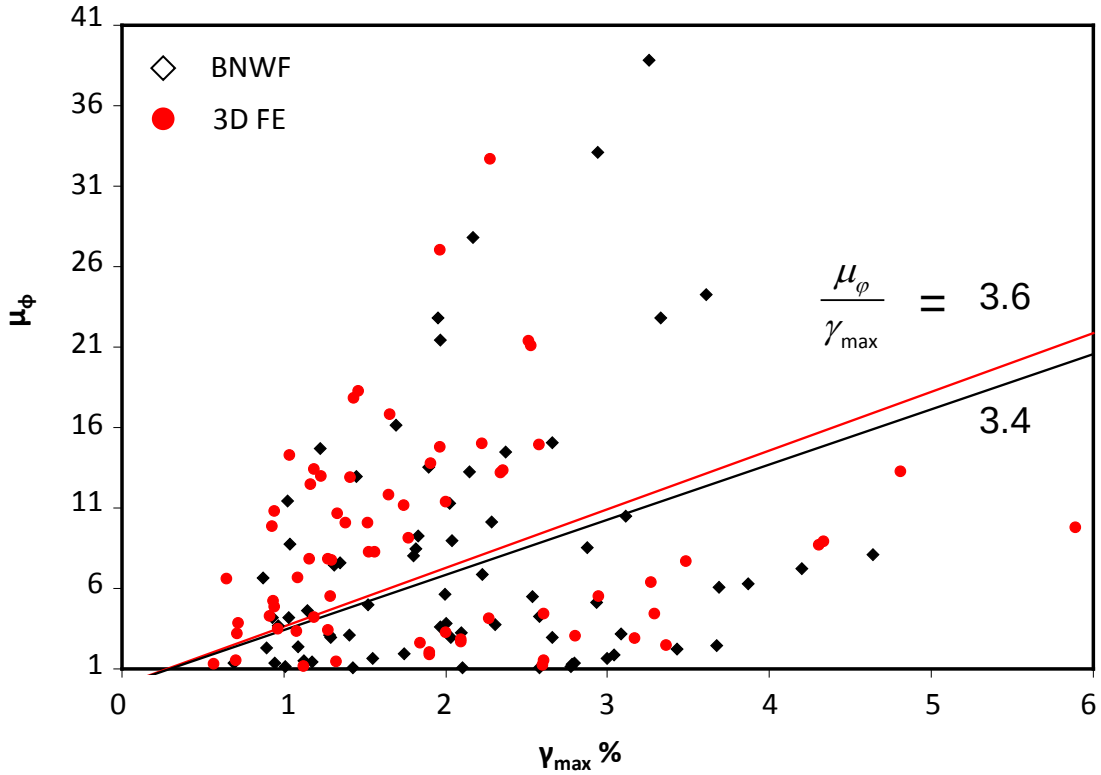

Figure 6.51: Correlation of local ductility demand and maximum drift ratio calculated with the 3D Finite Element Model and the Beam-on-nonlinear-Winkler-foundation Model

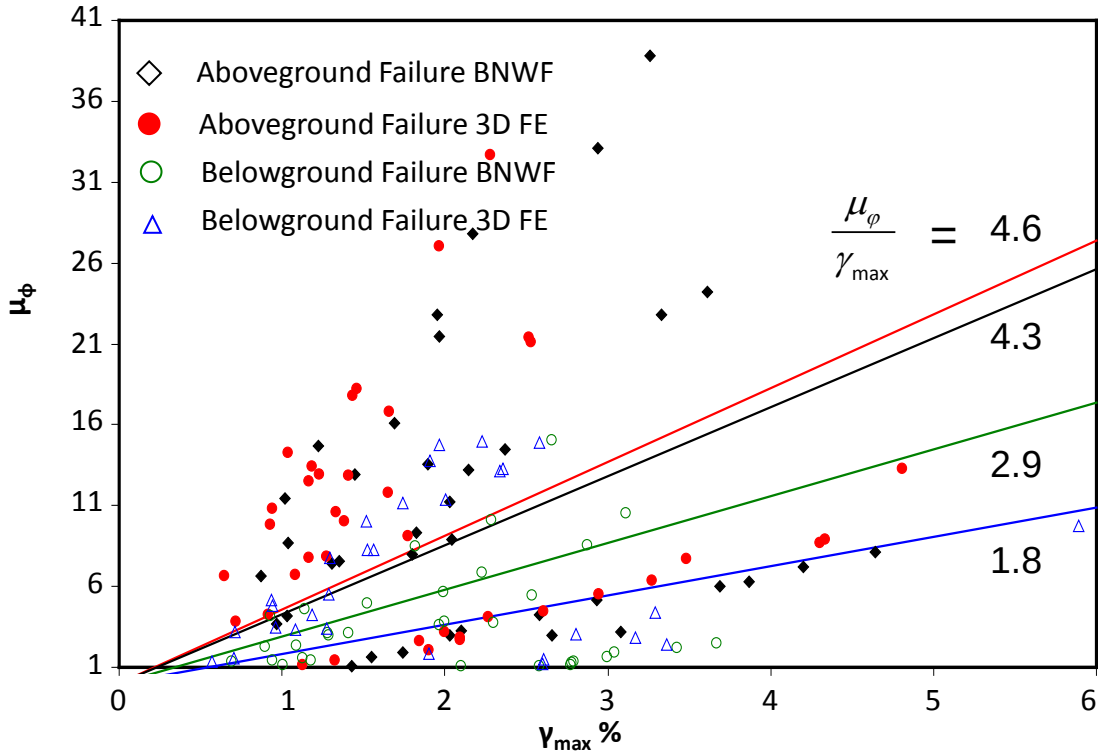

Figure 6.52: Correlation of local ductility demand and maximum drift ratio for different plastic hinge locations

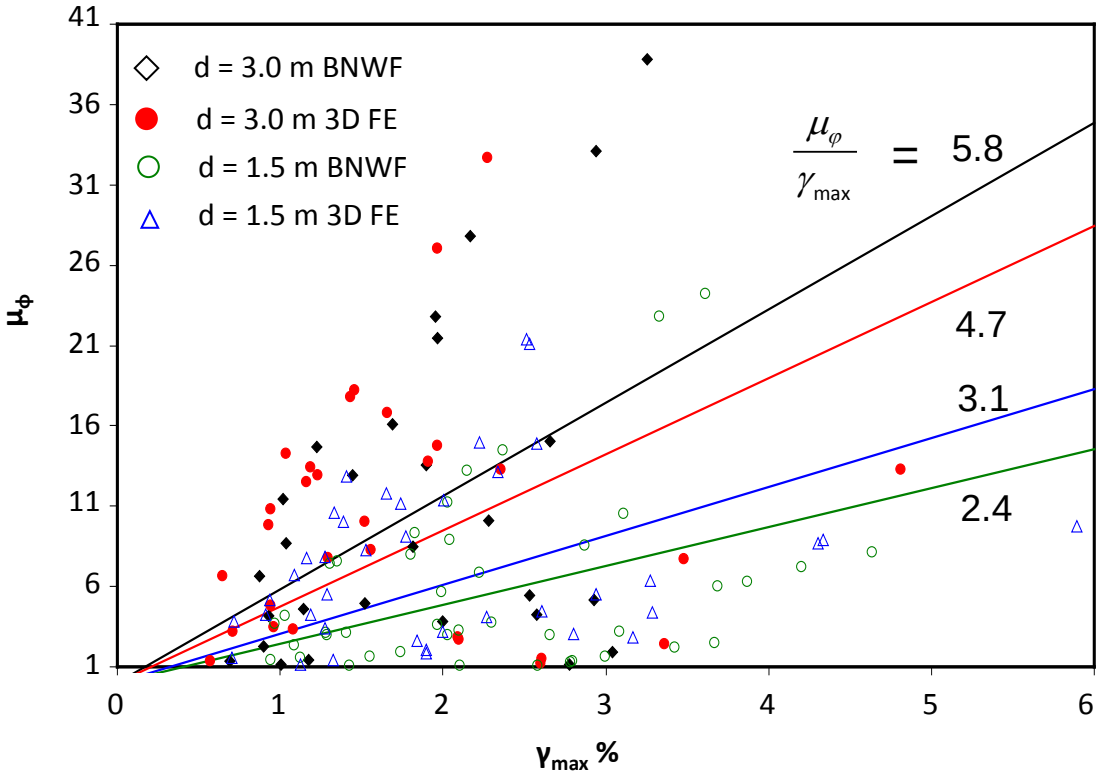

Figure 6.53: Correlation of local ductility demand and maximum drift ratio for different pier diameters

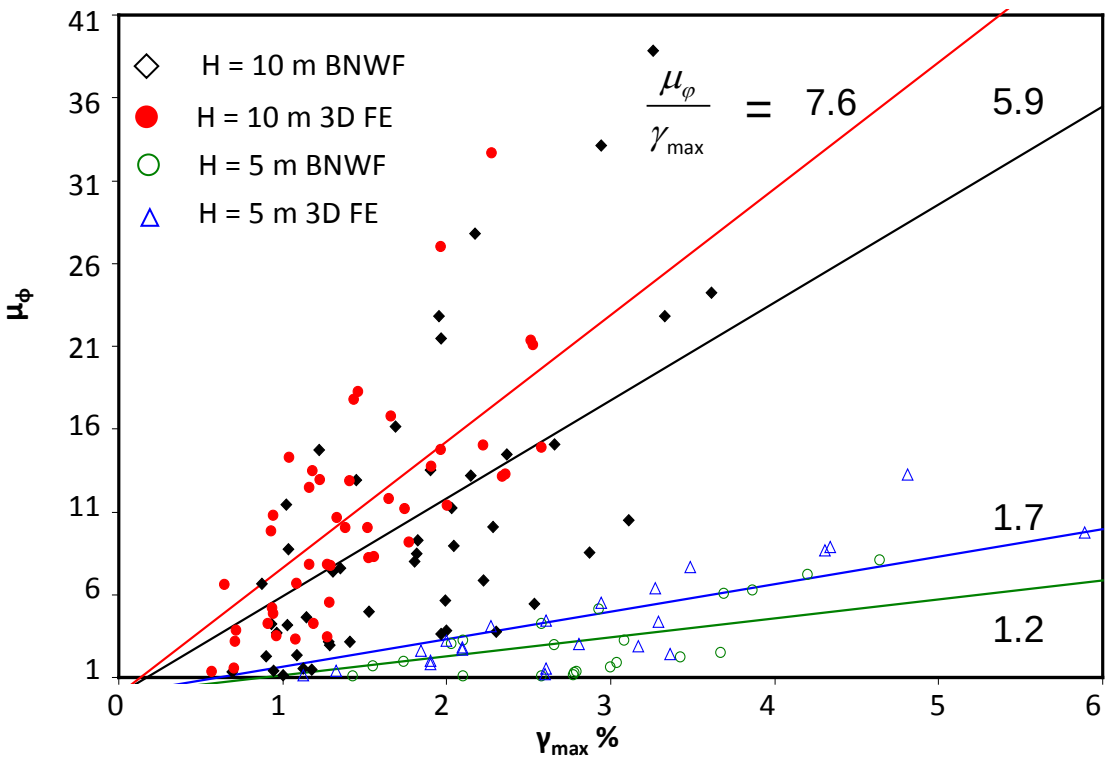

Figure 6.54: Correlation of local ductility demand and maximum drift ratio for different pier heights

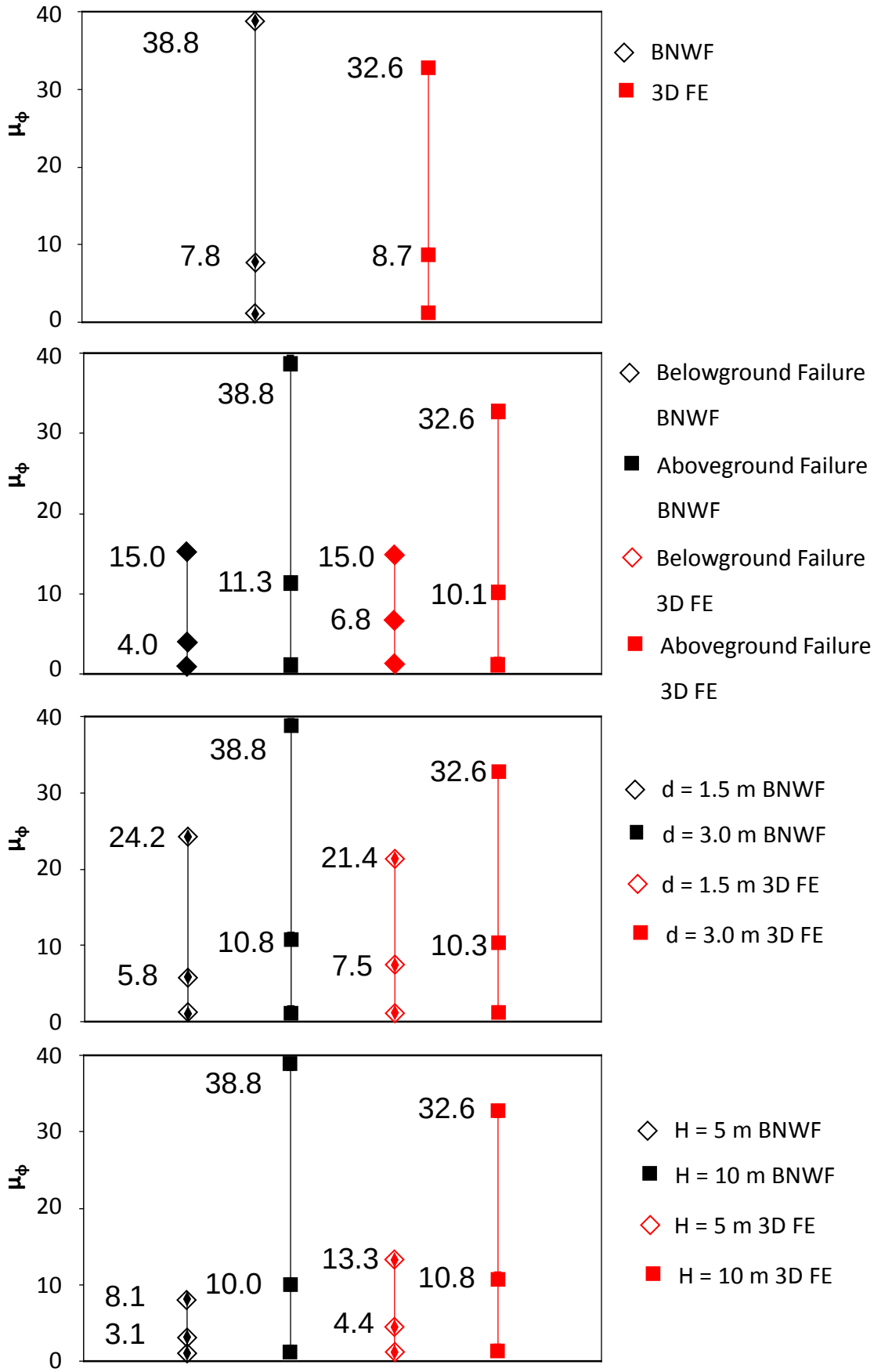

Figure 6.55: Variation of local curvature ductility demand μ_ϕ for different parameters examined

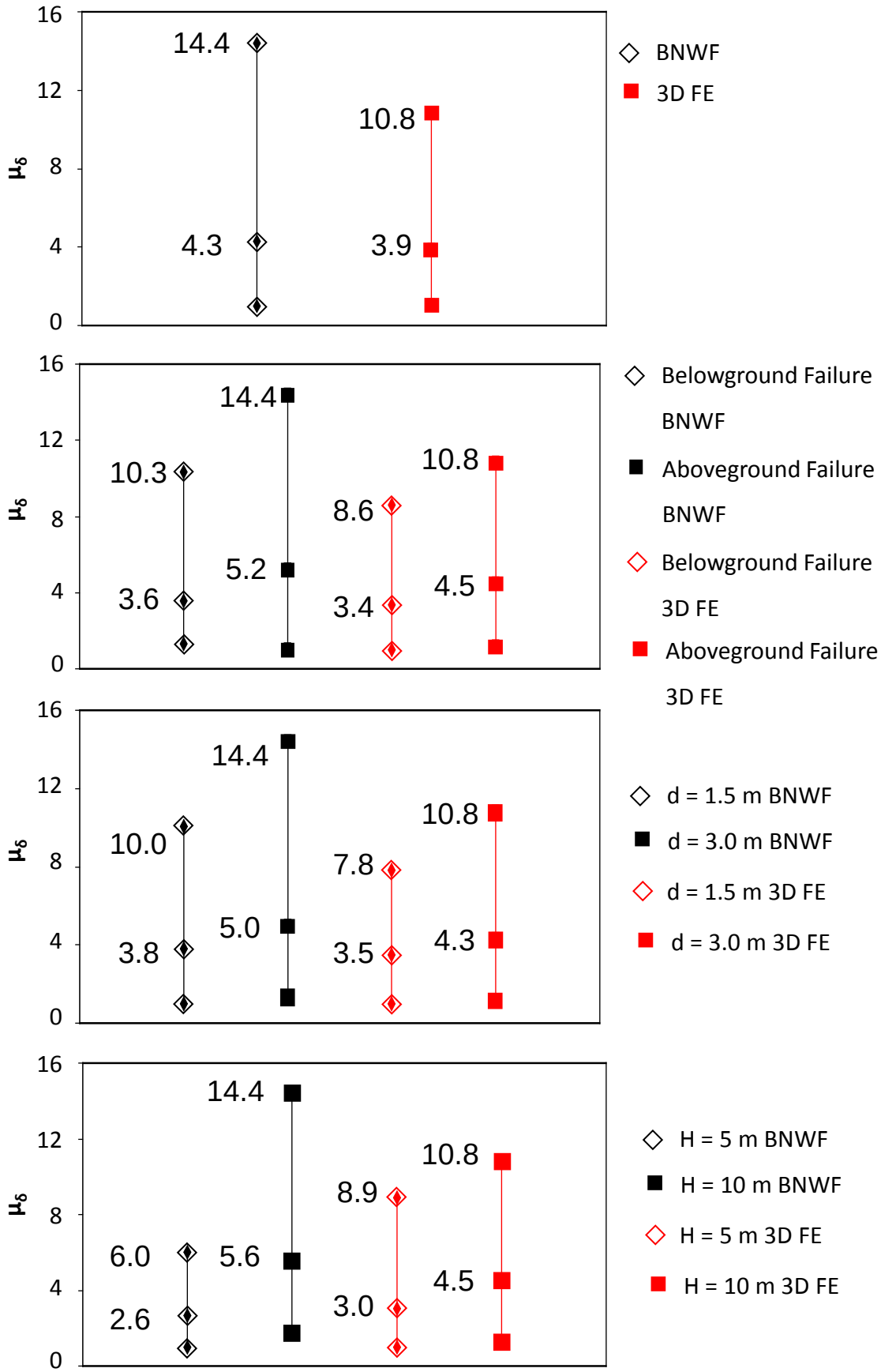

Figure 6.56: Variation of global displacement ductility demand μ_δ for different parameters examined

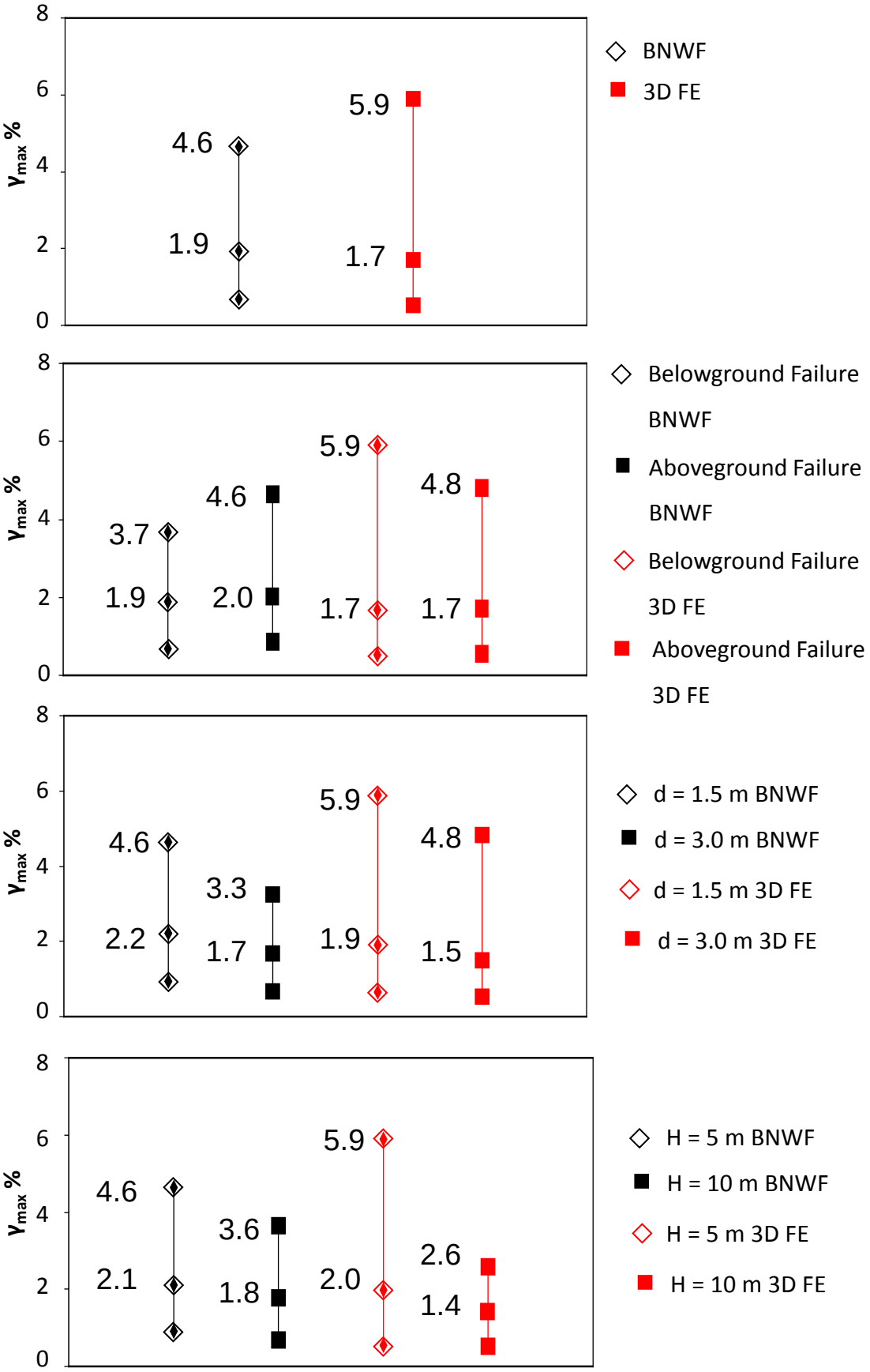

Figure 6.57: Variation of maximum drift ratio (γ_{max} %) for different parameters examined

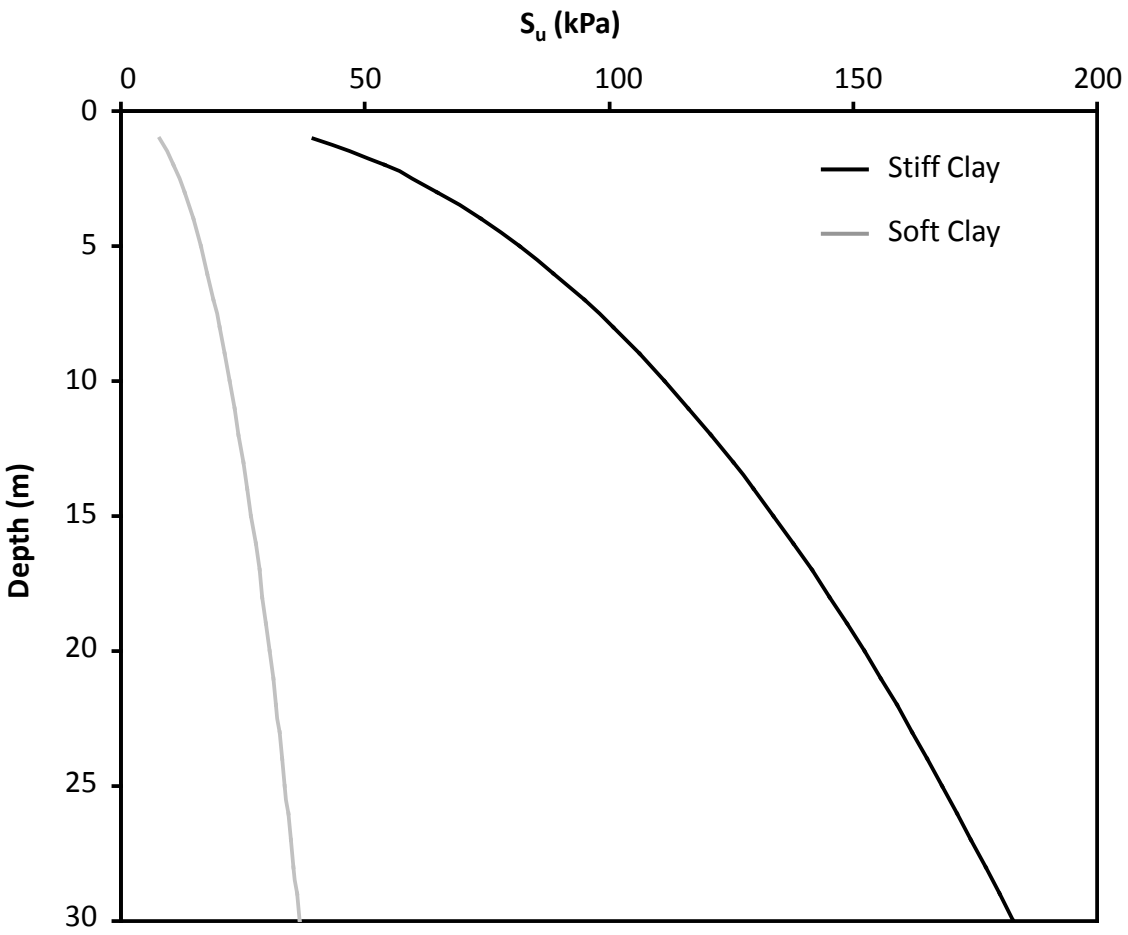

Figure 6.58: Undrained shear strength distribution of the stiff and soft clay deposit examined.

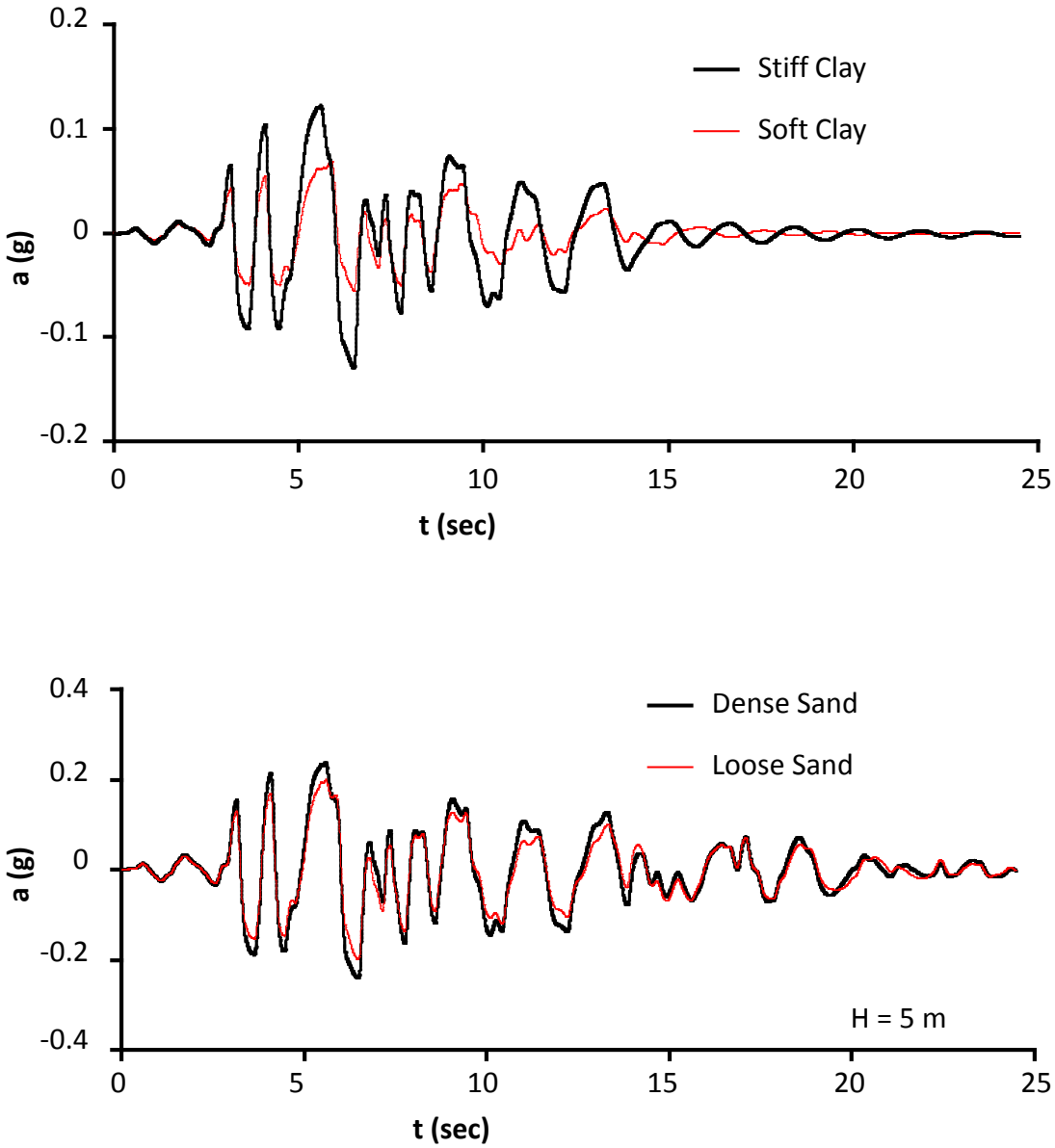

Figure 6.59: Acceleration time histories at the deck for pile-columns with diameter d = 3 m and aboveground height H = 5 m for different soil profiles (excitation at ground surface: JMA 1995 scaled at a_g = 0.8 g)

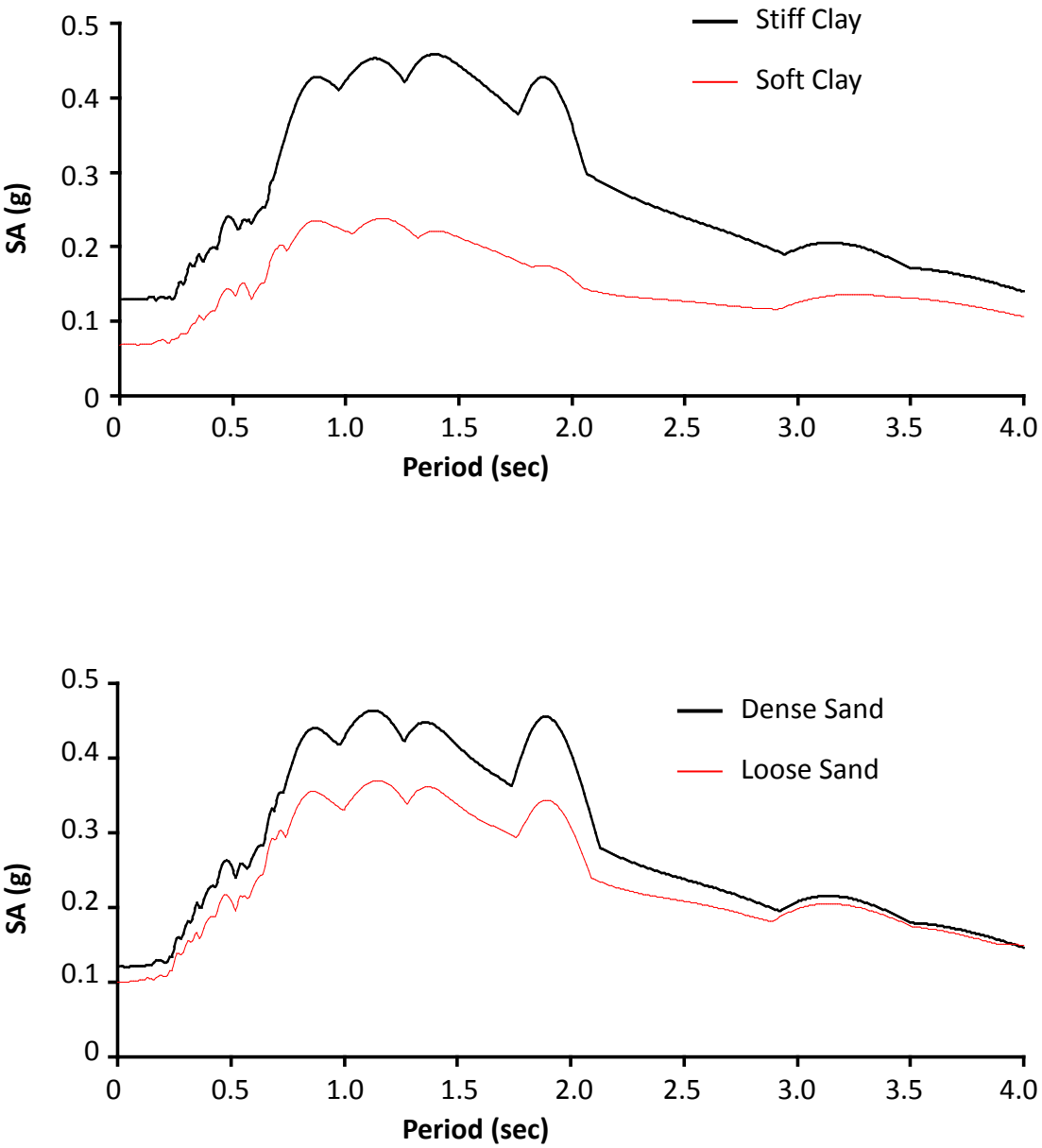

Figure 6.60: Response spectra at the deck (ξ = 5%) for pile-columns with diameter d = 3 m and aboveground height H = 5 m for different soil profiles

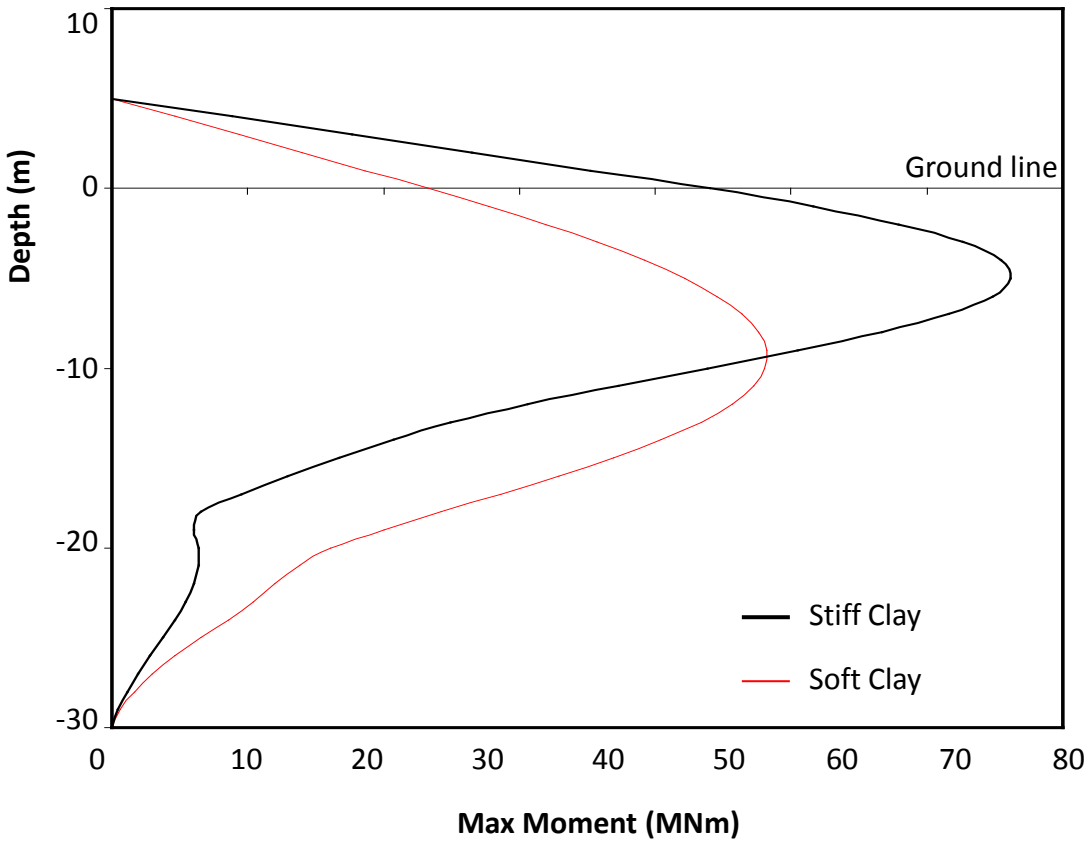

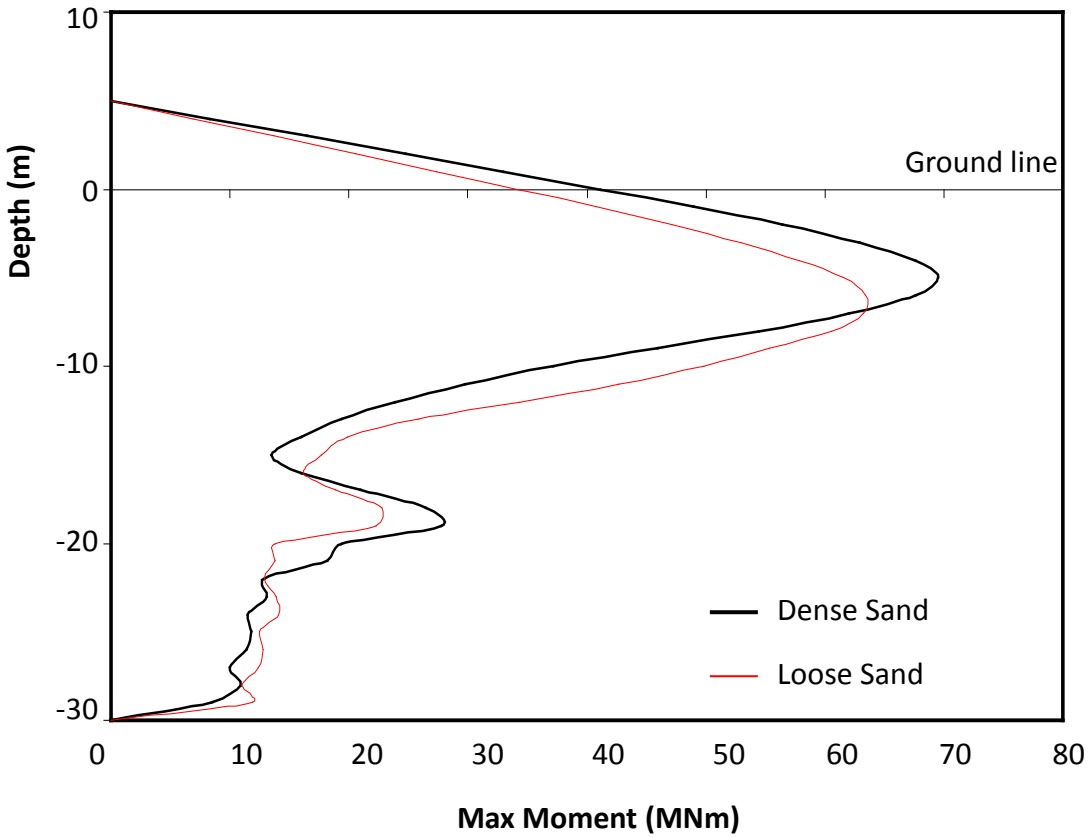

Figure 6.61: Maximum bending moment distributions for pile-columns with diameter d = 3 m and aboveground height H = 5 m for different soil profiles (excitation at ground surface: JMA 1995 scaled at a_g = 0.8 g)

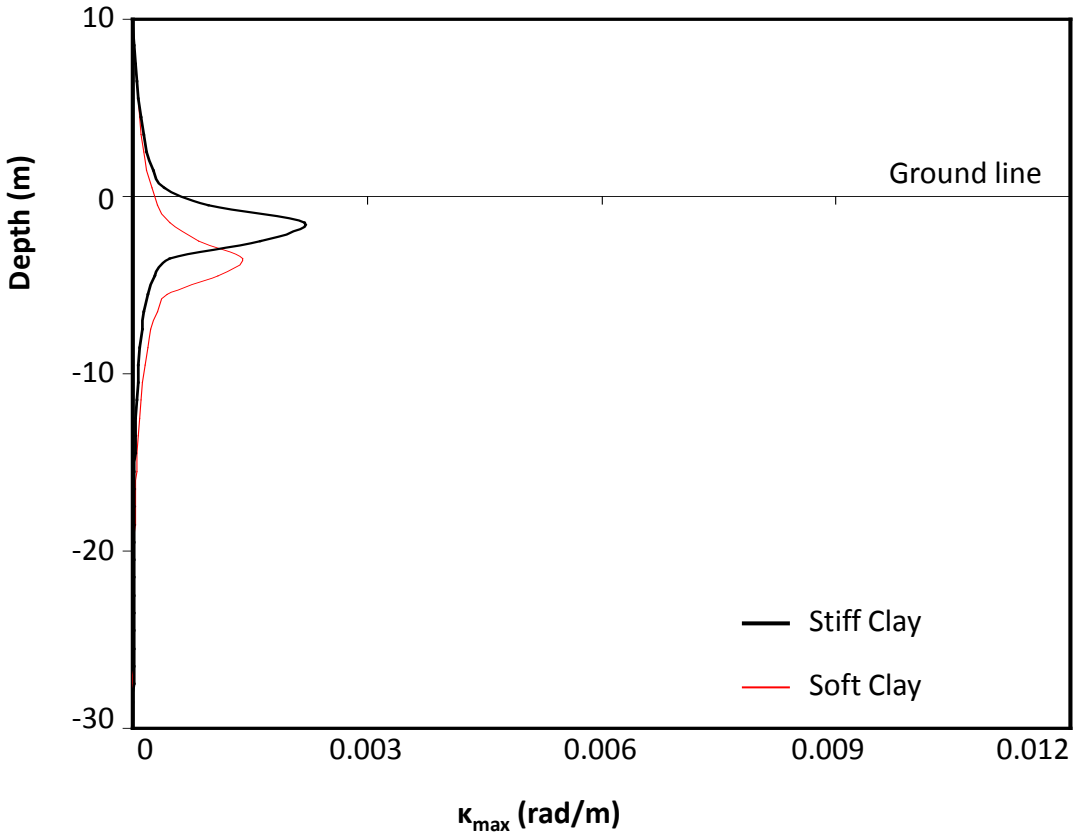

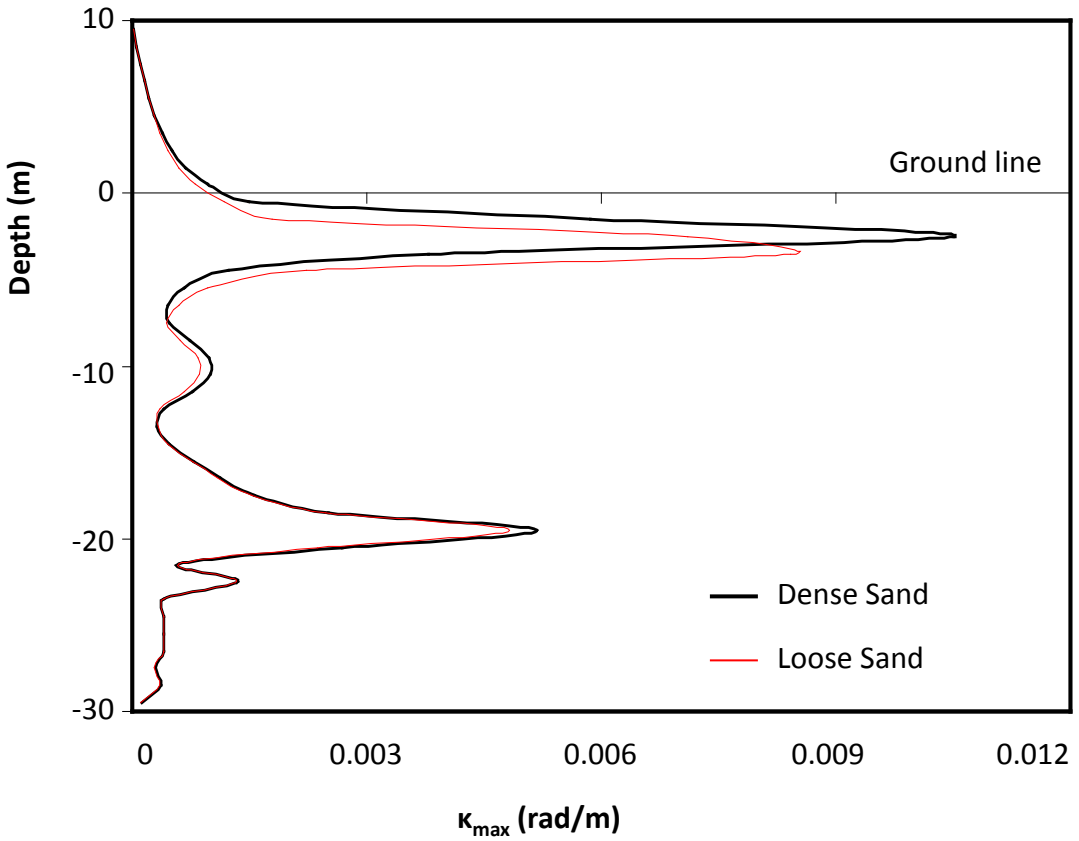

Figure 6.62: Maximum curvature distributions for pile-columns with diameter d = 3 m and aboveground height H = 10 m for different soil profiles (excitation at ground surface: JMA 1995 scaled at a_g = 0.8 g)

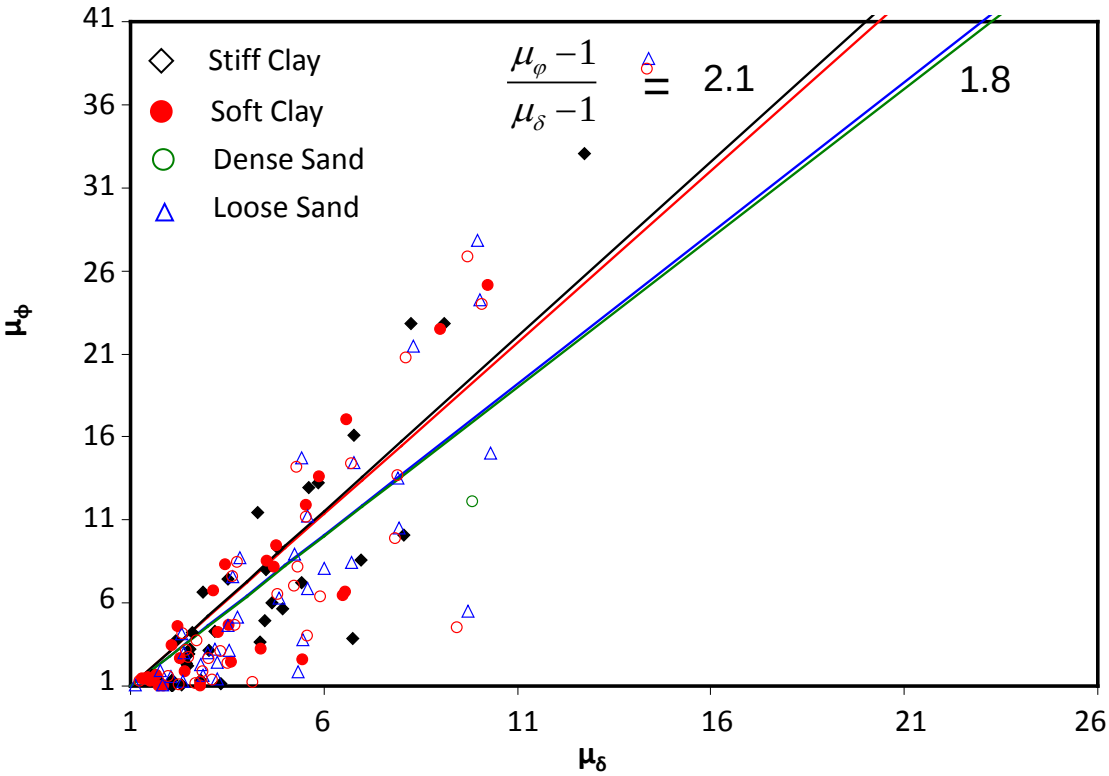

Figure 6.63: Correlation of local and global ductility demands for different soil types

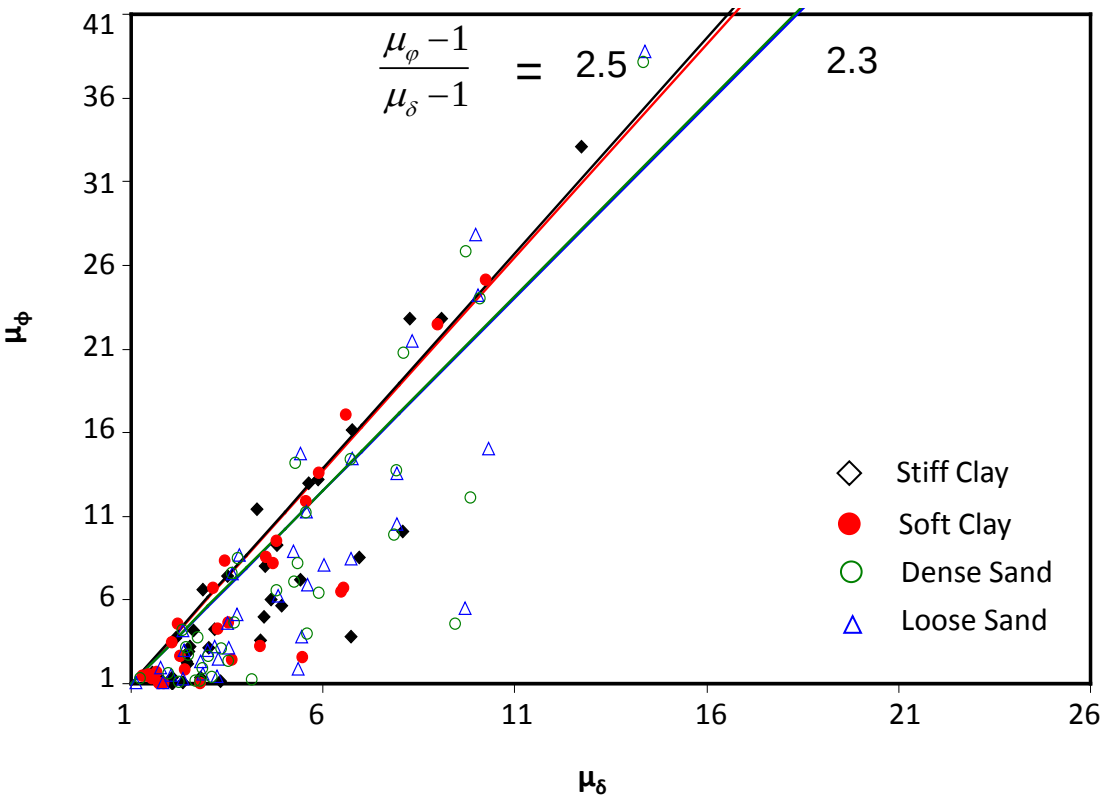

Figure 6.64: Correlation of local and global ductility demands for different soil types for aboveground failure

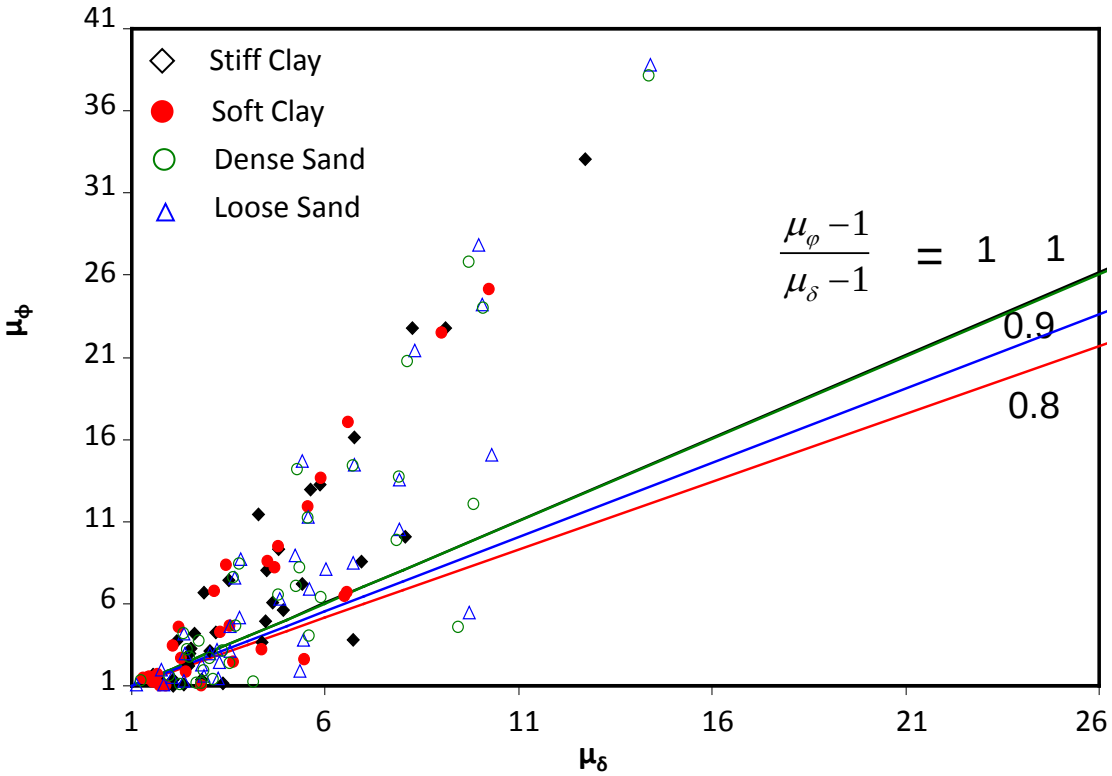

Figure 6.65: Correlation of local and global ductility demands for different soil types for belowground failure

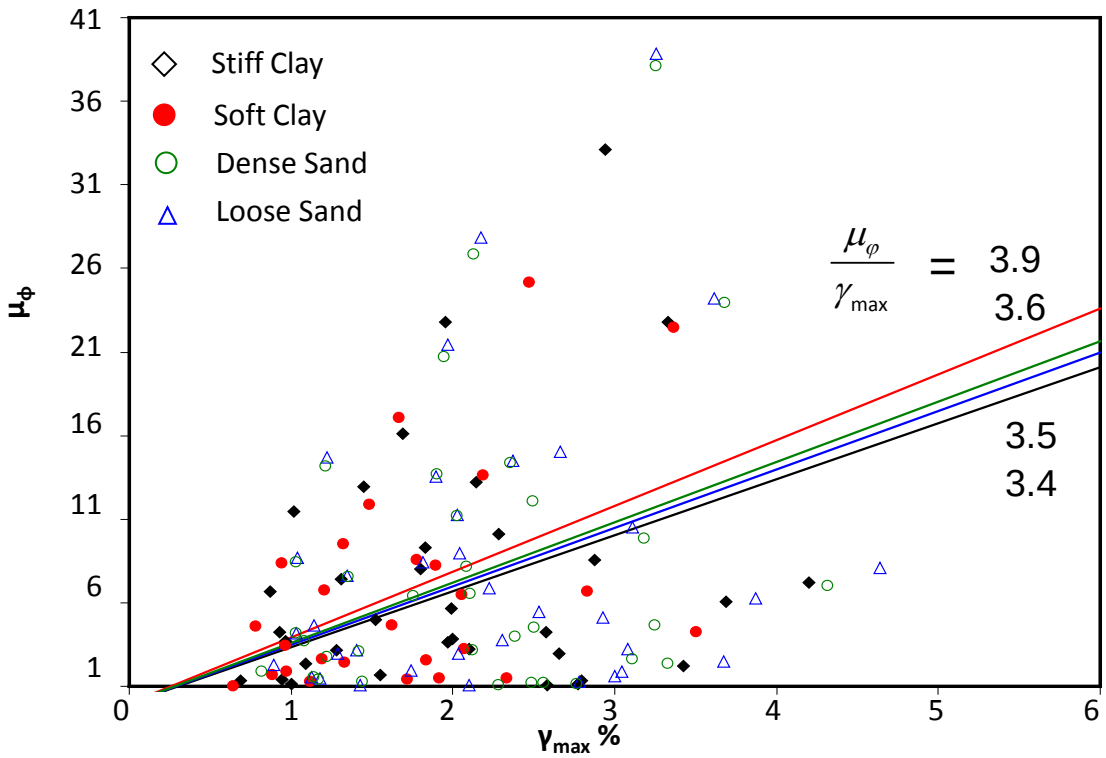

Figure 6.66: Correlation of local ductility demand and maximum drift ratio for different soil types

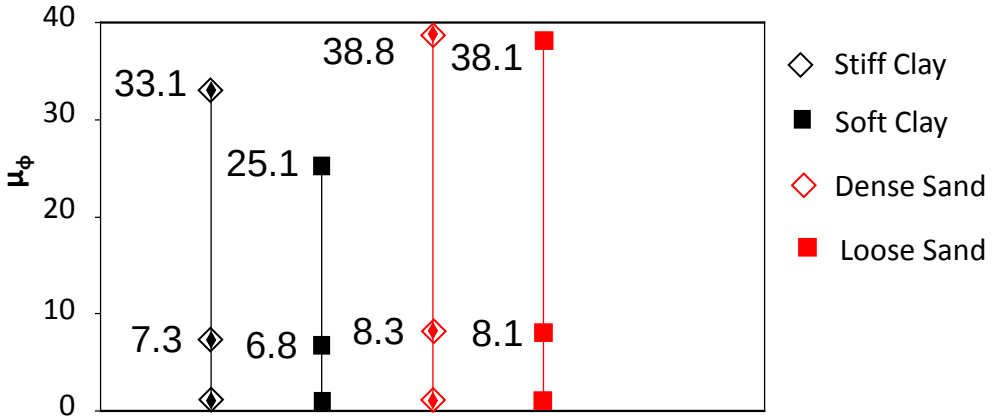

Figure 6.67: Variation of local curvature ductility demand μ_ϕ for different soil types

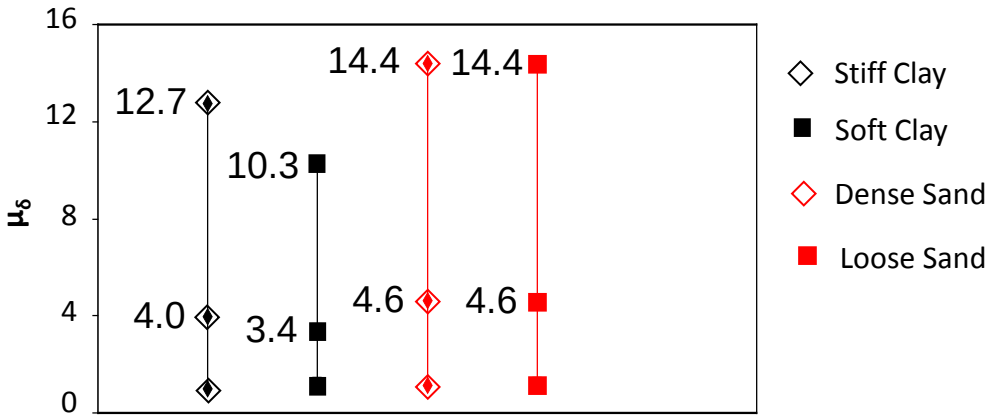

Figure 6.68: Variation of global displacement ductility demand μ_δ for different soil types

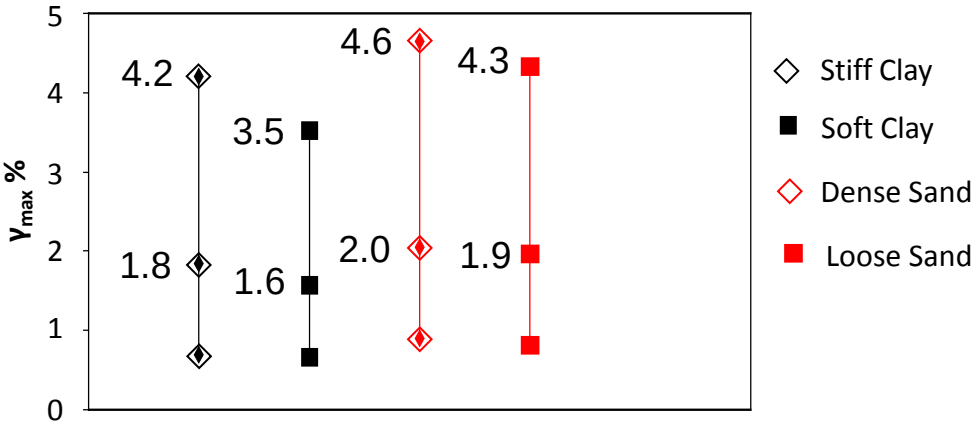

Figure 6.69: Variation of maximum drift ratio (γ_{max} %) for different soil types

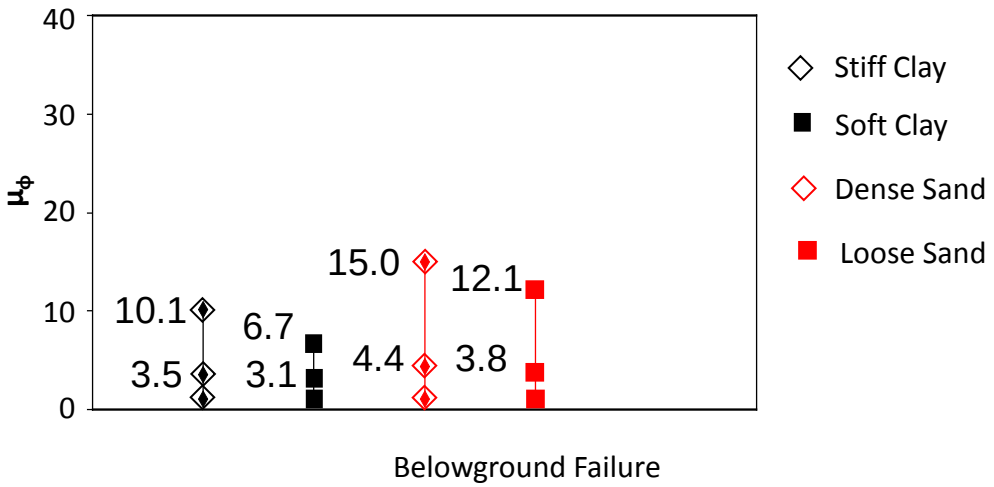

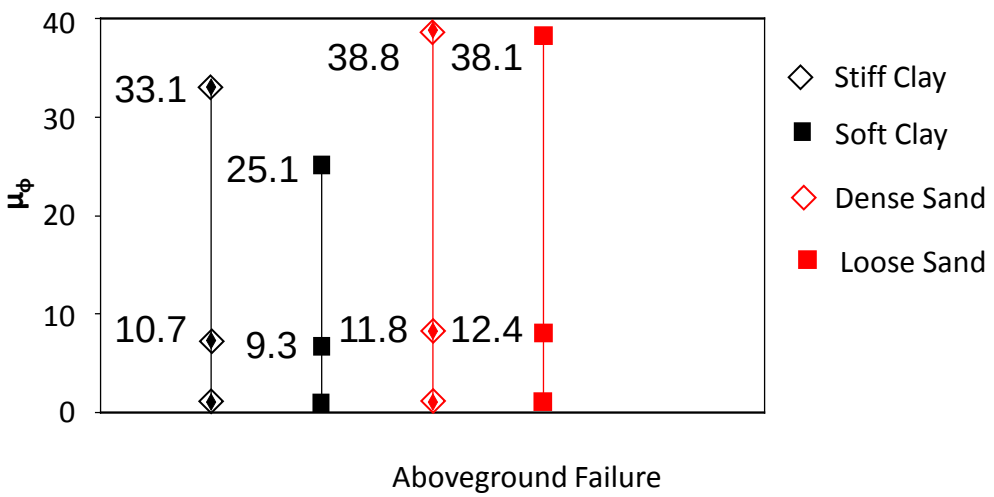

Figure 6.70: Variation of local curvature ductility demand μ_ϕ for different soil types for (a) belowground, and (b) aboveground failure

LIST OF REFERENCES

Achmus M., Kuo Y., Abdel-Rahman K., 2009, “Behavior of monopile foundations under cyclic lateral load”, *Computers and Geotechnics*, 36, pp 725-735

Allotey N., El Naggar M.H., 2008, “Generalized dynamic Winkler model for nonlinear soil-structure interaction analysis”, *Canadian Geotechnical Journal*, 45, pp 560-573

Alloptey N, El Naggar M.H., 2008, “A numerical study into lateral cyclic nonlinear soil-pile response”, *Canadian Geotechnical Journal*, 45 (9), pp 1268-1281

American Petroleum Institute (API), 2000, Recommended practice for planning, designing and constructing fixed offshore platforms-working stress design, *API Recommended Practice 2A-WSD (RP 2A-WSD)*, 21st edn

Anastasopoulos I., Gazetas G., Loli M., Apostolou M., Gerolymos N., 2010, “Soil failure can be used for seismic protection of structures”, *BEE*, 8, pp 309-326

Anastasopoulos, I., Georgarakos, P., Georgiannou, V., Drosos, V., Kourkoulis, R., 2010, "Seismic performance of bar-mat reinforced-soil retaining wall: Shaking table testing versus numerical analysis with modified kinematic hardening constitutive model", *Soil Dynamics and Earthquake Engineering*, 30, pp 1089–1105

Anthes R.J., 1997, “Modified rainflow counting keeping the load sequence”, *International Journal of Fatigue*, 19, pp 529-535

Apostolou M., Gazetas G., Garini E., 2007, “Seismic response of slender rigid structures with foundation uplifting”, *Soil Dynamics and Earthquake Engineering*, 27(7), pp 642-654

Ashour M., Norris G., 2000, “Modeling lateral soil-pile response based on soil-pile interaction”, *Journal of Geotechnical and Geoenvironmental Engineering*, 126 (5), pp 420-428

ASTM D3966 – 07, *Standard Test Methods for Deep Foundations under Lateral Load*

Badoni D., Makris N., 1996, “Nonlinear response of single piles under lateral inertial and seismic loads”, *Soil Dynamics and Earthquake Engineering*, 15, pp 29-43

Basu D., Salgado R., 2007, “Elastic analysis of laterally loaded pile in multi-layered soil”, *Geomechanics and Geoengineering: An International Journal*, 2 (3), pp 183-196

Bentley K., El Naggar M.H, 2000, “Numerical analysis of kinematic response of single piles”, *Canadian Geotechnical Journal*, 37, pp 1368-1382

Bolton M.D., 1986, “The strength and dilatency of sands”, *Geotechnique*, 36 (2), pp 65-78

Bouc R., 1971, “Modele mathematique d’ hysterisis”, *Acustica*, 21, pp 16-25

Boulanger, R., Curras, C., Kutter, B., Wilson, D., Abghari, A., 1999, ”Seismic soil-pile-structure interaction experiments and analyses”, *Journal of Geotechnical and Geoenvironmental Engineering*, 125 (9), pp 750–759

Bourgeois E., Rakotonindriana M.H.J., Le Kouby A., Mestat P., Serratrice J.F., 2010, “Three-dimensional numerical modeling of the behaviour of a pile subjected to cyclic lateral loading”, *Computers and Geotechnics*, Vol. 37, pp 999-1007

Bransby M.F., Randolph M.F., 1998, “Combined loading of skirted foundations”, *Geotechnique*, 48 (5), pp 637-655

Bransby M.F., Randolph M.F., 1999, “The effect of skirted foundation shape on response to combined V-M-H loadings”, *International Journal of Offshore and Polar Engineering*, 9 (3), pp 214-218

Bransby M.F., Randolph M.F., 1999, “The effects of embedment on the undrained response of caisson foundations to combined loadings”, *Soils and Foundations*, 39 (4), pp 19-34

Broms B., 1964, “Lateral resistance of piles in cohesive soils”, *Journal of Soil Mechanics and Foundation Division*, ASCE, 90 (2), pp 27-63

Broms B., 1964, “Lateral resistance of piles in cohesionless soils”, *Journal of Soil Mechanics and Foundation Division*, ASCE, 90 (3), pp 123-156

Broms B., 1965, “Design of laterally loaded piles”, *Journal of Soil Mechanics and Foundation Division*, ASCE, 91 (3), pp 77-99

Brown D.A, Reese L.C., O’Neill M.W., 1987, “Cyclic Lateral Loading of a large-scale pile group”, *Journal of Geotechnical Engineering*, 113 (11), pp 1326-1343

Brown D.A., Shie C., 1990, “Three dimensional finite element model of laterally loaded piles”, *Computers and Geotechnics*, 10, pp 59-79

Budek A.M., Priestley M.J.N., Benzoni G., 2000, “Inelastic seismic response of bridge drilled-shaft rc pile/columns”, Journal of Structural Engineering, 126 (4), pp 510-517

Budhu M., Davies, T., 1987, ”Nonlinear analysis of laterally loaded piles in cohesionless soils”, *Canadian Geotechnical Journal*, 24 (2), pp 289–296

Budhu M., Davies, T., 1988, ”Analysis of laterally loaded piles in soft clays”, *Journal of Geotechnical Engineering*, 114 (1), pp 21–39

Butterfield R., Gottardi G., 1994, “A complete three dimensional failure envelope for shallow footings on sand”, *Geotechnique*, 44 (1), pp 181–184

Butterfield R., Houlsby G.T., Gottardi G., 1997, “Standardized sign conventions and notations for generally loaded foundations”, *Geotechnique*, 47 (4), pp. 1051–1054

Cassidy M.J., Byrne B.W., Randolph M.F., 2004, “A comparison of the combined load behavior of spudcan and caisson foundations on soft normally consolidated clay”, *Geotechnique*, 54 (2), pp 91-106

CEN, “Eurocode 8: Design of structures for earthquake resistance. Part 2: Bridges”, Final Draft prEN 1998-2, Brussels, Belgium: European Committee for Standardization, 2005

Chatzigogos CT, Pecker A, Salençon J., 2007, “Seismic bearing capacity of a circular footing on a heterogeneous cohesive soil”, *Soils and Foundations*, 47 (4), pp. 783-797

Chatzigogos C.T., Pecker A., Salencon J., 2009, “Macroelement modeling of shallow foundations”, *Soil Dynamics and Earthquake Engineering*, 29 (6), pp 765-781

Chatzigogos CT, Figini R, Pecker A, Salençon J., 2011, “A macroelement formulation for shallow foundations on cohesive and frictional soils”, *International Journal for Numerical and Analytical Methods in Geomechanics*, 35, pp. 902–935

Chen W.F., Mizuno E., 1990, *Nonlinear Analysis in Soil Mechanics: Theory and Implementation*, Elsevier, New York

Chenaf N., Chazelas J., Escoffier S., Pecker A., 2012, ”Independent experimental observations of kinematic and inertial soil–pile interactions”, *International Journal of Physical Modelling in Geotechnics*, 12 (1), pp 1-14

Cho Y., Bang S., 2002, “Inclined Loading Capacity of Suction Piles”, *Proceedings of the 12th International Offshore and Polar Engineering Conference*, Kitakyushu, Japan May 26-31, pp 827-832

Correia A.A., Pecker A, Kramer S.L., Pinho R., 2012, “A pile-head macro-element approach to seismic design of extended pile-shaft-supported bridges”, *Second International Conference on performance-based design in earthquake geotechnical engineering*, Taormina, Italy, pp. 862–873

Correia A.A., Pecker A., Kramer S.L., Pinho R., 2012, “Nonlinear pile-head macro-element model: SSI effects on seismic response of a monoshaft-supported bridge”,

Proceedings of the 15th World Conference on Earthquake Engineering, Lisbon, Portugal, September

Crémer C., Pecker A., Davenne L., 2001, "Cyclic macro-element for soil structure interaction - Material and geometrical nonlinearities", *Numerical Methods in Geomechanics*, 25, pp 1257 – 1284

Crémer C, Pecker A, Davenne L., 2002, "Modelling of non-linear dynamic behaviour of a strip foundation with macroelement", *Journal of Earthquake Engineering*, 6, pp 175 – 212

Crémer C., Figini R., Pecker A., Salençon J, 2011, "A macroelement formulation for shallow foundations on cohesive and frictional soils", *International Journal for Numerical and Analytical Methods in Geomechanics*, 35, pp 902-931

Cubrinovski, M., Kokusho, T., Ishihara, K., 2006, "Interpretation from large-scale shake table tests on piles undergoing lateral spreading in liquefied soils*", Soil Dynamics and Earthquake Engineering*, 26 (2-4), pp. 275-286

Curras C.J., Boulanger R.W., Kutter B.L., Wilson D.W., 2001, "Dynamic experiments and analyses of a pile-group-supported structure", *Journal of Geotechnical and Geoenvironmental Engineering*, 127 (7), pp. 585–596

Dassault Systèmes Simulia Corp, 2009, *ABAQUS User's Manual, Providence*, RI, USA

Dawson T.H., 1980, "Simplified analysis of offshore piles under cyclic lateral loads", *Ocean Engineering*, Vol 7., pp 553-562

De Simone P., 2012, "Head embedment in Broms pile lateral capacity theory for cohesionless soils", *Computers and Geotechnics*, 43, pp 51-60

Di Laora R., Mandolini A., Mylonakis G., 2012, "Insight on kinematic bending of flexible piles in layered soil", *Soil Dynamics and Earthquake Engineering*, 43, pp 309–322.

Di Prisco C, Nova R, Sibilia A., 2003, "Shallow footings under cyclic loading: experimental behaviour and constitutive modeling", *Geotechnical Analysis of Seismic Vulnerability of Historical Monuments*, Maugeri M, Nova R (eds), Pàtron: Bologna

Drosos V., 2007, "*Inelastic dynamic soil-structure interaction*", Doctoral Dissertation, National Technical University of Athens

Drosos, V., Georgarakos, T., Loli, M., Anastasopoulos, I., Zarzouras, O., Gazetas, G., 2012, "Soil-Foundation-Structure interaction with mobilization of bearing capacity:

Experimental study on sand", *Journal of Geotechnical and Geoenvironmental Engineering*, 138 (11), pp 1369–1386

Duncan J., Evans L., Ooi P., 1994, "Lateral load analysis of single piles and drilled shafts", *Journal of Geotechnical Engineering*, 120 (6), pp 1018–1033

El Naggar M.H., Novak M., 1996, "Nonlinear analysis for dynamic lateral pile response", *Journal of Soil Dynamics and Earthquake Engineering*, 14 (3), pp 141-157

El Naggar M.H., Bentley K.J., 2000, "Dynamic analysis for laterally loaded piles and dynamic p-y curves", *Canadian Geotechnical Journal*, 37, pp 1166-1183

Fan K., Gazetas G., Kaynia A., Kausel E., Ahmad, S., 1991, "Kinematic seismic response of single piles and pile groups", *Journal of Geotechnical Engineering*, 117 (12), pp 1860–1879

Figini R., Paolucci R., Chatzigogos C., 2011, "A macro-element model for non-linear soil-shallow foundation-structure interaction under seismic loads: theoretical development and experimental validation on large scale tests", *Earthquake Engineering and Structural Dynamics*, 41 (3), pp 475-493

Fleming W.G.K., Weltman A.J., Randolph M.F., Elson W. K., 1992, *Piling Engineering*, Surrey University Press, London

Garnier J., 2002, "Properties of soil samples used in centrifuge models", *Invited Keynote Lecture, International Conference on Physical Modelling in Geotechnics – ICPMG '02*, R. Phillips et al. (Eds), published by A.A. Balkema, Rotterdam, 1, pp 5-19

Gazetas G., 1984, "Seismic response of end-bearing single piles", *Soil Dynamics and Earthquake Engineering*, 3 (2), pp 82-93

Gazetas G., Dobry R., 1984, "Horizontal response of piles in layered soils", *Journal of Geotechnical Engineering*, 110 (1), pp 20-40

Gazetas G., 1991, "Foundation vibrations", *Foundation Engineering Handbook*, 2nd edition, editor Fang, H.Y., Van Nostrand Reinhold, New York, USA, pp 553-593

Georgiadis M., 1983, "Development of p-y curves for layered soils", *Proceedings of the Geotechnical Practice in Offshore Engineering*, ASCE, pp 536-545

Georgiadis K., Georgiadis M., 2010, "Undrained lateral pile response in sloping ground", *Journal of Geotechnical and Geoenvironmental Engineering*, 136 (11), pp 1489–1500

Gerolymos N., 2002, "*Constitutive model for the static and dynamic response of soil, soi-pile and soil-caissonl*", Doctoral Dissertation, National Technical University of Athens

Gerolymos N., Gazetas G., 2005, “Phenomenological model applied to inelastic response of soil-pile interaction systems”, *Soils and Foundations*, 45 (4), pp 119-132

Gerolymos N., Gazetas G., 2005, “Constitutive model for 1-D cyclic soil behavior applied to seismic analysis of layered deposits”, *Soils and Foundations*, 45 (3), pp 147-159

Gerolymos N., Gazetas G., Tazoh T., 2005, “Static and Dynamic Response of Yielding Pile in Nonlinear Soil”, *Proceedings of the 1st Greece-Japan Workshop: Seismic Design, Observation and Retrofit of Foundations*, Athens, pp 25-35

Gerolymos N., Gazetas G., 2006, “Static and Dynamic Response of Massive Caisson Foundations with Soil and Interface Nonlinearities–Validation and Results”, *Soil Dynamics and Earthquake Engineering*, 26 (5), pp. 377-394

Gerolymos N., Drosos V., Gazetas G., 2009, “Seismic response of single-column bent on pile: evidence of beneficial role of pile and soil inelasticity”, *BEE*, 7, pp 547-573

Gerolymos N., Escoffier S., Gazetas G., Garnier J., 2009, “Numerical Modeling of centrifuge cyclic lateral pile load experiments”, *Earthquake Engineering and Engineering Vibration*, 8, pp 61-76

Gerolymos N., Zafeirakos A., Souliotis C., 2012, “Lateral response of caisson foundations: a macroelement approach”, *Proceedings of the 15th World Conference on Earthquake Engineering*, Lisbon, Portugal, September

Gerolymos N., 2013, *Geotechnical Report for METKA S.A: Geotechnical calculation for pile lateral pushover test*, Al-Basra Power Plant Project, Iraq

Gottardi G., Houlsby G.T., Butterfield R., 1999, “Plastic response of circular footings on sand under general planar loading”, *Geotechnique*, 49 (4), pp. 453-469

Gourvenec S., 2004, “Bearing capacity under combined loading – a study of the effect of shear strength heterogeneity”, *9th Australian and New Zealand Conference on Geomechanics*, Auckland, New Zealand, pp 527-533

Gourvenec S., 2007, “Shape effects on the capacity of rectangular footings under general loading”, *Geotechnique*, 57 (8), pp 637-646

Grashuls A.J., Dieterman H.A., Zorn N.F., 1990, “Calculation of Cyclic Response of Laterally Loaded Piles”, *Computers and Geotechnics*, 10, pp 287-305

Green R.A., Olson S.M., Cox B.R., Rix G.J., Rathje E., Bachhuber J., French J., Lasley S., Martin N., 2011, “Geotechnical Aspects of Failures at Port-au-Prince Seaport during

the 12 January 2010 Haiti Earthquake", *Earthquake Spectra*, Vol. 27, No. S1, pp. S43-S65

Hansen J.B., 1961, "The ultimate resistance of rigid piles against transversal forces", *Bulletin* 12: 5-9, Danish Geotechnical Institute, Copenhagen, Denmark

Hardin B.O., 1978, "Nature of stress-strain behavior of soils", *Proceedings of the Specialty Conference on Earthquake Engineering and Soil Dynamics*", ASCE, 1, pp 3-90

Houlsby G.T., Cassidy M.J., 2002, "A plasticity model for the behaviour of footings on sand under combined loading", *Geotechnique*, 52 (2), pp 117-129

Hutchinson T.C., Chai Y.H., Boulanger R.W., Idriss I.M., 2004, "Inelastic seismic response of extended pile-shaft-supported bridge structures", *Earthquake Spectra*, 20 (4), pp 1057-1080

Hutchinson T.C., Chai Y.H., Boulanger R.W., 2005, "Simulation of full-scale cyclic lateral load tests on piles", *Journal of Geotechnical and Geoenvironmental Engineering*, Vol. 131, No. 9, pp 1172-1175

Idriss I.M.., Sun J.I., 1991, "SHAKE91: A computer program for conducting equivalent linear seismic response analyses of horizontally layered soil deposits", *Center for Geotechnical Modeling Report*, Department of Civil and Environmental Engineering, University of California, Davis

Ishibashi I., Zhang X., 1993, "Unified dynamic shear moduli and damping ratios of sand and clay", *Soils and Foundations*, Vol. 33 (1), pp 182-191

Jeremic B., Jie G., Preisig M., Tafazzoli N., 2009, "Time domain simulation of soil–foundation–structure interaction in non-uniform soils", *Earthquake Engineering and Structural Dynamics*, 38, pp 699-718

Kagawa T., Kraft L., 1980, "Seismic p-y response of flexible piles," *Journal of the Geotechnical Engineering Division*, 106 (8), pp 899-918

Kavvadas M., Gazetas G., 1993, "Kinematic seismic response and bending of free-head piles in layered soil", *Geotechnique*, 43 (2), pp 207–222

Kramer S.L., 1996, *Geotechnical Earthquake Engineering*, Prentice Hall, Upper Saddle River, NJ

Lambe, T.W., 1973, "Predictions in soil engineering", *Geotechnique*, 23 (2), pp 149-202

LeBlanc C., Houlsby G.T., Byrne B.W., 2010, "Response of stiff piles in sand to long-term cyclic lateral loading", *Geotechnique*, 60 (2), pp 79–90

Lemaitre J., Chaboche J., 1990, *Mechanics of Solid Materials*, Cambridge University Press

Lin S., Liao J., 1999, "Permanent strains of piles in sand due to cyclic lateral loads", *Journal of Geotechnical and Geoenvironmental Engineering*, Vol. 125, No 9., pp 798-802

Loli M., Anastasopoulos I., Gelagoti F., Kourkoulis R., Gazetas G., 2011, "Inelastic response of footings: Numerical analysis against experimental simulation", *Research Report*, Laboratory of Soil Mechanics, NTUA

Long J.H., Vanneste G., 1994, "Effects of cyclic lateral loads on piles in sand", *Journal of Geotechnical Engineering*, 120(1), pp 33-42

Maheshwari B.K., Truman K.Z., El Naggar M.H., Gould P.L., 2004, "Three-dimensional nonlinear analysis for seismic soil-pile-structure interaction", *Soil Dynamics and Earthquake Engineering*, 24, pp 343-356

Maiorano R.M.S., de Sanctis L., Aversa S., Mandolini A., 2009, "Kinematic response analysis of piled foundations under seismic excitations", *Canadian Geotechnical Journal*, 46 (5), pp 571–84

Makris N., Gazetas G., 1992, "Dynamic pile-soil-pile interaction. Part II: Lateral and seismic response", *Earthquake Engineering and Structural Dynamics*, 21, pp 145-162

Makris N., Roussos Y.S., 2000, "Rocking response of rigid blocks under near-source ground motions", *Geotechnique*, 50 (3), pp 243-262

Martin C.M., 1994, "*Physical and numerical modeling of offshore foundations under combined loads*", Doctoral Dissertation, University of Oxford

Martin C.M., Houlsby G.T., 2001, "Combined loading of spudcan foundations on clay: numerical modeling", *Geotechnique*, Vol 51 (8), pp 687-699

Martin C.M., Houlsby G.T., 2001, "Combined loading of spudcan foundations on clay: numerical modeling", *Geotechnique*, Vol 51 (8), pp 687-699

Martin C. M., Randolph M. F., 2006, "Upper-bound analysis of lateral pile capacity in cohesive soil", *Geotechnique*, 56 (2), pp 141–145

Matlock H., 1970, "Correlations for design of laterally loaded piles in soft clay", *Proceedings of the 2nd Annual Offshore Technology Conference*, Houston, Texas, pp 577-594

Matlock H., Foo S.H., Bryant L.L., 1978, ''Simulation of lateral pile behavior'', Proc Earthquake Engineering and Soil Dynamics, ASCE, New York, 600–619

Mazzoni S., McKenna F., Fenves G.L., 2005, “OpenSees command language manual”, The Regents of the University of California

Meyerhof G., 1995, “Behaviour of pile foundations under special loading conditions: 1994 R.M. Hardy keynote address”, *Canadian Geotechnical Journal*, Vol 32 (2), pp 204-222

Meyerhof G., Sastry V.V.R.N., 1985, “Bearing capacity of rigid piles under eccentric and inclined loads”, *Canadian Geotechnical Journal*, Vol 24 (3), pp 471-478

Mindlin D., 1936, “Force at a point in the interior of a semi-infinite solid”, *Physics*, 7, pp 195-202

Murff J.D., 1987, “Technical notes on practical applications, plastic collapse of long piles under inclined loading”, *International Journal for Numerical and Analytical Methods in Geomechanics*, Vol 11, pp 185-192

Murff J., Hamilton J., 1993, ”P-Ultimate for undrained analysis of laterally loaded piles” *Journal of Geotechnical Engineering*, 119 (1), pp 91–107

Mylonakis G., 1995, “Contributions to static and seismic analysis of piles and pile-supported bridge piers”, *Doctoral Dissertation*, New York, State University of New York at Buffalo

Mylonakis, G. and Gazetas, G. 1998, “Vertical Vibration and Distress of Piles and Pile Groups in Layered Soil”, *Soils and Foundations*, Vol. 38, No 1, pp. 1-14

Nikolaou S., Mylonakis G., Gazetas G., Tazoh T., 2001, “Kinematic pile bending during earthquakes: analysis and field measurements”, *Geotechnique*, 51 (5), pp 425-440

Nogami T., Otani J., Konagai K., Chen H., 1992, “Nonlinear soil-pile interaction model for dynamic lateral motion”, *Journal of Geotechnical Engineering*, 118 (1), pp 89-106

Nova R., Montrasio L., 1991, “Settlements of shallow foundations on sand”, *Geotechnique*, 41(2), pp. 243-256

Nova R., Montrasio L., 1997, “Settlements of shallow foundations on sand: Geometric effects”, *Geotechnique*, 47 (1), pp. 49-60

Novak M., 1974, “Dynamic stiffness and damping of piles”, *Canadian Geotechnical Journal*, 11, pp 574-598

O’Neil M.W., Murchison J.M., 1983, “An evaluation of p-y relationships in sands”, A report to the American Petroleum Institute, *PRAC 82-41-1*, University of Houston, Texas

Ooi P., Chang B., Wang S., 2004, ”Simplified lateral load analyses of fixed-head piles and pile groups”, *Journal of Geotechnical Engineering*, 130 (11), pp 1140–1151

Paolucci R., 1997, “Simplified evaluation of earthquake induced permanent displacements of shallow foundations”, *Journal of Earthquake Engineering*, 1, pp. 563–579

Paolucci R, Pecker A., 1997, “Seismic bearing capacity of shallow strip foundations on dry soils”, *Soils and Foundations*, 37(3), pp. 95-105

Papadopoulou M.C., Comodromos E.M., 2010, “On the response prediction of horizontally loaded fixed-head pile groups in sands”, *Computers and Geotechnics*, Vol. 37, Issue 7-8, pp 930-941

Pecker A., 1998, “Capacity design principles for shallow foundations in seismic areas”, P*roceedings of the 11th European Conference on Earthquake Engineering*, Paris

Pender M.J, 1995, *Aseismic Foundation Design Analysis*, Continuing Education Course, University of Auckland, New Zealand

Penzien J., Scheffy C., Parmelee R., 1964, “Seismic analysis of bridges on long piles”, *Journal Engineering Mechanics Division., ASCE*, Vol. 90 (3), pp. 223-254

Poulos H.G., 1971, “Behavior of laterally loaded piles: I - single piles”, *Journal of Soil Mechanics and Foundation Division*, *ASCE*, 97 (5), pp 711-731

Poulos H.G., Davis E.H., 1980, *Pile Foundation Analysis and Design*, John Wiley and Sons, New York

Poulos H.G., 1982, “Single pile response to cyclic lateral load”, *Journal of Geotechnical and Geoenvironmental Engineering*, Vol 108, pp 355-375

Pyke R., 1979, “Nonlinear soil models for irregular cyclic loadings”, *Journal of the Geotechnical Engineering Division*, *ASCE*, Vol 105, GMT6, pp 715-726

Randolph M.F., 1981, “The response of flexible piles to lateral loading”, *Geotechnique,* 31 (2), pp. 247-259

Randolph M., Houlsby G., 1984, “The limiting pressure on a circular pile loaded laterally in cohesive soil”, *Geotechnique,* 34 (4), pp. 613-623

Reese L.C., Cox W.R., Koop F.D., 1974, “Analysis of laterally loaded piles in sand”, *Proceedings of the VI Annual Offshore Technology Conference*, Houston, Texas, 2: 473-485

Reese L.C., Cox W.R., Koop F.D., 1975, “Field testing and analysis of laterally loaded piles in stiff clay”, *Proceedings of the VII Annual Offshore Technology Conference*, Houston, Texas, 2: 672-690

Reese L.C., Van Impe W.F., 2001, *Single Piles and Pile Groups under Lateral Loading*, A.A.Balkema, Rotterdam

Riks E., 1979, “An incremental approach to the solution of snapping and buckling problems”, *International Journal of Solids and Structures*, 15, pp 524-551

Rollins K., Lane J., Gerber T., 2005, ”Measured and Computed Lateral Response of a Pile Group in Sand”, *Journal of Geotechnical and Geoenvironmental Engineering*, 131 (1), pp 103–114

Rollins K.M., Olsen R.J., Egbert J.J., Jensen D.H., Olsen K.G., Garrett B.H., 2006, “Pile spacing effects on lateral pile group behavior: Load Tests”, *Journal of Geotechnical and Geoenvironmental Engineering*, Vol. 132, No. 10, pp 1262-1271

Rosquoët F., Garnier J., Thorel L., Canepa Y., 2004, “Horizontal cyclic loading of piles installed in sand : Study of the pile head displacement and maximum bending moment”, *Proceedings of the International Conference on Cyclic Behaviour of Soils and Liquefaction Phenomena*, Bochum, T. Triantafyllidis (Ed.), Taylor & Francis, pp 363-368

Rovithis E.N., Pitilakis K.D., Mylonakis G.E., 2009, “Seismic analysis of coupled soil-pile-structure systems leading to the definition of a pseudo-natural SSI frequency”, *Soil Dynamics and Earthquake Engineering*, 29, pp 1005–1015

Sa’don N.M., Pender M.J., Orense R.P., Abdul Karim A.R., 2009, “A macro-element for pile-head response to cyclic lateral loading”, *Proceedings of the 2009 NZSEE Conference*, Paper Number 47

Salençon J, Pecker A., 1995, “Ultimate bearing capacity of shallow foundations under inclined and eccentric loading. Part I: Purely cohesive soil”, *European Journal of Mechanics*, 14 (3), pp. 349-375

Salençon J, Pecker A., 1995, “Ultimate bearing capacity of shallow foundations under inclined and eccentric loading. Part II: Purely cohesive soil without tensile strength”, *European Journal of Mechanics*, 14 (3), pp. 377-396

Sastry V.V.R.N., Meyerhof G., 1990, “Behavior of flexible piles under inclined loads”, *Canadian Geotechnical Journal*, 27 (1), pp 19-28

SDC, 2010, *Seismic Design Criteria – Version 1.6*, California Department of Transportation (Caltrans), USA

Seed H.B., Idriss I.M., 1970, "Soil modulii and damping factors for dynamic response analysis", *Report No. UCB/EERC-70/10*, University of California, Berkeley

Stroud M.A., Butler F.G., 1975, "The standard penetration test and the engineering properties of glacial materials", *Proceedings of the Symposium on Engineering Properties of Glacial Materials*, Birmingham, pp 117-128

Sun K., 1994, "Laterally loaded piles in elastic media", *Journal of Geotechnical Engineering*, 120 (8), pp 1324-1344.

Tabesh A., Poulos H.G., 2001, "Pseudostatic Approach for Seismic Analysis of Single Piles", *Journal of Geotechnical and Geoenvironmental Engineering*, 127 (9), pp 757-765

Taiebat H.A., Carter J.P., 2000, "Numerical studies of the bearing capacity of shallow foundations on cohesive soil subjected to combined loading", *Geotechnique*, 50 (4), pp 409-418

Taiebat H.A., Carter J.P., 2010, "A failure surface for circular footings on cohesive soils", *Geotechnique*, 60 (4), pp 265-273

Tasiopoulou P., Smyrou, E., Bal, İ. E., Gazetas, G., Vintzileou, E., 2011, Geotechnical and Structural Field Observations from Christchurch, February 2011 Earthquake, in New Zealand, *Research Report*, National Technical University of Athens, Greece

Thavaraj T., Finn W.D.L., Wu G., 2010, "Seismic response analysis of pile foundations", *Geotechnical and Geological Engineering*, 28, pp 275-286

Ticof J., 1977, "Surface footings on sand under general planar loads", Doctoral Dissertation, Southampton University, Southampton, U.K.

Trochanis A., Bielak J., Christiano P., 1991, "Simplified Model for Analysis of One or Two Piles", *Journal of Geotechnical Engineering*, 117 (3), pp 448–466

Trochanis A., Bielak J., Christiano P., 1991, "Three-Dimensional Nonlinear Study of Piles", *Journal of Geotechnical Engineering*, 117 (3), pp 429–447

Tuladhar R., Maki T., Mutsuyoshi H., 2008, "Cyclic behavior of laterally loaded concrete piles embedded into cohesive soil", *Earthquake Engineering and Structural Dynamics*, 37, pp 43-59

Vlasov V.Z., Leontiev N.N., 1966, "Beams, plates and shells on elastic foundations", *NTIS Accession No. N67-14238*, Israel Program for Scientific Translations, Washington, D.C

Velez A., Gazetas G., Krishnan R., 1983, "Lateral dynamic response of constrained-head piles", *Journal of Geotechnical Engineering*, 109 (8), pp 1063–1081

Verdure L., Garnier J., Levacher D., 2003, "Lateral cyclic loading of single piles in sand", *International Journal of Physical Modelling in Geotechnics*, 3, pp17-28

Villalobos F., Ovando E., Mendoza M., Oróstegui P., 2011, "Damages observed in the 2010 Concepcion earthquake and related soil phenomena", *Proceedings of the 5th International Conference on Earthquake Geotechnical Engineering*, Santiago, Chile, 10-13 January

Wang S., Kutter B.L., Chacko J.M., Wilson D.W., Boulanger R.W., Abghari A., 1998, "Nonlinear seismic soil-pile-superstructure interaction", *Earthquake Spectra*, 14 (2), pp 377-396.

Wen Y., 1976, "Method for random vibration of hysteretic systems", *Journal of the Engineering Mechanics Division*, 102 (2), pp 249-264

Wu G., Finn W.D.L., 19971, "Dynamic elastic analysis of pile foundations using finite element method in the frequency domain", *Canadian Geotechnical Journal*, 34, pp 34-43

Wu G., Finn W.D.L., 1997b, "Dynamic nonlinear analysis of pile foundations using finite element method in the time domain", *Canadian Geotechnical Journal*, 34, pp 44-52

Yang Z., Jeremic B., 2002, "Numerical analysis of pile behavior under lateral loads in layered elastic-plastic soils", *International Journal for Numerical and Analytical Methods in Geomechanics*, 26, pp 1385-1406

Yang Z., Elgamal A., 2008, "Multi-surface Cyclic Plasticity Sand Model with Lode Angle Effect", *Geotechnical and Geological Engineering*, 26, pp 335-348

Zhang F., Kimura M., Nakai T., Hoshikawa T., 2000, "Mechanical behavior of pile foundations subjected to cyclic lateral loading up to the ultimate state", *Soils and Foundations*, 40 (5), pp 1-17

Zhang L.M., Ng C.W.W., Lee, 2004, "Effects of slope and sleeving on the behavior of laterally loaded piles", *Soils and Foundations*, 44 (4), pp 99-108